Computational Studies of the Stability of Carbon-based Fuel Cell Materials

Patniboon, Tipaporn

Publication date:
2022

Document Version
Publisher's PDF, also known as Version of record

Citation (APA):
Patniboon, T. (2022). *Computational Studies of the Stability of Carbon-based Fuel Cell Materials*. Technical University of Denmark.

TIPAPORN PATNIBOON

Computational Studies of the Stability of Carbon-based Fuel Cell Materials

Ph.D. Thesis
October 2022

Department of Energy Conversion and Storage
Technical University of Denmark

Computational Studies of the Stability of Carbon-based Fuel Cell Materials

Author
Tipaporn Patniboon
E-mail: tipapa@dtu.dk

Supervisors
Associate Professor Heine Anton Hansen
Department of Energy Conversion and Storage
Technical University of Denmark
E-mail: heih@dtu.dk

Professor Tejs Vegge
Department of Energy Conversion and Storage
Technical University of Denmark
E-mail: teve@dtu.dk

Department of Energy Conversion and Storage
Section for Atomic Scale Materials Modelling
Technical University of Denmark
Anker Engelunds Vej, Building 301
2800 Kgs. Lyngby
Denmark
www.energy.dtu.dk
E-mail: info@energy.dtu.dk

Abstract

With the increase in global pollution and electricity use, a clean energy sources and energy conversion technologies are needed. An attractive alternative is using a fuel cell to convert chemical energy into electrical energy. Still, a durability is a critical concern for fuel cell development. In this thesis, two degradation concerns related to the materials in the fuel cell are investigated by density functional theory (DFT).

Firstly, the stability of a single metal atom catalyst (M/N/C) is investigated. The M/N/C catalyst is a promising catalyst at the cathode of the fuel cell. However, under an acid condition of the fuel cell, it has poor stability. The thermodynamic model of the dissolution reaction for the M/N/C catalyst with various local carbon structures and metal atoms is investigated. The results reveal a significant role of both local carbon structure and the metal atom in the stability. The computational screening considering both activity and stability suggests the MN_4 site on the bulk graphene, and graphene edge with M = Fe, Co, and Ru as a stable catalyze in the acid condition. The adsorption of the anion in the electrolyte is then further included in the activity and stability calculations for the MN_4 site on bulk graphene and graphene edge. Under the ORR-related condition, the electrolyte anions compete with water on the single metal site, in some cases either poisoning or modifying the catalyst activity and thermodynamic stability. The catalytic activity and stability descriptor suggest promising electrolyte and metal atom combinations that result in an active and durable catalyst.

Finally, the alkaline stability of the polybenzimidazole molecule is investigated. The polybenzimidazole molecule is a promising material for anion exchange membranes in alkaline fuel cells, but the degradation at a higher KOH concentration limits its practical use. It is found that the polybenzimidazole molecule undergoes deprotonation, forming the ionized molecule in an alkaline solution. In highly alkaline conditions, the fully deprotonated molecule is dominant and unlikely to degrade. In contrast, the non- and partially deprotonated molecules can undergo degradation. The effective energy barrier depends on the KOH concentration and becomes lower as the concentration increases. Also, it is found that the barrier along the reaction pathway and the availability of the vulnerable species in the solution both can affect the degradation rate, suggesting a significant role of pK_a value in the degradation.

Résumé

Med stigningen i den globale forurening og elektricitetsforbrug er der behov for rene energikilder samt teknologi til energikonvertering. Et attraktivt alternativ er at bruge en brændselscelle til at omdanne kemisk energi til elektrisk energi. Durabiliteten er dog stadig et kritisk problem for udviklingen af brændselsceller. I denne afhandling undersøges to nedbrydningsproblemer relateret til materialerne i brændselsceller ved hjælp af tæthedsfunktionalteori (DFT).

Først undersøges stabiliteten af en single-metalatom katalysator (M/N/C). M/N/C-katalysatoren er en lovende katalysator ved brændselscellens katode. Under sure betingelser i brændselscellen har den dog dårlig stabilitet. Den termodynamiske model for opløsningsreaktionen for M/N/C-katalysatoren med forskellige lokale carbonstrukturer og metalatomer undersøges. Resultaterne afslører at både den lokale carbonstruktur og metalatomet spiller væsentlige roller i forhold til at afgøre stabiliteten. Den beregningsbaserede screening, der tager både aktivitet og stabilitet i betragtning, antyder at MN_4-sitet på bulk grafen og grafenkanten med M = Fe, Co og Ru er stabile katalysatorer under sure betingelser. Adsorption af anionen i elektrolytten er yderligere inkluderet i aktivitets- og stabilitetsberegningen for MN_4-sitet på bulk grafen og grafenkanten. Under ORR-relevante betingelser konkurrerer elektrolytanionerne med vand om single-metalsitet, hvilket i nogle tilfælde kan lede til enten blokering eller modificering af katalysatoraktiviteten og den termodynamiske stabilitet. Den katalytiske aktivitet- og- stabilitetsdeskriptor antyder lovende elektrolyt- og metalatomkombinationer, der resulterer i en aktiv og holdbar katalysator.

Til sidst undersøges den basiske stabilitet af polybenzimidazolmolekylet. Polybenzimidazol-molekylet er et lovende materiale til anion exchangemembraner i basiske brændselsceller, men nedbrydningen ved højere KOH-koncentration begrænser dets praktiske anvendelse. Det findes, at polybenzimidazol-molekylet gennemgår deprotonering og danner det ioniserede molekyle i basisk opløsning. Under stærkt basiske betingelser er det fuldt deprotonerede molekyle dominerende og vil sandsynligvis ikke nedbrydes. Derimod kan de ikke- og delvist deprotonerede molekyler undergå nedbrydning. Den effektive energibarriere afhænger af KOH-koncentrationen og bliver lavere, når koncentrationen stiger. Det findes endvidere, at barrieren langs reaktionsvejen og tilgængeligheden af de sårbare molekyler i opløsningen begge kan påvirke nedbrydningshastigheden, hvilket tyder på at pKa-værdien spiller en væsentlig rolle i nedbrydningen.

Preface

This thesis is submitted in candidacy for a Ph.D. from Technical University of Denmark (DTU). The work was conducted between October 2019 and October 2022 at the Section of Atomic Scale Modelling and Materials at the Department of energy conversion and storage. The studies have been supervised by Heine Anton Hansen and Tejs Vegge. The Ph.D. project was financially supported by the Ministry of Science and Technology, Royal Thai Government.

I am thankful for many people I met during my time at DTU. First and foremost, I would like to thank my supervisor, Heine Anton Hansen, for his continuous support and guidance. I am thankful for his patience in explaining things to me, and I appreciate all the help and advice he has given. I also would like to thank my co-supervisor, Tejs Vegge, for his suggestions and kindness over the past three years.

Many thanks to all current and past members of the Atomic Scale Materials Modelling (ASM) and Autonomous Materials Discovery (AMD) section. I would like to thank Changzhi Ai, Benjamin Heckscher Sjølin, Nis Fisker-Bødker, Smobin Vincent, and Williams Agyei Appiah for the positive working environments in the office. In addition, I am very thankful to Arghya Bhowmik and Peter Bjørn Jørgensen for their help and discussion. It was a pleasure to meet and work with Haobo Li during my virtually external stay at Fritz-Haber-Institut der Max-Planck-Gesellscha, Germany. I am grateful to David Aili, Dmytro Serhiichuk, and Yang Hu for their valuable discussion of experimental findings. Special thanks to Pernille Pedersen for her help translating the abstract to Danish. I would also like to thank Changzhi Ai, Benjamin Heckscher Sjølin, Surajit Nandi, Xueping Qin, Leonardo Evaristo de Sousa, Xin Yang, and Xiaotong Zhang for proofreading the thesis and providing valuable suggestions for improvements.

Last but not least, many thanks to my parents, sister, and friends for always supporting and encouraging me. I appreciate your time with me, hearing me out, and cheering me up.

Tipaporn Patniboon
October 2022

List of Publications

Publications included in this thesis

Paper I

Acid-Stable and Active M-N-C Catalysts for the Oxygen Reduction Reaction: The Role of Local Structure
Tipaporn Patniboon and Heine Anton Hansen
ACS Catalysis, 2021, 11, 21, 1310213118

Paper II

Effects of Electrolyte Anion Adsorption on the Activity and Stability of Single Atom Electrocatalysts
Tipaporn Patniboon and Heine Anton Hansen
In preparation

Paper III

Degradation of Polybenzimidazole in Alkaline Solution with First-principles Modeling
Tipaporn Patniboon and Heine Anton Hansen
Electrochimica Acta, 2021, 398, 139329,

Contents

Chapter 1

Introduction

1.1 Fuel Cell Technology

Growing concerns about global pollution and increasing electricity use drive us to find less polluting energy sources and clean energy conversion technology. An attractive alternative is a conversion of chemical energy into electrical energy. A fuel cell is an electrochemical device that can convert the chemical energy of H_2 into electricity [1]. Among the different types of fuel cells, a proton exchange membrane fuel cell (PEMFC) and anion exchange membrane fuel cell (AMFC) are perceived as promising fuel cells, especially for mobile applications, due to their high energy efficiency and zero emission [1]. The PEMFC and AMFC are similar in principle. The main difference is that a solid membrane separates an anode and a cathode. As shown in Figure 1.1, protons conduct through a proton exchange membrane from the anode to the cathode in the PEMFC. In the AMFC, hydroxide ions are transported through an anion exchange membrane from the cathode to the anode. Under an acid condition of the PEMFC, the hydrogen oxidation reaction (HOR) occurs at the anode, and the oxygen reduction reaction (ORR) occurs at the cathode, which can be expressed as follows

$$\begin{aligned} &\mathrm{HOR}: \mathrm{H_2} \rightarrow 2\mathrm{H}^+ + 2\mathrm{e}^- \\ &\mathrm{ORR}: \frac{1}{2}\mathrm{O_2} + 2\mathrm{e}^- + 2\mathrm{H}^+ \rightarrow \mathrm{H_2O} \end{aligned} \tag{1.1}$$

Similarly, the HOR at the anode and the ORR at the cathode under an alkaline condition in the AMFC can be written as follows

$$\begin{aligned} &\mathrm{HOR}: \mathrm{H_2} + 2\mathrm{OH}^- \rightarrow 2\mathrm{H_2O} + 2\mathrm{e}^- \\ &\mathrm{ORR}: \frac{1}{2}\mathrm{O_2} + \mathrm{H_2O} + 2\mathrm{e}^- \rightarrow 2\mathrm{OH}^- \end{aligned} \tag{1.2}$$

Both types of fuel cells lead to the same overall reaction, which is

$$\mathrm{H_2} + \frac{1}{2}\mathrm{O_2} \rightarrow \mathrm{H_2O} \tag{1.3}$$

However, some differences can be seen in the fuel cell electrode reactions, and both types have their advantages and disadvantages.

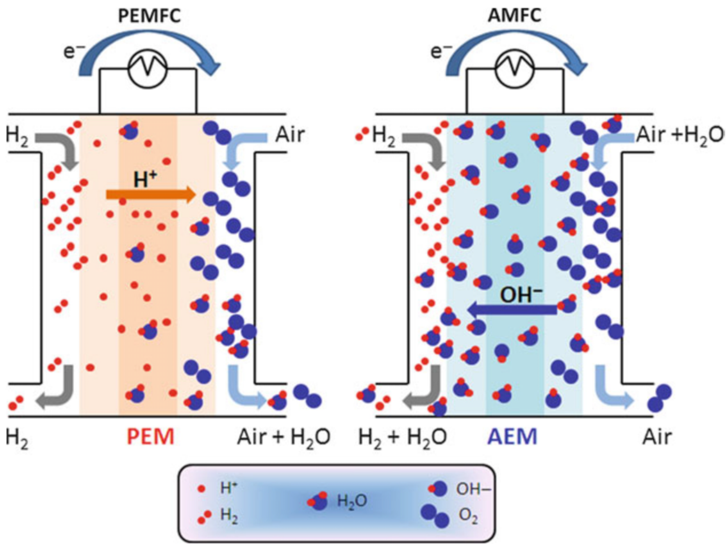

Figure 1.1: Schematic illustration of proton exchange membrane fuel cell (PEMFC) and anion membrane fuel cells (AMFC). Reproduced from [2], Copyright 2014, with permission from Springer Nature.

1.2 Degradation of M/N/C Electrocattalyst

The PEMFC has attracted attention due to its favorable power-to-weight ratio, quick start-up, and low operating temperature [3, 4]. The development of the PEMFC for commercialization has also made significant progress. Still, its large-scale commercialization is hampered by high cost and low performance. A highly efficient electrocatalyst is required to drive the sluggish ORR at the cathode. Carbon-support platinum-based particles are the most efficient and commercialized ORR catalysts. However, due to the high Pt-loading required at the cathode and the scarcity of Pt, the catalyst cost is the largest component of the PEMFC stack [5]. In addition, a lack of durability can also lead to the limited performance of the PEMFC. Under the acidic condition of the PEMFC, the corrosion of the carbon-based material, dissolution of catalyst, and polymer decomposition are the degradation that can be observed [6, 7]. Hence, it still has room to be improved regarding durability. In this thesis, the focus is on the catalyst component.

In developing advanced Pt-free cathode catalysts, the requirements for inexpensive but more active and durable ORR electrocatalysts are challenging. A single metal site incorporated in N-doped carbon (M/N/C catalyst) has emerged as a promising low-cost ORR catalyst. Many experimental and theoretical studies have already demon-

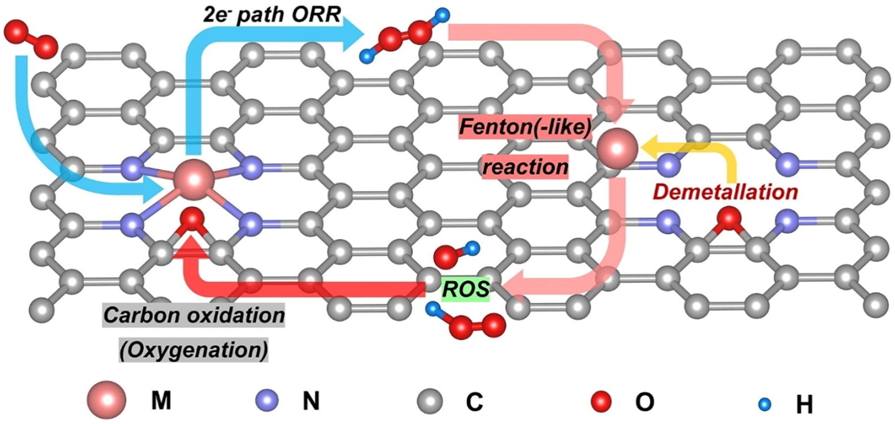

Figure 1.2: Schematic illustration of the degradation of M/N/C electrocatalysts via the demetallation and oxidation of the carbon matrix. Reproduced from [8], Copyright 2021, with permission from Elsevier.

strated the impressive utilization and initial ORR activity of the M/N/C catalyst, especially Fe/N/C catalysts [9–12]. However, a significant challenge of the M/N/C electrocatalysts is their poor stability, especially in acidic media.

Several possible degradation processes have been proposed to cause the instability of the Fe/N/C catalysts, e.g., the leaching of the metal atom from the MN_yC_x motif [13, 14], the carbon surface oxidation [15, 16] and the corrosion of the carbon matrix [17]. These mechanisms may occur parallel during the fuel cell operation and may be interrelated [18, 19]. For example, as shown in Figure 1.2, the demetallation could cause a direct loss of the active site density, and the leached metal ion could indirectly catalyze the oxidation of carbon materials. In addition, the oxidation of the carbon matrix could further accelerate the demetallation. Still, the dominating factor contributing to the M/N/C catalyst degradation is elusive and needs further investigation.

The carbon oxidation can occur by the direct electrochemical carbon oxidation at a higher potential [16, 20], leading to the destruction of the MN_yC_x site and the removal of the metal center atom. Its kinetics depend on temperature and defects in the carbon matrix. The carbon corrosion rate increases with temperature [16, 20], and the rate becomes faster on the graphene edge than on the basal plane [16]. As a result, the micropore-hosted MN_yC_x site could be eliminated faster than the bulk-hosted site [16]. The chemical oxidation of M/N/C catalysts surface by H_2O_2-derived radicals rather than by electrochemical carbon oxidation has been proposed as one of the degradation mechanisms of the Fe/N/C catalyst during the fuel cell operation [15, 21]. H_2O_2 can be electrochemically generated by ORR [22–24], and the reactions between H_2O_2 and dissolved metal ions or MN_y site, especially Fe ions and FeN_y site, lead to active oxygen species (ROS). The ROS has higher oxidative strength than H_2O_2 and can oxidize carbon matrix [15, 21, 25]. Upon damaging the carbon matrix, the metal atom could be more prone to detach from the M/N/C structures [15, 26], reducing the active site density. The ROS can also modify the carbon surface near the active site, reducing the turnover frequency (TOF) of the Fe/N/C catalyst [17]. The latter effect is partially reversible upon reduction of the carbon surface [17].

The demetallation could process by direct leaching of the Fe center [13, 14] or the loss of FeN_x species due to carbon corrosion [15, 16]. The demetallation of the Fe ion from the Fe/N/C catalyst is dominating at low potential (< 0.7 V) [20]. Using density functional theory (DFT) calculations to study the dissolution reaction of the FeN_4 sited embedded on a bilayer-graphene, Holby *et al.* suggested the demetallation of the FeN_4 site is thermodynamically favored under the PEMFC-relevant environment [27]. In contrast to the thermodynamic dissolution of the FeN_4 structures toward aqueous Fe^{2+} studied by Glibin *et al.* [28] and Chenitz *et al.* [29], the FeN_4 structures are thermodynamically stable in acidic conditions, but they can be demetallated by the driving force of water running into the micropores [29]. This specific demetallation has been proposed as the cause of the initial loss of ORR activity, especially for highly microporous catalysts[29].

The atomic structures and working environments play essential roles in the stability and catalytic activity of the Fe/N/C catalyzes [18, 29, 30]. While, the structure of pyrolyzed Fe/N/C materials highly depends on the synthetic path where various Fe species may form at high temperatures, ranging from metallic, metal-carbide, and metal-nitride Fe particles to FeN_x moieties. Many detail structures of the FeN_4 sites with different local carbon structure have been proposed as the active site for the ORR by both experimental and theoretical studies (e.g., FeN_4C_8 [31, 32], FeN_4C_{10} [18, 33], FeN_4C_{12} [9, 18, 33], edge-hosted FeN_4 [34]).

In a previous experiment by Santori *el al.*, two Fe/N/C catalysts comprising only atomically dispersed FeN_y moieties; one is an NH_3-pyrolyzed Fe/N/C catalyst, and the other is the Ar-pyrolyzed Fe/N/C catalyst [14]. The NH_3-pyrolyzed Fe/N/C catalyst results in a higher ORR activity in alkaline electrolyte and approximately ten times higher Fe leaching in the acid electrolyte relative to the Ar-pyrolyzed Fe/N/C catalyst. Furthermore, the Fe leaching rate is strongly enhanced when the potential is 0.75 to 0.3 V_{RHE}. By using operando X-ray absorption spectroscopy (XAS), Santori *el al.* has also suggested that the instability in the acidic medium of the NH_3-pyrolyzed catalysts relates to the lower oxidation state of the Fe atom litigated with highly basic nitrogen ligands [14].

Recent studies have shown that two FeN_4 sites with different local carbon structures have different stability under the operation in the acid eletrolyte[18]. Combining operando ^{57}Fe Mössbauer spectroscopy and XAS, Li *et al.* have identified two initial types of FeN_4 sites in the Fe/N/C catalysts, including a high-spin FeN_4C_{12} moiety (S1) and a low- or intermediate-spin FeN_4C_{10} moiety (S2), as shown in Figure 1.3. Both sites initially contribute to the ORR activity in the acid electrolyte. However, the FeN_4C_{12} site, which is more active for the ORR, irreversibly converts to inactive ferric oxides during the operation, especially at low potentials [18]. In contrast, the FeN_4C_{10} site, which has relatively low activity, is found to be more stable against demetallation and insensitive to local carbon surface oxidation [18]. This study has suggested a significant role of the local carbon around the FeN_4 sites in their stability, bringing up a potential pathway to achieve a Fe/N/C catalyst with activity and stability by regulating the local carbon structure. Nonetheless, the underlying driving force for different stability of these two FeN_4 sites is still unclear, and there is a wide debate about the active and stable site of the Fe/N/C catalysts [26, 35–37].

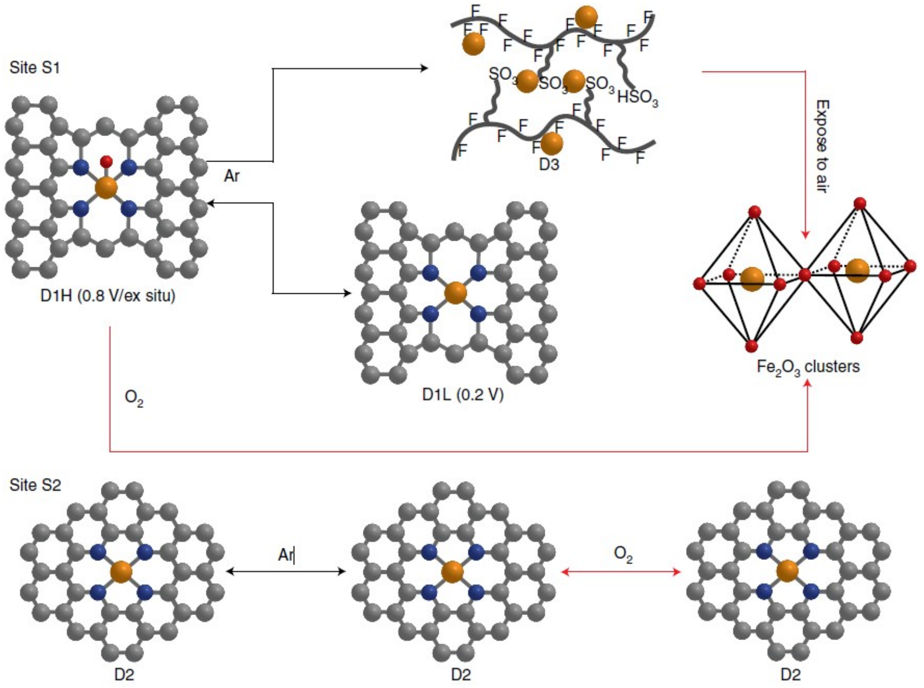

Figure 1.3: Schematic illustration of the conversion of two types of FeN_4 sites under acidic fuel cell operation. The highly active FeN_4C_{12} site (S1) is not durable and quickly converts into inactive ferric oxide. The less-active FeN_4C_{10} site is durable and retain fuel cell performance. Reproduced from [18], Copyright 2020, with permission from Springer Nature.

Since the dissolved Fe ions from the Fe/N/C catalyst and the Fe/N/C site itself can catalyze the formation of radicals from H_2O_2 [21, 25, 38], further deteriorating the catalyst surface and proton exchange membrane [17, 39]. The replacement of Fe with other metals that do not promote the formation of H_2O_2-derived radicals are also desirable. A previous study by Xie *et al.* [19] has reported a similar catalytic activity toward ORR of the Co/N/C catalyst to the Fe/N/C catalyst. In contrast, the Co/N/C catalyst has lower metal reaching and lower activity for promoting radicals from H_2O_2, resulting in significant resistance to demetallation and carbon surface oxidation under acid conditions, compared to the Fe/N/C catalysts [19]. By using X-ray absorption near-edge structure (XANES), extended X-ray absorption fine structure (EXAFS), magnetic susceptibility measurements, and DFT calculations, the structure of the Co/N/C catalysts has been identified by Zitolo *et al.* [12]. Like the Fe/N/C catalyst, the CoN_yC_x moieties are an active site toward the ORR. Unlike the FeN_yC_x moieties, the CoN_yC_x moieties do not experience structural and electronic-state changes under the ORR operation. In addition to the Co/N/C catalysts, the excellent structural stability of Ru/N/C catalyst in acid electrolytes has also been reported. Cao *el al.* have detected the Ru dissolution ratio of as low as 5% within 30 hours operation for Ru/N/C catalyst in O_2-saturated 0.5 M H_2SO_4 electrolyte [40]. Also, using transmission electron microscopy (TEM), X-ray diffraction (XRD), and EXAFS, they have found that the morphology and structure of the Ru/N/C catalyst remain nearly unchanged after the operation.

Understanding the degradation mechanism of the Fe/N/C catalyst is beneficial for the rational design of durable M/N/C catalysts. However, the complexity of the degradation becomes a big challenge to reveal the underlying dominant one. In this thesis, we try to understand how the nature of the metal atoms, the local carbon structures, and chemical environments, i.e., electrolyte anions affect the demetallation of the single metal atom and its catalytic activity. Although other degradation reactions could occur and contribute to the degradation, the ambiguous interaction between each possible degradation reaction makes it hard to explore simultaneously. We believe that the relation between the atomic structure and chemical environment of the MN_y motif with the demetallation will provide a better understanding of the degradation and helps design intrinsic stable and active catalysts. Other possible degradation reactions could be further included.

The development of new materials using the first principle calculations has been possible thanks to the increased computational power over the decades. As a result, a computational screen process can rapidly reduce the number of candidates to investigate experimentally. The DFT calculations have been successfully used for describing the electronic structure, and catalytic activity of the single atom catalyst [41–44]. This thesis uses the DFT calculations to study the relationship between the demetallation of the MN_yC motifs with their structure and chemical environments, i.e., electrolyte adsorption. Using the computation screening approach, we also suggest interesting candidates that can result in active and stable M/N/C catalysts.

1.3 Degradation of Polybenzimidazole Membrane

The AMFC is effectively an alkaline analogy of the PEMFC. Working under alkaline conditions offers several advantages over the PEMFC, including low dissolution rates of catalysts, less expensive Pt-free electrocatalysts, and wide selections of materials and components that are stable at high pH [45]. However, there are still concerns regarding the performance achieved by the AMFC. The most critical concern is the poor ionic conductivity and stability of the anion exchange membranes [2].

As shown in Figure 1.4 (a), the electrodes are separated by an aqueous potassium hydroxide solution confined in a porous diaphragm. The porous diaphragm is a separator material made from a stable, inert polymer, solely relying on a liquid electrolyte to establish percolating pathways throughout the porous structure. The diaphragm must have a significant thickness to secure gas separation. However, this, unfortunately, causes the increased ohmic resistance [46]. Replacing the diaphragm with an ion-conducting membrane reduces inter-electrode thickness, thus reducing the internal resistance [47]. A typical anion exchange membrane comprises polymer backbones with pendant fixed organic cations such as ammonium [11, 48], imidazolium cation [49–52], benzimidazolium [50, 53, 54] to allow hydroxide-ion conduction. However, both polymer backbones and organic cations could be potentially attacked by hydroxide ions, leading to the loss of mechanical strength and ion conductivity [55–58].

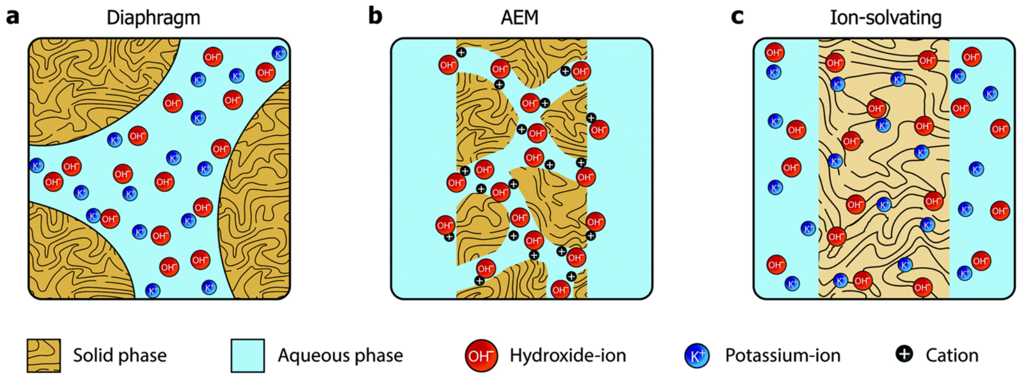

Figure 1.4: Three approaches towards hydroxide conducting separators: (a) a porous diaphragm, (b) an anion exchange membrane, (c) an ion-solvating membrane [47]

An alternative is an ion-solvating membrane which consists of a water-soluble polymer and a hydroxide salt (i.e., potassium hydroxide) [47, 59]. These combinations have the mechanical properties of the polymer and conductive properties of the alkaline salt. The polymer contains electronegative heteroatoms such as oxygen, nitrogen, or sulfur, which interact with the cations of the salt. Ionic conduction within the structure is based on these heteroatom-cation interactions, so it does not need the cation moieties [59] and can be prepared as thin as other polymeric membranes [47, 60].

Recently, the ion-solvating membrane based on polybenzimidazoles (mPBI) have been studied for the AMFC, and alkaline water electrolysis [60–63]. As shown in Figure 1.5, when combined with a strong concentrated base, the mPBI undergoes ionization, forming the polybenzimidazolides that allow the uptake of water and base to facilitate the hydroxide-ion transport in the membranes [64–66]. Compared to a porous separator such as Zirfon, the mPBI-based membrane has a lower ohmic polarization and hydrogen crossover but a higher ionic conductivity [60, 67]. The composite of the mPBI-based membrane depends on the KOH concentration. The mPBI-based membrane exhibits high ionic conductivity and chemical stability at low concentration (5 - 10 wt% KOH at T = 88°) [61]. The ionic conductivity can be further increased by two orders of magnitude and peaks at 20 - 25 % KOH [61]. However, a long-term operation at this high KOH concentration can lead to the degradation of the mPBI-based polymer [60, 61, 68]. Thus, the practical use is still limited.

A structure optimization has been found as a possible way to improve the alkaline stability of the mPBI-based membrane. The chemical stability of mPBI has been studied by Aili *et al.* [68], and they have found no change in the mPBI structure under 6 M KOH at 85 °C for 116 days. A polybenzimidazole derivative, poly(2,2-(m-mesitylene)-5,5-bibenzimidazole) (mesPBI), has been synthesized and was stable in 0 - 10 wt% KOH at T = 88 °C for 207 days [69]. Recently, a poly(2,2-(1,4-naphthalene)-5,5-bibenzimidazole) (NPBI); also a polybenzimidazole derivative, was successfully synthesized and used in alkaline water electrolysis by Hu *et al.* [70] and they have found no chemical degradation at T = 80 °C in 6 M KOH for 180 days.

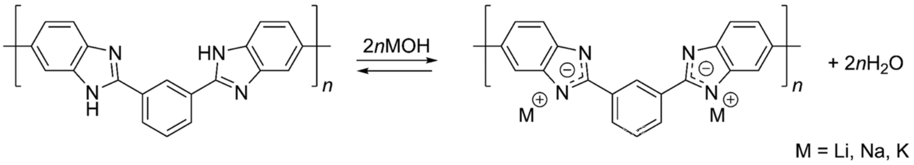

Figure 1.5: Formation of polybenzimidazolides in the alkaline solution. Reproduced from [71], Copyright 2020, with permission from Royal Society of Chemistry.

The degradation of the mPBI-based membrane could happen via a nucleophilic attack by hydroxide ions at the benzimidazole ring, similar to that of imidazolium cation [68–70]. However, under an alkaline condition, the mPBI undergoes deprotonation. The negative charge could be localized at the benzimidazole ring of the mPBI; thus, a predominant degradation mechanism could differ from the imidazolium cation. In order to develop mitigating degradation, a detailed mapping of the degradation pathway is needed. This thesis uses the DFT calculations to understand how the mPBI molecules degrade in an alkaline solution.

1.4 Outline of the Thesis

This thesis comprises six chapters and is organized as follows

- **Chapter 1 - Introduction**
  The introduction of the fuel cell technology and two degradation issues related to the materials inside the fuel cell which is the main focus of this thesis. A brief review of the degradation of the M/N/C catalyst in an acid condition and polybenzimidazole membrane in an alkaline solution.

- **Chapter 2 - Theoretical Framework**
  A brief introduction to the electronic structure problem in condensed matter physics, the DFT calculations, and an overview of exchange-correlation functionals used in this thesis.

- **Chapter 3 - Effect of Local Carbon Structure on the Activity and Stability of Single-atom Electrocatalyse**
  An investigation of the stability and ORR activity under acidic conditions of the M/N/C catalyst with different local carbon surrounding the MN_y site and different metal atoms.

- **Chapter 4 - Effect of Electrolyte Anion Adsorption on the Activity and Stability of Single Atom Electrocatalysts**
  A study of the effect of electrolyte anion adsorption on catalytic activity and stability of the M/N/C catalyst under two electrochemical conditions, which are the ORR and the CO_2 reduction reaction (CO_2RR).

- **Chapter 5 - Degradation of Polybenzimidazole in Alkaline Solution**
  The DFT investigation of the minimum degradation pathway of the mPBI molecule in an alkaline solution. The role of explicit water molecules and the effect of hydroxide ion concentration on the free energy barrier

- **Chapter 6 - Summary and Outlook**
  Main findings and an outlook for future work.

Chapter 2

Theoretical Framework

Density functional Theory (DFT) calculations are widely used as a standard tool for materials modeling problems in physics, chemistry, and materials science. This chapter briefly introduces the basic theoretical framework, including the electronic structure problem in condensed matter physics and DFT, as used in this thesis.

2.1 Electronic Structure Problem

A piece of any material consists of atoms, a set of atomic nuclei, and electrons interacting via electrostatic force. One of the fundamental ground state properties of such a system is its energy which changes when atomic positions are altered. The ground state properties can be determined by solving the time-independent Schrödinger equation.

$$\hat{H}\Psi(R,r) = \varepsilon\Psi(R,r) \tag{2.1}$$

where ε is the energy eigenvalue, and $\Psi(R,r)$ is the wavefunction of the system, depending on both the electron coordinates (r) and the nuclei coordinates (R). The Hamiltonian can be written as follows

$$\begin{aligned}\hat{H} =& -\sum_{I=1}^{P}\frac{\hbar^2}{2M_I}\nabla_I^2 - \sum_{i=1}^{N}\frac{\hbar^2}{2m}\nabla_i^2\\ &+\frac{e^2}{2}\sum_{I=1}^{P}\sum_{J\neq I}^{P}\frac{Z_I Z_J}{|R_I - R_J|} + \frac{e^2}{2}\sum_{i=1}^{N}\sum_{i\neq j}^{N}\frac{1}{|r_i - r_j|} - e^2\sum_{I=1}^{P}\sum_{i=1}^{N}\frac{Z_I}{|R_I - r_j|}\\ \hat{H} =& \hat{T}_n + \hat{T}_e + \hat{U}_{nn}(R) + \hat{U}_{ee}(r) + \hat{V}_{ne}(R,r)\end{aligned} \tag{2.2}$$

where $R = R_I; I = 1, ..., P$ is a set of P nuclei coordinates and $r = r_i; i = 1, .., N$ is a set of N electron coordinates. Z_I and M_I are the nucleus charge and mass, respectively, while m is the electron mass. $\hat{T}_n$ of the Hamiltonian is the kinetic energy of the nucleus. $\hat{T}_e$ is the kinetic energy of the electrons. $\hat{U}_{nn}(R)$ is the nucleus-nucleus interaction. $\hat{U}_{ee}(r)$ is the electron-electron interaction. $\hat{V}_{ne}$ is the interaction between the nucleus and electron. The final term makes the nucleus and electron parts inseparable.

The nucleus is considered to be much heavier and slower than the electrons. Therefore, the nucleus can be assumed stationary from the point of the electron. Then, the electrons are considered moving in the potential corresponding to the configuration of the nuclei and instantaneously adapting to nuclei motions [72]. This approximation is known as Born-Oppenheimer approximation [72]. For a given set of nuclei with coordinate R, the electronic part related to electron motion can be separated and solved.

$$\Psi(R, r) = \Psi_e(r; R)\Psi_n(R) \tag{2.3}$$

where $\Psi_e(r; R)$ is the many-body electronic wave function and $\Psi_n(R)$ is the nuclear wave function. The electronic Schrödinger equation can be expressed as follows

$$\hat{H}_e\Psi_e(r; R) = E(R)\Psi_e(r; R) \tag{2.4}$$

where E(R) are the electronic eigenvalues corresponding to the given nuclei configuration. The nuclei coordinates are only a parameter in $\hat{H}_e$, $\Psi_e(r; R)$ and E(R). The electronic Hamiltonian ($\hat{H}_e$) can be written as follows

$$\begin{aligned} \hat{H}_e &= -\sum_{i=1}^{N}\frac{\hbar^2}{2m}\nabla_i^2 + \frac{e^2}{2}\sum_{i=1}^{N}\sum_{i\neq j}^{N}\frac{1}{|r_i - r_j|} - e^2\sum_{I=1}^{P}\sum_{i=1}^{N}\frac{Z_I}{|R_I - r_j|} \\ \hat{H}_e &= \hat{T}_e + \hat{U}_{ee}(r) + \hat{V}_{ext}(r) \end{aligned} \tag{2.5}$$

where $\hat{T}_e$ is the kinetic energy of the electron. $\hat{U}_{ee}(r)$ is the electron-electron interaction. $\hat{V}_{ext}(r)$ is the nucleus-electron interaction, which is an interaction between electrons and the external potential generated by the given configuration of the nuclei. The electronic Schrödinger equation is still complicated to solve as the electrons interact among themselves via electrostatic forces. The presence of electrons in one region can influence the behavior of electrons in other regions. In other words, the probability of finding two electrons (two particles with the same charge) is reduced due to Coulomb repulsion, known as correlation interaction. Furthermore, the probability of finding two electrons is further depleted if they have the same spin due to Pauli's exchange principle, known as an exchange interaction. Thus, the electrons cannot be treated individually. Also, the electronic wavefunction cannot be written simply as a product of single-electron wavefunctions. As a many-body problem, the exact solution of the electronic Schrödinger equation consisting of N electrons will solve the equation in 3N degrees of freedom. Instead of doing so, the many-body wave function in the DFT is solved in terms of electronic density; n(r). Thus, it solves the equation in only the three spatial degrees of freedom.

2.2 Density Functional Theory

Hohenberg-Kohn Theorem

DFT is based on the Hohenberg-Kohn theorem [73], proposing the formal theoretical basis for obtaining electronic energies through electronic density.

Theorem 1 states that the external potential; $v_{ext}(r)$, is a unique functional of the density; n(r), apart from a trivial additive constant. Hence, the energies and other properties of the system at the ground state are determined by the ground state electronic density. Given the external potential; $v_{ext}(r)$, the total energy can be represented as a functional of the electronic density.

$$E[n(r)] = T[n(r)] + U_{ee}[n(r)] + \int v_{ext}(r)n(r)dr \tag{2.6}$$

where T[n(r)] is the kinetic energy of the electron. $U_{ee}[n(r)]$ is the potential energy due to electron-electron interaction. These two terms depend on the electron density. The final term is the potential energy due to the interaction between electrons and the external potential from the nuclei.

Theorem 2 states that the ground state energy can be obtained from the ground state electronic density, which minimizes the total energy. Thus, the energy functional; E[n(r)] is minimized for the ground state density; $n_0(r)$, whose energy is the ground state energy; E_0.

$$E_0 = \min_{n(r)} E[n(r)] \tag{2.7}$$

However, to get the exact ground state electron density, the exact expression of the first two terms in Equation 2.6 must be known.

Kohn-Sham Equations

Instead of considering a system of interacting electrons, the exact ground-state electron density is obtained from the non-interacting electron system subjected to an effective external potential; $v_{eff}(r)$, such that the same ground-state electron density as the interacting electron system is obtained [74]. As a result, the Hamiltonian can be written for the non-interacting electron system consisting of N electrons as follows

$$\hat{H}_s = \sum_{i=1}^{N} \left[-\frac{\hbar^2}{2m} \nabla_i^2 + v_{eff}(r_i) \right] \tag{2.8}$$

where $v_{eff}(r)$ is the effective external potential, which ensures that the electron density of the non-interacting electron system is the same as the electron density of the interacting electron system. A many-body wavefunction of the non-interacting electron system can be expressed as a Slater determinant of a single-electron wavefunction; Φ_i (called Kohn-Sham orbitals). The Kohn-Sham orbitals, Φ_i, can be obtained by solving the one-electron Schrödinger equation, the Kohn-Sham equation.

$$\hat{H}_{KS}\Phi_i = \left[-\frac{\hbar^2}{2m} \nabla_i^2 + v_{eff}(r_i) \right] \Phi_i = \varepsilon_i \Phi_i \tag{2.9}$$

The electron density of the non-interacting electron system can be written as

$$n(r) = 2 \sum_{i=1}^{N} |\Phi_i|^2 \tag{2.10}$$

The total energy of the non-interacting electron system with electron density, n(r), can be written as

$$E_s = T_s[n(r)] + \int v_{eff}(r)n(r)dr \tag{2.11}$$

where $T_s[n(r)]$ is the kinetic energy of the electrons in the non-interacting electron system. Applying the variational principle to the total energy of the non-interaction electron system results in the following equation.

$$\frac{\delta T_s[n(r)]}{\delta n(r)} + v_{eff}(r) = \mu_s \tag{2.12}$$

For the interacting electron system, the total energy in Equation 2.6 can be rewritten in terms of the kinetic energy of the non-interacting electron system.

$$E[n(r)] = T_s[n(r)] + \frac{1}{2}\int\int \frac{n(r)n(r')}{|r-r'|}drdr' + \int v_{ext}(r)n(r)dr + E_{xc}[n(r)] \tag{2.13}$$

where the second term is the Hartree energy which is the classical electrostatic energy from a charge distribution given by n(r). $E_{xc}[n(r)]$ is the exchange and correlation energy which is a correction term, including the kinetic correlation energy and exchange-correlation energy. The kinetic correlation energy accounts for the fact that the many-body electronic wavefunction of the interacting electron system cannot be written as Slater determinants of the single-electron wavefunction. The exchange-correlation energy accounts for other missing parts, including exchange energy and correlation energy of electrons. Furthermore, the Hartree energy also includes the interaction of an electron with itself. In order to cancel out this nonphysical contribution, $E_{xc}[n(r)]$ is expected to account for this contribution error. However, the exact mathematical expression of $E_{xc}[n(r)]$ term is unknown.

Minimizing the total energy of the interaction electron system with respect to the density, under the constraint that this density integrates into N particles, the following equation is obtained for the ground state density.

$$\frac{\delta T_s[n(r)]}{\delta n(r)} + \int \frac{n(r')}{|r-r'|}dr' + v_{ext}(r) + \frac{\delta E_{xc}[n(r)]}{\delta n(r)} = \mu \tag{2.14}$$

Since the interacting and non-interacting electron systems have the same ground state density and ground state energy, the chemical potentials must be equal. Thus $v_{eff}(r)$ can be expressed as the following equation.

$$\begin{aligned} v_{eff}(r) =& v_{ext}(r) + \int \frac{n(r')}{|r-r'|}dr' + \frac{\delta E_{xc}[n(r)]}{\delta n(r)} \\ =& v_{ext}(r) + v_H(r) + v_{xc}[n(r)] \end{aligned} \tag{2.15}$$

As a result, the problem can be solved self-consistently. From a given external potential of the system, the initial guess of electron density is used to formulate the effective potential. Then, the Kohn-Sham equation can be solved to give a new electron density.

The Kohn-Sham equation has to be solved self-consistently to ensure the input electron density equals the output electron density. The exact ground state electron density can be obtained only if the exact exchange-correlation functional is known. However, the exact exchange-correlation functional, including all the exchange and correlation contributions to the energy from the real many-body wave function, is not known. In order to make the DFT procedure practical, approximations for the exchange-correlation functional are required. Consequently, the accuracy of DFT calculations relies on accurate approximations of the exchange-correlation functional.

2.3 Exchange-correlation functional

The exchange-correlation functional can be approximated in several ways. Each gives different results and uses different amounts of resources. The simplest approximation is a Local Density Approximation (LDA) where the exchange-correlation functional at each position is the exchange-correlation of the homogeneous electron gas with the same electron density [74]. In this way, the exchange-correction functional is a local functional that depends only on the electron density at the considered position. The functional may be written as follows

$$E_{xc}^{LDA}[n(r)] = \int n(r)\varepsilon_{xc}^{HEG}[n(r)]dr \tag{2.16}$$

where ε_{xc}^{HEG} is the exchange-correlation energy density of the homogeneous electron gas with a uniform density n. As its name implies, the electron density is constant at all points in the space of the homogeneous electron gas. The LDA functional is exact for the homogeneous electron and is expected to be a good approximation for a system with a uniform electron density or where the electron density varies slowly in space, like bulk metals [75]. However, it fails for systems where the electron density changes rapidly through space, such as molecules and surfaces.

An extension of the LDA functional using information about the local electron density; n(r), and the local gradient in the electron density; $\nabla n(r)$, is a Generalized Gradient Approximation (GGA) [76]. There are many ways in which information from the electron density gradient can be included. Generally, the exchange-correlation functional in the GGA can be written as

$$E_{xc}^{GGA}[n(r)] = \int n(r)\varepsilon_{xc}^{HEG}[n(r)]F_{xc}[n(r), \nabla n(r)]dr \tag{2.17}$$

where F_{xc} is the enhancement factor that modifies the local LDA contribution to the energy. The exchange-correction functional depends on the electron density at the considered position and the nearest neighbor, containing a semi-local interaction. Two of the most widely used functionals in calculations involving solids are the Perdew-Wang functional (PW91) [77] and the Perdew-Burke-Ernzerhof functional (PBE) [76], which have proven quite successful in calculating many properties, most notably lattice constants [78].

However, the local and semi-local correction hardly captures the non-local interaction in the long-range such as van der Waals (vdW) dispersion interactions which fundamentally occur due to correlations that exist between temporary fluctuations in the electron density of one molecule and the energy of the electrons in another molecule responding to these fluctuations [75]. Including the non-local vdW interactions could have the advantage of describing the surface chemical reaction where the non-local vdW interaction plays an important role. A Bayesian Ensemble Error functional with van der Waals correlations (BEEF-vdW) [79] is another GGA functional with added vdW interaction. The general expression of the BEEF-vdW functional can be written as

$$E_{xc}^{BEEF-vdw}[n(r)] = \sum_{m=0}^{M-1} a_m E_m^{GGA-x} + \alpha_c E^{LDA-c} + (1-\alpha_c)E^{LDA-c} + E^{nl-c} \tag{2.18}$$

where E^{nl-c} is the non-local correlation which is the vdW-DF2 functional [80]. The correlation contribution is a linear combination of LDA and PBE correlation functional with a mixing parameter (α_c), determining the LDA and PBE correlation functional ratio. The exchange contribution is an empirically fit functional of the GGA exchange functional. The enhancement factor (E_m^{GGA-x}) is expanded based on M Legendre polynomial with the expansion coefficient (a_m). The parameters of the functional a_m and α_c are optimized with respect to a collection of experimental data in such a way that the uncertainty of the calculation can be quantified. Thus, the BEEF-vdw functional can further provide an uncertainty of DFT calculations.

An extension of the approach is using a mixture of the exchange-correlation density functional from LDA or GGA with the exact exchange energy calculated as in a Hartree-Fock method, the hybrid functional. In the Hartree-Fock method, the many-body wave function is approximated by a single Slater determinant, and the total electron energy can be written as follows

$$E_{HF} = T_s + E_H + E_x^{HF} + V_{ext} \tag{2.19}$$

where T_s is kinetic energy calculated in the same way as in Equation 2.11, E_H is the Hartree energy which is the classical electrostatic energy from the charge distribution, and E_x^{HF} is the exact exchange energy where the self-interaction is canceled out exactly. The limitation of the Hartree-Fock approximation is that the many-body wave function is not well-represented by a single Slater determine; the exact correlation term (E_c) is still missing.

The hybrid functional can generally be expressed as follows

$$E_{xc}^{HF} = \alpha E_x^{HF} + (1-\alpha)E_x^{LDA/GGA} + E_c^{LDA/GGA} \tag{2.20}$$

where the coefficient α is either chosen to assume a specific value or is fitted to some properties of the molecule database. An example of this approximation is the B3LYP functional [81] which successfully predicts small molecule properties [75]. While the hybrid functional aim at reducing the self-interaction error by including the exact exchange, computing the exact exchange can be very computationally demanding.

Chapter 3

Effect of Local Carbon Structure on the Activity and Stability of Single-atom Electrocatalyse

This chapter is based on the work presented in Paper I as given in Appendix D, covering the main points and results.

3.1 Introduction

A single metal atom supported on nitrogen-doped carbon (M/N/C) has gained much attention as a low-cost ORR catalyst due to its high initial activity, especially Fe/N/C catalysts [82–84]. The FeN_4 site has been proposed as the active site for the Fe/N/C catalysts [9, 31, 85]. Depending on the synthesis approach, which involves pyrolysis at a high temperature of iron, nitrogen, and carbon precursor [14, 86], various local carbon structures around the FeN_4 site. For instance, FeN_4C_8 [31, 32], FeN_4C_{10} [18, 33], FeN_4C_{12} [9, 18, 33], edge-hosted FeN_4 sites [34] have been proposed as the active site for the ORR. The local carbon structures are also important in the ORR activity [18, 30, 33, 42, 87].

On top of the ORR activity, one issue facing the Fe/N/C catalysts is insufficient stability. The Fe/N/C catalysts tend to degrade quickly under acidic environments [88]. While the degradation mechanism remains elusive. Many possible degradation processes have been proposed, such as carbon surface oxidation [17, 39], demetallation [13, 89], and carbon corrosion [16, 20]. The stability is also affected by the synthesis process [14]. A previous study has shown a higher ORR activity in alkaline media of the Fe/N/C catalysts prepared via the pyrolysis in NH_3 atmosphere than those prepared in inert gas [14]. At the same time, the Fe leaching rate in acid media has also been enhanced for the NH_3 pyrolyzed Fe/N/C catalysts [14]. It has been suggested that the pyrolysis in the flowing of NH_3 promotes basicity and porosity in the Fe/N/C catalysts [14, 29], resulting in enhanced ORR activity [18, 90]. While the demetallation of the FeN_4 motifs near the micropores could cause the initial activity to lose [29]. Using operando x-ray absorption spectroscopy to study the Fe/N/C catalysts, Li *et al.* [18] have reported two FeN_4 motifs in the Fe/N/C catalysts which are a low spin site; FeN_4C_{10} site and a high spin site; FeN_4C_{12} site. They have found that both sites initially contribute to the ORR activity, but only the FeN_4C_{10} site is durable in acid conditions [18], suggesting a significant role of the local carbon structure on the stability. Besides the Fe/N/C catalyst, the pyrolyzed M/N/C catalysts with M = Mn, Co, and Ru have resulted in a substantial active site for the ORR under acid conditions [12, 19, 91, 92]. Understanding how the local carbon structures and the nature of metal center atoms affect the catalytic activity and stability are thus beneficial for designing active and durable M/N/C catalysts.

While the materials screening for the ORR catalyst have focused on the catalytic activity [93–95], stability under working conditions is also an important criterion [96–99]. The demetallation of the metal atom due to protons attack has been used to determine the stability of the M/N/C catalyst under acid conditions [100–102]. The embedding energy, indicating the bonding strength between the embedded metal atom with the N-doped carbon structure against the cohesion energy of the bulk metal, is often used to represent thermodynamic stability for the M/N/C catalysts [94, 102, 103]. Previous work on the thermodynamic dissolution of the FeN_4 structures on two different local carbon structures toward aqueous Fe^{2+} has been studied by Glibin *et al.* [104], suggesting acid stability of the FeN_4 sites. In contrast, Holby *et al.* [27] have indicated the acid instability and likelihood of the dissolution of the FeN_4 site. Also, they have suggested that the FeN_4 site is stable only when OH is adsorbed on the FeN_4 motif. The absolute thermodynamic stability of FeN_4 sites remains controversial [27, 104].

This chapter studies the stability under acid ORR conditions of the MN_y motif with different local carbon surroundings and metal atoms. The stability is considered based on the tendency of the metal atom to dissolve from the carbon structure. The acid stability descriptor is then determined and used along with the ORR activity descriptor to suggest promising acid-stable and active M/N/C catalysts.

3.2 Structural Models

The model structures of the M/N/C catalyst considered in this chapter are shown in Figure 3.1. The MN_4C_{10} structure is the MN_4 motif embedded on the bulk graphene. Ten carbon atoms in this structure surround the MN_4 site. The MN_4C_Z and MN_4C_A structure are the MN_4 motifs at the zigzag and armchair edge, respectively. The MN_4C_{12} structure is the MN_4 motif near the micropores with a porphyrin-like structure where twelve carbon atoms surround the MN_4 site. The MN_4C_8 structure is the MN_4 motif bridging between two armchair edges, and eight carbon atoms surround the MN_4 site.

The FeN_4C_{12} structure has been identified by X-ray absorption spectroscopy and proposed as the active site toward the ORR by Zitolo *et al.* [9]. The FeN_4C_8 site has been proposed as the ORR active site in the Fe/N/C catalyst by several experimental studies [31, 34, 85]. Li *et al.* [18] and Mineva *et al.* [33] have identified both of the FeN_4C_{10} and

FeN_4C_{12} structure in the Fe/N/C catalysts.

Furthermore, defining a single metal atom coordinated with four neighbor atoms is saturated; two unsaturated sites, which are the MN_3C_Z and MN_3C_A site, are included. According to Cheng *et al.* [105], these unsaturated motifs at the graphene edge are thermodynamically favorable under the synthesis environments. The MN_3C_{10} motifs where the single metal atom coordinated with three nitrogen atoms and one carbon atom embedded on the bulk graphene are also included. The metal atom considered in this chapter is Cr, Mn, Fe, Co, Ni, and Ru. These transition metal elements were considered because of either relatively cheap and abundant 3d transition metals or already being synthesized and showing promising ORR activity in the experiments [12, 19, 91, 92]. For all considered structural models, the unit cell dimensions in the structure plane are 16.9 x 9.8 Å, with variations due to different metal atoms. The vacuum layer added perpendicular to the structure plane is about 15 Å.

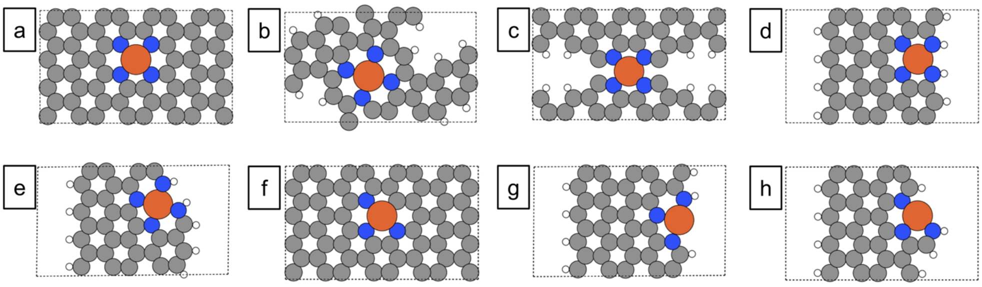

Figure 3.1: Structural models of the M/N/C catalysts: (a) MN_4C_{10}, (b) MN_4C_{12}, (c) MN_4C_8, (d) MN_4C_Z, (e) MN_4C_A, (f) MN_3C_{10}, (g) MN_3C_Z, (h) MN_3C_A. (C = gray, N = blue, H = white, M = orange).

3.3 Computational Details

The calculations in this chapter were performed using spin-polarized density functional theory (DFT) calculations as implemented in the Vienna ab initio simulation package (VASP) [106]. The projector augmented wave (PAW) [107] is used to describe the core electron. A plane-wave basis function with a kinetic energy cutoff of 600 eV defines the valence electron. A Fermi smearing is used with a width of 0.1 eV. The exchange and correlation energy are described using the BEEF-vdW functional [79]. The self-consistent electron density loop is converged to 10^{-5} eV. The structures are prepared using the atomic simulation environments (ASE) package [108]. The lattice relaxation of the single metal atom embedded on the carbon surface is relaxed in a vacuum until all forces are below 0.025 eV/Å. For binding energy calculations, the solvent effect is included during the relaxation. The implicit solvation implemented in VASPsol [109, 110] with a dielectric constant of 80 representing the water medium is used. A dipole correction is used perpendicular to the catalyst surface to decouple the electrostatic potentials on the two sides of the catalyst. The Brillouin zone is sampled with a 3 × 3 × 1 Monkhorst Pack k-point mesh [111] for all structural models in Figure 3.1. The calculations are submitted, managed, and received using the MyQueue [112] workflow tool, a python front-end to the job scheduler, in combination with ASE.

It is assumed that the adsorbate on a catalyst surface has only a vibration degree of freedom and only this vibration contributes to its free energy. The free energies (G) of the adsorbate on the catalyst surface are the calculated DFT energy (E_{DFT}), including zero point energy (ZPE), vibrational internal energy (U_{vib}), and vibrational entropy (S_{vib}) of the adsorbate.

$$G = E_{DFT} + ZPE + U_{vib} - TS_{vib}$$

$$ZPE = \sum_i \frac{hv_i}{2}$$

$$U_{vib} = \sum_i \frac{hv_i}{\exp(\frac{hv_i}{k_B T}) - 1}$$

$$S_{vib} = k_B \sum_i \left(\frac{hv_i}{k_B T(\exp(\frac{hv_i}{k_B T}) - 1)} - \ln\left(1 - \exp(-\frac{hv_i}{k_B T})\right) \right)$$

where v_i is the vibration frequencies of the adsorbate approximated as a quantum harmonic oscillation and calculated using a thermochemistry class in the ASE package [108]. k_B is the Boltzmann constant and T is temperature (K). The calculations are considered at T = 298.15 K.

For the gas molecule, the free energy is also considered at T = 298.15 K and pressure = 1 bar. The free energies of the gas molecule is the calculated DFT energy (E_{DFT}) corrected by including ZPE, enthalpy (H), and entropy (S): $G = E_{DFT} + ZPE + H - TS$. These values (ZPE, H, S) for the gas molecules are taken from the thermochemical database [113]. For O_2 gas molecule, the DFT calculations poorly describe its energy in the gas phase (in the GGA levels) [79]. Thus, the free energy of O_2 gas molecule is calculated in the way to reproduce the experimental free formation energy of liquid water: $2H_2 + O_2 \rightarrow 2H_2O$ where $\Delta G_{H_2O} = -4.92$ eV at T = 298.15 K and $p_{H_2} = p_{O_2} = 1$ bar [114].

According to Christensen's scheme, the energies of H_2, H_2O gas molecule, and binding energy of *OOH are corrected by 0.09 eV, -0.03 eV, and 0.20 eV, respectively, due to the error in the energy levels of the ORR intermediates specific to the BEEF-vdW functional [115, 116].

The change in free reaction energy with potential (U_{SHE}) and pH was calculated using the computational hydrogen electrode (CHE) [117]. By definition of the standard hydrogen electrode (SHE) at 0 V_{SHE}, there is an equilibrium between hydrogen molecules in the gas phase with solvated protons and electrons.

$$H^+ + e^- \rightleftharpoons \frac{1}{2}H_2$$

The free reaction energy of hydrogen adsorption on the catalyst surface at any considered potential (U_{SHE}) and pH can, for example, be written as

$$H^+ + e^- + ^* \rightarrow ^* H$$

$$\Delta G_{*H}(U_{SHE}, pH) = G(^*H) - G(^*) - \frac{1}{2}G(H_2) + eU_{SHE} + k_BTpH\ln(10) \tag{3.1}$$

$$= G(^*H) - G(*) - \frac{1}{2}G(H_2) - \Delta G_e - \Delta G_H \tag{3.2}$$

$$= \Delta G_{*H} - \Delta G_e - \Delta G_H \tag{3.3}$$

where * denotes the adsorbed site on the catalyst surface. $G(^*)$ and $G(^*H)$ are the total free energy of the catalyst surface and the catalyst surface with $^*H$, respectively. $\Delta G_H = -k_BTpH\ln(10)$ and $\Delta G_e = -eU_{SHE}$ where e is the numerical charge of an electron. ΔG_{*H} is the free adsorption energy of hydrogen at pH = 0 and U = 0 V_{SHE} which can be expressed as follows

$$\Delta G_{*H} = G(^*H) - G(^*) - \frac{1}{2}G(H_2) \tag{3.4}$$

3.4 Stability Diagram and Relative Stability

The stability under electrochemical environments is evaluated by considering the likelihood of the metal center atom dissolving from the M/N/C structures. It should be noted that other degradation reactions have also been suggested to cause the instability of the Fe/N/C catalysts, especially in acidic conditions. For instance, the carbon surface oxidation by H_2O_2-derived radicals. The carbon surface oxidation could lead to an inactive FeN_4 site toward the ORR [17] or the dissolution of the Fe atom [18, 26]. The carbon corrosion has been observed at high potential and can lead to the destruction of the FeN_4 motif [16, 20]. The demetallation has also been proposed to cause a fast activity decay of the Fe/N/C catalyst under acid conditions [29]. These possible degradation reactions could coincide and be interrelated [18]. The ambiguous interaction between each possible degradation reaction makes it difficult to explore them simultaneously. We believe that the relation between the local carbon structure and the metal center atom with the demetallation could provide a better understanding of the degradation of the M/N/C catalysts.

According to a theoretical study on the dissolution reaction of the FeN_4C_{10} site on a bilayer-graphene structure by Holby *et al.* [27], the metal atom (M) leaves the MN_yC structure, resulting in an aqueous metal ion with a charge x (M^{x+}), and the dissolved-metal carbon cavity (N_yC). Different degrees of protonation at the N-dangle bonds of the dissolved-metal carbon cavity is possible under acid conditions, resulting in the N_yCH_n structure.

$$MN_yC + nH^+ \rightarrow M^{x+} + N_yCH_n + (x-n)e^- \tag{3.5}$$

The reaction free energy for dissolving the metal atom from the graphene host structure at the potential U_{SHE} and pH can be expressed as follows [27].

$$\Delta G_{diss} = G(M^{x+}) + G(N_yCH_n) + (x-n)\Delta G_e - G(MN_yC) - n\Delta G_H - \frac{n}{2}G(H_2) \tag{3.6}$$

where $G(M^{x+})$ is the free energy of the dissolved metal ion, and it is approximated as

$$G(M^{x+}) = E_M(\text{bulk}) + \Delta G_x \tag{3.7}$$

where E_{DFT}(bulk) is the total energy per atom of the metal in the bulk structure obtained from the DFT calculations. ΔG_x is reaction free energy for the dissolution of the bulk metal, taken from the literature [114, 118, 119] and given in Table A.1. The ΔG_x depends on the dissolved metal concentration, and so does the $\Delta G_{diss}(U_{SHE}, pH)$. This chapter considers the dissolved metal ion concentration of 10^{-6} M. The dissolved metal ions considered in this chapter are Cr^{2+}, Cr^{3+}, $CrOH^{2+}$ for Cr; Mn^{2+}, Mn^{3+} for Mn; Fe^{2+}, Fe^{3+}, $FeOH^{2+}$ for Fe; Co^{2+}, Co^{3+} for Co; Ni^{2+}, Ni^{3+} for Ni; and Ru^{2+}, Ru^{3+} for Ru. The dissolution of the M/N/C catalyst is considered at T = 298.15 K. The N_yCH_n structure is the dissolved-metal carbon cavity with n H atoms bonded at the carbon cavity where n = 0 - 4 is considered for the structural model (a)-(f) in Figure 3.1 and n = 0 - 3 is considered for the structural model (g)-(h) in Figure 3.1. The minimum energy structures of the dissolved-metal $N_yC_{10}H_n$ carbon cavity structure can be found in Figure 3.2 and for other local carbon structures are given in Figure A.1 of Appendix A.

Furthermore, it is assumed that the catalyst surface is in equilibrium with protons, electrons, and liquid water, so oxygen and hydroxyl may be exchanged between the catalyst surface and a reference electrolyte [96].

$$^* + H_2O \rightleftharpoons {}^* OH + H^+ + e^- \tag{3.8}$$

$$^* + H_2O \rightleftharpoons {}^* O + 2H^+ + 2e^- \tag{3.9}$$

The change in free energy for the forward reactions in Equation 3.8 and 3.9 at the potential U_{SHE} and pH can be expressed as follows

$$\Delta G_{*OH}(U_{SHE}, pH) = G(^*OH) + \frac{1}{2}G(H_2) + \Delta G_H + \Delta G_e - G(^*) - G(H_2O) \tag{3.10}$$

$$\Delta G_{*O}(U_{SHE}, pH) = G(^*O) + G(H_2) + 2\Delta G_H + 2\Delta G_e - G(^*) - G(H_2O) \tag{3.11}$$

After all, the dissolution reaction of the M/N/C catalyst in an aqueous environment can generally be expressed as follows

$$^*O_aH_bMN_yC + (2a - b + n)H^+ \rightarrow aH_2O + M^{x+} + N_yCH_n + (x - n - 2a + b)e^- \tag{3.12}$$

where a, b, n, and x are an integer. Additionally, the relative stability denoted as ΔG_R is calculated to represent a thermodynamic driving force toward the dissolution of the catalyst surface [120]. The ΔG_R is defined as the free energy difference between the catalyst surface (either with or without the adsorbate) and the most stable dissolved species at each condition. The more positive the relative stability, the less stable the catalyze surface is against the dissolution.

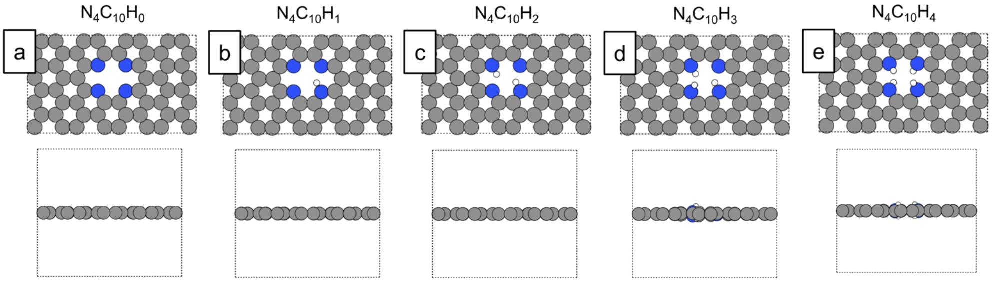

Figure 3.2: The minimum energy structures of the dissolved-metal $N_yC_{10}H_n$ carbon cavity with n = 0 - 4 (a - e): top view (top) and side view (bottom). (C = gray, N = blue, H = white, M = orange).

3.4.1 Stability of the Fe/N/C catalyst

The stability of the Fe/N/C catalysts under electrochemical environments is firstly discussed. Figure 3.3 shows the stability diagram of considered Fe/N/C structures. Only the most stable phase at each condition is shown in the stability diagrams. The stability diagram is divided into different areas with different colors based on the most stable dissolved metal ion and the most stable adsorbate on the metal site. For instance, all Fe^{2+} + $N_4C_{10}H_n$ phases (where n = 0 - 4) are represented with the same color in the stability diagram. Under the acidic ORR-related condition (U $\approx$ 0.6 - 0.8 V_{SHE} and pH = 0), the most stable phase is the dissolved Fe ion, suggesting that all considered Fe/N/C structures are prone to leach under the acidic ORR-related condition. At the same potential range in alkaline conditions (pH = 14), either *OH or *O adsorbats on the Fe atom. Then, the adsorbate stabilizing the Fe atom becomes the most stable phase for the FeN_4C_{10}, FeN_4C_{12}, FeN_4C_A, FeN_4C_Z, and FeN_3C_{10} structure. However, the FeN_4C_8, FeN_3C_Z, and FeN_3C_A structures are still prone to the dissolution under the alkaline conditions.

In Figure 3.3, the ΔG_R at pH = 0 of the Fe/N/C structure is plotted as a function of potential. The most stable dissolved species used as the reference for ΔG_R are superimposed as horizontal bars at the bottom. For the bare Fe/N/C structure at U = 0.8 V_{SHE} and pH = 0, the following order of ΔG_R is found: $FeN_4C_A < FeN_4C_Z < FeN_4C_{10} < FeN_3C_{10} < FeN_4C_{12} < FeN_3C_Z < FeN_4C_8 < FeN_3C_A$, suggesting that the stability against the dissolution decreases from the FeN_4C_A to FeN_3C_A. The formation of *OH and *O on the Fe/N/C structure reduces the thermodynamic driving force toward the dissolution. Considering the most stable surface at U = 0.8 V_{SHE} and pH = 0, the following order of ΔG_R is found: *O-FeN_4C_A < *O-FeN_4C_Z < *O-FeN_4C_{10} < *OH-FeN_3C_{10} < *O-FeN_4C_{12} < *O-FeN_3C_Z < *O-FeN_3C_A < *OH-FeN_4C_8.

At 0.2 - 0.9 V_{SHE} and pH = 0; the thermodynamic driving force toward the dissolution of the FeN_4C_{12} site is about 0.70 eV greater than that of the FeN_4C_{10} site, suggesting that the FeN_4C_{10} site is more stable than FeN_4C_{12} site under acid condition, in line with the experiments by Li *et al.* [18]. The horizontal bars in Figure 3.3 indicate the most stable dissolved species at each condition. The dissolution reactions change with the working condition (U_{SHE} and pH) and the local carbon structures. For the FeN_4C_8, FeN_3C_A, and FeN_3C_Z structure, the dissolution reaction results in 0-1 proton transferred to the carbon cavity, while 1 - 3 protons are transferred to the carbon cavity of the other structures. The protonation reaction at the carbon cavity is thermodynamically favorable for the N_4C_{12}, N_3C_{10}, N_4C_Z, N_4C_A, N_4C_{10}, and N_3C_Z dissolved-metal carbon cavity, but it is thermodynamically unfavorable for the N_3C_A and N_4C_8 structure, see Figure A.2 in Appendix A.

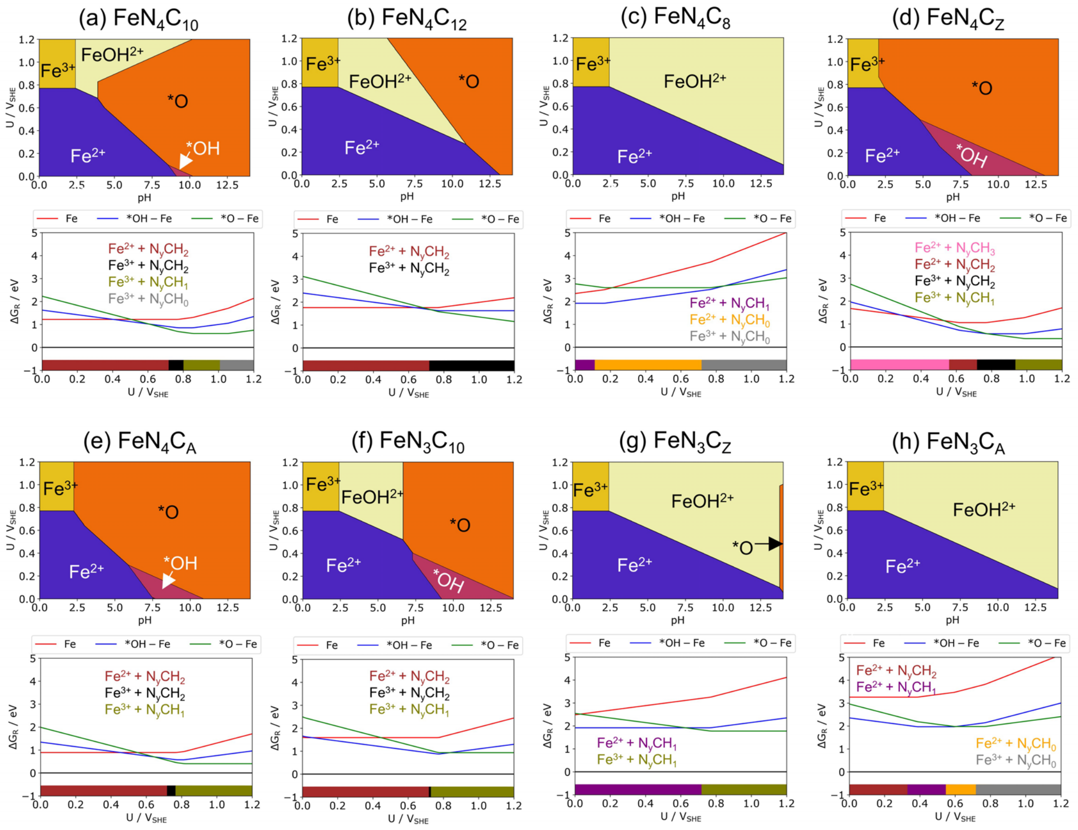

Figure 3.3: (top) Stability diagram and (bottom) ΔG_R at pH = 0 of the considered Fe/N/C structures without and with the adsorbate (Fe, *OH-Fe, and *O-Fe): (a) FeN_4C_{10}, (b) FeN_4C_{12}, (c) FeN_4C_8, (d) FeN_4C_Z, (e) FeN_4C_A, (f) FeN_3C_{10}, (g) FeN_3C_Z, and (h) FeN_3C_A.

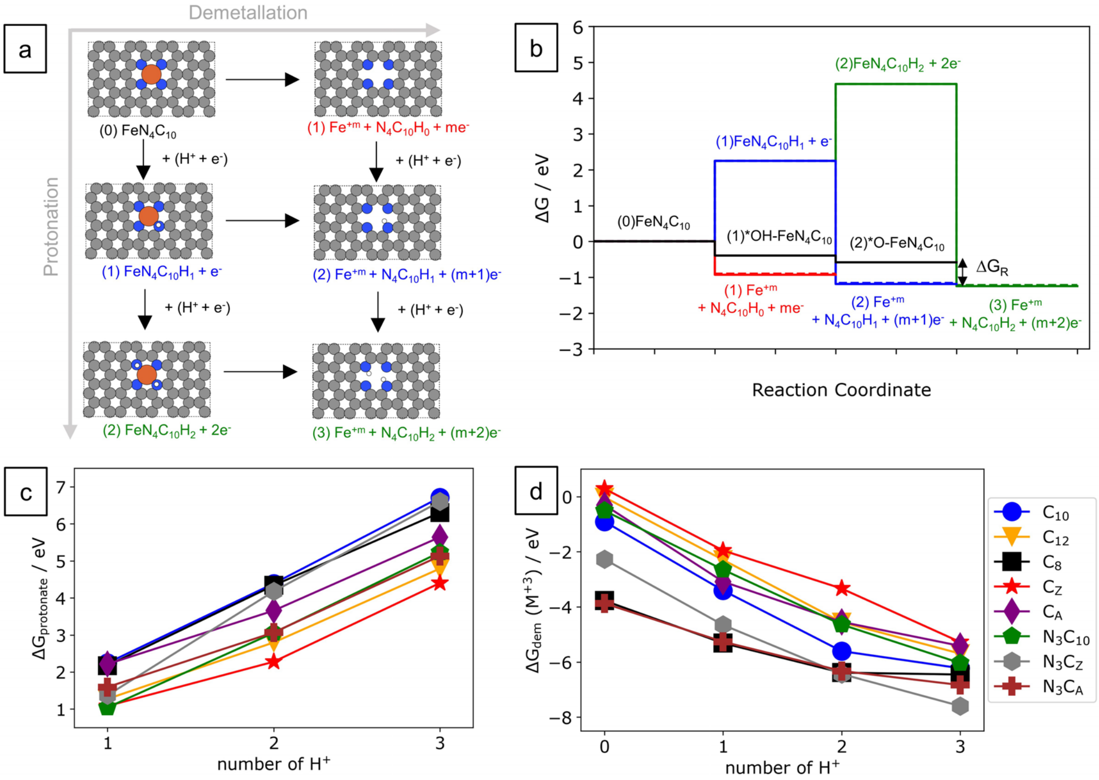

Figure 3.4: (a) Scheme illustration of a possible dissolution mechanism of FeN_4C_{10} structure. (C = gray, N = blue, H = white, M = orange), (b) Free energy diagram corresponding to the possible dissolution mechanisms of FeN_4C_{10} structure with up to $3H^+$ at U = 0.8 V_{SHE} and pH = 0, (c) $\Delta G_{protonate}$ at the atoms surrounding the Fe atom in considered Fe/N/C structures as a function of number of H^+ at pH = 0 and U = 0.8 V_{SHE}, (d) ΔG_{dem} for the Fe atom from the considered Fe/N/C structures to dissolved Fe^{3+} ion as a function of number of H^+ at pH = 0 and U = 0.8 V_{SHE}. Figure (c-d) uses the same markers and colors.

From a thermodynamic perspective, whether the protonation occurs before or after the demetallation leads to the same overall dissolution reaction and relative stability as shown in Figure 3.4 (a-b). However, the proton transfers might not necessarily affect the kinetic dissolution rate if they occur late in the exothermic process. Therefore, the protonation reaction occurring at the atoms surrounding the Fe atom, followed by the demetallation, is considered. The reaction free energies for the protonation at the atoms coordinated with the Fe atom ($\Delta G_{protonate}$) and the followed demetallation of the Fe atom to dissolved Fe ion (G_{dem}) are calculated as the following equations and shown in Figure 3.4 (c-d).

$$FeN_yC + n(H^+ + e^-) \rightarrow FeN_yCH_n$$

$$FeN_yCH_n \rightarrow Fe^{x+} + N_yCH_n + xe^-$$

$$\Delta G_{\text{protonate}}(U_{\text{SHE}}, \text{pH}) = G(\text{FeN}_y\text{CH}_n) - G(\text{FeN}_y\text{C}) - n\Delta G_H - n\Delta G_e \tag{3.13}$$

$$\Delta G_{\text{dem}}(U_{\text{SHE}}) = G(\text{N}_y\text{CH}_n) + G(\text{Fe}^{+x}) + x\Delta G_e - G(\text{FeN}_y\text{CH}_n) \tag{3.14}$$

where $G(\text{FeN}_y\text{CH}_n)$ is the total free energy of the FeN_yC with n H atoms at the atoms coordinated with the Fe atom. The protonation at the atoms coordinated with the Fe atom is an endothermic process and becomes more thermodynamically unfavorable as the potential increases or more protons are added. On the other hand, the demetallation becomes more favorable after the atoms coordinated with the Fe atom are protonated and become more thermodynamically favorable as the potential increases or more protons are added. At the potential U = 0.8 V_{SHE} and pH = 0, the reaction free energy for the protonation at the atoms surrounding the Fe atom is likely to increase from the $\text{FeN}_4\text{C}_Z < \text{FeN}_4\text{C}_{12} \approx \text{FeN}_3\text{C}_{10} \approx \text{FeN}_3\text{C}_A < \text{FeN}_3\text{C}_Z \approx \text{FeN}_4\text{C}_A < \text{FeN}_4\text{C}_{10} < \text{FeN}_4\text{C}_8$. After the protonation, the reaction free energy for the demetallation is likely to increase from the $\text{FeN}_4\text{C}_8 \approx \text{FeN}_3\text{C}_A < \text{FeN}_3\text{C}_Z < \text{FeN}_4\text{C}_{10} < \text{FeN}_4\text{C}_A \approx \text{FeN}_3\text{C}_{10} \approx \text{FeN}_4\text{C}_{12} < \text{FeN}_4\text{C}_Z$.

It is found that the Fe atom in the FeN_4C_8, FeN_3C_Z, and FeN_3C_A structure bond weakly with the carbon structure, compared to the others. As a result, the Fe atom in these structures can easily leave the carbon structure, even without the protonation at the atoms around the Fe atom. A previous DFT study by Tan *et al.* [26] also reported the weak bonding between the single Fe atom with the carbon structure in the FeN_4C_8 structure and suggested the thermodynamic instability of FeN_4C_8 structure.

The protonation at the atoms surrounding the Fe atom in the considered Fe/N/C structures weakens the bond between the Fe atom and the carbon host structure, making the followed demetallation more facile. Thus, the basicity of neighboring atoms and the bonding strength between the single Fe atom and the carbon host structure contribute to the stability of the Fe/N/C catalyst under acidic conditions. The $\text{FeN}_4\text{C}_{12}$ has a strong bonding between the Fe atom and the carbon host structure, but the nitrogen atoms around the Fe metal site are vulnerable to proton. While the nitrogen ligand in the FeN_4C_8 structure can resist the action of protons in an acid solution but the bonding between the Fe atom and the carbon host structure is too weak. Therefore, both structures are predicted to be less stable than the $\text{FeN}_4\text{C}_{10}$ structure under the same acid conditions. It should be noted that the stability calculation is here analyzed from thermodynamic trends, whereas the kinetic activation energy determines the rate of metal leaching. Therefore, a complete stability descriptor would require kinetic analysis of the dissolution mechanism.

According to the previous study on the dissolution of the $\text{FeN}_4\text{C}_{10}$ motif on the bilayer-graphene by Holby *et al.* [27], the unit cell size and the graphene underlayer can influence the calculated stability. In order to assess the sensitivity to these choices, the FeN_4C structures with a bigger unit cell are given in Figure A.3 of Appendix A. It can be seen that there is an influence of the size of the unit cell on the calculated stability. The change in the unit cell size leads to the variation in the dissolution potential toward the dissolved Fe^{2+} ion (n = a = b = 0 and x = 2 in Equation 3.12) about 0.08 V_{SHE}. However, the same trend in the dissolution potential order is obtained from both of the unit cell size which is FeN_4C_8 (-1.09, -0.98) < $\text{FeN}_4\text{C}_{10}$ (0.35, 0.27) < FeN_4C_A (0.65, 0.52)

$< \mathrm{FeN_4C_{12}}$ (0.79, 0.73) $< \mathrm{FeN_4C_Z}$ (0.94, 0.97). The numbers in the parentheses are the dissolution potential to Fe^{+2} in $\mathrm{V_{RHE}}$ unit obtained from the unite cells in Figure 3.1 and bigger unit cells, respectively. The dissolution potential order here agrees with the trend reported by Tan *et al.* [26]. The variation in adsorption free energy of $^*\mathrm{O}$ and $^*\mathrm{OH}$ on the Fe atom due to the change in the unit cell size is about 0.08 and 0.07 eV, respectively. The ΔG_R trend at $U = 0.8\ \mathrm{V_{SHE}}$ and $\mathrm{pH} = 0$ obtained from the bigger unit cell is $^*\mathrm{O}-\mathrm{FeN_4C_A} < {}^*\mathrm{O}-\mathrm{FeN_4C_{10}} < {}^*\mathrm{O}-\mathrm{FeN_4C_Z} < {}^*\mathrm{O}-\mathrm{FeN_4C_{12}} < {}^*\mathrm{OH}-\mathrm{FeN_4C_8}$, largely agree with results obtained from the unit cells in Figure 3.1. The effect of graphene underlayer on the dissolution potential has been reported by Holby *et al.* [27], causing a higher dissolution potential (about 0.08 $\mathrm{V_{RHE}}$) compared to that on the graphene monolayer. The difference in local atomic structures around the $\mathrm{FeN_4}$ motif; however, cause the variation in the dissolution potential to about 0.30 - 1.43 $\mathrm{V_{RHE}}$, greater than the effect of the graphene underlayer. Thus, the $\mathrm{FeN_4}$ motif embedded on the graphene monolayer is expected to be able to capture the effect of the local carbon structure on the stability.

Up to this point, the calculations use the implicit solvent. The explicit solvent effects on the catalyst surface and adsorbates are investigated in the following section. A single water layer containing 16 H_2O molecules is applied for the catalyst surface without any adsorbate, and a single water layer containing 15 H_2O molecules surrounding the intermediate $^*\mathrm{O}$, $^*\mathrm{OH}$, or $^*\mathrm{OOH}$) is applied for the catalyst surface with the adsorbate. The explicit water layer is applied on only one side of the catalyst surface, the same side as the adsorbate. According to a previous DFT study by Svane *et al.* [121], there is no further stabilization effect when adding explicit water layers on both sides of the $\mathrm{CoN_4C_{12}}$ structure compared to the explicit water layer on only one side [121].

In order to find the minimum energy structure of the explicit water layer, the minima hopping algorithm implemented in the ASE package [122–124] is used. The explicit water layer, either with or without adsorbate, is placed on the $\mathrm{FeN_4C_{10}}$ structure. The minima hopping algorithm is performed to find at least 30 local minima with the maximum force on each atom less than 0.05 eV/Å. Then, the lowest energy structure and the structures within 0.1 eV of the lowest structure are relaxed further until the maximum force on each atom less than 0.025 eV/Å. The minimum energy structure is then used for the binding energy and stability calculations. The minimum energy structures of the explicit water layer on the $\mathrm{FeN_4C_{10}}$ structure without and with intermediate obtained from the minima hopping algorithm are shown in Figure 3.5.

The adsorption energy of the ORR intermediates in the explicit solvation is calculated by replacing one water molecule from the explicit water layer with the adsorbate [125]. This way, the total number of adsorbate and water molecules is kept constant for all situations. The energy of one water molecule in the explicit water layer is assumed to be the average energy of water molecules in the explicit water layer and can be calculated as follows

$$E^{WL}(H_2O) = \frac{1}{16}\Big(E(^*16H_2O) - E(^*)\Big) \tag{3.15}$$

where $E(^*16H_2O)$ and $E(^*)$ are the total energy of the catalyst surface with and without the explicit water layer, respectively. The adsorption energy of $^*\mathrm{O}$ on the metal site with the explicit water layer (at $U_{SHE} = 0$ and pH = 0) can, for the example given by

$$^{*}16H_2O + H_2O \rightarrow ^{*} O \mid ^{*}15H_2O + H_2$$

$$\Delta G^{WL}_{*O} = G(^{*}O \mid ^{*}15H_2O) + G(H_2) - G(^{*}15H_2O) - G(H_2O) \tag{3.16}$$

where $G(^{*}O \mid ^{*}15H_2O)$ is the total free energy of the catalyst surface with the *O adsorbate on the metal site and 15 explicit water molecules around the *O adsorbate. One water molecule in the single water layer is removed to be placed by the *O adsorbate, so $G(^{*}15H_2O)$ is calculated as

$$E(^{*}15H_2O) = E(^{*}16H_2O) - E^{WL}(H_2O) \tag{3.17}$$

It should be noted that only the vibration of the reaction intermediate X is considered and contributes to the $G(^{*}X \mid ^{*}15H_2O)$, where X = O, OH, and OOH.

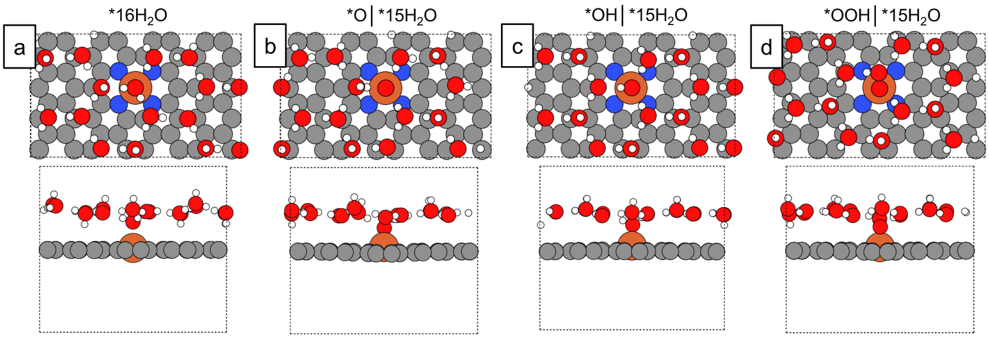

Figure 3.5: The minimum energy structures of the explicit water layer on the FeN_4C_{10} structure obtained from the minimahopping algorithm: (a) $^{*}16H_2O$, (b) $^{*}O \mid ^{*}15H_2O$, (c) $^{*}OH \mid ^{*}15H_2O$, (d) $^{*}OOH \mid ^{*}15H_2O$. (C = gray, N = blue, H = white, O = red, M = orange).

For simplicity, the same single water layer obtained with the FeN_4C_{10} structure is also used for other considered Fe/N/C structures. The explicit solvation effect is investigated on the FeN_4C_{10}, FeN_4C_{12}, FeN_4C_8 and FeN_4C_Z structure as shown in Figure A.4 of Appendix A. The water-to-adsorbate ratios are the same for all considered Fe/N/C structures. However, it should be noted that the explicit water molecules configuration on other considered Fe/N/C structures can be different from that of the FeN_4C_{10} structure, especially for the edged hosted FeN_4 structures. In order to get a more accurate explicit solvation model, the minimahopping algorithm or the ab initio molecular dynamics simulation might be needed for each specific Fe/N/C structure. The trend in the dissolution potential order is likely to be FeN_4C_8 (-1.09, -1.02, -0.93) < FeN_4C_{10} (0.35, 0.47, 0.46) < FeN_4C_{12} (0.79, 1.08, 0.95) < FeN_4C_Z (0.94, 1.04, 0.84). The numbers in the parentheses are the dissolution potential to Fe^{+2} in V_{RHE} unit obtained from each structure with implicit, vacuum, and explicit solvation, respectively. The dissolution potentials toward Fe^{2+} with the implicit solvation are about 0.14 V_{RHE}, lower than those in a vacuum. With explicit solvation, the dissolution potential is close to those in a vacuum, with a variation of about 0.06 V_{RHE}. The except is for the FeN_4C_Z structure. There is about 0.20 V_{RHE} difference in the dissolution potential obtained in a vacuum and explicit solvation. The difference here could be due to the distortion of the structure. With the explicit water layer, the nitrogen atoms of the $N_4C_ZH_0$ structure are distorted out of the plane, see Figure A.4 (d) in Appendix A. While these nitrogen atoms are still on the plane for the other solvations.

With the explicit solvation, $\Delta G(^*O)$ and $\Delta G(^*OH)$ on the Fe atom is stabilized (relative to vacuum) about 0.41 eV and 0.22 eV, respectively. With the implicit solvation, a similar magnitude of the stabilization energy (relative to vacuum) is found, which is 0.30 eV and 0.22 eV for $\Delta G(^*O)$ and $\Delta G(^*OH)$, respectively. For the the considered FeN_4C structures with the explicit solvation, the trend of ΔG_R at U = 0.8 V_{SHE} and pH = 0 is found to be $^*O-FeN_4C_Z < {}^*O-FeN_4C_{10} < {}^*O-FeN_4C_{12} < {}^*O-FeN_4C_8$. Meanwhile, it is found to be $^*OH-FeN_4C_Z < {}^*OH-FeN_4C_{10} < {}^*OH-FeN_4C_{12} < {}^*OH-FeN_4C_8$ in vacuum. The difference in ΔG_R is mainly due to the different stabilization on the adsorbate via the different solvations. It is seen that there is an influence of solvation on the stability calculations. The implicit solvation, which stabilizes about the same as the explicit solvation, is used in the further calculations to avoid structural distortion.

3.4.2 Stability of the M/N/C catalyst

The thermodynamic stability analysis is extended to other transition metal elements (M = Cr, Mn, Co, Ni, and Ru). The stability diagrams of these M/N/C structures are given in Figure A.5 - A.9. Under the ORR-related condition (U ≈ 0.6 - 0.8 V_{SHE} and pH = 0), all considered M/N/C structures are likely to dissolve, so the considered M/N/C structures are unstable under the acidic ORR condition. Figure 3.6 (a) shows ΔG_R of the bare M/N/C structures at U = 0.8 V_{SHE} and pH = 0. Regardless of the metal atom, the MN_4C_8, MN_3C_Z, and MN_3C_A structures are less stable than the others. On the other hand, the MN_4C_A structure is likely to be the most stable structure against dissolution. The general trend in the thermodynamic driving force toward the dissolution of the bare M/N/C structure at U = 0.8 V_{SHE} and pH = 0 is Cr > Mn > Ru > Fe > Co > Ni. In order to understand the stability trend among different metal elements, the dissolution reaction of the bare M/N/C surfaces without the protonation at the carbon cavity is considered.

The energy of the metal atom in the M/N/C structure against forming a bulk metal is investigated as follows

$$\Delta E_{bulk} = E_{DFT}(bulk) + E(N_yCH_0) - E(FeN_yC) \tag{3.18}$$

Figure 3.6 (c) shows ΔE_{bulk} for considered metal atom on different considered local carbon structures. Among considered structures, the metal atom in the MN_4C_8, MN_3C_Z, and MN_3C_A structure is unstable, preferring the bulk metal over the M/N/C structure. Furthermore, the following equation considers the energy for oxidizing the metal atom at a working potential (U = 0.8 V_{SHE}).

$$\Delta E_{oxidize} = G(M^{x+}) - x\Delta G_e - E_{DFT}(bulk) \tag{3.19}$$

where $G(M^{x+})$ is considered to be the free energy of the most stable dissolved metal ion at U = 0.8 V_{SHE} for each metal elements, thus x = 2 for Co, Ni; x = 3 for Cr, Mn, Fe, and Ru. Figure 3.6 (d) shows $\Delta E_{oxidize}$ for considered metal elements. The oxidization energy increases from Cr < Mn < Fe < Co < Ni. For the 3d metals, the metal oxidation energy plays an important role in the dissolution reaction, causing a significant difference in the acid stability among the 3d elements. The stability of the bare M/N/C structures toward the dissolution increases from Cr < Mn < Fe < Co < Ni, following the oxidation trend. For Ru (4d element), the bond strength between the single Ru atom and the carbon structure is weaker than other metal elements in the same carbon structure. However, the Ru atom is more difficult to oxidize. Overall, the stability of the bare Ru/N/C structure is likely to be between the Mn/N/C and Fe/N/C structures.

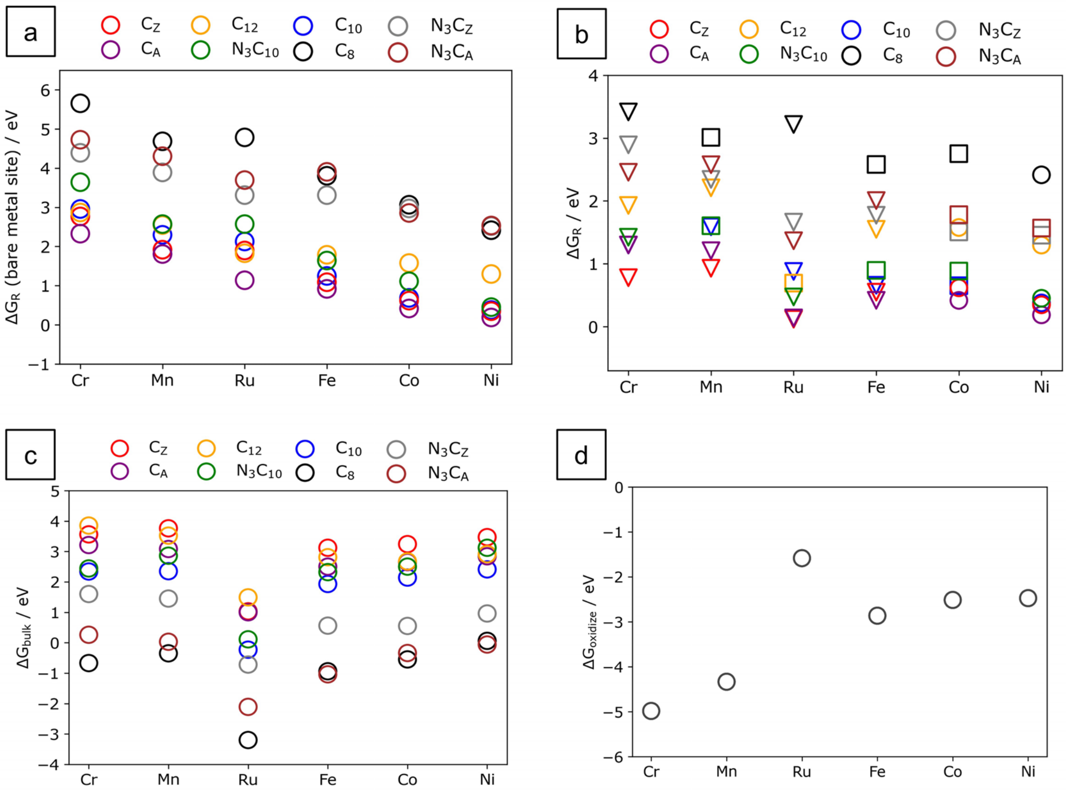

Figure 3.6: ΔG_R at U = 0.8 V_{SHE} and pH = 0 of (a) the bare M/N/C structures and (b) the most stable phase (at U = 0.8 V_{SHE} and pH = 0) of the M/N/C structures. The marker for the surface: M = circle, *OH-M = square, *O-M = triangle. (c) ΔE_{bulk} of M/N/C structures. (d) $\Delta E_{oxidized}$ for metal elements at U = 0.8 V_{SHE}

The formation of *O and *OH is thermodynamically favorable on the Cr, Mn, Ru, and Fe atoms on most considered structures at U = 0.8 V_{SHE} and pH = 0 and results in increased stability against the dissolution. Under the same conditions, the bare metal site is the most stable phase of the considered Co/N/C and Ni/N/C structures. Figure 3.6 (b) shows ΔG_R for the most stable phase of considered M/N/C structures at pH = 0 and U = 0.8 V_{SHE}. In general, the MN_4C_{10} or MN_3C_{10} sites, embedding on the bulk graphene, and the MN_4 site on the graphene edge (MN_4C_Z, MN_4C_A) are more stable than the MN_4 site hosted near micropores (MN_4C_{12}, MN_4C_8) and the unsaturated MN_3 site at the graphene edge (MN_3C_Z, MN_3C_A). Still, the stability of the most stable phase of the M/N/C structure toward the dissolution is likely to increase from Cr < Mn < Fe < Ru < Co < Ni.

A previous study by Singh *et al.* [120] has suggested that the materials with relative stability up to 0.5 eV/atom can persist in electrochemical environments due to insufficient energy gained via dissociation to the Pourbaix stable domains to overcome the energy barrier for the dissociation reaction. Thus, according to our study, the Fe, Co, Ru, and Ni atom in the MN_4C_{10}, MN_4C_Z and MN_4C_A structure can well be kinetically stable under acid conditions. The Ru atom in the MN_4C_Z and MN_4C_A structure, and the Ni atom in the MN_4C_A structure are the most promising stable structure under the acid conditions as the thermodynamic driving force toward the dissolution is less than about 0.2 eV. These results align with the experiment by Cao *et al.*, which found that the dissolution rate of the Ru atom was less than 5% when the Ru/N/C catalyst was operated in the acid solution for 30 hours at the applied potential of 1.5 V_{RHE} [40].

Meanwhile, the Cr and Mn atoms in most considered M/N/C structures have a considerable driving force toward dissolution (> 0.5 eV), so these catalysts are likely to be unstable in the acid condition. According to the experimental study by Sahraie *et al.* [126], the Mn/N/C catalysts lose the ORR activity more than the Fe/N/C catalyst during the stability test (0.5 - 1.3 V_{RHE}) in both acid and alkaline electrolyte.

Additionally, the previous experimental study by Xie *et al.* [19] has reported that in the acid conditions where the potential is cycled between 0.5 - 1.0 V_{RHE}, the Co/N/C catalyst has significantly lower metal leaching compared to the Fe/N/C catalyst, especially when purged with O_2. According to our calculations, the thermodynamic driving force toward the dissolution of the bare Fe/N/C structures is about 0.56 eV higher than that of the Co/N/C structures under acid conditions. When either the *OH or *O adsorbs on the metal site, the relative stability of the most stable phase of both metal atoms is comparable. The experimental study by Xie *et al.* has also reported lower carbon oxidation on the Co/N/C catalyze surface than on the Fe/N/C catalyst surface [19]. While the carbon surface oxidation has been proposed to be able to inactivate the M/N/C catalyst toward the ORR [17] and trigger the demetallation [26]. Thus, Xie *et al.* have suggested the reasons for the enhanced durability of the Co/N/C catalyst under the acid conditions compared to the Fe/N/C catalyst are because the degradation via the chemical oxidation on the catalyst surface and the active site demetallation is alleviated [19]. The effect of carbon surface oxidation on the stability of the M/N/C catalysts would undoubtedly be interesting to study.

The formation of *O and *OH on carbon atoms adjacent to the FeN_4 center in the FeN_4C_{10}, FeN_4C_{12} and FeN_4C_Z structure is investigated. The catalyst surface is assumed to be in equilibrium with protons, electrons, and liquid water. As given in Figure A.10 of Appendix A, the formation of *O or *OH on the adjacent carbons is not thermodynamically favored at pH = 0 in the potential range of 0 - 1.2 V_{SHE}. In previous studies by Zhang *et al.* [91] and Jung *et al.* [127], the formation energies of *O from water on various carbon atoms near the CoN_4C_{10} structure is higher than 2.8 eV, also suggesting thermodynamically unfavorable to form *O on the adjacent carbon atoms. However, the carbon surface oxidation could occur via other reactions such as the dissociation of H_2O_2 [17] or *OOH [26].

Furthermore, the effect of the nearby *O and *OH on the dissolution reaction of the FeN_4C_{10} structure is investigated as given in Figure A.11 (a-c). The Fe-N bonding in the FeN_4C_{10} structure and the H-N bonding in the N_4C_{10} structure is strengthened (about 0.49 eV, and 0.86 eV, respectively) by a nearby *OH. Thus, breaking the Fe-N bonds requires more energy. However, the H binding with the carbon cavity is also more energetically favorable. The dissolution reaction of the bare FeN_4C_{10} structure with nearby *OH at U = 0.8 V_{SHE} and pH = 0 occurs via the n = 1 reaction and ΔG_R is about 0.37 eV higher than that of the clean surface. With the nearby *O on the FeN_4C_{10} structure, the Fe-N and H-N bindings become weaker compared to the clean surface (about 0.78 eV and 0.39 eV, respectively). The dissolution reaction of the bare FeN_4C_{10} structure with nearby *O at U = 0.8 V_{SHE}, pH = 0 occurs occur via the n = 0 reaction and ΔG_R is about 0.66 eV higher than that of the clean surface. It can be seen that the oxygen functional groups near the Fe site can affect the stability. While, the formation of these oxygen functional groups (*O, *OH) could depend on the carbon structures [18, 26]. Also, the nature of the metal atom is important to be considered in the formation of oxygen functional groups via the dissociation of H_2O_2 [17] or *OOH[19, 92]. Such an investigation would certainly be interesting but it is beyond the scope of the present study.

In addition to the oxygen functional groups on the carbon surface, the carbon surface could contain additional N heteroatoms. The graphitic N atoms surrounding the FeN_4 site have been reported to improve ORR activity in alkaline, and acidic electrolytes [128]. The stability diagrams of the FeN_4C_{10} with two graphitic N atoms are given in Figure A.11 (d-e). It can be seen that the graphitic N atoms near the FeN_4 center also affect the stability. The thermodynamic driving force toward the dissolution of the bare Fe site in both considered Fe/N/C structures with additional graphitic N atoms at pH = 0, U = 0.8 V_{SHE} is increased compared to the clean surfaces. However, only some specific configurations of the graphitic N atoms are considered here. Different configurations could affect stability so does the activity [128]. The effect of N atoms or other hetero atoms on the carbon surface on the stability and activity of the Fe/N/C catalyst would certainly be interesting but is out of the scope of this present study.

Additionally, the anion-selective adsorption on the active site on the M/N/C catalyst can occur. It has been reported that various anions from the electrolytes are competitive with the adsorption of water on the MN_4C_{12} structure (M = Fe, Cr, Mn, and

Co) and can promote the ORR activity [93, 129, 130]. The effect of the electrolyte anion adsorption on the stability of the single atom catalyst will be discussed in Chapter 4.

3.5 ORR Activity

The ORR is considered to proceed through a four-electron associative pathway, and the metal site is considered the active site. A previous theoretical study by Liu *et al.* [30] has reported that the activation energy for the direct O_2 dissociation reaction is higher for the OOH dissociation reaction on the FeN_4C_{10}, FeN_4C_{12}, and FeN_4C_8 structure; thus, the OOH dissociation path is kinetically more feasible than the O_2 dissociation pathway. It is assumed that the ORR will proceed without hindrance if the reaction free energy of all elementary steps is negative, assuming no kinetic barrier for each step. The four elementary steps can be expressed as

$$O_2 + H^+ + e^- + ^* \rightarrow ^* OOH$$
$$^*OOH + H^+ + e^- \rightarrow ^* O + H_2O$$
$$^*O + H^+ + e^- \rightarrow ^* OH$$
$$^*OH + H^+ + e^- \rightarrow ^* + H_2O$$

At pH = 0 and U = 0 V_{SHE}, the reaction free energy of the consecutive step along the ORR can be expressed as follows

$$\Delta G_1 = \Delta G_{*OOH} + \Delta G_{H_2O} \tag{3.20}$$
$$\Delta G_2 = \Delta G_{*O} - \Delta G_{*OOH} \tag{3.21}$$
$$\Delta G_3 = \Delta G_{*OH} - \Delta G_{*O} \tag{3.22}$$
$$\Delta G_4 = -\Delta G_{*OH} \tag{3.23}$$

where ΔG_{*OOH}, ΔG_{*O} and ΔG_{*OH} are the adsorption free energy of *OOH, *O and *OH on the metal site at pH = 0 and U = 0 V_{SHE}, which are defined relative to water.

$$\Delta G_{*OOH} = G(^*OOH) + \frac{3}{2}G(H_2) - G(^*) - 2G(H_2O) \tag{3.24}$$
$$\Delta G_{*O} = G(^*O) + G(H_2) - G(^*) - G(H_2O) \tag{3.25}$$
$$\Delta G_{*OH} = G(^*OH) + \frac{1}{2}G(H_2) - G(^*) - G(H_2O) \tag{3.26}$$

At any considered pH and U_{SHE}, the reaction free energy of the consecutive step along the ORR can be expressed as follows

$$\Delta G_i(U_{SHE}, pH) = \Delta G_i - \Delta G_H - \Delta G_e \tag{3.27}$$

where ΔG_i (i = 1 - 4) is the reaction free energy of the consecutive step along the ORR at pH = 0 and U = 0 V_{SHE}. An initial chemical step of O_2 adsorption is not explicitly considered. A previous theoretical study by Svane *et al.* [93] has reported that the

O_2 adsorption on the bare metal sites in the MN_4C_{12} structure is exothermic ($\Delta H < 0$ eV), ranging from -0.57 eV on the CrN_4C_{12} to 0.03 eV on the FeN_4C_{12}. Furthermore, a previous theoretical study by Liu *et al.* [30] has predicted that the adsorption energy for O_2 is -0.63 eV on the FeN_4C_{12} structure, -0.95 eV on the FeN_4C_{10} structure and -1.67 eV on the FeN_4C_8 structure. These suggest that the O_2 adsorption has surmountable barriers at room temperature.

The thermodynamic limiting potential (U_L) is defined as the highest potential at which all elementary steps are downhill in free energy. The elementary step with the most positive free energy at U = 0 V_{SHE} is the potential determining step which firstly becomes uphill in free energy when the potential increases. The U_L and overpotential can be calculated as follows

$$U_L = -\max\{\Delta G_1, \Delta G_2, \Delta G_3, \Delta G_4\}/e \tag{3.28}$$

$$\text{overpotential} = U_{eq} - U_L \tag{3.29}$$

The equilibrium potential of the ORR is U_{eq} = 1.23 V, corresponding to the situation where the reaction has the maximum potential allowed by thermodynamics. Therefore, $U_L = U_{eq}$ for the ideal catalyst. However, the U_L is generally lower than U_{eq}, and the overpotential represents the additional potential needed to proceed with the ORR. The larger the overpotential, the lower activity of the catalyst.

Depending on the local carbon structures and the metal atom, the formation of *OH and *O on the metal site can be thermodynamically favorable. The *OH or *O binds strongly on the metal site in the MN_4C_8, MN_3C_Z, and MN_3C_A structures compared to the others. The metal site in these structures is likely to be occupied by *OH or *O under the ORR-related condition. Due to the metal site embedded on the two-dimensional nitrogen-doped carbon surface, two sides of the metal atom can expose to the electrolyte. The metal site already occupied by one *OH or *O would still have the other side available for the ORR to proceed. The adsorbate ligand can modify the electronic states of the metal site, affecting the binding of the second adsorbate on the other side [10, 93, 121, 131, 132]. The ORR activity of the M/N/C structures, including the adsorbate ligand (OH or O), is considered in the following section. The adsorbate ligand is the most stable adsorbate on the metal site at U = 0.8 V_{SHE} and pH = 0, a representative condition at which the PEMFC would be operated.

There is a scaling relation between $\Delta G(^*OH)$ and $\Delta G(^*OOH)$ on considered structures including ligand on the back side of the metal atom (with the mean absolute erre (MEA) of 0.11 eV). This scaling relation is known for metal and oxide surfaces [133].

$$\Delta G(^*OOH) = \Delta G(^*OH) + 3.23 \tag{3.30}$$

A similar scaling relation obtained from the MN_4C_{12} structures has been previously reported by Svane et al. [93]. This scaling relationship implies that the best liming potential is 0.83 V_{SHE}, resulting in the minimum overpotential of 0.4 V_{SHE}. The limiting potential as a function of $\Delta G(^*OH)$ for each metal atom in considered M/N/C structures is shown in Figure 3.7.

The ORR activity of the Fe/N/C structures is firstly discussed. The adsorption of the *OH on the bare Fe site is strong. Thus the ORR is limited by the reduction of *OH to H_2O. The order of the overpotential on the bare Fe site is found to be: FeN_4C_{12} (0.60 V_{SHE}) < FeN_4C_A (0.77 V_{SHE}) < FeN_4C_{10} (0.83 V_{SHE}) < FeN_4C_Z (0.95 V_{SHE}) < FeN_3C_{10} (1.18 V_{SHE}) < FeN_4C_8 (1.65 V_{SHE}) < FeN_3C_Z (1.79 V_{SHE}) < FeN_3C_A (2.13), agreeing with a previous theoretical study by Yang *et al.* [134]. At U = 0.8 V_{SHE} and pH = 0, the either *OH or *O can be formed on the metal site, depending of the local carbon structures. The presence of OH and O ligands weakens the binding strengths of the ORR intermediates on the Fe site compared to the bare Fe site. Considering the ORR activity on the Fe/N/C structures with the most stable adsorbate at U = 0.8 V_{SHE} and pH = 0 as a ligand on the back side, the following order of the overpotential is found: *OH-FeN_4C_8 (0.43 V_{SHE}) < *O-FeN_3C_Z (0.54 V_{SHE}) ≈ *OH-FeN_3C_{10} (0.54 V_{SHE}) < *O-FeN_3C_A (0.56 V_{SHE}) < *O-FeN_4C_{10} (0.63 V_{SHE}) < *O-FeN_4C_{12} (0.80 V_{SHE}) < *O-FeN_4C_A (0.81 V_{SHE}) < *O-FeN_4C_Z (1.06 V_{SHE}).

For other considered metal elements, the ORR intermediates bind strongly on the bare Cr, Mn, and Ru sits, especially in the MN_4C_8, MN_3C_Z, and MN_3C_A structures. The ORR activity is located on the left leg of the volcano plot, restricted by the reduction of *OH to H_2O. The OH and O ligands, which are also expected on these metal atoms under the ORR-related condition, can weaken the binding strengths of the ORR intermediates on the metal site. Thus, the OH and O ligand can enhance the ORR activity. Especially on the unsaturated MN_3C_Z, and MN_3C_A structures, it is found that the OH and O ligand results in higher ORR activity than the bare metal site in the same local carbon structure.

The binding strengths of the ORR intermediates on the bare Co site are weaker than the previously discussed metal elements. Still, the ORR intermediates are found to strongly bind on the bare Co site, especially on the MN_4C_8, MN_3C_Z, and MN_3C_A structures. The ORR activities of the considered Co/N/C structures are also on the left leg of the volcano but located nearer to the top than previously discussed metal elements. Except for the bare CoN_4C_{12} site, the ORR is limited by the reduction of *OH to H_2O. The OH and O ligands weaken the ORR intermediates' binding strengths on the Co site. Unlike previously discussed metal atoms, the ligand negatively affects the ORR activity on the CoN_4C_{12}, CoN_4C_Z, and CoN_4C_A structure. This is becuase the activity of these structures without the ligand is already near the top of the volcano. However, under the ORR-related condition (U = -0.8 V_{SHE}, pH = 0), the ligand is expected only on the CoN_3C_{10}, CoN_3C_Z, and CoN_3C_A structure which can substantially enhance the ORR activity, compared to the bare Co site with the same local carbon structures.

For the Ni/N/C structures, the ORR intermediates bond weakly with the bare Ni site, and the adsorption of O and OH ligands are not thermodynamically favorable under the considered condition, except on the NiN_3C_A and NiN_3C_Z structure. The ORR activity on considered Ni/N/C structures under the ORR-related condition is limited by the formation of *OOH, and is lower than other metal elements.

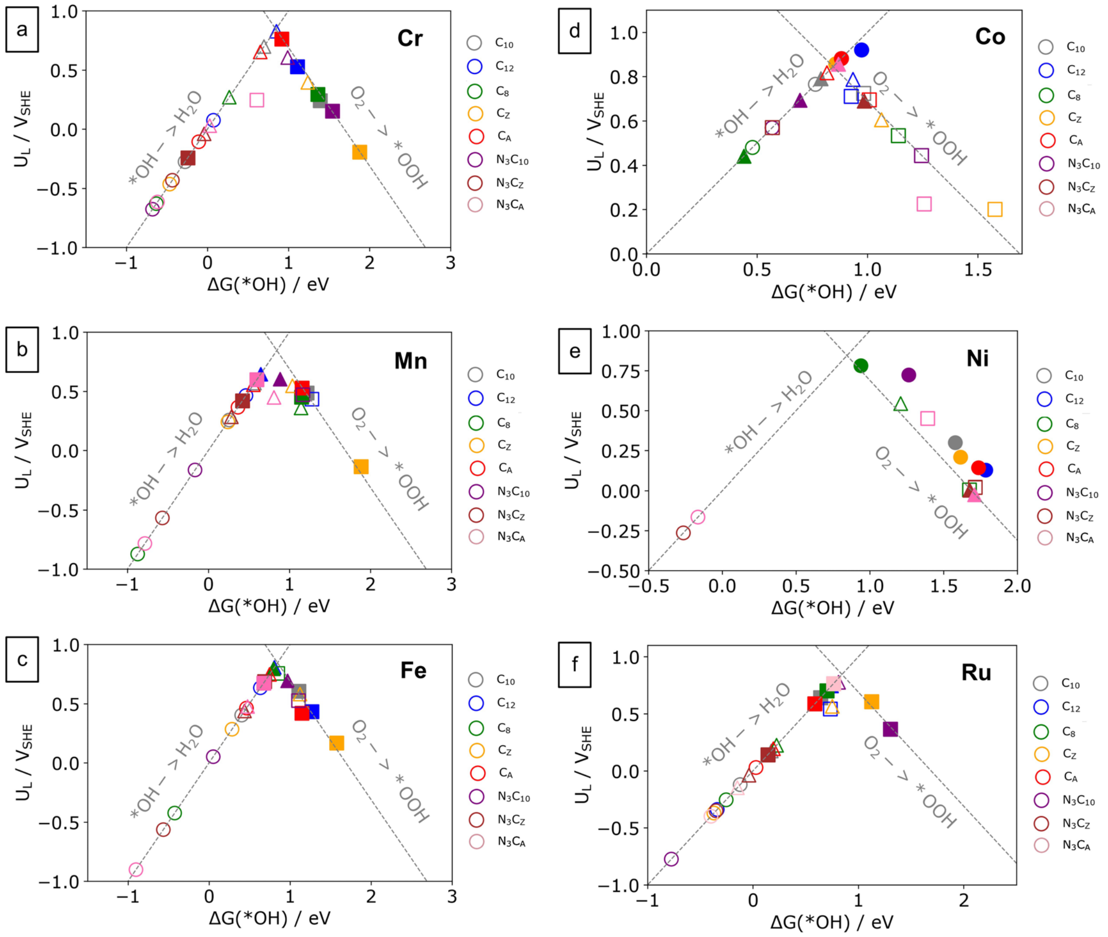

Figure 3.7: U_L as a function of $\Delta G(^*OH)$: (a) Cr/N/C, (b) Mn/N/C, (c) Fe/N/C, (d) Co/N/C, (e) Ni/N/C, (f) Ru/N/C structure. The U_L of the most stable phase (at pH = 0 and U = 0.8 V_{SHE}) are marked with filled color. The marker for the surface: M = circle, *O-M = square, *OH-M = triangle.

In general, the adsorption free energy of the ORR intermediate on the bare metal site embedded in the same local carbon structures is likely to increase from: Cr < Mn < Ru < Fe < Co < Ni. Under the ORR-related condition, the ligand atom is likely to occur on the Cr, Mn, Fe, and Ru atoms. The presence of O or OH ligand weakens the binding strength of the ORR intermediate, leading to a modified ORR activity. Among the different local carbon structures, the binding strength of the ORR intermediate on the bare metal site in the MN_4C_8, MN_3C_Z, MN_3C_A structure is stronger than the others. Under the ORR-related condition, the ORR on these structures always proceeds with the ligand on the back side, also leading to a substantial change in the ORR activity compared to the bare metal site with these local carbon structures.

With the presence of one adsorbate on MN_4C_8 structure, it is found that the metal atom is likely to lay above the basal plane, forming a distorted square-pyramidal geometry instead of a square-pyramidal geometry. The metal site then prefers a higher magnetization state (the number of spin up - the number of spin down) and stronger binding with the adsorbate compared to the square-pyramidal geometry.

Considering the FeN_4C_{12}, FeN_4C_{10}, and FeN_4C_8 structures as an example in Figure 3.8. The pristine structures of the FeN_4C_{12}, FeN_4C_{10}, and FeN_4C_8 structure are in a square planar geometry. The d-orbitals splitting of the metal center is based on the crystal field theory. The oxidation station on the metal center in the pristine FeN_4 structure is considered to be 2+, and the electronic configuration in the d-orbitals of the metal center is considered based on the converged magnetization projected on the metal atom. In this way, the Fe^{+2} in the square planar geometry has two unpaired electrons in the d-orbitals. When *OH bonds with the Fe center, one d-electron is transferred to the *OH. The *OH-FeN_4C_{12} and *OH-FeN_4C_{10} structure are in the square pyramidal geometry where the Fe^{3+} has only one unpaired electron in their d-orbitals. For the *OH-FeN_4C_8 structure, the *OH adsorption causes the elevation of the Fe atom about 0.80 Åabove the catalyst plane. The distortion could lead to a different orbital configuration, as suggested by Jurca *et al.* [135]. The possible electron configuration in the d-orbital splitting associated with the distortion is shown in Figure 3.8 (b). Three unpaired electrons remain in the d-orbital, resulting in a higher magnetization state. This electron configuration could have lower energy than those in the square-pyramidal geometry or allow the d-electron donated from the metal atom to be more facile. As a results, the *OH adsorption on the FeN_4C_8 structure is more energetically favorable than on the FeN_4C_{12} and FeN_4C_{10} structure.

It should be noted that the pristine structure of the edge-hosted MN_4C_Z and MN_4C_A site is also in a square planar geometry and have a similar converged magnetic moment on the metal atom as the bulk-hosted MN_4C_{10} structure either with and without one *OH. Thus, we expect a similar d-electronic configuration for both edge-hosted and bulk-hosted MN_4 sites. Additionally, the d-band center change due to the structure change from the bulk-hosted MN_4 site to the edge-hosted MN_4 site varies with the metal center atom, and there is no correlation between the d-band center and the adsorption energy strength of the reaction intermediate.

According to Figure A.12, the distorted square-pyramidal geometry upon the intermediate adsorption resulting in a high magnetization is seen in the *OH-MN_4C_8 structure with M = Mn, Ru and Co, compared to those on *OH-$MN_4C_{x=10,12}$ structure. Although the magnetization of the metal atom in the *OH-MN_4C_8 structure with M = Cr and Ni are not different from other *OH-$MN_4C_{x=10,12}$ structures, the elevation of the metal atom and the adsorption strength is relatively higher than the other *OH-$MN_4C_{x=10,12}$ structure.

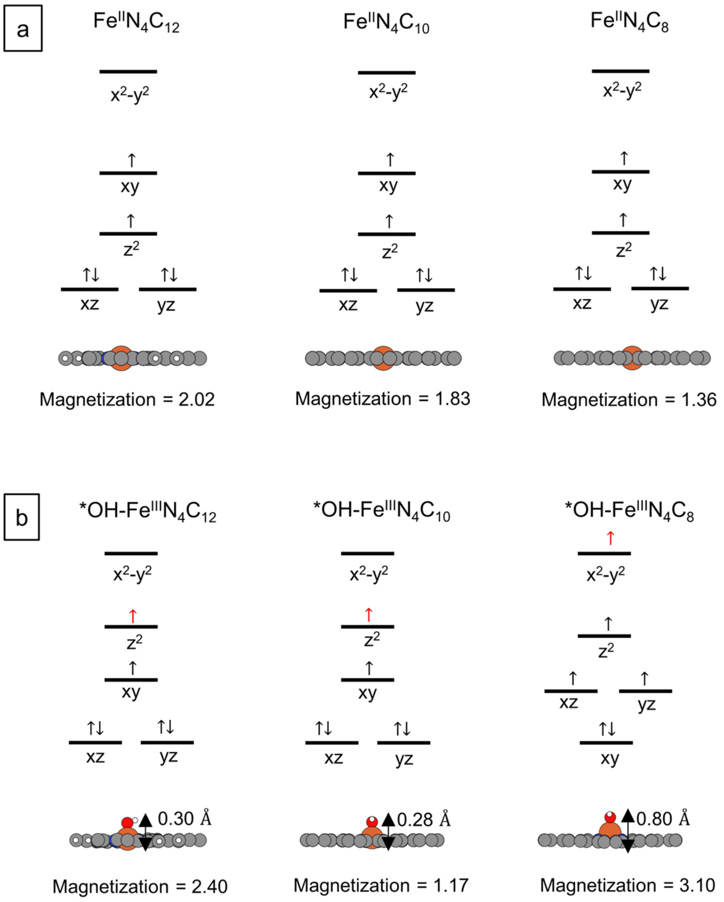

Figure 3.8: The d-orbital splitting and electronic configuration in d-orbitals for Fe atom in (a) FeN_4C_{12}, FeN_4C_{10}, and FeN_4C_8 structure in a square-planar geometry. (b) *OH-FeN_4C_{12}, *OH-FeN_4C_{10} structure in a square pyramidal geometry and *OH-FeN_4C_8 structure in a distorted square pyramidal geometry. The electron donated to the adsorbate is red, and the remaining electrons in the d-orbitals are black. The relative position of the energy level is qualitative only. Magmom is the converged magnetization (number of spin-up + spin-down) projected on the Fe atom. The insets show the structures with the height of the Fe atom above the N_4 plane. (C = grey, N = blue, H = white, Fe = orange, O = red). The oxidation of the Fe atom in the pristine FeN_4C structure is 2+, and it is 3+ with *OH.

Furthermore, the MN_3C_Z and MN_3C_A structures also bond with the adsorbate strongly, regardless of the metal atom. The possible explanation is that the metal atom in these two unsaturated structures has an oxidation state of 1+. Therefore, the metal atom prefers at least one bonding with the adsorbate to change the oxidation from 1+

to 2+ (or 3+), which is generally favorable for transition metal elements.

Let us consider the Ni/N/C system as an example. It is found that the Ni atom in the NiN_3C_A and NiN_3C_Z structure has the magnetization of 0.96, 0.80, respectively. If the oxidation state is 2+ (Ni^{2+}), there are eight d-electrons arranged in five d-orbitals. Then, a possible magnetization is 0 or 2. If the oxidation state is 1+ (Ni^{1+}), there are nine d-electrons arranged in five d-orbitals. Thus, a possible magnetization is 1, which is found in our calculation results. Furthermore, with the *O or *OH adsorption, the magnetization projected on the Ni atom in these two unsaturated structures is found to be 0. This magnetization value is the same as the Ni atom in the pristine NiN_4C structures with the oxidation state of 2+. Also, the bonding strength with the second adsorbate becomes comparable to that of other pristine NiN_4C structures.

3.6 Stability vs Activity

Combining the stability and activity descriptors, ΔG_R of the most stable surface at U = 0.8 V_{SHE}, pH = 0 is plotted against the overpotential (see Figure 3.9). It can be seen that the FeN_4, CoN_4, and RuN_4 sites mainly on the bulk graphene (MN_4C_{10}, MN_3C_{10}) and the graphene edges (MN_4C_A, MN_4C_Z) are a promising candidates with $\Delta G_R <$ 1.0 eV and the overpotential < 1.0 V_{SHE}. These promising candidates are already well-known M/N/C catalysts and have been experimentally tested as ORR catalysts in acid conditions [12, 19, 90, 91, 95, 128, 136]. The MN_yC structures with M = Cr, Mn are predicted to be unstable under the considered condition as the thermodynamic driving force toward the dissolution is greater than 1 eV. Also, the unsaturated MN_3C_A, and MN_3C_Z structures that exhibit high catalytic activity are not in Figure 3.9 as they are also not stable under the acidic ORR conditions.

It can be seen that Ru/N/C structures are active and stable under the ORR-related condition. Furthermore, the Ru atom has either OH or O ligand on the back side at the considered condition. These results are in line with the experiments by Xiao *et al.* [137], which have reported a higher activity and stability of the Ru/N/C catalyst than the Fe/N/C catalyst in 0.1 M $HClO_4$. Also, they have suggested that the *OH-RuN_4 site is the active and durable site for the Ru/N/C catalyst under acid conditions. In addition, a previous experimental study by Cao *et al.* [40], and Zhang *et al.* [90] have suggested the RuN_4 site with O or OH ligand as the active and durable site of the Ru/N/C catalyst in acid solution.

The experimental study by Zitolo *et al.* [12] has found that the Fe-based moieties experience a structural change and an electronic-state change, implying the formation of O and OH ligand on the Fe site under the operating condition. At the same time, they have found no structural and electronic change for the Co-based moieties. In our study, most considered Fe/N/C structures can have either O or OH ligand on the Fe atom at pH = 0 and U = 0.8 V_{SHE}. While at the same condition, only some of the considered Co/N/C structures have the OH ligand.

It is seen that the stable Co/N/C structures in Figure 3.9 are more active than the stable Fe/N/C structures. The experimental study by Martinez *et al.* [10] reported the

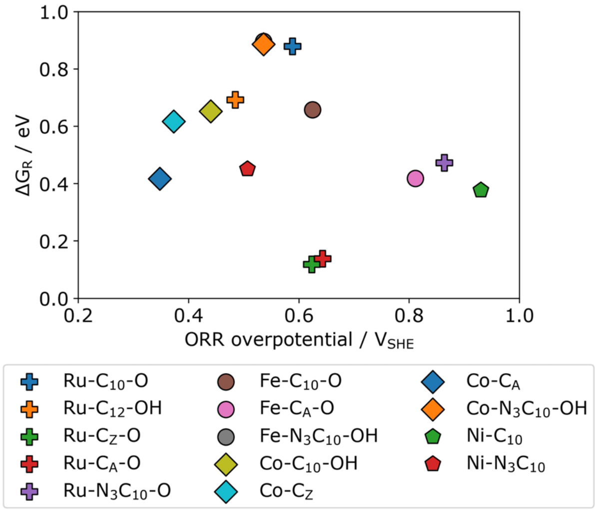

Figure 3.9: ΔG_R of the most stable phase at U = 0.8 V_{SHE} and pH = 0 vs ORR overpotential with nonadsorbing electrolyte ions. The catalysts close to the bottom left corner are expected to be active toward ORR and stable in acid conditions

ORR activity in 0.5 H_2SO_4 in the order of Fe > Co > Mn, suggesting that the Fe/N/C catalyst is more active than the Co/N/C catalyst. Their DFT calculations have suggested the OH ligand on the zigzag-edge host MN_4 as the active site [10]. A previous computational study by Svane *et al.* [93] has identified the ligand on the FeN_4C_{12} and MnN_4C_{12} site in 0.5 M H_2SO_4 solution is HSO_4 and H_2O for CoN_4C_{12} structure, giving the ORR limiting potential order (Fe > Co > Mn) in agreement with the experiments by Martinez *et al.* [10]. The interaction between the M/N/C catalysts with relevant species present in the electrolyte would be interesting to consider and may give a better model that can accurately describe the catalytic activity under experimental conditions. Another possible explanation could be highly selective for the two-electron ORR pathway, potentially lowering catalytic activity for the four-electron ORR pathway. According to the experimental study by Martinez *et al.* [10], the Fe/N/C catalyst has a half-wave potential of 0.80 V_{RHE} and selectivity for the four-electron pathway is more than 95% while the Co/N/C catalyst has a lower half-wave potential of 0.77 V_{RHE} and a lower selectivity for the four-electron path of 90%. Gao *et al.* [138] have also reported high onset potential at around 0.7 V_{RHE} for the Co/N/C and Fe/N/C catalyst, but the Co/N/C catalyst is more selective for the two-electron pathway than the Fe/N/C catalyst.

Additionally, some of the promising stable and active structures in acid conditions are the FeN_3C_{10}, CoN_3C_{10}, and NiN_3C_{10} structures, suggesting that the nearest neighbor interaction can tune the catalytic activity of the M/N/C catalyst on the graphene plane. Therefore, carefully manipulating the heteroatoms around the active site can further improve the catalytic activity while maintaining acid stability. Additionally, for the design strategies to achieve both an active site and stable M/N/C catalyst, the synthesis should aim to increase the site density of MN_4 bulk-hosted structures or the MN_4 on the edge-hosted graphene structure. Avoiding the formation of unsaturated MN_3C_Z or MN_3C_A structure as well as the MN_4C_8 site will increase the stability of the M/N/C catalyst under acid conditions. Further stability improvement for the active M/N/C structures like MN_4C_{12}, MN_4C_8 and the unsaturated structure (MN_3C_Z, MN_3C_A) might be achieved by forming these active structures over another graphitic layer [27]. The metal choice also significantly affects stability and activity, so it should be considered when designing the catalyst. Integrating Fe, Co, and Ru metal elements into graphitic carbon supports like the MN_4C_{10}, MN_4C_Z and MN_4C_A structure would be a promising catalyst for the ORR in acid conditions.

3.7 Conclusions

The systematic investigation of the stability and the ORR catalytic activity of the M/N/C structure with different local carbon structures around the MN_y motif under acid conditions was carried out in this chapter. The stability was considered from the tendency of the metal atom to dissolve into the electrolyte. The results revealed that the local carbon structures play a crucial role in the stability and ORR catalytic activity. All considered M/N/C structures with M = Cr, Mn, Fe, Co, Ni, and Ru are thermodynamically unstable in acidic ORR conditions. The thermodynamic driving forces toward the dissolution suggest that the MN_4 site on the bulk graphene and graphene edge (MN_4C_{10}, MN_4C_A, MN_4C_Z) are more stable against the dissolution than that hosted by the microporous (MN_4C_{12}, MN_4C_8) or in the unsaturated structure (MN_3C_Z, MN_3C_A). The stability also depends on the choice of a metal atom. The M/N/C structures with Fe, Co, Ni, and Ru are more stable under acid conditions than those with Mn and Cr metal atoms. Under the ORR-related conditions, we predicted the most stable phase of the active site in which O or OH ligands can occur on the back side and become a part of the active center. The ORR activity also depends on the choice of the metal atom and the local atomic structure. Combining both stability and activity descriptors, we suggested that the Fe, Co, and Ru atom mostly on the MN_4C_{10}, MN_4C_Z, MN_4C_A, and MN_3C_{10} structure are the promising acid-stable and active ORR catalyst. Rational modification of the carbon matrix and appropriate selection of metal atoms could be carefully used to optimize the activity and stability of the M/N/C catalysts.

Chapter 4

Effect of Electrolyte Anion Adsorption on the Activity and Stability of Single Atom Electrocatalysts

This chapter is based on the work presented in Paper II as given in Appendix D. The stability and activity of the M/N/C catalysts are further studied, including the effect of the electrolyte anion adsorption. This chapter covers the main points and results.

4.1 Introduction

The single metal atom coordinated N-doped carbon (M/N/C) has been recognized as an efficient electrocatalyst. In many experimental and theoretical studies, the Fe/N/C and Co/N/C materials have been identified as active ORR catalysts in acid electrolytes [9, 12, 31, 90, 136]. More recent studies have evidence that the M/N/C catalyst can also be an efficient catalyst for the CO_2RR [139–141]. In the previous Chapter 3, we found that the local coordination plays an important role in catalytic activity and stability of the M/N/C catalyst [18, 30, 35].

Furthermore, since the M/N/C catalysts possess two-dimensional properties, it is distinct from bulk materials, where only one exposed side is responsible for their catalytic activity. Ideally, both sides of the M/N/C catalyst are exposed to electrolytes so they can interact with an adsorbate. It is, therefore, possible that an electrolyte anion or a gas molecule from the environment adsorbs on one side of the M/N/C structure while the other side is still available for the reaction to proceed [129, 130]. The presence of the adsorbate on one side of the single metal atom will modify its electronic states, affecting the binding of the second adsorbate on the other side [93, 142, 143]. Experimental and theoretical studies have considered the effect of anions from the electrolyte or a gas molecule impurity on ORR activity. For instance, Holst-Olesen *et al.* have found that the anions from H_3PO_4- and CH_3COOH-containing electrolytes are beneficial for the ORR activity on the Fe/N/C catalysts [129, 130]. Various combinations of the electrolyte anion ligand and the single metal center in the MN_4C_{12} structures (M = Cr, Mn, Fe, and Co) for improving the ORR activity have studied in a previous theoretical study by Svane *et al.* [93]. Recently, many studies have also reported that the introduction of axial oxygen [13, 144] and halogen atom [90] on the MN_4 site can achieve an efficient catalyst for the CO_2RR.

The stability of the MN_4 site with the presence of a fifth ligand was recently discussed. Glibin *et al.* have previously studied the dissolution reaction of two different FeN_4 sites with the *F ligand. Based on a thermodynamic model, the fluorination on the FeN_4 site can increase the resistance of the single metal site against acid dissolution [104]. The DFT calculations have been used to study the dissolution reaction of the FeN_4 site embedded on a bilayer-graphene by Holby *et al.* [27]. The presence of *OH ligand on the FeN_4C_{10} site has been found to prevent the single Fe site from dissolution [27]. By using in situ Raman spectroscopy to study the Fe phthalocyanine (FePc) molecules and pyrolyzed Fe/N/C catalysts, Wei *et al.* have reported the structural dynamics of the FeN_4 active site in 0.1 M $HClO_4$ solution [145]. At a high potential of about 1.0 V_{RHE}, a non-planar structure is induced by the presence of an adsorbate on the FeN_4 site, preventing FeN_4 site from the dissolution. At a lower potential of about 0.05 V_{RHE}, they have found the irreversible attenuation of the planar Fe-N vibration, which is the evidence for dissolution of the bare Fe center [145]. Using DFT simulations with ^{57}Fe Mössbaur spectroscopy data, Nematollahi *et al.* have compared the DFT calculated and experimental quadrupole splitting energy of doublets (ΔE_{QS}) for different FeN_4 structures (FeN_4C_{10}, FeN_4C_{12}, FeN_4C_8) both with and without ligands [36]. They have suggested that the FeN_4C_8 structure with a fifth ligand such as OH^- and NH^{2-} could be an active and durable site under the acidic ORR conditions [36].

In this chapter, the systematic exploration of the electrolyte anion adsorption effect on the stability and activity of a single metal atom incorporated with N atoms doped into a bulk graphene terrace (MN_4C_{10}) and a graphene edge (MN_4C_A) with M = 3d, 4d, 5d, or p-block (Sn, Sb, and Bi) metal atoms. The interaction between the single metal site and the electrolyte anion is evaluated to understand how the electrolyte anion adsorption thermodynamically influences the dissolution of the single metal site under electrochemical conditions relevant to the ORR and the CO_2RR. In addition, the catalytic activity with the presence of an electrolyte anion ligand for the ORR and CO_2RR is also studied. Finally, the results are used to suggest combinations of metal atom center, local carbon structure, and electrolyte for active and stable catalysts under working conditions.

4.2 Computational Details

The structural models based on the MN_4C_{10} and MN_4C_A sites, as shown in Figure 3.1(a) and (e) are used to investigate the effect of electrolyte anion adsorption in this chapter. These graphene sites are selected because they are among the most stable type of sites, as previously found in Chapter 3. The DFT calculation details are the same as described in Section 3.3. Except that the thermal corrections for the adsorbates (ZPE + U_{vib} - TS_{vib}) at T = 298.15 K are calculated from the adsorbates on the FeN_4C_{10} and FeN_4C_A sites and applied to other metal sites with the same local carbon structure. The thermal corrections for the adsorbates are given in Table B.1 of Appendix B.

4.3 Formation Energy

The formation free energy of the single metal atom doped into the bulk graphene and the graphene edge is calculated as follows

$$\Delta G_f = E(MN_4C) - E(C) + 6\mu_C - \mu_M - 4\mu_N \tag{4.1}$$

where $E(MN_4C)$ is the total energy of the single metal atom doped into graphene. E(C) is the total energy of a pristine graphene sheet or pristine graphene nanoribbon. μ_C is the total energy of the pristine graphene sheet per carbon atom. μ_M is the total energy of metal in its bulk structure per metal atom. The nitrogen chemical potential (μ_N) is treated as a parameter for using different nitrogen precursors in experiments [14, 33, 140, 141, 146, 147]. μ_N is referenced to NH_3, N_2, and H_2 gas molecule at 1 bar.

$$\mu_N(n) = n[G(NH_3) - \frac{3}{2}G(H_2)] + \frac{1}{2}(1 - n)G(N_2) \tag{4.2}$$

where $G(NH_3)$, $G(H_2)$, and $G(N_2)$ are the free energy of NH_3, H_2, and N_2 gas molecule at 1 bar, respectively and n is an integer. When n = 0, the nitrogen reference source is the N_2 gas molecule, and when n = 1, the nitrogen reference source is the NH_3 gas molecule. It is assumed that the nitrogen chemical potential can vary as a function of NH_3, H_2, and N_2 content during the synthesis. The $n < 0$ situation corresponds to the synthesis under the high content of $(N_2 + H_2)$ condition and the $n > 1$ situation corresponds to the synthesis under the high content of NH_3 condition.

Figure 4.1 (a) shows the ΔG_f for MN_4C_{10} and MN_4C_A sites at two different $\mu_N(n)$ with n = 1, 3. When n is more than 1, this can correspond to increasing NH_3 partial pressure during the synthesis. The temperature is considered at T = 1100 °C, a typical temperature in the M/N/C synthesis [12, 14, 139]. Regardless of the metal atom and $\mu_N(n)$, the single atom site is thermodynamically preferred to form at the graphene edge over the bulk graphene. A pyridine vacancy ($PorN_4$) is slightly more stable on the graphene edge than the bulk graphene, and it is likely to be further stabilized if the bulk metal atom is supplied, forming the MN_4 site. Most 3d elements are thermodynamically more favorable to dope into the pyridine vacancy than the 4d-5d elements and p-elements. The formation at T = 1100 °C, becomes thermodynamic favourable when n increases from 1 to 3 (e.g., under the elevated NH_3 partial pressure).

As shown in Figure 4.1 (b), the nitrogen chemical potential changes with the temperature. Thus, the formation free energy depends on the temperature and the nitrogen chemical potential. Considering the formation energy of the CoN_4C_{10} site in Figure 4.1 (c) as an example, with increasing temperature, the formation energy becomes more favorable when $n > 1$. In other words, the synthesis under the high NH_3 partial pressure and high temperature (T > 500 °C) is favorable for the single atom formation. At low temperatures (T < 100 °C), the formation energy become thermodynamic favourable when $n < 0$ (e.g., under high ($N_2 + H_2$) content). The formation energies of other structures as a function of the nitrogen chemical potential at T = 25 and 1100 °C are given in Figure B.2 of Appendix B, where similar results are found. The results suggest that considered single metal sites doped into graphene can be synthesized in a controlled experiment.

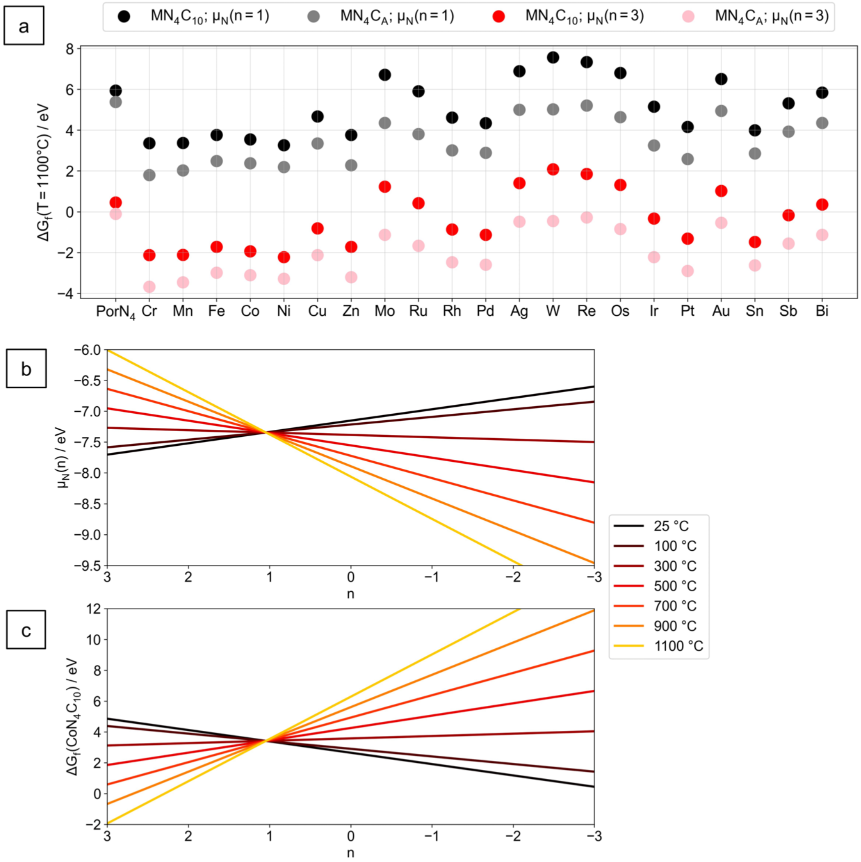

Figure 4.1: (a) ΔG_f for MN_4C_{10} and MN_4C_A sites at T = 1100 °C. (b) $\mu_N(n)$ and (c) ΔG_f of the CoN_4C_{10} site as a function of n at different temperatures.

4.4 Stability Diagram and Relative Stability

Under an electrochemical environment, the single metal atom in the M/N/C structures can interact with anions from the electrolyte. We consider the anions from commonly used electrolytes for the ORR [148, 149] and the CO_2RR [150], e.g., $H_2PO_4^-$, HPO_4^{2-}, PO_4^{3-} in H_3PO_4 solution; HSO_4^-, SO_4^{2-} in H_2SO_4 solution; Cl^- in HCl solution; ClO_4^- in $HClO_4$ solution; NO_3^- in HNO_3 solution; HCO_3^- and CO_3^{2-} in H_2CO_3 solution. Additionally, NO and CO gas molecules and CN^- in HCN solution are included as they have been found to affect the catalytic activity [65, 151, 152]. The complete list of electrolyte anions and poisoning gas molecules considered here is given in Table B.2 and Table B.3 of the Appendix B. It should be noted that the adsorption of CO and NO on the metal site considered in this study does not depend on the pH and applied potential. The adsorption of the anion from the electrolyte on the single metal atom can compete with the water molecule. Thus, in each solution, the adsorption of anion or gas molecules on the metal site competes with the formation of $^*H_2O$, $^*OH$, $^*O$ from the water oxidation or reduction. Also, it is assumed that the catalyst surface is in equilibrium with protons, electrons, and liquid water [96]. Thus, the hydrogen adsorption on the metal site ($^*H$) is also included.

Figure 4.2: Thermodynamic cycle for the calculation of the free adsorption energy of the electrolyte anion in added 0.1 M electrolyte: $\Delta G(^*A^{n-})$ [93, 129].

The adsorption free energy of electrolyte anions is calculated using the thermodynamic cycle [93, 129] as shown in Figure 4.2. The adsorption free energy of the electrolyte anion in added 0.1 M electrolyte at T = 298.15 K can be expressed as follows

$$\Delta G(^*A^{n-}) = \Delta_{CHE}G(^*A) - \Delta G_{sol}(H_nA) - \Delta G_{dilute}(A^{n-}) \tag{4.3}$$

$\Delta_{CHE}G(^*A)$ is calculated according to the computational hydrogen electrode (CHE) [117] and can be written as follows

$$\Delta_{CHE}G(^*A) = G(^*A) + \frac{n}{2}G(H_2) + n\Delta G_e + n\Delta G_H - G(^*) - G(H_nA_{(gas)}) \tag{4.4}$$

$\Delta G_{sol}(H_nA)$ is the free energy for dissolving gaseous H_nA (at 1 bar) in water to form anion and proton at the standard state where $[A^{n-}_{(aq)}] = [H^+_{(aq)}] = 1$ M.

$$\begin{aligned}\Delta G_{sol}(H_nA) &= G(A^{n-}_{(aq,1M)}) + \frac{n}{2}G(H_2) - G(HA_{(gas)}) \\ &= \Delta G_f(A^{n-}_{(aq,1M)}) - \Delta G_f(HA_{(gas)})\end{aligned} \tag{4.5}$$

where $\Delta G_f(A^{n-}_{(aq,1M)})$ and $\Delta G_f(HA_{(gas)})$ are the formation energy of A^{n-} in solution phase (1 M) and H_nA in gas phase (1 bar), respectively.

$\Delta G_{dilute}(A^{n-})$ in Figure 4.2 is the free energy accounting for the concentration difference from the standard state and can be expressed as follows

$$\Delta G_{dilute}(A^{n-}) = RT\ln\left((a_{H^+})^n \gamma [A^{n-}]\right) \tag{4.6}$$

where a_{H^+} and $a_{A^{n-}}$ are the activity of H^+ and A^{n-}, respectively. γ is an activity coefficient of A^{n-}, and $[A^{n-}]$ is the concentration of the electrolyte anion. The electrolyte concentration is 0.1 M, and the pressure of the poisoning gas molecule is 1 bar. At different pH, it is assumed that pH is adjusted by adding non-adsorbing acid and a_{H^+} is calculated from: $\mathrm{pH} = -\log(a_{H^+})$. The concentration of electrolyte anion species ($[A^{n-}]$) in the 0.1 M solutions at each pH is calculated based on its pK_a value. The value of γ, ΔG_f and pK_a are taken from literature [93, 113, 114, 153, 154] and listed in Table B.3 of Appendix B.

Along with the adsorption of the adsorbate, the dissolution of the single metal atom from the graphene host into the electrolyte can occur and result in the dissolved metal ion with charge +x (M^{x+}) and the graphene host cavity (N_4CH_n) as described in Section 3.4. A completed list of E_M(bulk) and ΔG_x for all metal elements considered in this chapter are given in Table B.4 of Appendix B. ΔG_x is taken from literature [113, 118, 119]. The concentration of the dissolved metal ion in the calculations is 10^{-6} M. Furthermore, the stability calculations are considered at T = 298.15 K.

As an example, Figure 4.3 (a) and Figure B.3 (a) show the stability diagram of the CoN_4C_{10} and CoN_4C_A sites in 0.1 M solutions, respectively. Only the most stable phase at each condition is shown in the stability diagram. The stability diagram is divided into different areas with different colors based on the most stable dissolved metal ion and the most stable adsorbate on the metal site, the same way as in the previous chapter. It is seen that the electrolyte anion can compete with water adsorption and become the most favorable adsorbate on a single Co atom. Like the previous chapter, we also consider the relative stability (ΔG_R), which is the free energy difference between the M/N/C catalyst surface (either with or without the adsorbate) and the most stable dissolved species (the dissolved metal ion and carbon host cavity). The ΔG_R indicates the thermodynamic driving force for the dissolution of the metal atom. The more positive the relative stability, the less stable the single metal atom is against the dissolution. As shown in Figure 4.3 (b) and Figure B.3 (b), ΔG_R of the CoN_4 sites is plotted as a function of applied potential at a specific pH (pH = 1 for H_3PO_4, H_2SO_4, and $HClO_4$ solution and pH = 7 for H_2CO_3 + CO solution). The most stable dissolved species for each potential used as a reference for ΔG_R are superimposed as horizontal bars at the bottom in Figure 4.3 (b) and Figure B.3 (b). At potentials above 0.6 V_{SHE} and pH = 1, in 0.1 M H_3PO_4, H_2SO_4, and $HClO_4$ solution, it is seen that $^*H_2PO4$, $^*SO_4$, and $^*ClO_4$ are thermodynamically preferred on the single Co atom and further reduce the thermodynamic driving force toward dissolution compared to $^*OH$ on the single Co atom in H_2O.

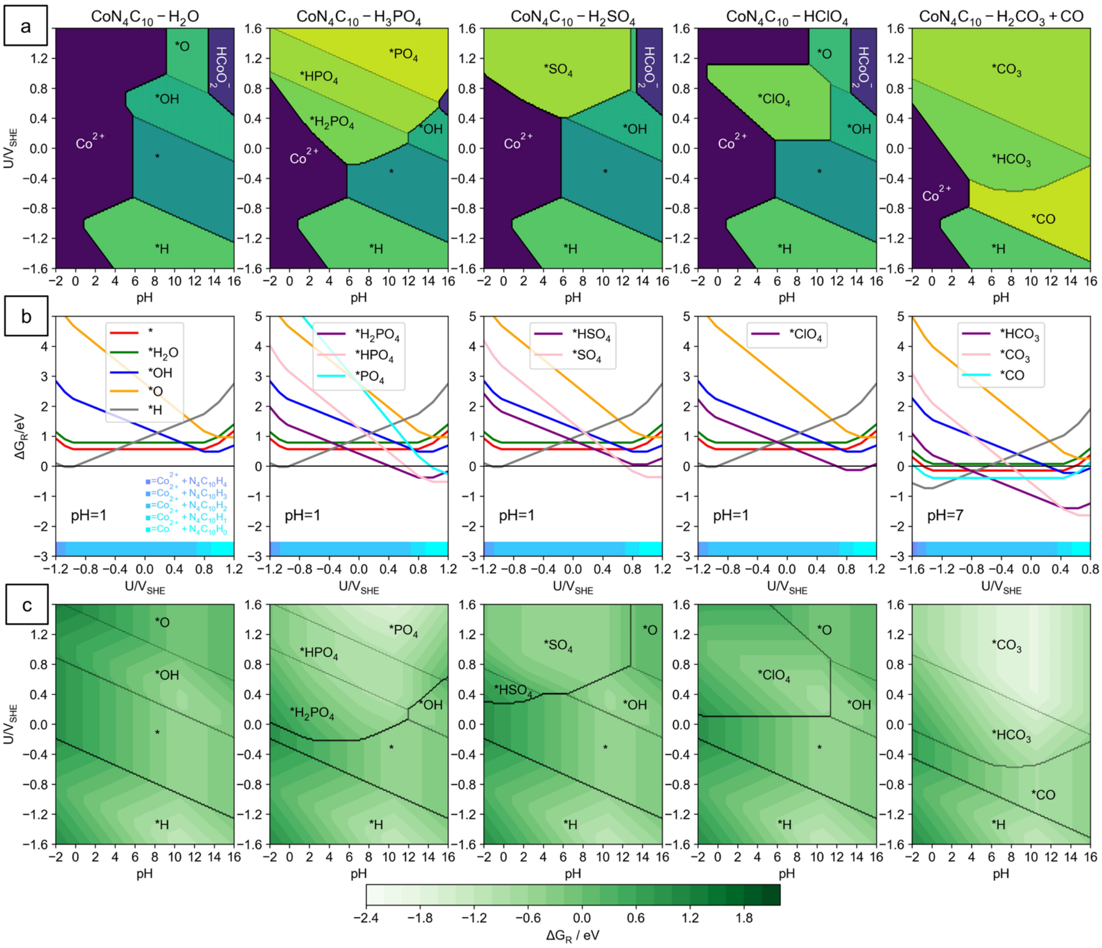

Figure 4.3: (a) Stability diagrams for the CoN_4C_{10} site in 0.1 M solutions. (b) ΔG_R for the sites at specific pH, and (c) stability diagrams for the CoN_4C_{10} site showing the most stable surface, and the background color corresponds to the value of ΔG_R.

The stability and relative stability plots of the FeN_4 site on both bulk graphene and the graphene edge are given in Figure B.4 and B.5 of Appendix B. We find a similar trend where the electrolyte anion is thermodynamically stable on the single metal site at high potential, and the corresponding thermodynamic driving force is lower than the same single metal site in H_2O. Furthermore, the thermodynamic driving force toward the dissolution decreases as the potential increases, suggesting that the demetallation could be dominant at the low potential in the acid condition. These results are in line with the experiments by Choi *et al.* where the Fe demetallation from the Fe/N/C catalyst in 0.1 M $HClO_4$ was observed at potentials below 0.7 V_{RHE} [20].

Under a neutral condition (pH = 7) in 0.1 M H_2CO_3 solution with CO, at U < -0.4 V_{SHE}, it is seen that *H is thermodynamically favorable on the single Co atom over the electrolyte anions. When the potential increases, the anions become the most stable adsorbate on the Co atom. $^*HCO_3$ is at potential around -0.6 to 0.4 V_{SHE} and $^*CO_3$ is at potential above 0.4 V_{SHE}. The thermodynamic driving force toward dissolution is lowered by about 0.46 and 2.18 eV when the $^*HCO_3$ and $^*CO_3$ are stabilized on the Co atom, compared to the $^*CO\text{-}CoN_4C_{10}$ site in H_2O + CO solution, respectively.

4.5 Stability under the ORR-related Condition

The ΔG_R of the most stable surface in 0.1 M electrolytes at pH = 1, and U = 0.80 V_{SHE} for other MN_4 sites is shown in Figure 4.4. Except for $PtN_4C_{x=10,A}$, $PdN_4C_{x=10,A}$, and $AuN_4C_{x=10,A}$ sites, the other MN_4 sites are likely to be stabilized by the adsorbate. Therefore the thermodynamic driving force toward dissolution is reduced compared to the bare metal site. The $PtN_4C_{x=10,A}$, $PdN_4C_{x=10,A}$, and $AuN_4C_{x=10,A}$ sites weakly interact with both electrolyte anions and water molecules, but they are stable against the dissolutions in a wide range of pH and potentials, even without any adsorbate. For the PtN_4 site, our calculation results are in line with a previous experimental study by Li *et al.* [92]. They have found a minor change in the current density of a Pt/N/C catalyst under the accelerated durability tests in 0.5 M H_2SO_4. The relative stability of $IrN_4C_{x=10,A}$ is below zero in the considered electrolytes, so it is stable under the considered ORR-related condition, in agreement with the experiment by Liu *et al.* [155]. During the durability test of the Ir/N/C catalyst in 0.1 M $HClO_4$, they found about 97% current density retention of the Ir/N/C catalyst [155].

For $CrN_4C_{x=10,A}$, $MoN_4C_{x=10,A}$, $RuN_4C_{x=10,A}$, $ReN_4C_{x=10,A}$, and $OsN_4C_{x=10,A}$ sites, the binding strength of the electrolyte anion is weaker than *O in most considered electrolytes. Thus, these metal sites are covered by *O. For the Ru/N/C catalyst, the experimental studies by Zhang *et al.* [91] and Xiao *et al.* [137] have tested its ORR performance in 0.1 M $HClO_4$ and suggested that the active center is the RuN_4 site bonds with axial *O or *OH, agreeing with our calculations.

A previous experimental study has shown a higher activity loss of the Mn/N/C catalyst than the Fe/N/C catalyst in 0.1 M $HClO_4$ under an accelerated stress test where the potential was cycled between 0.5 and 1.3 V_{RHE} [126]. In agreement with this experiment, in 0.1 M $HClO_4$ at U = 0.5 - 1.3 V_{RHE}, the thermodynamic driving force toward the dissolution of the MnN_4C_{10} site is about 0.78 eV higher than that of the FeN_4C_{10} site. For the MnN_4C_A site, it is about 0.57 eV higher than that of the FeN_4C_A site.

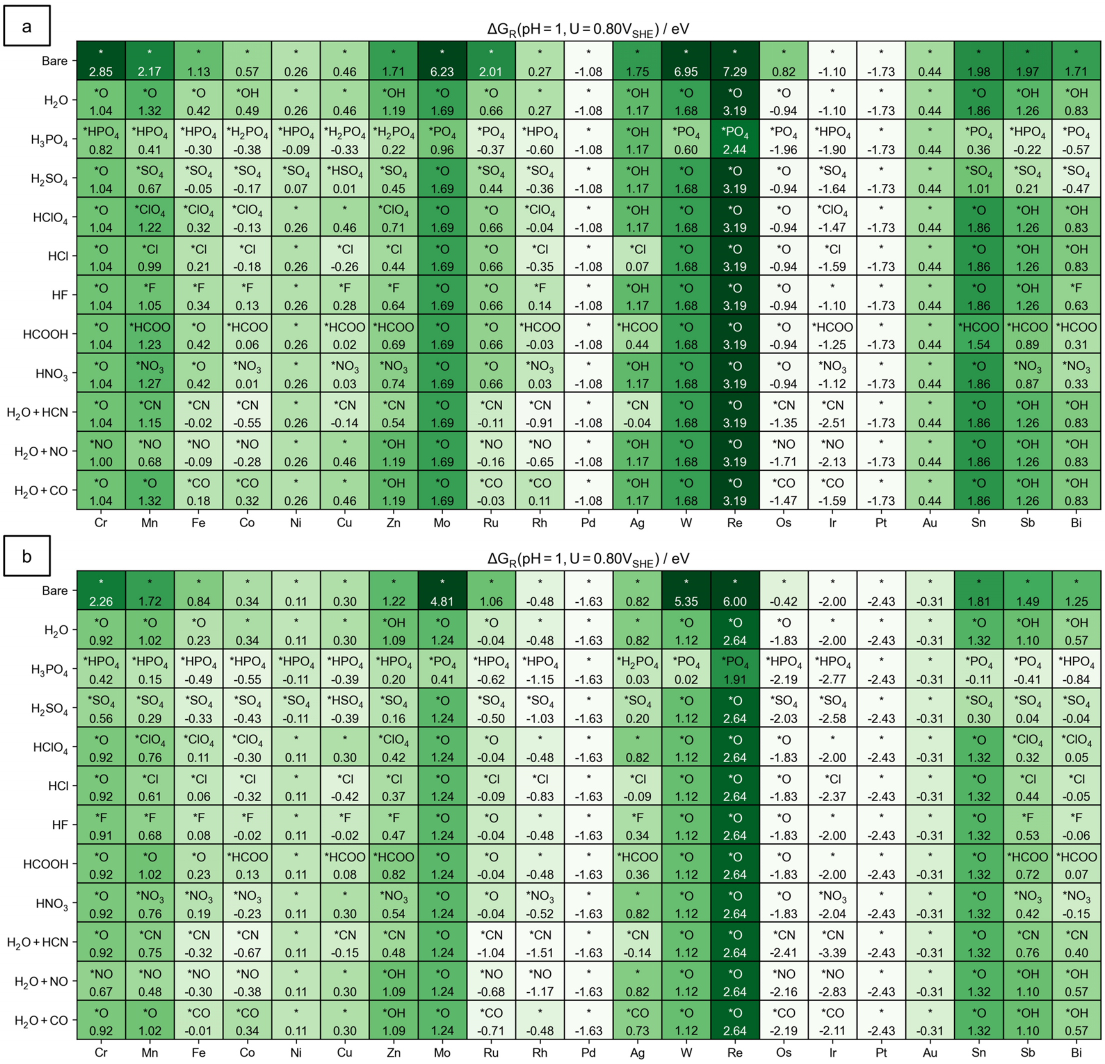

a

$\Delta G_R(pH = 1, U = 0.80V_{SHE})$ / eV

	Cr	Mn	Fe	Co	Ni	Cu	Zn	Mo	Ru	Rh	Pd	Ag	W	Re	Os	Ir	Pt	Au	Sn	Sb	Bi
Bare	* 2.85	* 2.17	* 1.13	* 0.57	* 0.26	* 0.46	* 1.71	* 6.23	* 2.01	* 0.27	* -1.08	* 1.75	* 6.95	* 7.29	* 0.82	* -1.10	* -1.73	* 0.44	* 1.98	* 1.97	* 1.71
H_2O	*O 1.04	*O 1.32	*O 0.42	*OH 0.49	* 0.26	* 0.46	*OH 1.19	*O 1.69	*O 0.66	* 0.27	* -1.08	*OH 1.17	*O 1.68	*O 3.19	*O -0.94	* -1.10	* -1.73	* 0.44	*O 1.86	*OH 1.26	*OH 0.83
H_3PO_4	$*HPO_4$ 0.82	$*HPO_4$ 0.41	$*HPO_4$ -0.30	$*H_2PO_4$ -0.38	$*HPO_4$ -0.09	$*H_2PO_4$ -0.33	$*H_2PO_4$ 0.22	$*PO_4$ 0.96	$*PO_4$ -0.37	$*HPO_4$ -0.60	* -1.08	*OH 1.17	$*PO_4$ 0.60	$*PO_4$ 2.44	$*PO_4$ -1.96	$*HPO_4$ -1.90	* -1.73	* 0.44	$*PO_4$ 0.36	$*HPO_4$ -0.22	$*PO_4$ -0.57
H_2SO_4	*O 1.04	$*SO_4$ 0.67	$*SO_4$ -0.05	$*SO_4$ -0.17	$*SO_4$ 0.07	$*HSO_4$ 0.01	$*SO_4$ 0.45	*O 1.69	$*SO_4$ 0.44	$*SO_4$ -0.36	* -1.08	*OH 1.17	*O 1.68	*O 3.19	*O -0.94	$*SO_4$ -1.64	* -1.73	* 0.44	$*SO_4$ 1.01	$*SO_4$ 0.21	$*SO_4$ -0.47
$HClO_4$	*O 1.04	$*ClO_4$ 1.22	$*ClO_4$ 0.32	$*ClO_4$ -0.13	* 0.26	* 0.46	$*ClO_4$ 0.71	*O 1.69	*O 0.66	$*ClO_4$ -0.04	* -1.08	*OH 1.17	*O 1.68	*O 3.19	*O -0.94	$*ClO_4$ -1.47	* -1.73	* 0.44	*O 1.86	*OH 1.26	*OH 0.83
HCl	*O 1.04	*Cl 0.99	*Cl 0.21	*Cl -0.18	* 0.26	*Cl -0.26	*Cl 0.44	*O 1.69	*O 0.66	*Cl -0.35	* -1.08	*Cl 0.07	*O 1.68	*O 3.19	*O -0.94	*Cl -1.59	* -1.73	* 0.44	*O 1.86	*OH 1.26	*OH 0.83
HF	*O 1.04	*F 1.05	*F 0.34	*F 0.13	* 0.26	*F 0.28	*F 0.64	*O 1.69	*O 0.66	*F 0.14	* -1.08	*OH 1.17	*O 1.68	*O 3.19	*O -0.94	* -1.10	* -1.73	* 0.44	*O 1.86	*OH 1.26	*F 0.63
HCOOH	*O 1.04	*HCOO 1.23	*O 0.42	*HCOO 0.06	* 0.26	*HCOO 0.02	*HCOO 0.69	*O 1.69	*O 0.66	*HCOO -0.03	* -1.08	*HCOO 0.44	*O 1.68	*O 3.19	*O -0.94	*HCOO -1.25	* -1.73	* 0.44	*HCOO 1.54	*HCOO 0.89	*HCOO 0.31
HNO_3	*O 1.04	$*NO_3$ 1.27	*O 0.42	$*NO_3$ 0.01	* 0.26	$*NO_3$ 0.03	$*NO_3$ 0.74	*O 1.69	*O 0.66	$*NO_3$ 0.03	* -1.08	*OH 1.17	*O 1.68	*O 3.19	*O -0.94	$*NO_3$ -1.12	* -1.73	* 0.44	*O 1.86	$*NO_3$ 0.87	$*NO_3$ 0.33
$H_2O + HCN$	*O 1.04	*CN 1.15	*CN -0.02	*CN -0.55	* 0.26	*CN -0.14	*CN 0.54	*O 1.69	*CN -0.11	*CN -0.91	* -1.08	*CN -0.04	*O 1.68	*O 3.19	*CN -1.35	*CN -2.51	* -1.73	* 0.44	*O 1.86	*OH 1.26	*OH 0.83
$H_2O + NO$	*NO 1.00	*NO 0.68	*NO -0.09	*NO -0.28	* 0.26	* 0.46	*OH 1.19	*O 1.69	*NO -0.16	*NO -0.65	* -1.08	*OH 1.17	*O 1.68	*O 3.19	*NO -1.71	*NO -2.13	* -1.73	* 0.44	*O 1.86	*OH 1.26	*OH 0.83
$H_2O + CO$	*O 1.04	*O 1.32	*CO 0.18	*CO 0.32	* 0.26	* 0.46	*OH 1.19	*O 1.69	*CO -0.03	*CO 0.11	* -1.08	*OH 1.17	*O 1.68	*O 3.19	*CO -1.47	*CO -1.59	* -1.73	* 0.44	*O 1.86	*OH 1.26	*OH 0.83

b

$\Delta G_R(pH = 1, U = 0.80V_{SHE})$ / eV

	Cr	Mn	Fe	Co	Ni	Cu	Zn	Mo	Ru	Rh	Pd	Ag	W	Re	Os	Ir	Pt	Au	Sn	Sb	Bi
Bare	* 2.26	* 1.72	* 0.84	* 0.34	* 0.11	* 0.30	* 1.22	* 4.81	* 1.06	* -0.48	* -1.63	* 0.82	* 5.35	* 6.00	* -0.42	* -2.00	* -2.43	* -0.31	* 1.81	* 1.49	* 1.25
H_2O	*O 0.92	*O 1.02	*O 0.23	* 0.34	* 0.11	* 0.30	*OH 1.09	*O 1.24	*O -0.04	* -0.48	* -1.63	* 0.82	*O 1.12	*O 2.64	*O -1.83	* -2.00	* -2.43	* -0.31	*O 1.32	*OH 1.10	*OH 0.57
H_3PO_4	$*HPO_4$ 0.42	$*HPO_4$ 0.15	$*HPO_4$ -0.49	$*HPO_4$ -0.55	$*HPO_4$ -0.11	$*HPO_4$ -0.39	$*HPO_4$ 0.20	$*PO_4$ 0.41	$*HPO_4$ -0.62	$*HPO_4$ -1.15	* -1.63	$*H_2PO_4$ 0.03	$*PO_4$ 0.02	$*PO_4$ 1.91	$*HPO_4$ -2.19	$*HPO_4$ -2.77	* -2.43	* -0.31	$*PO_4$ -0.11	$*PO_4$ -0.41	$*HPO_4$ -0.84
H_2SO_4	$*SO_4$ 0.56	$*SO_4$ 0.29	$*SO_4$ -0.33	$*SO_4$ -0.43	$*SO_4$ -0.11	$*HSO_4$ -0.39	$*SO_4$ 0.16	*O 1.24	$*SO_4$ -0.50	$*SO_4$ -1.03	* -1.63	$*SO_4$ 0.20	*O 1.12	*O 2.64	$*SO_4$ -2.03	$*SO_4$ -2.58	* -2.43	* -0.31	$*SO_4$ 0.30	$*SO_4$ 0.04	$*SO_4$ -0.04
$HClO_4$	*O 0.92	$*ClO_4$ 0.76	$*ClO_4$ 0.11	$*ClO_4$ -0.30	* 0.11	* 0.30	$*ClO_4$ 0.42	*O 1.24	*O -0.04	* -0.48	* -1.63	* 0.82	*O 1.12	*O 2.64	*O -1.83	* -2.00	* -2.43	* -0.31	*O 1.32	$*ClO_4$ 0.32	$*ClO_4$ 0.05
HCl	*O 0.92	*Cl 0.61	*Cl 0.06	*Cl -0.32	* 0.11	*Cl -0.42	*Cl 0.37	*O 1.24	*Cl -0.09	*Cl -0.83	* -1.63	*Cl -0.09	*O 1.12	*O 2.64	*O -1.83	*Cl -2.37	* -2.43	* -0.31	*O 1.32	*Cl 0.44	*Cl -0.05
HF	*F 0.91	*F 0.68	*F 0.08	*F -0.02	* 0.11	*F -0.02	*F 0.47	*O 1.24	*O -0.04	* -0.48	* -1.63	*F 0.34	*O 1.12	*O 2.64	*O -1.83	* -2.00	* -2.43	* -0.31	*O 1.32	*F 0.53	*F -0.06
HCOOH	*O 0.92	*O 1.02	*O 0.23	*HCOO 0.13	* 0.11	*HCOO 0.08	*HCOO 0.82	*O 1.24	*O -0.04	* -0.48	* -1.63	*HCOO 0.36	*O 1.12	*O 2.64	*O -1.83	* -2.00	* -2.43	* -0.31	*O 1.32	*HCOO 0.72	*HCOO 0.07
HNO_3	*O 0.92	$*NO_3$ 0.76	$*NO_3$ 0.19	$*NO_3$ -0.23	* 0.11	* 0.30	$*NO_3$ 0.54	*O 1.24	*O -0.04	$*NO_3$ -0.52	* -1.63	* 0.82	*O 1.12	*O 2.64	*O -1.83	$*NO_3$ -2.04	* -2.43	* -0.31	*O 1.32	$*NO_3$ 0.42	$*NO_3$ -0.15
$H_2O + HCN$	*O 0.92	*CN 0.75	*CN -0.32	*CN -0.67	* 0.11	*CN -0.15	*CN 0.48	*O 1.24	*CN -1.04	*CN -1.51	* -1.63	*CN -0.14	*O 1.12	*O 2.64	*CN -2.41	*CN -3.39	* -2.43	* -0.31	*O 1.32	*CN 0.76	*CN 0.40
$H_2O + NO$	*NO 0.67	*NO 0.48	*NO -0.30	*NO -0.38	* 0.11	* 0.30	*OH 1.09	*O 1.24	*NO -0.68	*NO -1.17	* -1.63	* 0.82	*O 1.12	*O 2.64	*NO -2.16	*NO -2.83	* -2.43	* -0.31	*O 1.32	*OH 1.10	*OH 0.57
$H_2O + CO$	*O 0.92	*O 1.02	*CO -0.01	*CO 0.34	* 0.11	* 0.30	*OH 1.09	*O 1.24	*CO -0.71	* -0.48	* -1.63	*CO 0.73	*O 1.12	*O 2.64	*CO -2.19	*CO -2.11	* -2.43	* -0.31	*O 1.32	*OH 1.10	*OH 0.57

Figure 4.4: ΔG_R of the most stable adsorbate on MN_4 site in 0.1 M electrolytes at pH = 1, U = 0.80 V_{SHE}: (a) MN_4C_{10}, (b) MN_4C_A. The inserted text indicates the most stable adsorbate on the metal site and its corresponding ΔG_R in eV. The background color corresponds to the ΔG_R value. The brighter the background color, the more stable it is against the dissolution.

In 0.1 M $HClO_4$ at U = 0.5 - 1.0 V_{RHE}, both the MnN_4 and FeN_4 sites are stabilized by $*ClO_4$. Comparing these metal sites in H_2O where the metal sites are covered by *O, ΔG_R for FeN_4 site in 0.1 M $HClO_4$ is about 0.18 eV lower than in H_2O and it is about 0.13 eV lower than in H_2O for MnN_4 site in 0.1 M $HClO_4$. However, in both H_2O and 0.1 M $HClO_4$, the MnN_4 sites are found to be less stable than the FeN_4 sites.

Another experimental study by Xie *et al.* [19] has determined the amount of metal leaching out from the Fe/N/C and Co/N/C catalyst when the potential was cycled between 0.6 - 1.0 V_{RHE} in 0.5 M H_2SO_4. They have found a lower metal leaching from the Co/N/C catalyst than the Fe/N/C catalyst [19]. At this potential range, we find that the FeN_4 and CoN_4 sites on both bulk graphene and the graphene edge in 0.1 M H_2SO_4 are occupied by $^*SO_4$. The thermodynamic driving force toward the dissolution of the $^*SO_4$-CoN_4 sites are about 0.14 eV lower than the $^*SO_4$-FeN_4 sites, agreeing with the experiment. In the previous chapter, where the electrolyte anion adsorption has not been included, we find that the thermodynamic driving force of the most stable phase of the $FeN_4C_{x=10,A}$ sites in H_2O is about 0.02 eV higher than those of the CoN_4 sites. It is seen that the stability calculations, including the electrolyte anion adsorption, compare well with the experimental results for M/N/C catalysts.

For CO adsorption, the CO chemisorption experiment on the M/N/C catalyst (M = Fe and Mn) has suggested a stronger CO binding on the Fe-containing site over the Mn-containing site [126]. In agreement with the experiment, we find a stronger CO adsorption on the FeN_4 sites than on the MnN_4 sites on both bulk graphene and graphene edge. Similar results have been reported by Svane *et al.* [93] where the M/N/C catalysts are modeled based on the MN_4C_{12} structures.

Besides the nature of the metal atom center, the stability against dissolution depends on the local carbon structure around the MN_4 motif. The MN_4 site on the graphene edge is more stable than that on the bulk graphene. The thermodynamic driving force toward the dissolution at U = 0.80 V_{SHE} and pH = 1 of the most stable phase of the MN_4C_A structures is about 0.52 eV lower than those of MN_4C_{10} structures.

4.6 ORR Activity

Considering the MN_4 site embedded in a two-dimensional carbon sheet, the adsorbates could interact with the metal atom from both sides. The electrolyte anion can strongly adsorb on both sides, blocking the metal site from the reaction intermediates. Alternatively, the electrolyte anion adsorbs only on one side, allowing the intermediate adsorbates to interact from the other side. In this chapter, the ORR is also considered to proceed through the four-electron associative pathway, and the metal site is considered as the active site. If the electrolyte anion is found to interact with MN_4 site under the ORR-related condition, the ORR activity of the MN_4 site is considered as the following mechanism [129].

$$\begin{gathered}
{}^*A/{}^*A + ne^- \rightarrow {}^* /{}^*A + A^{n-} \\
O_2 + H^+ + e^- + {}^* /{}^*A \rightarrow {}^* OOH/{}^*A \\
{}^*OOH/{}^*A + H^+ + e^- \rightarrow {}^* O/{}^*A + H_2O \\
{}^*O/{}^*A + H^+ + e^- \rightarrow {}^* OH/{}^*A \\
{}^*OH/{}^*A + H^+ + e^- \rightarrow {}^* /{}^*A + H_2O
\end{gathered}$$

where $^*A/^*A$ stands for the electrolyte anions on both sides of the metal site. $^*X/^*A$ stands for the electrolyte anion on one side and the reaction intermediate on the other side (X = O, OH, and OOH). At any considered pH and U_{SHE}, the reaction free energy of the consecutive step along the ORR can be expressed as follows

$$\Delta G_0(U_{SHE}, pH) = \Delta G({}^*A^{n-}/{}^*A) \tag{4.7}$$

$$\Delta G_1(U_{SHE}, pH) = \Delta G_{*OOH/*A} + \Delta G_{H_2O} - \Delta G_e - \Delta G_H \tag{4.8}$$

$$\Delta G_2(U_{SHE}, pH) = \Delta G_{*O/*A} - \Delta G_{*OOH/*A} - \Delta G_e - \Delta G_H \tag{4.9}$$

$$\Delta G_3(U_{SHE}, pH) = \Delta G_{*OH/*A} - \Delta G_{*O/*A} - \Delta G_e - \Delta G_H \tag{4.10}$$

$$\Delta G_4(U_{SHE}, pH) = -\Delta G_{*OH/*A} - \Delta G_e - \Delta G_H \tag{4.11}$$

where $\Delta G_{*X/*A}$ is the adsorption free energy of reaction intermediate X (X = O, OH and OOH) on the metal site with the electrolyte anion on the back side of the metal atom at pH = 0 and U = 0 V_{SHE}. $\Delta G_{*OOH/*A}$ and $\Delta G_{*O/*A}$ are obtained from a scaling relation established between ΔG_{*O} vs. ΔG_{*OH} and ΔG_{*OOH} vs. ΔG_{*OH} on the bare metal site, given in Equation 4.12 - 4.15 (Figure B.1 in Appendix B). Note that MEA is a mean absolute error. Only $\Delta G_{*OH/*A}$ is explicitly calculated in this chapter. A previous study by Svan *et al.* [93] has also reported a similar scaling relation between ΔG_{*OH} and ΔG_{*OOH} ($\Delta G_{*OOH} = \Delta G_{*OH} + 3.24$) obtained from the MN_4C_{12} structures, including the adsorption free energy with the electrolyte anion on the back side of the metal atom.

$$\text{For } MN_4C_{10}\text{: } \Delta G_{*OOH/*A} = \Delta G_{*OH/*A} + 3.22\text{ ; MAE} = 0.15\text{ eV} \tag{4.12}$$

$$\Delta G_{*O/*A} = 2\Delta G_{*OH/*A} + 0.65\text{ ; MAE} = 0.59\text{ eV} \tag{4.13}$$

$$\text{For } MN_4C_A\text{: } \Delta G_{*OOH/*A} = \Delta G_{*OH/*A} + 3.16\text{ ; MAE} = 0.14\text{ eV} \tag{4.14}$$

$$\Delta G_{*O/*A} = 2\Delta G_{*OH/*A} + 0.44\text{ ; MAE} = 0.39\text{ eV} \tag{4.15}$$

$$\text{where } \Delta G_{*OH/*A} = G({}^*OH/{}^*A) + \frac{1}{2}G(H_2) - G({}^*/{}^*A) - G(H_2O) \tag{4.16}$$

$\Delta G({}^*A^{n-}/{}^*A)$ in Equation 4.7 is the free adsorption energy of the second electrolyte anion on the metal atom. It can be calculated using the thermodynamic cycle in Figure 4.2 and can be written as follows

$$\Delta G({}^*A^{n-}/{}^*A) = \Delta_{CHE}G({}^*A/{}^*A) - \Delta G_{sol}(H_nA) - \Delta G_{dilute}(A^{n-}) \tag{4.17}$$

where $\Delta_{CHE}G({}^*A/{}^*A)$ is calculated according to the computational hydrogen electrode (CHE) [117] and can be written as follows

$$\Delta_{CHE}G({}^*A) = G({}^*A/{}^*A) + \frac{n}{2}G(H_2) + n\Delta G_e + n\Delta G_H - G({}^*A) - G(H_nA_{(gas)}) \tag{4.18}$$

The possible electrolyte anion participating in the ORR is the most stable adsorbate at pH = 1, U = 0.80 V_{SHE}. The corresponding ORR activity is also considered at this condition by calculating the thermodynamic barrier of the limiting step (ΔG_{max}). The thermodynamic barrier of the limiting step at specific U_{SHE} and pH indicates the minimum energy required to run the reaction at that specific condition, assuming no kinetic barrier between each elementary step. The limiting potential (U_L) is also calculated if all of the elementary steps along the ORR path are electrochemical reactions.

This situation includes when two NO and CO gas molecules are not thermodynamically stable on both sides of the metal atom. The U_L is the highest potential where all of the elementary steps are still downhill in free energy. The U_L and overpotential are considered at pH = 1 and can be calculated as follows

$$U_L = -\max\{\frac{\Delta G_0}{n}, \Delta G_1, \Delta G_2, \Delta G_3, \Delta G_4\}/e \tag{4.19}$$

$$\text{overpotential} = U_{eq} - U_L \tag{4.20}$$

where ΔG_i (i = 0 - 4) is the reaction free energy of the consecutive step along the ORR path in Equation 4.7 - 4.11, at pH = 1 and U = 0 V_{SHE}. n is the number of electrons transferred during the adsorption/desorption of the second electrolyte anion on the metal site (n = 0 for the neutral gas molecule, such as CO and NO).

The ORR activity of the FeN_4C_{10} and FeN_4C_A sites in 0.1 M H_3PO_4, H_2SO_4, $HClO_4$, and HCl is firstly discussed. At U = 0.8 V_{SHE} and pH = 1, the electrolyte anion ($^*HPO_4$, $^*SO_4$, $^*ClO_4$, and *Cl) bonds to the FeN_4 sites stronger than the water. Thus, these electrolyte anions can affect the ORR. Free energy diagrams of the ORR on the FeN_4C_{10} and FeN_4C_A site in these solutions at U = 0.80 V_{SHE} and pH = 1 are given in Figure 4.5.

The ORR on the FeN_4C_{10} site in 0.1 M $HClO_4$, and HCl is thermodynamically limited by the anion removal step, which is the change from the reaction state 0 to 1 in Figure 4.5 (a). In 0.1 M H_3PO_4, the thermodynamic barrier of the limiting step is the energy to remove one anion plus the energy to form *OOH, which is the relative energy between the reaction state 0 and 2 in Figure 4.5 (a). While in 0.1 M H_2SO_4, the limiting step is the reduction of *OH to H_2O, which is the change from the reaction state 4 to 5 in Figure 4.5 (a). The ΔG_{max} at U = 0.80 V_{SHE}, pH = 1 for the FeN_4C_{10} site in these considered electrolytes is H_2SO_4 (0.02 eV) < $HClO_4$ (0.13 eV) < H_3PO_4 (0.26 eV) < HCl (0.56 eV). The U_L at pH = 1 with the most stable adsorbate at U = 0.80 V_{SHE} and pH = 1 as the ligand on the back side of the metal atom is H_2SO_4 (0.78 V_{SHE}) > $HClO_4$ (0.67 V_{SHE}) > H_3PO_4 (0.60 V_{SHE}) > HCl (0.24 V_{SHE}). These results suggest that the ORR activity of the FeN_4C_{10} site in theses considered solutions is H_2SO_4 > $HClO_4$ > H_3PO_4 > HCl.

For the FeN_4C_A site in 0.1 M H_3PO_4 and HCl, the ORR is thermodynamically limited by the anion removal step. In 0.1 M H_2SO_4, the thermodynamic barrier of the limiting step is the energy to remove one anion plus the energy to form *OOH. The ORR is limited by the reduction of *OH to H_2O for the FeN_4C_A site in 0.1 M $HClO_4$. The ΔG_{max} at U = 0.80 V_{SHE} and pH = 1 for the FeN_4C_A site in these electrolytes is H_3PO_4 (0.01 eV) < H_2SO_4 (0.08 eV) < $HClO_4$ (0.13 eV) < HCl (0.54 eV). The U_L (at pH = 1) is in the following order: H_3PO_4 (0.79 V_{SHE}) > H_2SO_4 (0.76 V_{SHE}) > $HClO_4$ (0.67 V_{SHE}) > HCl (0.26 V_{SHE}). These results suggest that the ORR activity of the FeN_4C_A site in these considered solutions is H_3PO_4 > H_2SO_4 > $HClO_4$ > HCl. It is seen that the ORR activity obtained from FeN_4C_{10} and FeN_4C_A site is different, implying a significant role of the local carbon structure around the FeN_4 site in the catalytic activity.

Previous experimental results by Holst-Olesen *et al.* [129], and Hu *et al.* [156] have reported that the ORR activity of the Fe/N/C catalyst in H_3PO_4 are higher than

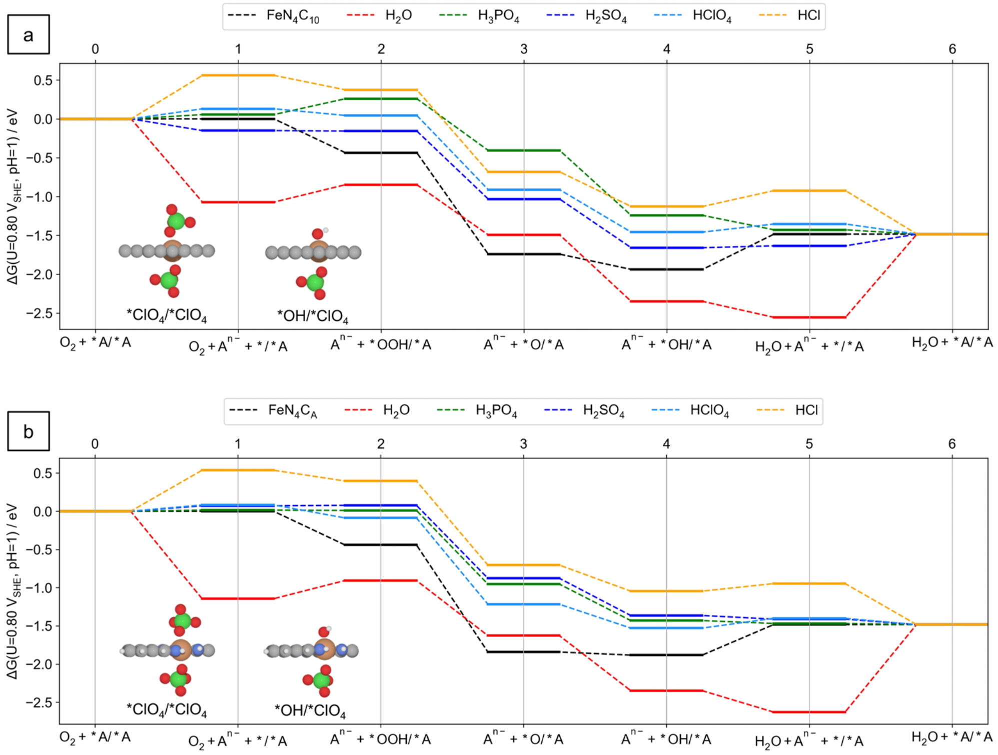

Figure 4.5: Free energy diagram of the ORR at pH = 1, U = 0.80 V_{SHE} on: (a) FeN_4C_{10}, (b) FeN_4C_A in H_2O, 0.1 M H_3PO_4, 0.1 M $HClO_4$, 0.1 M H_2SO_4 and 0.1 M HCl. In each solution, the ligand on the back side of the Fe atom is the most stable adsorb at pH = 1, U = 0.80 V_{SHE}. The insets show the side view of the $*OH/*ClO_4$ and $*ClO_4/*ClO_4$ on the FeN_4 site. (C = gray, N = blue, H = white, O = red, Fe = orange, Cl = lime green).

in the other electrolytes. Holst-Olesen *et al.* [129] have reported the ORR activity in the following order for the Fe/N/C catalysts in 0.5 M electrolyte: H_3PO_4 > $HClO_4$ ≈ H_2SO_4 > HCl. At 0.8 V_{RHE}, Hu *et al.* [156] have reported the ORR activity of the Fe/N/C catalyst as the following order: H_3PO_4 > H_2SO_4 > $HClO_4$ > HCl. Modeling the Fe/N/C catalyst by the FeN_4C_{12} structure, Holst-Olesen *et al.* [129] have reported a good agreement between the theoretical and experimental ORR activity trends. Our calculation results obtained from the FeN_4C_A structure agree with the experiments by Hu *et al.* and Holst-Olesen *et al.*. While the results obtained from FeN_4C_{10} sites disagree with the experiments. Both experimental studies by Holst-Olesen *et al.* [129] and Hu *et al.* [156] have suggested a strong poison effect on the Fe/N/C catalyst by Cl^- in HCl. In our calculations, the thermodynamic barrier of the limiting step in 0.1 M HCl is also higher than in other solutions. Additionally, Hu *et al.* have suggested that the catalytic activity of the Fe/N/C catalyst can be poisoned by ClO_4^- in $HClO_4$ solution, implying the interaction between the FeN_4 sites and ClO_4^- in $HClO_4$ solution [156]. In our calculation results, the $*ClO_4$ can be adsorbed on the FeN_4C_{10} and FeN_4C_A sites at U =

0.80 V_{SHE} and pH = 1. Furthermore, we find that the $^*ClO_4/^*ClO_4$ can thermodynamically block the FeN_4C_{10} site at this condition. These results disagree with a previous study by Holst-Olesen *et al.* [129] where the $^*ClO_4$ has been found not to adsorb on the FeN_4C_{12} site at U = 0.75 V_{RHE} in 0.5 M $HClO_4$. The discrepancy could be due to the different local carbon structures around the FeN_4 site, which could also be different in each experiment, depending on the synthesis process.

The ΔG_{max} at pH = 1 and U = 0.80 V_{SHE} is considered as the ORR activity descriptor and is given in Figure B.6. The U_L at pH = 1 is also given in Figure B.7 of Appendix B. Evaluating the ORR catalytic activity in 0.5 M H_2SO_4, Martinez *et al.* [10] have reported the following order of the onset potential for the M/N/C catalysts: Mn < Co < Fe. Their theoretical study using the MN_4 at the zigzag edge of the graphene has suggested the $^*OH$ ligand as a part of the active site. The theoretical study by Svane *et al.* [93] has reported the same order of U_L calculated from the MN_4C_{12} structure in 0.5 M H_2SO_4. According to our calculation results, the U_L at pH = 1 on these metal atoms in the MN_4C_{10} structure in 0.1 M H_2SO_4 differs by 0.01 V_{SHE} and the order is Mn (0.77 V_{SHE}) < Fe (0.78 V_{SHE}) < Co (0.79 V_{SHE}). While, the U_L calculated from the MN_4C_A structure is in the following order: Mn (0.70 V_{SHE}) < Co (0.71 V_{SHE}) < Fe (0.76 V_{SHE}), agreeing with the onset potential order from the experiments by Martinez *et al.* Another experimental study testing the ORR performance of the Co/N/C and Mn/N/C catalyst in 0.1 M $HClO_4$ solution has reported the onset potential of the Co/N/C and Mn/N/C catalyst in the order of Mn < Co [157]. For both MN_4C_{10} and MN_4C_A structures in 0.1 M $HClO_4$, we find the $^*ClO_4$-MN_4 site as the active center for MnN_4 and CoN_4 structures on bulk graphene and graphene edge. The order of U_L is found to be Co < Mn. Based on the MN_4C_{12} structure, Svane *et al.* [93] have found the $^*OH$-MnN_4C_{12} and $^*H_2O$-CoN_4C_{12} sites as the active center in 0.5 M $HClO_4$. Their calculated U_L is in the order of Mn < Co [93], which is in agreement with the experiment [157]. Previous experimental results have shown that the Fe/N/C catalysts can be poisoned by CN^- under the acid condition[158]. In our calculation results, we also find that at U > 0 V_{SHE} and pH = 1, the FeN_4C_{10} and FeN_4C_A sites are thermodynamically blocked by two $^*CN$. As a result, the ORR proceeds by at least a thermodynamic barrier for removing one $^*CN$ from FeN_4 sites. Previous theoretical study by Svane *et al.* [93] have also reported a similar results for the FeN_4C_{12} structure. Furthermore, we find that other MN_4 sites with M = Mn, Co, Ru, Rh, Os, and Ir can be blocked by two $^*CN$ at pH = 1 and U > 0 V_{SHE}. Additionally, it is found that two NO gas molecules can be adsorbed on both sides of IrN_4C_{10} and IrN_4C_A structures. At U = 0 - 0.8 V_{SHE} and pH = 1, the ORR proceeds with at least the thermodynamic hindrance to remove one $^*NO$ from the IrN_4 site. Furthermore, two $^*CO$ or $^*NO$ adsorbates are thermodynamically stable on the RuN_4C_A and OsN_4C_A structure at U = 0.80 V_{SHE}, pH = 1. However, as a second adsorbate, the binding of $^*OH$ on the metal site is stronger than the $^*CO$ and $^*NO$. Thus, the ORR on these metal sites is limited by the reduction of $^*OH$ to H_2O.

Comparing our calculation results with previous studies [93, 129], it is seen that the nature of the metal atom and the local carbon structure play a crucial role in determining the electrolyte adsorption and its corresponding catalytic activity.

4.7 Stability under the CO_2RR-related condition

Figure 4.6 shows ΔG_R of the most stable adsorbate on the MN_4C_{10} and MN_4C_A site in 0.1 M electrolytes at pH = 7, and U = -0.8 V_{SHE}. The 0.1 M H_2CO_3 solution is included as the electrolyte used in the experiments [139, 141, 150]. In contrast to the ORR conditions, the anion from most of the considered electrolytes does not bind with the single metal site, except from the 0.1 M H_2CO_3. Thus, most considered electrolytes possibly have little impact on catalytic activity and stability of the MN_4 site under the CO_2RR-related condition. Except for the 0.1 M H_2CO_3, we refer to the stability and catalytic activity under the CO_2RR-related condition in the considered electrolytes as same as in H_2O.

In H_2O, we find that *H can occupy on the CoN_4, RuN_4, RhN_4, OsN_4, and IrN_4 sites on both bulk graphene and graphene edge. While the $MoN_4C_{x=10,A}$, $WN_4C_{x=10,A}$, and ReN_4C_{10} sites are occupied by *O, same as in the ORR-related condition, but with a lower thermodynamic driving force toward the dissolution. It is also seen that *CO (in H_2O + CO solution) and *NO (in H_2O + CO + NO solution) can be thermodynamically stable on many metal sites both on bulk graphene and the graphene edge. It is found that *NO is likely to bind stronger than *CO to the metal site. Thus, it is possible that the *NO can block the metal site or participate in the reaction. Although *CN can adsorb on the metal atom at pH = 7 and U = -0.8 V_{SHE}, the binding strength of *CN with the metal atom is weaker than that of *CO. Thus, *CN does not block the metal site or participate in the reaction.

In 0.1 M H_2CO_3, the $MoN_4C_{x=10,A}$, $WN_4C_{x=10,A}$, and ReN_4C_{10} sites bind with $*CO_3$ via two oxygen atoms. we find that $*HCO_3$ is stable on $CrN_4C_{x=10,A}$, $MnN_4C_{x=10,A}$, FeN_4C_{10}, ZnN_4C_{10}, $SbN_4C_{x=10,A}$, and $BiN_4C_{x=10,A}$ sites. In 0.1 M H_2CO_3 + CO solution, CO gas molecule can compete with electrolyte anions (HCO_3^-, CO_3^{2-}) and bind to the metal sites. The most stable adsorbate on both MN_4C_{10} and MN_4C_A sites in H_2O + CO solution and 0.1 M H_2CO_3 + CO solution is slightly different. Similar to what is under the ORR condition, the NiN_4, CuN_4, PdN_4, PtN_4, AuN_4, and SnN_4 sites on both bulk graphene and the graphene edge are likely to be unoccupied.

Recently, a kinetic model fitted by the experimental data by Zeng *et al.* [159] has demonstrated the role of the bicarbonate buffer on the CO_2RR catalyzed by cobalt phthalocyanine (CoPC). They have suggested that the active site can be poisoned by HCO_3^- via the electrosorption at low overpotential, and the bicarbonate acts as a proton donor at a higher overpotential. Defining the onset potential for CO production to be the applied electrode potential at which the TOF of the CO formation exceeds 0.2 mmol/(h $m^2{}_{active}$), the experiments have found that the Co/N/C catalyst starts producing CO at U = -0.36 V_{RHE} [139]. Around this potential (U = -0.77 V_{SHE} at pH = 7), it is seen from our calculations in Figure 4.3 and Figure B.3 that *H, *CO, and $*HCO_3$ could thermodynamically be absorbed on the CoN_4 site on both bulk graphene and the graphene edge. At more positive potential, the $*HCO_3$ becomes the most stable adsorbate on the CoN_4 site. while the *H becomes more stable than *CO and $*HCO_3$ at more negative potential (higher overpotential).

(a) MN_4C_{10}: ΔG_R(pH = 7, -0.80 V_{SHE}) / eV

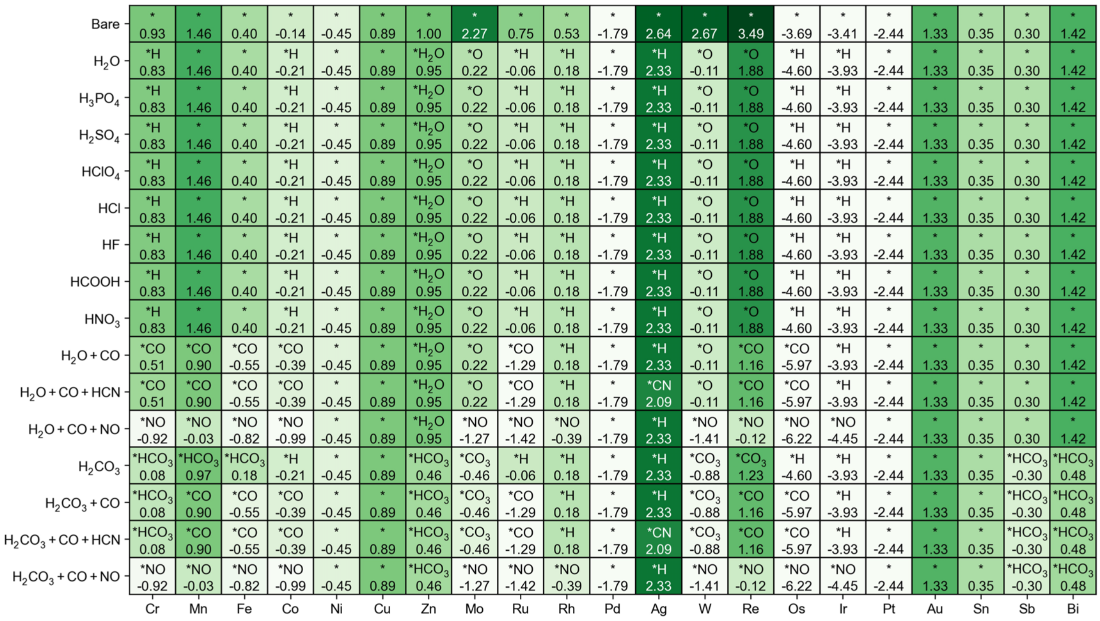

	Cr	Mn	Fe	Co	Ni	Cu	Zn	Mo	Ru	Rh	Pd	Ag	W	Re	Os	Ir	Pt	Au	Sn	Sb	Bi
Bare	* 0.93	* 1.46	* 0.40	* -0.14	* -0.45	* 0.89	* 1.00	* 2.27	* 0.75	* 0.53	* -1.79	* 2.64	* 2.67	* 3.49	* -3.69	* -3.41	* -2.44	* 1.33	* 0.35	* 0.30	* 1.42
H_2O	*H 0.83	* 1.46	* 0.40	*H -0.21	* -0.45	* 0.89	*H_2O 0.95	*O 0.22	*H -0.06	*H 0.18	* -1.79	*H 2.33	*O -0.11	*O 1.88	*H -4.60	*H -3.93	* -2.44	* 1.33	* 0.35	* 0.30	* 1.42
H_3PO_4	*H 0.83	* 1.46	* 0.40	*H -0.21	* -0.45	* 0.89	*H_2O 0.95	*O 0.22	*H -0.06	*H 0.18	* -1.79	*H 2.33	*O -0.11	*O 1.88	*H -4.60	*H -3.93	* -2.44	* 1.33	* 0.35	* 0.30	* 1.42
H_2SO_4	*H 0.83	* 1.46	* 0.40	*H -0.21	* -0.45	* 0.89	*H_2O 0.95	*O 0.22	*H -0.06	*H 0.18	* -1.79	*H 2.33	*O -0.11	*O 1.88	*H -4.60	*H -3.93	* -2.44	* 1.33	* 0.35	* 0.30	* 1.42
$HClO_4$	*H 0.83	* 1.46	* 0.40	*H -0.21	* -0.45	* 0.89	*H_2O 0.95	*O 0.22	*H -0.06	*H 0.18	* -1.79	*H 2.33	*O -0.11	*O 1.88	*H -4.60	*H -3.93	* -2.44	* 1.33	* 0.35	* 0.30	* 1.42
HCl	*H 0.83	* 1.46	* 0.40	*H -0.21	* -0.45	* 0.89	*H_2O 0.95	*O 0.22	*H -0.06	*H 0.18	* -1.79	*H 2.33	*O -0.11	*O 1.88	*H -4.60	*H -3.93	* -2.44	* 1.33	* 0.35	* 0.30	* 1.42
HF	*H 0.83	* 1.46	* 0.40	*H -0.21	* -0.45	* 0.89	*H_2O 0.95	*O 0.22	*H -0.06	*H 0.18	* -1.79	*H 2.33	*O -0.11	*O 1.88	*H -4.60	*H -3.93	* -2.44	* 1.33	* 0.35	* 0.30	* 1.42
HCOOH	*H 0.83	* 1.46	* 0.40	*H -0.21	* -0.45	* 0.89	*H_2O 0.95	*O 0.22	*H -0.06	*H 0.18	* -1.79	*H 2.33	*O -0.11	*O 1.88	*H -4.60	*H -3.93	* -2.44	* 1.33	* 0.35	* 0.30	* 1.42
HNO_3	*H 0.83	* 1.46	* 0.40	*H -0.21	* -0.45	* 0.89	*H_2O 0.95	*O 0.22	*H -0.06	*H 0.18	* -1.79	*H 2.33	*O -0.11	*O 1.88	*H -4.60	*H -3.93	* -2.44	* 1.33	* 0.35	* 0.30	* 1.42
$H_2O + CO$	*CO 0.51	*CO 0.90	*CO -0.55	*CO -0.39	* -0.45	* 0.89	*H_2O 0.95	*O 0.22	*CO -1.29	*H 0.18	* -1.79	*H 2.33	*O -0.11	*CO 1.16	*CO -5.97	*H -3.93	* -2.44	* 1.33	* 0.35	* 0.30	* 1.42
$H_2O + CO + HCN$	*CO 0.51	*CO 0.90	*CO -0.55	*CO -0.39	* -0.45	* 0.89	*H_2O 0.95	*O 0.22	*CO -1.29	*H 0.18	* -1.79	*CN 2.09	*O -0.11	*CO 1.16	*CO -5.97	*H -3.93	* -2.44	* 1.33	* 0.35	* 0.30	* 1.42
$H_2O + CO + NO$	*NO -0.92	*NO -0.03	*NO -0.82	*NO -0.99	* -0.45	* 0.89	*H_2O 0.95	*NO -1.27	*NO -1.42	*NO -0.39	* -1.79	*H 2.33	*NO -1.41	*NO -0.12	*NO -6.22	*NO -4.45	* -2.44	* 1.33	* 0.35	* 0.30	* 1.42
H_2CO_3	*HCO_3 0.08	*HCO_3 0.97	*HCO_3 0.18	*H -0.21	* -0.45	* 0.89	*HCO_3 0.46	*CO_3 -0.46	*H -0.06	*H 0.18	* -1.79	*H 2.33	*CO_3 -0.88	*CO_3 1.23	*H -4.60	*H -3.93	* -2.44	* 1.33	* 0.35	*HCO_3 -0.30	*HCO_3 0.48
$H_2CO_3 + CO$	*HCO_3 0.08	*CO 0.90	*CO -0.55	*CO -0.39	* -0.45	* 0.89	*HCO_3 0.46	*CO_3 -0.46	*CO -1.29	*H 0.18	* -1.79	*H 2.33	*CO_3 -0.88	*CO 1.16	*CO -5.97	*H -3.93	* -2.44	* 1.33	* 0.35	*HCO_3 -0.30	*HCO_3 0.48
$H_2CO_3 + CO + HCN$	*HCO_3 0.08	*CO 0.90	*CO -0.55	*CO -0.39	* -0.45	* 0.89	*HCO_3 0.46	*CO_3 -0.46	*CO -1.29	*H 0.18	* -1.79	*CN 2.09	*CO_3 -0.88	*CO 1.16	*CO -5.97	*H -3.93	* -2.44	* 1.33	* 0.35	*HCO_3 -0.30	*HCO_3 0.48
$H_2CO_3 + CO + NO$	*NO -0.92	*NO -0.03	*NO -0.82	*NO -0.99	* -0.45	* 0.89	*HCO_3 0.46	*NO -1.27	*NO -1.42	*NO -0.39	* -1.79	*H 2.33	*NO -1.41	*NO -0.12	*NO -6.22	*NO -4.45	* -2.44	* 1.33	* 0.35	*HCO_3 -0.30	*HCO_3 0.48

(b) MN_4C_A: ΔG_R(pH = 7, -0.80 V_{SHE}) / eV

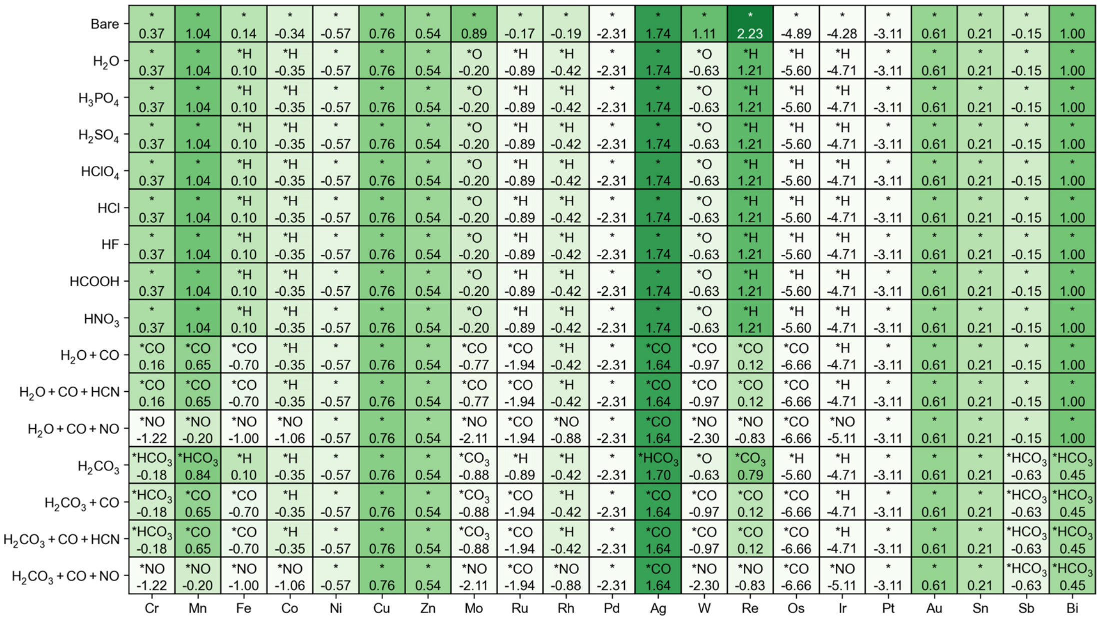

	Cr	Mn	Fe	Co	Ni	Cu	Zn	Mo	Ru	Rh	Pd	Ag	W	Re	Os	Ir	Pt	Au	Sn	Sb	Bi
Bare	* 0.37	* 1.04	* 0.14	* -0.34	* -0.57	* 0.76	* 0.54	* 0.89	* -0.17	* -0.19	* -2.31	* 1.74	* 1.11	* 2.23	* -4.89	* -4.28	* -3.11	* 0.61	* 0.21	* -0.15	* 1.00
H_2O	* 0.37	* 1.04	*H 0.10	*H -0.35	* -0.57	* 0.76	* 0.54	*O -0.20	*H -0.89	*H -0.42	* -2.31	* 1.74	*O -0.63	*H 1.21	*H -5.60	*H -4.71	* -3.11	* 0.61	* 0.21	* -0.15	* 1.00
H_3PO_4	* 0.37	* 1.04	*H 0.10	*H -0.35	* -0.57	* 0.76	* 0.54	*O -0.20	*H -0.89	*H -0.42	* -2.31	* 1.74	*O -0.63	*H 1.21	*H -5.60	*H -4.71	* -3.11	* 0.61	* 0.21	* -0.15	* 1.00
H_2SO_4	* 0.37	* 1.04	*H 0.10	*H -0.35	* -0.57	* 0.76	* 0.54	*O -0.20	*H -0.89	*H -0.42	* -2.31	* 1.74	*O -0.63	*H 1.21	*H -5.60	*H -4.71	* -3.11	* 0.61	* 0.21	* -0.15	* 1.00
$HClO_4$	* 0.37	* 1.04	*H 0.10	*H -0.35	* -0.57	* 0.76	* 0.54	*O -0.20	*H -0.89	*H -0.42	* -2.31	* 1.74	*O -0.63	*H 1.21	*H -5.60	*H -4.71	* -3.11	* 0.61	* 0.21	* -0.15	* 1.00
HCl	* 0.37	* 1.04	*H 0.10	*H -0.35	* -0.57	* 0.76	* 0.54	*O -0.20	*H -0.89	*H -0.42	* -2.31	* 1.74	*O -0.63	*H 1.21	*H -5.60	*H -4.71	* -3.11	* 0.61	* 0.21	* -0.15	* 1.00
HF	* 0.37	* 1.04	*H 0.10	*H -0.35	* -0.57	* 0.76	* 0.54	*O -0.20	*H -0.89	*H -0.42	* -2.31	* 1.74	*O -0.63	*H 1.21	*H -5.60	*H -4.71	* -3.11	* 0.61	* 0.21	* -0.15	* 1.00
HCOOH	* 0.37	* 1.04	*H 0.10	*H -0.35	* -0.57	* 0.76	* 0.54	*O -0.20	*H -0.89	*H -0.42	* -2.31	* 1.74	*O -0.63	*H 1.21	*H -5.60	*H -4.71	* -3.11	* 0.61	* 0.21	* -0.15	* 1.00
HNO_3	* 0.37	* 1.04	*H 0.10	*H -0.35	* -0.57	* 0.76	* 0.54	*O -0.20	*H -0.89	*H -0.42	* -2.31	* 1.74	*O -0.63	*H 1.21	*H -5.60	*H -4.71	* -3.11	* 0.61	* 0.21	* -0.15	* 1.00
$H_2O + CO$	*CO 0.16	*CO 0.65	*CO -0.70	*H -0.35	* -0.57	* 0.76	* 0.54	*CO -0.77	*CO -1.94	*H -0.42	* -2.31	*CO 1.64	*CO -0.97	*CO 0.12	*CO -6.66	*H -4.71	* -3.11	* 0.61	* 0.21	* -0.15	* 1.00
$H_2O + CO + HCN$	*CO 0.16	*CO 0.65	*CO -0.70	*H -0.35	* -0.57	* 0.76	* 0.54	*CO -0.77	*CO -1.94	*H -0.42	* -2.31	*CO 1.64	*CO -0.97	*CO 0.12	*CO -6.66	*H -4.71	* -3.11	* 0.61	* 0.21	* -0.15	* 1.00
$H_2O + CO + NO$	*NO -1.22	*NO -0.20	*NO -1.00	*NO -1.06	* -0.57	* 0.76	* 0.54	*NO -2.11	*CO -1.94	*NO -0.88	* -2.31	*CO 1.64	*NO -2.30	*NO -0.83	*CO -6.66	*NO -5.11	* -3.11	* 0.61	* 0.21	* -0.15	* 1.00
H_2CO_3	*HCO_3 -0.18	*HCO_3 0.84	*H 0.10	*H -0.35	* -0.57	* 0.76	* 0.54	*CO_3 -0.88	*H -0.89	*H -0.42	* -2.31	*HCO_3 1.70	*O -0.63	*CO_3 0.79	*H -5.60	*H -4.71	* -3.11	* 0.61	* 0.21	*HCO_3 -0.63	*HCO_3 0.45
$H_2CO_3 + CO$	*HCO_3 -0.18	*CO 0.65	*CO -0.70	*H -0.35	* -0.57	* 0.76	* 0.54	*CO_3 -0.88	*CO -1.94	*H -0.42	* -2.31	*CO 1.64	*CO -0.97	*CO 0.12	*CO -6.66	*H -4.71	* -3.11	* 0.61	* 0.21	*HCO_3 -0.63	*HCO_3 0.45
$H_2CO_3 + CO + HCN$	*HCO_3 -0.18	*CO 0.65	*CO -0.70	*H -0.35	* -0.57	* 0.76	* 0.54	*CO_3 -0.88	*CO -1.94	*H -0.42	* -2.31	*CO 1.64	*CO -0.97	*CO 0.12	*CO -6.66	*H -4.71	* -3.11	* 0.61	* 0.21	*HCO_3 -0.63	*HCO_3 0.45
$H_2CO_3 + CO + NO$	*NO -1.22	*NO -0.20	*NO -1.00	*NO -1.06	* -0.57	* 0.76	* 0.54	*NO -2.11	*CO -1.94	*NO -0.88	* -2.31	*CO 1.64	*NO -2.30	*NO -0.83	*CO -6.66	*NO -5.11	* -3.11	* 0.61	* 0.21	*HCO_3 -0.63	*HCO_3 0.45

Figure 4.6: ΔG_R of the most stable adsorbate on MN_4 site in 0.1 M electrolytes at pH = 7, U = -0.80 V_{SHE}: (a) MN_4C_{10}, (b) MN_4C_A. The inserted text indicates the most stable adsorbate on the metal site and its corresponding ΔG_R in eV. The background color corresponds to the ΔG_R value. The brighter the background color, the more stable it is against the dissolution.

Furthermore, a series of M/N/C catalysts (M = Mn^{3+}, Fe^{3+}, Co^{2+}, Ni^{2+}, Cu^{2+}, Zn^{2+}, and Sn^{2+}) has been synthesized and evaluated for the CO_2 reduction in 0.5 M $KHCO_3$ + 0.5 M K_2SO_4 [141]. The Cu/N/C catalyst has been found to produce hydrocarbon products with significant amounts, which correlates with a partial reduction of Cu^{2+} to Cu^0 and a partial demetallation of the CuN_4 site. According to our calculation at CO_2RR condition in 0.1 M H_2CO_3 + CO, both the CuN_4 and the MnN_4 sites on both bulk graphene and the graphene edge have a relatively higher thermodynamic driving force toward the dissolution than other metal elements considered in the experiment. Our calculation results for the CuN_4 site agree with the experiment [141].

4.8 CO_2RR Activity

Similar to the ORR mechanism with the electrolyte anion ligand on the back side of the metal atom, the following mechanism for CO_2 to CO formation is considered.

$$\begin{aligned} {}^*A/{}^*A + ne^- &\rightarrow {}^* /{}^*A + A^{n-} \\ CO_2 + H^+ + e^- + {}^* /{}^*A &\rightarrow {}^* COOH/{}^*A \\ {}^*COOH/{}^*A + H^+ + e^- &\rightarrow {}^* CO/{}^*A + H_2O \\ {}^*CO/{}^*A &\rightarrow {}^* /{}^*A + CO \end{aligned}$$

At any considered pH and U_{SHE}, the reaction free energy of the consecutive step along the CO_2 to CO can be expressed as

$$\Delta G_0(U_{SHE}, pH) = \Delta G({}^*A^{n-}/{}^*A) \tag{4.21}$$

$$\Delta G_1(U_{SHE}, pH) = G({}^*COOH/{}^*A) - G({}^*/{}^*A) - G(CO_2) - \frac{1}{2}G(H_2) - \Delta G_e - \Delta G_H \tag{4.22}$$

$$\Delta G_2(U_{SHE}, pH) = G({}^*CO/{}^*A) + G(H_2O) - G({}^*COOH/{}^*A) - \frac{1}{2}G(H_2) - \Delta G_e - \Delta G_H \tag{4.23}$$

$$\Delta G_3(U_{SHE}, pH) = G({}^*/{}^*A) + G(CO) - G({}^*CO/{}^*A) \tag{4.24}$$

It should be noted that G(CO) and G(CO_2), which are the free energy of CO and CO_2 gas molecule, are corrected by 0.15 eV and 0.30 eV, respectively, considering for the systematic DFT errors originated from an inaccurate description of C=O double bond [115]. The possible electrolyte anion participating in the CO_2RR is the most stable adsorbate at pH = 7 and U = -0.8 V_{SHE}. The catalytic activity is also considered at this condition by calculating the thermodynamic barrier of the limiting step.

As an example, the free energy diagrams of the CO_2RR to CO for some MN_4C_{10} structures (M = Mn, Fe, Co, Ni, Cu, Zn and Sn) in 0.1 M H_2CO_3 + CO solution are given in Figure 4.7 (a). At pH = 7, U = -0.80 V_{SHE}, the *CO is more stable than water on the MnN_4C_{10}, FeN_4C_{10}, CoN_4C_{10} structure. At the same time, the *HCO_3 is the most stable adsorbate on the ZnN_4C_{10} structure but there is no adsorbate on the

NiN_4C_{10}, CuN_4C_{10} and SnN_4C_{10} structures. It is found that the ligands are not thermodynamically favorable on both sides of the metal atom. Thus the other side of the metal atom is available for the reaction intermediate. The CO_2RR on the considered MN_4C_{10} structure in 0.1 M H_2CO_3 + CO solution at pH = 7 and U = -0.8 V_{SHE} is limited by the reduction of CO_2 to *COOH which is the change from the reaction state 1 to 2 in Figure 4.7 (a). Thus, the thermodynamic barrier of the limiting step is the energy barrier for reducing CO_2 to *COOH. Under the same condition, the ligand atom on the considered MN_4C_A structures is slightly different. However, the thermodynamic barrier of the limiting step is still the energy barrier for the reduction of CO_2 to *COOH, as shown in Figure 4.7 (b).

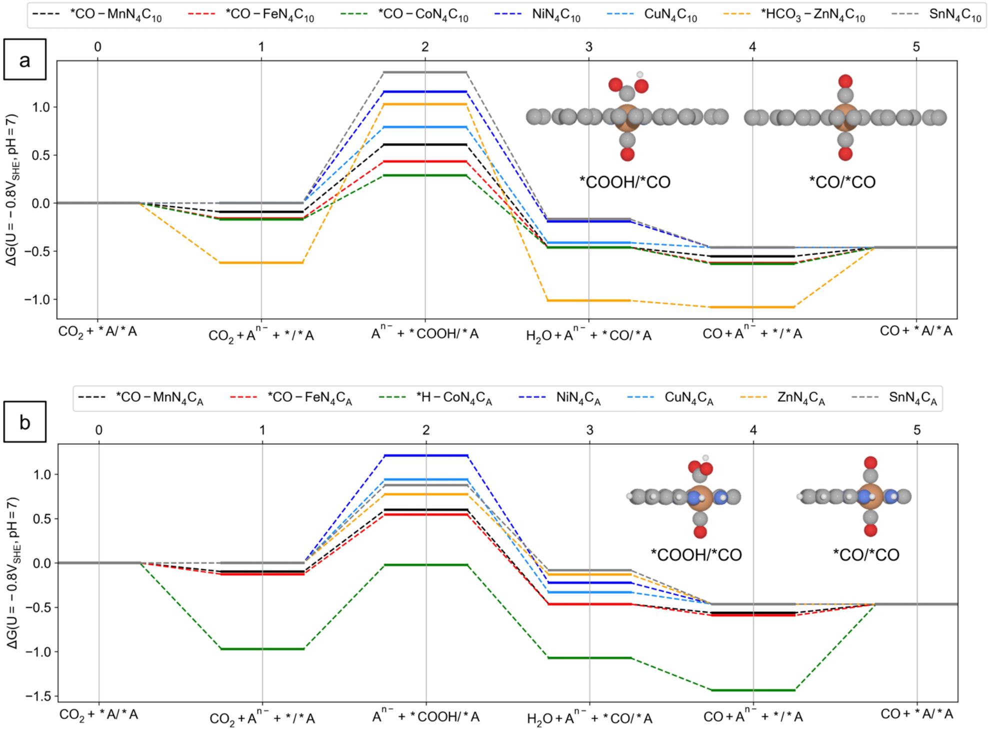

Figure 4.7: Free energy diagram of the CO_2RR to CO at pH = 7, U = -0.80 V_{SHE} on: (a) MN_4C_{10}, (b) MN_4C_A in 0.1 M H_2CO_3 + CO solution, where M = Mn, Fe, Co, Ni, Zn, Cu and Sn. The ligand on the back side of the metal atom is the most adsorbate at pH = 7, U = -0.80 V_{SHE}. The insets show the side view of the *COOH/*CO and *CO/*CO on the FeN_4 site. (C = gray, N = blue, H = white, O = red, Fe = orange).

Further comparison between the calculation results and the experiments [139, 141] is shown in Figure 4.8 (a). An experimental study by Ju *et al.* [139] has evaluated the electrochemical performance of the M/N/C catalyst (M = Mn, Fe, Co, Ni, and Cu) for CO_2 to CO formation and reported the order of the onset potential in 0.1 M $KHCO_3$ as follows: Co (-0.36 V_{RHE}) > Fe (-0.37 V_{RHE}) > Mn (-0.41 V_{RHE}) > Cu (-0.52

V_{RHE}) > Ni (-0.36 V_{RHE}). Their theoretical results have suggested that the potential-determining step on these M/N/C catalysts is the first proton-coupled electron transfer reduction of CO_2 to *COOH [139]. The experimental onset potentials reported by Ju *et al.* [139] are marked with red stars in Figure 4.8 and use the y-axis on the right.

Based on the MN_4C_{10} structure in 0.1 M H_2CO_3 with CO, we find the thermodynamic barrier of the limiting step at U = -0.80 V_{SHE} and pH = 7 in the following order: Co (0.46 eV) < Fe (0.59 eV) < Mn (0.70 eV) < Cu (0.79 eV) < Ni (1.16 eV), agreeing with the onset potential order reported by Ju *et al.* [139]. For the MN_4C_A structure in 0.1 M H_2CO_3 with CO, the thermodynamic barrier of the limiting step at the same condition is in the following order: Fe (0.67 eV) < Mn (0.70 eV) < Cu (0.94 eV) < Co (0.95 eV) < Ni (1.21 eV), deviating from the experimental trend.

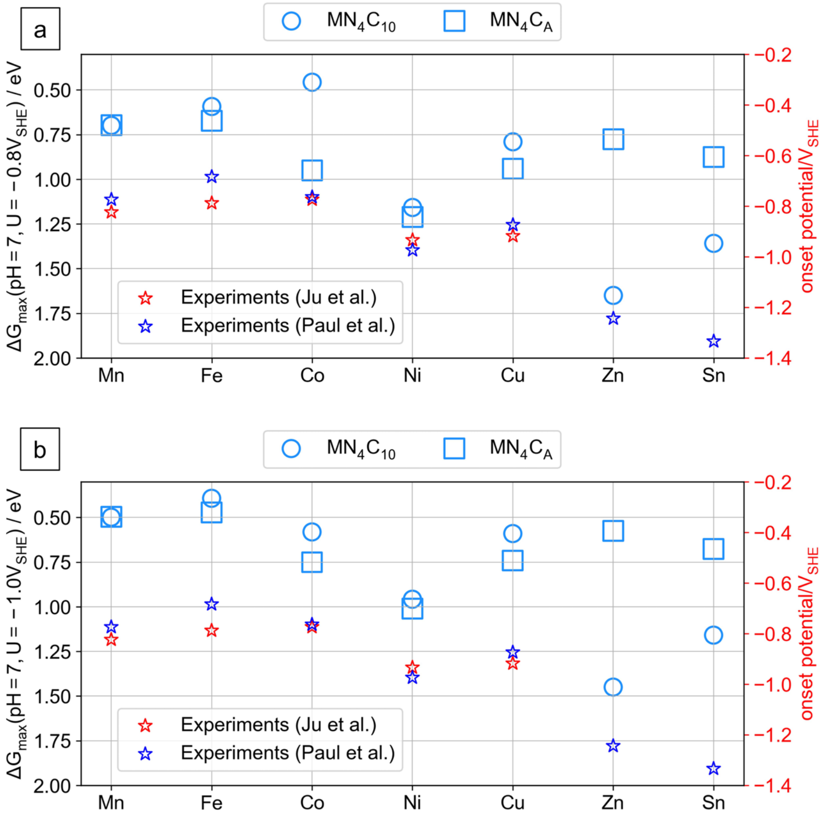

Figure 4.8: Comparison the onset potentials from the experiments [139, 141] and calculated ΔG_{max} for the CO_2RR to CO on MN_4C_{10} (circle) and MN_4C_A (square) with M = Mn, Fe, Co, Ni, Cu, Zn, and Sn at pH = 7: (a) U = -0.8 V_{SHE} and (b) U = -1.0 V_{SHE}. The ligand on the back side of the metal atom is the most stable adsorbate at pH = 7: (a) U = -0.8 V_{SHE} and (b) U = -1.0 V_{SHE}.

Recently, Li *et al.* [140] have synthesized and evaluated the activity toward CO formation in 0.1 M $KHCO_3$ for the M/N/C catalysts with M = Mn, Fe, Co, Ni, and Cu. They have reported the following order of CO partial current density at U = -0.6 V_{RHE} : Co > Fe > Ni > Cu > Mn. The thermodynamic barrier order obtained from the MN_4C_{10} structure agrees with this experimental results only for the relative order between Co, Fe, and Mn.

In another experimental study by Paul *et al.* [141], the M/N/C catalyst with M = Mn, Fe, Co, Ni, Cu, Zn, and Sn was synthesized and evaluated the performance of the CO_2RR in gas diffusion electrodes. The experimental onset potential for the CO formation in 0.5 M $KHCO_3$ + 0.5 M K_2SO_4 at pH = 7.5 has been reported in the following order: Fe (-0.27 V_{RHE}) > Co (-0.35 V_{RHE}) > Mn (-0.36 V_{RHE}) > Cu (-0.46 V_{RHE}) > Ni (-0.56 V_{RHE}) > Zn (-0.83 V_{RHE}) > Sn (-0.92 V_{RHE}). The onset potentials reported by Paul *et al.* [141] are marked with blue stars in Figure 4.8. Our thermodynamic barriers calculated from the MN_4C_{10} and MN_4C_A structures in 0.1 M H_2CO_3 with CO do not give the same order as this experiment.

It should be noted that other possible sites with different coordination environments [160–162] could be involved in the catalytic process and that the distribution of active sites could be different in each experiment, depending on the synthesis process. Also, the onset potential in each experiment is defined differently. Furthermore, it is assumed that the CO_2RR to CO in the experiments is limited by the reduction of CO_2 to *COOH step, same as in our calculation results.

On top of that, the ligand is defined as the most stable adsorbate at U = -0.8 V_{SHE} and pH = 7. The most stable ligand could be different when the potential slightly deviates from U = -0.8 V_{SHE} on some metal sites, i.e., the CoN_4C_{10} site. The thermodynamic barrier of the limiting step on the metal site in 0.1 M H_2CO_3 + CO at U = -1.0 V_{SHE} and pH = 7 is shown in Figure 4.8 (b). The most stable adsorbate at U = -1.0 V_{SHE} and pH = 7 is considered to be a ligand on the back side of the metal site. At this condition, most of the considered MN_4C_{10} sites still have the same ligand, except on the CoN_4C_{10} site where the ligand is now *H. For the MN_4C_{10} structure, the limiting step is still the reduction of CO_2 to *COOH as shown in Figure B.8 (a) of Appendix B. The thermodynamic barrier is in the following order: Fe < Mn < Co < Cu < Ni < Sn < Zn. The most active site is shifted from the CoN_4C_{10} to FeN_4C_{10} site. Still, this order is slightly different from the experimental trend reported by Paul *et al.* [141]. For the MN_4C_A structures at U = -1.0 V_{SHE}, pH = 7, we find the same order of thermodynamic barrier as the MN_4C_{10} structures.

It should be noted that the oxidation state on the single metal atom in the pristine MN_4 structure is considered to be 2+. Our calculations give a relatively high thermodynamic barrier for the NiN_4 site on both bulk graphene and graphene edge, compared to the FeN_4 site. While the Fe/N/C and particularly Ni/N/C catalyst have been suggested as a highly promising catalyst for selective CO production [139–141]. One possible explanation is that the $Ni^{2+}N_4$ site is not active for the CO_2RR. According to a previous study by Li *et al.* [140], the $Ni^{1+}N_4C_{10}$ site binds CO_2 more strongly than the $Ni^{2+}N_4C_{10}$ site, resulting in a higher activity toward CO formation for $Ni^{1+}N_4C_{10}$ than the $Ni^{2+}N_4C_{10}$ site. In fact, by the DFT calculations, they have found that the $Ni^{1+}N_4$ site has the highest activity among considered MN_4 sites in their study where M = Mn^{2+}(*O), Fe^{2+} (*H_2O), Co^{2+} (*H_2O), Ni^{1+}, and Cu^{2+}. The letter in parentheses is the ligand considered in their study [140].

The local environment could also influence the catalytic activity. According to a previous study by Yang *et al.*, the NiN_3 site has been found to be more active for the CO_2RR than the NiN_4 site [161]. Furthermore, it has been suggested that the NiN_4 site has a weaker binding to *H than the CoN_4 site, making the hydrogen evolution reaction (HER) unfavorable for the Ni/N/C catalyst compared to the Co/N/C catalyst. Also, the CO selectivity is higher for the Ni/N/C catalyst than the Co/N/C catalyst [139]. According to Figure B.8 in Appendix B, the binding energy of *H on the NiN_4 site is weaker than that on the CoN_4 site. Thus the NiN_4 sites in this study are also expected to have higher selectivity toward CO formation than the CoN_4 sites.

The ΔG_{max} along the CO_2RR to CO path at pH = 7, U = -0.80 V_{SHE} is shown in Figure B.9. It is seen that the two NO gas molecules can be adsorbed on both sides of $IrN_4C_{x=10,A}$ and ReN_4C_A structure. In 0.1 M H_2CO_3 + CO + NO solution at pH = 7 and U = -0.8 V_{SHE}, the thermodynamic barrier of the limiting step is the energy to remove one *NO plus the energy to form *COOH on theses metal site. Similarly, the two CO gas molecules can be adsorbed on both sites of $ReN_4C_{x=10,A}$, $OsN_4C_{x=10,A}$, RuN_4C_A, and WN_4C_A structure. In 0.1 M H_2CO_3 + CO solution at pH = 7 and U = -0.8 V_{SHE}, the thermodynamic barrier of the limiting step on these metal sites is also the energy to remove one *CO plus the energy to form *COOH.

4.9 Stability vs Activity

In order to identify the promising catalysts which are both electrochemically stable and active from our calculation results, the ΔG_R of the most stable surface of the MN_4 site is plotted against its corresponding thermodynamic barrier of the limiting step under the same condition.

For the ORR catalyst, it is considered at U = 0.80 V_{SHE} and pH = 1 as shown in Figure 4.9 (a-b). It is seen that the FeN_4, CoN_4, MnN_4, and RuN_4 sites on both bulk graphene and graphene in many electrolytes emerge as promising candidates, as many previous experimental studies have reported [9, 12, 19, 91, 92, 136, 146]. In the previous chapter, where the electrolyte adsorption was not included, the MnN_4C_{10} and MnN_4C_A structures were not promising candidates for the ORR in the acid condition. However, the MnN_4 site becomes more stable against the dissolution through electrolyte adsorption in this study. Other promising combinations between metal elements and acid electrolytes are shown in Table 4.1. It is seen that p-block metals, mainly on the graphene edge, have comparable stability and activity to the transition metal site. The Sn/N/C catalysts have been synthesized and exhibited similar activity, and selectivity toward the four-electron ORR to the Fe/N/C catalyst in 0.1 M $HClO_4$ [163]. The Sb/N/C catalyst has also been synthesized and exhibited promising activity toward the ORR, although in 0.1 M KOH [144].

In the case of the catalyst for CO_2RR to CO, it is considered at U = -0.80 V_{SHE} and pH = 7 as shown in Figure 4.9 (b-c). Besides the FeN_4, CoN_4, NiN_4 and MnN_4 sites which have been experimentally suggested for CO production [139–141, 164], other promising combinations between metal elements and electrolytes or gas molecules are identified as shown in Table 4.2.

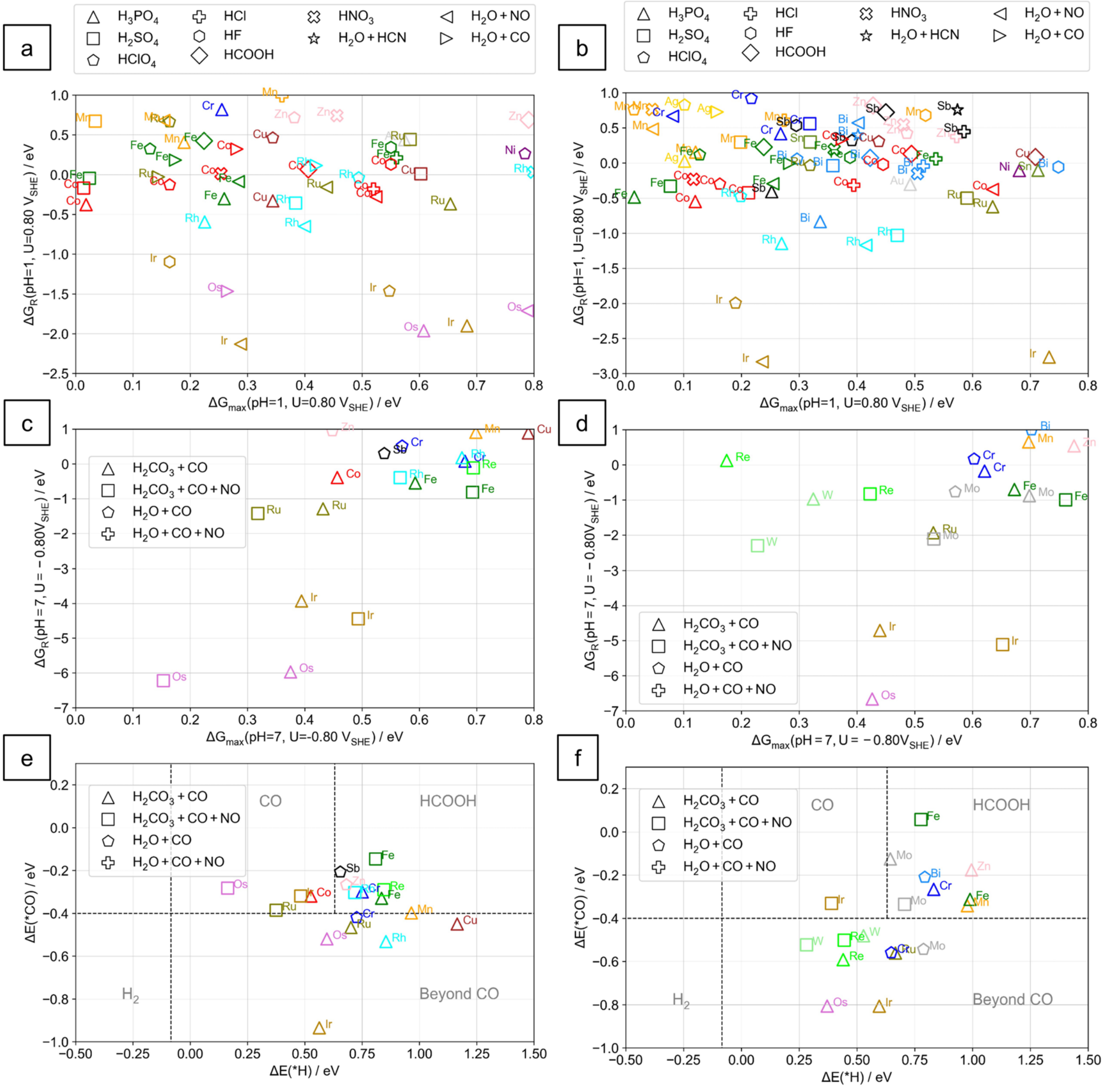

Figure 4.9: ΔG_R vs ΔG_{max} for the ORR: (a) MN_4C_{10} (b) MN_4C_A. ΔG_R vs ΔG_{max} for the CO_2RR to CO: (c) MN_4C_{10} (d) MN_4C_A. Classification plot for possible CO_2RR products of promising candidates based upon the binding energies of H and CO criterion by Bagger *et al.* [165, 166]: (e) MN_4C_{10} and (f) MN_4C_A

Table 4.1: Promising combinations between metal and electrolytes for ORR

structure	electrolyte
$CrN_4C_{x=10,A}$	H_3PO_4
CrN_4C_A	H_2O+NO, H_2SO_4, a non adsorbing electrolyte (e.g. $HClO_4$, HCl, HCOOH)
$CuN_4C_{x=10,A}$	a non-adsorbing electrolyte (e.g. $HClO_4$, HNO_3)
CuN_4C_{10}	H_2SO_4, H_3PO_4
$ZnN_4C_{x=10,A}$	$HClO_4$, HNO_3
ZnN_4C_A	HCOOH, HCl
$RhN_4C_{x=10,A}$	H_2SO_4, H_2O+NO, H_3PO_4
RhN_4C_{10}	H_2O+CO, $HClO_4$
RhN_4C_A	a non-adsorbing electrolyte (e.g. $HClO_4$, HF, HCOOH)
AgN_4C_A	H_3PO_4
OsN_4C_{10}	H_3PO_4, H_2O+CO, H_2O+NO
$IrN_4C_{x=10,A}$	H_2O+NO, H_3PO_4
IrN_4C_{10}	$HClO_4$, a non-adsorbing electrolyte (e.g. HF)
IrN_4C_A	a non-adsorbing electrolyte (e.g. $HClO_4$, HF, HCOOH)
$AuN_4C_{x=10,A}$	a non-adsorbing electrolyte (e.g. all considered electrolytes)
SnN_4C_A	H_2SO_4, H_3PO_4
SbN_4C_A	HCOOH, HCl, H_3PO_4
BiN_4C_A	H_3PO_4, $HClO_4$, H_2SO_4,HCOOH

Table 4.2: Promising combinations between metal and electrolytes for CO_2RR to CO

structure	electrolyte
$OsN_4C_{x=10,A}$	H_2CO_3+CO
OsN_4C_{10}	H_2CO_3+CO+NO
$IrN_4C_{x=10,A}$	H_2CO_3+CO, H_2CO_3+CO+NO
$RuN_4C_{x=10,A}$	H_2CO_3+CO
RuN_4C_{10}	H_2CO_3+CO+NO
RhN_4C_{10}	H_2CO_3+CO, H_2CO_3+CO+NO
$FeN_4C_{x=10,A}$	H_2CO_3+CO+NO
$ReN_4C_{x=10,A}$	H_2CO_3+CO+NO
$CrN_4C_{x=10,A}$	H_2O+CO, H_2CO_3+CO
SbN_4C_{10}	H_2O+CO
ZnN_4C_{10}	H_2O+CO
ZnN_4C_A	H_2CO_3+CO
CuN_4C_{10}	H_2CO_3+CO
WN_4C_A	H_2CO_3+CO, H_2CO_3+CO+NO
BiN_4C_A	a non-adsorbing electrolyte (e.g. H_2O)
MoN_4C_{10}	H_2CO_3+CO, H_2CO_3+CO+NO, H_2O+CO.

Additionally, the competing HER is crucial in determining the catalytic efficiency. It has been shown that the binding strengths of *CO and *H play the role of a descriptor for CO_2RR selectivity on transition metal surfaces [166] and single site porphyrin-like structures [165]. Figure 4.9 (e) and (f) show the classification of possible products from CO_2RR on the single metal sites. It is seen that the promising candidates are selective toward CO over H_2 production. As shown in Figure B.10 in Appendix B, the effect of the ligand is clearly observed on the MoN_4, RuN_4, WN_4, ReN_4, and OsN_4 sites where the bare metal sites strongly bond with *H. Thus these sites are highly selective for the HER. However, the binding of *H becomes weaker with the presence of the ligand. As a result, the competing HER can be suppressed. In addition to the CO formation, it is found that $IrN_4C_{x=10,A}$ in H_2CO_3+CO; OsN_4C_A in H_2CO_3+CO solution potentially reduce CO_2 to the products beyond CO. Other promising candidates that can produce the products beyond CO are $RuN_4C_{x=10,A}$, RhN_4C_{10}, OsN_4C_{10} in H_2CO_3+CO solution; ReN_4C_A, WN_4C_A in H_2CO_3+CO or H_2CO_3+CO+NO solution; and CrN_4C_A, MoN_4C_{10} in H_2O + CO solution.

For the transition metal single atom considered in this study, it is found that the reaction intermediate binding on the MN_4 site on the graphene edge is generally weaker than that on the MN_4 site on the bulk graphene. Figure 4.10 illustrates the projected density of states (PDOS) for the CoN_4C_{10} and CoN_4C_A sites without and with adsorbate (either one *OH or *COOH adsorbate). In the pristine structure of the CoN_4C_{10} site, we find the $3d_{xy}$ hybridization with the 2p orbitals of the surrounding N atoms forms the Co-N bonds. While the other 3d orbitals are non-binding orbitals. For the pristine structure of the CoN_4C_A site, both $3d_{xy}$ and $3d_{x^2-y^2}$ orbitals overlap with the 2p orbitals for the surrounding N atoms. When either *OH or *COOH adsorbs on the Co center atom, the 2p orbitals of *OH or *COOH overlap with $3d_{z^2}$ and $3d_{yz}$ orbitals of the Co atom on both the CoN_4C_{10} and CoN_4C_A sites. However, it is found that in the CoN_4C_{10} site, the Co $3d_{x^2-y^2}$ orbital locates below, while the Co $3d_{xy}$ orbital locates above the Fermi energy. The opposite trend is found for the CoN_4C_A site. It appears that the difference in d-orbitals located near the Fermi level, possibly caused by different local carbon structures, could affect the binding strength of the adsorbates [30].

Furthermore, with the ligand on the other side of the single metal atom, the adsorption of the reaction intermediate is likely to become weaker. The change in adsorption behavior of the ORR intermediate with the ligand on the back side in the CrN_4C_{12} and the CoN_4C_{12} structure has been previously explained by Svane *et al.* [93, 121] using the crystal field theory. Figure 4.11 shows the possible electronic configuration in the d-orbitals of the metal center in the MN_4C_{10} (M = Cr, Mn, Fe, and Co) structure with one and two adsorbates, based on the converged magnetization projected on the metal atom and the crystal field theory. The MN_4 site with two adsorbates adopts an octahedral structure. According to the crystal field theory, the d-orbitals of the metal center are split into two different energy levels, t_{2g} and e_g. For Co^{2+} with a low spin configuration in the octahedral geometry, transferring more than one electron to the adsorbates may not be thermodynamically favorable. Since after the first unpaired electron is transferred from the e_g d-orbitals, the remaining electrons are paired and placed in the lower t_{2g} d-orbitals. Similarly, for Fe^{2+} in the octahedral geometry with a low spin configuration, all d-electrons are placed in the lower t_{2g} d-orbitals. Removing electrons from these fully occupied orbitals may not be thermodynamically favorable. After all, this could destabilize *COOH and *OH when they bind as the second adsorbate. A similar value of the converged magnetization projected on the metal center in the MN_4 site is found on both bulk graphene and graphene edge. Thus, the metal center in both structures should have a similar electronic configuration in their d-orbitals.

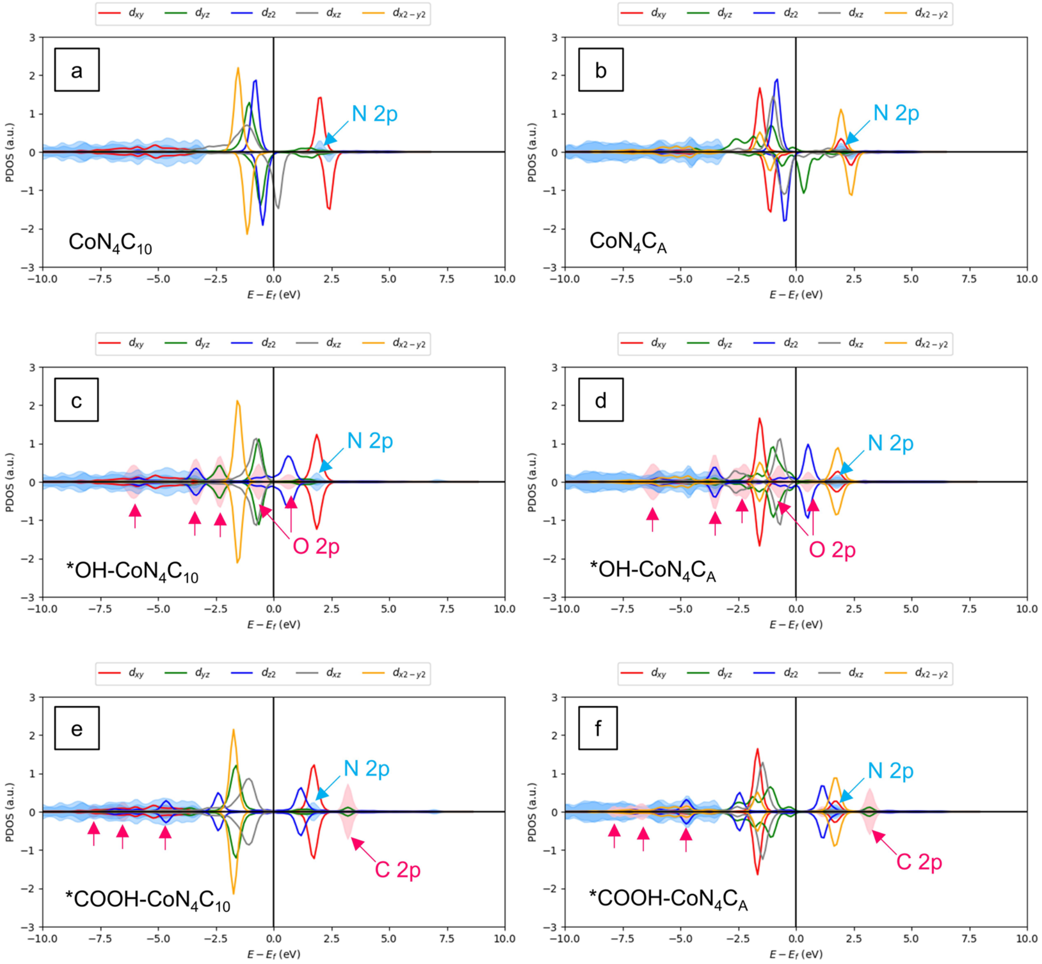

Figure 4.10: Spin-polarized density of states for: (a-b) the pristine CoN_4C_{10} and CoN_4C_A site projected onto Co 3d, N 2p orbital. (c-d) The CoN_4C_{10} and CoN_4C_A site with *OH projected onto Co 3d, N 2p and O 2p (*OH) orbital. (e-f) The CoN_4C_{10} and CoN_4C_A with *COOH projected onto Co 3d, N 2p and C 2p (*COOH) orbital.

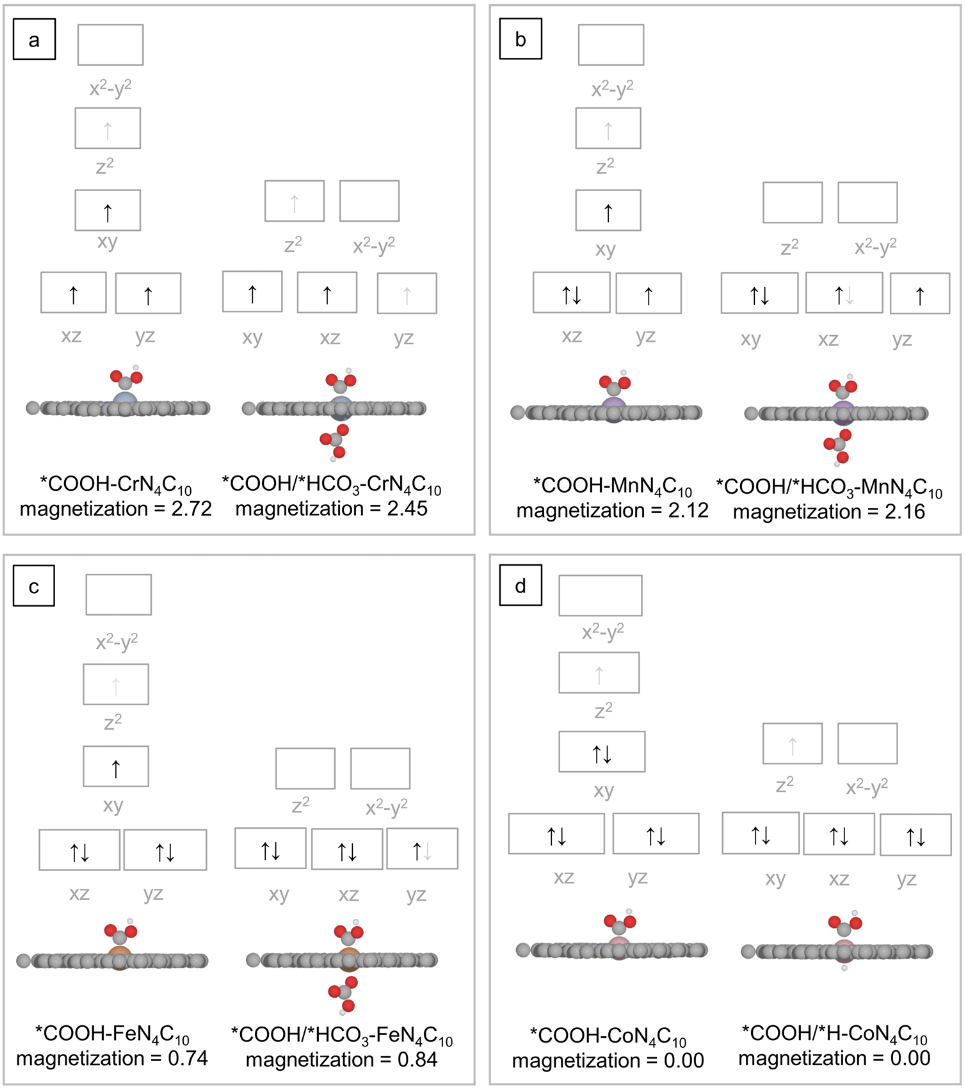

Figure 4.11: Illustration of d-orbital splitting and possible electron configurations for a single metal atom on bulk graphene (MN_4C_{10}) in square pyramidal geometry (with one adsorbate), octahedral geometry (two adsorbates): (a) Cr, (b) Mn, (c) Fe and (d) Co. The possible electron configuration is based on the converged magnetization projected on the metal center (number of spin-up - number of spin-down), and it is assumed that the oxidation of the metal center atom of the pristine structure (without adsorbates) is 2+. Only electrons in the black arrows remain on the metal center atom, while the electrons in the grey arrows are donated to the adsorbates. The relative position of energy level is qualitative only.

4.10 Conclusions

The effect of electrolyte anion adsorption on the stability and activity of single metal atom catalysts was studied. We considered two structural models of the M/N/C catalysts: the MN_4 motif on the bulk graphene terrace and the graphene edge with 3d, 4d, 5d, or p-block (Sn, Sb, and Bi) metal atoms. It was found that the armchair edge is thermodynamically favored to form the MN_4 site compared to the bulk graphene, especially for 3d transition metals. Under ORR conditions, various electrolyte anions can compete with water and adsorb on the single metal site. The electrolyte anion adsorption depends on the nature of the metal atom and local carbon structure around the MN_4 site. The ORR activity is either poisoned or altered by the electrolyte anion. If the electrolyte anion adsorbs on the single metal site, the single metal site can be further stabilized against dissolution in acid environments, compared to the stability in the pure water environment. It would be interesting to include the electrolyte stabilization effect on other MN_4 sites with different local carbon structures, although the sites considered here are expected to be among the most stable sites. Considering both stability in acid conditions and ORR activity, a single metal site based on Ir, Cu, Rh, Zn, Au, Os, Cr, and p-block elements (Sb, Sn, and Bi), especially on the graphene edge, has comparable ORR activity and stability to a single metal atom based on Fe and Co. Under the CO_2RR condition, most considered electrolyte anions, except in 0.1 M H_2CO_3 solution, do not interact with the single metal site. Still, water and gas molecules may form ligands on various single metal sites under the CO_2RR condition. It was found that the activity trend for the reduction of CO_2 to CO on the single metal site with the ligand from the solution compares well with the experimental trends. Besides the single-atom catalysts based on Fe, Co, Mn and Ni, we suggested promising single metal sites (Cr, Ru, W, Re, Os, Rh, Bi, Sb, Mo, Zn, and Ir) by including the adsorbate ligand from the solution. These promising candidates have comparable stability and activity to the Fe and Co-based catalysts. This study illustrated that the nature of the metal atom, the local carbon structure, and the chemical environment (i.e., electrolyte anions) play a critical role in the activity and stability of a single-atom electrocatalyst. A careful combination of electrolyte or gas ligand and a single metal atom with various local carbon structures could be a possible way to achieve an active and durable electrocatalyst.

Chapter 5

Degradation of Polybenzimidazole in Alkaline Solution

This chapter is based on the work presented in Paper III as given in Appendix D. The alkaline stability of the polybenzimidazole molecule is investigated as the polybenzimidazole molecule is a promising material for anion exchange membranes in alkaline fuel cells. This chapter covers the main points and results.

5.1 Introduction

Alkaline anion exchange membranes have gained increased attention due to their potential integration with a wide range of electrochemical energy storage and conversion devices, such as fuel cells and electrolyzers. Generally, in order to allow hydroxide ion conduction in an anion exchange membrane, cations, such as ammonium [11, 48], imidazolium cation [49–52] and benzimidazolium [50, 53, 54] are commonly attached to the polymer backbone. However, the hydroxide ion can react irreversibly with the polymer backbone and cations, causing the loss of ionic conductivity [55–57]. As a result, a chemical stability remains a significant challenge for anion exchange membranes. An alternative is an ion-solvating membrane where an aqueous electrolyte is dissolved in a polymer matrix, utilizing the uptake of the aqueous electrolyte to achieve ionic conductivity. Thus, there is no need for cation moieties [47, 60].

The poly(2,2-(m-phenylene)-5,5-bibenzimidazole) (mPBI) equilibrated in potassium hydroxide (KOH) solution can result in the ion-solvating membrane, consisting of KOH and water dissolved in the polymer matrix [66]. This alkaline doped mPBI system has high ionic conductivity, and excellent chemical stability in an alkaline condition [60, 66]. Also, it has been tested as an anion exchange membrane in direct alkaline alcohol fuel cells [167], alkaline fuel cells [159, 168], alkaline water electrolyzers [60, 62, 169], and vanadium redox flow batteries [170] with remarkable performance.

The composition of the alkaline doped mPBI system strongly depends on the KOH concentration, which significantly determines the ionic conductivity of the membrane. The mPBI undergoes deprotonation when it is immersed in an alkaline solution.

The acid-base equilibrium of mPBI in KOH solution is shown as reaction (0) in Figure 5.1. The system exhibits high ionic conductivity and chemical stability at low concentration (5 - 10 wt% KOH at T = 88°C) [60, 61]. Further increasing KOH concentration enhances the ionic conductivity [60, 61] but causes the degradation of the polymer as the gradually reduced molecular weight, mechanical strength, ionic conductivity, and structural change have also been reported [60, 61]. Thus, the actual use is still limited.

The mPBI-based membrane in an alkaline solution may degrade via a hydrolysis reaction [60, 61, 69]. Figure 5.1 shows the postulated degradation pathway. Reaction (1) is the nucleophilic addition of hydroxide ions at the benzimidazole ring. The following reactions are (2) ring-opening and (3) chain scissions [46, 61, 68]. The postulated degradation pathway is similar to the degradation of imidazolium and benzimidazolium cations [56, 57, 171, 172]. As shown in Figure 5.1, the negative charge may be delocalized over the benzimidazole ring after the deprotonation. The interaction between the deprotonated mPBI molecule and hydroxide ion in reaction (1) could differ from that of cations. Also, the following degradation reaction could be different. However, the degradation mechanism of the mPBI molecule in an alkaline solution has not been presented in detail. On top of that, it is still unclear which form of mPBI molecule undergoes the degradation in an alkaline solution since the equilibrium of the reaction (0) in Figure 5.1 strongly depends on the KOH concentration [64, 66].

In this chapter, we use the DFT calculations to evaluate the predominant species and the degradation mechanism of mPBI molecule in an alkaline solution. The postulated degradation pathway of the mPBI molecule, as shown in Figure 5.1, is investigated. The effect of explicit water molecules and hydroxide ion concentration on the degradation is considered. A comparison between experiment and theory is achieved by computing the effective energy barrier for the degradation against those estimated from experimental results.

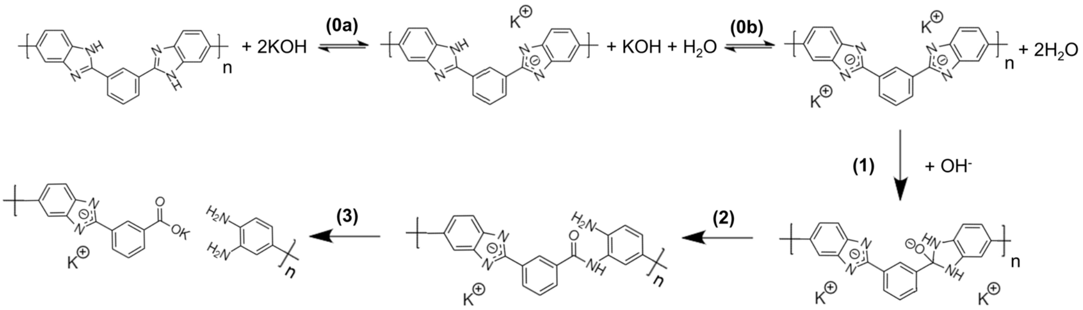

Figure 5.1: Schematic illustration: Reaction (0) is an acid-base equilibrium of mPBI molecule in KOH solution, and reaction (1)-(3) is a postulated degradation pathway of mPBI in alkaline solution

5.2 Computational Details

In this chapter, the DFT calculations were performed using the B3LYP functional [81] and 6-311++G(d, p) basis sets as implemented in Q-Chem 5.2 [173] for both optimized geometries and calculated energies. The threshold for the maximum gradient and the self-consistent field (SCF) energy change between consecutive optimization cycles was 3.0×10^{-3} Hartree/Bohr and 1.0×10^{-8} Hartree, respectively. The geometry optimizations for intermediate and transition states were carried out in gas phase. A freezing string method (FSM) [174, 175] was used to approximate the path connecting each intermediate state pair. The highest energy point on the path was taken as the first approximation for a transition state. The refined transition state was found using Baker's partitioned rational-function optimization (P-RFO) algorithm [176] also implemented in Q-chem 5.2. Each transition state was verified to connect the designated reactant and product by performing intrinsic reaction coordinate (IRC) [177] calculations. The vibrational frequencies were calculated to confirm the local minima on the potential energy surface with no imaginary frequencies for the reaction intermediates and one single imaginary frequency for the transition states. Single point energies were computed with the conductor-like polarization continuum model (C-PCM) [178–180] based on the optimized gas-phase geometries, and a dielectric constant of 78.39 corresponding to the bulk water was used to include the effect of the surrounding water medium.

Reaction free energy and free energy barrier are calculated at T = 88°C and pressure = 1 atm, which is the same as the experimental condition [61]. The free energy (G) of the model compound is the calculated DFT energy (E_{DFT}) included zero-point energy (ZPE), enthalpy contribution ($H = H_{vibration} + H_{rotation} + H_{translation}$), and entropy contribution ($S = S_{vibration} + S_{rotation} + S_{translation}$) calculated in the gas phase. The vibration calculations assume harmonic approximation. The reaction free energy in the solution phase is, for the example, given by

$$A + B \rightarrow C$$

$$\Delta G_{(sol)} = G(C_{(sol)}) - G(A_{(sol)}) - G(B_{(sol)}) \tag{5.1}$$

$$= \Delta E_{(sol)} + \Delta ZPE_{(gas)} + \Delta H_{(gas)} - T\Delta S_{(gas)} \tag{5.2}$$

$$\text{where } \Delta E_{(sol)} = E(C_{(sol)}) - E(A_{(sol)}) - E(B_{(sol)}) \tag{5.3}$$

$$\Delta ZPE_{(gas)} = ZPE(C_{(gas)}) - ZPE(A_{(gas)}) - ZPE(B_{(gas)}) \tag{5.4}$$

$$\Delta H_{(gas)} = H(C_{(gas)}) - H(A_{(gas)}) - H(B_{(gas)}) \tag{5.5}$$

$$\Delta S_{(gas)} = S(C_{(gas)}) - S(A_{(gas)}) - S(B_{(gas)}) \tag{5.6}$$

where $E(X_{(sol)})$ is the single point energy of species X (where X = A, B) computed with the presents of the implicit solvation based on the optimized gas-phase geometry. ZPE, H, and S are calculated in the gas phase.

5.3 Deprotonation Reaction

The mPBI-based membrane has been found to undergo deprotonation when it was soaked in KOH solution, and the ionized form has been found as a major species at high concentration [66]. At the same time the degradation has also been observed at high KOH concentration. Thus, it has been suggested that the degradation of the mPBI starts from the ionized species [66]. The $\mathrm{pK_a}$ of the mPBI molecule is firstly considered here to identify a predominant species at the high pH range, where degradation occurs.

$$\begin{tikzcd}
\mathrm{mPBI}(0)_{(\mathrm{gas,\,1atm})} \arrow[r, "\Delta G^{\mathrm{Depronation}}_{(\mathrm{gas})}"'] \arrow[d, "\Delta \mathrm{mPBI}(0)_{\mathrm{sol}}"] & \mathrm{mPBI}(-1)_{(\mathrm{gas,\,1atm})} \arrow[d, "\Delta \mathrm{mPBI}(-1)_{\mathrm{sol}}"] & + & \mathrm{H}^{+}{}_{(\mathrm{gas,\,1atm})} \arrow[d, "\Delta \mathrm{H}^{+}_{\mathrm{sol}}"] \\
\mathrm{mPBI}(0)_{(\mathrm{sol,\,1M})} \arrow[r, "\Delta G^{\mathrm{Depronation}}_{(\mathrm{sol})}"] & \mathrm{mPBI}(-1)_{(\mathrm{sol,\,1M})} & + & \mathrm{H}^{+}{}_{(\mathrm{sol,\,1M})}
\end{tikzcd}$$

Figure 5.2: Thermodynamic cycle for calculation of the first deprotonation reaction. Abbreviation in brackets: (gas) = gas phase and (sol) = solution phase (implicit solvation)

Two possible protons are deprotonated in mPBI molecule. The stepwise dissociation constant is defined for losing a single proton as illustrated in the reaction (0a) and (0b) in Figure 5.1. The dissociation constant for the first proton is denoted as $\mathrm{pK_a^1}$, and the successive proton is $\mathrm{pK_a^2}$. The acid deprotonation reaction of the mPBI molecule can be expressed as follows

$$\mathrm{mPBI(0)} \rightleftharpoons \mathrm{mPBI(-1)} + \mathrm{H^+} \rightleftharpoons \mathrm{mPBI(-2)} + 2\mathrm{H^+}$$

The number in parenthesis indicates the total charge on the molecule. Thus, mPBI(0) is the non-deprotonated form, mPBI(-1) is the partially deprotonated form after losing one proton, and mPBI(-2) is the fully deprotonated form after losing two protons. The $\mathrm{pK_a}$ is calculated from the deprotonation free energy in the solution phase.

$$\mathrm{pK_a} = \frac{1}{2.303RT}\Delta G^{\mathrm{Deprotonation}}_{(\mathrm{sol})} \tag{5.7}$$

where $\Delta G^{\mathrm{Deprotonation}}_{(\mathrm{sol})}$ is calculated from the thermodynamic cycle in Figure 5.2 and can be expressed as follows

$$\Delta G^{\mathrm{Deprotonation}}_{(\mathrm{sol})} = \Delta G^{\mathrm{Deprotonation}}_{(\mathrm{gas})} + \Delta \mathrm{mPBI}(-1)_{\mathrm{sol}} + \Delta \mathrm{H}^{+}_{\mathrm{sol}} - \Delta \mathrm{mPBI}(0)_{\mathrm{sol}} \tag{5.8}$$

where $\Delta G^{\mathrm{Deprotonation}}_{(\mathrm{gas})}$ is the deprotonation free energy in gas phase.

$$\Delta G^{\mathrm{Deprotonation}}_{(\mathrm{gas})} = G(\mathrm{mPBI}(-1)_{(\mathrm{gas})}) + G(\mathrm{H}^{+}_{(\mathrm{gas})}) - G(\mathrm{mPBI}(0)_{(\mathrm{gas})}) \tag{5.9}$$

where $G(\mathrm{mPBI}(-1)_{(\mathrm{gas})})$ and $G(\mathrm{mPBI}(0)_{(\mathrm{gas})})$ are the free energy of the mPBI(-1) and mPBI(0) molecule in gas phase. $\Delta\mathrm{mPBI}(0)_{\mathrm{sol}}$ and $\Delta\mathrm{mPBI}(-1)_{\mathrm{sol}}$ are the solvation energy of mPBI(0) and mPBI(-1) molecule, respectively, and can be calculated as

$$\Delta\mathrm{mPBI}(0)_{\mathrm{sol}} = E(\mathrm{mPBI}(0)_{(\mathrm{sol})}) - E(\mathrm{mPBI}(0)_{(\mathrm{gas})}) \tag{5.10}$$

$$\Delta\mathrm{mPBI}(-1)_{\mathrm{sol}} = E(\mathrm{mPBI}(-1)_{(\mathrm{sol})}) - E(\mathrm{mPBI}(-1)_{(\mathrm{gas})}) \tag{5.11}$$

where $E(\mathrm{mPBI}(0)_{(\mathrm{gas})})$ and $E(\mathrm{mPBI}(-1)_{(\mathrm{gas})})$ are the calculated DFT energy of mPBI(0), mPBI(-1) molecule in gas phase. $E(\mathrm{mPBI}(0)_{(\mathrm{sol})})$ and $E(\mathrm{mPBI}(-1)_{(\mathrm{sol})})$ are the single point energy of mPBI(0), mPBI(-1) molecule computed with the presence of the implicit solvation based on the optimized gas-phase geometry. $G(\mathrm{H}^+_{(\mathrm{gas})})$ is the free energy of the proton in the gas phase, which is calculated as

$$G(\mathrm{H}^+_{(\mathrm{gas})}) = E(\mathrm{H}^+_{(\mathrm{gas})}) + H(\mathrm{H}^+_{(\mathrm{gas})}) - TS(\mathrm{H}^+_{(\mathrm{gas})}) \tag{5.12}$$

where $E(\mathrm{H}^+_{(\mathrm{gas})}) = 0.00$ eV, $H(\mathrm{H}^+_{(\mathrm{gas})}) = \frac{5}{2}RT = 0.08$ eV and $S(\mathrm{H}^+_{(\mathrm{gas})}) = 0.41$ eV taken from the literature [181]. $\Delta\mathrm{H}^+_{\mathrm{sol}}$ is a solvation correction for a proton in solution phase, which is calculated as

$$\Delta\mathrm{H}^+_{\mathrm{sol}} = \Delta G_{1\mathrm{atm}\rightarrow 1\mathrm{M}} + \Delta G(\mathrm{H}^+)_{\mathrm{solvation}} \tag{5.13}$$

where $\Delta G_{1\mathrm{atm}\rightarrow 1\mathrm{M}}$ (= 0.08 eV) is the correction corresponding to the change in state from 1 atm to 1 M taken from the literature [181]. $\Delta G(\mathrm{H}^+)_{\mathrm{solvation}}$ (= -11.53 eV) is solvation free energy for proton taken from the literature [181].

For the mPBI molecule, we find that $\mathrm{pK}_a^1 = 12.46$ and $\mathrm{pK}_a^2 = 12.85$, suggesting that the mPBI(-2) molecule is the major species at high pH (high KOH concentration). Since there is a slight difference between successive $\mathrm{pK_a}$ values, there can be an overlap between the pH range and the existence of these three species. The mole fraction of the mPBI molecule in each deprotonation state is approximated using the relationship between pH and $\mathrm{pK_a}$ as described by the Henderson-Hasselbalch equation [182].

$$\mathrm{pH} = \mathrm{pK}_a^1 + \log\left(\frac{[\mathrm{mPBI}(-1)]}{[\mathrm{mPBI}(0)]}\right) \tag{5.14}$$

$$\mathrm{pH} = \mathrm{pK}_a^2 + \log\left(\frac{[\mathrm{mPBI}(-2)]}{[\mathrm{mPBI}(-1)]}\right) \tag{5.15}$$

$$f_0 = 1/\left(1 + 10^{(\mathrm{pH}-\mathrm{pKa}_1)} + 10^{(\mathrm{pH}-\mathrm{pKa}_1)}10^{(\mathrm{pH}-\mathrm{pKa}_2)}\right) \tag{5.16}$$

$$f_1 = f_0 10^{(\mathrm{pH}-\mathrm{pKa}_1)} \tag{5.17}$$

$$f_2 = f_1 10^{(\mathrm{pH}-\mathrm{pKa}_2)} \tag{5.18}$$

The square brackets indicate the concentration of mPBI molecule in each deprotonation state. f_0, f_1 and f_2 is the mole fraction of mPBI(0), mPBI(-1) and mPBI(-2), respectively, and $f_0 + f_1 + f_2 = 1$ at any pH. The conversion between pH and KOH concentration is calculated as follows

$$\mathrm{pH} = \mathrm{pK_w} + \log[\mathrm{OH}^-] \text{ where } [\mathrm{OH}^-] = \frac{0.01 X_{\mathrm{wt}} D_{\mathrm{KOH}}}{m_{\mathrm{KOH}}} \tag{5.19}$$

where X_{wt} is KOH concentration (in %wt KOH). D_{KOH} is the density of the KOH solution (in g/L). The density of KOH solution at each KOH concentration is taken from the literature (at T = 70°C [183]). m_{KOH} is the molar mass of KOH (= 56.11 g/mol). pK_w is the acid dissociation constant of water taken from literature (pK_w = 12.46 at T = 80°C [184])

Figure 5.3 shows the calculated mole fraction of mPBI molecule in each deprotonation state as a function of KOH concentration (and pH) at T = 88°C. The mole fraction of the mPBI(-1) and mPBI(-2) molecule increases as the KOH concentration increase from 0 to 10 %wt KOH, while the mole fraction of the mPBI(0) molecule decreases. At a higher concentration than 15 %wt KOH, mPBI(-2) becomes the predominant species. At the same time, the number of mPBI(0) and mPBI(-1) molecules keeps decreasing when the KOH concentration is higher than 15 %wt KOH. All three mPBI species can also be found at 5 - 15 wt% KOH. At 15 wt% KOH, there are approximately 10% of mPBI(0), 40% of mPBI(-1) and 50% of mPBI(-2) in the solution. At 50 wt % KOH, there are still approximately 10% of mPBI(-1) mixed with 90% of mPBI(-2) in the solution.

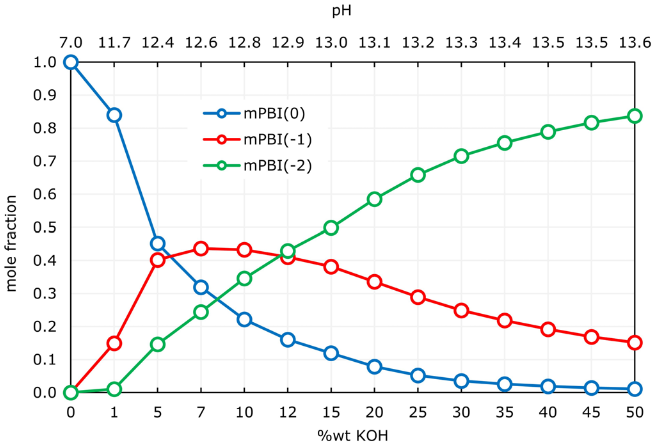

Figure 5.3: Calculated mole fraction of mPBI molecule in each deprotonated state as a function of KOH concentration (and pH) at T = 88°C.

It can be seen that the concentration of the ionized molecules increases with pH. Therefore, the ion conductivity can become higher by increasing KOH concentration. These calculation results are in line with a previous experiment by Kraglund *et al.*, which has reported an increase in the ionic conductivity of the mPBI-based membrane at T = 80°C of about two orders of magnitude from 0.7 to 72 mS/cm when the KOH concentration has been changed from 5 to 15 wt% KOH [60]. The ionic conductivity was further increased and peaked at the concentration around 20 - 25 wt% KOH; however, there were signs of structural change [60].

It should be noted that the bulk KOH concentration might not be directly applicable to the alkaline doped mPBI system. A previous study by Hou *et al.* has suggested that protons from the mPBI molecule can combine with hydroxide ions in the environment and form a more stable water molecule while the K^+ ion can integrate into the membrane [64, 185]. Therefore, due to water and K^+ uptake, the internal KOH concentration of the alkaline-doped mPBI system could be slightly different from the bulk KOH concentration.

5.4 Nucleophilic Addition

The degradation of mPBI-based membranes in alkaline solutions has been suggested to take place via hydrolysis reaction [46]. The first reaction involves nucleophilic addition at the carbon atom of the five-membered ring [46, 171]. Since all three forms of the mPBI molecule can be present in the alkaline solution at a high KOH concentration (> 15 %wt KOH), where the degradation is expected [46, 60, 61, 171], the reaction free energy of the first nucleophilic addition (ΔG_1) for all three forms of the mPBI molecule is investigated as follows

$$\Delta G_1 = G(\mathrm{OHmPBI(n)})_{(sol)} - G(\mathrm{mPBI(n)}_{(sol)}) - G(\mathrm{OH}^-_{(sol)}) \tag{5.20}$$

where OHmPBI(n) is the mPBI(n) molecule with a hydroxide ion bound with one of the carbon atoms of the five-membered ring and n = 0, -1, -2 for the non-, partially, and fully deprotonated mPBI molecule, respectively. There are three possible distinct carbon atoms of the five-membered ring of the mPBI(0) molecule, marked as C2, C4, and C5 in Figure 5.4, where hydroxide ions can attack. There are five possible positions in the mPBI(-1) molecule at C2, C4, C5, C2*, and C4*. The * denotes atoms located at the deprotonated part of the molecule. For the mPBI(-2) molecule, hydroxide attack on the carbon atom at the C2* or C5* position is possible. While the carbon atoms at C4* and C5* are symmetry equivalent.

As shown in Table 5.1, the hydroxide ion attack at the C2 position in the mPBI(0) and mPBI(-1) is more accessible than in other positions. Since these carbon atoms are located between two nitrogen atoms with higher negativity, these carbon atoms are more positively charged than the others. The more positive charge, the more favorably hydroxide ions attack. The deprotonated part is less vulnerable to hydroxide ions. The hydroxide ion attack at the C2* position in the mPBI(-1) molecule is more difficult than those at the C2 position. The lowest unoccupied molecular orbital (LUMO) energy of the molecule increases after deprotonation, and the atomic charge of atoms near the deprotonated part becomes slightly more negative. Figure 5.4 shows LUMO isosurfaces for mPBI molecules in different protonation states. The LUMO isosurface distributes all over the structure, including the C2 position on both sides in the mPBI(0) molecule. In comparison, the LUMO isosurface localizes in the C2 position in mPBI(-1) molecule. For the mPBI(-2) molecule, the LUMO energy is the highest among considered species, and the attack by hydroxide ion is also the most difficult. These results suggest that the susceptibility to hydroxide anion attack of the mPBI molecule can be related to the LUMO energy and isosurface [49, 186] and the formation of the deprotonated molecule can suppress the hydroxide ion attack.

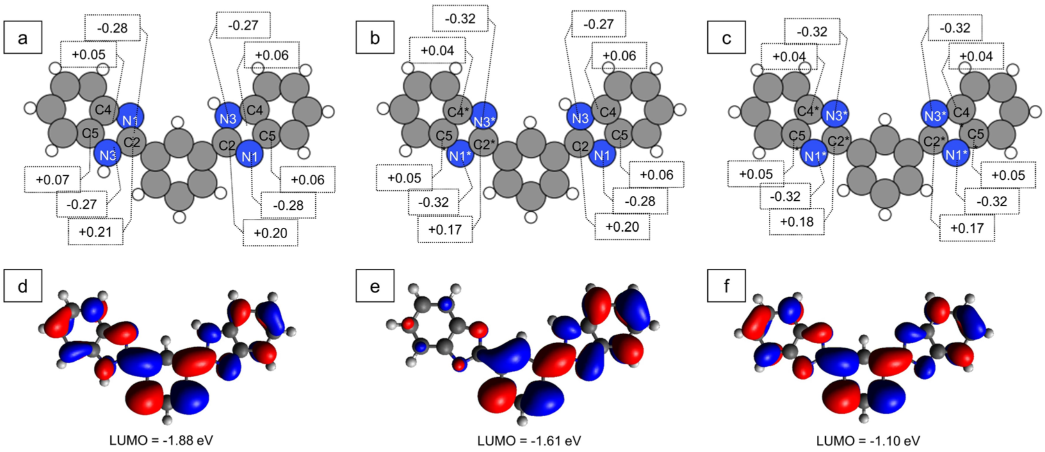

Figure 5.4: NBO atomic charge [187]: (a) mPBI(0), (b) mPBI(-1), (c) mPBI(-2). LUMO isosurface: (d) mPBI(0), (e) mPBI(-1), (f) mPBI(-2). (H = white, C = gray, N = blue)

Table 5.1: ΔG_1 (in eV) at the five-membered ring in mPBI molecule in each deprotonated state at T = 88 °C and atomic charge on the atom (in electron)

molecule	position	atomic charge	ΔG_1
mPBI(0)	C2	0.20	1.31
	C4	0.06	1.99
	C5	0.06	2.26
mPBI(-1)	C2*	0.17	2.43
	C4*	0.04	2.88
	C2	0.20	1.38
	C4	0.06	2.02
	C5	0.06	2.25
mPBI(-2)	C2*	0.17	2.66
	C4*	0.05	2.99

For the nucleophilic addition reaction at the C2 position, the free energy barrier is 1.42 eV for the mPBI(-1) and 1.35 eV for the mPBI(0) molecule. The free energy barrier for other positions in the mPBI(0) and mPBI(-1) molecule and in the mPBI(-2) molecule is 2.0 eV or greater, making the degradation unlikely. As there are more percentages of mPBI(-1) in solution than mPBI(0) at a high pH (pH > 13), the degradation could significantly be due to the mPBI(-1) species. Further investigation is continued from the hydroxide ion bond with the C2 position in the mPBI(-1) molecule.

5.5 Ring-opening Reaction

A ring-opening reaction follows the hydroxide ion attack. The possible mechanism for the mPBI(-1) molecule is that a hydroxyl proton at the C2 position is transferred to the nitrogen atom either at the N1 or N3 position, followed by a C-N bond breaking. The free energy barriers and rate constant along these two possible paths are calculated to identify the minimum reaction pathway.

For the calculated free energy barrier, an estimate of the reaction rate constant (k) is obtained from transition state theory [188].

$$k = \frac{k_B T}{h} \exp(\frac{-\Delta G^{TS}}{RT}) \tag{5.21}$$

where k_B is Boltzmann's constant, h is Planck's constant, ΔG^{TS} is the free energy barrier, R is the gas constant, and T is the temperature (K).

Due to its small mass, a hydrogen atom can be considered a wave packet, and it can penetrate regions forbidden for classical particles. During a hydrogen atom or proton transfer, the tunneling effects can increase the rate constant [189]. Thus, we also consider the tunneling effect for the reaction involving the hydrogen atom or proton transfer. Assuming the reaction path and the tunneling path coincide, the tunneling effect is included in the rate constant to obtain a tunneling corrected rate constants [190] as follows

$$k_{tunnelling} = \varkappa \frac{k_B T}{h} \exp(\frac{-\Delta G^{TS}}{RT}) \tag{5.22}$$

where $\varkappa$ is a tunneling correction adjusted the rate constant to include the tunneling effect along the reaction coordinate. Furthermore, assuming the shape of the potential energy barrier of the reaction is an inverted parabola. The probability of a particle with mass **m** and energy **E** penetrating the energy barrier with height **V** is approximated using the Wentzel-Kramers-Brillouin (WKB) approximation, leading to the following expression [191, 192].

$$\begin{aligned} P(E) &= \exp(-\frac{\pi^2 \omega}{h}\sqrt{2m(V-E)});\ 0 < E < V \\ P(E) &= 1;\ E > V \end{aligned} \tag{5.23}$$

where P(E) is the probability to find a particle on the other side of the barrier. ω is the energy barrier width estimated from the reaction path obtained from the IRC calculations. $\varkappa$ is the ratio between the quantum-mechanical rate to the classical rate [191].

Considering the particle with mass **m** and energy **E** moving toward the energy barrier with height **V**, if J_0 is the total flux of the inward particle to the barrier, the rate J at which particle appears on the other side of the barrier is given by

$$J = \frac{J_0}{k_B T} \int_0^{\infty} P(E) \exp(\frac{-E}{k_B T}) dE \tag{5.24}$$

For classical mechanism, P(E) = 0 for E < V and P(E) = 1 for E > V. Thus, J_C which is the classical flux of particle on the other side of the barrier is given by

$$J_C = \frac{J_0}{k_B T} \int_V^{\infty} \exp(\frac{-E}{k_B T}) dE = J_0 \exp(\frac{-V}{k_B T}) \tag{5.25}$$

Therefore, $\varkappa$ can be expressed as follows

$$\varkappa = \frac{J}{J_c} = \exp(\frac{V}{k_B T}) \int_0^{\infty} \frac{1}{k_B T} \exp(\frac{-E}{k_B T}) P(E)\, dE \tag{5.26}$$

If $\varkappa = 1$, there is no tunneling effect, and if $\varkappa > 1$, the tunneling effect contributes to the rate constant.

Let us consider the hydroxyl proton at the C2 position transfer to the nitrogen atom at the N3 position (see Figure 5.5). The ring-opening reaction occurs as a single step in path 1.1. The reaction goes through TS2-1.1 with a free energy barrier of 0.83 eV. The hydrogen tunneling effect in this step is negligible as $\varkappa = 1.00$. Alternatively, as the degradation occurs in an alkaline solution, water molecules and hydroxide ions are available in the environment, and both can participate in the reaction [171, 172]. The ring-opening with the presence of a hydroxide ion and a water molecule is shown as paths 1.2 and 1.3 in Figure 5.5, respectively.

For path 1.2, one hydroxide ion is explicitly added. This additional hydroxide ion spontaneously reacts with the hydroxyl proton at the C2 position, resulting in BX1-1.2, where one water molecule is formed. A transition state between intermediate B and BX1-1.2 could not be found. It is seen that the BX1-1.2 state is 0.31 eV less stable than the B state. The resulting water molecule further participates in the C2-N3 bond breaking, resulting in the ring-opening product C and one hydroxide ion. Compared to path 1.1, the additional hydroxide ion acts as a catalyst, lowering the energy barrier in path 1.2. The last reaction involves proton transfer from the water molecule to the nitrogen atom at the N3 position, where the tunneling correction is 1.07. Thus, the proton transfer rate constant increase from 1.33×10^9 s^{-1} to 1.43×10^9 s^{-1}.

For path 1.3, the reaction goes through TSY1-1.3, leading to the breaking of the C2-N3 bond. The free energy barrier for this step is 1.18 eV, including 0.25 eV for hydrogen-bond formation between structure B and the water molecule. After that, the hydroxyl proton at the C2 position is transferred to the nitrogen atom at the N3 position via the water molecule. The reaction gives the ring-opening product C and a water molecule. The free energy barrier for the hydroxyl proton transfer is only 0.02 eV, and the hydrogen tunneling correction for this step is 1.73. Thus, hydrogen tunneling significantly contributes to the rate constant which is increased from 3.67×10^{12} s^{-1} to 6.36×10^{12} s^{-1}. However, the highest transition state in path 1.3 is even higher than in the previous paths.

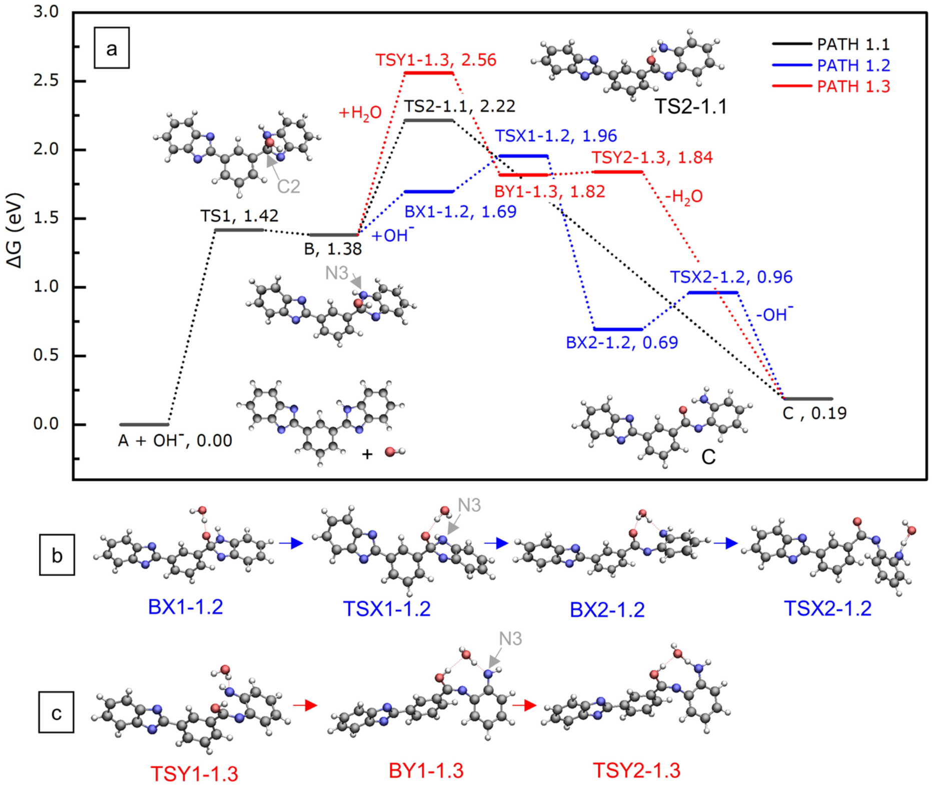

Figure 5.5: (a) Reaction energy profile for the ring-opening reaction of mPBI(-1) via path 1.1, 1.2 and 1.3 at T = 88 °C. The reference zero energy state for energies reported is A+OH^-, and the relative energies are in eV. The insets show the intermediate and transition state structure in (a) path 1.1, (b) path 1.2 and (c) path 1.3 (H = white, C = grey, N = blue, O = red).

Figure 5.6 shows an alternative path for the ring-opening reaction. First, the hydroxyl proton at the C2 position is transferred to a nitrogen atom at the N1 position. Then the C2-N1 (or C2-N3) bond is broken. It should be noted that after the hydroxyl proton transfer to the N2 position, the C2-N1 bond is equivalent to the C2-N3 bond.

We first consider the intramolecular proton transfer process (path 2.1). The hydroxyl proton at the C2 position is directly transferred to the nitrogen atom at the N1 position. A free energy barrier is found to be 0.91 eV. Due to the hydrogen tunneling effect ($\varkappa = 1.04$), the rate constant of 1.43 s^{-1} is increased to 1.48 s^{-1}

The hydroxyl proton transfer to the nitrogen atom at the N1 position via a hydroxide ion or water molecule is considered in paths 2.2 and 2.3, respectively. In path 2.2, the reaction goes through TS2-2.2. The water molecule donates one of its protons to the nitrogen atom at the N1 position, and then the hydroxide ion is obtained. The resulting hydroxide ion reacts with the hydroxyl proton at the C2 position, resulting in the intermediate C and water molecule. The free energy barrier for the hydroxyl proton transfer is 0.37 eV, including 0.25 eV for the hydrogen-bond formation between structure B and the water molecule. The TS2-2.2 state is about 0.54 eV lower than the TS2-2.1 state. Including the hydrogen tunneling correction of 1.26, the rate constant for the hydroxyl proton transfer is 5.55×10^7 s^{-1}, faster than the previous intramolecular proton transfer.

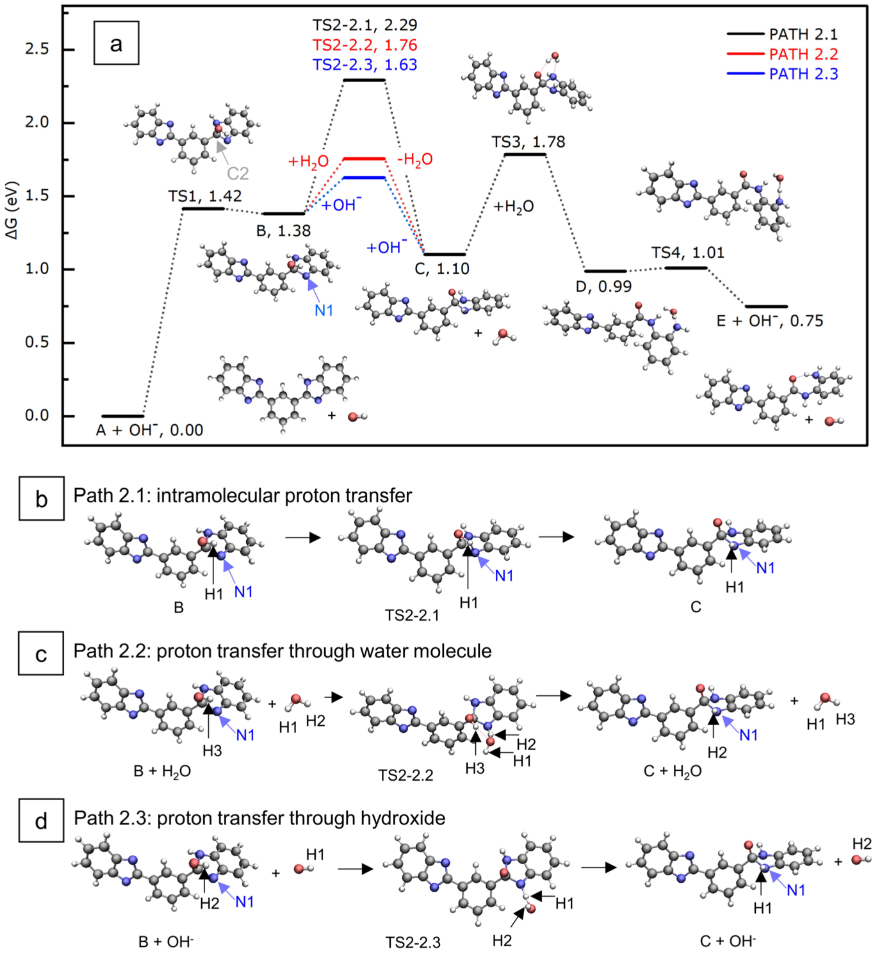

Figure 5.6: (a) Reaction energy profile for the ring-opening reaction of mPBI(-1) via path 2.1, 2.2 and 2.3 at T = 88 °C. The reference zero energy state for energies reported is A+OH^-, and the relative energies are in eV. The insets show the intermediate and transition state structure related to the hydroxyl proton transfer: (b) path 2.1, (c) path 2.2 and (d) path 2.3 (H = white, C = grey, N = blue, O = red)

In path 2.3, the additional hydroxide ion reacts with the hydroxyl proton at the C2 position, producing one water molecule. This water molecule later donates one of its protons to the nitrogen atom at the N1 position, resulting in the intermediate C and hydroxide ion. The reaction goes through TS2-2.3, and the free energy barrier is 0.25 eV, 0.66 eV lower than TS2-2.1, and 0.13 eV lower than TS2-2.2. Including the hydrogen tunneling correction, the rate constant for the hydroxyl proton transfer is 3.57x10^9 s^{-1}, faster than previous considerations.

The next step involves breaking the C-N bond (either C2-N1 or C2-N3 bond), resulting in an unstable N dangling bond in the structure D. This unstable N dangling bond can be stabilized by receiving a proton from a water molecule in its environment. The reaction gives the ring-opening product E and the hydroxide ion. The free energy barrier for the C-N bond breaking is 0.68 eV, including 0.23 eV for hydrogen-bond formation between the structure C and the water molecule. The free energy barrier for the proton transfer from the water molecule to the unstable N dangling atom is only 0.02 eV. With the hydrogen tunnelling correction of 1.33, the rate constant of the last step is 4.65x10^{12} s^{-1}.

It can be seen that path 2.2 and 2.3 has lower energy barrier than path 2.1. The highest transition state in path 2.2 and 2.3 is TS3 which is also lower than TSX1-1.2 in path 1. Thus, the ring-opening reaction of the mPBI(-1) molecules possibly occurs through path 2.2 or 2.3 with the assistance of water or hydroxide ions.

It should be noted that the hydroxide ion is unstable as it spontaneously reacts with the hydroxyl proton at the C2 position. It is also possible to spontaneously combine with the potassium ion instead of catalyzing the reaction if the explicit potassium ion is added. Still, the ring opening can occur via the water-assisted path.

5.6 Chain scission

The C2-N1 bond (amide linkage) in the structure E can be further hydrolyzed, leading to complete chain scission. As the degradation occurs in an alkaline solution, the hydroxide ion involves in the reaction. For path 3.1 in Figure 5.7 (b), the reaction begins with the nucleophilic addition at the C2 carbon atom in the structure E as it is the most positively charged position. The reaction goes through TS5 with a free energy barrier of 1.03 eV. The next step involves the C2-N1 bond cleavage, where the reaction goes through TS6-3.1 with a free energy barrier of 0.40 eV. The transition state mainly relates to the C2-N1 bond breaking. Then, the hydroxyl proton at the C2 position is transferred to the nitrogen atom at the N1 position without a transition state. The final product G is at -1.25 eV in the reaction energy profile and it is more stable than the E+OH$^-$ state.

The effect of explicit water on the energy profile is shown as path 3.2 in Figure 5.7 (b). One explicit water molecule is placed near the C2-N1 bond in structure E. The reaction goes through TS6-3.2 which relates to the C2-N1 bond breaking. The hydroxyl proton at the C2 position is spontaneously transferred to the nitrogen atom at the N1 position. The hydroxyl proton transfer can occur by passing the proton through the explicit water molecule but it is also barrierless. Thus, the tunneling correction is not taken into account in this step. The free energy barrier for the C2-N1 bond cleavage along path 3.2 is 0.70 eV, including 0.31 eV for hydrogen-bond formation between the structure F and water molecule. The free energy barrier is lowered by about 0.01 eV with the presence of explicit water molecules.

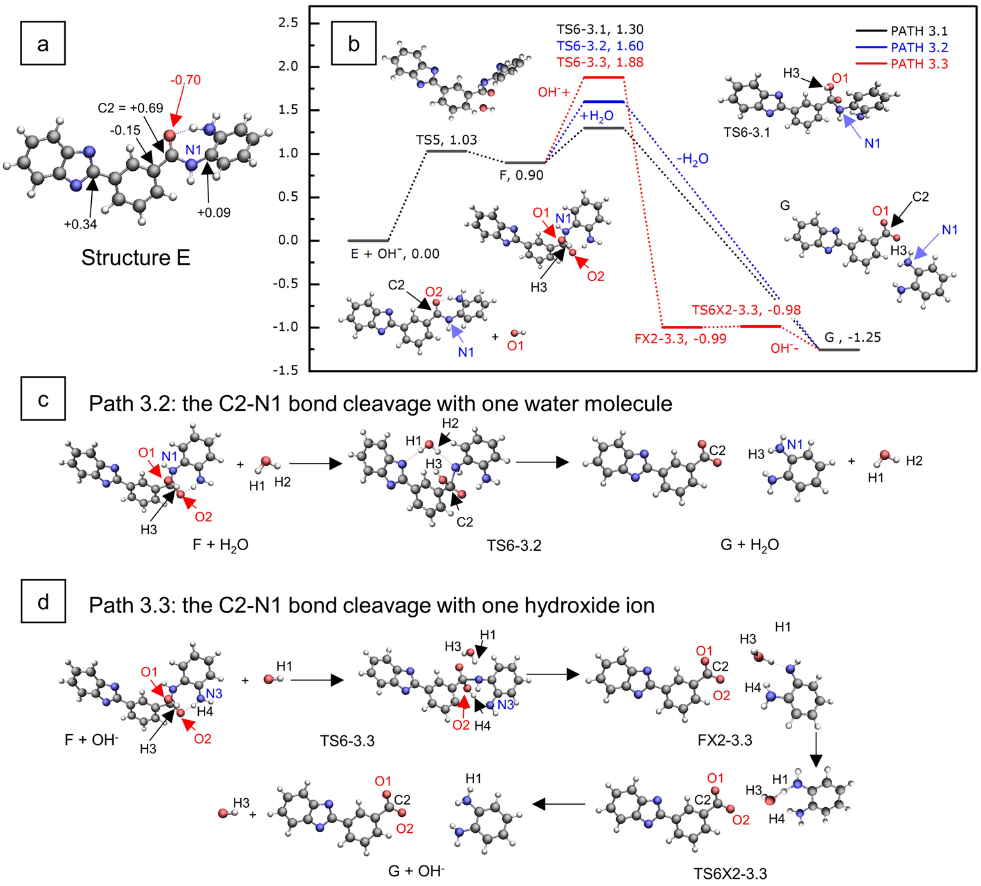

Figure 5.7: (a) NBO atomic charges on the structure E. (b) Reaction energy profile for the chain scission reaction of mPBI(-1) at T = 88 °C. The reference zero energy state for energies reported is E+OH$^-$, and the relative energies are in eV. The insets show structures for the intermediate and transition states in path 3.1. Structures for the intermediate and transition state related to the C-N bond cleavage: (c) path 3.2 (d) path 3.3 (H = white, C = grey, N = blue, O = red).

With an additional hydroxide ion (path 3.3), the additional hydroxide ion spontaneously reacts with a hydroxyl proton at the C2 position, forming a water molecule. The hydroxyl proton abstraction leads to the cleavage of the C2-N1 bond. The hydrogen atom (H4) is transferred back and forth between the nitrogen atom at the N3 position and the oxygen atom at the O2 position. The reaction goes through TS6-3.3 with a free energy barrier of 0.98 eV. The hydrogen tunneling correction for this step is only 1.02. The C2-N1 bond breaking creates an unstable N-dangling bond at the N2 position in structure FX2-3.3. A hydrogen atom can be transferred from the water molecule to stabilize this N-dangling bond. The free energy barrier for this step is only 0.01 eV and it results in the rate constant of 5.58×10^{12} s^{-1}. The hydrogen tunneling correction of

1.51 results in 8.45×10^{12} s^{-1}, implying that hydrogen transfer occurs very fast. The final products G and one hydroxide ion are obtained at the end. The free energy barrier in path 3.3 is higher than the previous paths.

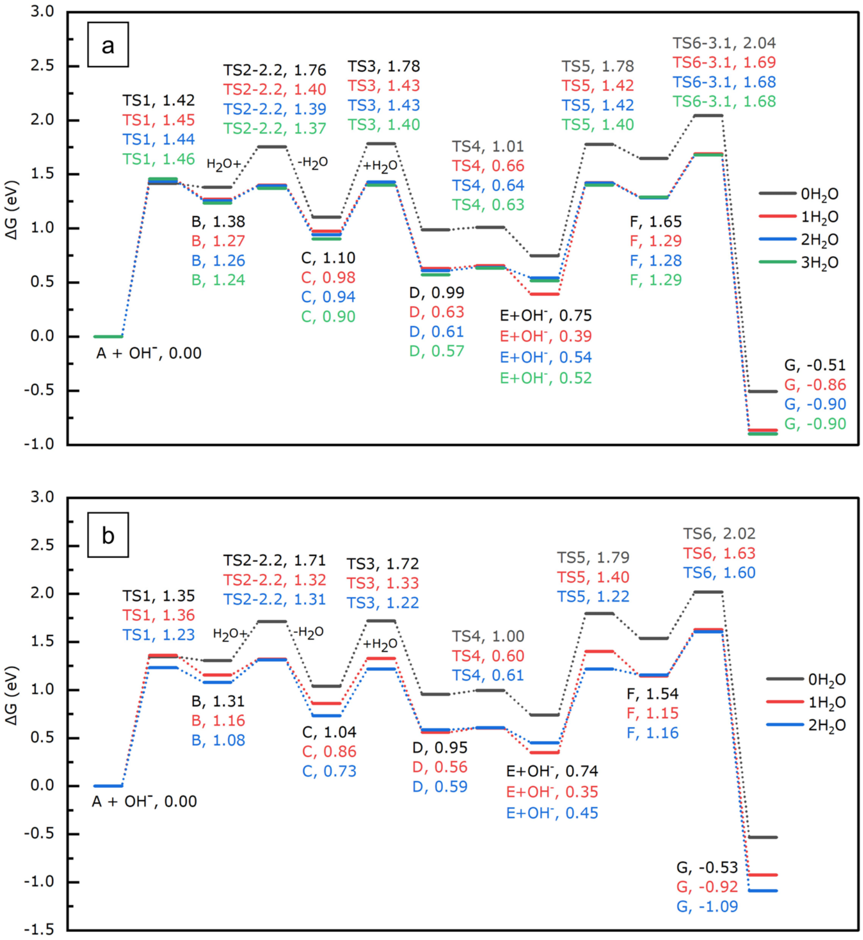

Figure 5.8: Reaction energy profile for the degradation path at T = 88 °C with a different number of explicit water molecules: (a) mPBI(-1) and (b) mPBI(0). The reference zero energy state for energies reported is A+OH^-, and the relative energies are in eV.

In summary, the degradation path for the mPBI(-1) is shown as the black line in Figure 5.8 (a). A water molecule catalyzes the pathway during the ring-opening reaction. The highest transition state along the degradation path is the TS6-3.1, located at 2.04 eV in the reaction profile. This state is the rate-limiting state. Therefore, the effective barrier for the degradation reaction which is calculated from the free energy of the TS6-3.1 relative to the initial state (A+OH^-), is found to be 2.04 eV. The final products from the chain scission contain free amino groups and a carbonyl group which are in line with the experimental study by Aili et al. [66] and Kraglund et al. [60]. For the mPBI(0) molecule, the degradation path is the same as the mPBI(-1) molecule and is given in Figure 5.8 (b) in the black line. The highest transition state is TS6-3.1 and the effective energy barrier is found to be 2.02 eV for the mPBI(0) molecule.

5.7 Reaction Path with Implicit-explicit Solvation

The implicit solvation model with the PCM is used in previous calculations to consider the effect of the surrounding water medium. However, it does not incorporate a short-range interaction between solutes and solvents, i.e., hydrogen bonding which can be important in the reaction path [181, 193]. In the following section, the combination between the explicit water molecules and the PCM implicit solvation is considered.

One Explicit Water Molecule

The first hydroxide ion attack at the C2 carbon atom in the mPBI(-1) molecule with one explicit water molecule at different hydrogen-bonding sites is considered. Among the considered positions in Figure C.1 of Appendix C. the explicit water molecule near the N1 position gives the lowest energy of ΔG_1. Thus, when we consider the reaction path with one explicit water molecule, the explicit water molecule is placed near the N1 position of the mPBI(-1) molecule. This position is also close to where the degradation occurs, and the explicit water molecule participates in the reaction as a reactant.

The free energy profile for the mPBI(-1) with one explicit water molecule is shown as the red line in Figure 5.8 (a). In this cases, ΔG_1 is 0.11 eV lower than that without the explicit water molecule. The free energy barrier for the water-assisted hydroxyl proton transfer ($\Delta G^{TS2\text{-}2.2}$) and the C-N bound breaking (ΔG^{TS3}) during the ring-opening step is 0.25 and 0.23 eV lower than that without the explicit water molecule. The ΔG^{TS4} and other reaction free energies during the chain scission are still the same as the path without the explicit water molecule. The highest transition state with one explicit water molecule is TS6-3.1, and the effective energy barrier is 1.69 eV, 0.35 eV lower than the path without the explicit water molecule.

Two and Three Explicit Water Molecules

When we consider more explicit water molecules in the reaction path, one explicit water molecule is placed near the N1 position and thus participates as a reactant. Then, additional explicit water molecules are placed near the N3* or N1* position, forming a hydrogen bond with the deprotonated site. The additional explicit water molecules are placed in the way to keep forming the hydrogen bond at the same site throughout the degradation path. With two explicit water molecules, it is found that the configuration with at least one explicit water molecule near the N1 position results in lower energy for ΔG_1 (see Table C.1). An increasing number of explicit water molecules from zero to three with at least one water molecule near the N1 position reduced ΔG_1 from 1.38 to 1.24 eV.

The reaction profile of the mPBI(-1) molecule with two and three explicit water molecules is given in the blue and green line in Figure 5.8 (a), and it is similar to the energy profile with one explicit water molecule. However, the reaction free energy for the proton transfer between structures D and E with two and three explicit water molecules is about 0.14 eV less negative than that with one explicit water molecule. The free energy barrier and reaction free energy for the second nucleophilic addition step (from E+OH^- to F) with two and three explicit water molecules are about 0.15 and 0.14 eV lower than those with one explicit water molecule. The free energy difference in each step along the reaction path, with two and three explicit water molecules, is less than 0.1 eV. These results suggest that a further increase in explicit water molecules may have no practical effect on the reaction profile. The highest transition state along the degradation pathway with two and three explicit water molecules is the TS6-3.1 state, which is only 0.1 eV lower than the degradation pathway with one explicit water molecule.

Additionally, the degradation pathway for the mPBI(0) with up to two explicit water molecules using the PCM implicit solvation is given in Figure 5.8 (b). The highest transition state is TS6-3.1, regardless of the number of explicit water molecules. The effective energy barrier in the reaction with zero, one, and two explicit water molecules is 2.02 eV, 1.63 eV, and 1.60 eV, respectively.

We employed the SMD implicit solvation model to test the sensitivity to the choice of implicit solvation model [194]. We use the same optimized structures in the gas phase and keep water as a solvent for the SMD implicit solvation. As shown in Figure C.2 (a) of Appendix C, the paths obtained from both implicit solvation models are similar, but the SMD implicit solvation results in higher reaction energy and energy barrier. As shown in Figure C.2 (b) of Appendix C, the effective barrier with the SMD implicit solvation also becomes smaller when including the explicit water molecules.

It is important to note that the effective energy barrier was approximated with specific static configurations and a limited amount of explicit water molecules around the mPBI molecule. A more elaborate model would require more number of explicit water molecules. A computational study of hydrolysis of imidazole-ylidenes by Hollóczki *et al.* has suggested that by increasing the number of water molecules, the calculated energy barriers trend agrees with the experimental results [195]. Also, it has been suggested that the alkaline stability of the imidazolium-based cation is determined by the hydration level, which is the number of water molecules per cation molecule [196–198]. Furthermore, a recent study by Wu *et al.* [198] investigating the distribution of water molecules and hydroxide ions around imidazolium-based molecules by molecular dynamic (MD) simulations with about 100 - 400 explicit water molecules has found that the alkaline stability of the imidazolium-based molecules significantly depends on the distribution of water molecules and hydroxide ions around the imidazolium structures. In our study, further increasing the number of explicit water molecules to complete the hydration shell for the mPBI molecule along the degradation by performing MD simulations would be required to achieve higher accuracy. However, such a simulation requires significantly more computational cost and time.

5.8 Effect of Hydroxide Ion Concentration

Previous experimental studies by Aili *et al.*[66] and Kraglund *et al.* [60] have reported that the mPBI-based membrane was stable at low KOH concentration (up to 5 wt% KOH at T = 80 - 88 °C) but it degraded when the KOH concentration was increased. In this following section, we consider the hydroxide ion concentration in the reaction free energy and free barrier calculations. The reaction free energy is, for example, calculated as follows

$$A + OH^- \rightarrow C$$

$$\Delta G(pH) = \Delta G_{(sol)} - RT \ln[OH^-] = \Delta G_{(sol)} - 2.303RT(pH - pK_W) \tag{5.27}$$

$$\Delta G_{(sol)} = G(C_{(sol)}) - G(A_{(sol)}) - G(OH^-_{(sol)}) \tag{5.28}$$

where $\Delta G_{(sol)}$ is the reaction free energy at standard condition in solution phase where $[A] = [OH^-] = [C] = 1$ M, and it is calculated in the same way as described in Section 5.2. pK_W is the acid dissociation constant of water taken from the literature ($pK_W = 12.46$ at T = 80°C [184]). It should be noted that the previous calculations apply for pH = 12.46.

Figure 5.9 (a) shows the reaction profile for the mPBI(-1) degradation with two explicit water molecules at different pH. For all considered pH values, the degradation rate is still determined by the TS6-3.1 state but the effective energy barrier becomes lower as pH increases, suggesting that the degradation becomes easier as the KOH concentrations is higher.

It should be noted that even though at a high pH range (pH > 13), the dominant species is mPBI(-2) which is unlikely to degrade, the degradation still can occur through the mPBI(-1) species which accounts for 10 - 20% of the mPBI molecules. The number of mPBI(-1) in the solution can be quickly reduced as the degradation reaction is also facile at this high pH. The mPBI(-2) species can then change to mPBI(-1) to maintain the equilibrium between all three mPBI species. The degradation can proceed further. Due to the degradation, the number of ionized species and mobile hydroxide ions in the solution is reduced. Thus, the reduction in the ionic conductivity and the changes in membrane structure are unavoidable. Working at a lower pH range to minimize degradation can be possible. However, this comes with a lower ionic conductivity as the percentage of the ionized form in the solution becomes lower at a lower pH [60].

5.9 Comparison with Experiment

An apparent free energy barrier can be approximated from a given experimental reaction rate. The apparent degradation rate is derived from the molecular weight loss of the mPBI membrane after being soaked in 5, 10, 25, 50 wt% KOH at T = 88 °C for 200 days reported by Aili *et al.* [66]. Therefore, the molecular weight loss rate of the mPBI at a specific KOH concentration (in s^{-1}) is approximated as follows

$$\text{rate} = \frac{1}{\Delta t}(1 - \frac{m_{200}}{m_1}) = k(f_0 + f_1) = k_0 f_0 + k_1 f_1 \tag{5.29}$$

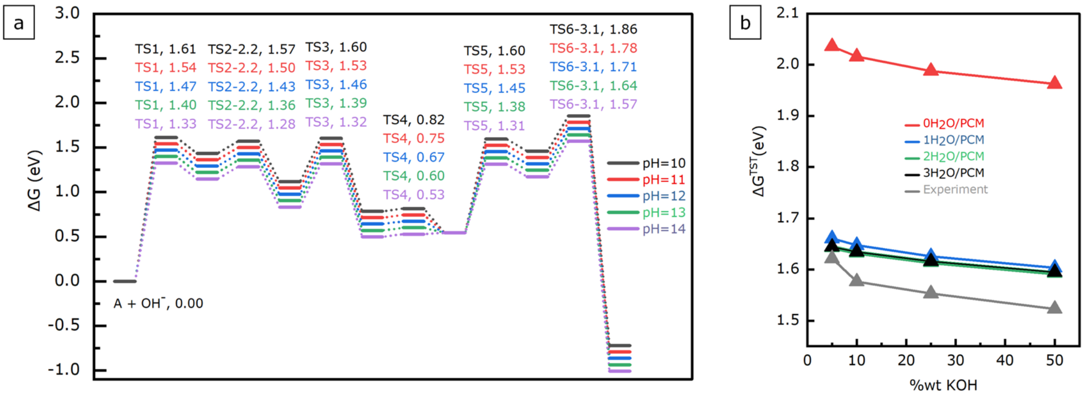

Figure 5.9: (a) Reaction energy profile for the mPBI(-1) degradation at T = 88 °C with two explicit water molecules and the PCM implicit solvation model at different pH. The reference zero energy state for energies reported is A+OH$^-$, and the relative energies are in eV. (b) The effective free energy barrier and the apparent energy barrier from the experiments at different KOH concentrations and T = 88 °C

where k is the apparent reaction rate constant (in s^{-1}). k_0, k_1 is the reaction rate constant (in s^{-1}) for the degradation of mPBI(0), and mPBI(-1), respectively. f_0, f_1 are the mole fraction of mPBI(0), and mPBI(-1), respectively. Δt is the duration for storing the mPBI in KOH solution (= 200 days); m_1 and m_{200} are the molecular weight of mPBI (in g/mol) before storing in KOH solution (day1) and after storing in KOH solution for 200 days, respectively. The apparent free energy barrier is calculated using Equation 5.21 with the approximated k from Equation 5.29.

The (total) effective barrier (ΔG^{TST}) from the theoretical model is a weighted average value, taking the mole fraction of mPBI(0) and mPBI(-1) at each KOH concentration into account, and can be expressed as follows

$$\Delta G^{TST} = -RT\ln(\frac{hk_{avg}}{k_B T}) \text{ and } k_{avg} = \frac{k_0 f_0}{f_0 + f_1} + \frac{k_1 f_1}{f_0 + f_1} \tag{5.30}$$

where k_0 , k_1 are calculated from the effective energy barrier for the degradation of the mPBI(-1) and mPBI(0) molecule using Equation 5.21.

Figure 5.9 (b) shows the apparent energy barrier derived from the experimental results and the effective free energy barrier from different implicit-explicit solvation models. Without the explicit water molecules, the PCM implicit solvation model predicts a much larger effective free energy barrier than the experiments, resulting in a mean absolute value (MAE) of 0.43 eV. However, the MAE is reduced to below 0.1 eV when including explicit water molecules in the simulation. On top of that, it is seen that both the apparent and effective free energy barriers decrease as the KOH concentration increases.

It should be noted that the contribution from the mPBI(-2) molecule to the total degradation rate is considered insignificant and is not included in the previous approximation. We find that the reaction free energy for the first nucleophilic addition reaction at the C2 position in the mPBI(-2) molecule is more than 2 eV, higher than those of the mPBI(-1) and mPBI(0) molecule. Thus, we consdiered that the mPBI(-2) molecule is unlikely to degrade. The approximated degradation rate includes the mPBI(-2) contribution as given in Figure C.3 (a) of Appendix C, demonstrating that there is no further improvement in the approximated rate.

Figure C.3 (b) in Appendix C show the approximated degradation (rate = $k_1f_1 + k_0f_0$) from the calculation model with different number of explicit water molecule. Like the effective energy barrier, the approximated degradation rate approaches the experimental results when explicit water molecules are included. The results show that the combined implicit and explicit solvation makes the predicted degradation rate and effective barrier move toward the experimental results, and at least two explicit water molecules should be considered along the degradation pathway.

The degradation rate becomes higher with KOH concentration, especially from 0 to 15 %wt KOH. After that, the degradation rate is slightly lower, mainly due to the reduced number of mPBI(0) molecules as the KOH concentration increase. Simultaneously, the degradation rate contribution from the mPBI(-1) molecule keeps increasing with the KOH concentration, see Figure C.3 (a) in Appendix C. These results suggest that both effective barriers and pK_a value play a significant role in the stability of the mPBI molecule in an alkaline solution.

5.10 Conclusions

This chapter investigated the degradation mechanism of the mPBI molecule in an alkaline solution. The mPBI molecule deprotonates when submerged in an alkaline solution. The fully deprotonated molecule (mPBI(-2)) is the predominant species at the high KOH concentration where degradation is expected. However, the formation of the fully deprotonated molecule suppresses the hydroxide ion attack. Still, the degradation possibly proceeds from the small fraction of non- and partially deprotonated molecules (mPBI(0) and mPBI(-1)). The hydroxide ion can attack the carbon atom at the C2 position in the non- and partially deprotonated molecule, initiating the degradation. The following reaction is the ring-opening reaction, where the hydroxyl proton transfer occurs via an ancillary hydroxide ion or water molecule. The product from the ring-opening reaction undergoes alkaline hydrolysis, leading to complete chain scission. The rate-determining state is associated with the amide cleavage during the chain scission reaction. An implicit solvation model predicts a relatively largest deviation of the degradation rate and effective barrier compared to the experiment. Combining explicit water molecules and implicit solvation lowers the effective barrier for the degradation, giving more agreement between the experiment and the calculations. The model additionally captures the experimental trend in which the degradation rate increases with KOH concentration.

Chapter 6

Summary and Outlook

In this thesis, the stabilities of carbon-based materials used in the fuel cell were studied by DFT calculations. These included the degradation of the M/N/C electrocatalyst in an acid solution and the degradation of the mPBI molecule in an alkaline solution.

We considered the stability of the M/N/C catalyst from the propensity of the metal center to dissolve from the carbon substrate. It was found that the local carbon structures around the metal center play a crucial role in its stability under the acid condition. Depending on the local carbon structures, the basicity of the atoms incorporated with the metal center and the bonding strength between the metal center and the carbon substrate influence the stability of the M/N/C structure under the acid condition. The choice of a metal center is also crucial to determining stability. We found that metal oxidation causes a significant difference in the acid stability among the 3d metal element. Using the computational screening approach, we suggested that the MN_4 sites on the bulk graphene and graphene edge with M = Fe, Co, and Ru are stable electrocatalysts in the acid condition.

Furthermore, the adsorption of the relevant species in the electrolytes was included in the stability and activity calculations for the MN_4 site on the bulk graphene and graphene edge. It was found that the electrolyte anions can compete with water and adsorb on the single metal site under the ORR-related condition. Then the single metal site can be further thermodynamically stabilized against dissolution, compared to the stability in the pure water environment. Unlike the ORR-related condition, most electrolyte anions do not adsorb on the single metal site at the lower potentials for the CO_2RR. Still, the adsorption of water and gas molecules can occur under CO_2RR-related conditions, resulting in modified catalytic activity. Through the catalytic activity and stability descriptor, we suggested promising combinations of the electrolyte and the metal center that result in an active and durable catalyst for the ORR and CO_2RR.

The stability calculations of the M/N/C catalyst in this thesis were based on the thermodynamic model. A kinetic analysis would be required for a better understanding and a complete stability descriptor. Also, the metal center can dynamically interact with the water and solvent molecules at the electrode-liquid interface. These interactions could affect the dissolution mechanism and the kinetic barrier. Thus the proper configurations of water and solvent molecules at the catalyst interface should be explicitly considered. The other reactions leading to the degradation of the M/N/C catalyst may occur in parallel during durability testing of the fuel cell, while only the demetallation was considered in this thesis. Therefore, the calculation models should be extended to consider other possible reactions, such as carbon surface oxidation and carbon corrosion. Also, it is interesting to study the stability of the M/N/C materials in other geometries, such as the dual metal site embedded in the graphene.

Apart from the stability of the M/N/C catalyst, we considered the stability of the mPBI molecule in an alkaline solution. The mPBI-based membrane is a promising material for anion exchange membranes in the alkaline fuel cell, but the degradation at high KOH concentrations limits its practical use. Under the alkaline condition, it was found that the mPBI molecule is deprotonated and thus forms the ionized molecule. The fully deprotonated molecule is the dominant species under the highly alkaline condition and is unlikely to be degraded. At the same time, the non- and partially-deprotonated molecules are vulnerable to hydroxide ion attack. Thus, the degradation possibly proceeds from the small fraction of non- and partially-deprotonated molecules. Furthermore, we found that the effective energy barrier depends on the KOH concentration and becomes lower as the KOH concentration increases, suggesting that degradation can become easier when the KOH concentration is higher. It was also found that the availability of vulnerable species in the solution can affect the degradation rate. These results suggested that the pK_a value is a crucial factor affecting the stability of the mPBI molecule. Finally, it was found that the calculation with the implicit-explicit solvation model agrees with the experiment more than the calculation with only the implicit solvation, and at least two explicit water molecules should be included along the degradation pathway.

Further investigating the distribution of explicit water molecules and hydroxide ions around the mPBI structures along the degradation would give a more accurate model and a better understanding of the degradation. Additionally, recent experiments have been carried out with derivatives of mPBI that are linked with steric trimethylphenyl units [69] or bulky naphthalene groups [70] and suggested improved stability in an alkaline solution. Further exploration of the degradation pathway of the derivatives will provide helpful information for designing new derivatives with improved long-term stability in alkaline solutions.

Bibliography

(1) Vielstich, W.; Lamm, A.; Gasteiger, H. A.; Wiley, J.; Kordesch, K.; Cifrain, M. Handbook of fuel cells, fundamentals technology and applications, 2003.

(2) Dekel, D. In *Encyclopedia of Applied Electrochemistry*, Kreysa, G., Ota, K.-i., Savinell, R. F., Eds.; Springer New York: New York, NY, 2014, pp 26–33.

(3) Pollet, B. G.; Kocha, S. S.; Staffell, I. *Current opinion in Electrochemistry* **2019**, *16*, 90–95.

(4) Colella, W.; OHayre, R.; Cha, S.-W.; Prinz, F. B. Fuel Cell Fundamentals, 2009.

(5) Thompson, S. T.; James, B. D.; Huya-Kouadio, J. M.; Houchins, C.; DeSantis, D. A.; Ahluwalia, R.; Wilson, A. R.; Kleen, G.; Papageorgopoulos, D. *Journal of Power Sources* **2018**, *399*, 304–313.

(6) Futter, G. A.; Latz, A.; Jahnke, T. *Journal of Power Sources* **2019**, *410-411*, 78–90.

(7) Borup, R. L.; Kusoglu, A.; Neyerlin, K. C.; Mukundan, R.; Ahluwalia, R. K.; Cullen, D. A.; More, K. L.; Weber, A. Z.; Myers, D. J. *Current Opinion in Electrochemistry* **2020**, *21*, 192–200.

(8) Yang, Y.; Lai, L.; Wei, L.; Chen, Y. *Journal of Energy Chemistry* **2021**, *63*, 667–674.

(9) Zitolo, A.; Goellner, V.; Armel, V.; Sougrati, M. T.; Mineva, T.; Stievano, L.; Fonda, E.; Jaouen, F. *Nature Materials* **2015**, *14*, 937–942.

(10) Martinez, U.; Holby, E. F.; Babu, S. K.; Artyushkova, K.; Lin, L.; Choudhury, S.; Purdy, G. M.; Zelenay, P. *Journal of The Electrochemical Society* **2019**, *166*, F3136–F3142.

(11) Cao, Y.-C.; Wu, X.; Scott, K. *International Journal of Hydrogen Energy* **2012**, *37*, 9524–9528.

(12) Zitolo, A.; Ranjbar-Sahraie, N.; Mineva, T.; Li, J.; Jia, Q.; Stamatin, S.; Harrington, G. F.; Lyth, S. M.; Krtil, P.; Mukerjee, S.; Fonda, E.; Jaouen, F. *Nature communications* **2017**, *8*, 957.

(13) Chen, Z.; Jiang, S.; Kang, G.; Nguyen, D.; Schatz, G. C.; Van Duyne, R. P. *Journal of the American Chemical Society* **2019**, *141*, 15684–15692.

(14) Santori, P. G.; Speck, F. D.; Li, J.; Zitolo, A.; Jia, Q.; Mukerjee, S.; Cherevko, S.; Jaouen, F. *Journal of The Electrochemical Society* **2019**, *166*, F3311–F3320.

(15) Kumar, K.; Dubau, L.; Mermoux, M.; Li, J.; Zitolo, A.; Nelayah, J.; Jaouen, F.; Maillard, F. *Angewandte Chemie International Edition* **2020**, *59*, 3235–3243.

(16) Goellner, V.; Baldizzone, C.; Schuppert, A.; Sougrati, M. T.; Mayrhofer, K.; Jaouen, F. *Physical Chemistry Chemical Physics* **2014**, *16*, 18454–18462.

(17) Choi, C. H. et al. *Energy and Environmental Science* **2018**, *11*, 3176–3182.
(18) Li, J. et al. *Nature Catalysis* **2021**, *4*, 10–19.
(19) Xie, X. et al. *Nature Catalysis* **2020**, *3*, 1044–1054.
(20) Choi, C. H.; Baldizzone, C.; Grote, J.-P.; Schuppert, A. K.; Jaouen, F.; Mayrhofer, K. J. J. *Angewandte Chemie* **2015**, *127*, 12944–12948.
(21) Bae, G.; Chung, M. W.; Ji, S. G.; Jaouen, F.; Choi, C. H. *ACS Catalysis* **2020**, *10*, 8485–8495.
(22) Shen, J.; Wen, Y.; Jiang, H.; Yu, S.; Dong, C.; Fan, Y.; Liu, B.; Li, C. *The Journal of Physical Chemistry C* **2022**, *126*, 10388–10398.
(23) Sun, Y.; Silvioli, L.; Sahraie, N. R.; Ju, W.; Li, J.; Zitolo, A.; Li, S.; Bagger, A.; Arnarson, L.; Wang, X.; Moeller, T.; Bernsmeier, D.; Rossmeisl, J.; Jaouen, F.; Strasser, P. *Journal of the American Chemical Society* **2019**, *141*, 12372–12381.
(24) Jiang, K.; Back, S.; Akey, A. J.; Xia, C.; Hu, Y.; Liang, W.; Schaak, D.; Stavitski, E.; Nørskov, J. K.; Siahrostami, S.; Wang, H. *Nature Communications* **2019**, *10*, DOI: `10.1038/s41467-019-11992-2`.
(25) Zhang, P.; Wang, Y.; You, Y.; Yuan, J.; Zhou, Z.; Sun, S. *The Journal of Physical Chemistry Letters* **2021**, *12*, 7797–7803.
(26) Tan, X.; Tahini, H. A.; Smith, S. C. *Journal of Materials Chemistry A* **2021**, *9*, 8721–8729.
(27) Holby, E. F.; Wang, G.; Zelenay, P. *ACS Catalysis* **2020**, *10*, 14527–14539.
(28) Glibin, V. P.; Dodelet, J.-P. *Journal of The Electrochemical Society* **2017**, *164*, F948–F957.
(29) Chenitz, R.; Kramm, U. I.; Lefèvre, M.; Glibin, V.; Zhang, G.; Sun, S.; Dodelet, J. P. *Energy and Environmental Science* **2018**, *11*, 365–382.
(30) Liu, K.; Wu, G.; Wang, G. *The Journal of Physical Chemistry C* **2017**, *121*, 11319–11324.
(31) Lefèvre, M.; Proietti, E.; Jaouen, F.; Dodelet, J.-P. *Science* **2009**, *324*, 71–74.
(32) Charreteur, F.; Jaouen, F.; Ruggeri, S.; Dodelet, J. P. *Electrochimica Acta* **2008**, *53*, 2925–2938.
(33) Mineva, T.; Matanovic, I.; Atanassov, P.; Sougrati, M. T.; Stievano, L.; Clémancey, M.; Kochem, A.; Latour, J. M.; Jaouen, F. *ACS Catalysis* **2019**, *9*, 9359–9371.
(34) Chung, H. T.; Cullen, D. A.; Higgins, D.; Sneed, B. T.; Holby, E. F.; More, K. L.; Zelenay, P. *Science* **2017**, *357*, 479–484.
(35) Hansen, H. A.; Patniboon, T. *ACS Catalysis* **2021**, *11*, 13102–13118.
(36) Nematollahi, P.; Barbiellini, B.; Bansil, A.; Lamoen, D.; Qingying, J.; Mukerjee, S.; Neyts, E. C. *ACS Catalysis* **2022**, 7541–7549.
(37) Sun, F.; Li, F.; Tang, Q. *The Journal of Physical Chemistry C* **2022**, DOI: `10.1021/acs.jpcc.2c03518`.
(38) Gubler, L.; Dockheer, S. M.; Koppenol, W. H. *Journal of The Electrochemical Society* **2011**, *158*, B755–B769.
(39) Ramaswamy, N.; Hakim, N.; Mukerjee, S. *Electrochimica Acta* **2008**, *53*, 3279–3295.

(40) Cao, L.; Luo, Q.; Chen, J.; Wang, L.; Lin, Y.; Wang, H.; Liu, X.; Shen, X.; Zhang, W.; Liu, W.; Qi, Z.; Jiang, Z.; Yang, J.; Yao, T. *Nature Communications* **2019**, *10*, 4849.
(41) Vijay, S.; Ju, W.; Brückner, S.; Tsang, S. C.; Strasser, P.; Chan, K. *Nature Catalysis* **2021**, *4*, 1024–1031.
(42) Liu, S. et al. *Nature Energy* **2022**, *7*, 652–663.
(43) Jin, Z.; Li, P.; Meng, Y.; Fang, Z.; Xiao, D.; Yu, G. *Nature Catalysis* **2021**, *4*, 615–622.
(44) *Nature Catalysis* **2018**, *1*, 63–72.
(45) Xiao, F.; Wang, Y.-C.; Wu, Z.-P.; Chen, G.; Yang, F.; Zhu, S.; Siddharth, K.; Kong, Z.; Lu, A.; Li, J.-C.; Zhong, C.-J.; Zhou, Z.-Y.; Shao, M. *Advanced Materials* **2021**, *33*, 2006292.
(46) Jensen, J. O.; Aili, D.; Hansen, M. K.; Li, Q.; Bjerrum, N. J.; Christensen, E. *ECS Transactions* **2014**, *64*, 1175–1184.
(47) Kraglund, M. R.; Carmo, M.; Schiller, G.; Ansar, S. A.; Aili, D.; Christensen, E.; Jensen, J. O. *Energy and Environmental Science* **2019**, *12*, 3313–3318.
(48) Leng, Y.; Chen, G.; Mendoza, A. J.; Tighe, T. B.; Hickner, M. A.; Wang, C. Y. *Journal of the American Chemical Society* **2012**, *134*, 9054–9057.
(49) Lee, B.; Yun, D.; Lee, J. S.; Park, C. H.; Kim, T. H. *Journal of Physical Chemistry C* **2019**, *123*, 13508–13518.
(50) Fan, J.; Willdorf-Cohen, S.; Schibli, E. M.; Paula, Z.; Li, W.; Skalski, T. J. G.; Sergeenko, A. T.; Hohenadel, A.; Frisken, B. J.; Magliocca, E.; Mustain, W. E.; Diesendruck, C. E.; Dekel, D. R.; Holdcroft, S. *Nature Communications* **2019**, *10*, 2306.
(51) Thomas, O. D.; Soo, K. J. W. Y.; Peckham, T. J.; Kulkarni, M. P.; Holdcroft, S. *Journal of the American Chemical Society* **2012**, *134*, 10753–10756.
(52) Yoshimura, K.; Zhao, Y.; Hasegawa, S.; Hiroki, A.; Kishiyama, Y.; Shishitani, H.; Yamaguchi, S.; Tanaka, H.; Koizumi, S.; Appavou, M.-S.; Radulescu, A.; Richter, D.; Maekawa, Y. *Soft Matter* **2017**, *13*, 8463–8473.
(53) Lin, B.; Xu, F.; Su, Y.; Han, J.; Zhu, Z.; Chu, F.; Ren, Y.; Zhu, L.; Ding, J. *ACS Applied Energy Materials* **2020**, *3*, 1089–1098.
(54) Sana, B.; Das, A.; Jana, T. *ACS Applied Energy Materials* **2022**, *5*, 3626–3637.
(55) Sturgeon, M. R.; Macomber, C. S.; Engtrakul, C.; Long, H.; Pivovar, B. S. *Journal of The Electrochemical Society* **2015**, *162*, F366–F372.
(56) Henkensmeier, D.; Kim, H. J.; Lee, H. J.; Lee, D. H.; Oh, I. H.; Hong, S. A.; Nam, S. W.; Lim, T. H. *Macromolecular Materials and Engineering* **2011**, *296*, 899–908.
(57) Henkensmeier, D.; Cho, H. R.; Kim, H. J.; Nunes Kirchner, C.; Leppin, J.; Dyck, A.; Jang, J. H.; Cho, E.; Nam, S. W.; Lim, T. H. *Polymer Degradation and Stability* **2012**, *97*, 264–272.
(58) Mohanty, A. D.; Tignor, S. E.; Krause, J. A.; Choe, Y.-K.; Bae, C. *Macromolecules* **2016**, *49*, 3361–3372.
(59) Merle, G.; Wessling, M.; Nijmeijer, K. *Journal of Membrane Science* **2011**, *377*, 1–35.
(60) Kraglund, M. R.; Aili, D.; Jankova, K.; Christensen, E.; Li, Q.; Jensen, J. O. *Journal of The Electrochemical Society* **2016**, *163*, F3125–F3131.
(61) Aili, D.; Jankova, K.; Li, Q.; Bjerrum, N. J.; Jensen, J. O. *Journal of Membrane Science* **2015**, *492*, 422–429.

(62) Borisov, G.; Penchev, H.; Maksimova-Dimitrova, K.; Ublekov, F.; Lefterova, E.; Sinigersky, V.; Slavcheva, E. *Materials Letters* **2019**, *240*, 144–146.

(63) Penchev, H.; Borisov, G.; Petkucheva, E.; Ublekov, F.; Sinigersky, V.; Radev, I.; Slavcheva, E. *Materials Letters* **2018**, *221*, 128–130.

(64) Babcock, E.; Szekely, N.; Konovalova, A.; Lin, Y.; Appavou, M. S.; Mangiapia, G.; Revay, Z.; Stieghorst, C.; Holderer, O.; Henkensmeier, D.; Lehnert, W.; Carmo, M. *Journal of Membrane Science* **2019**, *577*, 12–19.

(65) Zhang, Q.; Mamtani, K.; Jain, D.; Ozkan, U.; Asthagiri, A. *Journal of Physical Chemistry C* **2016**, *120*, 15173–15184.

(66) Aili, D.; Jankova, K.; Han, J.; Bjerrum, N. J.; Jensen, J. O.; Li, Q. *Polymer* **2016**, *84*, 304–310.

(67) Alam, A.; Park, C.; Lee, J.; Ju, H. *Renewable Energy* **2020**, *166*, 222–233.

(68) Aili, D.; Hansen, M. K.; Renzaho, R. F.; Li, Q.; Christensen, E.; Jensen, J. O.; Bjerrum, N. J. *Journal of Membrane Science* **2013**, *447*, 424–432.

(69) Aili, D.; Wright, A. G.; Kraglund, M. R.; Jankova, K.; Holdcroft, S.; Jensen, J. O. *J. Mater. Chem. A* **2017**, *5*, 5055–5066.

(70) Hu, B.; Huang, Y.; Liu, L.; Hu, X.; Geng, K.; Ju, Q.; Liu, M.; Bi, J.; Luo, S.; Li, N. *Journal of Membrane Science* **2022**, *643*, 120042.

(71) Aili, D.; Yang, J.; Jankova, K.; Henkensmeier, D.; Li, Q. *Journal of Materials Chemistry A* **2020**, *8*, 12854–12886.

(72) Born, M.; Oppenheimer, R. In *Quantum Chemistry: Classic Scientific Papers*; World Scientific: 2000, pp 1–24.

(73) Hohenberg, P.; Kohn, W. *Physical review* **1964**, *136*, B864.

(74) Kohn, W.; Sham, L. J. *Physical review* **1965**, *140*, A1133.

(75) In *Density Functional Theory*; John Wiley Sons, Ltd: 2009; Chapter 10, pp 209–233.

(76) Perdew, J. P.; Burke, K.; Ernzerhof, M. *Physical review letters* **1996**, *77*, 3865.

(77) Perdew, J. P.; Chevary, J. A.; Vosko, S. H.; Jackson, K. A.; Pederson, M. R.; Singh, D. J.; Fiolhais, C. *Physical review B* **1992**, *46*, 6671.

(78) Haas, P.; Tran, F.; Blaha, P. *Physical Review B* **2009**, *79*, 085104.

(79) Wellendorff, J.; Lundgaard, K. T.; Møgelhøj, A.; Petzold, V.; Landis, D. D.; Nørskov, J. K.; Bligaard, T.; Jacobsen, K. W. *Physical review B* **2012**, *85*, 235149.

(80) Lee, K.; Murray, É. D.; Kong, L.; Lundqvist, B. I.; Langreth, D. C. *Physical Review B* **2010**, *82*, 081101.

(81) Becke, A. D. *The Journal of Chemical Physics* **1993**, *98*, 1372–1377.

(82) He, Y.; Liu, S.; Priest, C.; Shi, Q.; Wu, G. *Chemical Society Reviews* **2020**, *49*, 3484–3524.

(83) Kaiser, S. K.; Chen, Z.; Faust Akl, D.; Mitchell, S.; Pérez-Ramírez, J. *Chemical Reviews* **2020**, *120*, 11703–11809.

(84) Peng, B.; Liu, H.; Liu, Z.; Duan, X.; Huang, Y. *The Journal of Physical Chemistry Letters* **2021**, *12*, 2837–2847.

(85) Kramm, U. I.; Herranz, J.; Larouche, N.; Arruda, T. M.; Lefèvre, M.; Jaouen, F.; Bogdanoff, P.; Fiechter, S.; Abs-Wurmbach, I.; Mukerjee, S., et al. *Physical Chemistry Chemical Physics* **2012**, *14*, 11673–11688.

(86) Kumar, K.; Asset, T.; Li, X.; Liu, Y.; Yan, X.; Chen, Y.; Mermoux, M.; Pan, X.; Atanassov, P.; Maillard, F.; Dubau, L. *ACS Catalysis* **2021**, *11*, 484–494.

(87) Xu, X.; Zhang, X.; Kuang, Z.; Xia, Z.; Rykov, A. I.; Yu, S.; Wang, J.; Wang, S.; Sun, G. *Applied Catalysis B: Environmental* **2022**, *309*, DOI: `10.1016/j.apcatb.2022.121290`.

(88) Osmieri, L.; Cullen, D. A.; Chung, H. T.; Ahluwalia, R. K.; Neyerlin, K. C. *Nano Energy* **2020**, *78*, 105209.

(89) Nabae, Y.; Yuan, Q.; Nagata, S.; Kusaba, K.; Aoki, T.; Takao, N.; Itoh, T.; Arao, M.; Imai, H.; Higashi, K.; Sakata, T.; Uruga, T.; Iwasawa, Y. *Journal of the Electrochemical Society* **2021**, *168*, 014513.

(90) Zhang, H.; Chung, H. T.; Cullen, D. A.; Wagner, S.; Kramm, U. I.; More, K. L.; Zelenay, P.; Wu, G. *Energy and Environmental Science* **2019**, *12*, 2548–2558.

(91) Zhang, C. et al. *ACS Nano* **2017**, *11*, 6930–6941.

(92) Li, T.; Liu, J.; Song, Y.; Wang, F. *ACS Catalysis* **2018**, *8*, 8450–8458.

(93) Svane, K. L.; Reda, M.; Vegge, T.; Hansen, H. A. *ChemSusChem* **2019**, *12*, 5133–5141.

(94) Deng, Q.; Zhao, J.; Wu, T.; Chen, G.; Hansen, H. A.; Vegge, T. *Journal of Catalysis* **2019**, *370*, 378–384.

(95) Zhao, C.; Gao, W.; Jiang, Q. *The Journal of Physical Chemistry C* **2020**, *124*, 25412–25420.

(96) Hansen, H. A.; Rossmeisl, J.; Nørskov, J. K. *Physical Chemistry Chemical Physics* **2008**, *10*, 3722–3730.

(97) Hansen, H. A.; Shi, C.; Lausche, A. C.; Peterson, A. A.; Nørskov, J. K. *Physical Chemistry Chemical Physics* **2016**, *18*, 9194–9201.

(98) Hubert, M. A.; Patel, A. M.; Gallo, A.; Liu, Y.; Valle, E.; Ben-Naim, M.; Sanchez, J.; Sokaras, D.; Sinclair, R.; Nørskov, J. K.; King, L. A.; Bajdich, M.; Jaramillo, T. F. *ACS Catalysis* **2020**, *10*, 12182–12196.

(99) Gunasooriya, G. T. K.; Nørskov, J. K. *ACS Energy Letters* **2020**, *5*, 3778–3787.

(100) Ha, M.; Kim, D. Y.; Umer, M.; Gladkikh, V.; Myung, C. W.; Kim, K. S. *Energy and Environmental Science* **2021**, *14*, 3455–3468.

(101) Calle-Vallejo, F.; Martínez, J. I.; García-Lastra, J. M.; Abad, E.; Koper, M. T. *Surface Science* **2013**, *607*, 47–53.

(102) Zhou, Y.; Gao, G.; Chu, W.; Wang, L. W. *Nanoscale Advances* **2020**, *2*, 710–716.

(103) Back, S.; Siahrostami, S. *Nanoscale Advances* **2019**, *1*, 132–139.

(104) Glibin, V. P.; Cherif, M.; Vidal, F.; Dodelet, J.-P.; Zhang, G.; Sun, S. *Journal of The Electrochemical Society* **2019**, *166*, F3277–F3286.

(105) Cheng, Y.; Zhao, S.; Li, H.; He, S.; Veder, J.-P.; Johannessen, B.; Xiao, J.; Lu, S.; Pan, J.; Chisholm, M. F.; Yang, S.-Z.; Liu, C.; Chen, J. G.; Jiang, S. P. *Applied Catalysis B: Environmental* **2019**, *243*, 294–303.

(106) Kresse, G.; Hafner, J. *Physical review B* **1993**, *47*, 558–561.

(107) Kresse, G.; Joubert, D. *Physical review B* **1999**, *59*, 1758–1775.

(108) Hjorth Larsen, A. et al. *Journal of Physics Condensed Matter* **2017**, *29*, 273002.

(109) Mathew, K.; Sundararaman, R.; Letchworth-Weaver, K.; Arias, T. A.; Hennig, R. G. *The Journal of Chemical Physics* **2014**, *140*, 84106.

(110) Mathew, K.; Kolluru, V. S.; Mula, S.; Steinmann, S. N.; Hennig, R. G. *Journal of Chemical Physics* **2019**, *151*, 1–8.

(111) Monkhorst, H. J.; Pack, J. D. *Physical review B* **1976**, *13*, 5188–5192.

(112) Mortensen, J.; Gjerding, M.; Thygesen, K. *The Journal of Open Source Software* **2020**, *5*, 1844.

(113) P.J. Linstrom; W.G. Mallard, E., *NIST Chemistry WebBook, NIST Standard Reference Database Number 69*; National Institute of Standards and Technology: Gaithersburg MD, 2022.

(114) *CRC Handbook of Chemistry and Physics*, 97th Edition; W. M. Haynes, David R. Lide, Thomas J. Bruno, Eds.; CRC Press: Boca Raton, 2016.

(115) Christensen, R.; Hansen, H. A.; Vegge, T. *Catalysis Science and Technology* **2015**, *5*, 4946–4949.

(116) Christensen, R.; Hansen, H. A.; Dickens, C. F.; Nørskov, J. K.; Vegge, T. *Journal of Physical Chemistry C* **2016**, *120*, 24910–24916.

(117) Nørskov, J. K.; Rossmeisl, J.; Logadottir, A.; Lindqvist, L.; Kitchin, J. R.; Bligaard, T.; Jónsson, H. *Journal of Physical Chemistry B* **2004**, *108*, 17886–17892.

(118) Marcel Pourbaix, *Atlas of electrochemical equilibria in aqueous solutions*, 2nd ed.; National Association of Corrosion Engineers: Houston, Tex, 1974.

(119) Bard, A. J.; Parsons, R.; Jordan, J., *Standard Potentials in Aqueous Solution*, 1st ed.; Routledge: 2017.

(120) Singh, A. K.; Zhou, L.; Shinde, A.; Suram, S. K.; Montoya, J. H.; Winston, D.; Gregoire, J. M.; Persson, K. A. *Chemistry of Materials* **2017**, *29*, 10159–10167.

(121) Svane, K. L.; Hansen, H. A.; Vegge, T. *Journal of Catalysis* **2021**, *393*, 230–237.

(122) Peterson, A. A. *Topics in Catalysis* **2014**, *57*, 40–53.

(123) Goedecker, S.; Hellmann, W.; Lenosky, T. *Physical review letters* **2005**, *95*, 55501.

(124) Goedecker, S. *Journal of Chemical Physics* **2004**, *120*, 9911–9917.

(125) Reda, M.; Hansen, H. A.; Vegge, T. *Catalysis Today* **2018**, *312*, 118–125.

(126) Sahraie, N. R.; Kramm, U. I.; Steinberg, J.; Zhang, Y.; Thomas, A.; Reier, T.; Paraknowitsch, J.-P.; Strasser, P. *Nature communications* **2015**, *6*, 8618.

(127) Jung, E.; Shin, H.; Lee, B. H.; Efremov, V.; Lee, S.; Lee, H. S.; Kim, J.; Hooch Antink, W.; Park, S.; Lee, K. S.; Cho, S. P.; Yoo, J. S.; Sung, Y. E.; Hyeon, T. *Nature Materials* **2020**, *19*, 436–442.

(128) Xia, D.; Yang, X.; Xie, L.; Wei, Y.; Jiang, W.; Dou, M.; Li, X.; Li, J.; Gan, L.; Kang, F. *Advanced Functional Materials* **2019**, *29*, 1–10.

(129) Holst-Olesen, K.; Reda, M.; Hansen, H. A.; Vegge, T.; Arenz, M. *ACS Catalysis* **2018**, *8*, 7104–7112.

(130) Holst-Olesen, K.; Silvioli, L.; Rossmeisl, J.; Arenz, M. *ACS Catalysis* **2019**, *9*, 3082–3089.

(131) Wang, Y.; Tang, Y.-J.; Zhou, K. *Journal of the American Chemical Society* **2019**, *141*, 14115–14119.

(132) Rebarchik, M.; Bhandari, S.; Kropp, T.; Mavrikakis, M. *ACS Catalysis* **2020**, *10*, 9129–9135.

(133) Viswanathan, V.; Hansen, H. A.; Rossmeisl, J.; Nørskov, J. K. *ACS Catalysis* **2012**, *2*, 1654–1660.

(134) Yang, X.; Xia, D.; Kang, Y.; Du, H.; Kang, F.; Gan, L.; Li, J. *Advanced Science* **2020**, *7*, 2000176.

(135) Jurca, T.; Farghal, A.; Lin, P.-H.; Korobkov, I.; Murugesu, M.; Richeson, D. S. *Journal of the American Chemical Society* **2011**, *133*, 15814–15817.

(136) He, Y.; Shi, Q.; Shan, W.; Li, X.; Kropf, A. J.; Wegener, E. C.; Wright, J.; Karakalos, S.; Su, D.; Cullen, D. A.; Wang, G.; Myers, D. J.; Wu, G. *Angewandte Chemie* **2021**, *60*, 9516–9526.

(137) Xiao, M.; Gao, L.; Wang, Y.; Wang, X.; Zhu, J.; Jin, Z.; Liu, C.; Chen, H.; Li, G.; Ge, J.; He, Q.; Wu, Z.; Chen, Z.; Xing, W. *Journal of the American Chemical Society* **2019**, *141*, 19800–19806.

(138) Gao, J.; Yang, H. b.; Huang, X.; Hung, S. F.; Cai, W.; Jia, C.; Miao, S.; Chen, H. M.; Yang, X.; Huang, Y.; Zhang, T.; Liu, B. *Chem* **2020**, *6*, 658–674.

(139) Ju, W.; Bagger, A.; Hao, G. P.; Varela, A. S.; Sinev, I.; Bon, V.; Roldan Cuenya, B.; Kaskel, S.; Rossmeisl, J.; Strasser, P. *Nature Communications* **2017**, *8*, DOI: `10.1038/s41467-017-01035-z`.

(140) Li, J.; Prlja, P.; Shinagawa, T.; Martín Fernández, A. J.; Krumeich, F.; Artyushkova, K.; Atanassov, P.; Zitolo, A.; Zhou, Y.; García-Muelas, R.; López, N.; Pérez-Ramírez, J.; Jaouen, F. *ACS Catalysis* **2019**, *9*, 10426–10439.

(141) Paul, S.; Kao, Y. L.; Ni, L.; Ehnert, R.; Herrmann-Geppert, I.; van de Krol, R.; Stark, R. W.; Jaegermann, W.; Kramm, U. I.; Bogdanoff, P. *ACS Catalysis* **2021**, *11*, 5850–5864.

(142) Zhang, B.; Zhang, J.; Shi, J.; Tan, D.; Liu, L.; Zhang, F.; Lu, C.; Su, Z.; Tan, X.; Cheng, X.; Han, B.; Zheng, L.; Zhang, J. *Nature Communications* **2019**, *10*, DOI: `10.1038/s41467-019-10854-1`.

(143) Liu, S.; Liu, Y.; Cheng, Z.; Tan, Y.; Ren, Y.; Yuan, T.; Shen, Z. *ACS Applied Materials & Interfaces* **2021**, *13*, 40590–40601.

(144) Wang, X.; Wang, Y.; Sang, X.; Zheng, W.; Zhang, S.; Shuai, L.; Yang, B.; Li, Z.; Chen, J.; Lei, L.; Adli, N. M.; Leung, M. K.; Qiu, M.; Wu, G.; Hou, Y. *Angewandte Chemie* **2021**, *60*, 4192–4198.

(145) Wei, J.; Xia, D.; Wei, Y.; Zhu, X.; Li, J.; Gan, L. *ACS Catalysis* **2022**, 7811–7820.

(146) Xiao, M. et al. Microporous Framework Induced Synthesis of Single-Atom Dispersed Fe-N-C Acidic ORR Catalyst and Its in Situ Reduced Fe-N4 Active Site Identification Revealed by X-ray Absorption Spectroscopy, 2018.

(147) He, J.; Zheng, T.; Wu, D.; Zhang, S.; Gu, M.; He, Q. *ACS Catalysis* **2022**, *12*, 1601–1613.

(148) Kamat, G. A.; Zamora Zeledón, J. A.; Gunasooriya, G. T. K.; Dull, S. M.; Perryman, J. T.; Nørskov, J. K.; Stevens, M. B.; Jaramillo, T. F. *Communications Chemistry* **2022**, *5*, DOI: `10.1038/s42004-022-00635-1`.

(149) Zamora Zeledón, J. A.; Kamat, G. A.; Gunasooriya, G. T. K.; Nørskov, J. K.; Stevens, M. B.; Jaramillo, T. F. *ChemElectroChem* **2021**, *8*, 2467–2478.

(150) Varela, A. S.; Kroschel, M.; Leonard, N. D.; Ju, W.; Steinberg, J.; Bagger, A.; Rossmeisl, J.; Strasser, P. *ACS Energy Letters* **2018**, *3*, 812–817.

(151) Kneebone, J. L.; Daifuku, S. L.; Kehl, J. A.; Wu, G.; Chung, H. T.; Hu, M. Y.; Alp, E. E.; More, K. L.; Zelenay, P.; Holby, E. F.; Neidig, M. L. *Journal of Physical Chemistry C* **2017**, *121*, 16283–16290.

(152) Cho, M.; Song, J. T.; Back, S.; Jung, Y.; Oh, J. *ACS Catalysis* **2018**, *8*, 1178–1185.

(153) C W Davies, *Ion association*, London, Butterworths, 1962.

(154) Ruscic, B.; Pinzon, R. E.; Von Laszewski, G.; Kodeboyina, D.; Burcat, A.; Leahy, D.; Montoy, D.; Wagner, A. F. In *Journal of Physics: Conference Series*, Institute of Physics Publishing: 2005; Vol. 16, pp 561–570.

(155) Liu, Q.; Li, Y.; Zheng, L.; Shang, J.; Liu, X.; Yu, R.; Shui, J. *Advanced Energy Materials* **2020**, *10*, DOI: `10.1002/aenm.202000689`.

(156) Hu, Y.; Jensen, J. O.; Pan, C.; Cleemann, L. N.; Shypunov, I.; Li, Q. *Applied Catalysis B: Environmental* **2018**, *234*, 357–364.

(157) Shah, S. S. A.; Najam, T.; Javed, M. S.; Rahman, M. M.; Tsiakaras, P. *ACS Applied Materials and Interfaces* **2021**, *13*, 23191–23200.

(158) Tylus, U.; Jia, Q.; Strickland, K.; Ramaswamy, N.; Serov, A.; Atanassov, P.; Mukerjee, S. *Journal of Physical Chemistry C* **2014**, *118*, 8999–9008.

(159) Zeng, L.; Zhao, T. S.; An, L.; Zhao, G.; Yan, X. H. *Journal of Membrane Science* **2015**, *493*, 340–348.

(160) Yan, C.; Li, H.; Ye, Y.; Wu, H.; Cai, F.; Si, R.; Xiao, J.; Miao, S.; Xie, S.; Yang, F.; Li, Y.; Wang, G.; Bao, X. *Energy and Environmental Science* **2018**, *11*, 1204–1210.

(161) Yang, J.; Qiu, Z.; Zhao, C.; Wei, W.; Chen, W.; Li, Z.; Qu, Y.; Dong, J.; Luo, J.; Li, Z.; Wu, Y. *Angewandte Chemie* **2018**, *130*, 14291–14296.

(162) Qin, X.; Zhu, S.; Xiao, F.; Zhang, L.; Shao, M. *ACS Energy Letters* **2019**, *4*, 1778–1783.

(163) Luo, F. et al. *Nature Materials* **2020**, *19*, 1215–1223.

(164) Varela, A. S.; Ranjbar Sahraie, N.; Steinberg, J.; Ju, W.; Oh, H.-S.; Strasser, P. *Angewandte Chemie* **2015**, *127*, 10908–10912.

(165) Bagger, A.; Ju, W.; Varela, A. S.; Strasser, P.; Rossmeisl, J. *Catalysis Today* **2017**, *288*, 74–78.

(166) Bagger, A.; Ju, W.; Varela, A. S.; Strasser, P.; Rossmeisl, J. *ChemPhysChem* **2017**, *18*, 3266–3273.

(167) Couto, R. N.; Linares, J. J. *Journal of Membrane Science* **2015**, *486*, 239–247.

(168) Luo, H.; Vaivars, G.; Agboola, B.; Mu, S.; Mathe, M. *Solid State Ionics* **2012**, *208*, 52–55.

(169) Diaz, L. A.; Hnát, J.; Heredia, N.; Bruno, M. M.; Viva, F. A.; Paidar, M.; Corti, H. R.; Bouzek, K.; Abuin, G. C. *Journal of Power Sources* **2016**, *312*, 128–136.

(170) Noh, C.; Serhiichuk, D.; Malikah, N.; Kwon, Y.; Henkensmeier, D. *Chemical Engineering Journal* **2021**, *407*, 126574.

(171) Long, H.; Pivovar, B. *Journal of Physical Chemistry C* **2014**, *118*, 9880–9888.

(172) Wang, W.; Wang, S.; Xie, X.; lv, Y.; Ramani, V. K. *Journal of Membrane Science* **2014**, *462*, 112–118.
(173) Epifanovsky, E. et al. *The Journal of Chemical Physics* **2021**, *155*, 084801.
(174) Mallikarjun Sharada, S.; Zimmerman, P. M.; Bell, A. T.; Head-Gordon, M. *Journal of Chemical Theory and Computation* **2012**, *8*, 5166–5174.
(175) Maeda, S.; Ohno, K.; Morokuma, K. *Journal of Chemical Theory and Computation* **2009**, *5*, 2734–2743.
(176) Baker, J. *Journal of Computational Chemistry* **1986**, *7*, 385–395.
(177) Fukui, K. *The Journal of Physical Chemistry* **1970**, *74*, 4161–4163.
(178) Cossi, M.; Rega, N.; Scalmani, G.; Barone, V. *Journal of Computational Chemistry* **2003**, *24*, 669–681.
(179) Barone, V.; Cossi, M. *Journal of Physical Chemistry A* **1998**, *102*, 1995–2001.
(180) Truong, T. N.; Stefanovich, E. V. *Chemical Physics Letters* **1995**, *240*, 253–260.
(181) Thapa, B.; Schlegel, H. B. *The Journal of Physical Chemistry A* **2015**, *119*, 5134–5144.
(182) Po, H. N.; Senozan, N. M. *Journal of Chemical Education* **2001**, *78*, 1499.
(183) Akerlof, G.; Bender, P. *Journal of the American Chemical Society* **1941**, *63*, 1085–1088.
(184) Sweeton, F. H.; Mesmer, R. E.; Baes, C. F. *Journal of Solution Chemistry* **1974**, *3*, 191–214.
(185) Hou, H.; Wang, S.; Jiang, Q.; Jin, W.; Jiang, L.; Sun, G. *Journal of Power Sources* **2011**, *196*, 3244–3248.
(186) Matsuyama, K.; Ohashi, H.; Miyanishi, S.; Ushiyama, H.; Yamaguchi, T. *RSC Advances* **2016**, *6*, 36269–36272.
(187) Glendening, E. D.; Landis, C. R.; Weinhold, F. *Journal of Computational Chemistry* **2013**, *34*, 1429–1437.
(188) Eyring, H. *The Journal of Chemical Physics* **1935**, *3*, 107–115.
(189) Jana, K.; Ganguly, B. *Physical Chemistry Chemical Physics* **2018**, *20*, 28049–28058.
(190) Vandeputte, A. G.; Sabbe, M. K.; Reyniers, M.-F.; Van Speybroeck, V.; Waroquier, M.; Marin, G. B. *The Journal of Physical Chemistry A* **2007**, *111*, 11771–11786.
(191) Bell, R. P. *Trans. Faraday Soc.* **1959**, *55*, 1–4.
(192) Griffiths, D. J.; Griffiths, P. D. J., *Introduction to Quantum Mechanics*; Pearson international edition; Pearson Prentice Hall: 2005.
(193) Xu, L.; Coote, M. L. *Journal of Physical Chemistry A* **2019**, *123*, 7430–7438.
(194) Marenich, A. V.; Cramer, C. J.; Truhlar, D. G. *Journal of Physical Chemistry B* **2009**, *113*, 6378–6396.
(195) Hollóczki, O.; Terleczky, P.; Szieberth, D.; Mourgas, G.; Gudat, D.; Nyulászi, L. *Journal of the American Chemical Society* **2011**, *133*, 780–789.
(196) Pusara, S.; Srebnik, S.; Dekel, D. R. *Journal of Physical Chemistry C* **2018**, *122*, 11204–11213.
(197) Dekel, D. R.; Willdorf, S.; Ash, U.; Amar, M.; Pusara, S.; Dhara, S.; Srebnik, S.; Diesendruck, C. E. *Journal of Power Sources* **2018**, *375*, 351–360.
(198) Wu, L.; Zhou, X.; Zhang, G.; Zhang, N.; Huang, Y.; Dai, S.; Shen, Y. *Industrial & Engineering Chemistry Research* **2021**, *60*, 2481–2491.

Appendix A

Supplementary material I

Table A.1: Reaction free energy for the dissolution of the bulk metal ($G(M^{x+})$) and calculated DFT energy per atom of the metal in their bulk structure (E_M(bulk)). E_0 is in V_{SHE} and E_M(bulk) is in eV/atom. The square brackets indicate the concentration of the dissolved metal ions.

ion	$G(M^{x+})$	E_0	E_M(bulk)
Cr^{2+}	$E_{Cr}(bulk) + 2(E_0 + (0.059/2) \log[Cr^{2+}])$	$E_0 = -0.91$	-7.17
Cr^{3+}	$E_{Cr}(bulk) + 3(E_0 + (0.059/3) \log[Cr^{3+}])$	$E_0 = -0.74$	
$CrOH^{2+}$	$G(Cr^{3+}) + G(H_2O) - (1/2)G(H_2) + 2.303\ k_BTpH_0$	$pH_0 = 3.81$	
Mn^{2+}	$E_{Mn}(bulk) + 2(E_0 + (0.059/2) \log[Mn^{2+}])$	$E_0 = -1.19$	-6.45
Mn^{3+}	$G(Mn^{2+}) + E_0 + (0.059) \log([Mn^{3+}]/[Mn^{2+}])$	$E_0 = 1.54$	
Fe^{2+}	$E_{Fe}(bulk) + 2(E_0 + (0.059/2) \log[Fe^{2+}])$	$E_0 = -0.45$	-5.65
Fe^{3+}	$E_{Fe}(bulk) + 3(E_0 + (0.059/3) \log[Fe^{3+}])$	$E_0 = -0.04$	
$FeOH^{2+}$	$G(Fe^{3+}) + G(H_2O) - (1/2)G(H_2) + 2.303\ k_BTpH_0$	$pH_0 = 2.43$	
Co^{2+}	$E_{Co}(bulk) + 2(E_0 + (0.059/2) \log[Co^{2+}])$	$E_0 = -0.28$	-4.29
Co^{3+}	$G(Co^{2+}) + E_0 + (0.059) \log([Co^{3+}]/[Co^{2+}])$	$E_0 = 1.92$	
Ni^{2+}	$E_{Ni}(bulk) + 2(E_0 + (0.059/2) \log[Ni^{2+}])$	$E_0 = -0.26$	-2.53
Ni^{3+}	$G(Ni^{2+}) + E_0 + (0.059) \log([Ni^{3+}]/[Ni^{2+}])$	$E_0 = 2.30$	
Ru^{2+}	$E_{Ru}(bulk) + 2(E_0 + (0.059/2) \log[Ru^{2+}])$	$E_0 = 0.46$	-6.26
Ru^{3+}	$G(Ru^{2+}) + E_0 + (0.059) \log([Ru^{3+}]/[Ru^{2+}])$	$E_0 = 0.25$	

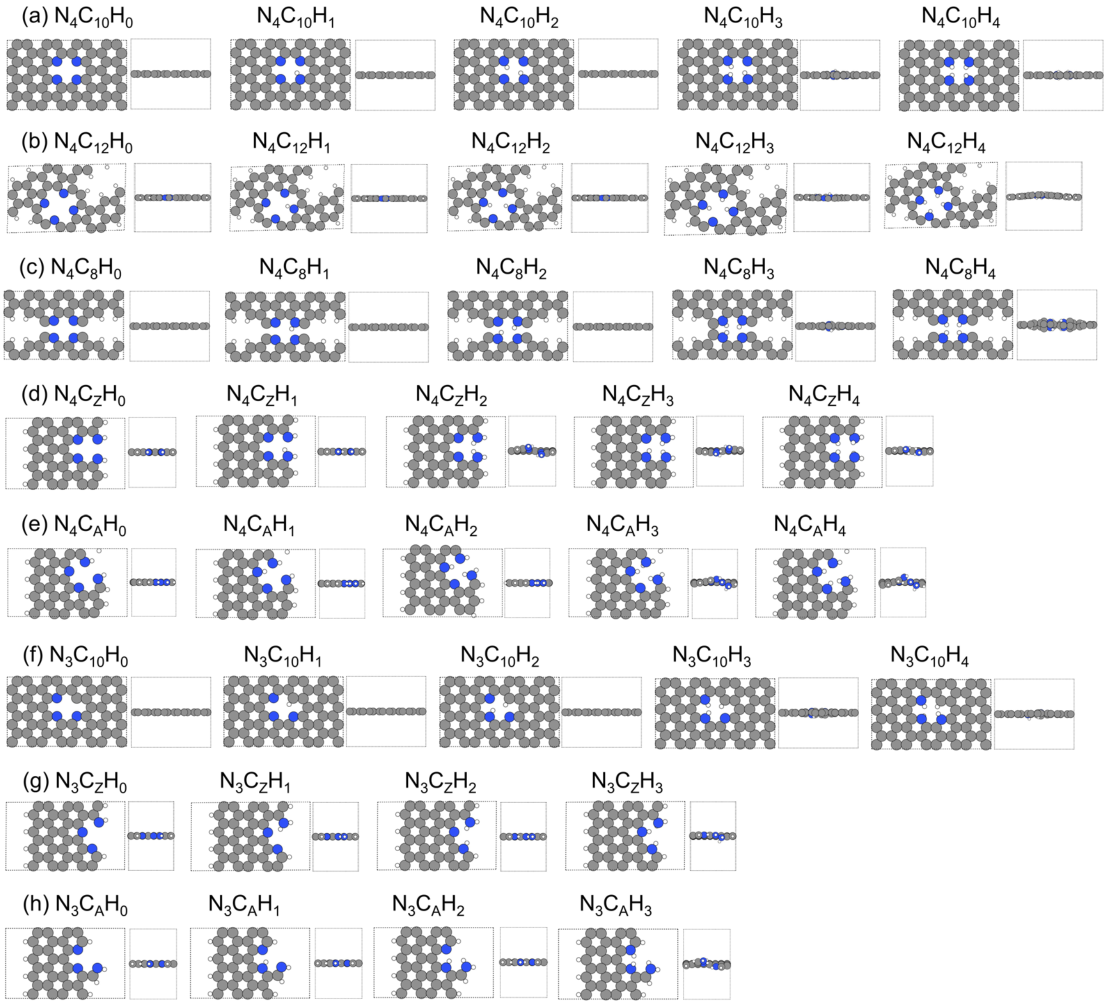

Figure A.1: The minimum energy structures of the dissolved-metal N_yCH_n carbon cavity with n = 0 - 4: (a) $N_4C_{10}H_n$, (b) $N_4C_{12}H_n$, (c) $N_4C_8H_n$, (d) $N_4C_ZH_n$, (e) $N_4C_AH_n$, (f) $N_3C_{10}H_n$, (g) $N_3C_ZH_n$, (h) $N_3C_AH_n$. (C = gray, N = blue, H = white, M = orange).

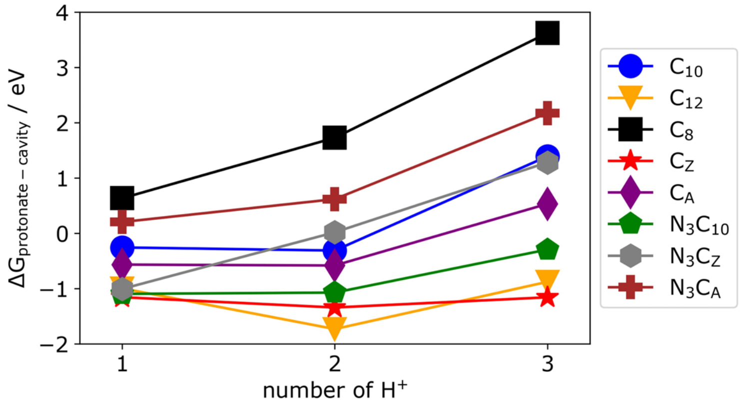

Figure A.2: Reaction free energy for protonation at the metal-dissolved carbon cavity ($\Delta G_{protonate-cavity}$) as a function of numer of H^+ at pH = 0 and U = 0.8 V_{SHE}.

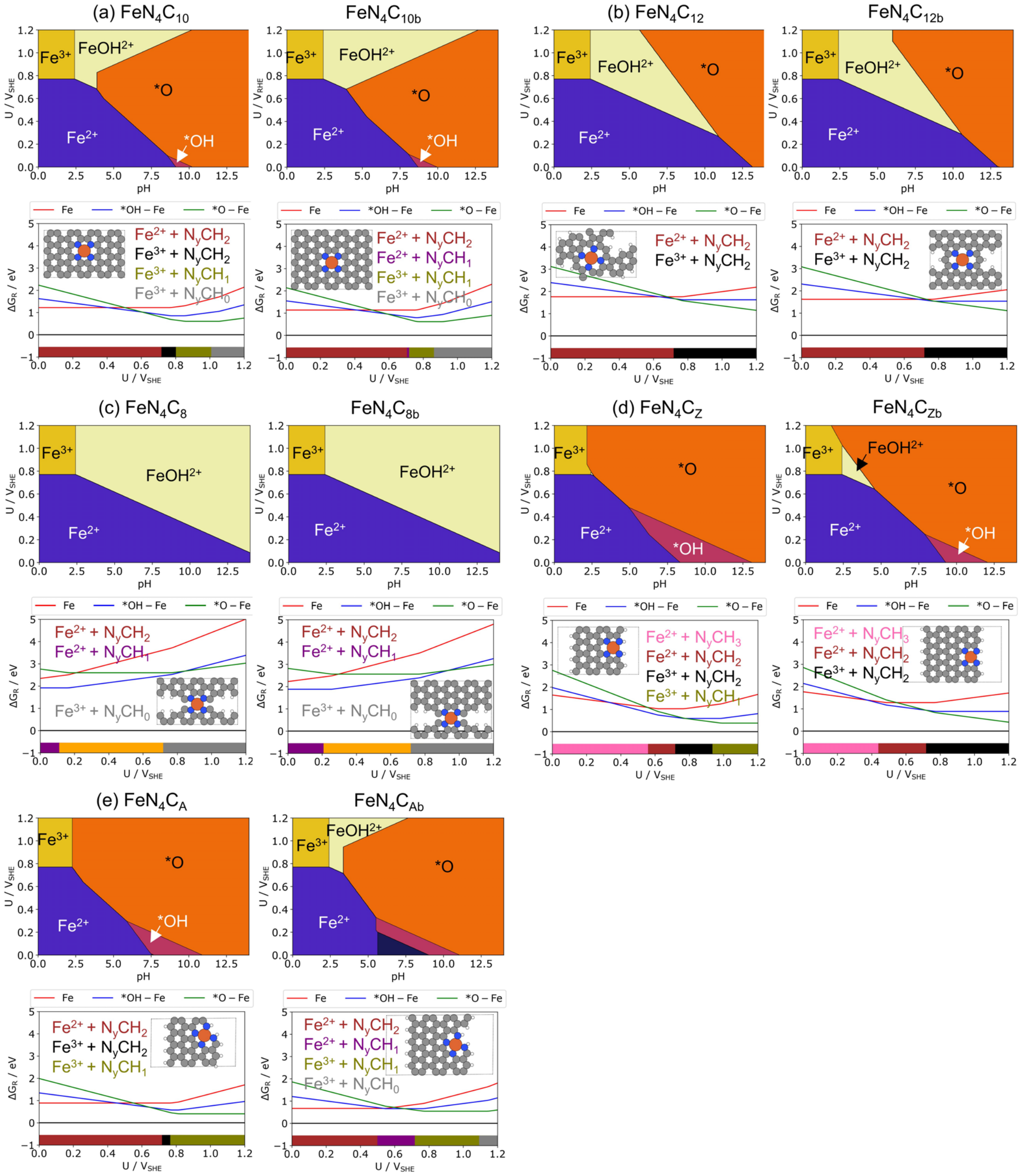

Figure A.3: (top) Stability diagram and (bottom) ΔG$_R$ at pH = 0 of the considered Fe/N/C structures without and with the adsorbate (Fe, *OH-Fe, and *O-Fe) obtained from two sizes of unit cell (b = bigger unit cell): (a) FeN$_4$C$_{10}$, (b) FeN$_4$C$_{12}$, (c) FeN$_4$C$_8$, (d) FeN$_4$C$_Z$, and (e) FeN$_4$C$_A$. The insets show the structural models used in the calculations (C = gray, N = blue, H = white, Fe = orange).

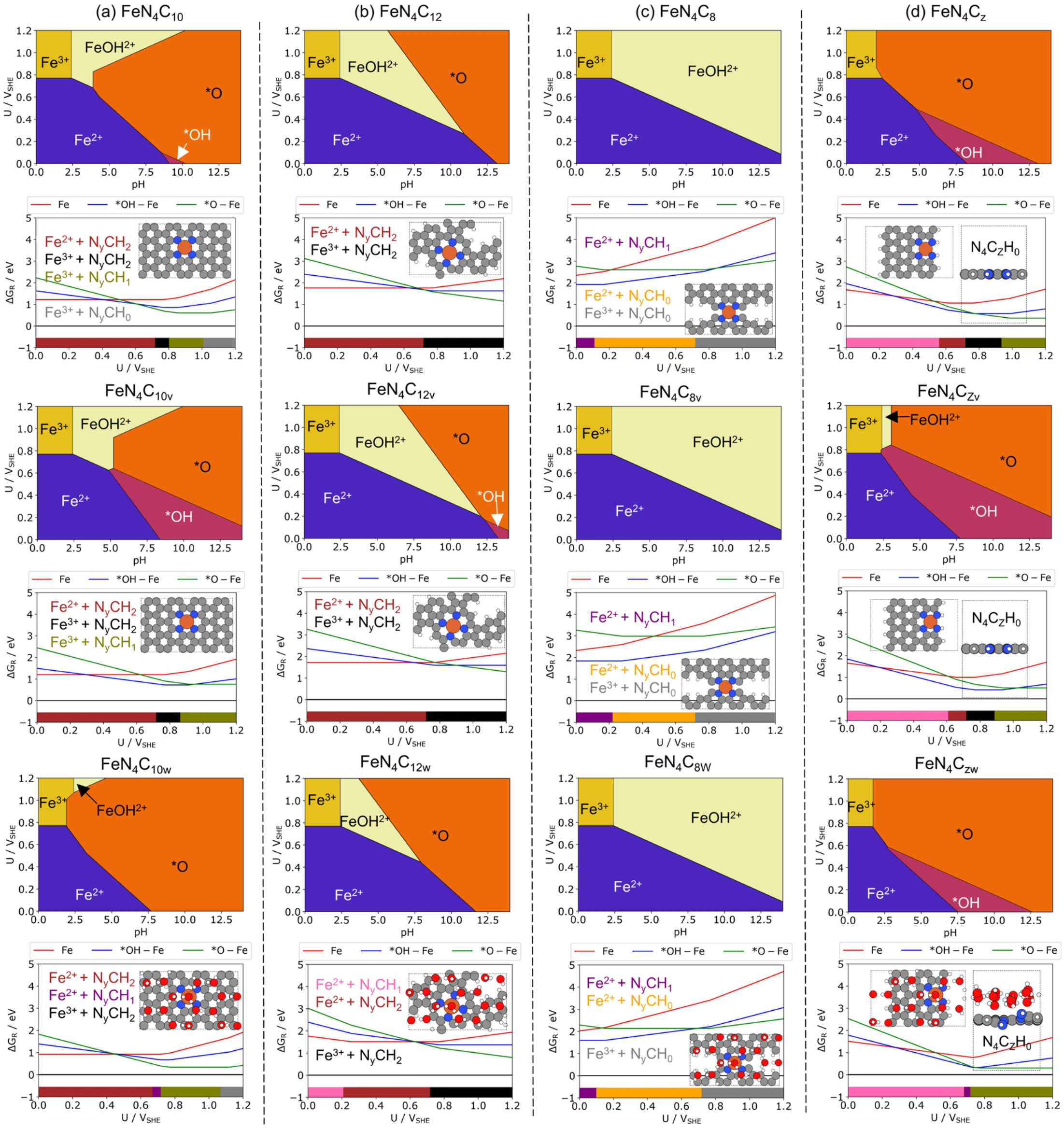

Figure A.4: Stability diagram and ΔG_R at pH = 0 of the considered Fe/N/C structures without and with the adsorbate (Fe, *OH-Fe, and *O-Fe) obtained from different solvation (v = vacuum, w = explicit solvation): (a) FeN_4C_{10}, (b) FeN_4C_{12}, (c) FeN_4C_8, and (d) FeN_4C_Z. The insets show the structural models used in the calculations (C = gray, N = blue, H = white, Fe = orange).

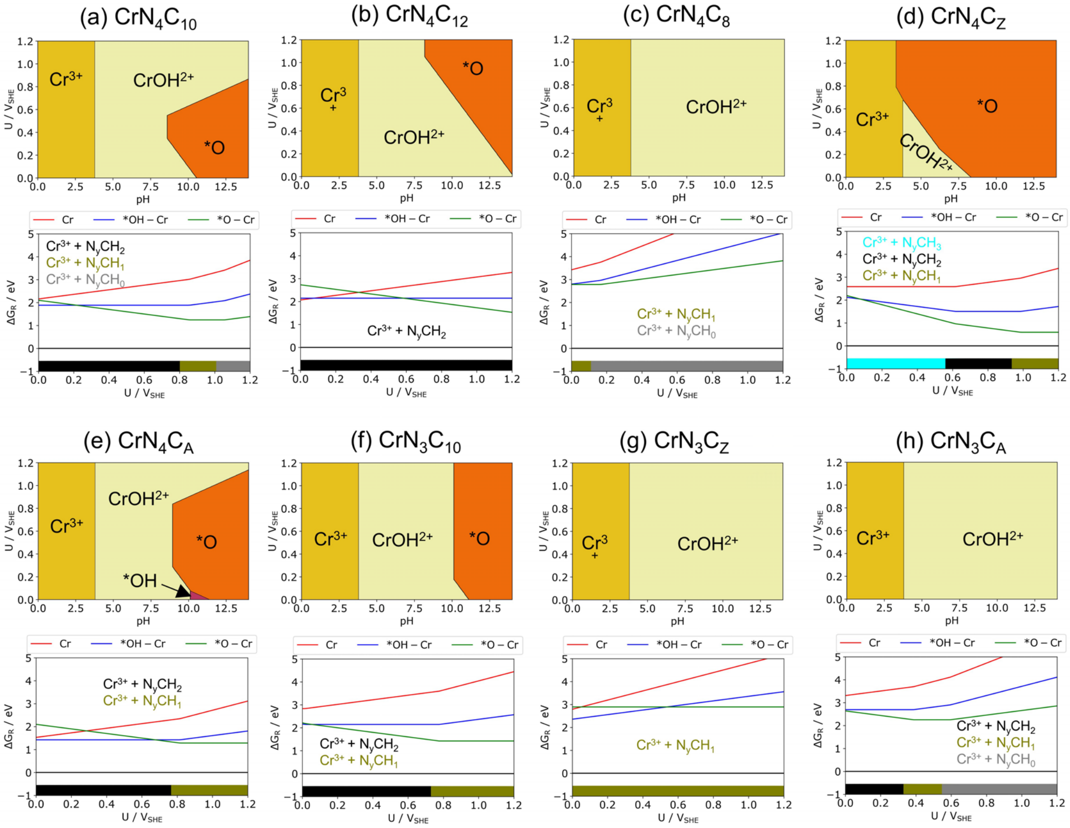

Figure A.5: (top) Stability diagram and (bottom) ΔG_R at pH = 0 of the considered Cr/N/C structures without and with the adsorbate (Cr, *OH-Cr, and *O-Cr): (a) CrN_4C_{10}, (b) CrN_4C_{12}, (c) CrN_4C_8, (d) CrN_4C_Z, (e) CrN_4C_A, (f) CrN_3C_{10}, (g) CrN_3C_Z, and (h) CrN_3C_A

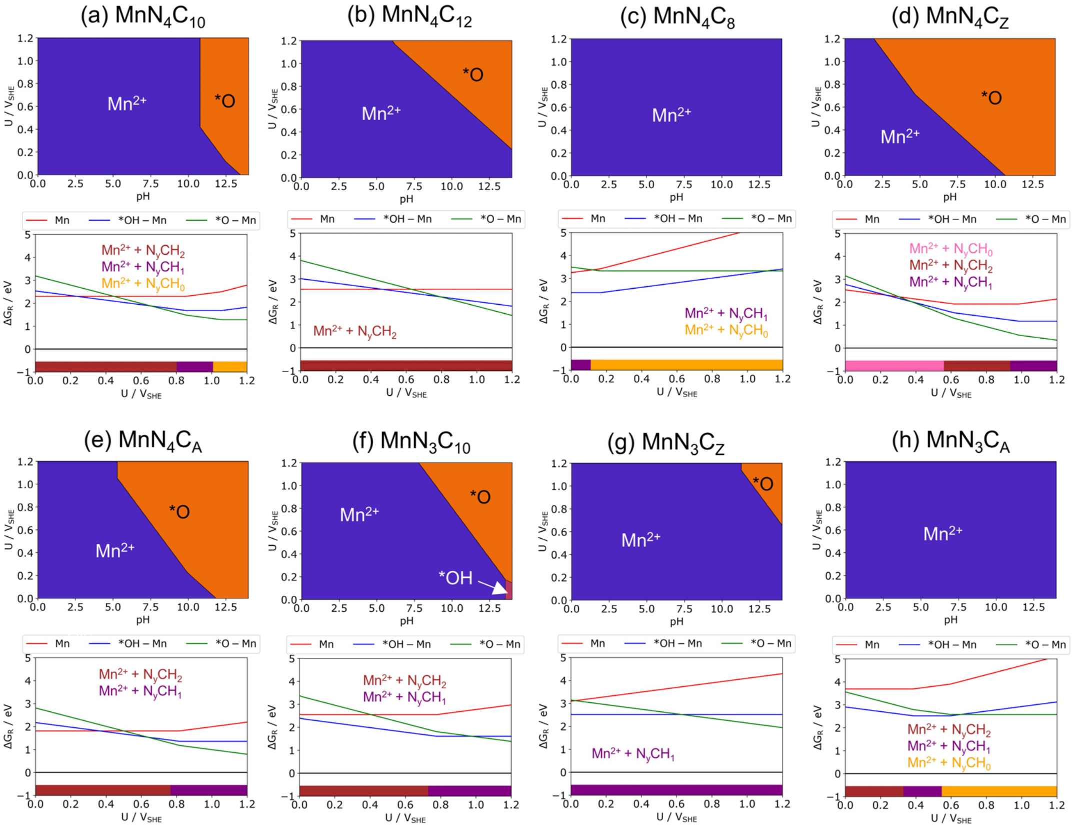

Figure A.6: (top) Stability diagram and (bottom) ΔG_R at pH = 0 of the considered Mn/N/C structures without and with the adsorbate (Mn, *OH-Mn, and *O-Mn): (a) MnN_4C_{10}, (b) MnN_4C_{12}, (c) MnN_4C_8, (d) MnN_4C_Z, (e) MnN_4C_A, (f) MnN_3C_{10}, (g) MnN_3C_Z, and (h) MnN_3C_A

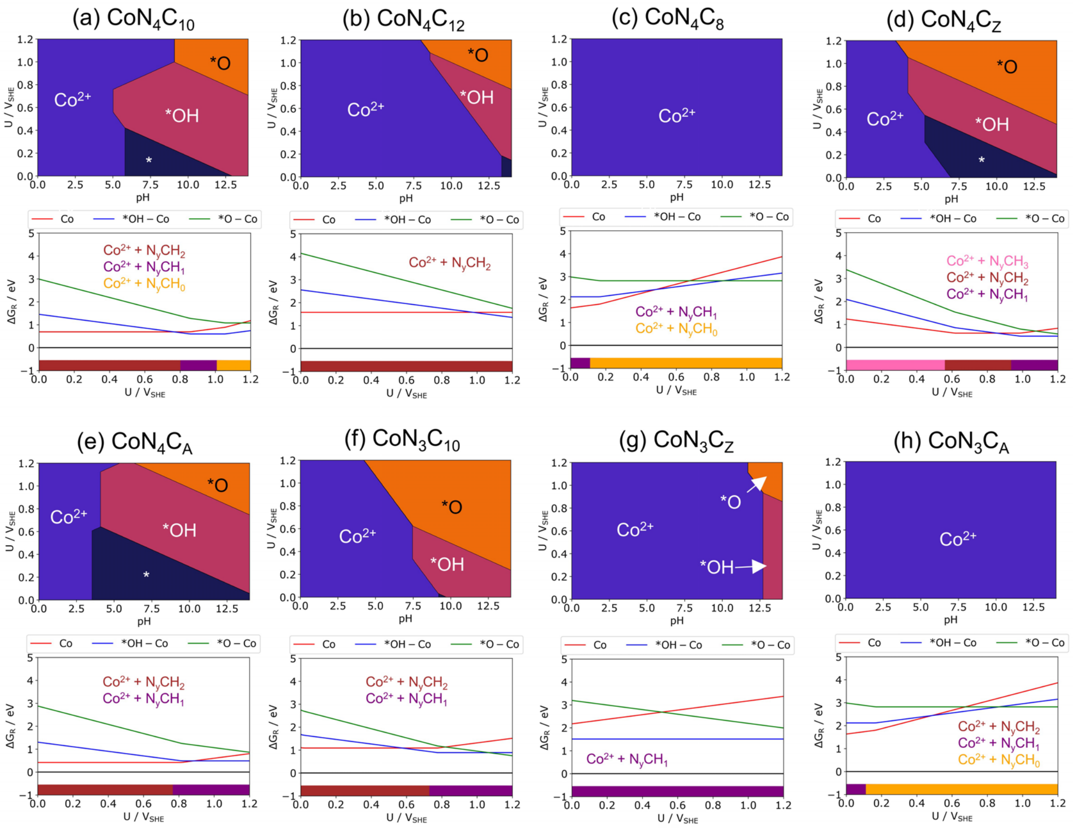

Figure A.7: (top) Stability diagram and (bottom) ΔG_R at pH = 0 of the considered Co/N/C structures without and with the adsorbate (Co, *OH-Co, and *O-Co): (a) CoN_4C_{10}, (b) CoN_4C_{12}, (c) CoN_4C_8, (d) CoN_4C_Z, (e) CoN_4C_A, (f) CoN_3C_{10}, (g) CoN_3C_Z,and (h) CoN_3C_A

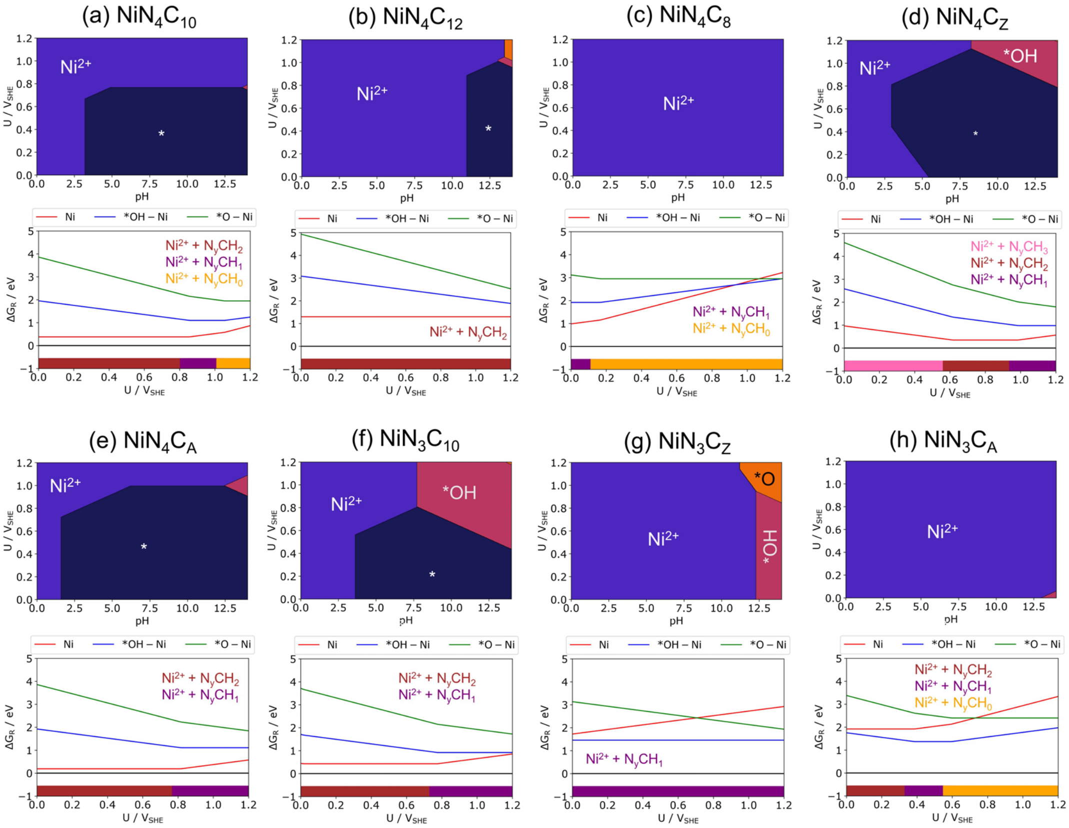

Figure A.8: (top) Stability diagram and (bottom) ΔG_R at pH = 0 of the considered Ni/N/C structures without and with the adsorbate (Ni, *OH-Ni, and *O-Ni): (a) NiN_4C_{10}, (b) NiN_4C_{12}, (c) NiN_4C_8, (d) NiN_4C_Z, (e) NiN_4C_A, (f) NiN_3C_{10}, (g) NiN_3C_Z, and (h) NiN_3C_A

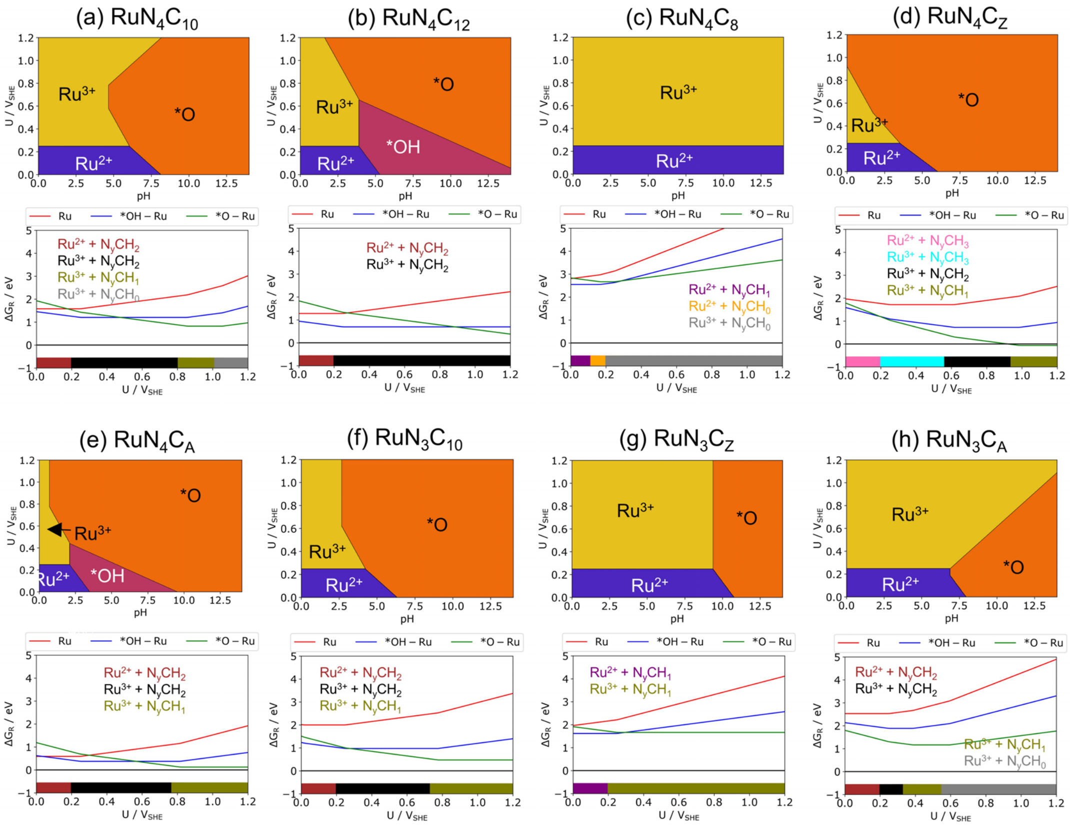

Figure A.9: (top) Stability diagram and (bottom) ΔG_R at pH = 0 of the considered Ru/N/C structures without and with the adsorbate (Ru, *OH-Ru, and *O-Ru): (a) RuN_4C_{10}, (b) RuN_4C_{12}, (c) RuN_4C_8, (d) RuN_4C_Z, (e) RuN_4C_A, (f) RuN_3C_{10}, (g) RuN_3C_Z, and (h) RuN_3C_A

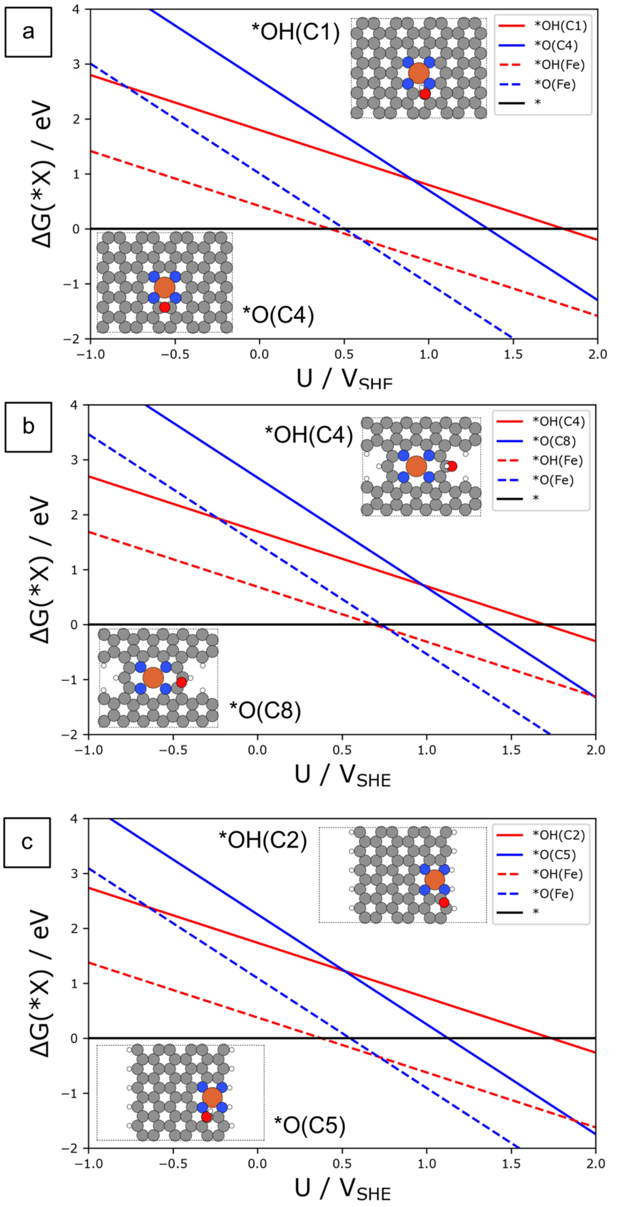

Figure A.10: Reaction free energy for the formation of *OH and *O on the FeN$_4$ center (in dashed lines) and carbon atoms adjacent to the FeN$_4$ center (in solid lines) at pH = 0; ΔG(*X) where X = O, OH: (a) FeN$_4$C$_{10b}$, (b) FeN$_4$C$_{12b}$ and (c) FeN$_4$C$_{Zb}$. The insets show the minimum energy positions for *OH and *O on the carbon atoms (C = gray, N = blue, H = white, Fe = orange).

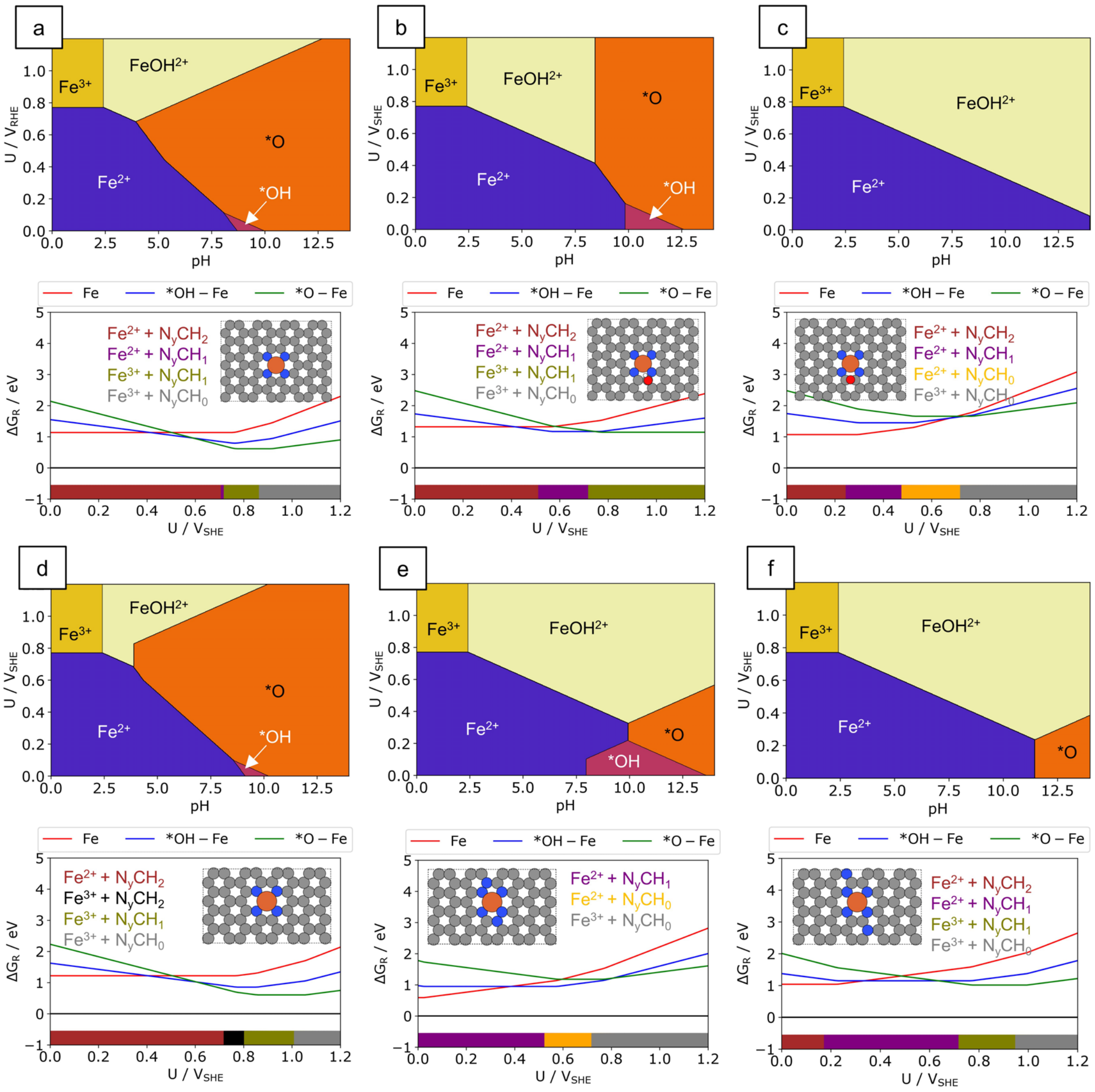

Figure A.11: Stability diagram and ΔG_R at pH = 0 of the considered FeN_4C_{10} structures without and with the adsorbate (Fe, *OH-Fe, and *O-Fe): (a) FeN_4C_{10b}, (b) FeN_4C_{10b} with near by *OH, (c) FeN_4C_{10b} with near by *O, (d) FeN_4C_{10}, (e) FeN_4C_{10} with nearby graphitic N atoms (configuration 1) and (f) FeN_4C_{10} with nearby graphitic N atoms (configuration 2). The insets show the structural models used in the calculations (C = gray, N = blue, H = white, Fe = orange).

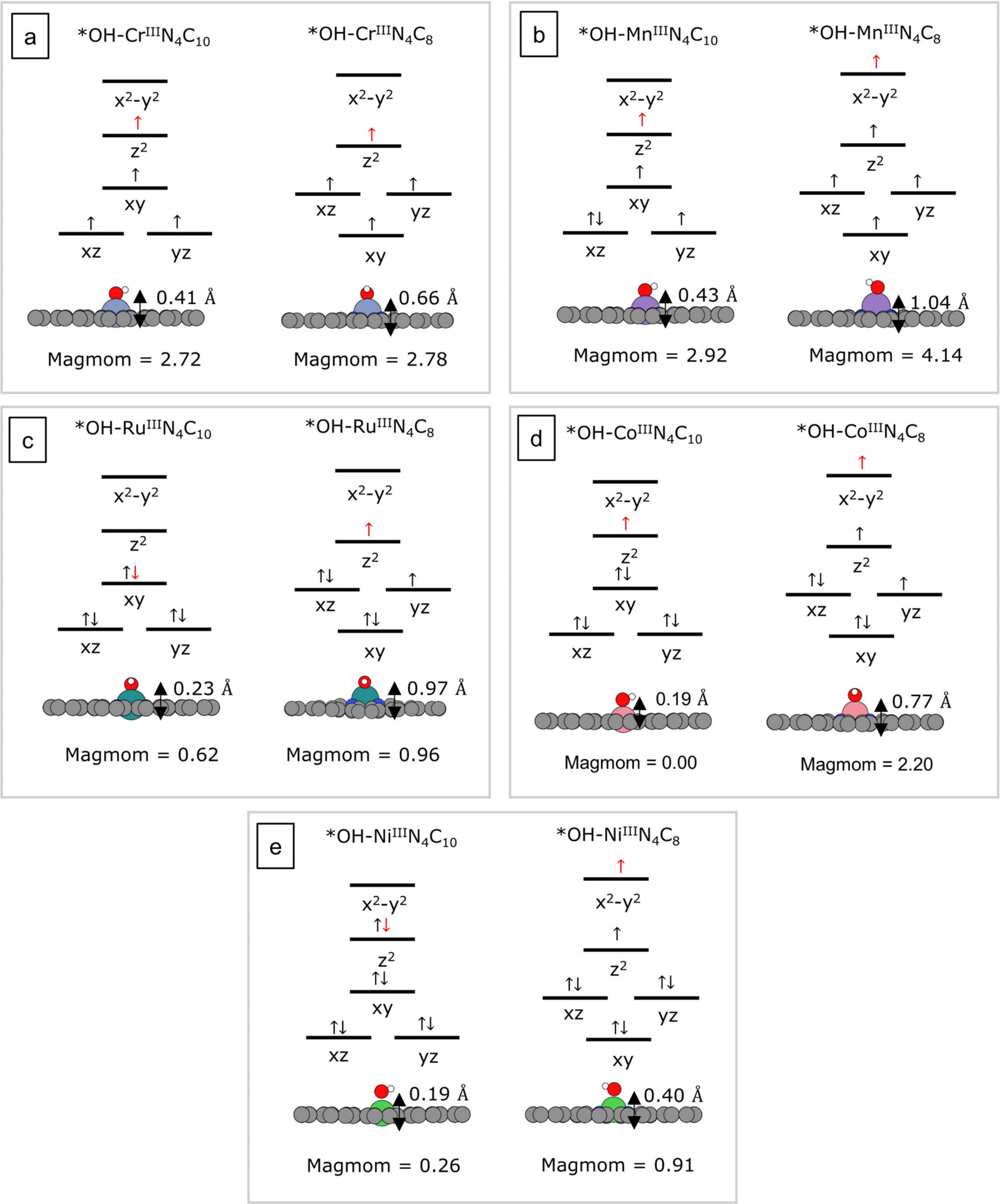

Figure A.12: The d-orbital splitting and electronic configuration for the metal atom in *OH-MN$_4$C$_{10}$ and *OH-MN$_4$C$_8$ structure: (a) M = Cr, (b) M = Mn, (c) M = Ru, (d) M = Co, and (e) M = Co. The electron donated to the adsorbate is red, and the remaining electrons in the d-orbitals are black.

Appendix B

Supplementary material II

Table B.1: Thermal correction ($ZPE + U_{vib} - TS_{vib}$) for the adsorbates at T = 298.15 K

Adsorbate I	Adsorbate II	$ZPE + U_{vib} - TS_{vib}$ (eV)	
		MN_4C_{10}	MN_4C_A
$^*H_2O$	-	0.60	0.65
*OOH	-	0.36	0.30
*OH	-	0.29	0.30
*O	-	0.03	0.04
*H	-	0.19	0.18
$^*HSO_4$	-	0.55	0.55
$^*SO_4$	-	0.28	0.26
$^*H_2PO_4$	-	0.81	1.12
$^*HPO_4$	-	0.48	0.53
$^*PO_4$	-	0.22	0.19
*Cl	-	-0.03	-0.03
$^*ClO_4$	-	0.19	0.24
*HCOO	-	0.49	0.69
*F	-	-0.02	-0.01
$^*NO_3$	-	0.23	0.18
*CN	-	0.14	0.10
*CO	-	0.11	0.12
*NO	-	0.10	0.09
$^*HCO_3$	-	0.64	0.77
$^*CO_3$	-	0.21	0.21
*COOH	-	0.51	0.53
$^*H_2O$	$^*H_2O$	1.13	1.62
*O	*O	0.67	0.62
*O	*O	0.07	0.07

Table B.1: Thermal correction ($ZPE + U_{vib} - TS_{vib}$) for the adsorbates at T = 298.15 K

Adsorbate I	Adsorbate II	$ZPE + U_{vib} - TS_{vib}$ (eV)	
		MN_4C_{10}	MN_4C_A
$^*HSO_4$	$^*HSO_4$	1.28	1.57
$^*SO_4$	$^*SO_4$	0.59	0.57
$^*H_2PO_4$	$^*H_2PO_4$	1.85	2.49
$^*HPO_4$	$^*HPO_4$	1.24	1.42
$^*PO_4$	$^*PO_4$	0.43	0.43
$^*Cl$	$^*Cl$	-0.03	-0.05
$^*ClO_4$	$^*ClO_4$	0.48	0.54
$^*HCOO$	$^*HCOO$	1.08	1.04
$^*F$	$^*F$	0.03	0.03
$^*NO_3$	$^*NO_3$	0.47	0.50
$^*CN$	$^*CN$	0.27	0.20
$^*CO$	$^*CO$	0.21	0.17
$^*OH$	$^*O$	0.36	0.35
$^*OH$	$^*HSO_4$	0.81	0.94
$^*OH$	$^*SO_4$	0.61	0.67
$^*OH$	$^*H_2PO_4$	1.27	1.24
$^*OH$	$^*HPO_4$	0.92	0.85
$^*OH$	$^*PO_4$	0.53	0.62
$^*OH$	$^*Cl$	0.30	0.32
$^*OH$	$^*F$	0.34	0.39
$^*OH$	$^*NO_3$	0.63	0.54
$^*OH$	$^*ClO_4$	0.63	0.60
$^*OH$	$^*HCOO$	0.85	0.87
$^*OH$	$^*CN$	0.56	0.52
$^*OH$	$^*CO$	0.51	0.05
$^*OH$	$^*NO$	0.46	0.45
$^*COOH$	$^*CO$	0.68	0.68
$^*COOH$	$^*HCO_3$	1.13	1.08
$^*CO$	$^*HCO_3$	0.66	0.70
$^*H$	$^*HCO_3$	0.89	1.07
$^*COOH$	$^*H$	0.88	0.92
$^*CO$	$^*H$	0.43	0.38
$^*COOH$	$^*CO_3$	0.75	0.82
$^*CO$	$^*CO_3$	0.26	0.42
$^*H$	$^*CO_3$	0.47	0.20
$^*CO$	$^*H_2O$	0.60	-
$^*COOH$	$^*H_2O$	1.04	-
$^*H$	$^*H_2O$	0.64	-

Table B.1: Thermal correction (ZPE + $U_{vib} - TS_{vib}$) for the adsorbates at T = 298.15 K

Adsorbate I	Adsorbate II	ZPE + $U_{vib} - TS_{vib}$ (eV)	
		MN_4C_{10}	MN_4C_A
*CO	*O	0.04	-0.03
*COOH	*O	0.39	0.50
*H	*O	0.21	0.22
*CO	*NO	0.18	0.76
*COOH	*NO	0.66	0.18
*H	*NO	0.42	0.53
*CO	*CN	0.21	0.50
*COOH	*CN	0.60	0.18
*H	*CN	0.41	0.40

Table B.2: List of gas molecules at T = 298.15 K and 1 bar. All energies are in eV.

	E_{DFT}	ZPE	$H_{(T=0K \rightarrow 298K)}$	TS	BEEF-vdW
H_2O	-12.83	0.56	0.10	0.67	-0.03
H_2	-7.18	0.27	0.09	0.40	0.09
H_3PO_4	-38.54	1.27	0.21	1.02	-
H_2SO_4	-29.87	1.04	0.17	0.93	-
HNO_3	-22.14	0.70	0.12	0.77	-
HCl	-4.54	0.18	0.09	0.58	-
HF	-6.20	0.25	0.09	0.54	-
HCOOH	-25.54	0.89	0.11	0.77	-
$HClO_4$	-16.85	0.73	0.16	0.92	-
HCN	-3.71	0.43	0.10	0.63	-
H_2CO_3	-31.00	1.05	0.13	0.82	-
NO	-9.33	0.12	0.10	0.65	-
CO	-12.10	0.13	0.09	0.61	0.15
CO_2	-18.43	0.31	0.10	0.66	0.30
NH_3	-18.46	0.89	0.11	0.60	-
N_2	-13.94	0.14	0.09	0.59	-

Table B.3: List of electrolyte anions: pK_a, formation energy in gas phase (ΔG_f(gas)) and solution phase (ΔG_f(aq, 1M)), solvation free energy (ΔG_{sol}), and activity coefficient for 0.1 M H_nA (γ). All energies are in eV.

Electrolyte	Anion	pK_a	ΔG_f(gas)	ΔG_f(aq, 1M)	ΔG_{sol}	γ
H_3PO_4	H_3PO_4	2.16	-11.36	-	-	-
	$H_2PO_4^-$	7.21	-	-11.75	-0.39	0.78
	HPO_4^{-2}	12.32	-	-11.33	0.03	0.51
	PO_4^{-3}	-	-	-10.59	0.77	0.34
H_2SO_4	H_2SO_4	-2.00	-6.75	-	-	-
	HSO_4^-	1.99	-	-7.86	-1.11	0.28
	SO_4^{-2}	-	-	-7.74	-0.99	0.14
HNO_3	HNO_3	-1.30	-0.57	-	-	-
	NO_3^-	-	-	-1.16	-0.59	0.79
HCl	HCl	-7.00	-0.99	-		-
	Cl^-	-	-	-1.36	-0.37	0.80
HF	HF	3.20	-2.84	-	-	-
	F^-	-	-	-2.90	-0.06	0.08
HCOOH	HCOOH	3.75	-3.64	-	-	-
	$HCOO^-$	-	-	-3.65	-0.01	0.78
$HClO_4$	$HClO_4$	-1.60	0.87	-	-	-
	ClO_4^-	-	-	-0.09	-0.96	0.80
HCN	HCN	9.21	1.30	-		-
	CN^-	-	-	1.79	0.50	0.78
H_2CO_3	H_2CO_3	6.35	-6.87	-	-	-
	HCO_3^-	10.33	-	-6.10	0.77	0.78
	CO_3^{-2}	-	-	-5.49	1.38	0.51

Table B.4: Free reaction energy of the dissolution reaction of the bulk metal and calculated DFT energy per atom of the metal in their bulk structure. E_0 is in V and E_M(bulk) is in eV/atom.

ion	$G(M^{x+})$	E_0 (V)	E_M(bulk)
Cr^{2+}	$E_{Cr}(bulk) + 2(E_0 + (0.059/2) \log[Cr^{2+}])$	$E_0 = -0.91$	-7.17
Cr^{3+}	$E_{Cr}(bulk) + 3(E_0 + (0.059/3) \log[Cr^{3+}])$	$E_0 = -0.74$	
$CrOH^{2+}$	$G(Cr^{3+}) + G(H_2O) - (1/2)G(H_2) + 2.303\ k_BTpH_0$	$pH_0 = 3.81$	
$HCrO_4^-$	$G(Cr^{3+}) + 4G(H_2O) - (7/2)G(H_2) + 3(E_0 + (0.059/3) \log([HCrO_4^-]/[Cr^{3+}]))$	$E_0 = 1.35$	
CrO_4^{2-}	$G(Cr^{3+}) + 3G(H_2O) - 4{*}G(H_2) + 3(E_0 + (0.059/3) \log([CrO_4^{2-}]/[Cr^{3+}]))$	$E_0 = 1.48$	
Mn^{2+}	$E_{Mn}(bulk) + 2(E_0 + (0.059/2) \log[Mn^{2+}])$	$E_0 = -1.19$	-6.45
Mn^{3+}	$G(Mn^{2+}) + E_0 + (0.059) \log([Mn^{3+}]/[Mn^{2+}])$	$E_0 = 1.54$	
MnO_4^{2-}	$G(Mn^{2+}) + 4G(H_2O) - 4G(H_2) + 4(E_0 + (0.059/4) \log([MnO_4^{2-}]/[Mn^{2+}]))$	$E_0 = 1.74$	
MnO_4^-	$G(Mn^{2+}) + 4G(H_2O) - 4G(H_2) + 5(E_0 + (0.059/5) \log([MnO_4^-]/[Mn^{2+}]))$	$E_0 = 1.51$	
MnO_4^{3-}	$G(MnO_4^{2-}) + E_0 + (0.059) \log([MnO_4^{3-}]/[MnO_4^{2-}])$	$E_0 = -0.27$	
Fe^{2+}	$E_{Fe}(bulk) + 2(E_0 + (0.059/2) \log[Fe^{2+}])$	$E_0 = -0.45$	-5.65
Fe^{3+}	$E_{Fe}(bulk) + 3(E_0 + (0.059/3) \log[Fe^{3+}])$	$E_0 = -0.04$	
$HFeO_4^-$	$G(Fe^{3+}) + 4G(H_2O) - (3/2)G(H_2) + 3(E_0 + (0.059/3) \log([HFeO_4^-]/[Fe^{3+}]))$	$E_0 = 2.07$	
FeO_4^{2-}	$G(Fe^{3+}) + 4G(H_2O) - 4G(H_2) + 3(E_0 + (0.059/3) \log([FeO_4^{2-}]/[Fe^{3+}]))$	$E_0 = 2.20$	
$FeOH^{2+}$	$G(Fe^{3+}) + G(H_2O) - (1/2)G(H_2) + 2.303\ k_BTpH_0$	$pH_0 = 2.43$	
$HFeO_2^-$	$G(Fe^{2+}) + 2G(H_2O) - (3/2)G(H_2) + 2.303\ k_BTpH_0$	$pH_0 = 31.58$	
FeO_2^-	$G(HFeO_2^-) - (1/2)G(H_2) + E_0 + (0.059) \log([FeO_2^-]/[HFeO_2^-])$	$E_0 = -0.69$	
Co^{2+}	$E_{Co}(bulk) + 2(E_0 + (0.059/2) \log[Co^{2+}])$	$E_0 = -0.28$	-4.29
Co^{3+}	$G(Co^{2+}) + E_0 + (0.059) \log([Co^{3+}]/[Co^{2+}])$	$E_0 = 1.92$	
$HCoO_2^-$	$G(Co^{2+}) + 2G(H_2O) - (3/2){*}G(H_2) + 2.303\ k_BTpH_0$	$pH_0 = 31.70$	
Ni^{2+}	$E_{Ni}(bulk) + 2(E_0 + (0.059/2) \log[Ni^{2+}])$	$E_0 = -0.26$	-2.53
Ni^{3+}	$G(Ni^{2+}) + E_0 + (0.059) \log([Ni^{3+}]/[Ni^{2+}])$	$E_0 = 2.30$	
$HNiO_2^-$	$G(Ni^{2+}) + 2G(H_2O) - (3/2)G(H_2) + 2.303\ k_BTpH_0$	$pH_0 = 30.40$	
Cu_{2+}	$E_{Cu}(bulk) + 2(E_0 + (0.059/2) \log[Cu_{2+}])$	$E_0 = 0.34$	-0.64
Cu_+	$E_{Cu}(bulk) + E_0 + (0.059) \log[Cu_+]$	$E_0 = 0.34$	
Cu_{3+}	$G(Cu_{2+}) + E_0 + (0.059) \log([Cu_{3+}]/[Cu_{2+}])$	$E_0 = 2.40$	
CuO_2^-	$G(Cu_{2+}) + 2G(H_2O) - 2G(H_2) + 2.303\ k_BTpH_0$	$pH_0 = 39.88$	
$HCuO_2^-$	$G(Cu_{2+}) + 2G(H_2O) - (3/2)G(H_2) + 2.303\ k_BTpH_0$	$pH_0 = 26.72$	
Zn^{2+}	$E_{Zn}(bulk) + 2(E_0 + (0.059/2) \log[Zn^{2+}])$	$E_0 = -0.76$	2.06
$ZnOH^+$	$G(Zn^{2+}) - (1/2)G(H_2) + G(H_2O) + 2.303\ k_BTpH_0$	$pH_0 = 9.67$	
$HZnO_2^-$	$G(Zn^{2+}) + 2G(H_2O) - (3/2){*}G(H_2) + 2.303\ k_BTpH_0$	$pH_0 = 27.63$	
ZnO_2^{2-}	$G(HZnO_2^-) - (1/2)G(H_2) + 2.303\ k_BTpH_0$	$pH_0 = 13.17$	
Mo^{3+}	$E_{Mo}(bulk) + 3(E_0 + (0.059/3) \log[Mo^{3+}])$	$E_0 = -0.20$	-8.17
$HMoO_4^-$	$G(Mo^{3+}) + 4G(H_2O) + 3(E_0 + (0.059/3) \log([HMoO_4^-]/[Mo^{3+}])) - (7/2)G(H_2)$	$E_0 = 0.39$	
MoO_4^{2-}	$G(Mo^{3+}) + 4G(H_2O) + 3(E_0 + (0.059/3) \log([MoO_4^{2-}]/[Mo^{3+}])) - 4G(H_2)$	$E_0 = 0.51$	
Ru^{2+}	$E_{Ru}(bulk) + 2(E_0 + (0.059/2) \log[Ru^{2+}])$	$E_0 = 0.46$	-6.26
Ru^{3+}	$G(Ru^{2+}) + E_0 + (0.059) \log([Ru^{3+}]/[Ru^{2+}])$	$E_0 = 0.25$	
RuO_4^{2-}	$G(Ru^{2+}) + 4G(H_2O) - 4G(H_2) + 4(E_0 + (0.059/4) \log([RuO_4^{2-}]/[Ru^{2+}]))$	$E_0 = 1.56$	
RuO_4^-	$G(Ru^{2+}) + 4G(H_2O) - 4G(H_2) + 5(E_0 + (0.059/5) \log([RuO_4^-]/[Ru^{2+}]))$	$E_0 = 1.37$	
Rh^+	$E_{Rh}(bulk) + E_0 + (0.059) \log[Rh^+]$	$E_0 = 0.60$	-4.24
Rh^{2+}	$G(Rh^+) + E_0 + (0.059) \log([Rh^{2+}]/[Rh^+])$	$E_0 = 0.60$	
Rh^{3+}	$E_{Rh}(bulk) + 3(E_0 + (0.059/3) \log[Rh^{3+}])$	$E_0 = 0.76$	
RhO_4^{2-}	$G(Rh^{2+}) + 4G(H_2O) - 4G(H_2) + 4(E_0 + (0.059/4) \log([RhO_4^{2-}]/[Rh^{2+}]))$	$E_0 = 2.00$	
$RhOH^{2+}$	$G(Rh^+) + G(H_2O) - (1/2)G(H_2) + 5(E_0 + (0.059/5) \log([RuOH^{2+}]/[Ru^+]))$	$E_0 = 0.23$	
Pd^{2+}	$E_{Pd}(bulk) + 2(E_0 + (0.059/2) \log[Pd^{2+}])$	$E_0 = 0.95$	-1.96
Ag^+	$E_{Ag}(bulk) + E_0 + (0.059) \log[Ag^+]$	$E_0 = 0.80$	0.55
Ag^{2+}	$G(Ag^+) + E_0 + (0.059) \log([Ag^{2+}]/[Ag^+])$	$E_0 = 1.98$	
Ag^{3+}	$G(Ag^{2+}) + E_0 + (0.059) \log([Ag^{3+}]/[Ag^+])$	$E_0 = 1.80$	
AgO^-	$G(Ag^+) - G(H_2) + G(H_2O) + 2.303\ k_BTpH_0$	$pH_0 = 24.04$	
AgO^+	$G(Ag^+) - G(H_2) + G(H_2O) + 2(E_0 + (0.059/2) \log([AgO^+]/[Ag^+]))$	$E_0 = 2.00$	
W^{3+}	$E_W(bulk) + 3(E_0 + (0.059/3) \log[W^{3+}])$	$E_0 = 0.10$	-0.43
WO_4^{2-}	$G(W^{3+}) + 4G(H_2O) - 4G(H_2) + 3(E_0 + (0.059/3) \log([WO_4^{2-}]/[W^{3+}]))$	$E_0 = 0.15$	

Table B.4: Free reaction energy of the dissolution reaction of the bulk metal and calculated DFT energy per atom of the metal in their bulk structure. E_0 is in V and E_M(bulk) is in eV/atom.

ion	$G(M^{x+})$	E_0 (V)	E_M(bulk)
Re^{3+}	$E_{Re}(bulk) + 3(E_0 + (0.059/3) \log[Re^{3+}])$	$E_0 = 0.30$	-9.59
Re^{-}	$G(Re^{3+}) + 4(E_0 + (0.059/4) \log([Re^{-}]/[Re^{3+}]))$	$E_0 = 0.13$	
ReO_4^-	$G(Re^{-}) + 4G(H_2O) - 4G(H_2) + 8(E_0 + (0.059/8) \log([ReO_4^-]/[Re^{-}]))$	$E_0 = 0.27$	
ReO_4^{2-}	$G(Re^{-}) + 4G(H_2O) - 4G(H_2) + 7(E_0 + (0.059/7) \log([ReO_4^{2-}]/[Re^{-}]))$	$E_0 = 0.41$	
OsO_4^{2-}	$E_{Os}(bulk) + 4G(H_2O) - 4G(H_2) + 6(E_0 + (0.059/6) \log[OsO_4^{2-}])$	$E_0 = 0.99$	-8.28
OsO_5^{2-}	$G(OsO_4^{2-}) + G(H_2O) - G(H_2) + 2(E_0 + (0.059/2) \log([OsO_5^{2-}]/[OsO_4^{2-}]))$	$E_0 = 1.14$	
$HOsO_4^-$	$G(OsO_4^{2-}) + G(H_2O) - (1/2)G(H_2) + 2(E_0 + (0.059/2) \log([HOsO_4^-]/[OsO_4^{2-}]))$	$E_0 = 0.71$	
Ir^{3+}	$E_{Ir}(bulk) + 3(E_0 + (0.059/3) \log[Ir^{3+}])$	$E_0 = 1.16$	-5.82
IrO_4^{-2}	$G(Ir^{3+}) - 4G(H_2) + 4G(H_2O) + 3(E_0 + (0.059/3) \log([IrO42-]/[Ir^{3+}]))$	$E_0 = 1.45$	
Pt^{2+}	$E_{Pt}(bulk) + 2(E_0 + (0.059/2) \log[Pt^{2+}])$	$E_0 = 1.18$	-3.13
Au^{+}	$E_{Au}(bulk) + E_0 + (0.059) \log[Au^{+}]$	$E_0 = 1.70$	-0.25
Au^{2+}	$G(Au^{+}) + E_0 + (0.059) \log([Au^{2+}]/ [Au^{+}])$	$E_0 = 1.80$	
Au^{3+}	$E_{Au}(bulk) + 3(E_0 + (0.059/3) \log[Au^{3+}])$	$E_0 = 1.50$	
$AuOH^{2+}$	$G(Au^{+}) + G(H_2O) - (1/2)G(H_2) + 2(E_0 + (0.059/2) \log([AuOH^{2+}]/[Au^{+}]))$	$E_0 = 1.32$	
$H_2AuO_3^-$	$G(Au^{+}) + 3G(H_2O) - 2G(H_2) + 2(E_0 + (0.059/2) \log([H_2AuO_3^-]/[Au^{+}]))$	$E_0 = 1.85$	
$HAuO_3^{2-}$	$G(Au^{+}) + 3G(H_2O) - (5/2)G(H_2) + 2(E_0 + (0.059/2) \log([HAuO_3^{2-}]/[Au^{+}]))$	$E_0 = 2.24$	
AuO_3^{3-}	$G(HAuO_3^{2-}) - (1/2)G(H_2) + 2.303\ k_BT\ pH_0$	$pH_0 = 15.99$	
Sn^{2+}	$ESn(bulk) + 2(E_0 + (0.059/2) \log[Sn^{2+}])$	$E_0 = -0.14$	-1.18
Sn4+	$G(Sn^{2+}) + 2(E_0 + (0.059/2) \log([Sn^{4+}]/[Sn^{2+}]))$	$E_0 = 0.15$	
SnO_3^{-2}	$G(Sn^{2+}) + 3G(H_2O) - 3G(H_2) + 2(E_0 + (0.059/2) \log([SnO32-]/[Sn^{2+}]))$	$E_0 = 0.84$	
$HSnO_2^-$	$G(SnO_3^{-2}) - G(H_2O) + (3/2)G(H_2) - 2(E_0 + (0.059/2) \log([HSnO_2^-]/[SnO_3^{-2}]))$	$E_0 = 0.37$	
$SnOH^{+}$	$G(Sn^{2+}) + G(H_2O) - (1/2)G(H_2) + 2.303\ k_BT\ E_0$	$E_0 = 0.56$	
SbO^{+}	$ESb(bulk) + 2G(H_2O) - G(H_2) + 3(E_0 + (0.059/3) \log[SbO^{+}])$	$E_0 = 0.21$	-2.09
$HSbO_2$	$G(SbO^{+}) - (1/2)G(H_2) + G(H_2O) + 2.303\ k_BTE_0$	$E_0 = 0.87$	
SbO_2^-	$G(HSbO_2) - (1/2)G(H_2) + 2.303\ k_BT\ E_0$	$E_0 = 11.00$	
SbO_2^+	$G(SbO^{-}) + G(H_2O) - G(H_2) + 2(E_0 + (0.059/2) \log([SbO_2^+]/[SbO_2^-]))$	$E_0 = 0.72$	
SbO_3^-	$G(SbO^{-}) + 2G(H_2O) - 2G(H_2) + 2(E_0 + (0.059/2) \log([SbO_3^-]/[SbO_2^-]))$	$E_0 = 0.70$	
Bi^{+}	$E_{Bi}(bulk) + E_0 + (0.059) \log[Bi^{+}]$	$E_0 = 0.50$	-1.19
Bi^{3+}	$E_{Bi}(bulk) + 3(E_0 + (0.059/3) \log[Bi^{3+}])$	$E_0 = 0.38$	
$BiOH^{2+}$	$G(Bi^{3+}) - (1/2)G(H_2) + G(H_2O) + 2.303\ k_BT\ E_0$	$E_0 = 2.00$	
BiO^{+}	$G(Bi^{3+}) - (1/2)G(H_2) + 2.303\ k_BT\ E_0$	$E_0 = 3.37$	

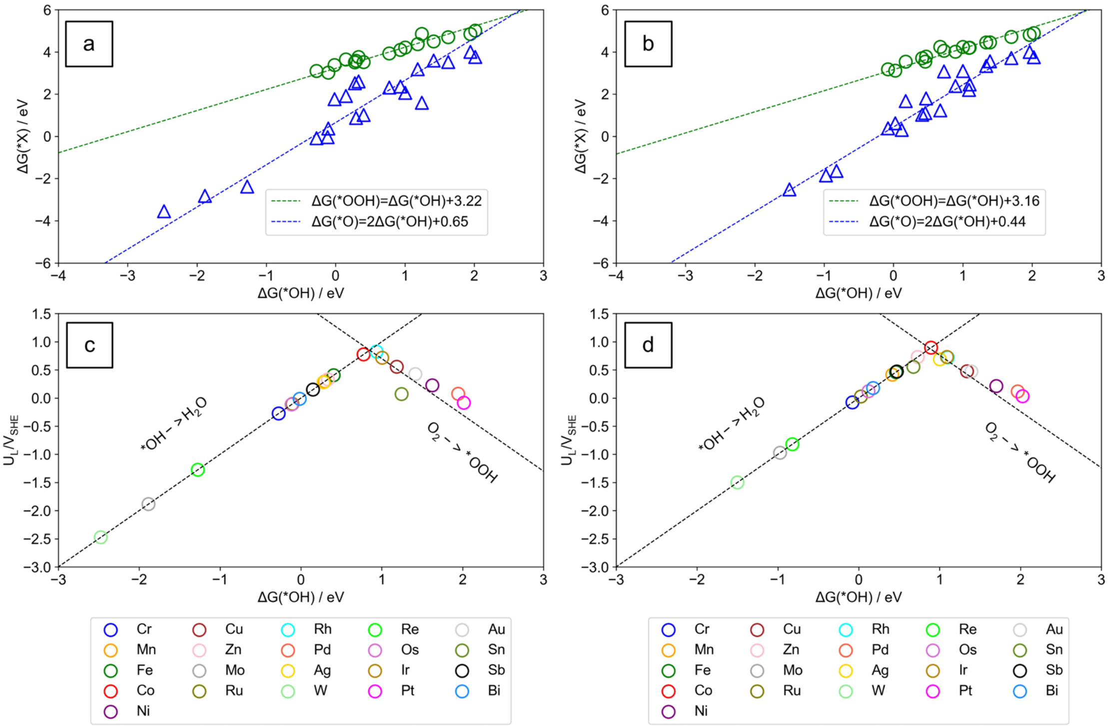

Figure B.1: Scaling relation between ΔG(*O) vs. ΔG(*OH) and ΔG(*OOH) vs. ΔG(*OH) on the bare metal site: (a) MN_4C_{10}, (b) MN_4C_A. Activity volcano plot as a function of ΔG(*O) for the bare metal site: (c) MN_4C_{10} and (d) MN_4C_A.

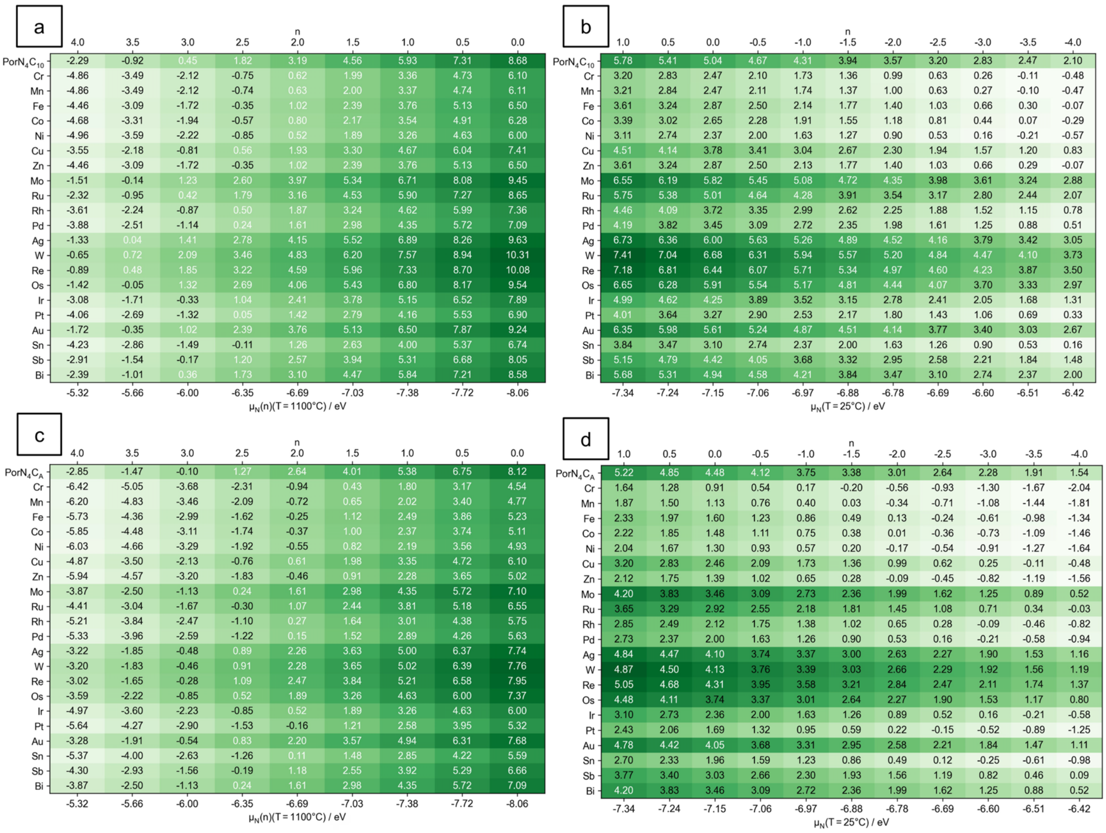

a

n	4.0	3.5	3.0	2.5	2.0	1.5	1.0	0.5	0.0
$PorN_4C_{10}$	-2.29	-0.92	0.45	1.82	3.19	4.56	5.93	7.31	8.68
Cr	-4.86	-3.49	-2.12	-0.75	0.62	1.99	3.36	4.73	6.10
Mn	-4.86	-3.49	-2.12	-0.74	0.63	2.00	3.37	4.74	6.11
Fe	-4.46	-3.09	-1.72	-0.35	1.02	2.39	3.76	5.13	6.50
Co	-4.68	-3.31	-1.94	-0.57	0.80	2.17	3.54	4.91	6.28
Ni	-4.96	-3.59	-2.22	-0.85	0.52	1.89	3.26	4.63	6.00
Cu	-3.55	-2.18	-0.81	0.56	1.93	3.30	4.67	6.04	7.41
Zn	-4.46	-3.09	-1.72	-0.35	1.02	2.39	3.76	5.13	6.50
Mo	-1.51	-0.14	1.23	2.60	3.97	5.34	6.71	8.08	9.45
Ru	-2.32	-0.95	0.42	1.79	3.16	4.53	5.90	7.27	8.65
Rh	-3.61	-2.24	-0.87	0.50	1.87	3.24	4.62	5.99	7.36
Pd	-3.88	-2.51	-1.14	0.24	1.61	2.98	4.35	5.72	7.09
Ag	-1.33	0.04	1.41	2.78	4.15	5.52	6.89	8.26	9.63
W	-0.65	0.72	2.09	3.46	4.83	6.20	7.57	8.94	10.31
Re	-0.89	0.48	1.85	3.22	4.59	5.96	7.33	8.70	10.08
Os	-1.42	-0.05	1.32	2.69	4.06	5.43	6.80	8.17	9.54
Ir	-3.08	-1.71	-0.33	1.04	2.41	3.78	5.15	6.52	7.89
Pt	-4.06	-2.69	-1.32	0.05	1.42	2.79	4.16	5.53	6.90
Au	-1.72	-0.35	1.02	2.39	3.76	5.13	6.50	7.87	9.24
Sn	-4.23	-2.86	-1.49	-0.11	1.26	2.63	4.00	5.37	6.74
Sb	-2.91	-1.54	-0.17	1.20	2.57	3.94	5.31	6.68	8.05
Bi	-2.39	-1.01	0.36	1.73	3.10	4.47	5.84	7.21	8.58
$\mu_N(n)(T = 1100°C)$ / eV	-5.32	-5.66	-6.00	-6.35	-6.69	-7.03	-7.38	-7.72	-8.06

b

n	1.0	0.5	0.0	-0.5	-1.0	-1.5	-2.0	-2.5	-3.0	-3.5	-4.0
$PorN_4C_{10}$	5.78	5.41	5.04	4.67	4.31	3.94	3.57	3.20	2.83	2.47	2.10
Cr	3.20	2.83	2.47	2.10	1.73	1.36	0.99	0.63	0.26	-0.11	-0.48
Mn	3.21	2.84	2.47	2.11	1.74	1.37	1.00	0.63	0.27	-0.10	-0.47
Fe	3.61	3.24	2.87	2.50	2.14	1.77	1.40	1.03	0.66	0.30	-0.07
Co	3.39	3.02	2.65	2.28	1.91	1.55	1.18	0.81	0.44	0.07	-0.29
Ni	3.11	2.74	2.37	2.00	1.63	1.27	0.90	0.53	0.16	-0.21	-0.57
Cu	4.51	4.14	3.78	3.41	3.04	2.67	2.30	1.94	1.57	1.20	0.83
Zn	3.61	3.24	2.87	2.50	2.13	1.77	1.40	1.03	0.66	0.29	-0.07
Mo	6.55	6.19	5.82	5.45	5.08	4.72	4.35	3.98	3.61	3.24	2.88
Ru	5.75	5.38	5.01	4.64	4.28	3.91	3.54	3.17	2.80	2.44	2.07
Rh	4.46	4.09	3.72	3.35	2.99	2.62	2.25	1.88	1.52	1.15	0.78
Pd	4.19	3.82	3.45	3.09	2.72	2.35	1.98	1.61	1.25	0.88	0.51
Ag	6.73	6.36	6.00	5.63	5.26	4.89	4.52	4.16	3.79	3.42	3.05
W	7.41	7.04	6.68	6.31	5.94	5.57	5.20	4.84	4.47	4.10	3.73
Re	7.18	6.81	6.44	6.07	5.71	5.34	4.97	4.60	4.23	3.87	3.50
Os	6.65	6.28	5.91	5.54	5.17	4.81	4.44	4.07	3.70	3.33	2.97
Ir	4.99	4.62	4.25	3.89	3.52	3.15	2.78	2.41	2.05	1.68	1.31
Pt	4.01	3.64	3.27	2.90	2.53	2.17	1.80	1.43	1.06	0.69	0.33
Au	6.35	5.98	5.61	5.24	4.87	4.51	4.14	3.77	3.40	3.03	2.67
Sn	3.84	3.47	3.10	2.74	2.37	2.00	1.63	1.26	0.90	0.53	0.16
Sb	5.15	4.79	4.42	4.05	3.68	3.32	2.95	2.58	2.21	1.84	1.48
Bi	5.68	5.31	4.94	4.58	4.21	3.84	3.47	3.10	2.74	2.37	2.00
$\mu_N(T = 25°C)$ / eV	-7.34	-7.24	-7.15	-7.06	-6.97	-6.88	-6.78	-6.69	-6.60	-6.51	-6.42

c

n	4.0	3.5	3.0	2.5	2.0	1.5	1.0	0.5	0.0
$PorN_4C_A$	-2.85	-1.47	-0.10	1.27	2.64	4.01	5.38	6.75	8.12
Cr	-6.42	-5.05	-3.68	-2.31	-0.94	0.43	1.80	3.17	4.54
Mn	-6.20	-4.83	-3.46	-2.09	-0.72	0.65	2.02	3.40	4.77
Fe	-5.73	-4.36	-2.99	-1.62	-0.25	1.12	2.49	3.86	5.23
Co	-5.85	-4.48	-3.11	-1.74	-0.37	1.00	2.37	3.74	5.11
Ni	-6.03	-4.66	-3.29	-1.92	-0.55	0.82	2.19	3.56	4.93
Cu	-4.87	-3.50	-2.13	-0.76	0.61	1.98	3.35	4.72	6.10
Zn	-5.94	-4.57	-3.20	-1.83	-0.46	0.91	2.28	3.65	5.02
Mo	-3.87	-2.50	-1.13	0.24	1.61	2.98	4.35	5.72	7.10
Ru	-4.41	-3.04	-1.67	-0.30	1.07	2.44	3.81	5.18	6.55
Rh	-5.21	-3.84	-2.47	-1.10	0.27	1.64	3.01	4.38	5.75
Pd	-5.33	-3.96	-2.59	-1.22	0.15	1.52	2.89	4.26	5.63
Ag	-3.22	-1.85	-0.48	0.89	2.26	3.63	5.00	6.37	7.74
W	-3.20	-1.83	-0.46	0.91	2.28	3.65	5.02	6.39	7.76
Re	-3.02	-1.65	-0.28	1.09	2.47	3.84	5.21	6.58	7.95
Os	-3.59	-2.22	-0.85	0.52	1.89	3.26	4.63	6.00	7.37
Ir	-4.97	-3.60	-2.23	-0.85	0.52	1.89	3.26	4.63	6.00
Pt	-5.64	-4.27	-2.90	-1.53	-0.16	1.21	2.58	3.95	5.32
Au	-3.28	-1.91	-0.54	0.83	2.20	3.57	4.94	6.31	7.68
Sn	-5.37	-4.00	-2.63	-1.26	0.11	1.48	2.85	4.22	5.59
Sb	-4.30	-2.93	-1.56	-0.19	1.18	2.55	3.92	5.29	6.66
Bi	-3.87	-2.50	-1.13	0.24	1.61	2.98	4.35	5.72	7.09
$\mu_N(n)(T = 1100°C)$ / eV	-5.32	-5.66	-6.00	-6.35	-6.69	-7.03	-7.38	-7.72	-8.06

d

n	1.0	0.5	0.0	-0.5	-1.0	-1.5	-2.0	-2.5	-3.0	-3.5	-4.0
$PorN_4C_A$	5.22	4.85	4.48	4.12	3.75	3.38	3.01	2.64	2.28	1.91	1.54
Cr	1.64	1.28	0.91	0.54	0.17	-0.20	-0.56	-0.93	-1.30	-1.67	-2.04
Mn	1.87	1.50	1.13	0.76	0.40	0.03	-0.34	-0.71	-1.08	-1.44	-1.81
Fe	2.33	1.97	1.60	1.23	0.86	0.49	0.13	-0.24	-0.61	-0.98	-1.34
Co	2.22	1.85	1.48	1.11	0.75	0.38	0.01	-0.36	-0.73	-1.09	-1.46
Ni	2.04	1.67	1.30	0.93	0.57	0.20	-0.17	-0.54	-0.91	-1.27	-1.64
Cu	3.20	2.83	2.46	2.09	1.73	1.36	0.99	0.62	0.25	-0.11	-0.48
Zn	2.12	1.75	1.39	1.02	0.65	0.28	-0.09	-0.45	-0.82	-1.19	-1.56
Mo	4.20	3.83	3.46	3.09	2.73	2.36	1.99	1.62	1.25	0.89	0.52
Ru	3.65	3.29	2.92	2.55	2.18	1.81	1.45	1.08	0.71	0.34	-0.03
Rh	2.85	2.49	2.12	1.75	1.38	1.02	0.65	0.28	-0.09	-0.46	-0.82
Pd	2.73	2.37	2.00	1.63	1.26	0.90	0.53	0.16	-0.21	-0.58	-0.94
Ag	4.84	4.47	4.10	3.74	3.37	3.00	2.63	2.27	1.90	1.53	1.16
W	4.87	4.50	4.13	3.76	3.39	3.03	2.66	2.29	1.92	1.56	1.19
Re	5.05	4.68	4.31	3.95	3.58	3.21	2.84	2.47	2.11	1.74	1.37
Os	4.48	4.11	3.74	3.37	3.01	2.64	2.27	1.90	1.53	1.17	0.80
Ir	3.10	2.73	2.36	2.00	1.63	1.26	0.89	0.52	0.16	-0.21	-0.58
Pt	2.43	2.06	1.69	1.32	0.95	0.59	0.22	-0.15	-0.52	-0.89	-1.25
Au	4.78	4.42	4.05	3.68	3.31	2.95	2.58	2.21	1.84	1.47	1.11
Sn	2.70	2.33	1.96	1.59	1.23	0.86	0.49	0.12	-0.25	-0.61	-0.98
Sb	3.77	3.40	3.03	2.66	2.30	1.93	1.56	1.19	0.82	0.46	0.09
Bi	4.20	3.83	3.46	3.09	2.72	2.36	1.99	1.62	1.25	0.88	0.52
$\mu_N(T = 25°C)$ / eV	-7.34	-7.24	-7.15	-7.06	-6.97	-6.88	-6.78	-6.69	-6.60	-6.51	-6.42

Figure B.2: ΔG_f (in eV) as a function of $\mu_N(n)$: (a) MN_4C_{10} at T = 1100 °C, (b) MN_4C_{10} at T = 25 °C, (c) MN_4C_A at T = 1100 °C, (d) MN_4C_A at T = 25 °C. At n = 0, $\mu_N(n = 0)$ is that of the N_2 molecule at 1 bar and at considered temperature in each subplot (T = 1100 °C for (a) and (c); T = 25 °C for (b) and (d)). Lower formation energy (brighter colour background) indicates more thermodynamically favourable to form.

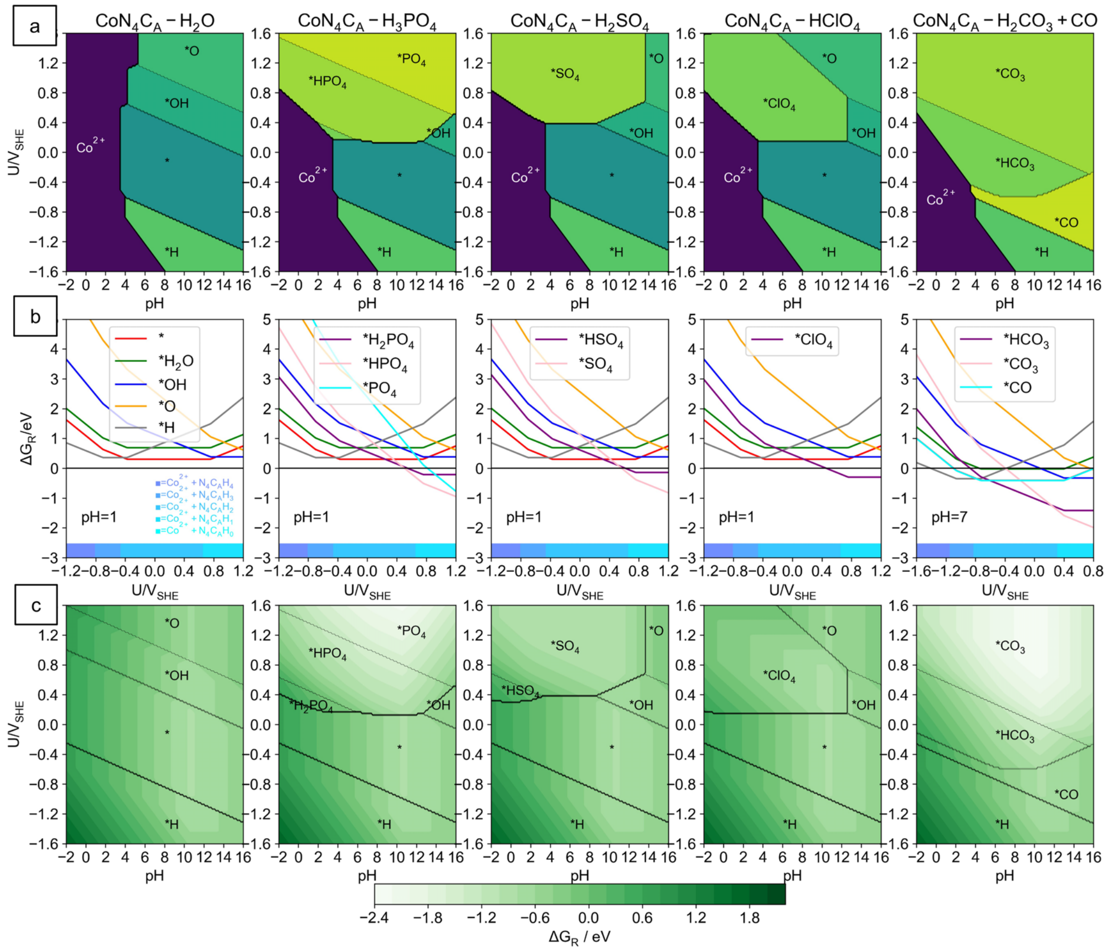

Figure B.3: (a) Stability diagrams for the CoN_4C_A site in 0.1 M solutions. (b) ΔG_R for the sites at specific pH, and (c) Stability diagrams for the CoN_4C_A site showing the most stable surface, and the background color corresponds to the value of ΔG_R

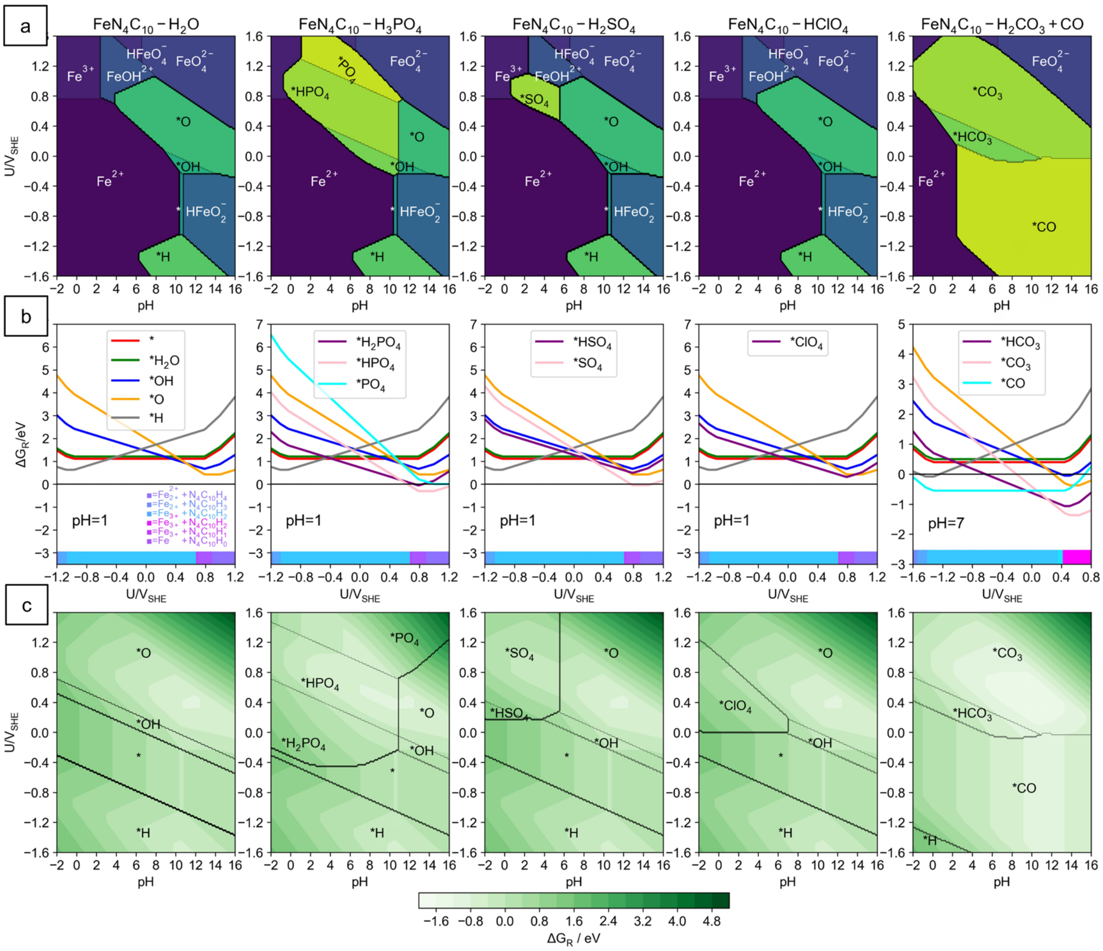

Figure B.4: (a) Stability diagrams for the FeN_4C_{10} site in 0.1 M solutions. (b) ΔG_R for the sites at specific pH, and (c) Stability diagrams for the FeN_4C_{10} site showing the most stable surface, and the background color corresponds to the value of ΔG_R

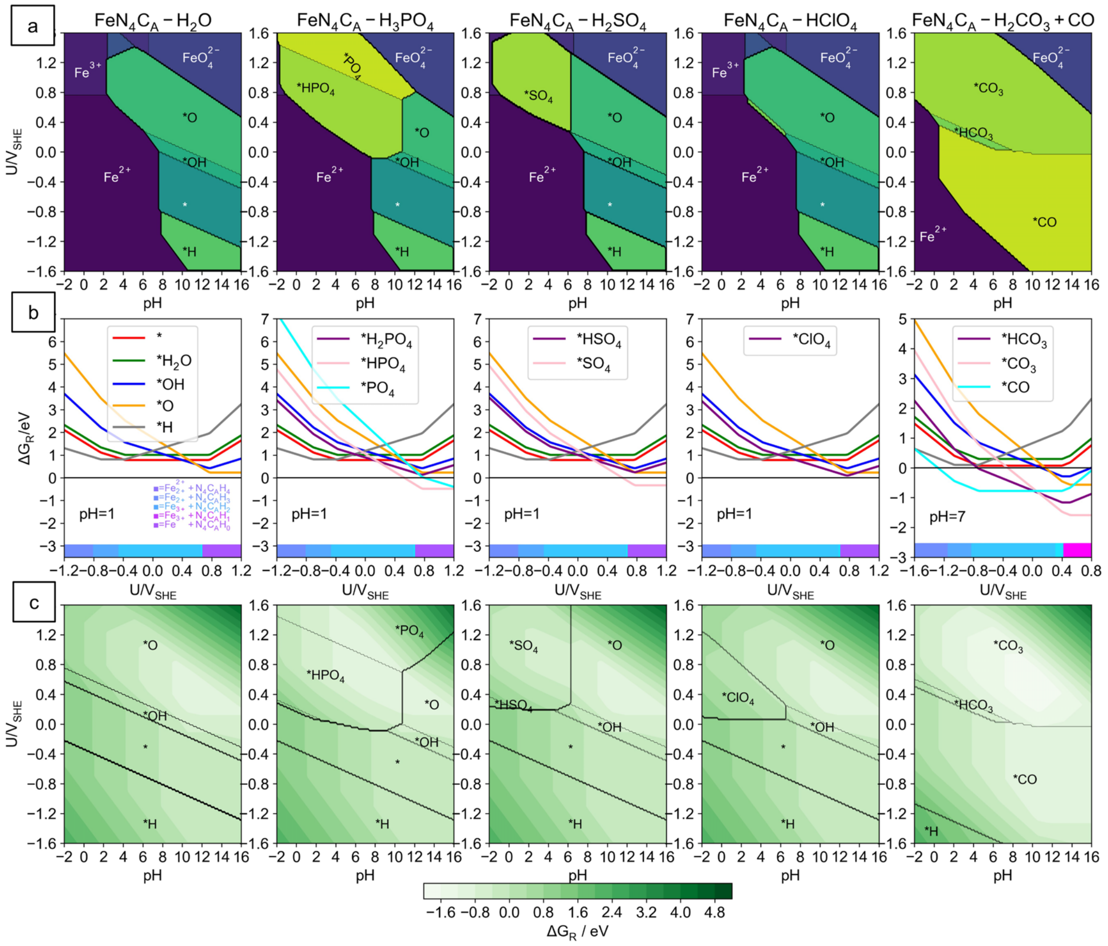

Figure B.5: (a) Stability diagrams for the FeN_4C_A site in 0.1 M solutions. (b) ΔG_R for the sites at specific pH, and (c) Stability diagrams for the FeN_4C_A site showing the most stable surface, and the background color corresponds to the value of ΔG_R

(a) MN_4C_{10}: ΔG_{max}(pH = 1, U = 0.8 V_{SHE}) / eV

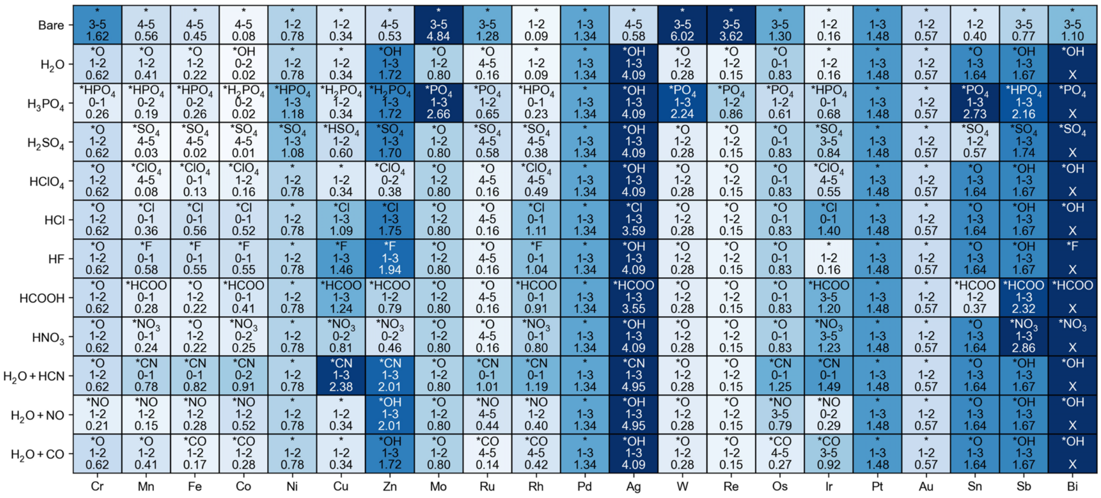

	Cr	Mn	Fe	Co	Ni	Cu	Zn	Mo	Ru	Rh	Pd	Ag	W	Re	Os	Ir	Pt	Au	Sn	Sb	Bi
Bare	* 3-5 1.62	* 4-5 0.56	* 4-5 0.45	* 4-5 0.08	* 1-2 0.78	* 1-2 0.34	* 4-5 0.53	* 3-5 4.84	* 3-5 1.28	* 1-2 0.09	* 1-3 1.34	* 4-5 0.58	* 3-5 6.02	* 3-5 3.62	* 3-5 1.30	* 1-2 0.16	* 1-3 1.48	* 1-2 0.57	* 1-2 0.40	* 3-5 0.77	* 3-5 1.10
H_2O	*O 1-2 0.62	*O 1-2 0.41	*O 1-2 0.22	*OH 0-2 0.02	* 1-2 0.78	* 1-2 0.34	*OH 1-3 1.72	*O 1-2 0.80	*O 4-5 0.16	* 1-2 0.09	* 1-3 1.34	*OH 1-3 4.09	*O 1-2 0.28	*O 1-2 0.15	*O 0-1 0.83	* 1-2 0.16	* 1-3 1.48	* 1-2 0.57	*O 1-3 1.64	*OH 1-3 1.67	*OH X
H_3PO_4	*HPO$_4$ 0-1 0.26	*HPO$_4$ 0-2 0.19	*HPO$_4$ 0-2 0.26	*H$_2$PO$_4$ 0-2 0.02	*HPO$_4$ 1-3 1.18	*H$_2$PO$_4$ 1-2 0.34	*H$_2$PO$_4$ 1-3 1.72	*PO$_4$ 1-3 2.66	*PO$_4$ 1-2 0.65	*HPO$_4$ 0-1 0.23	* 1-3 1.34	*OH 1-3 4.09	*PO$_4$ 1-3 2.24	*PO$_4$ 1-2 0.86	*PO$_4$ 1-2 0.61	*HPO$_4$ 0-1 0.68	* 1-3 1.48	* 1-2 0.57	*PO$_4$ 1-3 2.73	*HPO$_4$ 1-3 2.16	*PO$_4$ X
H_2SO_4	*O 1-2 0.62	*SO$_4$ 4-5 0.03	*SO$_4$ 4-5 0.02	*SO$_4$ 4-5 0.01	*SO$_4$ 1-3 1.08	*HSO$_4$ 1-2 0.60	*SO$_4$ 1-3 1.70	*O 1-2 0.80	*SO$_4$ 4-5 0.58	*SO$_4$ 4-5 0.38	* 1-3 1.34	*OH 1-3 4.09	*O 1-2 0.28	*O 1-2 0.15	*O 0-1 0.83	*SO$_4$ 3-5 0.84	* 1-3 1.48	* 1-2 0.57	*SO$_4$ 1-2 0.57	*SO$_4$ 1-3 1.74	*SO$_4$ X
$HClO_4$	*O 1-2 0.62	*ClO$_4$ 4-5 0.08	*ClO$_4$ 0-1 0.13	*ClO$_4$ 1-2 0.16	* 1-2 0.78	* 1-2 0.34	*ClO$_4$ 0-2 0.38	*O 1-2 0.80	*O 4-5 0.16	*ClO$_4$ 4-5 0.49	* 1-3 1.34	*OH 1-3 4.09	*O 1-2 0.28	*O 1-2 0.15	*O 0-1 0.83	*ClO$_4$ 4-5 0.55	* 1-3 1.48	* 1-2 0.57	*O 1-3 1.64	*OH 1-3 1.67	*OH X
HCl	*O 1-2 0.62	*Cl 0-1 0.36	*Cl 0-1 0.56	*Cl 0-1 0.52	* 1-2 0.78	*Cl 1-3 1.09	*Cl 1-3 1.75	*O 1-2 0.80	*O 4-5 0.16	*Cl 0-1 1.11	* 1-3 1.34	*Cl 1-3 3.59	*O 1-2 0.28	*O 1-2 0.15	*O 0-1 0.83	*Cl 0-1 1.40	* 1-3 1.48	* 1-2 0.57	*O 1-3 1.64	*OH 1-3 1.67	*OH X
HF	*O 1-2 0.62	*F 0-1 0.58	*F 0-1 0.55	*F 0-1 0.55	* 1-2 0.78	*F 1-3 1.46	*F 1-3 1.94	*O 1-2 0.80	*O 4-5 0.16	*F 0-1 1.04	* 1-3 1.34	*OH 1-3 4.09	*O 1-2 0.28	*O 1-2 0.15	*O 0-1 0.83	* 1-2 0.16	* 1-3 1.48	* 1-2 0.57	*O 1-3 1.64	*OH 1-3 1.67	*F X
HCOOH	*O 1-2 0.62	*HCOO 0-1 0.28	*O 1-2 0.22	*HCOO 0-1 0.41	* 1-2 0.78	*HCOO 1-3 1.24	*HCOO 1-2 0.79	*O 1-2 0.80	*O 4-5 0.16	*HCOO 0-1 0.91	* 1-3 1.34	*HCOO 1-3 3.55	*O 1-2 0.28	*O 1-2 0.15	*O 0-1 0.83	*HCOO 3-5 1.20	* 1-3 1.48	* 1-2 0.57	*HCOO 1-2 0.37	*HCOO 1-3 2.32	*HCOO X
HNO_3	*O 1-2 0.62	*NO$_3$ 0-1 0.24	*O 1-2 0.22	*NO$_3$ 0-2 0.25	* 1-2 0.78	*NO$_3$ 0-2 0.81	*NO$_3$ 0-2 0.46	*O 1-2 0.80	*O 4-5 0.16	*NO$_3$ 0-1 0.80	* 1-3 1.34	*OH 1-3 4.09	*O 1-2 0.28	*O 1-2 0.15	*O 0-1 0.83	*NO$_3$ 3-5 1.23	* 1-3 1.48	* 1-2 0.57	*O 1-3 1.64	*NO$_3$ 1-3 2.86	*NO$_3$ X
H_2O + HCN	*O 1-2 0.62	*CN 0-1 0.78	*CN 0-1 0.82	*CN 0-2 0.91	* 1-2 0.78	*CN 1-3 2.38	*CN 1-3 2.01	*O 1-2 0.80	*CN 0-1 1.01	*CN 0-1 1.19	* 1-3 1.34	*CN 1-3 4.95	*O 1-2 0.28	*O 1-2 0.15	*CN 0-1 1.25	*CN 0-1 1.49	* 1-3 1.48	* 1-2 0.57	*O 1-3 1.64	*OH 1-3 1.67	*OH X
H_2O + NO	*NO 1-2 0.21	*NO 1-2 0.15	*NO 1-2 0.28	*NO 1-2 0.52	* 1-2 0.78	* 1-2 0.34	*OH 1-3 2.01	*O 1-2 0.80	*NO 4-5 0.44	*NO 1-2 0.40	* 1-3 1.34	*OH 1-3 4.95	*O 1-2 0.28	*O 1-2 0.15	*NO 3-5 0.79	*NO 0-2 0.29	* 1-3 1.48	* 1-2 0.57	*O 1-3 1.64	*OH 1-3 1.67	*OH X
H_2O + CO	*O 1-2 0.62	*O 1-2 0.41	*CO 1-2 0.17	*CO 1-2 0.28	* 1-2 0.78	* 1-2 0.34	*OH 1-3 1.72	*O 1-2 0.80	*CO 4-5 0.14	*CO 4-5 0.42	* 1-3 1.34	*OH 1-3 4.09	*O 1-2 0.28	*O 1-2 0.15	*CO 4-5 0.27	*CO 3-5 0.92	* 1-3 1.48	* 1-2 0.57	*O 1-3 1.64	*OH 1-3 1.67	*OH X

(b) MN_4C_A: ΔG_{max}(pH = 1, U = 0.8 V_{SHE}) / eV

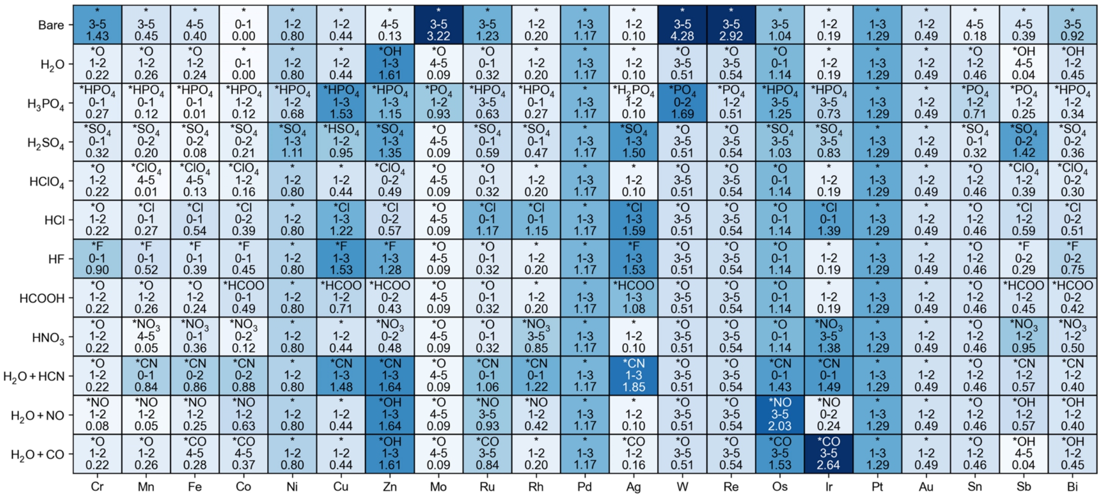

	Cr	Mn	Fe	Co	Ni	Cu	Zn	Mo	Ru	Rh	Pd	Ag	W	Re	Os	Ir	Pt	Au	Sn	Sb	Bi
Bare	* 3-5 1.43	* 3-5 0.45	* 4-5 0.40	* 0-1 0.00	* 1-2 0.80	* 1-2 0.44	* 4-5 0.13	* 3-5 3.22	* 3-5 1.23	* 1-2 0.20	* 1-3 1.17	* 1-2 0.10	* 3-5 4.28	* 3-5 2.92	* 3-5 1.04	* 1-2 0.19	* 1-3 1.29	* 1-2 0.49	* 4-5 0.18	* 4-5 0.39	* 3-5 0.92
H_2O	*O 1-2 0.22	*O 1-2 0.26	*O 1-2 0.24	* 0-1 0.00	* 1-2 0.80	* 1-2 0.44	*OH 1-3 1.61	*O 4-5 0.09	*O 0-1 0.32	* 1-2 0.20	* 1-3 1.17	* 1-2 0.10	*O 3-5 0.51	*O 3-5 0.54	*O 0-1 1.14	* 1-2 0.19	* 1-3 1.29	* 1-2 0.49	*O 1-2 0.46	*OH 4-5 0.04	*OH 1-2 0.45
H_3PO_4	*HPO$_4$ 0-1 0.27	*HPO$_4$ 0-1 0.12	*HPO$_4$ 0-1 0.01	*HPO$_4$ 1-2 0.12	*HPO$_4$ 1-2 0.68	*HPO$_4$ 1-3 1.53	*HPO$_4$ 1-3 1.15	*PO$_4$ 1-2 0.93	*HPO$_4$ 3-5 0.63	*HPO$_4$ 0-1 0.27	* 1-3 1.17	*H$_2$PO$_4$ 1-2 0.10	*PO$_4$ 0-2 1.69	*PO$_4$ 1-2 0.51	*HPO$_4$ 3-5 1.25	*HPO$_4$ 3-5 0.73	* 1-3 1.29	* 1-2 0.49	*PO$_4$ 1-2 0.71	*PO$_4$ 1-2 0.25	*HPO$_4$ 1-2 0.34
H_2SO_4	*SO$_4$ 0-1 0.32	*SO$_4$ 0-2 0.20	*SO$_4$ 0-2 0.08	*SO$_4$ 0-2 0.21	*SO$_4$ 1-3 1.11	*HSO$_4$ 1-2 0.95	*SO$_4$ 1-3 1.35	*O 4-5 0.09	*SO$_4$ 0-1 0.59	*SO$_4$ 0-1 0.47	* 1-3 1.17	*SO$_4$ 1-3 1.50	*O 3-5 0.51	*O 3-5 0.54	*SO$_4$ 3-5 1.03	*SO$_4$ 3-5 0.83	* 1-3 1.29	* 1-2 0.49	*SO$_4$ 0-1 0.32	*SO$_4$ 0-2 1.42	*SO$_4$ 0-2 0.36
$HClO_4$	*O 1-2 0.22	*ClO$_4$ 4-5 0.01	*ClO$_4$ 4-5 0.13	*ClO$_4$ 1-2 0.16	* 1-2 0.80	* 1-2 0.44	*ClO$_4$ 0-2 0.49	*O 4-5 0.09	*O 0-1 0.32	* 1-2 0.20	* 1-3 1.17	* 1-2 0.10	*O 3-5 0.51	*O 3-5 0.54	*O 0-1 1.14	* 1-2 0.19	* 1-3 1.29	* 1-2 0.49	*O 1-2 0.46	*ClO$_4$ 1-2 0.39	*ClO$_4$ 0-2 0.30
HCl	*O 1-2 0.22	*Cl 0-1 0.27	*Cl 0-1 0.54	*Cl 0-2 0.39	* 1-2 0.80	*Cl 1-3 1.22	*Cl 0-2 0.57	*O 4-5 0.09	*Cl 0-1 1.17	*Cl 0-1 1.15	* 1-3 1.17	*Cl 1-3 1.59	*O 3-5 0.51	*O 3-5 0.54	*O 0-1 1.14	*Cl 0-1 1.39	* 1-3 1.29	* 1-2 0.49	*O 1-2 0.46	*Cl 1-2 0.59	*Cl 0-2 0.51
HF	*F 0-1 0.90	*F 0-1 0.52	*F 0-1 0.39	*F 0-1 0.45	* 1-2 0.80	*F 1-3 1.53	*F 1-3 1.28	*O 4-5 0.09	*O 0-1 0.32	* 1-2 0.20	* 1-3 1.17	*F 1-3 1.53	*O 3-5 0.51	*O 3-5 0.54	*O 0-1 1.14	* 1-2 0.19	* 1-3 1.29	* 1-2 0.49	*O 1-2 0.46	*F 0-2 0.29	*F 0-2 0.75
HCOOH	*O 1-2 0.22	*O 1-2 0.26	*O 1-2 0.24	*HCOO 0-1 0.49	* 1-2 0.80	*HCOO 1-2 0.71	*HCOO 0-2 0.43	*O 4-5 0.09	*O 0-1 0.32	* 1-2 0.20	* 1-3 1.17	*HCOO 1-3 1.08	*O 3-5 0.51	*O 3-5 0.54	*O 0-1 1.14	* 1-2 0.19	* 1-3 1.29	* 1-2 0.49	*O 1-2 0.46	*HCOO 1-2 0.45	*HCOO 0-2 0.42
HNO_3	*O 1-2 0.22	*NO$_3$ 4-5 0.05	*NO$_3$ 0-1 0.36	*NO$_3$ 0-2 0.12	* 1-2 0.80	* 1-2 0.44	*NO$_3$ 0-2 0.48	*O 4-5 0.09	*O 0-1 0.32	*NO$_3$ 3-5 0.85	* 1-3 1.17	* 1-2 0.10	*O 3-5 0.51	*O 3-5 0.54	*O 0-1 1.14	*NO$_3$ 3-5 1.38	* 1-3 1.29	* 1-2 0.49	*O 1-2 0.46	*NO$_3$ 1-2 0.95	*NO$_3$ 1-2 0.50
H_2O + HCN	*O 1-2 0.22	*CN 0-1 0.84	*CN 0-2 0.86	*CN 0-2 0.88	* 1-2 0.80	*CN 1-3 1.48	*CN 1-3 1.64	*O 4-5 0.09	*CN 0-1 1.06	*CN 0-1 1.22	* 1-3 1.17	*CN 1-3 1.85	*O 3-5 0.51	*O 3-5 0.54	*CN 0-1 1.43	*CN 0-1 1.49	* 1-3 1.29	* 1-2 0.49	*O 1-2 0.46	*CN 1-2 0.57	*CN 1-2 0.40
H_2O + NO	*NO 1-2 0.08	*NO 1-2 0.05	*NO 1-2 0.25	*NO 1-2 0.63	* 1-2 0.80	* 1-2 0.44	*OH 1-3 1.64	*O 4-5 0.09	*NO 3-5 0.93	*NO 1-2 0.42	* 1-3 1.17	* 1-2 0.10	*O 3-5 0.51	*O 3-5 0.54	*NO 3-5 2.03	*NO 0-2 0.24	* 1-3 1.29	* 1-2 0.49	*O 1-2 0.46	*OH 1-2 0.57	*OH 1-2 0.40
H_2O + CO	*O 1-2 0.22	*O 1-2 0.26	*CO 4-5 0.28	*CO 4-5 0.37	* 1-2 0.80	* 1-2 0.44	*OH 1-3 1.61	*O 4-5 0.09	*CO 3-5 0.84	* 1-2 0.20	* 1-3 1.17	*CO 1-2 0.16	*O 3-5 0.51	*O 3-5 0.54	*CO 3-5 1.53	*CO 3-5 2.64	* 1-3 1.29	* 1-2 0.49	*O 1-2 0.46	*OH 4-5 0.04	*OH 1-2 0.45

Figure B.6: ΔG_{max} along the ORR pathway at U = 0.80 V_{SHE} and pH = 1 in 0.1 M electrolytes on: (a) MN_4C_{10}, (b) MN_4C_A. In each cell, the inserted text in the 1^{st} row shows the adsorbate ligand on the back side of the metal atom participating in the reaction. The adsorbate ligand is considered to be the most stable adsorbate on the MN_4 site at pH = 1, U = 0.80 V_{SHE}. The inserted text in the 2^{nd} row shows the determining reaction states for ΔG_{max} at pH = 1, U = 0.80 V_{SHE}. The number 0-6 is referred to the reaction state in Figure 4.5. The inserted number in the 3^{rd} row is ΔG_{max} value at pH = 1, U = 0.80 V_{SHE} in eV. The insert **X** in the 3^{rd} row means the second adsorbate moves away from the metal site with a distance > 3.0 Å; thus, the metal site is considered to be inactive for the ORR. The background color corresponds to the ΔG_{max} value. The brighter the background color, the lower the thermodynamic barrier.

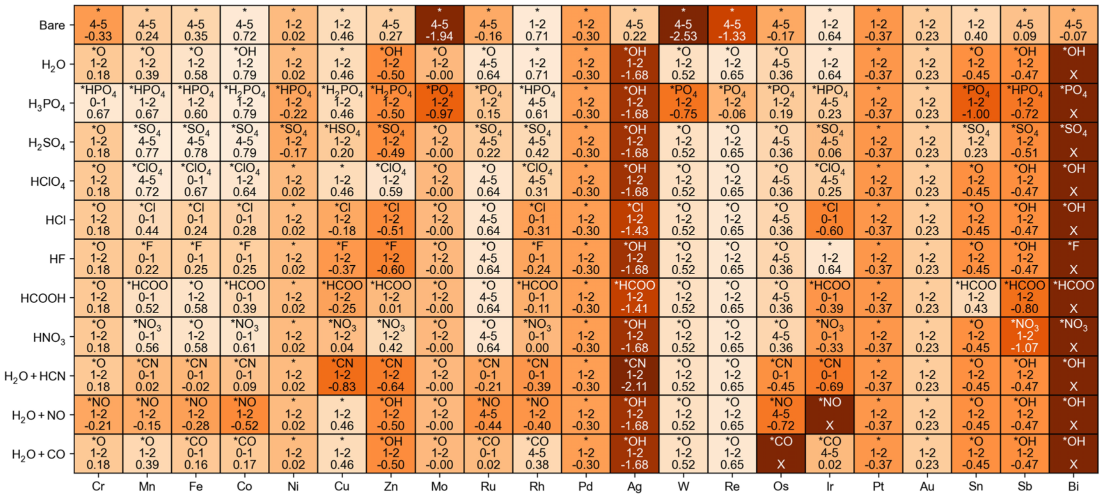

(a) MN_4C_{10}: $U_L(pH = 1) / V_{SHE}$

	Cr	Mn	Fe	Co	Ni	Cu	Zn	Mo	Ru	Rh	Pd	Ag	W	Re	Os	Ir	Pt	Au	Sn	Sb	Bi
Bare	* 4-5 -0.33	* 4-5 0.24	* 4-5 0.35	* 4-5 0.72	* 1-2 0.02	* 1-2 0.46	* 4-5 0.27	* 4-5 -1.94	* 4-5 -0.16	* 1-2 0.71	* 1-2 -0.30	* 4-5 0.22	* 4-5 -2.53	* 4-5 -1.33	* 4-5 -0.17	* 1-2 0.64	* 1-2 -0.37	* 1-2 0.23	* 1-2 0.40	* 4-5 0.09	* 4-5 -0.07
H_2O	*O 1-2 0.18	*O 1-2 0.39	*O 1-2 0.58	*OH 1-2 0.79	* 1-2 0.02	* 1-2 0.46	*OH 1-2 -0.50	*O 1-2 -0.00	*O 4-5 0.64	* 1-2 0.71	* 1-2 -0.30	*OH 1-2 -1.68	*O 1-2 0.52	*O 1-2 0.65	*O 4-5 0.36	* 1-2 0.64	* 1-2 -0.37	* 1-2 0.23	*O 1-2 -0.45	*OH 1-2 -0.47	*OH X
H_3PO_4	*HPO_4 0-1 0.67	*HPO_4 1-2 0.67	*HPO_4 1-2 0.60	*H_2PO_4 1-2 0.79	*HPO_4 1-2 -0.22	*H_2PO_4 1-2 0.46	*H_2PO_4 1-2 -0.50	*PO_4 1-2 -0.97	*PO_4 1-2 0.15	*HPO_4 4-5 0.61	* 1-2 -0.30	*OH 1-2 -1.68	*PO_4 1-2 -0.75	*PO_4 1-2 -0.06	*PO_4 1-2 0.19	*HPO_4 4-5 0.23	* 1-2 -0.37	* 1-2 0.23	*PO_4 1-2 -1.00	*HPO_4 1-2 -0.72	*PO_4 X
H_2SO_4	*O 1-2 0.18	*SO_4 4-5 0.77	*SO_4 4-5 0.78	*SO_4 4-5 0.79	*SO_4 1-2 -0.17	*HSO_4 1-2 0.20	*SO_4 1-2 -0.49	*O 1-2 -0.00	*SO_4 4-5 0.22	*SO_4 4-5 0.42	* 1-2 -0.30	*OH 1-2 -1.68	*O 1-2 0.52	*O 1-2 0.65	*O 4-5 0.36	*SO_4 4-5 0.06	* 1-2 -0.37	* 1-2 0.23	*SO_4 1-2 0.23	*SO_4 1-2 -0.51	*SO_4 X
$HClO_4$	*O 1-2 0.18	*ClO_4 4-5 0.72	*ClO_4 0-1 0.67	*ClO_4 1-2 0.64	* 1-2 0.02	* 1-2 0.46	*ClO_4 1-2 0.59	*O 1-2 -0.00	*O 4-5 0.64	*ClO_4 4-5 0.31	* 1-2 -0.30	*OH 1-2 -1.68	*O 1-2 0.52	*O 1-2 0.65	*O 4-5 0.36	*ClO_4 4-5 0.25	* 1-2 -0.37	* 1-2 0.23	*O 1-2 -0.45	*OH 1-2 -0.47	*OH X
HCl	*O 1-2 0.18	*Cl 0-1 0.44	*Cl 0-1 0.24	*Cl 0-1 0.28	* 1-2 0.02	*Cl 1-2 -0.18	*Cl 1-2 -0.51	*O 1-2 -0.00	*O 4-5 0.64	*Cl 0-1 -0.31	* 1-2 -0.30	*Cl 1-2 -1.43	*O 1-2 0.52	*O 1-2 0.65	*O 4-5 0.36	*Cl 0-1 -0.60	* 1-2 -0.37	* 1-2 0.23	*O 1-2 -0.45	*OH 1-2 -0.47	*OH X
HF	*O 1-2 0.18	*F 0-1 0.22	*F 0-1 0.25	*F 0-1 0.25	* 1-2 0.02	*F 1-2 -0.37	*F 1-2 -0.60	*O 1-2 -0.00	*O 4-5 0.64	*F 0-1 -0.24	* 1-2 -0.30	*OH 1-2 -1.68	*O 1-2 0.52	*O 1-2 0.65	*O 4-5 0.36	* 1-2 0.64	* 1-2 -0.37	* 1-2 0.23	*O 1-2 -0.45	*OH 1-2 -0.47	*F X
HCOOH	*O 1-2 0.18	*HCOO 0-1 0.52	*O 1-2 0.58	*HCOO 0-1 0.39	* 1-2 0.02	*HCOO 1-2 -0.25	*HCOO 1-2 0.01	*O 1-2 -0.00	*O 4-5 0.64	*HCOO 0-1 -0.11	* 1-2 -0.30	*HCOO 1-2 -1.41	*O 1-2 0.52	*O 1-2 0.65	*O 4-5 0.36	*HCOO 0-1 -0.39	* 1-2 -0.37	* 1-2 0.23	*HCOO 1-2 0.43	*HCOO 1-2 -0.80	*HCOO X
HNO_3	*O 1-2 0.18	*NO_3 0-1 0.56	*O 1-2 0.58	*NO_3 0-1 0.61	* 1-2 0.02	*NO_3 1-2 0.04	*NO_3 1-2 0.42	*O 1-2 -0.00	*O 4-5 0.64	*NO_3 0-1 0.00	* 1-2 -0.30	*OH 1-2 -1.68	*O 1-2 0.52	*O 1-2 0.65	*O 4-5 0.36	*NO_3 0-1 -0.33	* 1-2 -0.37	* 1-2 0.23	*O 1-2 -0.45	*NO_3 1-2 -1.07	*NO_3 X
$H_2O + HCN$	*O 1-2 0.18	*CN 0-1 0.02	*CN 0-1 -0.02	*CN 0-1 0.09	* 1-2 0.02	*CN 1-2 -0.83	*CN 1-2 -0.64	*O 1-2 -0.00	*CN 0-1 -0.21	*CN 0-1 -0.39	* 1-2 -0.30	*CN 1-2 -2.11	*O 1-2 0.52	*O 1-2 0.65	*CN 0-1 -0.45	*CN 0-1 -0.69	* 1-2 -0.37	* 1-2 0.23	*O 1-2 -0.45	*OH 1-2 -0.47	*OH X
$H_2O + NO$	*NO 1-2 -0.21	*NO 1-2 -0.15	*NO 1-2 -0.28	*NO 1-2 -0.52	* 1-2 0.02	* 1-2 0.46	*OH 1-2 -0.50	*O 1-2 -0.00	*NO 4-5 -0.44	*NO 1-2 -0.40	* 1-2 -0.30	*OH 1-2 -1.68	*O 1-2 0.52	*O 1-2 0.65	*NO 4-5 -0.72	*NO X	* 1-2 -0.37	* 1-2 0.23	*O 1-2 -0.45	*OH 1-2 -0.47	*OH X
$H_2O + CO$	*O 1-2 0.18	*O 1-2 0.39	*CO 0-1 0.16	*CO 0-1 0.17	* 1-2 0.02	* 1-2 0.46	*OH 1-2 -0.50	*O 1-2 -0.00	*CO 0-1 0.02	*CO 4-5 0.38	* 1-2 -0.30	*OH 1-2 -1.68	*O 1-2 0.52	*O 1-2 0.65	*CO X	*CO 4-5 0.02	* 1-2 -0.37	* 1-2 0.23	*O 1-2 -0.45	*OH 1-2 -0.47	*OH X

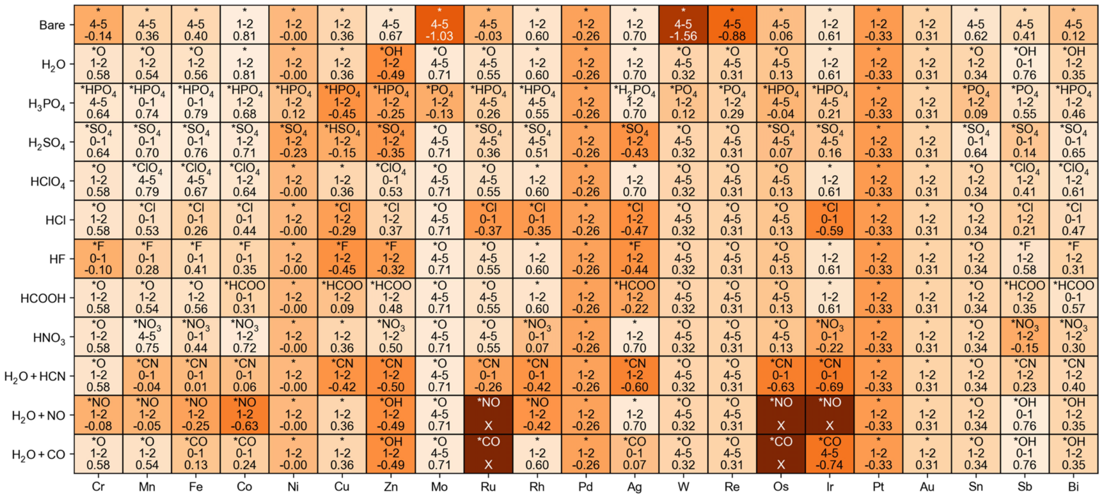

(b) MN_4C_A: $U_L(pH = 1) / V_{SHE}$

	Cr	Mn	Fe	Co	Ni	Cu	Zn	Mo	Ru	Rh	Pd	Ag	W	Re	Os	Ir	Pt	Au	Sn	Sb	Bi
Bare	* 4-5 -0.14	* 4-5 0.36	* 4-5 0.40	* 1-2 0.81	* 1-2 -0.00	* 1-2 0.36	* 4-5 0.67	* 4-5 -1.03	* 4-5 -0.03	* 1-2 0.60	* 1-2 -0.26	* 1-2 0.70	* 4-5 -1.56	* 4-5 -0.88	* 4-5 0.06	* 1-2 0.61	* 1-2 -0.33	* 1-2 0.31	* 4-5 0.62	* 4-5 0.41	* 4-5 0.12
H_2O	*O 1-2 0.58	*O 1-2 0.54	*O 1-2 0.56	* 1-2 0.81	* 1-2 -0.00	* 1-2 0.36	*OH 1-2 -0.49	*O 4-5 0.71	*O 4-5 0.55	* 1-2 0.60	* 1-2 -0.26	* 1-2 0.70	*O 4-5 0.32	*O 4-5 0.31	*O 4-5 0.13	* 1-2 0.61	* 1-2 -0.33	* 1-2 0.31	*O 1-2 0.34	*OH 0-1 0.76	*OH 1-2 0.35
H_3PO_4	*HPO_4 4-5 0.64	*HPO_4 0-1 0.74	*HPO_4 0-1 0.79	*HPO_4 1-2 0.68	*HPO_4 1-2 0.12	*HPO_4 1-2 -0.45	*HPO_4 1-2 -0.25	*PO_4 1-2 -0.13	*HPO_4 4-5 0.26	*HPO_4 4-5 0.55	* 1-2 -0.26	*H_2PO_4 1-2 0.70	*PO_4 1-2 0.12	*PO_4 1-2 0.29	*HPO_4 4-5 -0.04	*HPO_4 4-5 0.21	* 1-2 -0.33	* 1-2 0.31	*PO_4 1-2 0.09	*PO_4 1-2 0.55	*HPO_4 1-2 0.46
H_2SO_4	*SO_4 0-1 0.64	*SO_4 0-1 0.70	*SO_4 0-1 0.76	*SO_4 1-2 0.71	*SO_4 1-2 -0.23	*HSO_4 1-2 -0.15	*SO_4 1-2 -0.35	*O 4-5 0.71	*SO_4 4-5 0.36	*SO_4 4-5 0.51	* 1-2 -0.26	*SO_4 1-2 -0.43	*O 4-5 0.32	*O 4-5 0.31	*SO_4 4-5 0.07	*SO_4 4-5 0.16	* 1-2 -0.33	* 1-2 0.31	*SO_4 0-1 0.64	*SO_4 0-1 0.14	*SO_4 0-1 0.65
$HClO_4$	*O 1-2 0.58	*ClO_4 4-5 0.79	*ClO_4 4-5 0.67	*ClO_4 1-2 0.64	* 1-2 -0.00	* 1-2 0.36	*ClO_4 0-1 0.53	*O 4-5 0.71	*O 4-5 0.55	* 1-2 0.60	* 1-2 -0.26	* 1-2 0.70	*O 4-5 0.32	*O 4-5 0.31	*O 4-5 0.13	* 1-2 0.61	* 1-2 -0.33	* 1-2 0.31	*O 1-2 0.34	*ClO_4 1-2 0.41	*ClO_4 1-2 0.61
HCl	*O 1-2 0.58	*Cl 0-1 0.53	*Cl 0-1 0.26	*Cl 0-1 0.44	* 1-2 -0.00	*Cl 1-2 -0.29	*Cl 1-2 0.37	*O 4-5 0.71	*Cl 0-1 -0.37	*Cl 0-1 -0.35	* 1-2 -0.26	*Cl 1-2 -0.47	*O 4-5 0.32	*O 4-5 0.31	*O 4-5 0.13	*Cl 0-1 -0.59	* 1-2 -0.33	* 1-2 0.31	*O 1-2 0.34	*Cl 1-2 0.21	*Cl 0-1 0.47
HF	*F 0-1 -0.10	*F 0-1 0.28	*F 0-1 0.41	*F 0-1 0.35	* 1-2 -0.00	*F 1-2 -0.45	*F 1-2 -0.32	*O 4-5 0.71	*O 4-5 0.55	* 1-2 0.60	* 1-2 -0.26	*F 1-2 -0.44	*O 4-5 0.32	*O 4-5 0.31	*O 4-5 0.13	* 1-2 0.61	* 1-2 -0.33	* 1-2 0.31	*O 1-2 0.34	*F 1-2 0.58	*F 1-2 0.31
HCOOH	*O 1-2 0.58	*O 1-2 0.54	*O 1-2 0.56	*HCOO 0-1 0.31	* 1-2 -0.00	*HCOO 1-2 0.09	*HCOO 1-2 0.48	*O 4-5 0.71	*O 4-5 0.55	* 1-2 0.60	* 1-2 -0.26	*HCOO 1-2 -0.22	*O 4-5 0.32	*O 4-5 0.31	*O 4-5 0.13	* 1-2 0.61	* 1-2 -0.33	* 1-2 0.31	*O 1-2 0.34	*HCOO 1-2 0.35	*HCOO 0-1 0.57
HNO_3	*O 1-2 0.58	*NO_3 4-5 0.75	*NO_3 0-1 0.44	*NO_3 1-2 0.72	* 1-2 -0.00	* 1-2 0.36	*NO_3 1-2 0.50	*O 4-5 0.71	*O 4-5 0.55	*NO_3 0-1 0.07	* 1-2 -0.26	* 1-2 0.70	*O 4-5 0.32	*O 4-5 0.31	*O 4-5 0.13	*NO_3 0-1 -0.22	* 1-2 -0.33	* 1-2 0.31	*O 1-2 0.34	*NO_3 1-2 -0.15	*NO_3 1-2 0.30
$H_2O + HCN$	*O 1-2 0.58	*CN 0-1 -0.04	*CN 0-1 0.01	*CN 0-1 0.06	* 1-2 -0.00	*CN 1-2 -0.42	*CN 1-2 -0.50	*O 4-5 0.71	*CN 0-1 -0.26	*CN 0-1 -0.42	* 1-2 -0.26	*CN 1-2 -0.60	*O 4-5 0.32	*O 4-5 0.31	*CN 0-1 -0.63	*CN 0-1 -0.69	* 1-2 -0.33	* 1-2 0.31	*O 1-2 0.34	*CN 1-2 0.23	*CN 1-2 0.40
$H_2O + NO$	*NO 1-2 -0.08	*NO 1-2 -0.05	*NO 1-2 -0.25	*NO 1-2 -0.63	* 1-2 -0.00	* 1-2 0.36	*OH 1-2 -0.49	*O 4-5 0.71	*NO X	*NO 1-2 -0.42	* 1-2 -0.26	* 1-2 0.70	*O 4-5 0.32	*O 4-5 0.31	*NO X	*NO X	* 1-2 -0.33	* 1-2 0.31	*O 1-2 0.34	*OH 0-1 0.76	*OH 1-2 0.35
$H_2O + CO$	*O 1-2 0.58	*O 1-2 0.54	*CO 0-1 0.13	*CO 0-1 0.24	* 1-2 -0.00	* 1-2 0.36	*OH 1-2 -0.49	*O 4-5 0.71	*CO X	* 1-2 0.60	* 1-2 -0.26	*CO 0-1 0.07	*O 4-5 0.32	*O 4-5 0.31	*CO X	*CO 4-5 -0.74	* 1-2 -0.33	* 1-2 0.31	*O 1-2 0.34	*OH 0-1 0.76	*OH 1-2 0.35

Figure B.7: U_L of the ORR in 0.1 M electrolyte at pH = 1 on: (a) MN_4C_{10}, (b) MN_4C_A. In each cell, the inserted text in the 1st row shows the adsorbate ligand on the back side of the metal atom participating in the reaction. The adsorbate ligand is considered to be the most stable adsorbate on the MN_4 site at pH = 1, U = 0.80 V_{SHE}. The inserted text in the 2nd row shows the potential determining states for U_L at pH = 1. The number 0-6 is referred to the reaction state in Figure 4.5. The inserted number in the 3rd row is U_L value at pH = 1 in V_{SHE}. The insert **X** in the 3rd row means the second adsorbate moves away from the metal site with a distance > 3.0 Å; thus, the metal site is considered to be inactive for the ORR or the neutral gas molecules are thermodynamically favorable on both sides of the metal atom. The background color corresponds to the value of U_L. The brighter the background color, the higher the limiting potential.

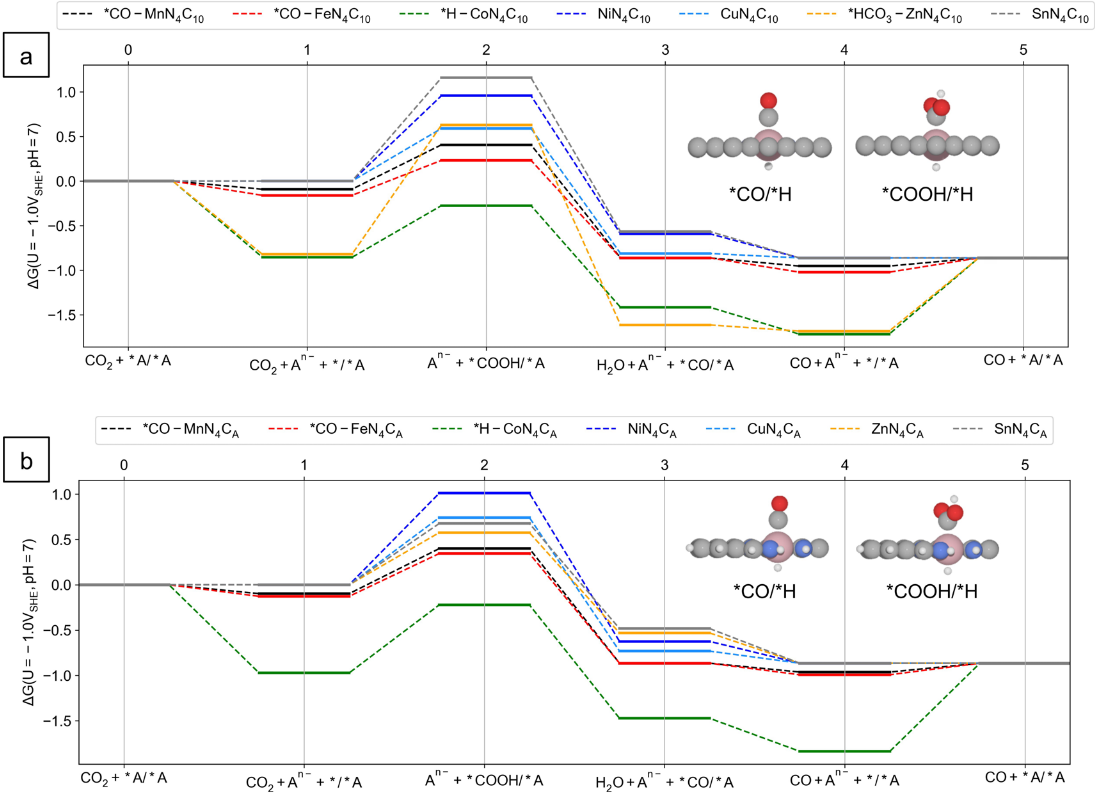

Figure B.8: Free energy diagram of the CO_2RR to CO at pH = 7, U = -1.0 V_{SHE} on: (a) MN_4C_{10}, (b) MN_4C_A structure in 0.1 M H_2CO_3 + CO solution, where M = Mn, Fe, Co, Ni, Zn, Cu and Sn. The ligand on the back side of the metal atom is the most adsorbate at pH = 7, U = -1.0 V_{SHE}. The insets show the side view of the *COOH/*H and *CO/*H on the CoN_4 site. (C = gray, N = blue, H = white, O = red, Co = pink)

(a) MN_4C_{10}: ΔG_{max}(pH = 7, -0.80 V_{SHE}) / eV

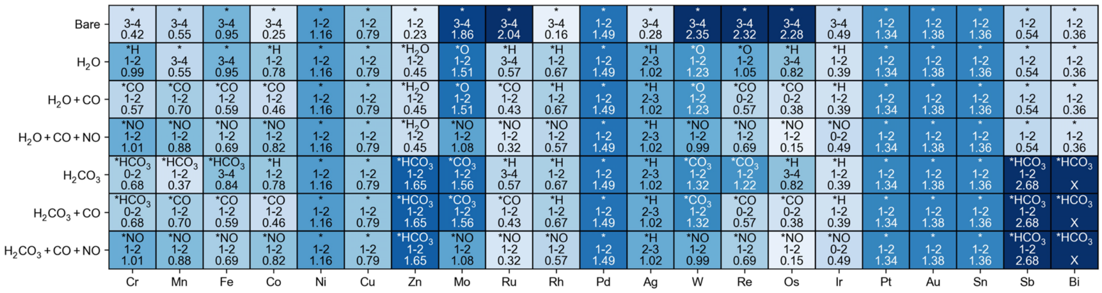

	Cr	Mn	Fe	Co	Ni	Cu	Zn	Mo	Ru	Rh	Pd	Ag	W	Re	Os	Ir	Pt	Au	Sn	Sb	Bi
Bare	* 3-4 0.42	* 3-4 0.55	* 3-4 0.95	* 3-4 0.25	* 1-2 1.16	* 1-2 0.79	* 1-2 0.23	* 3-4 1.86	* 3-4 2.04	* 3-4 0.16	* 1-2 1.49	* 3-4 0.28	* 3-4 2.35	* 3-4 2.32	* 3-4 2.28	* 3-4 0.49	* 1-2 1.34	* 1-2 1.38	* 1-2 1.36	* 1-2 0.54	* 1-2 0.36
H_2O	*H 1-2 0.99	* 3-4 0.55	* 3-4 0.95	*H 1-2 0.78	* 1-2 1.16	* 1-2 0.79	*H_2O 1-2 0.45	*O 1-2 1.51	*H 3-4 0.57	*H 1-2 0.67	* 1-2 1.49	*H 2-3 1.02	*O 1-2 1.23	*O 1-2 1.05	*H 3-4 0.82	*H 1-2 0.39	* 1-2 1.34	* 1-2 1.38	* 1-2 1.36	* 1-2 0.54	* 1-2 0.36
H_2O+CO	*CO 1-2 0.57	*CO 1-2 0.70	*CO 1-2 0.59	*CO 1-2 0.46	* 1-2 1.16	* 1-2 0.79	*H_2O 1-2 0.45	*O 1-2 1.51	*CO 1-2 0.43	*H 1-2 0.67	* 1-2 1.49	*H 2-3 1.02	*O 1-2 1.23	*CO 0-2 0.57	*CO 0-2 0.38	*H 1-2 0.39	* 1-2 1.34	* 1-2 1.38	* 1-2 1.36	* 1-2 0.54	* 1-2 0.36
$H_2O+CO+NO$	*NO 1-2 1.01	*NO 1-2 0.88	*NO 1-2 0.69	*NO 1-2 0.82	* 1-2 1.16	* 1-2 0.79	*H_2O 1-2 0.45	*NO 1-2 1.08	*NO 1-2 0.32	*NO 1-2 0.57	* 1-2 1.49	*H 2-3 1.02	*NO 1-2 0.99	*NO 1-2 0.69	*NO 1-2 0.15	*NO 0-2 0.49	* 1-2 1.34	* 1-2 1.38	* 1-2 1.36	* 1-2 0.54	* 1-2 0.36
H_2CO_3	*HCO_3 0-2 0.68	*HCO_3 1-2 0.37	*HCO_3 3-4 0.84	*H 1-2 0.78	* 1-2 1.16	* 1-2 0.79	*HCO_3 1-2 1.65	*CO_3 1-2 1.56	*H 3-4 0.57	*H 1-2 0.67	* 1-2 1.49	*H 2-3 1.02	*CO_3 1-2 1.32	*CO_3 1-2 1.22	*H 3-4 0.82	*H 1-2 0.39	* 1-2 1.34	* 1-2 1.38	* 1-2 1.36	*HCO_3 1-2 2.68	*HCO_3 X
H_2CO_3+CO	*HCO_3 0-2 0.68	*CO 1-2 0.70	*CO 1-2 0.59	*CO 1-2 0.46	* 1-2 1.16	* 1-2 0.79	*HCO_3 1-2 1.65	*CO_3 1-2 1.56	*CO 1-2 0.43	*H 1-2 0.67	* 1-2 1.49	*H 2-3 1.02	*CO_3 1-2 1.32	*CO 0-2 0.57	*CO 0-2 0.38	*H 1-2 0.39	* 1-2 1.34	* 1-2 1.38	* 1-2 1.36	*HCO_3 1-2 2.68	*HCO_3 X
$H_2CO_3+CO+NO$	*NO 1-2 1.01	*NO 1-2 0.88	*NO 1-2 0.69	*NO 1-2 0.82	* 1-2 1.16	* 1-2 0.79	*HCO_3 1-2 1.65	*NO 1-2 1.08	*NO 1-2 0.32	*NO 1-2 0.57	* 1-2 1.49	*H 2-3 1.02	*NO 1-2 0.99	*NO 1-2 0.69	*NO 1-2 0.15	*NO 0-2 0.49	* 1-2 1.34	* 1-2 1.38	* 1-2 1.36	*HCO_3 1-2 2.68	*HCO_3 X

(b) MN_4C_A: ΔG_{max}(pH = 7, -0.80 V_{SHE}) / eV

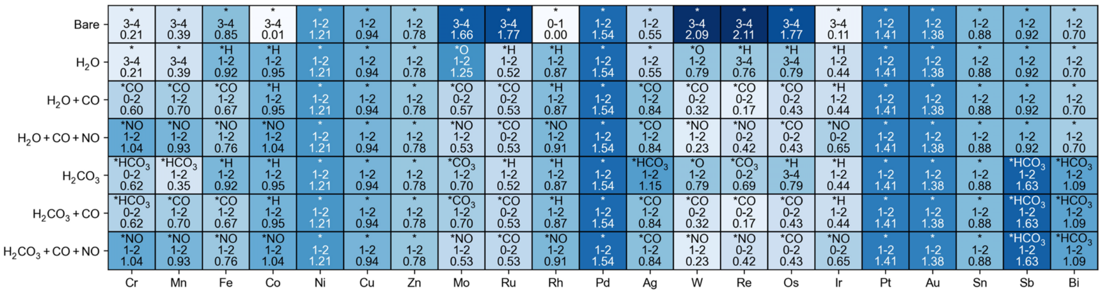

	Cr	Mn	Fe	Co	Ni	Cu	Zn	Mo	Ru	Rh	Pd	Ag	W	Re	Os	Ir	Pt	Au	Sn	Sb	Bi
Bare	* 3-4 0.21	* 3-4 0.39	* 3-4 0.85	* 3-4 0.01	* 1-2 1.21	* 1-2 0.94	* 1-2 0.78	* 3-4 1.66	* 3-4 1.77	* 0-1 0.00	* 1-2 1.54	* 1-2 0.55	* 3-4 2.09	* 3-4 2.11	* 3-4 1.77	* 3-4 0.11	* 1-2 1.41	* 1-2 1.38	* 1-2 0.88	* 1-2 0.92	* 1-2 0.70
H_2O	* 3-4 0.21	* 3-4 0.39	*H 1-2 0.92	*H 1-2 0.95	* 1-2 1.21	* 1-2 0.94	* 1-2 0.78	*O 1-2 1.25	*H 1-2 0.52	*H 1-2 0.87	* 1-2 1.54	* 1-2 0.55	*O 1-2 0.79	*H 3-4 0.76	*H 3-4 0.79	*H 1-2 0.44	* 1-2 1.41	* 1-2 1.38	* 1-2 0.88	* 1-2 0.92	* 1-2 0.70
H_2O+CO	*CO 0-2 0.60	*CO 1-2 0.70	*CO 1-2 0.67	*H 1-2 0.95	* 1-2 1.21	* 1-2 0.94	* 1-2 0.78	*CO 0-2 0.57	*CO 0-2 0.53	*H 1-2 0.87	* 1-2 1.54	*CO 1-2 0.84	*CO 0-2 0.32	*CO 0-2 0.17	*CO 0-2 0.43	*H 1-2 0.44	* 1-2 1.41	* 1-2 1.38	* 1-2 0.88	* 1-2 0.92	* 1-2 0.70
$H_2O+CO+NO$	*NO 1-2 1.04	*NO 1-2 0.93	*NO 1-2 0.76	*NO 1-2 1.04	* 1-2 1.21	* 1-2 0.94	* 1-2 0.78	*NO 1-2 0.53	*CO 0-2 0.53	*NO 1-2 0.91	* 1-2 1.54	*CO 1-2 0.84	*NO 1-2 0.23	*NO 0-2 0.42	*CO 0-2 0.43	*NO 0-2 0.65	* 1-2 1.41	* 1-2 1.38	* 1-2 0.88	* 1-2 0.92	* 1-2 0.70
H_2CO_3	*HCO_3 0-2 0.62	*HCO_3 1-2 0.35	*H 1-2 0.92	*H 1-2 0.95	* 1-2 1.21	* 1-2 0.94	* 1-2 0.78	*CO_3 1-2 0.70	*H 1-2 0.52	*H 1-2 0.87	* 1-2 1.54	*HCO_3 1-2 1.15	*O 1-2 0.79	*CO_3 0-2 0.69	*H 3-4 0.79	*H 1-2 0.44	* 1-2 1.41	* 1-2 1.38	* 1-2 0.88	*HCO_3 1-2 1.63	*HCO_3 1-2 1.09
H_2CO_3+CO	*HCO_3 0-2 0.62	*CO 1-2 0.70	*CO 1-2 0.67	*H 1-2 0.95	* 1-2 1.21	* 1-2 0.94	* 1-2 0.78	*CO_3 1-2 0.70	*CO 0-2 0.53	*H 1-2 0.87	* 1-2 1.54	*CO 1-2 0.84	*CO 0-2 0.32	*CO 0-2 0.17	*CO 0-2 0.43	*H 1-2 0.44	* 1-2 1.41	* 1-2 1.38	* 1-2 0.88	*HCO_3 1-2 1.63	*HCO_3 1-2 1.09
$H_2CO_3+CO+NO$	*NO 1-2 1.04	*NO 1-2 0.93	*NO 1-2 0.76	*NO 1-2 1.04	* 1-2 1.21	* 1-2 0.94	* 1-2 0.78	*NO 1-2 0.53	*CO 0-2 0.53	*NO 1-2 0.91	* 1-2 1.54	*CO 1-2 0.84	*NO 1-2 0.23	*NO 0-2 0.42	*CO 0-2 0.43	*NO 0-2 0.65	* 1-2 1.41	* 1-2 1.38	* 1-2 0.88	*HCO_3 1-2 1.63	*HCO_3 1-2 1.09

Figure B.9: ΔG_{max} along the CO_2RR to CO pathway at U = -0.80 V_{SHE} and pH = 7 in 0.1 M electrolytes on: (a) MN_4C_{10}, (b) MN_4C_A. In each cell, the inserted text in the 1st row shows the adsorbate ligand on the back side of the metal atom participating in the reaction. The adsorbate ligand is considered to be the most stable adsorbate on the MN_4 site at pH = 7, U = -0.80 V_{SHE}. For other considered electrolytes, except 0.1 M H_2CO_3, their catalytic activity under the CO_2RR-related condition is the same as in H_2O. The inserted text in the 2nd row shows the determining reaction states for ΔG_{max} at pH = 7, U = -0.80 V_{SHE}. The number 0-5 is referred to the reaction state in Figure 4.7. The inserted number in the 3rd row is ΔG_{max} value at pH = 7, U = -0.80 V_{SHE} in eV. The insert **X** in the 3rd row means the second adsorbate moves away from the metal site with a distance > 3.0 Angstrom. Thus, the metal site is considered to be inactive for the CO_2RR. The background color corresponds to the ΔG_{max} value. The brighter the background color, the lower the thermodynamic barrier of the limiting step.

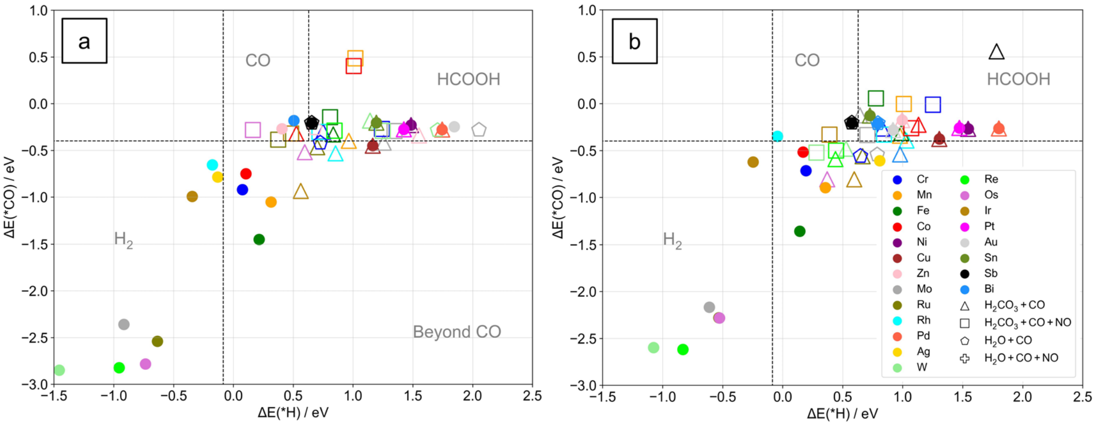

Figure B.10: Classification plot for possible CO_2RR products based on ΔE(*H) and ΔE(*CO) of considered M/N/C catalyst with $\Delta G_R < 1.0$ eV in different solution: (a) MN_4C_{10} (b) MN_4C_A. The binding energies of the bare metal sites are included and are marked with filled color dots.

Appendix C

Supplementary material III

Table C.1: ΔG_1 (in eV) for the nucleophilic addition at the C2 position in the mPBI(-1) molecule with the different number of an explicit water molecules at different hydrogen-bonding sites (see Figure C.1) at T = 88 °C

	#water molecule	H-bonding site	ΔG_1
(1)	0	-	1.38
(2)	1	N1	1.27
(3)	1	N1*	1.42
(4)	1	N3*	1.34
(5)	2	N1, N3*	1.26
(6)	2	N1, N1*	1.26
(7)	2	N1*, N3*	1.31
(8)	3	N1, N1*, N3*	1.24

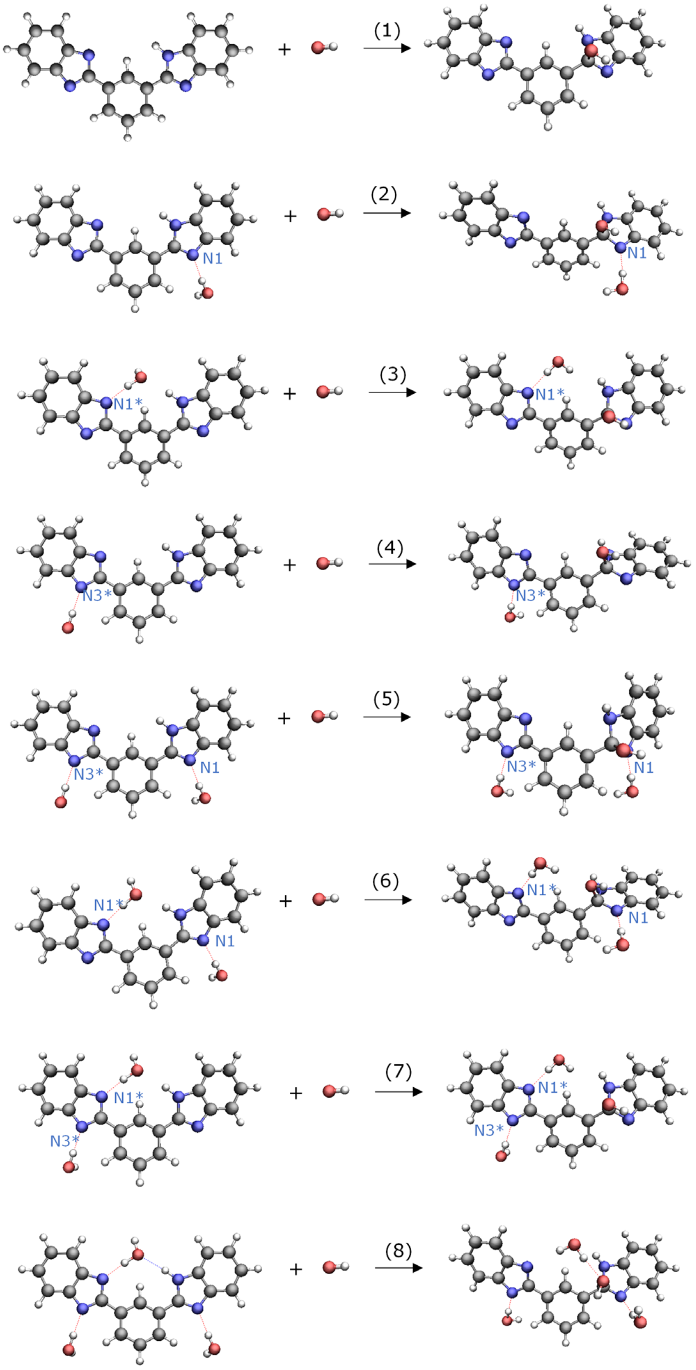

Figure C.1: Different explicit water molecules at different hydrogen-bonding sites around the mPBI(-1) molecule for calculation of ΔG_1 at the C2 position. (H = white, C = grey, N = blue, O = red)

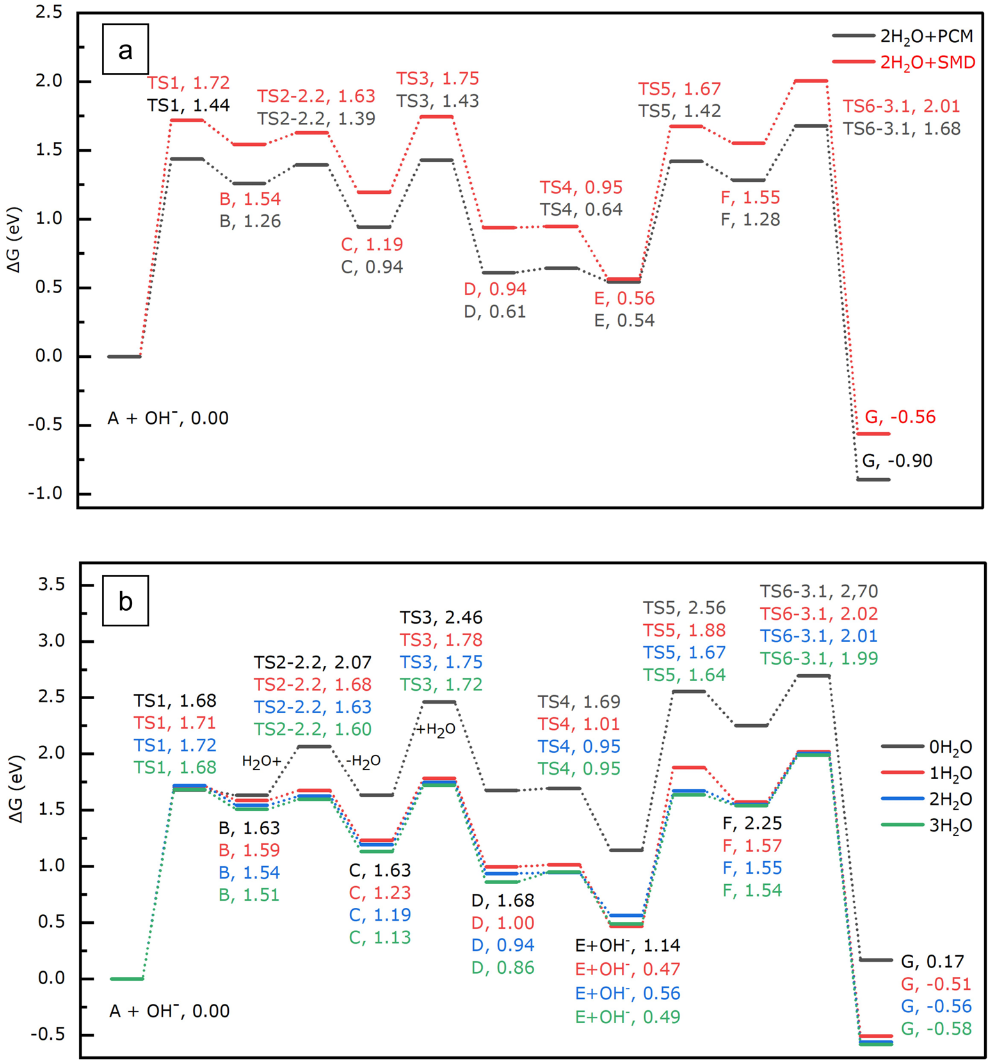

Figure C.2: Reaction energy profile for the degradation path of mPBI(-1) at T = 88 °C: (a) with two explicit water molecules using PCM and SMD implicit solvation model. (b) with different explicit water molecules using SMD implicit solvation model. The reference zero energy state for energies reported is A+OH^-, and the relative energies are in eV.

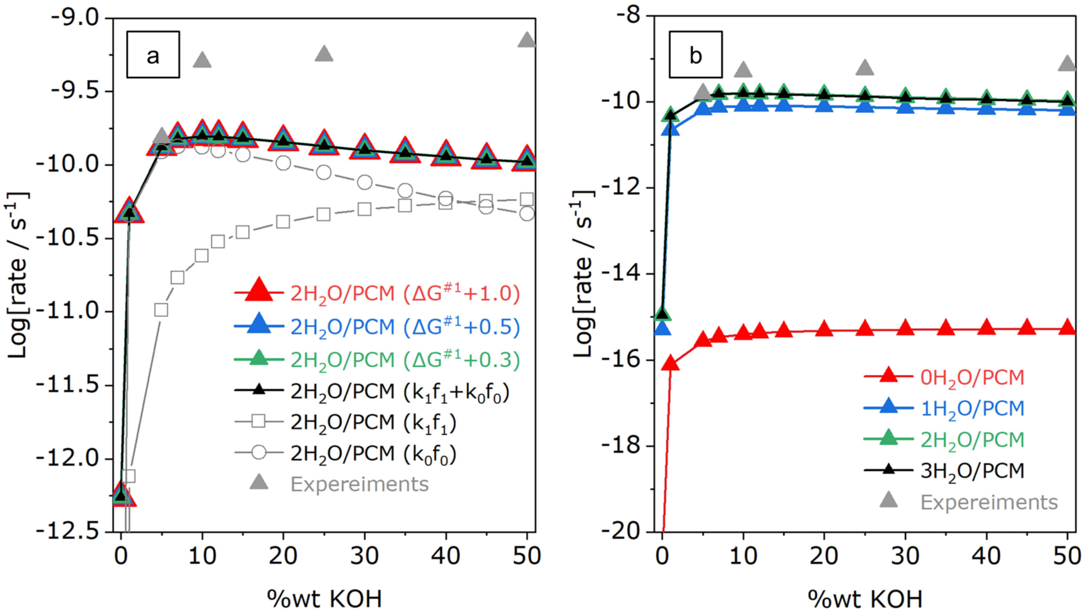

Figure C.3: (a) Calculated degradation rate including the contribution from the mPBI(-2) with the effective barrier 0.3, 0.5, and 1.0 eV higher than that of the mPBI(-1) with two explicit water molecules ($\Delta G^{\sharp 1}$). (b) Calculated degradation rate ($k_1 f_1 + k_0 f_0$) at different KOH concentrations and T = 88 °C.

Appendix D

Included Publications

D.1 Paper I

Acid-Stable and Active M-N-C Catalysts for the Oxygen Reduction Reaction: The Role of Local Structure
Tipaporn Patniboon and Heine Anton Hansen
ACS Catalysis, 2021, 11, 21, 1310213118

ACS Catalysis

pubs.acs.org/acscatalysis

Research Article

Acid-Stable and Active M−N−C Catalysts for the Oxygen Reduction Reaction: The Role of Local Structure

Tipaporn Patniboon and Heine Anton Hansen*

Cite This: *ACS Catal.* 2021, 11, 13102−13118

Read Online

ACCESS | Metrics & More | Article Recommendations | Supporting Information

ABSTRACT: Metal−nitrogen carbon (M−N−C) catalysts, atomically dispersed and nitrogen-coordinated MN_x sites embedded in carbon planes, have exhibited encouraging oxygen reduction reaction activity in an acidic environment. However, one challenge for these materials is their insufficient long-term stability in the acid environment. Herein, we systematically investigate both catalytic activity toward ORR and stability under acid conditions using density functional theory (DFT). Various local atomic structures around the MN_x site and different metal atoms (M = Cr, Mn, Fe, Co, Ni, and Ru) are considered in this study to understand the relation between atomic structures, stability, and catalytic activity. The stability of the M−N−C catalyst is considered from the propensity of the metal atom center to dissolve from the carbon host structure. The calculations reveal that the considered MN_x sites are thermodynamically unstable in acid ORR conditions. However, based on the calculated thermodynamic driving force toward the metal dissolution, the MN_4 sites with Fe, Co, Ni, and Ru metal atoms embedded on the graphene plane and at the graphene edge are more stable in the acid ORR condition than the other considered MN_x structures. Combining the stability and catalytic activity descriptor, we propose some acid-stable and active MN_x structures toward ORR. This computational study provides helpful guidance for the rational modification of the carbon matrix hosting MN_x moieties and the appropriate selection of a metal atom for optimizing the activity and stability toward the ORR reaction.

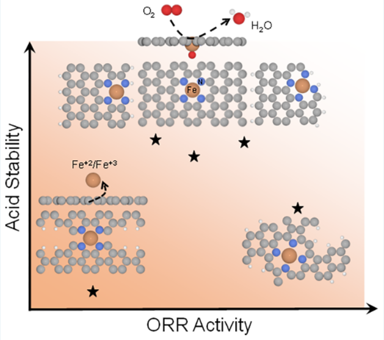

KEYWORDS: *density functional theory, carbon, oxygen reduction reaction, single-atom catalyst, stability, dissolution*

1. INTRODUCTION

The proton exchange membrane fuel cell (PEMFC) is a highly efficient clean energy conversion device that requires a highly active catalyst for the oxygen reduction reaction (ORR) at the cathode. Platinum-based catalysts now reach high activity and durability.[1] However, considering the high cost and lack of platinum-based catalysts, the catalyst-free platinum group remains an alternative catalyst for cost and sustainability reasons.

Among the catalysts free of platinum group metals, metal−nitrogen carbon (M−N−C) catalysts, where atomically dispersed and nitrogen-coordinate MN_x sites are embedded in carbon planes, have gained much attention because of their high initial activity toward the ORR in acid media, especially Fe−N−C catalysts.[2−4] However, the issue facing the Fe−N−C catalyst is an insufficiency of long-term stability. The Fe−N−C catalyst tends to degrade quickly in the acidic PEMFC environment,[5] but the degradation mechanism remains elusive; therefore, further investigations and improvements for the M−N−C catalysts are still needed. However, various degradation mechanisms have been proposed to degrade M−N−C catalysts, such as carbon oxidation by hydroxyl or hydroperoxyl radicals,[6,7] demetalation of metal sites,[8,9] and carbon corrosion.[10]

On top of that, the synthetic approaches that involve pyrolysis of the mixture of metal, nitrogen, and carbon precursor often result in the various local environment for the MN_x site,[11,12] and thus, the ORR catalytic activity and stability of the M−N−C materials is highly dependent on the synthesis path. Different configurations of the MN_x sites have been proposed as an active site for the ORR by experimental and theoretical studies,[13−15] but the specific MN_x sites, which are active and durable under working conditions, should be preferred targets for synthesis. The Fe−N−C catalyst prepared via pyrolysis in flowing NH_3 has been reported to have higher initial ORR activity in acid and alkaline conditions than similarly prepared Fe−N−C pyrolyzed in an inert atmosphere.[12,13] However, the NH_3 pyrolyzed Fe−N−C catalyst results in about 10 times enhanced Fe leaching rate than the inert gas pyrolyzed catalyst in acid.[12,13] It has been reported that the NH_3 pyrolysis promotes high basicity and porosity in the Fe−N−C catalyst surface.[12,13,16] The introduction of

Received: June 30, 2021
Revised: September 2, 2021
Published: October 14, 2021

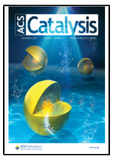

ACS Publications

https://doi.org/10.1021/acscatal.1c02941
ACS Catal. 2021, 11, 13102−13118

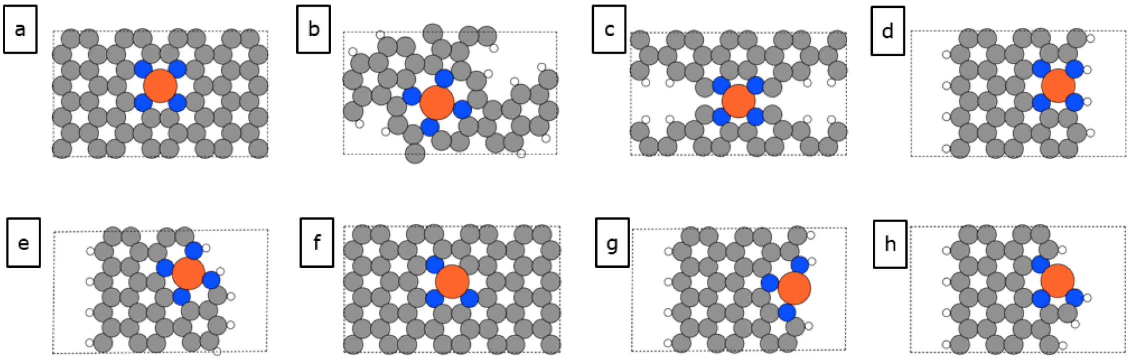

Figure 1. M−N−C model structures: (a) MN_4C_{10}, (b) MN_4C_{12}, (c) MN_4C_8, (d) MN_4C_Z, (e) MN_4C_A, (f) MN_3C_{10}, (g) FeN_3C_Z, (h) FeN_3C_A. Color codes for atom: C-gray, N-blue, H-white, M (= metal atom)-orange.

micropores has been suggested to enhance the catalytic activity for ORR.[17,18] In contrast, the initial ORR performance loss has also been proposed due to the demetalation of the FeN_4 site located in the micropore.[16] In addition, a recent experimental study by Li et al.[19] using operando X-ray absorption spectroscopy has reported that there are two types of FeN_4 sites identified in the Fe−N−C catalyst. These are FeN_4C_{10}, and FeN_4C_{12} sites, surrounded by a different local carbon structure. Both sites initially contribute to the ORR activity of the Fe−N−C in an acidic medium. However, the FeN_4C_{12} site is not durable under operation, rapidly converting into inactive ferric oxide particles as there is a decreasing ORR activity, decreasing numbers of this site, and increasing ferric oxide formation. The FeN_4C_{10} site is stable under the acid condition with no measurable decrease in the numbers of this active site after 50 h of operating at 0.5 V.[19] Therefore, the local atomic structures of the MN_x have been suggested to play a significant role in ORR catalytic activity and demetalation of the active site.[10,17,19,20]

Besides the Fe−N−C catalyst, the Co−N−C catalyst has been the most investigated as a replacement for Fe since the dissolved Fe ions from the Fe−N−C catalysts can further deteriorate the membrane durability by catalyzing the formation of radicals from H_2O_2, which degrade the membrane.[6,21] Thus, metal atom sites which do not promote the formation of H_2O_2 radicals are also needed. A previous study by Xie et al. has reported that the Co−N−C catalyst has inferior catalytic activity toward ORR and lower activity for promoting radicals from H_2O_2 but has significant resistance to demetalation in acid condition.[22] Since various CoN_x sites can be simultaneously formed during the synthesis,[23] specific knowledge of the detailed structures of the active and durable CoN_x site would be valuable. Furthermore, other M−N−C catalysts have also been reported to have structural stability under acid conditions, such as the Ru−N−C system.[24] Therefore, the insightful understanding of how catalytic activity and degradation of the MN_x site related to its electronic structures and local atomic configuration is critical for designing M−N−C catalyst.

Advancements in computing capability have helped to expand predictions from first-principles simulations of materials. While the materials screening for ORR to date have focused on the electrocatalytic activity,[25−27] stability under working conditions is also an essential criterion.[28−31] The demetalation of the metal atom center due to proton attack has been calculated and used to determine the acid stability of the M−N−C catalyst, identifying a specific potential or pH when the dissolution of the metal center is thermodynamically favorable.[32−34] Also, the embedding energy, indicating the bonding strength between the embedded isolated metal atom with N-doped carbon structure against the cohesion energy of the bulk metal, is often calculated and used to represent thermodynamic stability for the M−N−C cattalyts.[27,33,35] Previous work on the thermodynamic dissolution of the FeN_4 structures on two different local carbon structures toward aqueous Fe^{2+} has been studied by Glibin et al.,[36] suggesting acid stability of the FeN_4 site.[36] In contrast, Holby et al. found FeN_4 sites to be stable only when OH is adsorbed on the FeN_4 site, and the absolute thermodynamic stability of FeN_4 sites remains controversial.[37,38]

Various degradation mechanisms of the M−N−C catalyst have been suggested. The carbon oxidation is most probably from H_2O_2-derived radicals during the oxygen reduction, which leads to various oxygen functional groups on the carbon surface that can deactivate the metal site[7] and trigger irreversible leaching of the metal site.[19,39] This might depend on the morphology of the carbon surface.[19,39] However, the carbon surface oxidation is reversible, and the ORR activity can be recovered by electrochemical cycling or chemical treatment.[7,22] Additionally, carbon corrosion can occur and leads to carbon loss surrounding the FeN_x site, eventually resulting in metal site leaching.[10] The demetalation itself has also been proposed to cause fast activity decay of the Fe−N−C catalyst.[16] Thus, the degradation of M−N−C catalysts may have more than one cause. Nonetheless, how the M−N−C structure affects the stability against demetalation can be the first step to understand the M−N−C degradation, and it is a focus in this work. The relation between the structure and demetalation will be addressed before introducing other possible degradation pathways.

The thermodynamic understanding of dissolution in aqueous media can be obtained from the so-called Pourbaix diagrams, which indicates the potential and pH ranges where the different component oxidation state of materials exist.[29,30,40] A recent study by Holby et al. has proposed a dissolution reaction to determine the stability of FeN_4 embedded on a graphene layer as a function of pH and applied potential,[38] indicating the acid instability and likelihood to dissolve of the FeN_4 site. Here, we employ this proposed dissolution to further study the stability of MN_x with various local atomic structures and various metal atoms to understand how local atomic structures and different metal atoms affect the stability of M−N−C catalysts. Furthermore, the acid stability descriptor of the MN_x site under PEMFC conditions is determined by computing the relative stability with respect to the most stable species in the stability diagram, and it is used as a comparative stability descriptor. Thus, the stability descriptor can offer insight into how the M−N−C structure affects stability. The stability descriptor is then used along with the catalytic activity descriptor to identify promising acid-stable and active MN_x sites toward ORR.

2. METHODS

2.1. Computation Details. Spin-polarized density functional theory calculations are performed using the Vienna ab initio simulation package (VASP)[41] and project augmented wave (PAW)[42] pseudopotential. Structures are set up and analyzed using the atomic simulation environment (ASE).[43] The exchange and correlation energy are described using the BEEF-vdW functional to include the effects of dispersive interactions.[44] A plane-wave cutoff of 600 eV is used. The self-consistent electron density loop is converged to 10^{-5} eV, and the structures are relaxed until all forces are below 0.025 eV $Å^{-1}$. The calculations are submitted, managed, and received using the MyQueue[45] workflow tool, a python front-end to the job scheduler.

Eight different M−N−C model structures with different local atomic structure surrounding the metal site are investigated in this study and shown in Figure 1. The MN_4C_{10} structure is an MN_4 site embedded in an intact graphitic layer where the MN_4 site is surrounded by 10 carbon atoms, where M is a single metal atom. The MN_4C_Z and MN_4C_A structure represent the MN_4 site near the zigzag and armchair graphitic edge, respectively. For the active sites hosted in a micropore, we consider a MN_4C_{12} site near the micropore with a porphyrin-like structure and a MN_4C_8 site where the MN_4 moiety is bridging two adjacent armchair edges. The FeN_4C_{12} site has been identified by X-ray absorption spectroscopy and has been proposed as the active site toward the ORR reaction by Zitolo et al.[13] The FeN_4C_8 site has been proposed as the most active site in such Fe−N−C catalyst.[14,15,18,46] Li et al. have reported that the Fe−N−C catalyst initially comprises two distinct FeN_4 sites identified as the FeN_4C_{10} and FeN_4C_{12} strcuture.[19] Also, we further consider two defective sites derived from the MN_4C_Z and MN_4C_A structure, namely, MN_3C_Z and MN_3C_A. These edge-anchored unsaturated MN_3 structures are possible to form under a synthesis environment, as reported by Cheng et al.[47] The unit cell dimensions in the catalyst plane are 16.9 × 9.8 Å on average, with minor variations for the different metal atoms M (where M = Cr, Mn, Fe, Co, Ni, and Ru) and different local atomic structures. The vacuum layer in a perpendicular direction to the catalyst plane is about 15 Å, and a dipole correction is used in the perpendicular direction to the catalyst plane to decouple the electrostatic potentials on the two sides of the catalyst plane. The Brillouin zone is sampled with a (3 × 3 × 1) MonkhorstPack k-point mesh.[48]

Solvent effects on the surface and adsorbates are included using the implicit solvent model implemented in VASPsol with a dielectric constant of 80[49,50] representing water medium. Additional calculations with an explicit solvation effect are performed with one explicit water layer. First, the explicit water layer structure (16 H_2O molecules) and the explicit water layer with ORR intermediate structure (15 H_2O molecules surrounding an intermediate) on the FeN_4C_{10} structure are determined by the minima hopping algorithm implemented in ASE.[51−53] The minima hopping algorithm is performed to find at least about 30 local minima with the convergence criterion of maximum force on each atom less than 0.05 eV $Å^{-1}$. Next, the lowest energy local minima structure and the local minima structure within 0.1 eV of the lowest structure are relaxed further with maximum force on each atom less than 0.025 eV $Å^{-1}$. Then, the water layer structure with the lowest energy is used in the calculations for the FeN_4C_{10} and other Fe−N−C structures.

The change in reaction free energy with an applied potential, U, and pH was calculated using the computational hydrogen electrode (CHE),[1,54] the free energy of the reaction at a potential of U versus the reversible hydrogen electrode (SHE), and pH is given by

$$\Delta G(U,\ \mathrm{pH}) = \Delta G(U=0,\ \mathrm{pH}=0) - neU + nk_BT\mathrm{pH}\ln(10) \tag{1}$$

where n is the number of electrons involved in the reaction, e is the numerical charge of an electron, and k_B is the Boltzmann constant.

$$\Delta G(U=0,\ \mathrm{pH}=0) = \Delta E_{\mathrm{DFT}} + \Delta E_{\mathrm{ZPE}} + \Delta U_{\mathrm{vib}}(T) - T\Delta S_{\mathrm{vib}}(T) \tag{2}$$

where $\Delta G(U = 0,\ \mathrm{pH} = 0)$ is calculated from DFT and includes the change in electronic energy (ΔE_{DFT}), zero-point energy (ΔE_{ZPE}), vibration energy ($\Delta U_{\mathrm{vib}}(T)$), and entropy ($\Delta S_{\mathrm{vib}}(T)$) at T = 298.15K. In the case of adsorbates on the catalyst surface, only the vibration frequencies of adsorbate are considered, and the free energy is calculated following the quantum mechanical harmonic approximation.

The energy of O_2 in the gas phase is poorly described by DFT calculations;[44] thus, it is corrected to reproduce experimental free energy of liquid water formation ($2H_2 + O_2 \rightarrow 2H_2O$; $\Delta G_{H_2O} = -4.92$ eV). Furthermore, according to the Christensen scheme,[55,56] the error in the energy levels of the ORR intermediates specific to the BEEF-vdW functional are corrected as follows

$$\Delta E(\mathrm{O{-}O}) = 0.20\ \mathrm{eV} \tag{3}$$

$$\Delta E(\mathrm{H_2O}) = -0.03\ \mathrm{eV} \tag{4}$$

$$\Delta E(\mathrm{H_2}) = 0.09\ \mathrm{eV} \tag{5}$$

2.2. Stability Calculations. Our current investigation follows previous work on a dissolution reaction for the FeN_4 site on the bilayer graphene-host structure (which is similar to the FeN_4C_{10} structure defined in this study) by Holby et al.[38] During the dissolution, the Fe metal atom can leave the FeN_4 site on the carbon host structure (FeN_4C) and becomes an aqueous Fe ion, $Fe^{x+}{}_{(aq)}$ with a charge x, given the resulting metal-dissolved carbon host cavity with various possible degrees of protonation under the acid environment of the dangling bond, N_4CH_n as a product where n is the number of protons bonded with the carbon host cavity. It has been reported that the FeN_4 site embedded in graphene without ligands or ORR intermediates is unstable in acid conditions, whereas the adsorption of OH on FeN_4 makes the FeN_4 site thermodynamically stable.[38]

In this work, we employ the above dissolution mechanism to further investigate the stability trend of the M−N−C systems

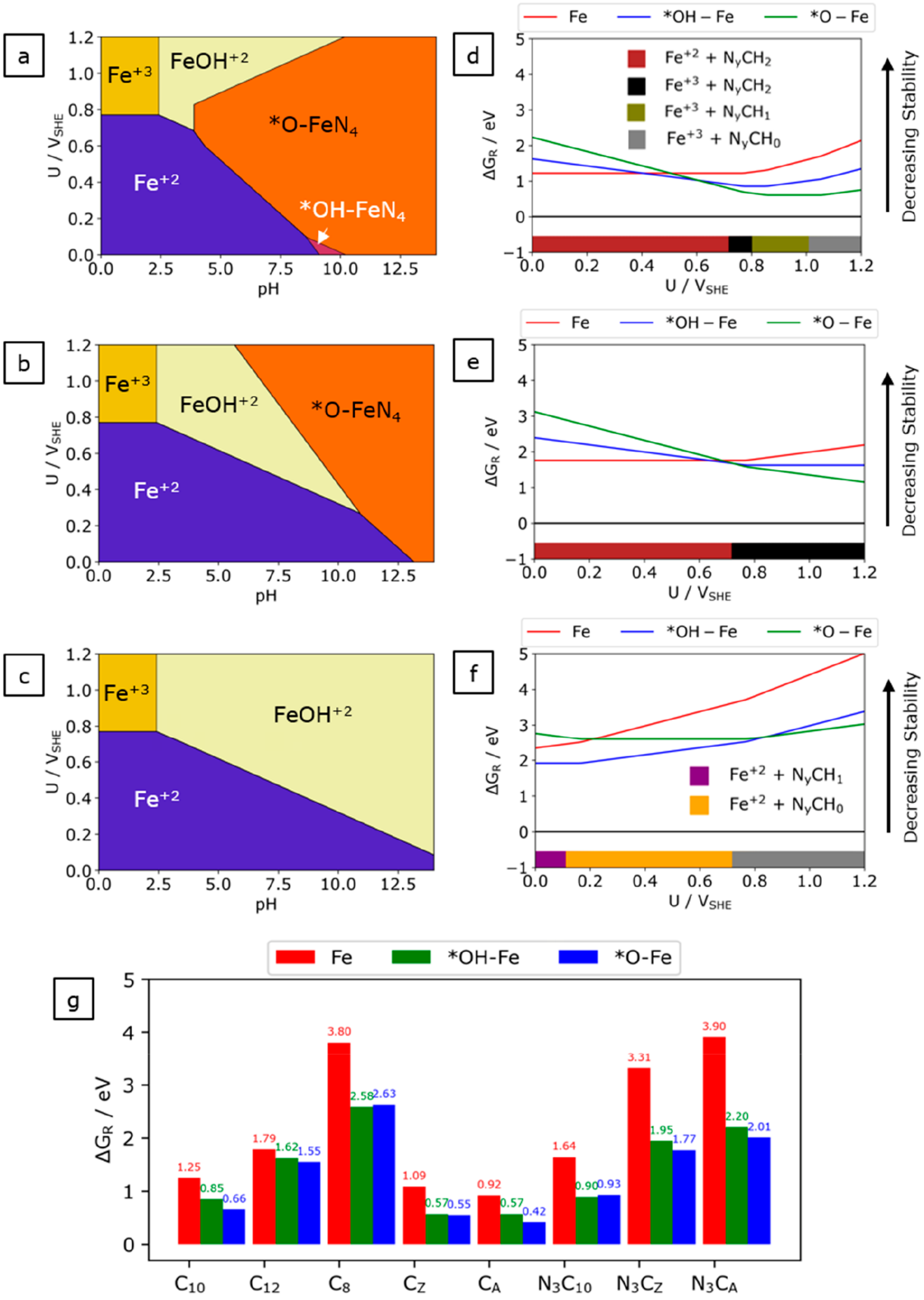

Figure 2. (a−c) Stability diagram of FeN_4C_{10}, FeN_4C_{12}, and FeN_4C_8 structure as a function of applied potential (U) and pH. (d−f) The relative stability (ΔG_R) for Fe, *OH-Fe, and *O-Fe phase as a function of potential U at pH = 0 for FeN_4C_{10}, FeN_4C_{12}, and FeN_4C_8 structure, the most energetically favorable dissolved species are superimposed as horizontal bars at the bottom of each relative stability plot. (g) Relative stability for Fe, *OH-Fe, and *O-Fe phase of different considered FeN_yC structures in Figure 1 at $U = 0.8$ V_{SHE} and pH = 0.

with different local atomic structures surrounding the metal site, as shown in Figure 1 and different metal atoms. The free energy of MN_yC, *OH-MN_yC, and *O-MN_yC phase relative to dissolved species as a function of potential U and pH are defined by using H_2O in a liquid phase and H_2 in a gas phase as a reference to avoid O_2 calculation and can be written as eqs 7−9. Note that y is the number of N atoms ligating the metal atom. The MN_yC denotes the bare metal site structure, while the *OH-MN_yC and *O-MN_yC denote one *OH and *O adsorbate bond with the metal site, respectively. It is assumed that the catalyst surface is in equilibrium with protons, electrons, and liquid water at $T = 298.15$ K, such that oxygen and hydroxyl may be exchanged between the surface and a reference electrolyte through Equation 6.[29]

$$\begin{aligned} MN_yC + H_2O(l) &\rightleftarrows {*OH\text{-}MN_yC} + (H^+_{(aq)} + e^-) \\ &\rightleftarrows {*O\text{-}MN_yC} + 2(H^+_{(aq)} + e^-) \end{aligned} \qquad (6)$$

$$\begin{aligned} &MN_yC + nH^+_{(aq)} \rightarrow M^{x+}_{(aq)} + N_yCH_n + (x - n)e^- \\ &\Delta G(MN_yC) = G(M^{x+}_{(aq)}) + G(N_yCH_n) - G(MN_yC) \\ &\quad - \frac{n}{2}G(H_2) - (x - n)U + nk_BT\ln(10)pH \end{aligned} \tag{7}$$

$$\begin{aligned} &{*OH\text{-}MN_yC} + (n + 1)H^+_{(aq)} \\ &\rightarrow M^{x+}_{(aq)} + N_yCH_n + (x - n - 1)e^- + H_2O \\ &\Delta G(*OH\text{-}MN_yC) = G(M^{x+}_{(aq)}) + G(N_yCH_n) + G(H_2O) \\ &\quad - G(MN_yC) - \frac{(n - 1)}{2}G(H_2) - (x - n - 1)U \\ &\quad + (n - 1)k_BT\ln(10)pH \end{aligned} \tag{8}$$

$$\begin{aligned} &{}^*O\text{-}MN_yC + (n + 2)H^+_{(aq)} \\ &\rightarrow M^{x+}_{(aq)} + N_yCH_n + (x - n - 2)e^- + H_2O \\ &\Delta G(*OH\text{-}MN_yC) = G(M^{x+}_{(aq)}) + G(N_yCH_n) + G(H_2O) \\ &\quad - G(MN_yC) - \frac{(n - 2)}{2}G(H_2) \\ &\quad - (x - n - 2)U + (n - 2)k_BT\ln(10)pH \end{aligned} \tag{9}$$

where $\Delta G(MN_yC)$, $\Delta G(*OH\text{-}MN_yC)$, $\Delta G(*O\text{-}MN_yC)$ are the free energy of the catalyst surface without and with one *OH, and one *O at the metal site, respectively. $\Delta G(N_yCH_n)$ is the free energy of the metal-dissolved carbon cavity with n H atoms bonded at the cavity. We consider from $n = 0$ up to $n = 4$ for the dissolution reaction in eqs 7−9. The optimized structures of nH-bond carbon cavity are shown in Figure S1. $G(M^{+x})$ is the free energy of the dissolved metal ion, is estimated as follows:

$$G(M^{+x}) = E_{DFT(bulk)} + \Delta G_x \tag{10}$$

where $E_{DFT(bulk)}$ is the total energy per metal atom in the bulk structure obtained from DFT calculations. ΔG_x is the free reaction energy of the dissolution reaction of the bulk metal, which is taken from the literature.[57−59] Table S1 shows the free energy of the dissolved metal ion and the dissolution potential used in each approximation ΔG_x. The free energy of the dissolved ion depends on the metal ion concentration, which is assumed to be 10^{-6} M for all dissolved metal ions in this work and all calculations are at $T = 298.15$ K.

2.3. ORR Catalyst Activity. We employ purely thermodynamic models when considering the ORR activity by assuming that all element steps have to be exergonic for the ORR to run and neglect the kinetic barrier for each elementary step. The ORR catalytic activity of the different surface structures is estimated by determining the theoretical overpotential and the potential-determining step in the four-electron associative mechanism with *O, *OH, and *OOH intermediates[60] as shown in eqs 11−14. The metal site is considered as the active site, so all ORR intermediates bond with the metal site. The potential and pH dependence of each reaction step is calculated by employing the CHE as shown in eq 1.

$$O_2(g) + H^+ + e^- + * \rightarrow *OOH \qquad ; \Delta G_1 \tag{11}$$

$$*OOH + H^+ + e^- \rightarrow *O + H_2O(l) \qquad ; \Delta G_2 \tag{12}$$

$$*O + H^+ + e^- + * \rightarrow *OH \qquad ; \Delta G_3 \tag{13}$$

$$*OH + H^+ + e^- \rightarrow * + H_2O(l) \qquad ; \Delta G_4 \tag{14}$$

where * denotes the active metal site. The limiting potential (U_L) is defined as the highest potential at which all four reaction steps are downhill in free energy.

$$\begin{aligned} \text{overpotential} &= 1.23\text{ V} - U_L \\ &= 1.23\text{ V} - \max\{\Delta G_1, \Delta G_2, \Delta G_3, \Delta G_4\}/e \end{aligned} \tag{15}$$

Adsorption energies of *O, *OH, and *OOH intermediate are defined relative to a water molecule from the following reactions.

$$* + H_2O \rightarrow *O + H_2 \qquad ; \Delta G(*O) \tag{16}$$

$$* + H_2O \rightarrow *OH + \frac{1}{2}H_2 \qquad ; \Delta G(*OH) \tag{17}$$

$$* + 2H_2O \rightarrow *OOH + \frac{3}{2}H_2 \qquad ; \Delta G(*OOH) \tag{18}$$

3. RESULTS AND DISCUSSION

3.1. Stability Diagram and Thermodynamic Driving Force toward Metal Dissolution. We first consider the Fe−N−C system. Figure 2 shows the stability diagram of the FeN_4C_{10}, FeN_4C_{12}, and FeN_4C_8 structures as a function of applied potential, U, and pH. The stability diagrams for other FeN_yC structures are shown in Figure S2. At acidic ORR relevant conditions ($U \sim 0.6$−0.8 V_{SHE} and pH = 0), the most stable phase is the dissolved Fe ions for all considered structures, so the single Fe metal atom is prone to leach. At the same potential range in alkaline conditions, *OH or *O can be formed from water on the Fe metal site on the FeN_4C_{10}, FeN_4C_{12}, FeN_4C_A, FeN_4C_Z, and FeN_3C_{10} structure and results in stabilization of the Fe metal site against the dissolution. However, the FeN_4C_8, FeN_3C_Z, and FeN_3C_A structures are still prone to dissolution even in alkaline conditions, as the most stable phase is still a dissolved Fe compound ion. In general, the calculation reveals that the dissolution is a greater problem in acidic than alkaline conditions, as reported by previous experiments.[12,61]

To further extend the stability diagram, we consider a thermodynamic driving force toward the dissolution. A previous study by Singh et al. suggests that materials with predicted free energy up to 0.5 eV/atom greater than the most stable species in the Pourbaix diagram can be stable against the corrosion in experiments due to a large kinetic barrier for structural reorganization.[40] We define the relative dissolution free energy (ΔG_R), which is the free energy difference between the most stable Fe, *OH-Fe, or *O-Fe phase and the most stable dissolved species at pH = 0. The ΔG_R represents a thermodynamic driving force for each phase toward the dissolution and is shown in Figure 2d−f, where the most stable dissolved species are superimposed as horizontal bars at the bottom. The phase with a higher driving force is likely to dissolve into the electrolyte, as reported by the previously combined experimental and theoretical study.[30]

For the considered FeN_yC structures, the relative dissolution free energy (ΔG_R) value of the bare Fe metal phase order at $U = 0.8$ V_{SHE} and pH = 0 is $FeN_4C_A < FeN_4C_Z < FeN_4C_{10} < FeN_3C_{10} < FeN_4C_{12} < FeN_3C_Z < FeN_4C_8 < FeN_3C_A$, see Figure 2g, suggesting that the stability against the dissolution decreases from FeN_4C_A to FeN_3C_A. The formation of one

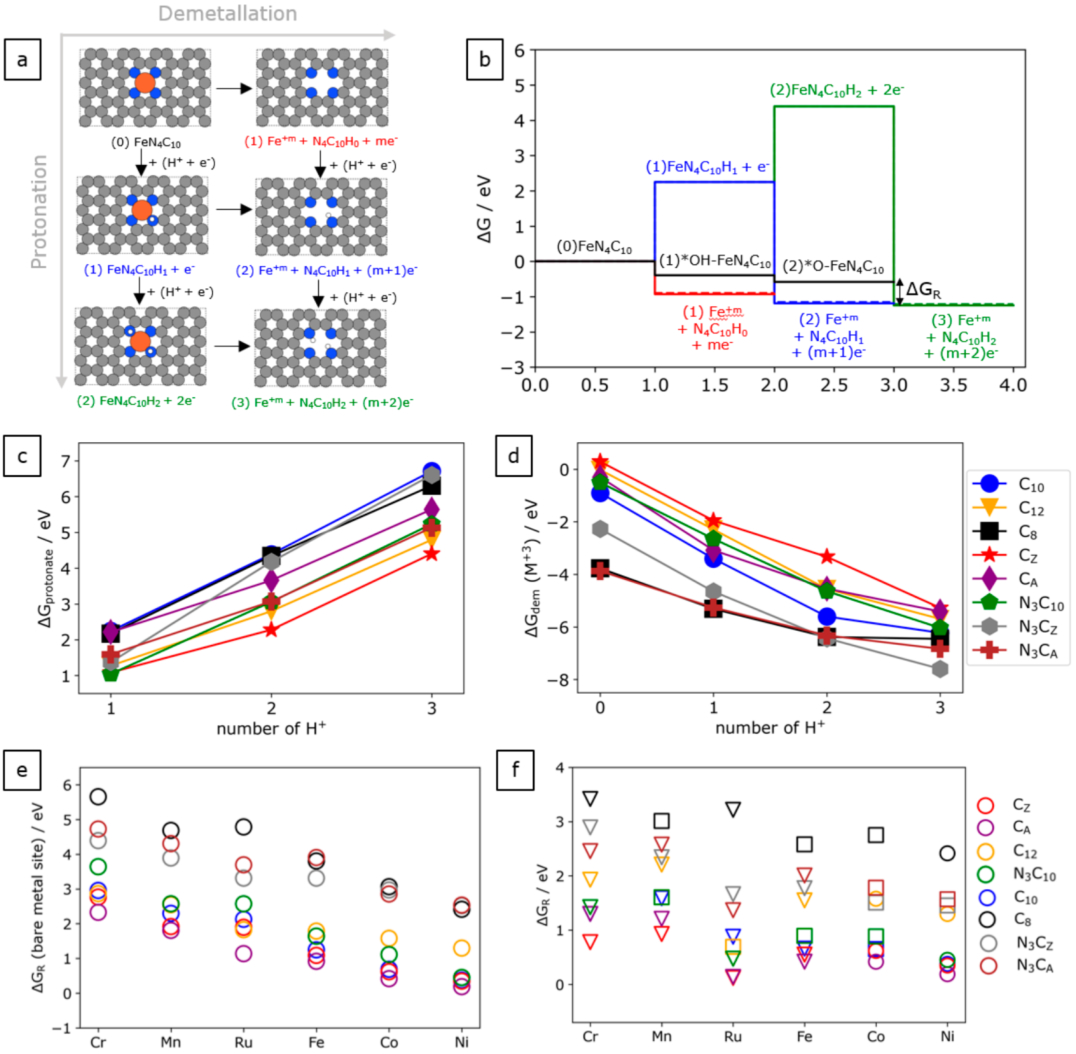

Figure 3. (a) Schematic illustration of possible dissolution mechanism of FeN_4C_{10} structure. Color codes for atoms are the same as Figure 1. (b) Free energy diagram related to possible dissolution mechanisms of FeN_4C_{10} structure with up to $3H^+$ at $U = 0.8$ V_{SHE} and pH = 0. (c) Protonation free reaction energy ($\Delta G_{protonate}$) at the atoms surrounding the Fe metal site and (d) demetalation free reaction energy (ΔG_{dem}) for Fe metal atom from the considered host carbon structures to dissolved Fe^{3+} ion as a function of H^+ number at pH = 0 and $U = 0.8$ V_{SHE}. (e) The relative stability (ΔG_R) of the bare metal phase and (f) the most stable phase MN_yC structures at $U = 0.8$ V_{SHE} and pH = 0. The symbols for the surface: *M = circle, *OH-M = square, *O-M = triangle.

*OH and *O on the bare Fe metal site at higher potential thermodynamically stabilizes the Fe metal atom against the dissolution. At $U = 0.8$ V_{SHE} and pH = 0, the relative free energy (ΔG_R) order of the most stable phase is found to be *O-FeN_4C_A < *O-FeN_4C_Z < *O-FeN_4C_{10} < *OH-FeN_3C_{10} < *O-FeN_4C_{12} < *O-FeN_3C_Z < *O-FeN_3C_A < *OH-FeN_4C_8, see Figure 2g.

At potentials in the range of 0.2−0.9 V_{SHE} and pH = 0, we find that the FeN_4C_{10} structure is more stable than the FeN_4C_{12} site as the thermodynamic driving force for the most stable phase of the FeN_4C_{12} structure is about 0.70 eV greater than that of the FeN_4C_{10} structure, on average. These results agree with the experimental results reported by Li et al.[19]

The horizontal bars at the bottom of each relative stability plot indicate the most energetically favorable dissolved species, suggesting that the dissolution reactions depend not only on the working condition (U and pH) but also on the local atomic structure around the metal site. For example, for the FeN_4C_8, FeN_4C_A, and FeN_4C_Z structures, the dissolution reaction results in 0 or one proton transferred to the cavity site, while 1−3 protons are transferred to the cavity site of the other structures.

Considering the dissolution reaction in more detail, we find that the protonation at the metal-dissolved host carbon structure is thermodynamically favorable for the N_4C_{12}, N_3C_{10}, N_4C_Z, N_4C_A, N_4C_{10}, and N_3C_Z structure, but it is endothermic for the N_3C_A and N_4C_8 structure (Figure S3). However, these proton transfers might not necessarily affect the kinetic dissolution rate if they occur late in the exothermic process. During the dissolution, we therefore also consider that the protonation reaction occurs at the atoms surrounding the Fe metal atom and is followed by the demetalation reaction, as eqs 19 and 20. Figure 3a,b illustrates the possible dissolution mechanism and corresponding free energy diagram of the dissolution process. From a thermodynamic perspective, whether the protonation reaction occurs before or after the demetalation leads to the same overall dissolution reaction as eq 7 and the same relative stability.

$$\mathrm{FeN}_y\mathrm{C} + n(\mathrm{H}^+ + e^-) \rightarrow \mathrm{FeN}_y\mathrm{CH}_n \tag{19}$$

$$\mathrm{FeN}_y\mathrm{CH}_n \rightarrow \mathrm{Fe}^{+m} + \mathrm{N}_y\mathrm{CH}_n + me^- \tag{20}$$

We find that the protonation at the atoms surrounding the Fe metal atom is endothermic and becomes more difficult as the potential increases or more protons are added (Figure 3c). At the potential $U = 0.8\ \mathrm{V_{SHE}}$ and pH = 0, the order of the protonation (from easy to difficult) is $\mathrm{FeN_4C_Z} > \mathrm{FeN_4C_{12}} \sim \mathrm{FeN_3C_{10}} \sim \mathrm{FeN_3C_A} > \mathrm{FeN_3C_Z} \sim \mathrm{FeN_4C_A} > \mathrm{FeN_4C_{10}} > \mathrm{FeN_4C_8}$. On the other hand, the demetalation reaction becomes more favorable after the atoms surrounding the Fe metal atoms are protonated and become more favorable as potential increases or more protons are added (Figure 3d). The order of the demetalation at $U = 0.8\ \mathrm{V_{SHE}}$ and pH = 0 (from easy to difficult), regardless of the number of additional protons before the demetalation is $\mathrm{FeN_4C_8} \sim \mathrm{FeN_3C_A} > \mathrm{FeN_3C_Z} > \mathrm{FeN_4C_{10}} > \mathrm{FeN_4C_A} \sim \mathrm{FeN_3C_{10}} \sim \mathrm{FeN_4C_{12}} > \mathrm{FeN_4C_Z}$. Additionally, we find that the Fe metal atom in the $\mathrm{FeN_4C_8}$, $\mathrm{FeN_3C_Z}$, and $\mathrm{FeN_3C_A}$ structure bond quite weakly with the host carbon structure compared with the others, as reported by Tan et al.[39] Therefore, the Fe metal atom in these structures can more easily leave the host carbon structure.

The demetalation reaction relates to the bond strength between the Fe metal atom and the host carbon structure. The protonation at the ligand atoms surrounding the Fe metal atom can weaken the bond between the Fe and the surrounding ligand atoms, resulting in the following demetalation step being facile. Consequently, the basicity of ligand atoms contributes to the stability of the Fe−N−C catalyst in the acidic condtion[12,20] as same as the bonding strength between the metal atom with the carbon host structure. The different trade-offs between the demetalation reaction and the protonation reaction due to the different local atomic structures surrounding the Fe metal site enable different n values for the dissolution reaction.

It is important to note that the real degradation mechanism is still unknown, and other possible mechanisms such as carbon corrosion,[10,18] hydroxyl radical attraction,[6,62] and carbon oxidation[7] have been proposed as a degradation mechanism of the Fe−N−C catalyst can simultaneously occur and might be coupled. Also, the stability is here analyzed from thermodynamic trends, whereas the rate of metal leaching is determined by the kinetic activation energy. Thus, a kinetic analysis of the dissolution mechanism would be required for a complete theoretical description.

Furthermore, Holby et al. suggest the computational unit cell size and a graphene underlayer to host the $\mathrm{FeN_4}$ actives site influence the calculated stability.[38] To assess the sensitivity to these choices, we performed additional stability calculations for some Fe−N−C structures with a bigger unit cell (Figure S5). Table S4 shows the dissolution potential to $\mathrm{Fe^{2+}}$ ion obtained from two sizes of a unit cell. The size of the unit cell can lead to variation in the dissolution potential of about 0.08 $\mathrm{V_{SHE}}$. However, we find the same trend in the dissolution potential obtained from both sizes of unit cells which is $\mathrm{FeN_4C_8}$ (−1.09 $\mathrm{V_{SHE}}$) < $\mathrm{FeN_4C_{10}}$ (0.35 $\mathrm{V_{SHE}}$) < $\mathrm{FeN_4C_A}$ (0.65 $\mathrm{V_{SHE}}$) < $\mathrm{FeN_4C_{12}}$ (0.79 $\mathrm{V_{SHE}}$) < $\mathrm{FeN_4C_Z}$ (0.94 $\mathrm{V_{SHE}}$) for the unit cell in Figure 1 and $\mathrm{FeN_4C_{8b}}$ (−0.98 $\mathrm{V_{SHE}}$) < $\mathrm{FeN_4C_{10b}}$ (0.27 $\mathrm{V_{SHE}}$) < $\mathrm{FeN_4C_{Ab}}$ (0.52 $\mathrm{V_{SHE}}$) < $\mathrm{FeN_4C_{12b}}$ (0.73 $\mathrm{V_{SHE}}$) < $\mathrm{FeN_4C_{Zb}}$ (0.97 $\mathrm{V_{SHE}}$) for the bigger unit cell in Figure S5. This dissolution trend agrees with the trend reported by Tan et al.[39] However, we find the dissolution to $\mathrm{Fe^{2+}}$ ion of 0.35 $\mathrm{V_{SHE}}$ and 0.27 $\mathrm{V_{SHE}}$ for the $\mathrm{FeN_4C_{10}}$ and $\mathrm{FeN_4C_{10b}}$ structure, respectively, which are quite different from the value reported by Holby et al. using the $\mathrm{FeN_4C_{10}}$ structure on a 6 × 6 graphene monolayer structure in a vacuum, in which the dissolution potential is 0.57 $\mathrm{V_{SHE}}$. We find that the dissolution potential of 0.47 $\mathrm{V_{SHE}}$ for the $\mathrm{FeN_4C_{10}}$ structure (Table S5) in a vacuum. Thus, there may be some influence of solvation on the calculated stability as well as the strain associated with the smaller cell.[38] The variation in *O and *OH free adsorption energy due to the size of the unit cell is 0.08 and 0.07 eV on average for both *O and *OH, respectively. The trend in the relative dissolution free energy (ΔG_R) value of the most stable phase at $U = 0.8\ \mathrm{V_{SHE}}$ and pH = 0 obtained from the bigger unit cell is *O-$\mathrm{FeN_4C_{Ab}}$ < *O-$\mathrm{FeN_4C_{10b}}$ < *O-$\mathrm{FeN_4C_{Zb}}$ < *O-$\mathrm{FeN_4C_{12b}}$ < *OH-$\mathrm{FeN_4C_{8b}}$, largely in agreement with results on the unit cell in Figure 1. Therefore, the unit cells in Figure 1 are used in our further calculations.

Besides the stabilization by the graphene underlayer reported by Holby et al., the dissolution potential of 0.65 $\mathrm{V_{SHE}}$ has been reported for the $\mathrm{FeN_4C_{10}}$ configuration on a 6 × 6 graphene bilayer structure (0.08 higher than the monolayer structure).[38] Thus, it has been recommended to use a larger and bilayer graphene structure for the stability calculation.[38] However, we find that different local atomic structures around the Fe metal site cause the change in the dissolution potential in the range of 0.30−1.43 $\mathrm{V_{SHE}}$, which is greater than the effect of a graphene underlayer. Thus, only a monolayer structure is considered here.

So far, the solvent effect is considered implicitly in this work. We further investigate the effect of the explicit water layer on the stability calculation. We consider the explicit water layer only on the same side of the catalyst as the *O and *OH adsorbates (Figure S6). A previous study by Svane et al.[63] studied the explicit solvation effect on a $\mathrm{CoN_4C_{12}}$ structure suggests that the explicit water on the same side of the adsorbate can result in stabilization about 0.27 eV for *OH relative to a solvent-free model. However, there is no further stabilization effect when adding explicit water layers on both sides of the catalyst surface, as the stabilization is only about 0.1 eV for *O, *OH, and *OOH relative to the one explicit water on the same side with the adsorbates. Table S5 shows the dissolution potential to $\mathrm{Fe^{2+}}$ obtained from different solvation models. The dissolution potentials obtained from implicit solvation are 0.14 $\mathrm{V_{SHE}}$ lower, on average, than those obtained in a vacuum. The dissolution potential with the explicit solvation is close to those in a vacuum with a variation of 0.06 $\mathrm{V_{SHE}}$, on average. However, there is a big difference in dissolution potential between $\mathrm{FeN_4C_Z}$ in a vacuum and explicit solvation. We find that, in the optimized structure of the $\mathrm{N_4C_{Zw}H_0}$ structure with one explicit water layer, the nitrogen atoms are out of a carbon plane while the nitrogen atoms in a vacuum and implicit solvation model remain in the carbon plane. The distortion with the explicit solvation leads to 0.20 $\mathrm{V_{SHE}}$ lower dissolution potential for the $\mathrm{FeN_4C_{Zw}}$ compared with the solvation-free model. The explicit water layer surrounding *O and *OH adsorbates leads to stabilization relative to the vacuum of 0.41 and 0.22 eV, respectively. The stabilization relative to the vacuum due to the implicit solvation is 0.30 and 0.22 eV for *O and *OH, respectively. Thus, the stabilization is similar in magnitude for implicit and explicit solvation. For the most stable phase at $U = 0.8$ V_{SHE} and pH = 0, the relative dissolution free energy (ΔG_R) value with explicit solvation is *O-FeN4C10$_{Zw}$ < *O-FeN4C$_{10w}$ < *O-FeN4C$_{12w}$ < *O-FeN4C$_{8w}$. Meanwhile, we find the relative dissolution free energy (ΔG_R) value in a vacuum to be *OH-FeN$_4$C10$_{Zv}$ < *OH-FeN4C$_{10v}$ < *OH-FeN4C$_{12v}$ < *OH-FeN4C$_{8v}$. The difference in the relative stability of the most stable phase is mainly due to the different stabilization effects on *O and *OH via different solvation models. There is an obvious influence of solvation on the stability calculation; to avoid the structural distortion in the calculations, we use the implicit solvation, which leads to a similar solvation stabilization as the explicit solvation in our further calculations.

We further extend the thermodynamic stability analysis with different metal atoms, changing the metal atom to Cr, Mn, Co, Ni, and Ru. The stability diagrams are shown in Figures S10−S15, indicating that all considered MN$_x$ sites on the considered structures prefer to dissolve under the acid condition as the most stable species at pH = 0 are an aqueous metal ion. Figure 3e shows the relative stability for the bare metal site at $U = 0.8$ V_{SHE} and pH = 0; the MN$_4$C$_8$, MN$_3$C$_Z$, and MN$_3$C$_A$ structures, regardless of the metal atom, are less stable than other structures. On the other hand, the MN$_4$C$_A$ structure is the most stable structure against the dissolution under the same acid conditions, regardless of the metal atoms. The general trend in the thermodynamic driving force toward the dissolution of the bare metal site at $U = 0.8$ V_{SHE} and pH = 0 is Cr > Mn > Ru > Fe > Co > Ni. To understand this trend, we have considered the dissolution of the bare MN$_x$ site without the protonation at the cavity. We first consider the energy of the metal atom being in the MN$_x$ site on the carbon host structure against the formation of metal atom in the bulk structure by the following equation:

$$\Delta G_{\text{bulk}} = E_M + E(N_xC_y) - E(MN_xC_y) \tag{21}$$

where E_M is the total energy per atom of the metal in bulk structure, $E(MN_xC_y)$ is the total energy of the MN$_4$ structure and $E(N_xC_y)$ is the total energy of the metal-dissolved cavity structure (N_xC_y). The calculated ΔE_{metal} for different metal centers on different carbon host structures are shown in Figure S16a and Table S6. The ΔE_{metal} values indicate that the metal atom in the MN$_4$C$_8$, MN$_3$C$_Z$, and MN$_3$C$_A$ structure is unstable and prefers to form the bulk metal rather than be embedded in the carbon host structure compared with other structures. Second, we consider the energy for oxidizing the metal atom at a working potential ($U = 0.8$ V_{SHE}) by the following equation:

$$\Delta E_{\text{oxidize}} = G(M^{+x}) - xU - E_M \tag{22}$$

where $G(M^{+x})$ is free energy of the most stable dissoved metal ion at the considered condition ($x = 2$ for M = Co and Ni; $x = 3$ for M = Cr, Mn, Ru and Fe). The calculated $\Delta E_{\text{oxidize}}$ is shown in Figure S16b and Table S6. The oxidization trend of the metal (from easy to difficult) is Cr < Mn < Fe < Co < Ni. For these 3d metals, the metal oxidation energy ($\Delta E_{\text{oxidize}}$) plays an important role in the dissolution reaction, causing a significant difference in the acid stability among 3d elements. The stability of the bare MN$_x$ site toward a dissolved metal cation is Cr < Mn < Fe < Co < Ni, following the oxidation trend.

For Ru, the bond strength between the Ru atom and the carbon hosts is weaker than other metal elements within the same carbon host structure. However, Ru is also more difficult to oxidize, and overall, the stability of the RuN$_x$ site is between Mn and Fe.

The formation of one *O and *OH from water mostly on Cr, Mn, Ru, and Fe metal sites at pH = 0 and $U = 0.8$ V_{SHE} is thermodynamically favorable on most of the considered structures, resulting in increased stability under acid conditions. However, under the same conditions, the most stable phase of the considered CoN$_y$C and NiN$_y$C structures is mostly the bare metal site (Figure 3f).

We consider the M−N−C catalyst by choosing M = Cr, Mn, Fe, Ru, Co, and Ni because these elements are either relatively cheap and abundant 3d metals or have shown promising ORR activity and stability. The thermodynamic stability analysis of the Pt−N−C structures is also considered and shown in Figure S17. Most of the considered Pt−N−C structures, except PtN$_4$C$_8$, are thermodynamically stable against dissolution at pH = 0, $U = 0.8$ V_{RHE}, and even more stable than other considered metal elements. However, all considered Pt−N−C structures are inactive toward the ORR as the overpotential of all considered Pt−N−C structures is more than 1.00 eV (Table S18).

In general, we find that the metal atom on the graphene plane (MN$_4$C$_{10}$ or MN$_3$C$_{10}$) and the MN$_4$ site on the graphene edge (MN$_4$C$_Z$ and MN$_4$C$_A$) are more stable than the MN$_4$ site hosted near micropores (MN$_4$C$_{12}$) or bridging between two zigzag edges (MN$_4$C$_8$) and the MN$_3$ structures at the graphene edge (MN$_3$C$_Z$ and MN$_3$C$_A$).

The Fe, Co, Ru, and Ni metal atoms on the MN$_4$C$_{10}$, MN$_4$C$_Z$, and MN$_4$C$_A$ can well be kinetically stable under acid conditions as the thermodynamic driving force is less than 0.70 eV at $U = 0.8$ V_{SHE} and pH = 0. On top of that, the Ru metal atom on the MN$_4$C$_Z$, MN$_4$C$_A$ structure, and Ni metal atom on the MN$_4$C$_A$ structure are the most promising stable structure under the acid condition as the thermodynamic driving force toward the dissolution is less than 0.2 eV. Previous experimental results have found that the Ru−N−C catalyst is rather stable in the acid environment with a dissolution rate of less than 5% over 30 h of operation at 1.5 V_{SHE}.[24] Meanwhile, the Cr and Mn metal atoms on considered structures have a considerable driving force toward dissolution (>0.7 eV), so these catalysts are unstable during the PEMFC operation. A previous experimental study has reported that the Mn−N−C catalyst is likely to lose its ORR catalytic activity more than the Fe−N−C catalyst in acid and alkaline conditions during the stability test cycling the potential between 0.5 and 1.3 V_{SHE}.[61] Furthermore, the previous experiments have suggested that the Co−N−C catalyst has significantly enhanced resistance to demetalation compared to the Fe−N−C catalyst in acid conditions, especially under O$_2$ purged testing.[22] For the FeN$_y$C and CoN$_y$C structure without any adsorbate, the thermodynamic driving force of the bare Fe metal atom toward the dissolution is about 0.56 eV bigger than for the bare Co metal site, on average. With the formation of one *OH or *O on the metal site, the relative stabilities of the most stable phase under acid conditions for both metal atoms are comparable. This suggests that other mechanisms such as carbon surface oxidation[7] as well as the H$_2$O$_2$ derived radicals attack stabilized *OH or *O ligand[22,62] possibly occur along with the demetalation reaction or deactivate the active site. These possible processes should be included in the calculation model to get a complete theoretical description.

Different metal atoms on the same carbon structure dissolve with the same dissolution reaction; the same n value in eqs

7−9). With the $n = 0$ dissolution reaction, the primary contribution to acid instability is the bond strength between the single metal atom and the host carbon structure. However, with increasing n, more contributions from the protonation reaction at the atom surrounding the metal site are included. Thus, the thermodynamic acid stability of the M−N−C catalyst is determined by both the bonding strength of the metal atom with the host carbon structure and the basicity of the ligand atom around the metal atoms. In the Fe−N−C system, the FeN_4C_{12} has strong bonding between the Fe metal atom and the host carbon structure, but the nitrogen atoms around the Fe metal site are vulnerable to proton attack. The nitrogen ligand in the FeN_4C_8 structure can resist the action of protons in acid solution, but the bonding between the Fe metal atom and the carbon host structure is too weak. Consequently, both structures are predicted to be less stable than the FeN_4C_{10} structure under the same acid conditions.

Additionally, previous studies by Zhang et al.[64] and Jung et al.[65] have suggested that the oxygen functional groups near the CoN_4 site can be formed via electrochemical or chemical treatment. The formation energies of *O from water on various carbon sites near the CoN_4C_{10} structure reported by Zhang et al.[64] and Jung et al.[65] are more than 2.8 eV, suggesting weak adsorption of *O on the adjacent carbons. The oxidation of the surface carbon adjacent to the FeN_4 sites has also been reported, decreasing the four-electron ORR activity. However, the deactivation is reversible, and the ORR activity can be recovered upon electrochemical reduction of the carbon surface.[7] We consider *O or *OH formation on carbon adjacent to the Fe center on the FeN_4C_{10b}, FeN_4C_{12b}, and FeN_4C_{Zb} structures, assuming that the catalyst surface is in equilibrium with protons, electrons, and liquid water at $T = 298.15$ K (Figure S19). The *O or *OH on adjacent carbon is not thermodynamically favored in the potential range of 0−1.2 V_{SHE}. Thus, we exclude the formation of *O and *OH next to the MN_x site from our further considerations.

However, the surface carbon oxidation can possibly occur via other such as the dissociation of H_2O_2[7] or *OOH.[39] The surface carbon oxidation may directly or indirectly affect the dissolution of the MN_x site.[19] Tan et al.[39] has suggested that the stable oxygen functional group site next to the FeN_4 site can be different, depending on the local carbon structure.

We consider the effect of nearby *O and *OH on the dissolution reaction for some specific Fe−N−C structures. The carbon surface oxidation potentially affects the stability of the MN_x site and the dissolution reaction. As shown in Table S8, the bond strength between Fe and carbon host in the FeN_4C_{10} structure and bond strength between one H with the carbon cavity in the N_4C_{10} structure is strengthened by the nearby *OH functional but weakened by the nearby *O functional. Breaking the Fe−N bonds require more energy with nearby *OH; however, the H binding with the cavity is also more energetically favorable in the final product. Overall, at pH = 0 and $U = 0.8$ V_{SHE}, the pristine FeN_4C_{10} with the nearby *OH has the same dissolution ($n = 1$) reaction product as the pristine FeN_4C_{10} structure but the dissolution reaction is more thermodynamically favorable than the pristine FeN_4C_{10} structure (Figure S20). The thermodynamic driving force toward the dissolution of the pristine FeN_4C10_{bOH} is found to be 1.58 eV, 0.37 eV higher than that of the pristine FeN_4C_{10}. For the FeN_4C_{10} with nearby *O functional, the Fe−N and H−N bonding become weak. At pH = 0 and $U = 0.8$ V_{SHE}, the overall dissolution reaction is more thermodynamically favorable to occur via the n = 0 reaction for the pristine FeN_4C10_{bO}, and it is more thermodynamically favorable than the pristine FeN_4C_{10} structure. The thermodynamic driving force toward the dissolution for the pristine $FeN4C_{10bO}$ is 1.87 eV, 0.66 eV higher than the pristine FeN_4C_{10} structure.

In the cases of the pristine FeN_4C_{12}, the Fe−N and H−N bond strength are weakened by both the nearby *O and *OH functional groups. The same dissolution ($n = 2$) reaction as the pristine FeN_4C_{12} structure becomes more energetically favorable with nearby *O and *OH. The thermodynamic driving force toward the dissolution is 2.01, 1.98 eV for the pristine FeN_4C_{12bOH} and FeN_4C_{12bO} structure (0.36, 0.33 eV higher than that of the pristine FeN_4C_{12}).

At the same time, the formation site of these stable oxygen functional groups can depend on the carbon structure around the active site (Table S7). Therefore, the effect of the carbon surface oxidation on the stability of the MN_x site can vary for different local carbon structures.[39] How carbon surface oxidation forms on various carbon structures and its corresponding effect on the dissolution reaction of the MN_x active site would certainly be interesting to study. However, such an investigation is beyond the scope of the current study.

In addition to the carbon surface oxidation resulting in *O or *OH on the adjacent carbon atoms to the FeN_x site, the carbon surface could possibly contain additional N heteroatoms. The graphitic N atoms surrounding the FeN_x site have been reported to improve ORR activity in both alkaline and acidic electrolyte. It has been reported that the neighboring graphitic nitrogen induces a higher filling degree of d-orbit and decreases on-site magnetic, which can optimize the binding energy of the ORR intermediates.[66] The stability diagrams of some structures with one and two graphitic N atoms are shown in Figure S22. The structures show no distortion because of the added graphitic N atoms (Figure S23). However, the Fe−N bond strength and the first H−N bonding strength on the cavity are weakened due to the added graphic N (Table S9). Consequently, the additional graphitic N atoms are likely to destabilize the surface and increase the thermodynamic driving force toward the dissolution. At pH = 0, $U = 0.8$ V_{SHE}, the thermodynamic driving force toward dissolution increases 0.09 and 0.26 eV on average for the FeN_4C_{12} structures with one and two graphitic N atoms, respectively. For the FeN_4C_{10} structure, the thermodynamic driving force toward the dissolution at pH = 0 and $U = 0.8$ V_{SHE} increase from 1.25 eV to 1.56 and 1.83 eV on average with one and two graphitic N atoms, respectively. Note that only some specific configurations of the graphitic N on the carbon plane are considered here; different configurations could affect the measured activity[66] and stability. However, the exploration of all such configurations is beyond the scope of this work.

The anion-selective adsorption on the active site of the M−N−C catalyst can occur, and it has been previously reported[25,67] that the effect of anions on the Pt and the Fe−N−C catalyst is different. For Pt, the anion in the electrolyte solution can block the active site, decreasing ORR activity. While the M−N−C catalyst is a two-dimensional material, both sides of the catalyst can be exposed to the electrolyte with anions adsorbing on one or both sides of the catalyst. The adsorption of various anions has been reported to be competitive with formation of *O, *OH on the MN_4C_{12} structure (where M = Fe, Cr, Mn, and Co) and can even promote the ORR activity, depending on the metal center as previously reported Svane et al.[25]

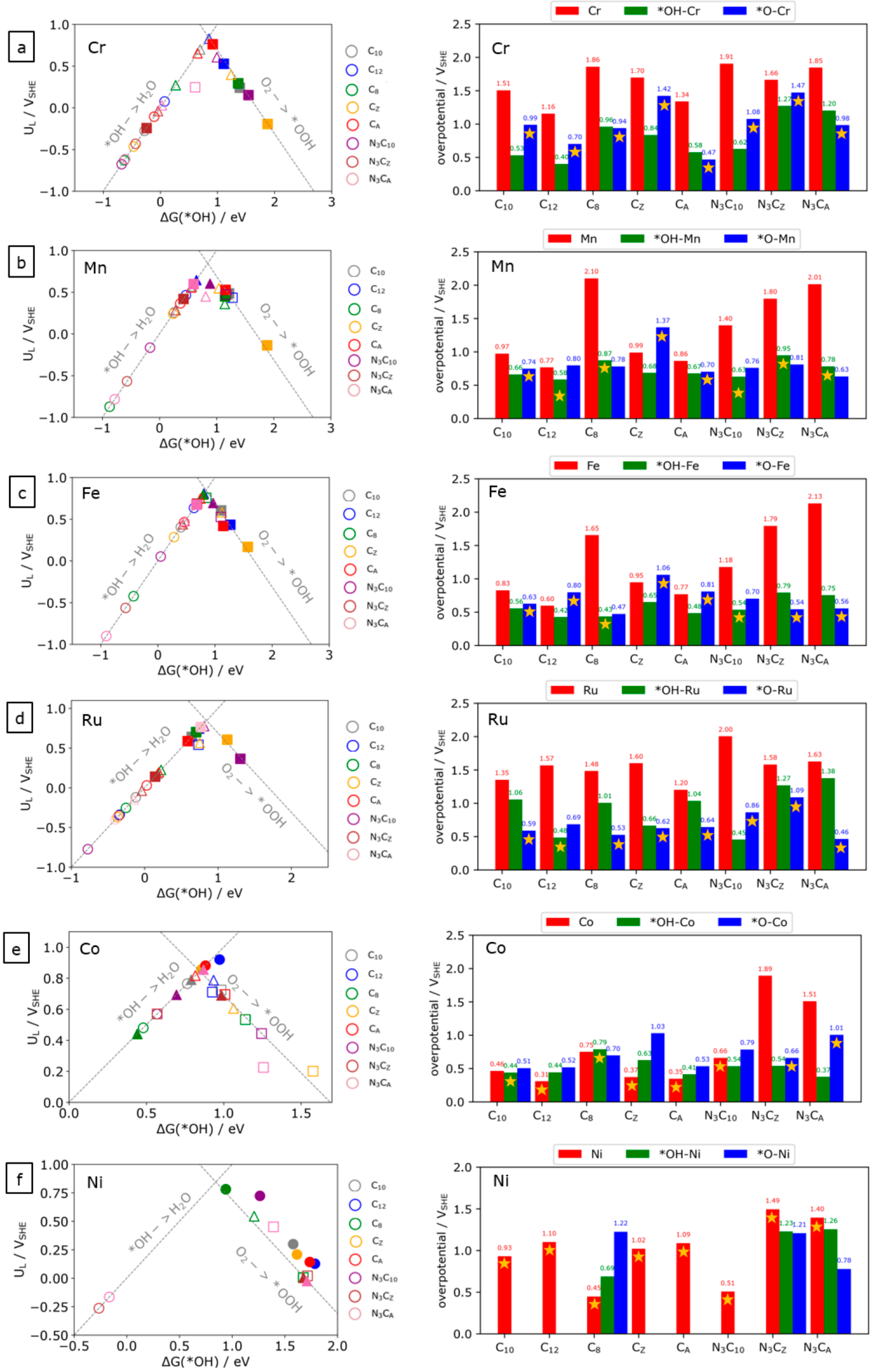

Figure 4. Limiting potential as a function of ΔG(*OH) (left) and ORR overpotential of the corresponding M−N−C systems (right): (a) Cr, (b) Co, (c) Mn, (d) Ni (e) Fe, and (f) Ru. The most stable phase at pH = 0 and U = 0.8 V_{SHE} are filled color and symbol for the surface: *M = circle, *O-M = square, *OH-M = triangle in the volcano plot. The most stable phases are marks with a yellow star in the overpotential plot.

3.2. ORR Catalytic Activity.

As previously seen from the thermodynamic stability results, the formation of one *OH and *O adsorbate from water on the metal site is thermodynamic favorable and stabilizes the metal site against the dissolution. Due to the two-dimensional structure of the MN_y motif, when the formation of one *OH or *O adsorbate from water occurs on the metal site, it can become a part of the active metal site where the other side of the metal atom is still available for the ORR intermediates to react. Thus, in this work, we consider that both metal sides can bond with the adsorbate. At a relevant PEMFC condition, we can identify the most stable adsorbate, which is likely to occupy one of the metal atom sides and become a part of the active metal site, as shown in Figure 3f.

In general, we find that one *O or *OH adsorbate is absorbed strongly on the metal site in the MN_4C_8, MN_3C_Z, and MN_3C_A structures compared with other MN_yC structures, even in the case of inactive Ni metal atoms. Thus, one *O or *OH mostly becomes a part of the active metal site in these structures, regardless of the metal atom.

Having identified the most stable phase of the considered MN_yC structures, we investigate how the ORR activity was affected by the local atomic structure around the metal atom as well as the presence of *O and *OH adsorbate as a part of the active metal site. The adsorption free energy of the reaction intermediate *OOH, *O, and *OH and the limiting potential for the associative ORR pathway is calculated as defined in the Methods section. An initial chemical step of O_2 adsorption is not explicitly considered. Liu et al.[17] reported that the activation energy for the direct O_2 dissociation reaction is always higher for the OOH dissociation reaction on the FeN_4C_{10}, FeN_4C_{12}, and FeN_4C_8 structure; thus, the OOH dissociation path is kinetically more feasible than the O_2 dissociation pathway.

The MN_yC catalyst follows the scaling relation between the adsorption energies of the *OH and *OOH intermediates, which is known for metal and oxide surface.[68]

$$\Delta G(\text{*OOH}) = \Delta G(\text{*OH}) + 3.23, \text{ MEA} = 0.11 \text{ eV} \tag{23}$$

A similar scaling relation obtained from the MN_4 catalyst has been previously reported by Svane et al.[25] This scaling relationship implies that the best liming potential is 0.83 V_{SHE}, resulting in the minimum overpotential of 0.4 V_{SHE}. The limiting potential plotted as a function of $\Delta G(\text{*OH})$ for each metal atom, and the corresponding ORR overpotential is shown in Figure 4.

We first consider the Fe−N−C system, the bare Fe metal site bond with *OH intermediate quite strongly, so the reaction is limited by the reduction of *OH (Equation 14) for the considered carbon host structures. The trend in ORR overpotential for the bare Fe metal site is found to be FeN_4C_{12} < FeN_4C_A < FeN_4C_{10} < FeN_4C_Z < FeN_3C_{10} < FeN_4C_8 < FeN_3C_Z < FeN_3C_A. This trend agrees with a previous theoretical prediction by Yang et al.[69] At $U = 0.8$ V_{SHE} and pH = 0, we find that one side of the Fe atom is likely to be ligated by either *OH or *O adsorbate. The active site with the *O or *OH ligand is denoted as *OH-Fe and *O-Fe in Figure 4. The ORR intermediate binds with the Fe metal site more weakly with the presence of *OH ligand, compared with those on the bare Fe metal site. The ORR intermediate binding becomes even weaker with the presence of the *O ligand. The *OH ligand is found to improve ORR activity on the FeN_4C_{10}, FeN_4C_{12}, FeN_4C_8, FeN_4C_Z, and FeN_3C_{10} structure as reported by previous studies.[69−72] However, the *O ligand promotes the ORR activity on the FeN_3C_Z and FeN_3C_A structures. Considering the ORR activity on the most stable phase under the PEMFC relevant condition in Figure 3f, we find the ORR overpotential trend to be *OH-FeN_4C_8 (0.43) < *O-FeN_3C_Z (0.54) ∼ *OH-FeN_3C_{10} (0.54) < *O-FeN_3C_A (0.56) < *O-FeN_4C_{10} (0.63) < *O-FeN_4C_{12} (0.80) < *O-FeN_4C_A (0.81) < *O-FeN_4C_Z (1.06).

We find that the ORR intermediates bind strongly on the bare metal site for Cr, Mn, and Ru metal atoms, especially on the MN_4C_8, MN_3C_Z, and MN_3C_A structures. Thus, the ORR activity of the bare metal site locates on the left leg of the volcano plot, and the desorption of the *OH step restricts the reaction (ΔG_4). The *OH and *O ligands are found to decrease the ORR adsorption strength on the metal site, as previously found in the FeN_yC system. We find that the formation of OH ligand at the metal site enhance the ORR activity for the MN_4C_{10}, MN_4C_Z, MN_4C_A, and MN_3C_{10} structure with the Mn and Cr metal atom, while the *O ligand positively affects the ORR activity on the MN_4C_8, MN_3C_Z, and the MN_3C_A structure with the Mn and Cr metal atom.

For the RuN_yC structures, we find that the formation of one *OH and *O ligand, which is expected under the working condition, is also beneficial for the ORR activity, especially *O. It turns out that the *O-Ru site has higher ORR activity than the bare metal site or the *OH-Ru site for the RuN_4C_{10}, RuN_4C_8, RuN_4C_Z, RuN_4C_A, RuN_3C_Z, and RuN_3C_A structure.

The ORR intermediate adsorption on the bare Co metal site is weaker than the previous metal atoms. Still, the ORR intermediate strongly binds on the bare metal site in the MN_4C_8, MN_3C_Z, and MN_3C_A structures. For the Co bare metal site, the ORR activity is still on the left leg of the volcano plot but locates near the peak of the volcano plot. The strong bonding of the *OH has restricted the reaction, except for the CoN_4C_{12} structure where ΔG_1 limits the reaction. The *OH and *O ligands are found to decrease the ORR adsorption strength on the Co metal site. Unlike previously considered metal atoms, the effect of *OH and *O ligands on the Co metal site negatively affects the ORR activity on the CoN_4C_{12}, CoN_4C_Z, and CoN_4C_A structure because the activity of the Co bare metal site is already near the top of the activity volcano. With *OH and *O ligands on these structures, the *OH adsorption strength is decreased, moving the active sites to the right leg of the volcano plot. However, under working conditions, the *OH ligand is expected to spontaneously evolve only on the Co metal site in the CoN_3C_{10}, CoN_3C_Z, and CoN_3C_A structure which can substantially enhance the ORR activity.

In the NiN_yC structures, the ORR intermediate bond is too weak with the bare Ni metal site in most considered host carbon structures, and no *O and *OH ligands are expected on most NiN_yC sites. Thus, the first reaction step restricts the reaction ($O_2 \rightarrow$ *OOH; ΔG_1), and most NiN_yC structures are less active toward the ORR than other metal atoms, except for the NiN_4C_8 structure. The NiN_4C_8 structure turns out to have high ORR activity with the overpotential of 0.45 V_{SHE}. This is due to the stronger bonding between the Ni metal and the ORR intermediate on the NiN_4C_8 compared with other host structures.

For the bare metal site, the binding energy of the ORR intermediate in the same carbon host structure is likely to follow the ordering (from strong to weak): Cr > Mn > Ru > Fe > Co > Ni. Among the different carbon host structures, the bare metal atom on the MN_4C_8, MN_3C_Z, MN_3C_A structure is likely to bond with the adsorbate too strongly. We find that in the optimized structure of the MN_4C_8 with an adsorbate, the metal atom is likely to lay above the basal plane, forming a distorted square-pyramidal geometry instead of a square-pyramidal geometry. Also, we find that the metal atom (with adsorbate) in this distorted square-pyramidal geometry prefers a higher spin state than in other structures with a square-pyramidal geometry.

Consider the FeN_4C_{12}, FeN_4C_{10}, and FeN_4C_8 structures as an example in Figure S24. The optimized structures of the FeN_4C_{12}, FeN_4C_{10}, and FeN_4C_8 are in a square planar geometry. The Fe^{2+} have a spin configuration with two (or almost two) unpaired d electrons in these structures. Due to the *OH adsorption, the d electron in the highest level is transferred to the *OH adsorbate. The *OH-FeN_4C_{12} and *OH-FeN_4C_{10} structures are in the square pyramidal geometry where the Fe^{3+} has only one unpaired electron in their orbital configuration. For the *OH-FeN_4C_8 structure, the *OH adsorption causes the elevation of the Fe metal about 0.80 Å above the N_4 plane. The distortion could lead to a different orbital configuration, as suggested by Jurca et al.[73] The possible d electron configuration in an orbital configuration associated with the distortion has three unpaired d electrons, resulting in a higher spin state configuration. The electron configuration in the *OH-FeN_4C_8 structure has lower energy than those in the *OH-FeN_4C_{12} and *OH-FeN_4C_{10} structure. Therefore, the *OH adsorption on the FeN_4C_8 is more energetically favorable than the FeN_4C_{12} and FeN_4C_{10} structure. The degree of distortion depends on the choice of the metal center. The distorted square-pyramidal geometry upon the intermediate adsorption also causes the high spin configuration on the Mn^{3+} and Co^{3+}, which also has strong binding energy with the adsorbate (Figure S25). There is no significant difference in the spin state of Cr^{3+} in the *OH-CrN_4C_8, *OH-CrN_4C_{12}, and *OH-CrN_4C_{10} structure since both geometries have the same three unpaired d-electrons; however, the elevation of the Cr metal atom in the *OH-CrN_4C_8 is relatively higher and the *OH adsorption is stronger compared with that of the CrN_4C_{10} and CrN_4C_{12} structure (Figure S26). The distorted square-pyramidal geometry may be the energetically favored structure. Like the Cr−N−C system, the Ni^{3+} has the same d electron configuration for both distorted and undistorted square-pyramidal geometry; thus, there is no different spin state among considered structures as observed in the previous Fe−N−C system, but the Ni site in the NiN_4C_8 structure still bonds with the adsorbate stronger than other structures. However, the Ni metal atom is unlikely to react with the ORR intermediate, so the evaluation of the Ni atom out of the N_4 plane upon the intermediate adsorption is relatively small compared to other MN_4C_8 structures. For the *OH-RuN_4C_8, the Ru metal atom with *OH adsorbate is about 0.97 Å above the N_4 plane (Figure S27). The Ru^{3+} in the RuN_4C_8 structure also has a higher spin state and stronger *OH bonding than in the *OH-RuN_4C_{12} and *OH-RuN_4C_{10} structure.

Note that the pristine structure of the bulk-host (MN_4C_{10}) and edge-hosted MN_4 site (MN_4C_Z and MN_4C_A) is a square planar geometry. The metal center in these pristine structures has a similar converged magnetic moment on the metal atom (Table S10), implying a similar spin state. For the Fe−N−C system, the magnetic moment is 1.83, 1.92, and 1.91 for the pristine FeN_4C_{10}, FeN_4C_Z, and FeN_4C_A structures, respectively. The change in the d band center due the change in structure from the bulk-hosted MN_4 site to the edge-hosted MN_4 sites varies with the metal center element (Table S10). In the Fe−N−C system, the d-band center shifts up from −1.13 eV to −0.91 and −0.94 eV when the structure changes from the FeN_4C_{10} to the FeN_4C_Z and FeN_4C_A structure, respectively. While the *OH adsorption free energy is 0.40, 0.28, and 0.46 eV for the FeN_4C_{10}, FeN_4C_Z, and FeN_4C_A structure, respectively. In these cases, the adsorption of *OH is more energetically favorable on the zigzag edge host (FeN_4C_Z) structure than the others (FeN_4C_{10}, FeN_4C_A). After one *OH adsorption, the bulk-hosted MN_x site and edge-hosted MN_x sites adopt a square-pyramidal geometry. In the case of the Fe−N−C system, the elevation of the metal center upon the *OH adsorption is 0.28, 0.45, and 0.26 Å for the *OH-FeN_4C_{10}, *OH-FeN_4C_Z, and *OH-FeN_4C_A structures, respectively (Figure S28) This elevation is significantly smaller than the elevation in the *OH-FeN_4C_8 structure, which is 0.80 Å. The magnetic moment on the metal atom is 1.17, 1.70, and 1.00 for the *OH-FeN_4C_{10}, *OH-FeN_4C_Z, and *OH-FeN_4C_A structures, respectively, resulting in a low spin configuration. The ORR activity can be found in Table S14 for the Fe−N−C system. The pristine FeN_4C_A structure, which the FeN_4 site located at the armchair edge, is slightly more active toward the ORR than the bulk-host FeN_4 site (overpotential is 0.08 V lower than the FeN_4C_{10} site). However, the ORR activity also depends on the *OH and *O ligands which can form in closed potential. With the *OH, the FeN_4 site at the armchair edge still has better ORR activity than the bulk-hosted one (overpotential is 0.08 V lower than the *OH-FeN_4C_{10} site)—however, the ORR activity order changes with the *O ligand. The formation energies of the bulk-hosted and edged-host MN_4 sites are calculated and presented in Table S10. Our results suggest that forming the MN_4 site at the edge, either on a zigzag or armchair edge, is energetically favorable compared to forming it on the graphene bulk structure for all considered metal elements.

The MN_3C_Z and MN_3C_A structures are also likely to bond with the adsorbate strongly, regardless of the metal atom. This is possible because the metal atom has a possible oxidation state of +1 in these two structures. Thus, the metal atom prefers to form at least one more bond with the adsorbate, changing the oxidation from +1 to +2 or +3, which is generally favorable for transition metal atoms. To consider the NiN_3C_A and NiN_3C_Z structures as examples, see Table S11, we find that the pristine structures are converted into +1 spin states (one unpaired electron). The *O and *OH bond strongly with the bare Ni metal site in the NiN_3C_A and NiN_3C_Z, and the spin states become +0, which is the same as other NiN_4C_y structures without adsorbates. The bonding with another ORR intermediate as a second adsorbate on the NiN_3C_A and NiN_3C_Z structure becomes too weak, and it is comparable to that on the bare Ni atom on other NiN_4C_y structures. In other words, the metal atom in the MN_3C_A and MN_3C_Z structure is unsaturated and prefers to form a bond with the adsorbate. The preference of *O and *OH on these unsaturated structures is advantageous for Fe and Co catalysts. We find that *O strongly adsorbs on the FeN_3C_Z and FeN_3C_A structures and becomes a part of the active site where the theoretical overpotential can be as low as 0.54 and 0.56 V_{SHE}, respectively. Similarly, the *OH-CoN_3C_Z and *OH-CoN_3C_A active sites can reach as low theoretical overpotential as 0.54 and 0.37 V_{SHE}.

3.3. Stability vs Activity.

Combining the acid stability and activity descriptors, we plot the relative stability of the most stable phase at $U = 0.8$ V_{SHE}, pH = 0 against the ORR activity in Figure 5. We consider the structure with the relative stability lower than 1 eV and the overpotential less than 1 V_{SHE}. The stable and active sites shown in Figure 5 are from the Fe, Co, Ni, and Ru metal atom mainly on the graphene plane (both

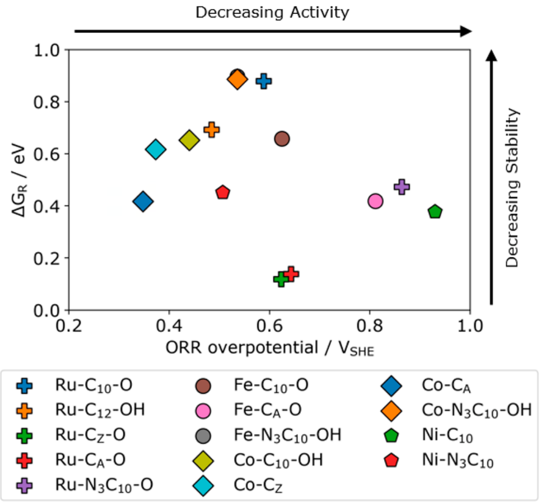

Figure 5. Relative stability of the most stable phase at U = 0.8 V_{SHE} and pH = 0 vs theoretical ORR overpotential with nonadsorbing electrolyte ions. The catalysts close to the bottom left corner are expected to be active toward ORR and stable in acid conditions.

MN_4C_{10} and MN_3C_{10} structure) and at the edge of the graphene (Table 1). The MN_yC structure with Cr ad Mn metal atoms is predicted to be unstable under the considered condition as the thermodynamic driving force toward the dissolution is greater than 1 eV. Also, most MN_yC structures hosted by the micropore and the unsaturated MN_y structures that exhibit higher catalytic activity than the active site on the graphene plane for some metal atoms are not in Figure 5 because of the same reason.

Table 1. Promising Structures with the ORR Overpotential Less than 1 V_{SHE} and Relative Stability at U = 0.8 V_{SHE} and pH = 0 Less than 1.0 eV

system	active site	ΔG_R/eV	overpotential/V_{SHE}
RuN_4C_{10}	*O-Ru	0.88	0.59
RuN_4C_{12}	*OH-Ru	0.69	0.49
RuN_4C_Z	*O-Ru	0.12	0.62
RuN_4C_A	*O-Ru	0.14	0.64
RuN_3C_{10}	*O-Ru	0.47	0.86
FeN_4C_{10}	*O-Fe	0.66	0.63
FeN_4C_A	*O-Fe	0.42	0.81
FeN_3C_{10}	*OH-Fe	0.90	0.54
CoN_4C_{10}	*OH-Co	0.65	0.44
CoN_4C_Z	*Co	0.62	0.37
CoN_4C_A	*Co	0.42	0.35
CoN_3C_{10}	*OH-Co	0.89	0.54
NiN_4C_{10}	*Ni	0.38	0.93
NiN_3C_{10}	*Ni	0.45	0.51

Besides the well-known Fe−N−C catalyst, the Ru−N−C,[74,75] Co−N−C,[22,23,76,77] and Mn−N−C[78,79] catalysts have already been synthesized and tested as an ORR catalyst in acid conditions. However, when we compare theoretical and experimental results, we need to keep in mind that the variation in catalyst preparation and different metal precursor[80] can possibly lead to a different configuration of MN_y site for different metal atoms.

Xiao et al. have reported that the RuN_4 single-atom catalyst exhibits oxygen reduction reaction turnover frequency in 0.1 M $HClO_4$ exceeding the FeN_4 single atom in the same solution while the activity loss is less than that of the FeN_4 single atom.[74] Furthermore, the *OH-RuN_4 site has be suggested as an active site for the ORR activity in acid conditions.[74] The experimental study by Cao et al.[24] and Zhang et al.[75] suggests that under working potential in acid solution, the active and stable site for the RuN_4 single-atom catalyst is the Ru metal site bond with an oxygen atom, in agreement with our finding. Furthermore, Zitolo et al.[23] has suggested that the Fe-based moieties experience a structural change and an electronic-state change, implying that the *O and *OH ligand originating from H_2O can exist under operating while it does not occur for the Co-based moieties. This partially agrees with this study. Most of the Fe−N−C sites have either one *O or *OH on one side of the Fe metal, while only some of the Co−N−C sites have the *O or *OH ligand at the ORR relevant condition.

We find that the stable CoN_yC structures in Table 1 and Figure 5 are more active than the stable FeN_yC structures. Previous experimental studies have reported that the Co−N−C catalyst exhibits high stability in acid condition.[22,77] However, Martinez et al. have found the ORR activity order in 0.5 H_2SO_4 to be Fe > Co > Mn.[78] To match the experimental results and DFT calculations, Martinez et al. have also suggested that the *OH ligand must be adsorbed on one side of the metal atom in the MN_4C_A. While not included in this study, it is well-known that impurities or anions from the electrolyte can be adsorbed on an MN_4 motif site and can either enhance or deteriorate the catalytic activity.[67,81] The computational study by Svane et al. has found that the ligand under H_2SO_4 solution for the FeN_4C_{12} and MnN_4C_{12} structure is HSO_4 and H_2O for CoN_4C_{12} structure, giving good ORR catalytic activity (Fe > Co > Mn)[25] in agreement with the experimental trend in the same solution reported by Martinez et al.[78] The interaction of the single metal site on different local carbon structures with the relevant species in the electrolyte should be further considered to create a model that can accurately describe both the catalytic activity and stability under experimental conditions.[25,67] Another possible explanation for this could be that the Co−N−C catalyst is highly selective for the two-electron pathway, potentially lowering catalytic activity for the four-electron pathway. Martinez et al. has reported that the Fe−N−C catalyst has a half-wave potential of 0.80 V_{RHE} and a selectivity for the four-electron pathway more than 95% while the Co−N−C catalyst has a lower half-wave potential of 0.77 V_{RHE} and a lower selectivity for the four-electron path (90%).[78] Similarly, Gao et al. has reported that the Co−N−C and Fe−N−C catalyst both show high onset potential at around 0.7 V_{RHE}, but the Co−N−C catalyst is more selective for the two-electron pathway than the Fe−N−C catalyst,[82] also agreeing with Zitolo et al.[23]

Some of the promising stable and active structures in acid condition are the FeN_3C_{10}, CoN_3C_{10}, and NiN_3C_{10} structures, suggesting that the catalytic activity of the MN_x on the graphene plane can be tuned by the nearest neighbor interaction; therefore, careful manipulation of the heteroatoms around the active site can possibly further improve the catalytic activity of the MN_yC_{10} structure while maintaining acid stability. Additionally, for the design strategies to achieve both active site and stable M−N−C catalyst, the synthesized aim should be increasing the site density of MN_x bulk-hosted structures (MN_4C_{10} or MN_3C_{10}) or the MN_4 on the edge-hosted graphene structure. Also, avoiding the formation of unsaturated MN_3C_Z or MN_3C_A structure as well as the MN_4C_8

site, which bridged between two armchair edges, will increase the stability of the M−N−C catalyst under acid conditions. Further stability improvement for the active M−N−C structures hosted by the micropores (MN_4C_{12}, MN_4C_8) or the unsaturated structure (MN_3C_Z, MN_3C_A) might be achieved by forming these active structures over another graphitic layer. The metal choice also significantly affects both stability and activity and should be considered when designing the catalyst. Integrating Fe, Co, and Ru metal elements into graphitic carbon supports like the MN_xC_{10} structure would be a promising catalyst for the ORR in acid conditions.

4. CONCLUSION

To summarize, we have systematically investigated stabilities and ORR catalytic activity of the MN_x site on different local atomic structures in acid conditions using DFT calculations, which reveal that the local atomic structure plays a crucial role in both stability and ORR catalytic activity. The stability is here considered from the tendency of a single metal atom to dissolve into the electrolyte. The calculation reveals that all considered MN_x structures are thermodynamically unstable in acid ORR conditions. The thermodynamic driving forces toward the dissolution suggest that the single metal site on the graphene plane and at the edge of the graphene (MN_4C_{10}, MN_4C_A, and MN_4C_Z) are more stable against the dissolution than the single metal sites host by the microporous (i.e., MN_4C_{12}, MN_4C_8) or in the unsaturated single metal site at the edge (MN_3C_Z and MN_3C_A). The stability also depends on the choice of metal site. The MN_x sites with Fe, Co, Ni, and Ru metal atoms are more stable under the acid conditions than those with Mn and Cr metal atoms. Under reaction conditions, we predict the most stable phase of the active site in which *O or *OH ligands occur and become a part of the active site. The ORR activity also depends on the choice of metal and the local atomic structure around the metal site. The MN_4C_8, MN_3C_Z, and MN_3C_A structures are likely to bond with the intermediate too strongly, generally having one *O or *OH ligand on the metal site. For different metal atoms, the Cr, Mn, Ru, and Fe metal bond with the ORR intermediate quite strongly, and the ORR occurs with *O or *OH ligands. The bonding strength becomes weak for the Ni metal atom compared to other considered metal atoms, and most considered structures with Ni are not active toward ORR. Combining both stability and activity descriptors, we identify that single Fe, Co, and Ru metal atoms mostly on the MN_4C_{10}, MN_4C_Z, MN_4C_A, and MN_3C_{10} structure are the promising acid-stable active ORR catalyst. Therefore, rational modification of carbon matrix hosting MN_y moieties and appropriate selection of a metal atom could be carefully used to optimize the activity and stability toward the reaction. This computational study provides useful guidance to rational design and controlled synthesis of M−N−C electrocatalyst to achieve both active and stable catalyst under working conditions not only for the ORR but also the OER due to their similar operating conditions and reaction intermediates. Our study highlights the improved stability of MN_4C_{10}, MN_4C_Z, and MN_4C_A sites against the demetalation and metal clustering compared to, e.g., MN_4C_8 and MN_4C_{12} sites. The approach can be further applied to the N_2[83] and CO_2 reduction reactions,[84,85] and refined by including relevant reaction intermediates such as *H, *CO, and *NH_3 at the more reducing reaction conditions. Figure S30 is an example of extending stability diagrams and relative stability plots at different pH, showing that the approach is flexible and can be applied for varied electrochemical environments. Furthermore, these computational approaches are of interest to the further understanding of acid stability of other geometries of M−N−C materials, such as the dual metal site embedded on the graphene[61,63,86] or a diporphyrin complex.[84,87]

ASSOCIATED CONTENT

Supporting Information

The Supporting Information is available free of charge at https://pubs.acs.org/doi/10.1021/acscatal.1c02941.

> Images of optimized structures; free energy of dissolved metal ions; stability diagrams of the Fe−N−C system; protonation free reaction energy at the metal dissolved carbon cavity; dissolution potential to Fe^{2+}; free adsorption energy of ORR intermediates, the relative stability of Fe, *OH-Fe, *O-Fe with different unit cells and solvation models; stability diagrams for Fe−N−C, Cr−N−C, Mn−N−C, Co−N−C, Ni−N−C, Ru−N−C, Pt−N−C systems; the energy of the MN_x site against metal clustering and energy for oxidizing metal atom; stability diagrams and relative stability for Fe−N−C system with nearby *O, *OH and graphitic N atoms; orbital splitting of d-state and occupancy; possible oxidation and spin state of Ni−N−C system; d-band center and formation energy for the bulk-hosted and edged hosted MN_x site; adsorption free energy of ORR intermediates, ORR overpotentials, and relative stability for Fe−N−C, Cr−N−C, Mn−N−C, Co−N−C, Ni−N−C, Ru−N−C, and Pt−N−C system (PDF)

AUTHOR INFORMATION

Corresponding Author

Heine Anton Hansen − *Technical University of Denmark, Kongens Lyngby 2800, Denmark*; orcid.org/0000-0001-7551-9470; Email: heih@dtu.dk

Author

Tipaporn Patniboon − *Technical University of Denmark, Kongens Lyngby 2800, Denmark*

Complete contact information is available at: https://pubs.acs.org/10.1021/acscatal.1c02941

Notes

The authors declare no competing financial interest.

ACKNOWLEDGMENTS

Funding from the Villum Foundation grant 9455 to the Villum Center for the Science of Sustainable Fuels and Chemicals (V-SUSTAIN) and a scholarship from the Ministry of Science and Technology, Royal Thai Government are acknowledged.

REFERENCES

(1) Nørskov, J. K.; Rossmeisl, J.; Logadottir, A.; Lindqvist, L.; Kitchin, J. R.; Bligaard, T.; Jónsson, H. Origin of the Overpotential for Oxygen Reduction at a Fuel-Cell Cathode. *J. Phys. Chem. B* **2004**, *108* (46), 17886−17892.

(2) Peng, B.; Liu, H.; Liu, Z.; Duan, X.; Huang, Y. Toward Rational Design of Single-Atom Catalysts. *J. Phys. Chem. Lett.* **2021**, *12* (11), 2837−2847.

(3) He, Y.; Liu, S.; Priest, C.; Shi, Q.; Wu, G. Atomically Dispersed Metal-Nitrogen-Carbon Catalysts for Fuel Cells: Advances in Catalyst

Design, Electrode Performance, and Durability Improvement. *Chem. Soc. Rev.* **2020**, *49* (11), 3484−3524.

(4) Kaiser, S. K.; Chen, Z.; Faust Akl, D.; Mitchell, S.; Pérez-Ramírez, J. Single-Atom Catalysts across the Periodic Table. *Chem. Rev.* **2020**, *120* (21), 11703−11809.

(5) Osmieri, L.; Cullen, D. A.; Chung, H. T.; Ahluwalia, R. K.; Neyerlin, K. C. Durability Evaluation of a Fe−N−C Catalyst in Polymer Electrolyte Fuel Cell Environment via Accelerated Stress Tests. *Nano Energy* **2020**, *78* (August), 105209.

(6) Ramaswamy, N.; Hakim, N.; Mukerjee, S. Degradation Mechanism Study of Perfluorinated Proton Exchange Membrane under Fuel Cell Operating Conditions. *Electrochim. Acta* **2008**, *53* (8), 3279−3295.

(7) Choi, C. H.; Lim, H. K.; Chung, M. W.; Chon, G.; Ranjbar Sahraie, N.; Altin, A.; Sougrati, M. T.; Stievano, L.; Oh, H. S.; Park, E. S.; Luo, F.; Strasser, P.; Dražić, G.; Mayrhofer, K. J. J.; Kim, H.; Jaouen, F. The Achilles' Heel of Iron-Based Catalysts during Oxygen Reduction in an Acidic Medium. *Energy Environ. Sci.* **2018**, *11* (11), 3176−3182.

(8) Nabae, Y.; Yuan, Q.; Nagata, S.; Kusaba, K.; Aoki, T.; Takao, N.; Itoh, T.; Arao, M.; Imai, H.; Higashi, K.; Sakata, T.; Uruga, T.; Iwasawa, Y. In Situ X-Ray Absorption Spectroscopy to Monitor the Degradation of Fe/N/C Cathode Catalyst in Proton Exchange Membrane Fuel Cells. *J. Electrochem. Soc.* **2021**, *168* (1), 014513.

(9) Chen, Z.; Jiang, S.; Kang, G.; Nguyen, D.; Schatz, G. C.; Van Duyne, R. P. Operando Characterization of Iron Phthalocyanine Deactivation during Oxygen Reduction Reaction Using Electrochemical Tip-Enhanced Raman Spectroscopy. *J. Am. Chem. Soc.* **2019**, *141* (39), 15684−15692.

(10) Goellner, V.; Baldizzone, C.; Schuppert, A.; Sougrati, M. T.; Mayrhofer, K.; Jaouen, F. Degradation of Fe/N/C Catalysts upon High Polarization in Acid Medium. *Phys. Chem. Chem. Phys.* **2014**, *16* (34), 18454−18462.

(11) Kumar, K.; Asset, T.; Li, X.; Liu, Y.; Yan, X.; Chen, Y.; Mermoux, M.; Pan, X.; Atanassov, P.; Maillard, F.; Dubau, L. Fe-N-C Electrocatalysts' Durability: Effects of Single Atoms' Mobility and Clustering. *ACS Catal.* **2021**, *11* (2), 484−494.

(12) Santori, P. G.; Speck, F. D.; Li, J.; Zitolo, A.; Jia, Q.; Mukerjee, S.; Cherevko, S.; Jaouen, F. Effect of Pyrolysis Atmosphere and Electrolyte PH on the Oxygen Reduction Activity, Stability and Spectroscopic Signature of FeN x Moieties in Fe-N-C Catalysts. *J. Electrochem. Soc.* **2019**, *166* (7), F3311−F3320.

(13) Zitolo, A.; Goellner, V.; Armel, V.; Sougrati, M. T.; Mineva, T.; Stievano, L.; Fonda, E.; Jaouen, F. Identification of Catalytic Sites for Oxygen Reduction in Iron- and Nitrogen-Doped Graphene Materials. *Nat. Mater.* **2015**, *14* (9), 937−942.

(14) Lefèvre, M.; Proietti, E.; Jaouen, F.; Dodelet, J. P. Iron-Based Catalysts with Improved Oxygen Reduction Activity in Polymer Electrolyte Fuel Cells. *Science (Washington, DC, U. S.)* **2009**, *324* (5923), 71−74.

(15) Kramm, U. I.; Herranz, J.; Larouche, N.; Arruda, T. M.; Lefèvre, M.; Jaouen, F.; Bogdanoff, P.; Fiechter, S.; Abs-Wurmbach, I.; Mukerjee, S.; Dodelet, J. P. Structure of the Catalytic Sites in Fe/N/C-Catalysts for O 2-Reduction in PEM Fuel Cells. *Phys. Chem. Chem. Phys.* **2012**, *14* (33), 11673−11688.

(16) Chenitz, R.; Kramm, U. I.; Lefèvre, M.; Glibin, V.; Zhang, G.; Sun, S.; Dodelet, J. P. A Specific Demetalation of Fe-N4 Catalytic Sites in the Micropores of NC-Ar + NH3 Is at the Origin of the Initial Activity Loss of the Highly Active Fe/N/C Catalyst Used for the Reduction of Oxygen in PEM Fuel Cells. *Energy Environ. Sci.* **2018**, *11* (2), 365−382.

(17) Liu, K.; Wu, G.; Wang, G. Role of Local Carbon Structure Surrounding FeN4 Sites in Boosting the Catalytic Activity for Oxygen Reduction. *J. Phys. Chem. C* **2017**, *121* (21), 11319−11324.

(18) Zhang, H.; Chung, H. T.; Cullen, D. A.; Wagner, S.; Kramm, U. I.; More, K. L.; Zelenay, P.; Wu, G. High-Performance Fuel Cell Cathodes Exclusively Containing Atomically Dispersed Iron Active Sites. *Energy Environ. Sci.* **2019**, *12* (8), 2548−2558.

(19) Li, J.; Sougrati, M. T.; Zitolo, A.; Ablett, J. M.; Oğuz, I. C.; Mineva, T.; Matanovic, I.; Atanassov, P.; Huang, Y.; Zenyuk, I.; Di Cicco, A.; Kumar, K.; Dubau, L.; Maillard, F.; Dražić, G.; Jaouen, F. Identification of Durable and Non-Durable FeNx Sites in Fe−N−C Materials for Proton Exchange Membrane Fuel Cells. *Nat. Catal.* **2021**, *4* (1), 10−19.

(20) Speck, F. D.; Paul, M. T. Y.; Ruiz-Zepeda, F.; Gatalo, M.; Kim, H.; Kwon, H. C.; Mayrhofer, K. J. J.; Choi, M.; Choi, C. H.; Hodnik, N.; Cherevko, S. Atomistic Insights into the Stability of Pt Single-Atom Electrocatalysts. *J. Am. Chem. Soc.* **2020**, *142* (36), 15496−15504.

(21) Gubler, L.; Dockheer, S. M.; Koppenol, W. H. Radical (HO●, H● and HOO●) Formation and Ionomer Degradation in Polymer Electrolyte Fuel Cells. *J. Electrochem. Soc.* **2011**, *158* (7), B755.

(22) Xie, X.; He, C.; Li, B.; He, Y.; Cullen, D. A.; Wegener, E. C.; Kropf, A. J.; Martinez, U.; Cheng, Y.; Engelhard, M. H.; Bowden, M. E.; Song, M.; Lemmon, T.; Li, X. S.; Nie, Z.; Liu, J.; Myers, D. J.; Zelenay, P.; Wang, G.; Wu, G.; Ramani, V.; Shao, Y. Performance Enhancement and Degradation Mechanism Identification of a Single-Atom Co−N−C Catalyst for Proton Exchange Membrane Fuel Cells. *Nat. Catal.* **2020**, *3* (12), 1044−1054.

(23) Zitolo, A.; Ranjbar-Sahraie, N.; Mineva, T.; Li, J.; Jia, Q.; Stamatin, S.; Harrington, G. F.; Lyth, S. M.; Krtil, P.; Mukerjee, S.; Fonda, E.; Jaouen, F. Identification of Catalytic Sites in Cobalt-Nitrogen-Carbon Materials for the Oxygen Reduction Reaction. *Nat. Commun.* **2017**, *8* (1), 957.

(24) Cao, L.; Luo, Q.; Chen, J.; Wang, L.; Lin, Y.; Wang, H.; Liu, X.; Shen, X.; Zhang, W.; Liu, W.; Qi, Z.; Jiang, Z.; Yang, J.; Yao, T. Dynamic Oxygen Adsorption on Single-Atomic Ruthenium Catalyst with High Performance for Acidic Oxygen Evolution Reaction. *Nat. Commun.* **2019**, *10* (1), 4849.

(25) Svane, K. L.; Reda, M.; Vegge, T.; Hansen, H. A. Improving the Activity of M−N4 Catalysts for the Oxygen Reduction Reaction by Electrolyte Adsorption. *ChemSusChem* **2019**, *12* (23), 5133−5141.

(26) Zhao, C.; Gao, W.; Jiang, Q. Scheme for Screening O2 Reduction Electrocatalysts: From Pure Metals and Alloys to Single-Atom Catalysts. *J. Phys. Chem. C* **2020**, *124* (46), 25412−25420.

(27) Deng, Q.; Zhao, J.; Wu, T.; Chen, G.; Hansen, H. A.; Vegge, T. 2D Transition Metal−TCNQ Sheets as Bifunctional Single-Atom Catalysts for Oxygen Reduction and Evolution Reaction (ORR/OER). *J. Catal.* **2019**, *370*, 378−384.

(28) Hansen, H. A.; Shi, C.; Lausche, A. C.; Peterson, A. A.; Nørskov, J. K. Bifunctional Alloys for the Electroreduction of CO2 and CO. *Phys. Chem. Chem. Phys.* **2016**, *18* (13), 9194−9201.

(29) Hansen, H. A.; Rossmeisl, J.; Nørskov, J. K. Surface Pourbaix Diagrams and Oxygen Reduction Activity of Pt(111), Ag(111) and Ni(111) Surfaces Studied by DFT. *Phys. Chem. Chem. Phys.* **2008**, *10* (25), 3722−3730.

(30) Hubert, M. A.; Patel, A. M.; Gallo, A.; Liu, Y.; Valle, E.; Ben-Naim, M.; Sanchez, J.; Sokaras, D.; Sinclair, R.; Nørskov, J. K.; King, L. A.; Bajdich, M.; Jaramillo, T. F. Acidic Oxygen Evolution Reaction Activity-Stability Relationships in Ru-Based Pyrochlores. *ACS Catal.* **2020**, *10* (20), 12182−12196.

(31) Gunasooriya, G. T. K. K.; Nørskov, J. K. Analysis of Acid-Stable and Active Oxides for the Oxygen Evolution Reaction. *ACS Energy Lett.* **2020**, *5* (12), 3778−3787.

(32) Calle-Vallejo, F.; Martínez, J. I.; García-Lastra, J. M.; Abad, E.; Koper, M. T. M. Oxygen Reduction and Evolution at Single-Metal Active Sites: Comparison between Functionalized Graphitic Materials and Protoporphyrins. *Surf. Sci.* **2013**, *607*, 47−53.

(33) Zhou, Y.; Gao, G.; Chu, W.; Wang, L. W. Computational Screening of Transition Metal-Doped Phthalocyanine Monolayers for Oxygen Evolution and Reduction. *Nanoscale Adv.* **2020**, *2* (2), 710−716.

(34) Ha, M.; Kim, D. Y.; Umer, M.; Gladkikh, V.; Myung, C. W.; Kim, K. S. Tuning Metal Single Atoms Embedded in NxCy Moieties toward High-Performance Electrocatalysis. *Energy Environ. Sci.* **2021**, *14* (6), 3455−3468.

(35) Back, S.; Siahrostami, S. Noble Metal Supported Hexagonal Boron Nitride for the Oxygen Reduction Reaction: A DFT Study. *Nanoscale Adv.* **2019**, *1* (1), 132−139.

(36) Glibin, V. P.; Dodelet, J.-P. Thermodynamic Stability in Acid Media of FeN 4 -Based Catalytic Sites Used for the Reaction of Oxygen Reduction in PEM Fuel Cells. *J. Electrochem. Soc.* **2017**, *164* (9), F948−F957.

(37) Yin, X.; Holby, E. F.; Zelenay, P. Comment on 'Non-PGM Electrocatalysts for PEM Fuel Cells: Effect of Fluorination on the Activity and Stability of a Highly Active NC_Ar + NH3catalyst' by Gaixia Zhang, Xiaohua Yang, Marc Dubois, Michael Herraiz, Régis Chenitz, Michel Lefèvre, Mohamed Cheri. *Energy Environ. Sci.* **2021**, *14* (2), 1029−1033.

(38) Holby, E. F.; Wang, G.; Zelenay, P. Acid Stability and Demetalation of PGM-Free ORR Electrocatalyst Structures from Density Functional Theory: A Model for "Single-Atom Catalyst" Dissolution. *ACS Catal.* **2020**, *10* (24), 14527−14539.

(39) Tan, X.; Tahini, H. A.; Smith, S. C. Unveiling the Role of Carbon Oxidation in Irreversible Degradation of Atomically-Dispersed FeN4moieties for Proton Exchange Membrane Fuel Cells. *J. Mater. Chem. A* **2021**, *9* (13), 8721−8729.

(40) Singh, A. K.; Zhou, L.; Shinde, A.; Suram, S. K.; Montoya, J. H.; Winston, D.; Gregoire, J. M.; Persson, K. A. Electrochemical Stability of Metastable Materials. *Chem. Mater.* **2017**, *29* (23), 10159−10167.

(41) Kresse, G.; Hafner, J. Ab Initio Molecular Dynamics for Liquid Metals. *Phys. Rev. B: Condens. Matter Mater. Phys.* **1993**, *47* (1), 558−561.

(42) Blöchl, P. E. Projector Augmented-Wave Method. *Phys. Rev. B: Condens. Matter Mater. Phys.* **1994**, *50* (24), 17953−17979.

(43) Hjorth Larsen, A.; JØrgen Mortensen, J.; Blomqvist, J.; Castelli, I. E.; Christensen, R.; Dułak, M.; Friis, J.; Groves, M. N.; Hammer, B.; Hargus, C.; Hermes, E. D.; Jennings, P. C.; Bjerre Jensen, P.; Kermode, J.; Kitchin, J. R.; Leonhard Kolsbjerg, E.; Kubal, J.; Kaasbjerg, K.; Lysgaard, S.; Bergmann Maronsson, J.; Maxson, T.; Olsen, T.; Pastewka, L.; Peterson, A.; Rostgaard, C.; SchiØtz, J.; Schütt, O.; Strange, M.; Thygesen, K. S.; Vegge, T.; Vilhelmsen, L.; Walter, M.; Zeng, Z.; Jacobsen, K. W. The Atomic Simulation Environment - A Python Library for Working with Atoms. *J. Phys.: Condens. Matter* **2017**, *29* (27), 273002.

(44) Wellendorff, J.; Lundgaard, K. T.; Møgelhøj, A.; Petzold, V.; Landis, D. D.; Nørskov, J. K.; Bligaard, T.; Jacobsen, K. W. Density Functionals for Surface Science: Exchange-Correlation Model Developmentwith Bayesian Error Estimation. *Phys. Rev. B: Condens. Matter Mater. Phys.* **2012**, *85* (23), 235149.

(45) Mortensen, J.; Gjerding, M.; Thygesen, K. MyQueue: Task and Workflow Scheduling System. *J. Open Source Softw.* **2020**, *5* (45), 1844.

(46) Charreteur, F.; Jaouen, F.; Ruggeri, S.; Dodelet, J. P. Fe/N/C Non-Precious Catalysts for PEM Fuel Cells: Influence of the Structural Parameters of Pristine Commercial Carbon Blacks on Their Activity for Oxygen Reduction. *Electrochim. Acta* **2008**, *53* (6), 2925−2938.

(47) Cheng, Y.; Zhao, S.; Li, H.; He, S.; Veder, J. P.; Johannessen, B.; Xiao, J.; Lu, S.; Pan, J.; Chisholm, M. F.; Yang, S. Z.; Liu, C.; Chen, J. G.; Jiang, S. P. Unsaturated Edge-Anchored Ni Single Atoms on Porous Microwave Exfoliated Graphene Oxide for Electrochemical CO2. *Appl. Catal., B* **2019**, *243* (June 2018), 294−303.

(48) Monkhorst, H. J.; Pack, J. D. Special Points for Brillouin-Zone Integrations. *Phys. Rev. B* **1976**, *13* (12), 5188−5192.

(49) Mathew, K.; Sundararaman, R.; Letchworth-Weaver, K.; Arias, T. A.; Hennig, R. G. Implicit Solvation Model for Density-Functional Study of Nanocrystal Surfaces and Reaction Pathways. *J. Chem. Phys.* **2014**, *140* (8), 084106.

(50) Mathew, K.; Kolluru, V. S. C.; Mula, S.; Steinmann, S. N.; Hennig, R. G. Implicit Self-Consistent Electrolyte Model in Plane-Wave Density-Functional Theory. *J. Chem. Phys.* **2019**, *151* (23), 234101.

(51) Goedecker, S. Minima Hopping: An Efficient Search Method for the Global Minimum of the Potential Energy Surface of Complex Molecular Systems. *J. Chem. Phys.* **2004**, *120* (21), 9911−9917.

(52) Goedecker, S.; Hellmann, W.; Lenosky, T. Global Minimum Determination of the Born-Oppenheimer Surface within Density Functional Theory. *Phys. Rev. Lett.* **2005**, *95* (5), 55501.

(53) Peterson, A. A. Global Optimization of Adsorbate-Surface Structures While Preserving Molecular Identity. *Top. Catal.* **2014**, *57* (1−4), 40−53.

(54) Kulkarni, A.; Siahrostami, S.; Patel, A.; Nørskov, J. K. Understanding Catalytic Activity Trends in the Oxygen Reduction Reaction. *Chem. Rev.* **2018**, *118* (5), 2302−2312.

(55) Christensen, R.; Hansen, H. A.; Dickens, C. F.; Nørskov, J. K.; Vegge, T. Functional Independent Scaling Relation for ORR/OER Catalysts. *J. Phys. Chem. C* **2016**, *120* (43), 24910−24916.

(56) Christensen, R.; Hansen, H. A.; Vegge, T. Identifying Systematic DFT Errors in Catalytic Reactions. *Catal. Sci. Technol.* **2015**, *5* (11), 4946−4949.

(57) Haynes, W. M. *CRC Handbook of Chemistry and Physics*, 94th ed.; Taylor & Francis, 2013.

(58) Pourbaix, M. *Atlas of Electrochemical Equilibria in Aqueous Solutions*, 2nd ed.; National Association of Corrosion Engineers: Houston, 1974; p 644.

(59) Bratsch, S. G. Standard Electrode Potentials and Temperature Coefficients in Water at 298.15 K. *J. Phys. Chem. Ref. Data* **1989**, *18* (1), 1−21.

(60) Hansen, H. A.; Viswanathan, V.; NØrskov, J. K. Unifying Kinetic and Thermodynamic Analysis of 2 E- and 4 e - Reduction of Oxygen on Metal Surfaces. *J. Phys. Chem. C* **2014**, *118* (13), 6706−6718.

(61) Sahraie, N. R.; Kramm, U. I.; Steinberg, J.; Zhang, Y.; Thomas, A.; Reier, T.; Paraknowitsch, J.-P.; Strasser, P. Quantifying the Density and Utilization of Active Sites in Non-Precious Metal Oxygen Electroreduction Catalysts. *Nat. Commun.* **2015**, *6*, 8618.

(62) Lefèvre, M.; Dodelet, J. P. Fe-Based Catalysts for the Reduction of Oxygen in Polymer Electrolyte Membrane Fuel Cell Conditions: Determination of the Amount of Peroxide Released during Electroreduction and Its Influence on the Stability of the Catalysts. *Electrochim. Acta* **2003**, *48* (19), 2749−2760.

(63) Svane, K. L.; Hansen, H. A.; Vegge, T. A Comparison of Single and Double Co Sites Incorporated in N-Doped Graphene for the Oxygen Reduction Reaction. *J. Catal.* **2021**, *393*, 230−237.

(64) Zhang, Q.; Tan, X.; Bedford, N. M.; Han, Z.; Thomsen, L.; Smith, S.; Amal, R.; Lu, X. Direct Insights into the Role of Epoxy Groups on Cobalt Sites for Acidic H2O2 Production. *Nat. Commun.* **2020**, *11* (1), 4181.

(65) Jung, E.; Shin, H.; Lee, B. H.; Efremov, V.; Lee, S.; Lee, H. S.; Kim, J.; Hooch Antink, W.; Park, S.; Lee, K. S.; Cho, S. P.; Yoo, J. S.; Sung, Y. E.; Hyeon, T. Atomic-Level Tuning of Co−N−C Catalyst for High-Performance Electrochemical H2O2 Production. *Nat. Mater.* **2020**, *19* (4), 436−442.

(66) Xia, D.; Yang, X.; Xie, L.; Wei, Y.; Jiang, W.; Dou, M.; Li, X.; Li, J.; Gan, L.; Kang, F. Direct Growth of Carbon Nanotubes Doped with Single Atomic Fe−N4 Active Sites and Neighboring Graphitic Nitrogen for Efficient and Stable Oxygen Reduction Electrocatalysis. *Adv. Funct. Mater.* **2019**, *29* (49), 1906174.

(67) Holst-Olesen, K.; Reda, M.; Hansen, H. A.; Vegge, T.; Arenz, M. Enhanced Oxygen Reduction Activity by Selective Anion Adsorption on Non-Precious-Metal Catalysts. *ACS Catal.* **2018**, *8* (8), 7104−7112.

(68) Viswanathan, V.; Hansen, H. A.; Rossmeisl, J.; Nørskov, J. K. Universality in Oxygen Reduction Electrocatalysis on Metal Surfaces. *ACS Catal.* **2012**, *2* (8), 1654−1660.

(69) Yang, X.; Xia, D.; Kang, Y.; Du, H.; Kang, F.; Gan, L.; Li, J. Unveiling the Axial Hydroxyl Ligand on Fe-N4-C Electrocatalysts and Its Impact on the PH-Dependent Oxygen Reduction Activities and Poisoning Kinetics. *Adv. Sci.* **2020**, *7* (12), 2000176.

(70) Wang, Y.; Tang, Y.-J.; Zhou, K. Self-Adjusting Activity Induced by Intrinsic Reaction Intermediate in Fe−N−C Single-Atom Catalysts. *J. Am. Chem. Soc.* **2019**, *141* (36), 14115−14119.

(71) Chung, H. T.; Cullen, D. A.; Higgins, D.; Sneed, B. T.; Holby, E. F.; More, K. L.; Zelenay, P. Direct Atomic-Level Insight into the Active Sites of a High-Performance PGM-Free ORR Catalyst. *Science (Washington, DC, U. S.)* **2017**, *357* (6350), 479−484.

(72) Rebarchik, M.; Bhandari, S.; Kropp, T.; Mavrikakis, M. How Noninnocent Spectator Species Improve the Oxygen Reduction Activity of Single-Atom Catalysts: Microkinetic Models from First-Principles Calculations. *ACS Catal.* **2020**, *10* (16), 9129−9135.

(73) Jurca, T.; Farghal, A.; Lin, P.-H.; Korobkov, I.; Murugesu, M.; Richeson, D. S. Single-Molecule Magnet Behavior with a Single Metal Center Enhanced through Peripheral Ligand Modifications. *J. Am. Chem. Soc.* **2011**, *133* (40), 15814−15817.

(74) Xiao, M.; Gao, L.; Wang, Y.; Wang, X.; Zhu, J.; Jin, Z.; Liu, C.; Chen, H.; Li, G.; Ge, J.; He, Q.; Wu, Z.; Chen, Z.; Xing, W. Engineering Energy Level of Metal Center: Ru Single-Atom Site for Efficient and Durable Oxygen Reduction Catalysis. *J. Am. Chem. Soc.* **2019**, *141* (50), 19800−19806.

(75) Zhang, C.; Sha, J.; Fei, H.; Liu, M.; Yazdi, S.; Zhang, J.; Zhong, Q.; Zou, X.; Zhao, N.; Yu, H.; Jiang, Z.; Ringe, E.; Yakobson, B. I.; Dong, J.; Chen, D.; Tour, J. M. Single-Atomic Ruthenium Catalytic Sites on Nitrogen-Doped Graphene for Oxygen Reduction Reaction in Acidic Medium. *ACS Nano* **2017**, *11* (7), 6930−6941.

(76) He, Y.; Shi, Q.; Shan, W.; Li, X.; Kropf, A. J.; Wegener, E. C.; Wright, J.; Karakalos, S.; Su, D.; Cullen, D. A.; Wang, G.; Myers, D. J.; Wu, G. Dynamically Unveiling Metal − Nitrogen Coordination during Thermal Activation to Design High-Efficient Atomically Dispersed CoN 4 Active Sites. *Angew. Chem.* **2021**, *133* (17), 9602−9612.

(77) Li, X.; Surkus, A. E.; Rabeah, J.; Anwar, M.; Dastigir, S.; Junge, H.; Brückner, A.; Beller, M. Cobalt Single-Atom Catalysts with High Stability for Selective Dehydrogenation of Formic Acid. *Angew. Chem., Int. Ed.* **2020**, *59* (37), 15849−15854.

(78) Martinez, U.; Holby, E. F.; Babu, S. K.; Artyushkova, K.; Lin, L.; Choudhury, S.; Purdy, G. M.; Zelenay, P. Experimental and Theoretical Trends of PGM-Free Electrocatalysts for the Oxygen Reduction Reaction with Different Transition Metals. *J. Electrochem. Soc.* **2019**, *166* (7), F3136−F3142.

(79) Li, J.; Chen, M.; Cullen, D. A.; Hwang, S.; Wang, M.; Li, B.; Liu, K.; Karakalos, S.; Lucero, M.; Zhang, H.; Lei, C.; Xu, H.; Sterbinsky, G. E.; Feng, Z.; Su, D.; More, K. L.; Wang, G.; Wang, Z.; Wu, G. Atomically Dispersed Manganese Catalysts for Oxygen Reduction in Proton-Exchange Membrane Fuel Cells. *Nat. Catal.* **2018**, *1* (12), 935−945.

(80) Peng, H.; Liu, F.; Liu, X.; Liao, S.; You, C.; Tian, X.; Nan, H.; Luo, F.; Song, H.; Fu, Z.; Huang, P. Effect of Transition Metals on the Structure and Performance of the Doped Carbon Catalysts Derived From Polyaniline and Melamine for ORR Application. *ACS Catal.* **2014**, *4* (10), 3797−3805.

(81) Holst-Olesen, K.; Silvioli, L.; Rossmeisl, J.; Arenz, M. Enhanced Oxygen Reduction Reaction on Fe/N/C Catalyst in Acetate Buffer Electrolyte. *ACS Catal.* **2019**, *9* (4), 3082−3089.

(82) Gao, J.; Yang, H. B.; Huang, X.; Hung, S. F.; Cai, W.; Jia, C.; Miao, S.; Chen, H. M.; Yang, X.; Huang, Y.; Zhang, T.; Liu, B. Enabling Direct H2O2 Production in Acidic Media through Rational Design of Transition Metal Single Atom Catalyst. *Chem.* **2020**, *6* (3), 658−674.

(83) Geng, Z.; Liu, Y.; Kong, X.; Li, P.; Li, K.; Liu, Z.; Du, J.; Shu, M.; Si, R.; Zeng, J. Achieving a Record-High Yield Rate of 120.9 MgNH3mgcat.−1h−1 for N2 Electrochemical Reduction over Ru Single-Atom Catalysts. *Adv. Mater.* **2018**, *30* (40), 1803498.

(84) Wan, H.; Jensen, A. W.; Escudero-Escribano, M.; Rossmeisl, J. Insights in the Oxygen Reduction Reaction: From Metallic Electrocatalysts to Diporphyrins. *ACS Catal.* **2020**, *10* (11), 5979−5989.

(85) Varela, A. S.; Ju, W.; Bagger, A.; Franco, P.; Rossmeisl, J.; Strasser, P. Electrochemical Reduction of CO2 on Metal-Nitrogen-Doped Carbon Catalysts. *ACS Catal.* **2019**, *9* (8), 7270−7284.

(86) Wang, J.; Huang, Z.; Liu, W.; Chang, C.; Tang, H.; Li, Z.; Chen, W.; Jia, C.; Yao, T.; Wei, S.; Wu, Y.; Li, Y. Design of N-Coordinated Dual-Metal Sites: A Stable and Active Pt-Free Catalyst for Acidic Oxygen Reduction Reaction. *J. Am. Chem. Soc.* **2017**, *139* (48), 17281−17284.

(87) Wan, H.; Jiao, Y.; Bagger, A.; Rossmeisl, J. Three-Dimensional Carbon Electrocatalysts for CO2or CO Reduction. *ACS Catal.* **2021**, *11* (2), 533−541.

D.2 Paper II

Effects of Electrolyte Anion Adsorption on the Activity and Stability of Single Atom Electrocatalysts
Tipaporn Patniboon and Heine Anton Hansen
In preparation

Effects of Electrolyte Anion Adsorption on the Activity and Stability of Single Atom Electrocatalysts

Tipaporn Patniboon and Heine Anton Hansen
Department of Energy Conversion and Storage, Technical University of Denmark
Anker Engelunds Vej, 2800 Kongens Lyngby, Denmark

ABSTRACT

A single metal site incorporated in N-doped carbon (M/N/C) is a promising electrocatalyst. Here, we perform a computation investigation of the effect of electrolyte anion adsorption on the activity and stability of single-atom catalysts (MN_4) with M as transition metal and p-block metal. The MN_4 site on two different graphene structures (bulk graphene and graphene edge) is studied under electrochemical conditions for the oxygen reduction reaction (ORR) and the CO_2 reduction reaction (CO_2RR). Because of the two-dimensional nature of the catalyst, reaction intermediates and electrolyte ions can interact with both sides of the single-atom catalyst. As a result, the electrolyte anions compete with water and adsorbate on the single metal site, in some cases either poisoning or modifying the catalyst activity and thermodynamic stability. We find most electrolyte anions adsorbs on the single metal site under ORR conditions but not at the lower potentials for the CO_2RR. Still, the adsorption of water and gas molecules can occur under CO_2RR conditions. For example, under ORR conditions, the thermodynamic driving force of the *SO_4-FeN_4 site in the 0.1 M H_2SO_4 solution is about 0.47-0.56 eV lower than the *O-FeN_4 site in water, depending on the local carbon structure. Additionally, the stabilization by electrolyte anions depends on the nature of the metal atom. Our study demonstrates the important role of electrolytes and the coordination environment for the activity and stability of the M/N/C catalyst.

INTRODUCTION

Single metal atom coordinated N-doped carbon (M/N/C) has been recognized as an efficient electrocatalyst. Compared to the bulk metal, the single-atom catalyst maximizes the metal atom utilization, thus exhibiting impressively high activity and selectivity. In many experimental and theoretical studies, the Fe/N/C and Co/N/C materials have been identified as active ORR catalysts in acid electrolytes[1–5]. More recent studies showed that the M/N/C catalyst is also an efficient catalyst for the CO_2RR[6–8]. The metal centers are crucial for the reaction, and the MN_y site is suggested as the active site for the ORR[4] and CO_2RR[9]. In addition, the coordination environment is suggested to play an important role in both catalytic activity and stability[10,11]. Many studies have been made to determine the detailed structure and map the relationship between catalyst structure, activity, and stability. Many structures of the MN_4 site with different local carbon structures (i.e., MN_4C_8[3,12,13], MN_4C_{10}[11,14], MN_4C_{12}[2,4,14]) have been proposed from experimental and theoretical studies. Still, there is a wide debate about the active and stable site in the M/N/C materials.[11,15–21]

Additionally, possessing two-dimensional structures, the M/N/C catalyst is distinct from the bulk materials, where only one exposed side is responsible for its catalytic activity. Ideally, both sides of the M/N/C catalyst are exposed to electrolyte so both sides can interact with an adsorbate. An electrolyte anion or a gas molecule from the environment may adsorb on one side of the MN_y site while the other side is still available for the reaction to proceed.[22,23] The presence of the adsorbate on one side of the single metal atom will modify its electronic states, affecting the binding of the second adsorbate on the other side[24,25]. Experimental and theoretical studies have considered the effect of anions from the electrolyte or a gas molecule impurity on ORR activity. For instance, Holst-Olesen *et al.* found that the presence of anions from H_3PO_4 or CH_3COOH-containing electrolytes is beneficial for the ORR activity on the Fe/N/C catalyst[22,23]. Various combinations of the electrolyte anion ligand and the single metal center in the MN_4C_{12} structure (M = Cr, Mn, Fe, and Co) for improving the ORR activity have also been suggested in a previous theoretical study by Svane *et al.*[24] Recently, studies have also reported that the introduction of axial oxygen[26,27] or halogen atom[25] on the MN_4C structure can achieve an efficient catalyst for the CO_2RR.

Besides the catalytic activity, the stability of the MN_4 site with the presence of a fifth ligand was recently discussed. Glibin *et al.* have previously studied the dissolution reaction of two different FeN_4 sites with *F ligand based on a thermodynamic model and suggested that the fluorination on the FeN_4 sites increases the resistance of the single metal site against acid leaching[28]. Density functional theory (DFT) calculations have been used to study the dissolution reaction of the FeN_4 site embedded on a bilayer-graphene by Holby *et al*. [19] This study has suggested the presence of *OH ligand on the FeN_4C_{10} site thermodynamically prevents the single Fe metal site from dissolution[19]. Using in situ Raman spectroscopy of molecule Fe phthalocyanine (FePc) model and pyrolyzed Fe/N/C catalyst, Wei *et al.* have reported the structural dynamics of the FeN_4 active site in acid solution (0.1 M $HClO_4$). At high potential (1.0 V_{RHE}), a non-planar structure is induced by the presence of an adsorbate on the FeN_4 site, and the structure is stable against the dissolution. In contrast, the irreversible attenuation of the planar Fe-N vibration after staying at a lower potential for a long time (at 0.05 V_{RHE} for 15 min) has been suggested as evidence for the dissolution of the Fe center[29]. Using DFT simulations with ^{57}Fe Mössbaur spectroscopy data, Nematollahi *et al.* have compared the DFT calculated and experimental quadrupole splitting energy of doublets (ΔE_{QS}) for different FeN_4 structures (FeN_4C_{10}, FeN_4C_{12}, FeN_4C_8) both with and without ligands. They have suggested the FeN_4C_8 structure with a fifth ligand such as OH^- and NH_2^- could be an active and durable site for the ORR in acid conditions[20].

Here, we systematically explore the effect of electrolyte anion adsorption on the stability and activity of a single metal atom with N ligands doped into a bulk graphene terrace (MN_4C_{10}) and a graphene edge (MN_4C_A) with M = 3d, 4d, 5d, or p-block (Sn, Sb, and Bi) metal atoms. These graphene sites are selected because they are among the most stable type of sites[18]. We determine the interaction between the single metal site with the electrolyte anion and evaluate how the electrolyte adsorption thermodynamically influences the dissolution of the single metal site under electrochemical conditions relevant to the ORR and CO_2RR. We then investigate the catalytic activity with the presence of an electrolyte anion ligand for the ORR and CO_2RR. Finally, the results are used to suggest combinations of a metal atom, local carbon structure, and electrolyte for active and stable catalysts under working conditions. We show how the chemical environment around the single-atom site plays a crucial role in determining the activity and stability of the catalyst.

RESULTS AND DISCUSSION

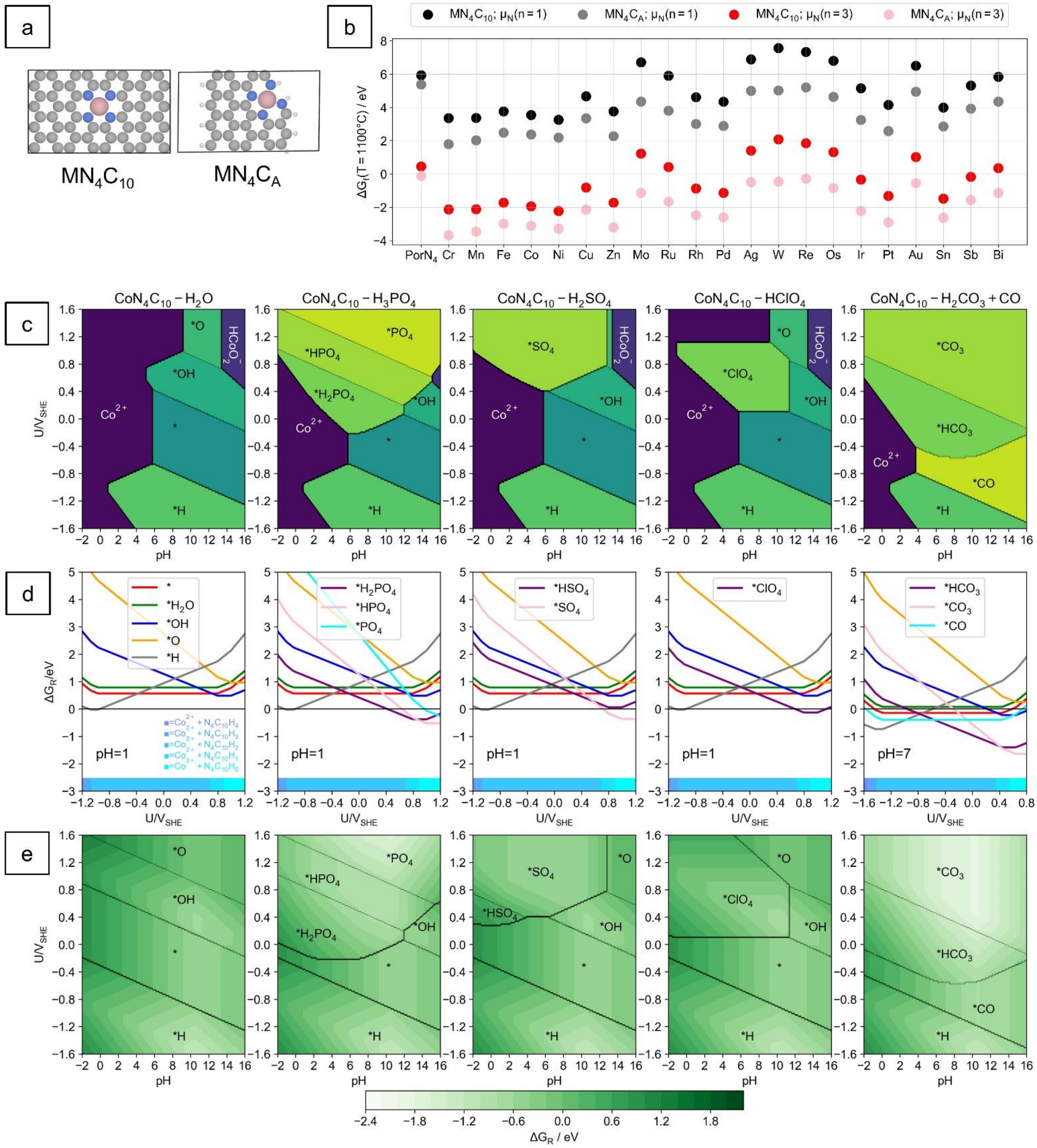

Figure 1 (a) Single atom site in bulk graphene (MN_4C_{10}) and a graphene edge (MN_4C_A) (C = grey, N = blue, H = white, M = pink). (b) ΔG_f for MN_4C_{10} and MN_4C_A sites. (c) Stability diagrams for the CoN_4C_{10} site in 0.1 M solutions. (d) ΔG_R for the sites at specific pH and (e) Stability diagrams for the CoN_4C_{10} site showing the most stable surface.

Here we consider the structural models of the MN_4C_{10} and MN_4C_A sites, as shown in **Figure 1 (a)**. The MN_4C_{10} site was previously reported as a durable site in acid[11,18,30]. Also, the MN_4C_A site, which represents the MN_4 site at the armchair edge is included in this study as previously found to be a stable and active site for the ORR under acid conditions[18,31]. We calculate the formation free energy of the single metal atom doped into bulk graphene and the graphene edge as follows:

$$\Delta G_f = E(MN_4C) - (E(C) - 6\mu_C - \mu_M - 4\mu_N) \qquad \text{Equation 1}$$

$E(MN_4C)$ is the total energy of the single metal atom doped into graphene. $E(C)$ is the total energy of a pristine graphene sheet or pristine graphene nanoribbon. μ_C is the total energy of the pristine graphene sheet per carbon atom. μ_M is the total energy of metal in its bulk structure per metal atom. The nitrogen chemical potential (μ_N) is treated as a parameter to account for the use of different nitrogen precursors in experiments[7,8,14,32–35]. μ_N is referenced to NH_3, N_2, and H_2 at 1 bar and can be expressed as $\mu_N(n) = n[G(NH_3) - (3/2)G(H_2)] + (1/2)(1 - n)G(N_2)$ where n is an integer. Thus, when n = 0, the nitrogen reference source is the N_2 gas molecule at 1 bar, and when n = 1, the nitrogen reference source is the NH_3 gas molecule. The nitrogen chemical potential can vary as a function of N_2, H_2, and NH_3 content in the environment gas during the synthesis. The n < 0 situation corresponds to synthesis under the high pressure of $N_2 + H_2$, and the n > 1 situation corresponds to the synthesis under the high pressure of NH_3.

Figure 1 (b) shows the ΔG_f of MN_4C_{10} and MN_4C_A at two different $\mu_N(n)$ with n=1,3. The temperature is considered at T=1100 ℃, a typical temperature in the M/N/C synthesis[4,6,36]. Regardless of the metal atom and $\mu_N(n)$, the single atom site is thermodynamically preferred to form at the graphene edge over bulk graphene. We find that a pyridine vacancy ($PorN_4$) is more stable on the graphene edge than the bulk graphene, and it is likely to be further stabilized if the bulk metal atom is supplied, forming the MN_4 site. Most 3d elements are thermodynamically more favorable to dope into the pyridine vacancy than the 4d-5d elements and p-elements. The formation at T=1100 ℃, becomes thermodynamic favorable when n increase from 1 to 3 (*e.g.*, under the elevated NH_3 partial pressure). Figure S1 (b) shows that the nitrogen chemical potential changes with temperature. Thus, the formation free energies depend on temperature and the nitrogen chemical potential. Let us consider the formation free energy of the CoN_4C_{10} site as an example, as shown in **Figure S1 (c)**. Increasing temperature makes the formation more favorable when n > 1. In other words, the synthesis under the high NH_3 partial pressure and high temperature (T > 500 ℃) is favorable for the single atom formation. At low temperatures (T < 100 ℃), the formation becomes thermodynamic favourable when n < 0 (*e.g.*, under high N_2+H_2 content). **Figure S2** shows the formation free energy of all considered MN_4 structures at T=25℃ and 1100 ℃ as a function of μ_N, suggesting that the considered single metal sites doped into graphene can be synthesized in a controlled experiment.

We then consider the stability of the MN_4 site in an electrochemical environment where the single metal atom can interact with anions from the electrolyte or reaction intermediates. We consider anions from commonly used electrolytes for the ORR or the CO_2RR[37–39], *e.g.*, $H_2PO_4^-$, HPO_4^{2-}, PO_4^{3-} in H_3PO_4 solution; HSO_4^-, SO_4^{2-} in H_2SO_4 solution; Cl^- in HCl solution; ClO_4^- in $HClO_4$ solution; NO_3^- in HNO_3 solution; HCO_3^- and CO_3^{2-} in H_2CO_3 solution. Furthermore, NO and CO gas molecules and CN^- in HCN solution are included as they have been found to affect the catalytic activity[40–42]. The complete list of the considered electrolyte anion and poisoning gas molecules is given in **Table S2** and **Table S3**. The adsorption of CO and NO on the single metal site considered in this study does not depend on pH and potential. We consider that the electrolyte anion adsorption on the single metal atom can compete with the water molecule. In each solution, the adsorption of anion or gas molecules on the single metal site competes with the formation of *OH, *O, and *H from water oxidation or reduction. The adsorption free energy of electrolyte anions is calculated using the thermodynamic cycle[23,24] shown in **Figure S3,** with additional calculation details in **Section 3** of the Supporting Information**.** Along with the adsorption of the adsorbate, the dissolution of the single metal atom from the graphene host into the electrolyte, resulting in dissolved metal ion (M^{x+}) and the graphene host cavity (N_4CH_n) is considered as follows[19]:

$$MN_4C + nH^+_{(aq)} \rightarrow M^{x+}_{(aq)} + N_4CH_n + (x-n)e^- \qquad \text{Equation 2}$$

More calculation details about the dissolution reaction can be found in **Section 4** of the supporting information. However, other possible degradation reactions besides the demetalltion[43,44] have been proposed to cause instability of the Fe/N/C catalyst, especially in an acidic environment. These include carbon corrosion[45], and carbon surface oxidation by H_2O_2-derived free radicals[45,46]. These possible degradation mechanisms might coincide and be interrelated[45]. Understanding the degradation mechanism is a prerequisite for the rational design of durable and stable M/N/C catalysts. We believe that the relation between the chemical environment, i.e., electrolyte and local carbon structure around the MN_y site with the demetallation, provides a better understanding of the degradation and is useful for designing intrinsic stable and active catalysts.

For example, **Figure 1 (c)** shows the stability diagram of the CoN_4C_{10} site in 0.1 M solutions. Only the most stable phase at each condition is shown in the stability diagram. It is seen that the electrolyte anion competes with water adsorption and becomes the most favorable adsorbate on a single Co atom. We further consider the relative stability (ΔG_R), which we define as the free energy difference between the M/N/C catalyst surface (either with or without the adsorbate) and the most stable dissolved species (the dissolved metal ion and carbon host cavity)[47]. Therefore**,** ΔG_R indicates the thermodynamic driving force for the dissolution of the metal atom. The more positive relative stability, the less stable the single metal atom is against dissolution. **Figure 1 (d)** shows ΔG_R as a function of applied potential at specific pH (pH = 1 for H_3PO_4, H_2SO_4, and $HClO_4$ solution and pH = 7 for H_2CO_3+CO solution). The most stable dissolved species for each potential used as a reference for ΔG_R are superimposed as horizontal bars at the bottom in **Figure 1 (d)**. At potentials above 0.6 V_{SHE} and pH=1, in 0.1 M H_3PO_4, H_2SO_4, and $HClO_4$ solution, it is seen that $*HPO_4$, $*SO_4$, and $*ClO_4$ are thermodynamically preferred on the single Co atom and further reduces the thermodynamic driving force toward dissolution compared to *OH on the single Co atom in H_2O. The relative stability of the CoN_4C_A site and the FeN_4 site on both bulk graphene and the graphene edge can be found in **Section 5** of the supplementary information, where similar trends are found. The electrolyte anion becomes thermodynamically stable on the single metal site as potential increases. Simultaneously, the corresponding thermodynamic force becomes lower than the same single metal site in H_2O. Furthermore, it is seen that the thermodynamic driving force toward the dissolution is likely to decrease as the potential increase, suggesting that the demetallation could be dominant at the low potential region in the acid condition. This is in line with the experimental study by Choi *et al.,* where the Fe demetallation from the Fe/N/C catalyst in 0.1 M $HClO_4$ was observed at potentials below 0.7 V_{RHE}[44].

At pH = 7 in 0.1 M H_2CO_3 solution with CO[6,39], at potentials below -0.4 V_{SHE}, *H is thermodynamically favorable on the single Co atom. When the potential increases, the anions become the most stable adsorbate on the Co atom ($*HCO_3$ at potential around -0.6 to 0.4 V_{SHE} and $*CO_3$ at potential above 0.4 V_{SHE}). The thermodynamic driving force is lowered by 0.46 eV when the $*HCO_3$ is stabilized on the Co atom (U = -0.6 to 0.4 V_{SHE}), and it is lowered by 2.18 eV when the $*CO_3$ is stabilized on the Co atom (U = 0.4 - 1.6 V_{SHE}), compared to the $*CO\text{-}CoN_4C_{10}$ site in H_2O+CO solution at the same potential ranges.

The ΔG_R of the most stable MN_4C_{10} and MN_4C_A surface in 0.1 M electrolytes under the ORR condition (pH=1, and U=0.80 V_{SHE}) is shown in **Figure 2(a)** and **Figure S9**, respectively. Except for $PtN_4C_{x=10,A}$, $PdN_4C_{x=10,A}$, and $AuN_4C_{x=10,A}$ sites, the other MN_4 sites are likely to be stabilized by the adsorbate. Therefore the thermodynamic driving force is reduced compared to the bare metal site. The $PtN_4C_{x=10,A}$, $PdN_4C_{x=10,A}$, and $AuN_4C_{x=10,A}$ sites weakly interact with electrolyte anions and water molecules. However, they are stable against dissolutions in a wide range of pH and potentials, even without any adsorbate. The stability of the Pt center is consistent with a previous experimental study by Li *et al.*[48], where a negligible change in the current density of a Pt/N/C catalyst under accelerated durability tests in 0.5 M H_2SO_4 has been reported. The relative stability of $IrN_4C_{x=10,A}$ is found to be lower than zero in the considered electrolytes, so it is stable under the considered ORR condition. This agrees with experiments where the Ir/N/C catalyst retains 97% of the current density during a durability test in 0.1 M $HClO_4$[49]. For $CrN_4C_{x=10,A}$, $MoN_4C_{x=10,A}$, $RuN_4C_{x=10,A}$, $ReN_4C_{x=10,A}$, and $OsN_4C_{x=10,A}$ sites, the binding strength of the anion is likely weaker than *O in most considered electrolytes. Thus, these metal sites are covered by *O. According to experimental studies by Zhang *et al.*[50] and Xiao *et al.*[51] testing the ORR performance of the Ru/N/C catalyst in 0.1 M $HClO_4$, the active RuN_4 site has been suggested to bond with axial *O or *OH.

Furthermore, a previous experimental study has shown a higher activity loss of the Mn/N/C catalyst than the Fe/N/C catalyst in 0.1 M $HClO_4$ under an accelerated stress test where the potential is cycled between 0.5 and 1.3 V_{RHE}[52]. In agreement with this experiment, in 0.1 M $HClO_4$ in the potential range of 0.5–1.3 V_{RHE} (0.44-1.25 V_{SHE} at pH = 1), we find the thermodynamic force toward the dissolution of the MnN_4 site on bulk graphene and graphene edge is about 0.78 eV and 0.57 eV higher than those of the FeN_4 site on bulk graphene and graphene edge, respectively. At U = 0.5–1.0 V_{RHE} in 0.1 M $HClO_4$, the MnN_4, and FeN_4 sites are stabilized by ClO_4. Then, ΔG_R is about 0.25 eV and 0.13 eV lower than in H_2O, respectively. However, in both H_2O and 0.1 M $HClO_4$, the MnN_4 site is found to be less stable than the FeN_4 site.

Another experimental study by Xie *et al.*[53] has determined the amount of metal leached out from the Fe/N/C and Co/N/C catalyst when the potential is cycled between 0.6–1.0 V_{RHE} in 0.5 M H_2SO_4. They have found a lower amount of metal leaching from the Co/N/C catalyst, compared to the Fe/N/C catalyst, especially when purged with O_2.[53] At U = 0.6–1.0 V_{RHE} (U=0.55–0.96 V_{SHE} at pH=1), we find that the FeN_4 and CoN_4 site on both bulk graphene and the graphene edge in 0.1 M H_2SO_4 are occupied by $*SO_4$. The thermodynamic driving force toward the dissolution of the $*SO_4\text{-}CoN_4$ site on bulk graphene and graphene edge is about 0.14 eV and 0.13 eV lower than the $*SO_4\text{-}FeN_4$ site, agreeing with the experiment. In our previous study[18], the electrolyte anion adsorption was not included. At the same condition, the $*O\text{-}FeN_4$ and $*OH\text{-}CoN_4$ is the most stable phase of the FeN_4 and CoN_4 site on both bulk and armchair edge in H_2O. The thermodynamic driving toward the dissolution of the most stable phase of the FeN_4 site on the bulk graphene and graphene edge in H_2O is only 0.04 eV and 0.00 eV higher than the CoN_4 site. This suggests that our stability calculations, including the electrolyte anion adsorption, compare well with the experimental results for M/N/C catalysts.

For CO adsorption, CO chemisorption experiments on the M/N/C catalyst (M = Fe and Mn) have suggested a stronger CO binding on the Fe-containing site over the Mn-containing site[52]. In agreement with these experiments, we find a stronger CO adsorption on the FeN_4 site than on the MnN_4 site on both bulk graphene and the graphene edge. Similar results have been reported by Svane *et al.*[54] where the

MN_4 structure is modeled based on the MN_4C_{12} structure. In addition, the stability against dissolution is also determined by the local carbon structure. We find that the MN_4 site on the graphene edge is more stable against dissolution than that on the bulk graphene. The thermodynamic driving at U = 0.8 V_{SHE}, pH = 1 of the most stable MN_4 site on the graphene edge is about 0.52 eV lower than those on the bulk graphene, on average.

Since the MN_4 site is embedded in a two-dimensional carbon sheet, the adsorbates may interact with the metal atom from both sides. The electrolyte anion can strongly adsorb on two sides, blocking the metal site from the intermediate adsorbates. Alternatively, if the interaction is weak, the electrolyte anion will adsorb only on one side, allowing the intermediate adsorbates to interact from the other. In the case of weak interaction, i.e., PdN_4C_x, PtN_4C_x, and AuN_4C_x, the bare metal site is responsible for their catalytic activity. In this work, the ORR is considered to proceed through a four-electron associative pathway, and the metal site is considered the active site. Most of the considered MN_4 sites interact with the electrolyte anion under the ORR condition. Thus, the activity of the MN_4 site toward the ORR by considering the following reaction mechanism[23] on the catalyst surface:

$$*A^n/*A^n + ne^- \rightarrow */*A^n + A^{n-} \quad ; \Delta G(ORR)_0 \qquad \text{Equation 3}$$
$$*A^n + O_2 + (H^+ + e^-) \rightarrow *OOH/*A^n \quad ; \Delta G(ORR)_1 \qquad \text{Equation 4}$$
$$*OOH/*A^n + (H^+ + e^-) \rightarrow *O/*A^n + H_2O \quad ; \Delta G(ORR)_2 \qquad \text{Equation 5}$$
$$*O/*A^n + (H^+ + e^-) \rightarrow *OH/*A^n \quad ; \Delta G(ORR)_3 \qquad \text{Equation 6}$$
$$*OH/*A^n + (H^+ + e^-) \rightarrow */*A^n + H_2O \quad ; \Delta G(ORR)_4 \qquad \text{Equation 7}$$

$*A^n/*A^n$ is the electrolyte anions (or gas molecules with n = 0) adsorbed on both sides. $*X/*A^n$ stands for the electrolyte anion adsorbs on one side and the reaction intermediate on another, where *X = *O, *OH, *OOH. $\Delta G(*O/*A^n)$ and $\Delta G(*OOH/*A^n)$ are obtained from a scaling relation established for $\Delta G(*O)$ vs. $\Delta G(*OH)$ and $\Delta G(*OH)$ vs. $\Delta G(*OOH)$ on the bare metal site (**Figure S12**), respectively. Thus, only $\Delta G(*OH/*A^n)$ is explicitly calculated in this study. The possible electrolyte anion participating in the reaction is considered the most stable adsorbate at pH = 1 and U = 0.80 $V_{SHE,}$ as shown in Figures 2 (a) and **S9**. The corresponding ORR activity is also calculated at this condition. The change in free reaction energy with an applied potential (U_{SHE}) and pH is calculated using the computational hydrogen electrode (CHE)[55]. The thermodynamic barrier of the limiting step (ΔG_{max}) along the ORR pathway at pH = 1, U = 0.80 V_{SHE} is considered the ORR activity descriptor, which is given in **Figure S14-S15**. The limiting potential (U_L) is also calculated if all elementary steps are electrochemical, as shown in **Figure S16-S17**. This includes when NO and CO gas molecules are not thermodynamically stable on both sides of the metal atom.

The ORR activity of the FeN_4 site in 0.1 M H_3PO_4, H_2SO_4, $HClO_4$, and HCl is firstly discussed. At U = 0.8 V_{SHE} and pH = 1, one electrolyte anion (HPO_4^{2-}, SO_4^{2-}, ClO_4^{-}, and Cl^-) bonds with the FeN_4C_{10} and FeN_4C_A sites stronger than the water molecule, so the electrolyte anion can affect the ORR. **Figure S13** shows free energy diagrams of the ORR on the FeN_4C_{10} and FeN_4C_A sites at U = 0.80 V_{SHE} and pH = 1. The anion removal step limits the ORR on the FeN_4C_{10} site in 0.1 M $HClO_4$ and HCl. In 0.1 H_3PO_4, the thermodynamic barrier of the limiting step is the barrier of the anion removal plus the barrier of the formation *OOH on the FeN_4C_{10} site. While in 0.1 M H_2SO_4, the ORR is limited by the reduction of *OH to H_2O. The lowest ΔG_{max} at U = 0.80 V_{SHE} and pH = 1 for the FeN_4C_{10} site in these electrolytes is found for H_2SO_4 (0.02 eV) < $HClO_4$ (0.13 eV) < H_3PO_4 (0.26 eV) < HCl (0.56 eV). The U_L with the most stable adsorbate at U = 0.80 V_{SHE} and pH = 1 as the ligand on the FeN_4C_{10} site is found in the following order:

H_2SO_4 (0.78 V_{SHE}) > $HClO_4$ (0.67 V_{SHE}) > H_3PO_4 (0.60 V_{SHE}) > HCl (0.24 V_{SHE}). These results suggest that the ORR activity of the FeN_4C_{10} site is in the following order: H_2SO_4 > $HClO_4$ > H_3PO_4 > HCl.

For the FeN_4C_A site in 0.1 M H_3PO_4, and HCl, the ORR at U = 0.80 $V_{SHE,}$ and pH = 1 is limited by the anion removal step. In 0.1 M H_2SO_4, the thermodynamic barrier of the limiting step is the barrier of the anion removal plus the formation of *OOH on the FeN_4C_A site. The ORR is limited by the reduction of *OH to H_2O for the FeN_4C_A site in 0.1 M $HClO_4$. The lowest ΔG_{max} at U = 0.80 V_{SHE} and pH = 1 for the FeN_4C_A site in these electrolytes is found to be H_3PO_4 (0.01 eV) < H_2SO_4 (0.08 eV) < $HClO_4$ (0.13 eV) < HCl (0.54 eV). The U_L is found in the following order: H_3PO_4 (0.79 V_{SHE}) > H_2SO_4 (0.76 V_{SHE}) > $HClO_4$ (0.67 V_{SHE}) > HCl (0.26 V_{SHE}). These results suggest that the ORR activity of the FeN_4C_A site is in the following order: H_3PO_4 > H_2SO_4 > $HClO_4$ > HCl. It is seen that the ORR activity obtained from FeN_4C_A and FeN_4C_{10} sites is different, implying a significant role of the local carbon structure around the FeN_4 site in the catalytic activity.

Previous experimental results by Holst-Olesen *et al.*[23] and Hu *et al.*[56] have reported that the ORR activity of the Fe/N/C catalyst in H_3PO_4 is higher than in the other considered electrolytes. Holst-Olesen *et al.*[23] reported the ORR activity in the following order: H_3PO_4 > $HClO_4$ ≈ H_2SO_4 > HCl in 0.5 M electrolyte. At 0.8 V_{RHE}, Hu *et al.*[56] reported the ORR activity of the Fe/N/C catalyst in the following order: H_3PO_4 > H_2SO_4 > $HClO_4$ > HCl. Modeling the Fe/N/C catalyst by the FeN_4C_{12} structure, Holst-Olesen *et al.*[23] have reported a good agreement between the theoretical and experimental ORR activity trend. Our calculation results obtained from the FeN_4C_A site agree with the experiments by Hu *et al.*[56] and Holst-Olesen *et al.*[23]. Both experimental studies by Holst-Olesen *et al.*[23] and Hu *et al.*[56] have suggested a strong poison effect on the Fe/N/C catalyst by Cl^- in HCl solution. In our findings, the thermodynamic barrier of the limiting step in 0.1 M HCl is also higher than in 0.1 M $HClO_4$ and H_2SO_4 solution. Additionally, Hu *et al.*[56] have also suggested that the catalytic activity of the Fe/N/C catalyst can be poisoned by ClO_4^- in the $HClO_4$ solution. Our calculation results show that the ClO_4^- can be adsorbed on the FeN_4 site on bulk graphene and graphene edge at U = 0.80 V_{SHE} and pH = 1. Also, we find that the ClO_4^- anions thermodynamically block the FeN_4C_{10} site at this condition. These results disagree with previous theoretical and experimental studies[22,24] based on the MN_4C_{12} (M = Cr, Fe, Mn, Co) structure where the ClO_4^- anion has been found not to adsorb on the MN_4 site at U = 0.75 V in 0.5 M $HClO_4$. As discussed previously, the discrepancy could be due to the different coordination environments around the MN_4 site, which could be different in each experiment, depending on the synthesis process.

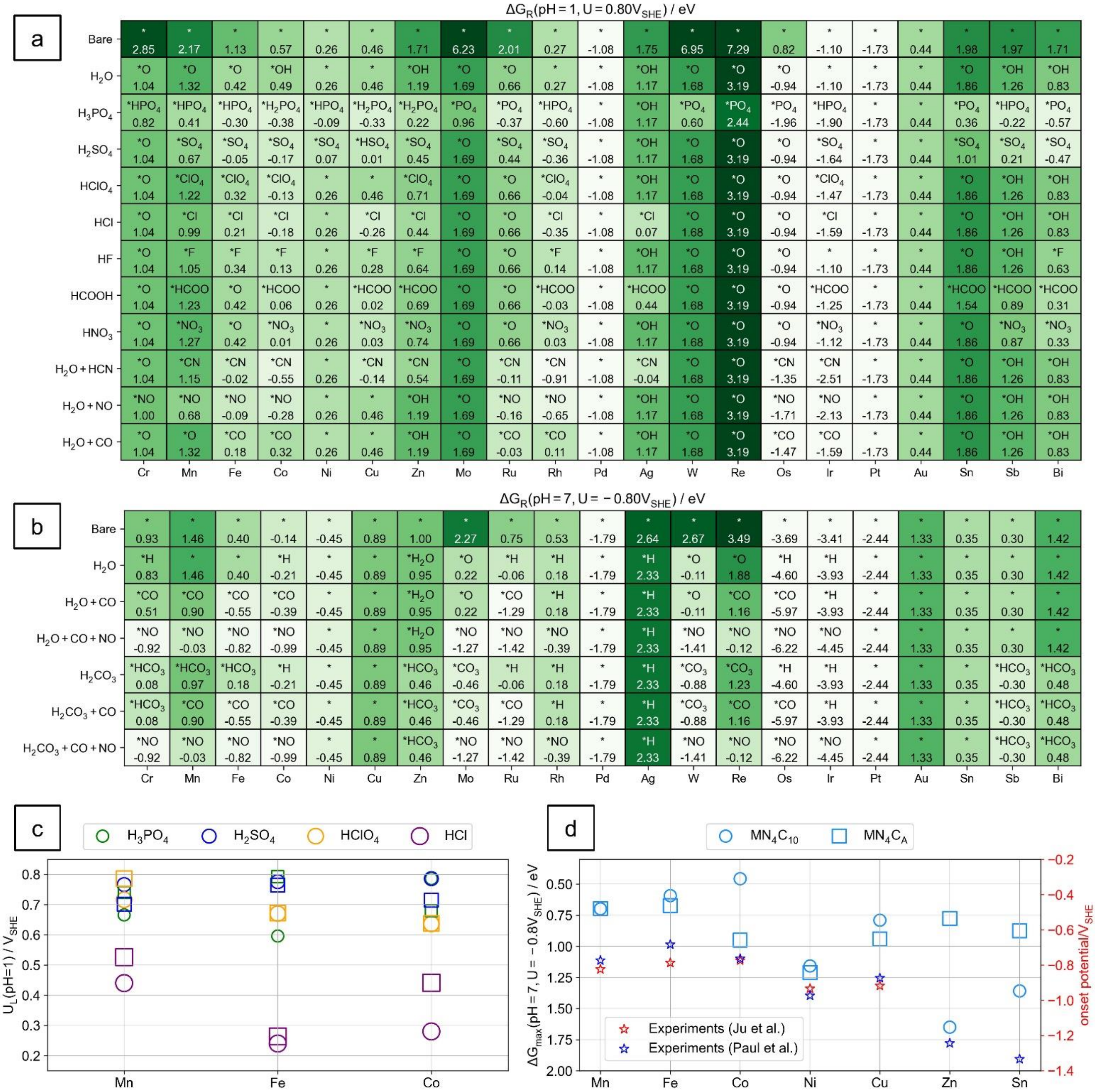

$\Delta G_R(pH=1, U=0.80V_{SHE})$ / eV

	Cr	Mn	Fe	Co	Ni	Cu	Zn	Mo	Ru	Rh	Pd	Ag	W	Re	Os	Ir	Pt	Au	Sn	Sb	Bi
Bare	* 2.85	* 2.17	* 1.13	* 0.57	* 0.26	* 0.46	* 1.71	* 6.23	* 2.01	* 0.27	* -1.08	* 1.75	* 6.95	* 7.29	* 0.82	* -1.10	* -1.73	* 0.44	* 1.98	* 1.97	* 1.71
H_2O	*O 1.04	*O 1.32	*O 0.42	*OH 0.49	* 0.26	* 0.46	*OH 1.19	*O 1.69	*O 0.66	* 0.27	* -1.08	*OH 1.17	*O 1.68	*O 3.19	*O -0.94	* -1.10	* -1.73	* 0.44	*O 1.86	*OH 1.26	*OH 0.83
H_3PO_4	$*HPO_4$ 0.82	$*HPO_4$ 0.41	$*HPO_4$ -0.30	$*H_2PO_4$ -0.38	$*HPO_4$ -0.09	$*H_2PO_4$ -0.33	$*H_2PO_4$ 0.22	$*PO_4$ 0.96	$*PO_4$ -0.37	$*HPO_4$ -0.60	* -1.08	*OH 1.17	$*PO_4$ 0.60	$*PO_4$ 2.44	$*PO_4$ -1.96	$*HPO_4$ -1.90	* -1.73	* 0.44	$*PO_4$ 0.36	$*HPO_4$ -0.22	$*PO_4$ -0.57
H_2SO_4	*O 1.04	$*SO_4$ 0.67	$*SO_4$ -0.05	$*SO_4$ -0.17	$*SO_4$ 0.07	$*HSO_4$ 0.01	$*SO_4$ 0.45	*O 1.69	$*SO_4$ 0.44	$*SO_4$ -0.36	* -1.08	*OH 1.17	*O 1.68	*O 3.19	*O -0.94	$*SO_4$ -1.64	* -1.73	* 0.44	$*SO_4$ 1.01	$*SO_4$ 0.21	$*SO_4$ -0.47
$HClO_4$	*O 1.04	$*ClO_4$ 1.22	$*ClO_4$ 0.32	$*ClO_4$ -0.13	* 0.26	* 0.46	$*ClO_4$ 0.71	*O 1.69	*O 0.66	$*ClO_4$ -0.04	* -1.08	*OH 1.17	*O 1.68	*O 3.19	*O -0.94	$*ClO_4$ -1.47	* -1.73	* 0.44	*O 1.86	*OH 1.26	*OH 0.83
HCl	*O 1.04	*Cl 0.99	*Cl 0.21	*Cl -0.18	* 0.26	*Cl -0.26	*Cl 0.44	*O 1.69	*O 0.66	*Cl -0.35	* -1.08	*Cl 0.07	*O 1.68	*O 3.19	*O -0.94	*Cl -1.59	* -1.73	* 0.44	*O 1.86	*OH 1.26	*OH 0.83
HF	*O 1.04	*F 1.05	*F 0.34	*F 0.13	* 0.26	*F 0.28	*F 0.64	*O 1.69	*O 0.66	*F 0.14	* -1.08	*OH 1.17	*O 1.68	*O 3.19	*O -0.94	* -1.10	* -1.73	* 0.44	*O 1.86	*OH 1.26	*F 0.63
HCOOH	*O 1.04	*HCOO 1.23	*O 0.42	*HCOO 0.06	* 0.26	*HCOO 0.02	*HCOO 0.69	*O 1.69	*O 0.66	*HCOO -0.03	* -1.08	*HCOO 0.44	*O 1.68	*O 3.19	*O -0.94	*HCOO -1.25	* -1.73	* 0.44	*HCOO 1.54	*HCOO 0.89	*HCOO 0.31
HNO_3	*O 1.04	$*NO_3$ 1.27	*O 0.42	$*NO_3$ 0.01	* 0.26	$*NO_3$ 0.03	$*NO_3$ 0.74	*O 1.69	*O 0.66	$*NO_3$ 0.03	* -1.08	*OH 1.17	*O 1.68	*O 3.19	*O -0.94	$*NO_3$ -1.12	* -1.73	* 0.44	*O 1.86	$*NO_3$ 0.87	$*NO_3$ 0.33
H_2O+HCN	*O 1.04	*CN 1.15	*CN -0.02	*CN -0.55	* 0.26	*CN -0.14	*CN 0.54	*O 1.69	*CN -0.11	*CN -0.91	* -1.08	*CN -0.04	*O 1.68	*O 3.19	*CN -1.35	*CN -2.51	* -1.73	* 0.44	*O 1.86	*OH 1.26	*OH 0.83
H_2O+NO	*NO 1.00	*NO 0.68	*NO -0.09	*NO -0.28	* 0.26	* 0.46	*OH 1.19	*O 1.69	*NO -0.16	*NO -0.65	* -1.08	*OH 1.17	*O 1.68	*O 3.19	*NO -1.71	*NO -2.13	* -1.73	* 0.44	*O 1.86	*OH 1.26	*OH 0.83
H_2O+CO	*O 1.04	*O 1.32	*CO 0.18	*CO 0.32	* 0.26	* 0.46	*OH 1.19	*O 1.69	*CO -0.03	*CO 0.11	* -1.08	*OH 1.17	*O 1.68	*O 3.19	*CO -1.47	*CO -1.59	* -1.73	* 0.44	*O 1.86	*OH 1.26	*OH 0.83

$\Delta G_R(pH=7, U=-0.80V_{SHE})$ / eV

	Cr	Mn	Fe	Co	Ni	Cu	Zn	Mo	Ru	Rh	Pd	Ag	W	Re	Os	Ir	Pt	Au	Sn	Sb	Bi
Bare	* 0.93	* 1.46	* 0.40	* -0.14	* -0.45	* 0.89	* 1.00	* 2.27	* 0.75	* 0.53	* -1.79	* 2.64	* 2.67	* 3.49	* -3.69	* -3.41	* -2.44	* 1.33	* 0.35	* 0.30	* 1.42
H_2O	*H 0.83	* 1.46	* 0.40	*H -0.21	* -0.45	* 0.89	$*H_2O$ 0.95	*O 0.22	*H -0.06	*H 0.18	* -1.79	*H 2.33	*O -0.11	*O 1.88	*H -4.60	*H -3.93	* -2.44	* 1.33	* 0.35	* 0.30	* 1.42
H_2O+CO	*CO 0.51	*CO 0.90	*CO -0.55	*CO -0.39	* -0.45	* 0.89	$*H_2O$ 0.95	*O 0.22	*CO -1.29	*H 0.18	* -1.79	*H 2.33	*O -0.11	*CO 1.16	*CO -5.97	*H -3.93	* -2.44	* 1.33	* 0.35	* 0.30	* 1.42
$H_2O+CO+NO$	*NO -0.92	*NO -0.03	*NO -0.82	*NO -0.99	* -0.45	* 0.89	$*H_2O$ 0.95	*NO -1.27	*NO -1.42	*NO -0.39	* -1.79	*H 2.33	*NO -1.41	*NO -0.12	*NO -6.22	*NO -4.45	* -2.44	* 1.33	* 0.35	* 0.30	* 1.42
H_2CO_3	$*HCO_3$ 0.08	$*HCO_3$ 0.97	$*HCO_3$ 0.18	*H -0.21	* -0.45	* 0.89	$*HCO_3$ 0.46	$*CO_3$ -0.46	*H -0.06	*H 0.18	* -1.79	*H 2.33	$*CO_3$ -0.88	$*CO_3$ 1.23	*H -4.60	*H -3.93	* -2.44	* 1.33	* 0.35	$*HCO_3$ -0.30	$*HCO_3$ 0.48
H_2CO_3+CO	$*HCO_3$ 0.08	*CO 0.90	*CO -0.55	*CO -0.39	* -0.45	* 0.89	$*HCO_3$ 0.46	$*CO_3$ -0.46	*CO -1.29	*H 0.18	* -1.79	*H 2.33	$*CO_3$ -0.88	*CO 1.16	*CO -5.97	*H -3.93	* -2.44	* 1.33	* 0.35	$*HCO_3$ -0.30	$*HCO_3$ 0.48
$H_2CO_3+CO+NO$	*NO -0.92	*NO -0.03	*NO -0.82	*NO -0.99	* -0.45	* 0.89	$*HCO_3$ 0.46	*NO -1.27	*NO -1.42	*NO -0.39	* -1.79	*H 2.33	*NO -1.41	*NO -0.12	*NO -6.22	*NO -4.45	* -2.44	* 1.33	* 0.35	$*HCO_3$ -0.30	$*HCO_3$ 0.48

Figure 2 ΔG_R of the most stable adsorbate on MN_4C_{10} in 0.1 M electrolytes at: (a) pH=1, U=0.80 V_{SHE}. (b) pH=7, U=-0.80 V_{SHE}. The text insert indicates the most stable adsorbate on the metal site and its corresponding ΔG_R in eV. (c) U_L for the ORR on MN_4C_{10} (circle) and MN_4C_A (square) at pH=1 with M = Mn, Fe, and Co and (d) ΔG_{max} for the CO_2RR to CO on MN_4C_{10} (circle) and MN_4C_A (square) at pH=7 and U=-0.8 V_{SHE} with M = Mn, Fe, Co, Ni, Cu, Zn, and Sn.

Evaluating the ORR catalytic activity in 0.5 M H_2SO_4, Martinez *et al.*[57] have reported the following order of onset for the M/N/C catalyst: Mn < Co < Fe and their theoretical study has suggested an *OH ligand as a part of the active site. The theoretical studies by Svane *et al.*[24] based on the MN_4C_{12} structure have reported the same order for the liming potential in 0.5 M H_2SO_4. They have found $*HSO_4$ as a ligand on the FeN_4C_{12} and MnN_4C_{12} site while $*H_2O$ on the CoN_4C_{12} site in 0.5 M H_2SO_4[24]. According to our calculations, the ligand on MnN_4, FeN_4, and CoN_4 sites on both bulk graphene and graphene edge in 0.1 M H_2SO_4 is $*SO_4$. As shown in **Figure 2 (c)**, the U_L on the MN_4C_{10} structure for these three elements in 0.1 M H_2SO_4 at pH = 1 differs by 0.01 V_{SHE}, and the U_L order is Mn (0.77 V_{SHE}) < Fe (0.78 V_{SHE}) < Co (0.79 V_{SHE}). While U_L calculated from the MN_4C_A structure in 0.1 M H_2SO_4 is in the following order: Mn (0.70 V_{SHE}) < Co (0.71 V_{SHE}) < (0.76 V_{SHE}), agreeing with the onset potential order from the experiments. Another experimental study testing the ORR performance of the Co/N/C and Mn/N/C catalyst in 0.1 M $HClO_4$ solution has reported the onset potential order as Mn < Co[58]. For both MN_4C_{10} and MN_4C_A sites in 0.1 M $HClO_4$, we find $*ClO_4$-MnN_4 and $*ClO_4$-CoN_4 sites serve as the active center, and the U_L is Co < Mn. Based on the MN_4C_{12} structure studied by Svane *et al.*, the ligand is *OH and $*H_2O$ on MnN_4C_{12} and CoN_4C_{12}, respectively, and the U_L is Mn < Co[2424].

Previous experimental results have shown a poisoning of Fe/N/C catalysts by CN^- in an acid environment[59]. This is consistent with our calculations on FeN_4C_{10} and FeN_4C_A structures and the FeN_4C_{12} site in the previous computational study[24]. At U > 0 V_{SHE}, pH = 1, the ORR on the FeN_4C_{10} and FeN_4C_A sites process by the least thermodynamic barrier for removing one *CN anion from the FeN_4 sites. The Fe site and other metal sites such as Mn, Co, Ru, Rh, Os, and Ir on both bulk graphene and graphene edge where two *CN can limit the ORR anions by blocking the metal site at U > 0 V_{SHE}, pH = 1. Additionally, we find that NO gas molecules are thermodynamically favorable on both sides of the IrN_4C_{10} and IrN_4C_A structure. In the potential range of 0 - 0.8 V_{SHE} and pH = 1, the ORR proceeds with the least thermodynamic hindrance for removing one *NO from the IrN_4 site. We find that both CO and NO gas molecules are thermodynamically stable on both sides of the RuN_4C_A and OsN_4C_A structures. However, at U = 0.80 V_{SHE}, pH = 1, the binding of *OH is stronger than the 2nd *CO or *NO. As a result, the ORR is thermodynamically limited by the reduction of *OH to H_2O.

Comparing our present calculation results with the previous studies[23,24], it is seen that the nature of the metal center of the M/N/C catalyst and the coordination environment plays a crucial role in determining the electrolyte adsorption and its corresponding catalytic performance in acid environments.

Figures 2 (b) and **S10-S11** show ΔG_R of the most stable MN_4C_{10} and MN_4C_A surface in 0.1 M electrolytes under the CO_2RR condition (pH = 7, and U = -0.8 V_{SHE}). At this condition, we include 0.1 M H_2CO_3 solution as the electrolyte used in the experiments[6,8,39]. In contrast to the ORR conditions, the anion from most of the considered electrolytes, except from 0.1 M H_2CO_3, do not bind with the single metal site. Thus, most considered electrolytes possibly have little impact on catalytic activity and stability of the MN_4 site under the CO_2RR. For all considered electrolytes, except 0.1 M H_2CO_3, the stability under the CO_2RR-related condition is the same as in H_2O. We find that *H can occupy the CoN_4, RuN_4, RhN_4, OsN_4, and IrN_4 sites on both bulk graphene and the graphene edge in H_2O. While the $MoN_4C_{x=10,A}$, $WN_4C_{x=10,A}$, and ReN_4C_{10} sites are occupied by *O. This is the same as under the ORR condition but with a lower thermodynamic driving force toward the dissolution. It is also seen that *CO (in H_2O+CO solution) and *NO (in H_2O+CO+NO solution) can be thermodynamically stable on many metal sites both on bulk graphene and the graphene edge. We find that NO is likely to bind stronger than CO to the metal site. The binding of CN^- is weaker than that of CO. Then CN^- is unlikely to either block the metal site or affect the CO_2RR. In 0.1 M H_2CO_3, the $MoN_4C_{x=10,A}$, $WN_4C_{x=10,A}$, and ReN_4C_{10} sites bind with the $*CO_3$ via two oxygen atoms. For other metal sites, we find that $^*HCO_3$ is thermodynamically stable on $CrN_4C_{x=10,A}$, $MnN_4C_{x=10,A}$, FeN_4C_{10}, ZnN_4C_{10}, $SbN_4C_{x=10,A}$, and $BiN_4C_{x=10,A}$ sites. When the CO gas molecule is present (such as in 0.1 M H_2CO_3 + CO), the *CO can compete with $^*HCO_3$ and $^*CO_3$ and bind to the metal sites. It can be seen that the most stable adsorbate on both MN_4C_{10} and MN_4C_A sites in H_2O+CO and 0.1 M H_2CO_3+CO is slightly different. Like the ORR above conditions, the NiN_4, CuN_4, PdN_4, PtN_4, and AuN_4 sites on both bulk graphene and the graphene edge are unoccupied by an adsorbate.

Recently, a kinetic model fit the experimental data by Zeng *et al.*[60] demonstrated the role of the bicarbonate (HCO_3) buffer on the electrochemical CO_2RR catalyzed by cobalt phthalocyanine (CoPC). They suggested that the active site can be poisoned by HCO_3^- via electrosorption at low overpotential while the bicarbonate acts as a proton donor at higher overpotential. Defining the onset potential for CO production to be the applied electrode potential at which the TOF of the CO formation exceeds 0.2 mmol/(h m^2_{active}), the experiments have found that the Co/N/C catalyst starts producing CO at around -0.36 V_{RHE}[6] (-0.77 V_{SHE} at pH = 7). Around this potential, it is seen from our calculations in **Figure 1 (c)** and **Figure S5** that *H, *CO, and $^*HCO_3$ could be absorbed on the CoN_4 site on both bulk graphene and the graphene edge. At more negative potential (high overpotential), the *H is more stable than *CO and $^*HCO_3$. At a more positive potential (low overpotential), the $^*HCO_3$ becomes the most favorable adsorbate. Furthermore, a series of M/N/C catalysts (M = Mn^{3+}, Fe^{3+}, Co^{2+}, Ni^{2+}, Cu^{2+}, Zn^{2+}, and Sn^{2+}) have been synthesized and evaluated for electrochemical CO_2 reduction in aqueous electrolyte (0.5 M $KHCO_3$ and 0.5 M K_2SO_4) by Paul *et al.*[8]. They have found that the Cu/N/C catalyst can produce hydrocarbon products in significant amounts which have also been demonstrated to correlate with a partial reduction of Cu^{2+} to Cu^0 accompanied by a partial demetallation of the CuN_4 site. According to our calculation at CO_2RR condition in 0.1 M H_2CO_3+CO, both the CuN_4 site and the MnN_4 site on both bulk graphene and the graphene edge have a relatively higher thermodynamic driving force than other metal elements. While our calculation agrees with the experiments for the CuN_4 site by Paul *et al.*[8], it is inconclusive for the MnN_4 site since there are no available experiments on the transformation of the Mn/N/C catalyst during the CO_2RR.

Similar to the ORR mechanism with the electrolyte anion ligand, the following mechanism for CO_2 to CO formation is considered:

$$^*A^n/^*A^n + ne^- \rightarrow {}^*/^*A^n + A^{n-} \quad ; \Delta G(CO_2RR)_0 \qquad \text{Equation 8}$$

$$^*/^*A^n + CO_2 + (H^+ + e^-) \rightarrow {}^*COOH/^*A^n \quad ; \Delta G(CO_2RR)_1 \qquad \text{Equation 9}$$

$$^*COOH/^*A^n + (H^+ + e^-) \rightarrow {}^*CO/^*A^n + H_2O \quad ; \Delta G(CO_2RR)_2 \qquad \text{Equation 10}$$

$$^*CO/^*A^n \rightarrow CO(g) + {}^*/^*A^n \quad ; \Delta G(CO_2RR)_3 \qquad \text{Equation 11}$$

The possible electrolyte anion participating in the reaction is considered to be the most stable adsorbate at pH = 7 and U = -0.8 V_{SHE}. The CO_2 to CO formation activity is also considered in this condition. **Figure S19-S20** shows the thermodynamic barrier of the limiting step (ΔG_{max}) for the CO_2 to CO formation at pH = 7 and U = -0.8 V_{SHE} on the MN_4 site. We find that the NO gas molecules thermodynamically prefer both sides of the IrN_4C_{10}, IrN_4C_A, and ReN_4C_A structures. In the H_2CO_3 + CO + NO solution at pH = 7 and U = -0.8 V_{SHE}, the limiting step is removing one NO gas molecule plus forming *COOH on these metal sites. Similarly, the CO gas molecules can be thermodynamically stable on both sites of $ReN_4C_{x=10,A}$, $OsN_4C_{x=10,A}$, RuN_4C_A, and WN_4C_A sites. In H_2CO_3 + CO solution at pH = 7 and U = -0.8 V_{SHE}, the limiting step on these metal sites is also the removal of one CO gas molecule plus the formation *COOH.

We compare our calculation results with the experimental studies shown in **Figure 2 (d).** An experimental study by Ju *et al.*[6]. has evaluated the electrochemical performance of the M/N/C catalyst (M=Mn. Fe. Co, Ni, and Cu) for CO_2 to CO formation and reported the order of the onset potential in 0.1 M $KHCO_3$ as follows: Co (-0.36 V_{RHE}) > Fe (-0.37 V_{RHE}) > Mn (-0.41 V_{RHE}) > Cu (-0.52 V_{RHE}) > Ni (-0.36 V_{RHE}). Their theoretical results have also suggested that the potential-determining step on these M/N/C catalysts is the first proton-coupled electron transfer reduction of CO_2 to form *COOH[6]. The experimental onset potentials reported by Ju *et al.* are marked with red stars in **Figure 2 (d)** and use the y-axis on the right. In 0.1 M H_2CO_3 with CO, the CO_2 to CO formation on the MN_4C_{10} structure is thermodynamically limited by the reduction of CO_2 to *COOH, as shown in **Figure S18 (a)**. The thermodynamic barrier of the limiting step for the CO_2 to CO formation at U = -0.80 $V_{SHE,}$ and pH = 7 is found to be in the following order: Co (0.46 eV) < Fe (0.59 eV) < Mn (0.70 eV) < Cu (0.79 eV) < Ni (1.16 eV), agreeing with the onset potential order reported by Ju *et al.*[6]. It should be noted that at this condition in 0.1 M H_2CO_3+CO, the ligand is found to be *CO on the CoN_4C_{10}, $FeN_4C_{10,}$ and MnN_4C_{10} sites. In contrast, the CuN_4C_{10} and NiN_4C_{10} site has no ligand on the metal site at this condition. For the MN_4C_A structure in 0.1 M H_2CO_3 with CO, the ligand at U = -0.80 $V_{SHE,}$ and pH = 7 is *H on the CoN_4C_A site and *CO on the FeN_4C_A and MnN_4C_A sites. There is also no ligand on both CuN_4C_A and NiN_4C_A under this condition. The CO_2RR to CO on these metal sites are also limited by the reduction of CO_2 to *COOH, as shown in **Figure S18 (b)**, and the thermodynamic barrier of the limiting step at U = -0.80 $V_{SHE,}$ and pH = 7 is in the following order: Fe (0.67 eV) < Mn (0.70 eV) < Cu (0.94 eV) < Co (0.95 eV) < Ni (1.21 eV), deviating from the experimental trend.

Furthermore, Li *et a*l.[7] have synthesized and evaluated the activity toward CO formation in 0.1 M $KHCO_3$ for the M/N/C catalysts with M = Mn, Fe, Co, Ni, and Cu. They have reported the following order of CO partial current density at U = -0.6 V_{RHE}: Co > Fe > Ni > Cu > Mn. Our thermodynamic barrier on the MN_4C_{10} structure agrees with this experiment only for the relative order between Co, Fe, and Mn. In another experimental study by Paul *et a*l. [8], the M/N/C catalyst with M = Mn, Fe, Co, Ni, Cu, Zn, and Sn was synthesized and tested for the CO_2RR in gas diffusion electrodes. The experimental onset potential for the CO formation in 0.5 M $KHCO_3$+0.5 M K_2SO_4 at pH=7.5 has been reported in the following order: Fe (-0.27 V_{RHE}) > Co (-0.35 V_{RHE}) > Mn (-0.36 V_{RHE}) > Cu (-0.46 V_{RHE}) > Ni (-0.56 V_{RHE}) > Zn (-0.83 V_{RHE}) > Sn (-0.92 V_{RHE}). The experiential onset potentials reported by Paul *et al.*[8] are marked with blue stars in **Figure 2 (d).** Our thermodynamic barrier based on the MN_4C_{10} and MN_4C_A structure in 0.1 M H_2CO_3 with CO does not give the exact order as the experimental results by Paul *et al.* [8] It should be noted that other possible sites with different coordination environments[60–62] could be involved in the catalytic process and that the distribution of active sites could be different in each experiment, depending on the synthesis process. Also, the onset potential is defined differently in these two experiments, and we assume that the CO_2RR to CO in the experiments is limited by the reduction of CO_2 to *COOH, similar to our calculations.

On top of that, the ligand on the metal site is defined to be the most stable adsorbate at U = -0.8 V_{SHE} and pH = 7. The most stable ligand could be different when the potential slightly deviates from U = -0.8 V_{SHE} on some metal sites, i.e., the CoN_4C_{10} site. In **Figure S22**, we consider the thermodynamic barrier of the limiting step on the metal site in 0.1 M H_2CO_3+CO at -1.0 V_{SHE} and pH = 7, and the most stable adsorbate at U=-1.0 V_{SHE}, pH = 7 is considered to be a ligand on the metal site. At this condition, most of the considered MN_4C_{10} sites still have the same ligand, except the CoN_4C_{10} site, where the ligand is now *H. For the MN_4C_{10} structure, the limiting step is still the reduction of CO_2 to *COOH step, as shown in **Figure S21(a)**. The thermodynamic barrier of the limiting step at U = -1.0 V_{SHE}, pH = 7 is found in the following order: Fe < Mn < Co < Cu < Ni < Sn < Zn. Due to the ligand change, the most active site among the considered MN_4C_{10} structures is shifted from the CoN_4C_{10} site to the FeN_4C_{10} site. Still, this order differs slightly from the experimental trend reported by Paul *et al.* [8]

It should be noted that the oxidation state on the single metal atom in the pristine MN_4 structure is considered to be +2 in this work. Our calculations give a relatively high thermodynamic barrier for the NiN_4 site on both bulk graphene and graphene edge, compared to the FeN_4 site. In contrast, the Fe/N/C and particularly Ni/N/C catalyst have been suggested as highly promising for selective CO production[6–8]. One possible explanation is that the $Ni^{2+}N_4$ site is not active for the CO_2RR. According to a previous study by Li *et al.*, the $Ni^{1+}N_4C_{10}$ site bind with CO_2 more strongly than the $Ni^{2+}N_4C_{10}$, so the $Ni^{1+}N_4C_{10}$ site is predicted to have higher activity toward CO formation than the $Ni^{2+}N_4C_{10}$ site. In fact, by DFT calculations, they have found that the $Ni^{1+}N_4C_{10}$ site has the highest activity among the considered MN_4 sites in their study where M = Mn^{2+}(*O), Fe^{2+}(*H_2O), Co^{2+}(*H_2O), Ni^{1+}, and Cu^{2+}. the letter in parentheses is the ligand considered in their study[7].

The local environment could also influence catalytic activity. For example, according to a previous study by Yang *et al.*, the NiN_3 sites have been calculated to be more active than the NiN_4 site[63]. Furthermore, it has been suggested that the NiN_y site has a weaker binding of *H than the CoN_y site, making the hydrogen evolution reaction (HER) unfavorable for the Ni/N/C catalyst. Also, the *CO selectivity is higher for the Ni/N/C catalyst than the Co/N/C catalyst[6]. As shown in **Figure S23**, the binding energy of *H on the NiN_4 site is weaker than on the CoN_4 site. Thus the NiN_4 site in our calculation is also expected to have higher selectivity toward CO formation than the CoN_4 sites.

In order to identify the promising catalysts that are electrochemically stable and active based on our computational analysis, the ΔG_R of the most stable phase is plotted against its corresponding thermodynamic barrier of the limiting step on that most stable phase at the same condition. We considered the ORR catalyst in acid at U = 0.80 V_{SHE} and pH = 1, as shown in Figures **3 (a)** and **3 (b)**. It is seen that the FeN_4, CoN_4, MnN_4, and RuN_4 sites on both bulk graphene and the graphene edge emerge as a promising candidates in many electrolytes, in agreement with several previous experimental studies[2,53,64,65]. In our previous study, where electrolyte adsorption was not included, the MnN_4C_{10} structure was not a promising candidate for the ORR in acid[18]. The MnN_4 site, however, becomes more stable against dissolution through electrolyte adsorption in the current study. We also identify new promising combinations between metal elements for acid electrolytes with $\Delta G_R < 1$ eV and $\Delta G_{max} < 0.8$ eV. These are IrN_4C_{10} in H_3PO_4, $HClO_4$, H_2O+NO, or non-adsorbing electrolyte (*e.g.,* HF); IrN_4C_A in H_3PO_4, H_2O+NO or non-adsorbing electrolyte (*e.g.,* $HClO_4$, HF, HCOOH); CuN_4C_A in a non-adsorbing electrolyte (*e.g.*, $HClO_4$, HNO_3); CuN_4C_{10} in H_2SO_4, H_3PO_4, non-adsorbing electrolyte (*e.g.*, $HClO_4$, HNO_3); RhN_4C_{10} in H_2O+CO, $HClO_4$, H_3PO_4, H_2SO_4, H_2O+NO; RhN_4C_A in H_2SO_4, H_2O+NO, H_3PO_4 or non-adsorbing electrolyte (*e.g.*, $HClO_4$, HF, HCOOH); AgN_4C_A in H_3PO_4; $AuN_4C_{x=10,A}$ in a non-adsorbing electrolyte (*e.g.*, all considered electrolytes in this study); ZnN_4C_{10} in $HClO_4$, HNO_3; ZnN_4C_A in $HClO_4$, HNO_3, HCOOH, HCl; OsN_4C_{10} in H_3PO_4 and H_2O+CO; BiN_4C_A in H_3PO_4, $HClO_4$, H_2SO_4, HCOOH; CrN_4C_A in H_2O+NO, H_2SO_4, or non-adsorbing electrolyte (*e.g.*, $HClO_4$, HCl, HCOOH); SnN_4C_A in H_2SO_4, H_3PO_4; and SbN_4C_A in HCOOH, HCl, H_3PO_4. It is seen that the p-block metals, mostly on the graphene edge, have comparable stability and activity to the transition metal sites. The Sn/N/C catalyst has been successfully synthesized, and it exhibits similar activity and selectivity for four-electron ORR to a Fe/N/C catalyst in 0.1 M $HClO_4$[66]. The Sb/N/C catalyst has also been synthesized and exhibits promising activity toward the ORR, although in 0.1 M KOH[67].

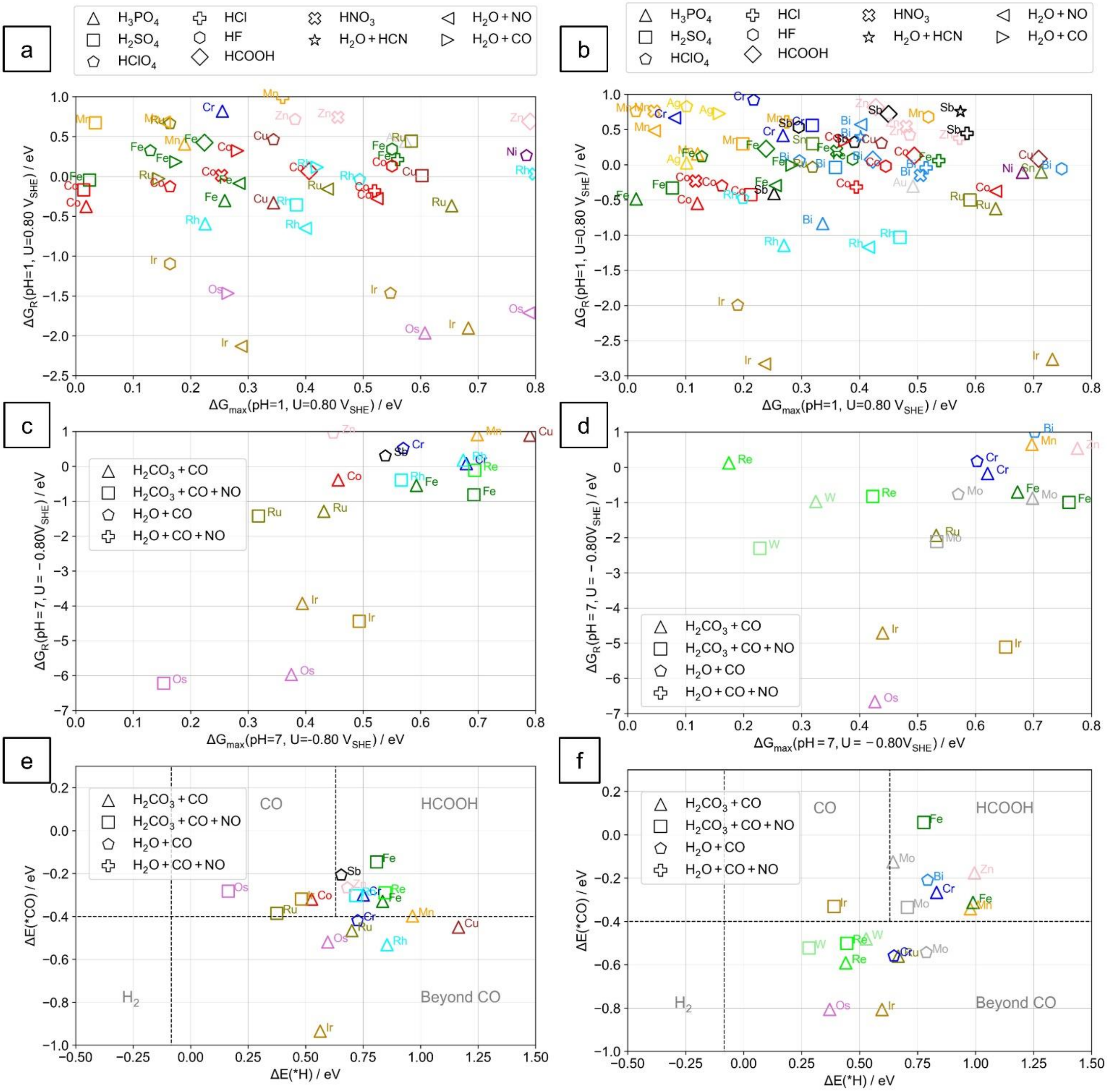

Figure 3 ΔG_R vs. ΔG_{max} for the ORR on the most stable surface in the different electrolytes at pH = 1 at U = 0.8 V_{SHE}: (a) MN_4C_{10} (b) MN_4C_A. ΔG_R vs. ΔG_{max} for the CO_2RR to CO on the most stable surface in different electrolytes at pH = 7 and U = -0.8 V_{SHE}: (c) MN_4C_{10} and (d) MN_4C_A. Classification plot for possible CO_2RR products of promising candidates: (e) MN_4C_{10} and (f) MN_4C_A.

For the CO_2RR toward CO, we consider the condition at U = -0.80 V_{SHE} and pH = 7, as shown in **Figure 3 (c)** and **(d)**. Besides the MnN_4, FeN_4, CoN_4, and NiN_4 which has been experimentally suggested for CO production[6–8], we show promising combinations (with ΔG_R < 1 eV and ΔG_{max} < 0.8 eV): $OsN_4C_{x=10,A}$,

$IrN_4C_{x=10,A}$, $RuN_4C_{x=10,A}$, RhN_4C_{10}, FeN_4C_{10}, $ReN_4C_{x=10,A}$, and WN_4C_A in H_2CO_3 (or H_2O) with NO or CO; $BiN_4C_{x=10,A}$ and $SbN_4C_{x=10,A}$ in non-adsorbing electrolyte (*e.g.* H_2O); ZnN_4C_{10} in H_2O with CO; $CrN_4C_{x=10,A}$ in H_2CO_3 with CO, H_2O with CO; MoN_4C_A in H_2CO_3 with CO or NO; and MoN_4C_A in H_2O with CO.

In addition to reducing CO_2 to CO, the competing HER is crucial in determining catalytic efficiency. It has been shown that the binding strength of *CO and *H are a descriptor of CO_2RR selectivity for both on transition metal surface[68] and single site porphyrin-like structure[69]. **Figure 3 (e)** and **(f)** show the classification of possible products from CO_2RR on the single metal sites, based on the binding energy of *CO and *H criteria suggested by Bagger *et al.*[69]. It is seen that the identified promising candidates are selective toward CO production over H_2 production. The effect of the ligand is seen on the MoN_4, RuN_4, WN_4, ReN_4, and OsN_4 sites, where the bare metal site strongly bonds with *H and will be highly selective for the HER. The binding of *CO and *H becomes weaker with the ligand; thus, the competing HER can be suppressed, as shown in **Figure S23**. Among the promising candidates, $IrN_4C_{x=10,A}$ in H_2CO_3 with CO, and OsN_4C_A in H_2CO_3+CO solution potentially reduces CO_2 to the product beyond CO. Other promising candidates that can produce products beyond CO are $RuN_4C_{x=10,A}$, RhN_4C_{10}, and OsN_4C_{10} in H_2CO_3+CO solution; ReN_4C_A and WN_4C_A in H_2CO_3+CO (or H_2CO_3+CO+NO solution); and CrN_4C_A and MoN_4C_A in H_2O+CO solution.

For the transition metal single atom considered in this study, we find that the reaction intermediate binding on the MN_4 site on the graphene edge is generally weaker than that on the MN_4 site on the bulk graphene. **Figure S24** illustrates the projected density of states (PDOS) for the CoN_4C_{10} and CoN_4C_A sites without and with adsorbate (either one *OH or *COOH adsorbate). In the pristine structure of the CoN_4C_{10} site, we observe that the $3d_{xy}$ hybridization with the 2p orbital of the surrounding N atoms forms the Co-N bonds, while the other 3d orbitals are non-binding orbitals. For the pristine structure of the CoN_4C_A site, not only $3d_{xy}$ but also $3d_{x2-y2}$ overlap with the 2p orbital for the surrounding N atoms. When *OH or *COOH adsorb on the Co atom, the 2p orbital of *OH or *COOH overlaps with the $3d_{z2}$ and $3d_{yz}$ orbital of the Co atom for the CoN_4C_{10} and CoN_4C_A site. In the CoN_4C_{10} site, the Co $3d_{x2}$ orbital locates below, while the Co $3d_{xy}$ locates above the Fermi energy. The opposite situation is found for the CoN_4C_A site, where the Co $3d_{x2}$ orbital locates below while the Co $3d_{xy}$ locates above the Fermi energy. A similar calculated PDOS pattern is found for other single metal atoms. Thus, it appears that the difference in d-orbitals located near the Fermi level, possibly caused by different local carbon atoms, affects the binding strength of the adsorbates[10].

Furthermore, with the presence of the ligand on the other side of the single metal atom, we find that the adsorption of the reaction intermediate likely weakens. The change in adsorption behavior of the ORR intermediate with the ligand on the CrN_4C_{12} and the CoN_4C_{12} structure has been previously explained by Svane *et al.* [24,70] using crystal field theory. In **Figure S25**, we show the possible electronic configuration in the d-orbital of the single metal atom in the MN_4C_{10} (M = Cr, Mn, Fe, and Co) structure with one and two adsorbates based on the converged magnetization and crystal field theory. The MN_4 site with two adsorbates adopts an octahedral structure, and the d-orbitals of the metal atom are split into two different energy levels, t_{2g} and e_g. For a Co^{2+} ion with a low spin configuration in the octahedral geometry, transferring more than one electron to the adsorbates may not be thermodynamically favorable since after the first unpaired electron is transferred from higher e_g d-orbitals, the remaining electrons are paired electrons and fully placed in the lower t_{2g} d-orbital.

Similarly, for a Fe^{2+} ion in the octahedral geometry with a low spin configuration, all d-electrons are placed in the lower t_{2g} d-orbital. Removing electrons from this fully occupied orbital may not be thermodynamically favorable. This could result in the destabilization of *COOH or *OH when binding as the second adsorbate. We find a similar value of the final magnetization for the MN_4 site on both bulk graphene and graphene edge; thus, we expect that both structure sites should have a similar d-orbital splitting pattern.

CONCLUSION

We have investigated the effect of electrolyte anion adsorption on the stability and activity of single metal atoms doped on two different graphenes: the bulk graphene terrace and a graphene edge with 3d, 4d, 5d, or p-block (Sn, Sb, and Bi) metal atoms. We find that the armchair edge is thermodynamically favored to form the MN_4 site compared to the bulk graphene, especially for 3d transition metals. Under ORR conditions (pH=1 and U=0.80 V_{SHE}), we find that various electrolyte anions can compete with water and adsorb on the single metal site. The electrolyte anion adsorption depends on the nature of the metal atom and local carbon around the MN_4 site. The ORR activity is either poisoned or altered by the electrolyte anion. If the electrolyte anion adsorbs on the single metal site, the single metal site can be further stabilized against dissolution in acid environments, compared to the stability in the pure water environment. We also find that the MN_4 site on the armchair edge is more stable than on the bulk graphene. Therefore, it would be interesting to include the electrolyte stabilization effect on other MN_4 sites with different local carbon structures, although the sites considered here are expected to be among the most stable sites. Considering both stability in acid conditions and ORR activity, we find a single metal site based on Ir, Cu, Rh, Zn, Au, Os, Cr, and p-block elements (Sb, Sn, and Bi), especially on the graphene edge, has comparable ORR activity and stability to a single metal atom based on Fe and Co. Under the CO_2RR condition (pH = 7 and U = -0.8 V_{SHE}), most considered electrolyte anions, except in 0.1 M H_2CO_3 solution, do not interact with the single metal site. Still, water and gas molecules may form ligands on various single metal sites under CO_2RR conditions. We find that the activity trend for reducing CO_2 to CO on the single metal site with the ligand from the solution compares well with the experimental trends. Besides the single atom catalyst-based Fe, Co, and Ni, we have identified promising single metal sites (Cr, Ru, W, Re, Os, Rh, Bi, Sb, Mo, Zn, and Ir), by including the adsorbate ligand from the solution. These promising candidates have comparable stability and activity to the Fe and Co-based catalysts. Our results illustrate that the nature of the metal atom, the local carbon structure, and the chemical environment, such as electrolytes, play a critical role in the activity and stability of a single-atom electrocatalyst. A careful combination of electrolyte or gas ligand and a single metal atom with various local carbon could be a possible way to achieve an active and durable electrocatalyst.

DATA AVAILABILITY

The data that supports the findings of this study are available within the article and its supplementary material. The DFT-optimized structures and calculation details in this study can be accessed from an online repository: DOI:10.5281/zenodo.7071450

ACKNOWLEDGMENTS

Funding from the Villum Foundation V-SUSTAIN grant 9455 to the Villum Center for the Science of Sustainable Fuels and Chemicals and a scholarship from the Ministry of Science and Technology, Royal Thai Government is acknowledged.

REFERENCE

(1) He, Y.; Shi, Q.; Shan, W.; Li, X.; Kropf, A. J.; Wegener, E. C.; Wright, J.; Karakalos, S.; Su, D.; Cullen, D. A.; Wang, G.; Myers, D. J.; Wu, G. Dynamically Unveiling Metal–Nitrogen Coordination during Thermal Activation to Design High-Efficient Atomically Dispersed CoN4 Active Sites. *Angewandte Chemie - International Edition* **2021**, *60* (17), 9516–9526. https://doi.org/10.1002/anie.202017288.

(2) Zitolo, A.; Ranjbar-Sahraie, N.; Mineva, T.; Li, J.; Jia, Q.; Stamatin, S.; Harrington, G. F.; Lyth, S. M.; Krtil, P.; Mukerjee, S.; Fonda, E.; Jaouen, F. Identification of Catalytic Sites in Cobalt-Nitrogen-Carbon Materials for the Oxygen Reduction Reaction. *Nat Commun* **2017**, *8* (1), 957. https://doi.org/10.1038/s41467-017-01100-7.

(3) Lefèvre, M.; Proietti, E.; Jaouen, F.; Dodelet, J. P. Iron-Based Catalysts with Improved Oxygen Reduction Activity in Polymer Electrolyte Fuel Cells. *Science (1979)* **2009**, *324* (5923), 71–74. https://doi.org/10.1126/science.1170051.

(4) Zitolo, A.; Goellner, V.; Armel, V.; Sougrati, M. T.; Mineva, T.; Stievano, L.; Fonda, E.; Jaouen, F. Identification of Catalytic Sites for Oxygen Reduction in Iron- and Nitrogen-Doped Graphene Materials. *Nat Mater* **2015**, *14* (9), 937–942. https://doi.org/10.1038/nmat4367.

(5) Zhang, H.; Chung, H. T.; Cullen, D. A.; Wagner, S.; Kramm, U. I.; More, K. L.; Zelenay, P.; Wu, G. High-Performance Fuel Cell Cathodes Exclusively Containing Atomically Dispersed Iron Active Sites. *Energy Environ Sci* **2019**, *12* (8), 2548–2558. https://doi.org/10.1039/c9ee00877b.

(6) Ju, W.; Bagger, A.; Hao, G. P.; Varela, A. S.; Sinev, I.; Bon, V.; Roldan Cuenya, B.; Kaskel, S.; Rossmeisl, J.; Strasser, P. Understanding Activity and Selectivity of Metal-Nitrogen-Doped Carbon Catalysts for Electrochemical Reduction of CO2. *Nat Commun* **2017**, *8* (1). https://doi.org/10.1038/s41467-017-01035-z.

(7) Li, J.; Pršlja, P.; Shinagawa, T.; Martín Fernández, A. J.; Krumeich, F.; Artyushkova, K.; Atanassov, P.; Zitolo, A.; Zhou, Y.; García-Muelas, R.; López, N.; Pérez-Ramírez, J.; Jaouen, F. Volcano Trend in Electrocatalytic Co2 Reduction Activity over Atomically Dispersed Metal Sites on Nitrogen-Doped Carbon. *ACS Catal* **2019**, *9* (11), 10426–10439. https://doi.org/10.1021/acscatal.9b02594.

(8) Paul, S.; Kao, Y. L.; Ni, L.; Ehnert, R.; Herrmann-Geppert, I.; van de Krol, R.; Stark, R. W.; Jaegermann, W.; Kramm, U. I.; Bogdanoff, P. Influence of the Metal Center in M−N−C Catalysts on the CO2 Reduction Reaction on Gas Diffusion Electrodes. *ACS Catal* **2021**, *11* (9), 5850–5864. https://doi.org/10.1021/acscatal.0c05596.

(9) Varela, A. S.; Ranjbar Sahraie, N.; Steinberg, J.; Ju, W.; Oh, H.-S.; Strasser, P. Metal-Doped Nitrogenated Carbon as an Efficient Catalyst for Direct CO 2 Electroreduction to CO and Hydrocarbons . *Angewandte Chemie* **2015**, *127* (37), 10908–10912. https://doi.org/10.1002/ange.201502099.

(10) Liu, K.; Wu, G.; Wang, G. Role of Local Carbon Structure Surrounding FeN4 Sites in Boosting the Catalytic Activity for Oxygen Reduction. *Journal of Physical Chemistry C* **2017**, *121* (21), 11319–11324. https://doi.org/10.1021/acs.jpcc.7b00913.

(11) Li, J.; Sougrati, M. T.; Zitolo, A.; Ablett, J. M.; Oğuz, I. C.; Mineva, T.; Matanovic, I.; Atanassov, P.; Huang, Y.; Zenyuk, I.; di Cicco, A.; Kumar, K.; Dubau, L.; Maillard, F.; Dražić, G.; Jaouen, F. Identification of Durable and Non-Durable FeNx Sites in Fe–N–C Materials for Proton Exchange Membrane Fuel Cells. *Nat Catal* **2021**, *4* (1), 10–19. https://doi.org/10.1038/s41929-020-00545-2.

(12) Charreteur, F.; Jaouen, F.; Ruggeri, S.; Dodelet, J. P. Fe/N/C Non-Precious Catalysts for PEM Fuel Cells: Influence of the Structural Parameters of Pristine Commercial Carbon Blacks on Their Activity for Oxygen Reduction. *Electrochim Acta* **2008**, *53* (6), 2925–2938. https://doi.org/10.1016/j.electacta.2007.11.002.

(13) Qin, X.; Zhu, S.; Xiao, F.; Zhang, L.; Shao, M. Active Sites on Heterogeneous Single-Iron-Atom Electrocatalysts in CO2 Reduction Reaction. *ACS Energy Lett* **2019**, *4* (7), 1778–1783. https://doi.org/10.1021/acsenergylett.9b01015.

(14) Mineva, T.; Matanovic, I.; Atanassov, P.; Sougrati, M. T.; Stievano, L.; Clémancey, M.; Kochem, A.; Latour, J. M.; Jaouen, F. Understanding Active Sites in Pyrolyzed Fe-N-C Catalysts for Fuel Cell Cathodes by Bridging Density Functional Theory Calculations and 57Fe Mössbauer Spectroscopy. *ACS Catal* **2019**, *9* (10), 9359–9371. https://doi.org/10.1021/acscatal.9b02586.

(15) Kumar, K.; Gairola, P.; Lions, M.; Ranjbar-Sahraie, N.; Mermoux, M.; Dubau, L.; Zitolo, A.; Jaouen, F.; Maillard, F. Physical and Chemical Considerations for Improving Catalytic Activity and Stability of Non-Precious-Metal Oxygen Reduction Reaction Catalysts. *ACS Catal* **2018**, *8* (12), 11264–11276. https://doi.org/10.1021/acscatal.8b02934.

(16) Glibin, V.; Zhang, G.; Dodelet, J.-P.; Sun, S. Non-PGM Electrocatalysts for PEM Fuel Cells: Thermodynamic Stability of Potential ORR CoNx-C Electrocatalytic Sites. *J Electrochem Soc* **2021**, *168* (9), 094502. https://doi.org/10.1149/1945-7111/ac1d03.

(17) Glibin, V. P.; Dodelet, J.-P. Thermodynamic Stability in Acid Media of FeN 4 -Based Catalytic Sites Used for the Reaction of Oxygen Reduction in PEM Fuel Cells . *J Electrochem Soc* **2017**, *164* (9), F948–F957. https://doi.org/10.1149/2.1041709jes.

(18) Hansen, H. A.; Patniboon, T. Acid-Stable and Active M−N−C Catalysts for the Oxygen Reduction Reaction: The Role of Local Structure. *ACS Catal* **2021**, *11* (21), 13102–13118. https://doi.org/10.1021/acscatal.1c02941.

(19) Holby, E. F.; Wang, G.; Zelenay, P. Acid Stability and Demetalation of PGM-Free ORR Electrocatalyst Structures from Density Functional Theory: A Model for “Single-Atom Catalyst” Dissolution. *ACS Catal* **2020**, *10* (24), 14527–14539. https://doi.org/10.1021/acscatal.0c02856.

(20) Nematollahi, P.; Barbiellini, B.; Bansil, A.; Lamoen, D.; Qingying, J.; Mukerjee, S.; Neyts, E. C. Identification of a Robust and Durable FeN 4 C x Catalyst for ORR in PEM Fuel Cells and the Role of the Fifth Ligand . *ACS Catal* **2022**, 7541–7549. https://doi.org/10.1021/acscatal.2c01294.

(21) Xu, X.; Zhang, X.; Kuang, Z.; Xia, Z.; Rykov, A. I.; Yu, S.; Wang, J.; Wang, S.; Sun, G. Investigation on the Demetallation of Fe-N-C for Oxygen Reduction Reaction: The Influence of Structure and Structural Evolution of Active Site. *Appl Catal B* **2022**, *309*. https://doi.org/10.1016/j.apcatb.2022.121290.

(22) Holst-Olesen, K.; Silvioli, L.; Rossmeisl, J.; Arenz, M. Enhanced Oxygen Reduction Reaction on Fe/N/C Catalyst in Acetate Buffer Electrolyte. *ACS Catal* **2019**, *9* (4), 3082–3089. https://doi.org/10.1021/acscatal.8b04609.

(23) Holst-Olesen, K.; Reda, M.; Hansen, H. A.; Vegge, T.; Arenz, M. Enhanced Oxygen Reduction Activity by Selective Anion Adsorption on Non-Precious-Metal Catalysts. *ACS Catal* **2018**, *8* (8), 7104–7112. https://doi.org/10.1021/acscatal.8b01584.

(24) Svane, K. L.; Reda, M.; Vegge, T.; Hansen, H. A. Improving the Activity of M−N4 Catalysts for the Oxygen Reduction Reaction by Electrolyte Adsorption. *ChemSusChem* **2019**, *12* (23), 5133–5141. https://doi.org/10.1002/cssc.201902443.

(25) Zhang, B.; Zhang, J.; Shi, J.; Tan, D.; Liu, L.; Zhang, F.; Lu, C.; Su, Z.; Tan, X.; Cheng, X.; Han, B.; Zheng, L.; Zhang, J. Manganese Acting as a High-Performance Heterogeneous Electrocatalyst in Carbon Dioxide Reduction. *Nat Commun* **2019**, *10* (1). https://doi.org/10.1038/s41467-019-10854-1.

(26) Chen, Z.; Huang, A.; Yu, K.; Cui, T.; Zhuang, Z.; Liu, S.; Li, J.; Tu, R.; Sun, K.; Tan, X.; Zhang, J.; Liu, D.; Zhang, Y.; Jiang, P.; Pan, Y.; Chen, C.; Peng, Q.; Li, Y. Fe1N4-O1site with Axial Fe-O Coordination for Highly Selective CO2reduction over a Wide Potential Range. *Energy Environ Sci* **2021**, *14* (6), 3430–3437. https://doi.org/10.1039/d1ee00569c.

(27) Wang, X.; Wang, Y.; Sang, X.; Zheng, W.; Zhang, S.; Shuai, L.; Yang, B.; Li, Z.; Chen, J.; Lei, L.; Adli, N. M.; Leung, M. K. H.; Qiu, M.; Wu, G.; Hou, Y. Dynamic Activation of Adsorbed Intermediates via Axial Traction for the Promoted Electrochemical CO2 Reduction. *Angewandte Chemie - International Edition* **2021**, *60* (8), 4192–4198. https://doi.org/10.1002/anie.202013427.

(28) Glibin, V. P.; Cherif, M.; Vidal, F.; Dodelet, J.-P.; Zhang, G.; Sun, S. Non-PGM Electrocatalysts for PEM Fuel Cells: Thermodynamic Stability and DFT Evaluation of Fluorinated FeN 4 -Based ORR Catalysts . *J Electrochem Soc* **2019**, *166* (7), F3277–F3286. https://doi.org/10.1149/2.0341907jes.

(29) Wei, J.; Xia, D.; Wei, Y.; Zhu, X.; Li, J.; Gan, L. Probing the Oxygen Reduction Reaction Intermediates and Dynamic Active Site Structures of Molecular and Pyrolyzed Fe–N–C Electrocatalysts by In Situ Raman Spectroscopy. *ACS Catal* **2022**, 7811–7820. https://doi.org/10.1021/acscatal.2c00771.

(30) Sun, F.; Li, F.; Tang, Q. Spin State as a Participator for Demetalation Durability and Activity of Fe–N–C Electrocatalysts. *The Journal of Physical Chemistry C* **2022**. https://doi.org/10.1021/acs.jpcc.2c03518.

(31) Zheng, F.; Ji, Y.; Dong, H.; Liu, C.; Chen, S.; Li, Y. Edge Effect Promotes Graphene-Confining Single-Atom Co–N4 and Rh–N4 for Bifunctional Oxygen Electrocatalysis. *Journal of Physical Chemistry C* **2022**, *126* (1), 30–39. https://doi.org/10.1021/acs.jpcc.1c07691.

(32) Cometto, C.; Ugolotti, A.; Grazietti, E.; Moretto, A.; Bottaro, G.; Armelao, L.; di Valentin, C.; Calvillo, L.; Granozzi, G. Copper Single-Atoms Embedded in 2D Graphitic Carbon Nitride for the CO2 Reduction. *NPJ 2D Mater Appl* **2021**, *5* (1). https://doi.org/10.1038/s41699-021-00243-y.

(33) Byon, H. R.; Suntivich, J.; Shao-Horn, Y. Graphene-Based Non-Noble-Metal Catalysts for Oxygen Reduction Reaction in Acid. *Chemistry of Materials* **2011**, *23* (15), 3421–3428. https://doi.org/10.1021/cm2000649.

(34) He, J.; Zheng, T.; Wu, D.; Zhang, S.; Gu, M.; He, Q. Insights into the Determining Effect of Carbon Support Properties on Anchoring Active Sites in Fe-N-C Catalysts toward the Oxygen Reduction Reaction. *ACS Catal* **2022**, *12* (3), 1601–1613. https://doi.org/10.1021/acscatal.1c04815.

(35) Xiao, M.; Zhu, J.; Ma, L.; Jin, Z.; Ge, J.; Deng, X.; Hou, Y.; He, Q.; Li, J.; Jia, Q.; Mukerjee, S.; Yang, R.; Jiang, Z.; Su, D.; Liu, C.; Xing, W. Microporous Framework Induced Synthesis of Single-Atom Dispersed Fe-N-C Acidic ORR Catalyst and Its in Situ Reduced Fe-N4 Active Site Identification Revealed by X-Ray Absorption Spectroscopy. *ACS Catalysis*. American Chemical Society April 6, 2018, pp 2824–2832. https://doi.org/10.1021/acscatal.8b00138.

(36) Santori, P. G.; Speck, F. D.; Li, J.; Zitolo, A.; Jia, Q.; Mukerjee, S.; Cherevko, S.; Jaouen, F. Effect of Pyrolysis Atmosphere and Electrolyte PH on the Oxygen Reduction Activity, Stability and Spectroscopic Signature of FeN x Moieties in Fe-N-C Catalysts . *J Electrochem Soc* **2019**, *166* (7), F3311–F3320. https://doi.org/10.1149/2.0371907jes.

(37) Zamora Zeledón, J. A.; Kamat, G. A.; Gunasooriya, G. T. K. K.; Nørskov, J. K.; Stevens, M. B.; Jaramillo, T. F. Probing the Effects of Acid Electrolyte Anions on Electrocatalyst Activity and Selectivity for the Oxygen Reduction Reaction. *ChemElectroChem* **2021**, *8* (13), 2467–2478. https://doi.org/10.1002/celc.202100500.

(38) Kamat, G. A.; Zamora Zeledón, J. A.; Gunasooriya, G. T. K. K.; Dull, S. M.; Perryman, J. T.; Nørskov, J. K.; Stevens, M. B.; Jaramillo, T. F. Acid Anion Electrolyte Effects on Platinum for Oxygen and Hydrogen Electrocatalysis. *Commun Chem* **2022**, *5* (1). https://doi.org/10.1038/s42004-022-00635-1.

(39) Varela, A. S.; Kroschel, M.; Leonard, N. D.; Ju, W.; Steinberg, J.; Bagger, A.; Rossmeisl, J.; Strasser, P. PH Effects on the Selectivity of the Electrocatalytic CO2 Reduction on Graphene-Embedded Fe-N-C Motifs: Bridging Concepts between Molecular Homogeneous and Solid-State Heterogeneous Catalysis. *ACS Energy Lett* **2018**, *3* (4), 812–817. https://doi.org/10.1021/acsenergylett.8b00273.

(40) Kneebone, J. L.; Daifuku, S. L.; Kehl, J. A.; Wu, G.; Chung, H. T.; Hu, M. Y.; Alp, E. E.; More, K. L.; Zelenay, P.; Holby, E. F.; Neidig, M. L. A Combined Probe-Molecule, Mössbauer, Nuclear Resonance Vibrational Spectroscopy, and Density Functional Theory Approach for Evaluation of Potential Iron Active Sites in an Oxygen Reduction Reaction Catalyst. *Journal of Physical Chemistry C* **2017**, *121* (30), 16283–16290. https://doi.org/10.1021/acs.jpcc.7b03779.

(41) Zhang, Q.; Mamtani, K.; Jain, D.; Ozkan, U.; Asthagiri, A. CO Poisoning Effects on FeNC and CNx ORR Catalysts: A Combined Experimental-Computational Study. *Journal of Physical Chemistry C* **2016**, *120* (28), 15173–15184. https://doi.org/10.1021/acs.jpcc.6b03933.

(42) Cho, M.; Song, J. T.; Back, S.; Jung, Y.; Oh, J. The Role of Adsorbed CN and Cl on an Au Electrode for Electrochemical CO2 Reduction. *ACS Catal* **2018**, *8* (2), 1178–1185. https://doi.org/10.1021/acscatal.7b03449.

(43) Chen, Z.; Jiang, S.; Kang, G.; Nguyen, D.; Schatz, G. C.; van Duyne, R. P. Operando Characterization of Iron Phthalocyanine Deactivation during Oxygen Reduction Reaction Using Electrochemical Tip-Enhanced Raman Spectroscopy. *J Am Chem Soc* **2019**, *141* (39), 15684–15692. https://doi.org/10.1021/jacs.9b07979.

(44) Choi, C. H.; Baldizzone, C.; Grote, J.-P.; Schuppert, A. K.; Jaouen, F.; Mayrhofer, K. J. J. Stability of Fe-N-C Catalysts in Acidic Medium Studied by Operando Spectroscopy. *Angewandte Chemie* **2015**, *127* (43), 12944–12948. https://doi.org/10.1002/ange.201504903.

(45) Kumar, K.; Dubau, L.; Mermoux, M.; Li, J.; Zitolo, A.; Nelayah, J.; Jaouen, F.; Maillard, F. On the Influence of Oxygen on the Degradation of Fe-N-C Catalysts. *Angewandte Chemie* **2020**, *132* (8), 3261–3269. https://doi.org/10.1002/ange.201912451.

(46) Choi, C. H.; Lim, H. K.; Chung, M. W.; Chon, G.; Ranjbar Sahraie, N.; Altin, A.; Sougrati, M. T.; Stievano, L.; Oh, H. S.; Park, E. S.; Luo, F.; Strasser, P.; Dražić, G.; Mayrhofer, K. J. J.; Kim, H.; Jaouen, F. The Achilles' Heel of Iron-Based Catalysts during Oxygen Reduction in an Acidic Medium. *Energy Environ Sci* **2018**, *11* (11), 3176–3182. https://doi.org/10.1039/c8ee01855c.

(47) Singh, A. K.; Zhou, L.; Shinde, A.; Suram, S. K.; Montoya, J. H.; Winston, D.; Gregoire, J. M.; Persson, K. A. Electrochemical Stability of Metastable Materials. *Chemistry of Materials* **2017**, *29* (23), 10159–10167. https://doi.org/10.1021/acs.chemmater.7b03980.

(48) Li, T.; Liu, J.; Song, Y.; Wang, F. Photochemical Solid-Phase Synthesis of Platinum Single Atoms on Nitrogen-Doped Carbon with High Loading as Bifunctional Catalysts for Hydrogen Evolution and Oxygen Reduction Reactions. *ACS Catal* **2018**, *8* (9), 8450–8458. https://doi.org/10.1021/acscatal.8b02288.

(49) Liu, Q.; Li, Y.; Zheng, L.; Shang, J.; Liu, X.; Yu, R.; Shui, J. Sequential Synthesis and Active-Site Coordination Principle of Precious Metal Single-Atom Catalysts for Oxygen Reduction Reaction and PEM Fuel Cells. *Adv Energy Mater* **2020**, *10* (20). https://doi.org/10.1002/aenm.202000689.

(50) Zhang, C.; Sha, J.; Fei, H.; Liu, M.; Yazdi, S.; Zhang, J.; Zhong, Q.; Zou, X.; Zhao, N.; Yu, H.; Jiang, Z.; Ringe, E.; Yakobson, B. I.; Dong, J.; Chen, D.; Tour, J. M. Single-Atomic Ruthenium Catalytic Sites on

Nitrogen-Doped Graphene for Oxygen Reduction Reaction in Acidic Medium. *ACS Nano* **2017**, *11* (7), 6930–6941. https://doi.org/10.1021/acsnano.7b02148.

(51) Xiao, M.; Gao, L.; Wang, Y.; Wang, X.; Zhu, J.; Jin, Z.; Liu, C.; Chen, H.; Li, G.; Ge, J.; He, Q.; Wu, Z.; Chen, Z.; Xing, W. Engineering Energy Level of Metal Center: Ru Single-Atom Site for Efficient and Durable Oxygen Reduction Catalysis. *J Am Chem Soc* **2019**, *141* (50), 19800–19806. https://doi.org/10.1021/jacs.9b09234.

(52) Sahraie, N. R.; Kramm, U. I.; Steinberg, J.; Zhang, Y.; Thomas, A.; Reier, T.; Paraknowitsch, J.-P.; Strasser, P. Quantifying the Density and Utilization of Active Sites in Non-Precious Metal Oxygen Electroreduction Catalysts. *Nat Commun* **2015**, *6*, 8618. https://doi.org/10.1038/ncomms9618.

(53) Xie, X.; He, C.; Li, B.; He, Y.; Cullen, D. A.; Wegener, E. C.; Kropf, A. J.; Martinez, U.; Cheng, Y.; Engelhard, M. H.; Bowden, M. E.; Song, M.; Lemmon, T.; Li, X. S.; Nie, Z.; Liu, J.; Myers, D. J.; Zelenay, P.; Wang, G.; Wu, G.; Ramani, V.; Shao, Y. Performance Enhancement and Degradation Mechanism Identification of a Single-Atom Co–N–C Catalyst for Proton Exchange Membrane Fuel Cells. *Nat Catal* **2020**, *3* (12), 1044–1054. https://doi.org/10.1038/s41929-020-00546-1.

(54) Dong, H.; Gu, F.; Li, M.; Lin, B.; Si, Z.; Hou, T.; Yan, F.; Lee, S. T.; Li, Y. Improving the Alkaline Stability of Imidazolium Cations by Substitution. *ChemPhysChem* **2014**, *15* (14), 3006–3014. https://doi.org/10.1002/cphc.201402262.

(55) Nørskov, J. K.; Rossmeisl, J.; Logadottir, A.; Lindqvist, L.; Kitchin, J. R.; Bligaard, T.; Jónsson, H. Origin of the Overpotential for Oxygen Reduction at a Fuel-Cell Cathode. *Journal of Physical Chemistry B* **2004**, *108* (46), 17886–17892. https://doi.org/10.1021/jp047349j.

(56) Hu, Y.; Jensen, J. O.; Pan, C.; Cleemann, L. N.; Shypunov, I.; Li, Q. Immunity of the Fe-N-C Catalysts to Electrolyte Adsorption: Phosphate but Not Perchloric Anions. *Appl Catal B* **2018**, *234*, 357–364. https://doi.org/10.1016/j.apcatb.2018.03.056.

(57) Martinez, U.; Holby, E. F.; Babu, S. K.; Artyushkova, K.; Lin, L.; Choudhury, S.; Purdy, G. M.; Zelenay, P. Experimental and Theoretical Trends of PGM-Free Electrocatalysts for the Oxygen Reduction Reaction with Different Transition Metals. *J Electrochem Soc* **2019**, *166* (7), F3136–F3142. https://doi.org/10.1149/2.0201907jes.

(58) Shah, S. S. A.; Najam, T.; Javed, M. S.; Rahman, M. M.; Tsiakaras, P. Novel Mn-/Co-N x Moieties Captured in N-Doped Carbon Nanotubes for Enhanced Oxygen Reduction Activity and Stability in Acidic and Alkaline Media. *ACS Appl Mater Interfaces* **2021**, *13* (19), 23191–23200. https://doi.org/10.1021/acsami.1c03477.

(59) Tylus, U.; Jia, Q.; Strickland, K.; Ramaswamy, N.; Serov, A.; Atanassov, P.; Mukerjee, S. Elucidating Oxygen Reduction Active Sites in Pyrolyzed Metal-Nitrogen Coordinated Non-Precious-Metal Electrocatalyst Systems. *Journal of Physical Chemistry C* **2014**, *118* (17), 8999–9008. https://doi.org/10.1021/jp500781v.

(60) Zeng, J. S.; Corbin, N.; Williams, K.; Manthiram, K. Kinetic Analysis on the Role of Bicarbonate in Carbon Dioxide Electroreduction at Immobilized Cobalt Phthalocyanine. *ACS Catal* **2020**, *10* (7), 4326–4336. https://doi.org/10.1021/acscatal.9b05272.

(61) Yan, C.; Li, H.; Ye, Y.; Wu, H.; Cai, F.; Si, R.; Xiao, J.; Miao, S.; Xie, S.; Yang, F.; Li, Y.; Wang, G.; Bao, X. Coordinatively Unsaturated Nickel-Nitrogen Sites towards Selective and High-Rate CO2 Electroreduction. *Energy Environ Sci* **2018**, *11* (5), 1204–1210. https://doi.org/10.1039/c8ee00133b.

(62) Cheng, Y.; Zhao, S.; Li, H.; He, S.; Veder, J. P.; Johannessen, B.; Xiao, J.; Lu, S.; Pan, J.; Chisholm, M. F.; Yang, S. Z.; Liu, C.; Chen, J. G.; Jiang, S. P. Unsaturated Edge-Anchored Ni Single Atoms on Porous Microwave Exfoliated Graphene Oxide for Electrochemical CO2. *Appl Catal B* **2019**, *243* (June 2018), 294–303. https://doi.org/10.1016/j.apcatb.2018.10.046.

(63) Yang, J.; Qiu, Z.; Zhao, C.; Wei, W.; Chen, W.; Li, Z.; Qu, Y.; Dong, J.; Luo, J.; Li, Z.; Wu, Y. In Situ Thermal Atomization To Convert Supported Nickel Nanoparticles into Surface-Bound Nickel Single-Atom Catalysts. *Angewandte Chemie* **2018**, *130* (43), 14291–14296. https://doi.org/10.1002/ange.201808049.

(64) Zhang, H.; Hwang, S.; Wang, M.; Feng, Z.; Karakalos, S.; Luo, L.; Qiao, Z.; Xie, X.; Wang, C.; Su, D.; Shao, Y.; Wu, G. Single Atomic Iron Catalysts for Oxygen Reduction in Acidic Media: Particle Size Control and Thermal Activation. *J Am Chem Soc* **2017**, *139* (40), 14143–14149. https://doi.org/10.1021/jacs.7b06514.

(65) Li, J.; Chen, M.; Cullen, D. A.; Hwang, S.; Wang, M.; Li, B.; Liu, K.; Karakalos, S.; Lucero, M.; Zhang, H.; Lei, C.; Xu, H.; Sterbinsky, G. E.; Feng, Z.; Su, D.; More, K. L.; Wang, G.; Wang, Z.; Wu, G. Atomically Dispersed Manganese Catalysts for Oxygen Reduction in Proton-Exchange Membrane Fuel Cells. *Nat Catal* **2018**, *1* (12), 935–945. https://doi.org/10.1038/s41929-018-0164-8.

(66) Luo, F.; Roy, A.; Silvioli, L.; Cullen, D. A.; Zitolo, A.; Sougrati, M. T.; Oguz, I. C.; Mineva, T.; Teschner, D.; Wagner, S.; Wen, J.; Dionigi, F.; Kramm, U. I.; Rossmeisl, J.; Jaouen, F.; Strasser, P. P-Block Single-Metal-Site Tin/Nitrogen-Doped Carbon Fuel Cell Cathode Catalyst for Oxygen Reduction Reaction. *Nat Mater* **2020**, *19* (11), 1215–1223. https://doi.org/10.1038/s41563-020-0717-5.

(67) Wang, T.; Cao, X.; Qin, H.; Shang, L.; Zheng, S.; Fang, F.; Jiao, L. P-Block Atomically Dispersed Antimony Catalyst for Highly Efficient Oxygen Reduction Reaction. *Angewandte Chemie - International Edition* **2021**, *60* (39), 21237–21241. https://doi.org/10.1002/anie.202108599.

(68) Bagger, A.; Ju, W.; Varela, A. S.; Strasser, P.; Rossmeisl, J. Electrochemical CO2 Reduction: A Classification Problem. *ChemPhysChem* **2017**, *18* (22), 3266–3273. https://doi.org/10.1002/cphc.201700736.

(69) Bagger, A.; Ju, W.; Varela, A. S.; Strasser, P.; Rossmeisl, J. Single Site Porphyrine-like Structures Advantages over Metals for Selective Electrochemical CO2 Reduction. *Catal Today* **2017**, *288*, 74–78. https://doi.org/10.1016/j.cattod.2017.02.028.

(70) Svane, K. L.; Hansen, H. A.; Vegge, T. A Comparison of Single and Double Co Sites Incorporated in N-Doped Graphene for the Oxygen Reduction Reaction. *J Catal* **2021**, *393*, 230–237. https://doi.org/https://doi.org/10.1016/j.jcat.2020.11.024.

Supporting Information

Effects of Electrolyte Anion Adsorption on the Activity and Stability of Single Atom Electrocatalysts

Tipaporn Patniboon and Heine Anton Hansen
Department of Energy Conversion and Storage, Technical University of Denmark
Anker Engelunds Vej, 2800 Kongens Lyngby, Denmark

1. Computational Details

The spin-polarized density functional theory calculations are performed using the Vienna ab initio simulation package (VASP)[1] and projector augmented wave (PAW)[2] is used to describe the core electrons. A plane-wave basis function with a kinetic energy cutoff of 600 eV is used to describe the valence electrons. The Fermi smearing is used with a width of 0.1 eV. The exchange and correlation energy are described using the BEEF-vdW[3] functional to include the effects of dispersive interactions. The self-consistent electron density loop is converged to 10^{-5} eV. The structure is prepared using the Atomic Simulation Environments (ASE)[4] package and the bare M/N/C catalyst models are similar to those used in our previous study[5]. The unit cell dimensions in the catalyst plane are 16.9 x 9.8 Å on average, with variations for the different metal atoms. The lattice relaxation of the single metal atom on bulk graphene (MN_4C_{10}) and graphene edged (MN_4C_A) are relaxed in a vacuum until all forces are below 0.025 eV $Å^-$ and a dipole correction is used in the perpendicular direction to the catalyst plane to decouple the electrostatic potentials on the two sides of the catalyst plane. The Brillouin zone is sampled with a (3×3×1) Monkhorst Pack k-point mesh[6]. For binding energy calculations, the solvent effect is included during the relaxation, using the implicit solvent model implemented in VASPsol[6] with a dielectric constant of 80, representing the water medium. The calculations are submitted, managed, and received using the MyQueue[7] workflow tool, a python front-end to the job scheduler.

The free energy for the adsorbate is calculated from DFT energy (E_{DFT}), including zero-point energy (ZPE), vibrational internal energy (U_{vib}), and vibrational entropy (S_{vib}) as a thermal correction.

$$G = E_{DFT} + ZPE + U_{vib} - TS_{vib} = E_{DFT} + \text{Thermal correction} \qquad \text{Equation S1}$$

The thermal correction term ($ZPE + U_{vib} - TS_{vib}$) is calculated only for the adsorbates on the FeN_4C_{10} and FeN_4C_A sites and applied to other single metal sites with the same local carbon structure. The thermal corrections for adsorbates are listed in Table S1. In the case of the adsorbates on the catalyst surface, only the vibration of the adsorbate is calculated, following the quantum mechanical harmonic approximation, by using the thermochemistry class in the ASE package[4]. For the gas molecule, the free energy the DFT energy is corrected by including ZPE, enthalpy (H), and entropy (S). These values (ZPE, H, S) for the gas molecules are taken from the thermochemical database[8] (if available). The free energy of O_2 is not directly obtained from the DFT calculation, it is calculated in the way to reproduce the experimental free energy of liquid water formation ($2H_2 + O_2 \rightarrow 2H_2O$; $\Delta G_{H2O} = -4.92$ eV[9]).

The change in free reaction energy with an applied potential (U_{SHE}) and pH is calculated using the computational hydrogen electrode (CHE)[10]. By the definition of the standard hydrogen electrode (SHE) at 0 V_{SHE}, there is an equilibrium between hydrogen molecules in the gas phase with solvated protons and electrons.

$$H^+ + e^- \leftrightarrow H_2$$

Thus, the free energy of hydrogen adsorption on the catalysts surface at any considered potential (U_{SHE}) and pH can for the example given by follows.

$$* + H^+ + e^- \leftrightarrow {}^*H$$

$$\Delta G_{*H}(U_{SHE}, pH) = G(*H) - G(*) - (1/2)G(H_2) + eU_{SHE} + k_BT\ pH\ ln(10) \qquad \text{Equation S2}$$

$$\Delta G_{*H}(U_{SHE}, pH) = G(*H) - G(*) - (1/2)G(H_2) - \Delta G_H - \Delta G_e \qquad \text{Equation S3}$$

where * denoted the adsorbed site on the catalyst surface, $\Delta G_H = -k_BT\ pH\ ln(10)$ and $\Delta G_e = -eU_{SHE}$, where e is the numerical charge of an electron, k_B is the Boltzmann constant and T is the temperature (in K). Furthermore, according to the Christensen scheme[11,12], the energies of molecular CO_2, CO, H_2, and H_2O are corrected by +0.3, +0.15, +0.09, and -0.03 eV, respectively, which is specific to the BEEF-vdW functional. When $\Delta G(*OOH)$ is calculated, it is also corrected by $\Delta E(O\text{-}O) = 0.20$ eV, for the same reason.

Table S1 Thermal correction for the adsorbates at T = 298.15 K

	$ZPE + U_{vib} - TS_{vib}$ / eV	
adsorbate	MN_4C_{10}	MN_4C_A
$*H_2O$	0.60	0.65
*OOH	0.36	0.30
*OH	0.29	0.30
*O	0.03	0.04
*H	0.19	0.18
$*HSO_4$	0.55	0.55
*SO4	0.28	0.26
$*H_2PO_4$	0.81	1.12
$*HPO_4$	0.48	0.53
$*PO_4$	0.22	0.19
*Cl	-0.03	-0.03
$*ClO_4$	0.19	0.24
*HCOO	0.49	0.69
*F	-0.02	-0.01
$*NO_3$	0.23	0.18
*CN	0.14	0.10
*CO	0.11	0.12
*NO	0.10	0.09
$*HCO_3$	0.64	0.77
$*CO_3$	0.21	0.21
*COOH	0.51	0.53

Table S1 (continue) Thermal correction of the adsorbates at T = 298.15 K

		ZPE + U_{vib} - TS_{vib} / eV	
adsorbate1	adsorbate2	MN_4C_{10}	MN_4C_A
$*H_2O$	$*H_2O$	1.13	1.62
*OH	*OH	0.67	0.62
*O	*O	0.07	0.07
$*HSO_4$	$*HSO_4$	1.28	1.57
$*SO_4$	$*SO_4$	0.59	0.57
$*H_2PO_4$	$*H_2PO_4$	1.85	2.49
$*HPO_4$	$*HPO_4$	1.24	1.42
$*PO_4$	$*PO_4$	0.43	0.43
*Cl	*Cl	-0.03	-0.05
$*ClO_4$	$*ClO_4$	0.48	0.54
*HCOO	*HCOO	1.08	1.04
*F	*F	0.03	0.03
$*NO_3$	$*NO_3$	0.47	0.50
*CN	*CN	0.27	0.20
*CO	*CO	0.21	0.17
*OH	*O	0.36	0.35
*OH	$*HSO_4$	0.81	0.94
*OH	$*SO_4$	0.61	0.67
*OH	$*H_2PO_4$	1.27	1.24
*OH	$*HPO_4$	0.92	0.85
*OH	$*PO_4$	0.53	0.62
*OH	*Cl	0.30	0.32
*OH	*F	0.34	0.39
*OH	$*NO_3$	0.63	0.54
*OH	$*ClO_4$	0.63	0.60
*OH	*HCOO	0.85	0.87
*OH	*CN	0.56	0.52
*OH	*CO	0.51	0.05
*OH	*NO	0.46	0.45

Table S1 (continue) Thermal correction for the adsorbates at T = 298.15 K

		ZPE + U_{vib} - TS_{vib} / eV	
adsorbate1	adsorbate2	MN_4C_{10}	MN_4C_A
*COOH	*CO	0.68	0.68
*COOH	*HCO_3	1.13	1.08
*CO	*HCO_3	0.66	0.70
*H	*HCO_3	0.89	1.07
*COOH	*H	0.88	0.92
*CO	*H	0.43	0.38
*COOH	*CO_3	0.75	0.82
*CO	*CO_3	0.26	0.42
*H	*CO3	0.47	0.20
*CO	*H_2O	0.60	-
*COOH	*H_2O	1.04	-
*H	*H_2O	0.64	-
*CO	*O	0.04	-0.03
*COOH	*O	0.39	0.50
*H	*O	0.21	0.22
*CO	*NO	0.18	0.76
*COOH	*NO	0.66	0.18
*H	*NO	0.42	0.53
*CO	*CN	0.21	0.50
*COOH	*CN	0.60	0.18
*H	*CN	0.41	0.40

2. Formation Energy Calculation

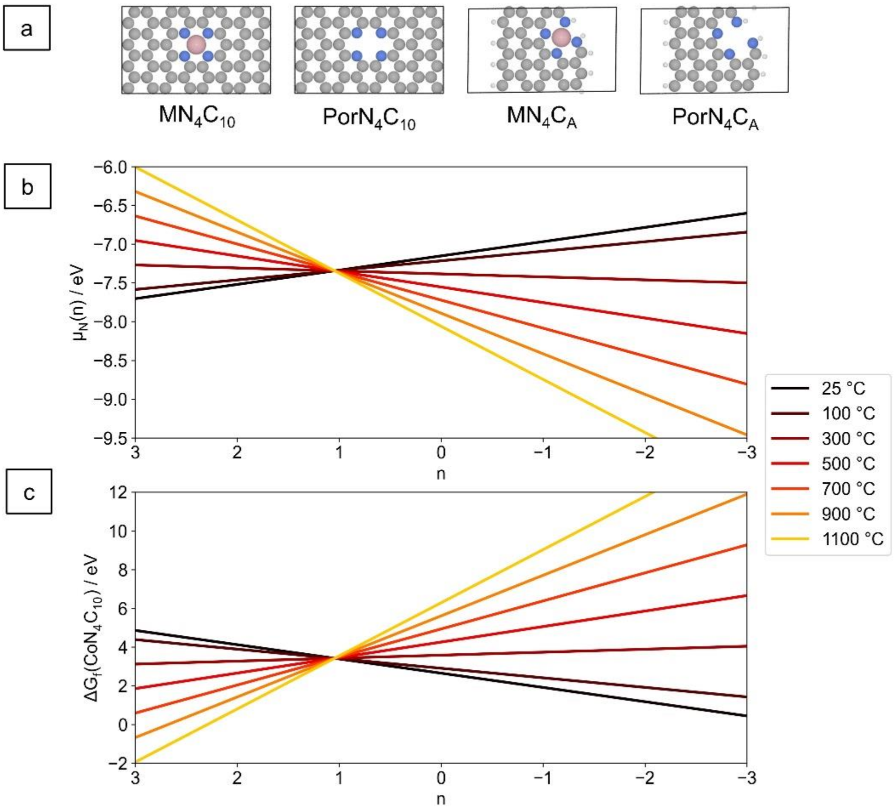

Figure S1 (a) Single metal atom site and pyridine vacancy site doped on bulk graphene (MN$_4$C$_{10}$, PorN$_4$C$_{10}$) and on graphene edge (MN$_4$C$_A$, PorN$_4$C$_A$) (C = grey, N = blue, H = white, M = pink). (b) $\mu_N(n)$ at different temperatures (c) ΔG_f of the CoN$_4$C$_{10}$ structure at different $\mu_N(n)$ and temperatures.

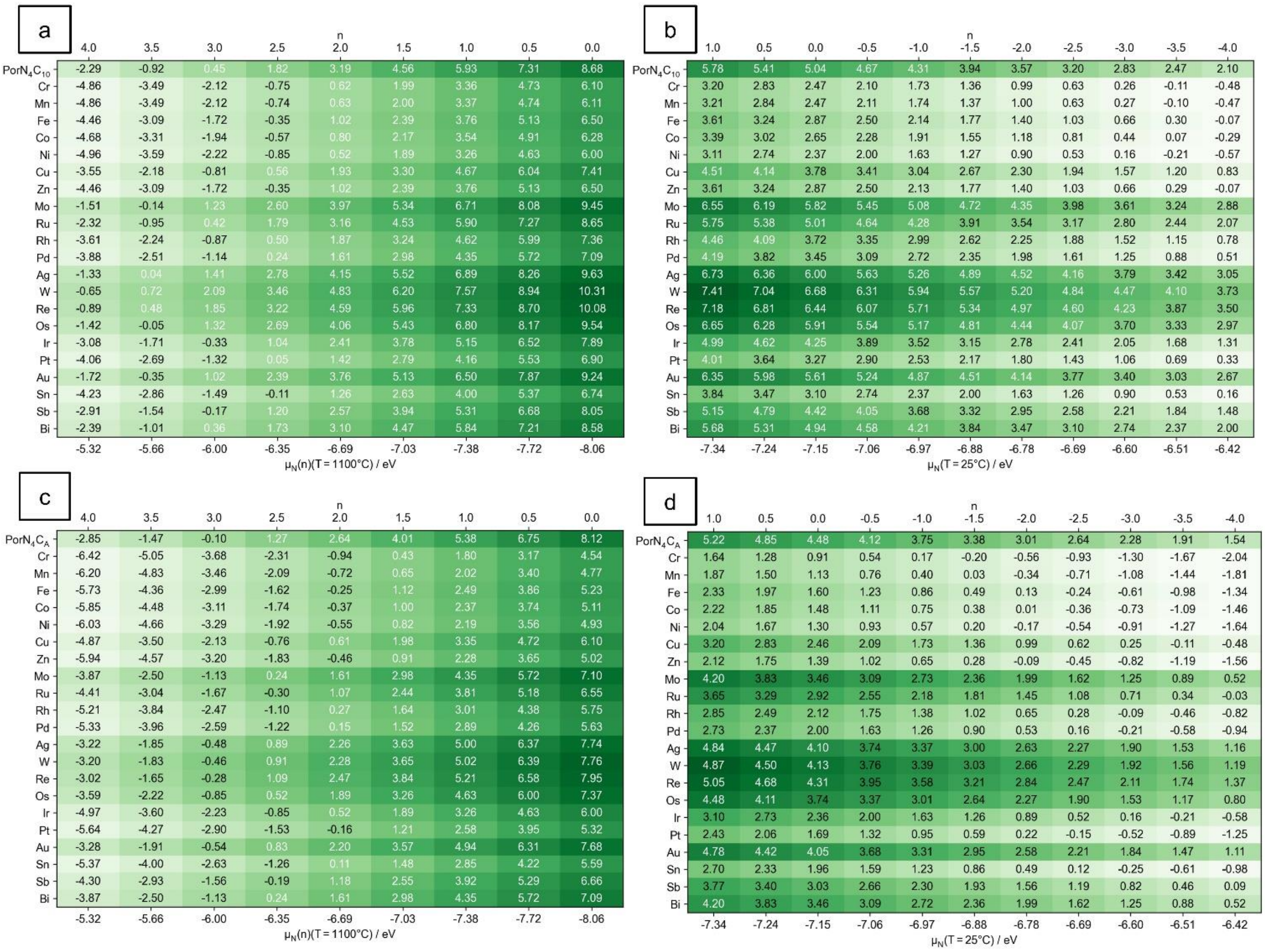

a

n	4.0	3.5	3.0	2.5	2.0	1.5	1.0	0.5	0.0
$PorN_4C_{10}$	-2.29	-0.92	0.45	1.82	3.19	4.56	5.93	7.31	8.68
Cr	-4.86	-3.49	-2.12	-0.75	0.62	1.99	3.36	4.73	6.10
Mn	-4.86	-3.49	-2.12	-0.74	0.63	2.00	3.37	4.74	6.11
Fe	-4.46	-3.09	-1.72	-0.35	1.02	2.39	3.76	5.13	6.50
Co	-4.68	-3.31	-1.94	-0.57	0.80	2.17	3.54	4.91	6.28
Ni	-4.96	-3.59	-2.22	-0.85	0.52	1.89	3.26	4.63	6.00
Cu	-3.55	-2.18	-0.81	0.56	1.93	3.30	4.67	6.04	7.41
Zn	-4.46	-3.09	-1.72	-0.35	1.02	2.39	3.76	5.13	6.50
Mo	-1.51	-0.14	1.23	2.60	3.97	5.34	6.71	8.08	9.45
Ru	-2.32	-0.95	0.42	1.79	3.16	4.53	5.90	7.27	8.65
Rh	-3.61	-2.24	-0.87	0.50	1.87	3.24	4.62	5.99	7.36
Pd	-3.88	-2.51	-1.14	0.24	1.61	2.98	4.35	5.72	7.09
Ag	-1.33	0.04	1.41	2.78	4.15	5.52	6.89	8.26	9.63
W	-0.65	0.72	2.09	3.46	4.83	6.20	7.57	8.94	10.31
Re	-0.89	0.48	1.85	3.22	4.59	5.96	7.33	8.70	10.08
Os	-1.42	-0.05	1.32	2.69	4.06	5.43	6.80	8.17	9.54
Ir	-3.08	-1.71	-0.33	1.04	2.41	3.78	5.15	6.52	7.89
Pt	-4.06	-2.69	-1.32	0.05	1.42	2.79	4.16	5.53	6.90
Au	-1.72	-0.35	1.02	2.39	3.76	5.13	6.50	7.87	9.24
Sn	-4.23	-2.86	-1.49	-0.11	1.26	2.63	4.00	5.37	6.74
Sb	-2.91	-1.54	-0.17	1.20	2.57	3.94	5.31	6.68	8.05
Bi	-2.39	-1.01	0.36	1.73	3.10	4.47	5.84	7.21	8.58
$\mu_N(n)(T = 1100°C)$ / eV	-5.32	-5.66	-6.00	-6.35	-6.69	-7.03	-7.38	-7.72	-8.06

b

n	1.0	0.5	0.0	-0.5	-1.0	-1.5	-2.0	-2.5	-3.0	-3.5	-4.0
$PorN_4C_{10}$	5.78	5.41	5.04	4.67	4.31	3.94	3.57	3.20	2.83	2.47	2.10
Cr	3.20	2.83	2.47	2.10	1.73	1.36	0.99	0.63	0.26	-0.11	-0.48
Mn	3.21	2.84	2.47	2.11	1.74	1.37	1.00	0.63	0.27	-0.10	-0.47
Fe	3.61	3.24	2.87	2.50	2.14	1.77	1.40	1.03	0.66	0.30	-0.07
Co	3.39	3.02	2.65	2.28	1.91	1.55	1.18	0.81	0.44	0.07	-0.29
Ni	3.11	2.74	2.37	2.00	1.63	1.27	0.90	0.53	0.16	-0.21	-0.57
Cu	4.51	4.14	3.78	3.41	3.04	2.67	2.30	1.94	1.57	1.20	0.83
Zn	3.61	3.24	2.87	2.50	2.13	1.77	1.40	1.03	0.66	0.29	-0.07
Mo	6.55	6.19	5.82	5.45	5.08	4.72	4.35	3.98	3.61	3.24	2.88
Ru	5.75	5.38	5.01	4.64	4.28	3.91	3.54	3.17	2.80	2.44	2.07
Rh	4.46	4.09	3.72	3.35	2.99	2.62	2.25	1.88	1.52	1.15	0.78
Pd	4.19	3.82	3.45	3.09	2.72	2.35	1.98	1.61	1.25	0.88	0.51
Ag	6.73	6.36	6.00	5.63	5.26	4.89	4.52	4.16	3.79	3.42	3.05
W	7.41	7.04	6.68	6.31	5.94	5.57	5.20	4.84	4.47	4.10	3.73
Re	7.18	6.81	6.44	6.07	5.71	5.34	4.97	4.60	4.23	3.87	3.50
Os	6.65	6.28	5.91	5.54	5.17	4.81	4.44	4.07	3.70	3.33	2.97
Ir	4.99	4.62	4.25	3.89	3.52	3.15	2.78	2.41	2.05	1.68	1.31
Pt	4.01	3.64	3.27	2.90	2.53	2.17	1.80	1.43	1.06	0.69	0.33
Au	6.35	5.98	5.61	5.24	4.87	4.51	4.14	3.77	3.40	3.03	2.67
Sn	3.84	3.47	3.10	2.74	2.37	2.00	1.63	1.26	0.90	0.53	0.16
Sb	5.15	4.79	4.42	4.05	3.68	3.32	2.95	2.58	2.21	1.84	1.48
Bi	5.68	5.31	4.94	4.58	4.21	3.84	3.47	3.10	2.74	2.37	2.00
$\mu_N(T = 25°C)$ / eV	-7.34	-7.24	-7.15	-7.06	-6.97	-6.88	-6.78	-6.69	-6.60	-6.51	-6.42

c

n	4.0	3.5	3.0	2.5	2.0	1.5	1.0	0.5	0.0
$PorN_4C_A$	-2.85	-1.47	-0.10	1.27	2.64	4.01	5.38	6.75	8.12
Cr	-6.42	-5.05	-3.68	-2.31	-0.94	0.43	1.80	3.17	4.54
Mn	-6.20	-4.83	-3.46	-2.09	-0.72	0.65	2.02	3.40	4.77
Fe	-5.73	-4.36	-2.99	-1.62	-0.25	1.12	2.49	3.86	5.23
Co	-5.85	-4.48	-3.11	-1.74	-0.37	1.00	2.37	3.74	5.11
Ni	-6.03	-4.66	-3.29	-1.92	-0.55	0.82	2.19	3.56	4.93
Cu	-4.87	-3.50	-2.13	-0.76	0.61	1.98	3.35	4.72	6.10
Zn	-5.94	-4.57	-3.20	-1.83	-0.46	0.91	2.28	3.65	5.02
Mo	-3.87	-2.50	-1.13	0.24	1.61	2.98	4.35	5.72	7.10
Ru	-4.41	-3.04	-1.67	-0.30	1.07	2.44	3.81	5.18	6.55
Rh	-5.21	-3.84	-2.47	-1.10	0.27	1.64	3.01	4.38	5.75
Pd	-5.33	-3.96	-2.59	-1.22	0.15	1.52	2.89	4.26	5.63
Ag	-3.22	-1.85	-0.48	0.89	2.26	3.63	5.00	6.37	7.74
W	-3.20	-1.83	-0.46	0.91	2.28	3.65	5.02	6.39	7.76
Re	-3.02	-1.65	-0.28	1.09	2.47	3.84	5.21	6.58	7.95
Os	-3.59	-2.22	-0.85	0.52	1.89	3.26	4.63	6.00	7.37
Ir	-4.97	-3.60	-2.23	-0.85	0.52	1.89	3.26	4.63	6.00
Pt	-5.64	-4.27	-2.90	-1.53	-0.16	1.21	2.58	3.95	5.32
Au	-3.28	-1.91	-0.54	0.83	2.20	3.57	4.94	6.31	7.68
Sn	-5.37	-4.00	-2.63	-1.26	0.11	1.48	2.85	4.22	5.59
Sb	-4.30	-2.93	-1.56	-0.19	1.18	2.55	3.92	5.29	6.66
Bi	-3.87	-2.50	-1.13	0.24	1.61	2.98	4.35	5.72	7.09
$\mu_N(n)(T = 1100°C)$ / eV	-5.32	-5.66	-6.00	-6.35	-6.69	-7.03	-7.38	-7.72	-8.06

d

n	1.0	0.5	0.0	-0.5	-1.0	-1.5	-2.0	-2.5	-3.0	-3.5	-4.0
$PorN_4C_A$	5.22	4.85	4.48	4.12	3.75	3.38	3.01	2.64	2.28	1.91	1.54
Cr	1.64	1.28	0.91	0.54	0.17	-0.20	-0.56	-0.93	-1.30	-1.67	-2.04
Mn	1.87	1.50	1.13	0.76	0.40	0.03	-0.34	-0.71	-1.08	-1.44	-1.81
Fe	2.33	1.97	1.60	1.23	0.86	0.49	0.13	-0.24	-0.61	-0.98	-1.34
Co	2.22	1.85	1.48	1.11	0.75	0.38	0.01	-0.36	-0.73	-1.09	-1.46
Ni	2.04	1.67	1.30	0.93	0.57	0.20	-0.17	-0.54	-0.91	-1.27	-1.64
Cu	3.20	2.83	2.46	2.09	1.73	1.36	0.99	0.62	0.25	-0.11	-0.48
Zn	2.12	1.75	1.39	1.02	0.65	0.28	-0.09	-0.45	-0.82	-1.19	-1.56
Mo	4.20	3.83	3.46	3.09	2.73	2.36	1.99	1.62	1.25	0.89	0.52
Ru	3.65	3.29	2.92	2.55	2.18	1.81	1.45	1.08	0.71	0.34	-0.03
Rh	2.85	2.49	2.12	1.75	1.38	1.02	0.65	0.28	-0.09	-0.46	-0.82
Pd	2.73	2.37	2.00	1.63	1.26	0.90	0.53	0.16	-0.21	-0.58	-0.94
Ag	4.84	4.47	4.10	3.74	3.37	3.00	2.63	2.27	1.90	1.53	1.16
W	4.87	4.50	4.13	3.76	3.39	3.03	2.66	2.29	1.92	1.56	1.19
Re	5.05	4.68	4.31	3.95	3.58	3.21	2.84	2.47	2.11	1.74	1.37
Os	4.48	4.11	3.74	3.37	3.01	2.64	2.27	1.90	1.53	1.17	0.80
Ir	3.10	2.73	2.36	2.00	1.63	1.26	0.89	0.52	0.16	-0.21	-0.58
Pt	2.43	2.06	1.69	1.32	0.95	0.59	0.22	-0.15	-0.52	-0.89	-1.25
Au	4.78	4.42	4.05	3.68	3.31	2.95	2.58	2.21	1.84	1.47	1.11
Sn	2.70	2.33	1.96	1.59	1.23	0.86	0.49	0.12	-0.25	-0.61	-0.98
Sb	3.77	3.40	3.03	2.66	2.30	1.93	1.56	1.19	0.82	0.46	0.09
Bi	4.20	3.83	3.46	3.09	2.72	2.36	1.99	1.62	1.25	0.88	0.52
$\mu_N(T = 25°C)$ / eV	-7.34	-7.24	-7.15	-7.06	-6.97	-6.88	-6.78	-6.69	-6.60	-6.51	-6.42

Figure S2 ΔG_f (in eV) as a function of $\mu_N(n)$: (a) MN_4C_{10} at T=1100 ℃, (b) MN_4C_{10} at T=25 ℃, (c) MN_4C_A at T=1100 ℃, (d) MN_4C_A at T=25 ℃. At n = 0, $\mu_N(n=0)$ is that of the N_2 molecule at 1 bar and at considered temperature in each subplot (T=1100 ℃ for (a) and (c); T=25℃ for (b) and (d)). Lower formation energy (brighter colour background) indicates more thermodynamically favourable to form.

3. Electrolyte Anion Adsorption

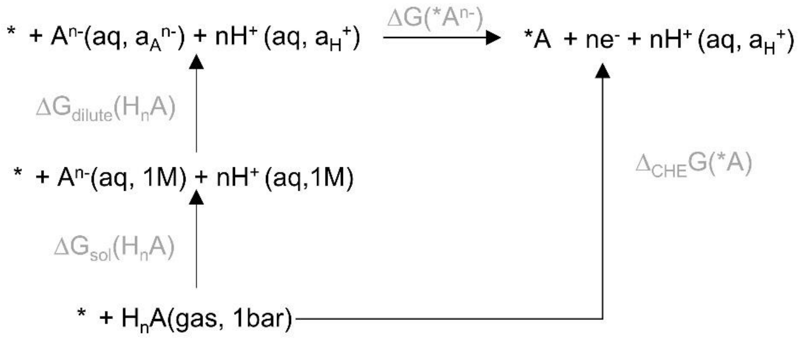

Figure S3 Thermodynamic cycle for the calculation of the free adsorption energy of the electrolyte anion in 0.1 M electrolyte: $\Delta G(*A^{n-})$ [13,14]

The adsorption free energy of the electrolyte anion in added 0.1 M electrolyte at T = 298.25 K is calculated from:

$$\Delta G(*A^{n-}) = G(*A) - neU_{SHE} - n\,pH\,k_BT\,\ln(10) - G(*) - G_{dilute}(A^{n-}) \qquad \text{Equation S4}$$

$\Delta G_{sol}(H_nA)$ is the free energy for dissolving gaseous H_nA (at 1 bar) in water to form anion and proton at the standards state where $[A^{n-}_{(aq)}] = [H^+_{(aq)}] = 1M$.

$$\Delta G_{sol}(H_nA) = G(A^{n-}_{(aq,\,1M)}) + (n/2)G(H_2) - G(H_nA_{(gas)}) = \Delta G_f(A^{n-}_{(aq,\,1M)}) - \Delta G_f(HA_{(gas)}) \qquad \text{Equation S5}$$

where $\Delta G_f(H_nA_{(gas)})$, $\Delta G_f(A^{n-}_{(aq,\,1M)})$ are formation energy of H_nA in gas phase and A^{n-} is solution phase at 1 M, respectively. $\Delta G_{dilute}(A^{n-})$ is the free energy for concentration difference from the standard state.

$$\Delta G_{dilute}(A^{n-}) = G(A^{n-}_{(dilute)}) - G(A^{n-}_{(aq,\,1M)}) = RT \times \ln((a_{H^+})^n \times a_{A^{n-}}) = RT \times \ln((a_{H^+})^n \times \gamma[A^{n-}]) \qquad \text{Equation S6}$$

where a_{H^+}, $a_{A^{n-}}$ are the activity of H^+ and A^{n-}, respective. γ is activity coefficient of A^{n-}, and $[A^{n-}]$ is the concentration of the electrolyte anion. The concentration of the added electrolyte is taken to be 0.1 M and the poisoning gas molecule is considered at 1 bar. At different pH, we assume that pH is adjusted by adding non-adsorbing acid and a_{H^+} is calculated from pH = $-\log(a_{H^+})$. The concentration of each electrolyte anion species in the 0.1 M solution at each pH is calculated based on its pK_a value. Then $G_{dilute}(A^{n-})$ in Equation S4 can be expressed as:

$$G_{dilute}(A^{n-}) = \Delta G_{sol}(H_nA) + \Delta G_{dilute}(A^{n-}) - (n/2)G(H_2) + G(H_nA_{(gas)}) \qquad \text{Equation S7}$$

Finally, the adsorption free energy of electrolyte anion can be calculated using the thermodynamic cycle in Figure S3 and can be expressed as follows:

$$\Delta G(*A^{n-}) = \Delta_{CHE}G(*A) - \Delta G_{sol}(H_nA) - \Delta G_{dilute}(A^{n-}) \qquad \text{Equation S8}$$

where $\Delta_{CHE}G(*A) = G(*A) + (1/2)G(H_2) + n\Delta G_H + n\Delta G_e - G(*) - G(H_nA_{(gas)})$ and $\Delta G_H = -k_BT$ pH ln(10) and $\Delta G_e = -eU_{SHE}$. All the relevant values (γ, ΔG_f, pK_a) are taken from literature and listed in Table S2 and Table S3.

Table S2 Gas molecules at T = 298.15 K and 1 bar.

	E_{DFT} / eV	ZPE / eV [8]	H(T=0→298K) / eV [8]	TS / eV [8]	BEEF-vdW / eV [11,12]
H_2O	-12.83	0.56	0.10	0.67	-0.03
H_2	-7.18	0.27	0.09	0.40	0.09
H_3PO_4	-38.54	1.27 [a]	0.21 [a]	1.02 [a]	-
H_2SO_4	-29.87	1.04	0.17	0.93	-
HNO_3	-22.14	0.70	0.12	0.77	-
HCl	-4.54	0.18	0.09	0.58	-
HF	-6.20	0.25	0.09	0.54	-
HCOOH	-25.54	0.89	0.11	0.77	-
$HClO_4$	-16.85	0.73	0.16	0.92	-
HCN	-3.71	0.43	0.10	0.63	-
H_2CO_3	-31.00	1.05 [a]	0.13 [a]	0.82 [a]	-
NO	-9.33	0.12	0.10	0.65	-
CO	-12.10	0.13	0.09	0.61	0.15
CO_2	-18.43	0.31	0.10	0.66	0.30
NH_3	-18.46	0.89	0.11	0.60	-
N_2	-13.94	0.14	0.09	0.59	-

[a] ZPE, enthalpy and entropy are calculated using thermochemistry class in ASE package, treating a molecule as an ideal gas.

Table S3 Electrolyte anions: pK_a, solvation free energy, and activity coefficient for 0.1 M H_nA.

Electrolyte	Anion	pK_a[9]	ΔG_f(gas) / eV	ΔG_f(aq, 1M) / eV	ΔG_{sol} / eV	γ ($a_{A^{-n}}$) (0.1M)
H_3PO_4	H_3PO_4	2.16	-11.36 [14]	-	-	-
	$H_2PO_4^-$	7.21	-	-11.75 [9]	-0.39	0.78 [b]
	HPO_4^{-2}	12.32	-	-11.33 [9]	0.03	0.51 [b]
	PO_4^{-3}	-	-	-10.59 [9]	0.77	0.34 [b]
H_2SO_4	H_2SO_4	-2.00	-6.75 [14]	-	-	-
	HSO_4^-	1.99	-	-7.86 [9]	-1.11	0.28 [9]
	SO_4^{-2}	-	-	-7.74 [9]	-0.99	0.14 [9]
HNO_3	HNO_3	-1.30	-0.57 [8]	-	-	-
	NO_3^-	-	-	-1.16 [9]	-0.59	0.79 [9]
HCl	HCl	-7.00	-0.99 [15]	-		-
	Cl^-	-	-	-1.36 [9]	-0.37	0.80 [9]
HF	HF	3.20	-2.84 [15]	-	-	-
	F^-	-	-	-2.90 [9]	-0.06	0.08 [9]
HCOOH	HCOOH	3.75	-3.64 [14]	-	-	-
	$HCOO^-$	-	-	-3.65 [9]	-0.01	0.78 [b]
$HClO_4$	$HClO_4$	-1.60	0.87 [14]	-	-	-
	ClO_4^-	-	-	-0.09 [9]	-0.96	0.80 [9]
HCN	HCN	9.21	1.30 [15]	-		-
	CN^-	-	-	1.79 [9]	0.50	0.78 [b]
H_2CO_3	H_2CO_3	6.35	-6.87 [16a]	-	-	-
	HCO_3^-	10.33	-	-6.10 [15]	0.78	0.77 [15]
	CO_3^{-2}			-5.49 [15]	0.51	1.38 [15]

[a] only enthalpy data was available. The entropy is calculated using thermochemistry class in ASE package, treating a molecule as an ideal gas and the formation energy in the gas phase is calculated from the following reaction: $H_2CO_{3(gas)} \rightarrow H_2O_{(gas)} + CO_{2(gas)}$

[b] The activity coefficients are estimated by using the Davies equation[17].

4. Dissolution Reaction

The dissolution of the single metal atom from the graphene host into the electrolyte, resulting in dissolved metal ion (M^{x+}) and the graphene host cavity (N_4CH_n) is considered as follows:

$$MN_4C + nH^+_{(aq)} \rightarrow M^{x+}_{(aq)} + N_4CH_n + (x-n)e^-$$

The reaction free energy for dissolving a single metal atom from the graphene host structure at the potential U_{SHE} and pH is considered as follows[18]:

$$\Delta G_{diss} = G(M^{x+}_{(aq)}) + G(N_4CH_n) + (x-n)\Delta G_e - G(MN_4C) - n\Delta G_H - (1/2)G(H_2) \qquad \text{Equation S9}$$

N_4CH_n is the graphene host after the single metal is dissolved and can have different protonation degrees at the N dangling bonds. We considered N_4CH_n with n = 0-4 for $N_4C_{10}H_n$ and $N_4C_AH_n$, where their free energy is taken from the previous study[5]. M^{x+} is a dissolved metal ion, U_{SHE} is the applied potential vs SHE and $G(M^{x+}_{(aq)}) = E_M(bulk) + \Delta G_x$, where $E_M(bulk)$ is energy per atom of the metal in their bulk structure and ΔG_x is the free reaction energy of the dissolution reaction of the bulk metal taken from literature and shown in Table S4. In this work, the concentration of dissolved metal ion is 10^{-6} M and T = 298.15 K.

Table S4 Free reaction energy of the dissolution reaction of the bulk metal and calculated DFT energy per atom of the metal in their bulk structure (E_0 is in V and E_M(bulk) is in eV/atom)

metal	ion	reaction	E_0 (V)	E_M(bulk) [a]
Cr	$1 = Cr^{2+}$	$G(Cr^{2+}) = E_{Cr}(bulk) + 2(E_0 + (0.0592/2)\log[Cr^{2+}])$	$E_0 = -0.91$ [9]	-7.17
	$2 = Cr^{3+}$	$G(Cr^{3+}) = E_{Cr}(bulk) + 3(E_0 + (0.0592/3)\log[Cr^{3+}])$	$E_0 = -0.74$ [9]	
	$3 = CrOH^{2+}$	$G(CrOH^{2+}) = G(Cr^{3+}) + G(H_2O) – (1/2)G(H_2) + 2.3026\ k_BT\ pH_0$	$pH_0 = 3.81$ [19]	
	$4 = HCrO_4^-$	$G(HCrO_4^-) = G(Cr^{3+}) + 4G(H_2O) - (7/2)G(H_2) + 3(E_0 + (0.0592/3)\log([HCrO4^-]/[Cr^{3+}]))$	$E_0 = 1.35$ [9]	
	$5 = CrO_4^{-2}$	$G(CrO_4^{-2}) = G(Cr^{3+}) + 3G(H_2O) - 4{*}G(H_2) + 3(E_0 + (0.0592/3)\log([CrO_4^{-2}]/[Cr^{3+}]))$	$E_0 = 1.48$ [19]	
Mn	$1 = Mn^{2+}$	$G(Mn^{2+}) = E_{Mn}(bulk) + 2(E_0 + (0.0592/2)\log[Mn^{2+}])$	$E_0 = -1.19$ [9]	-6.45
	$2 = Mn^{3+}$	$G(Mn^{3+}) = G(Mn^{2+}) + E_0 + (0.0592)\log([Mn^{3+}]/[Mn^{2+}])$	$E_0 = 1.54$ [9]	
	$3 = MnO_4^{-2}$	$G(MnO_4^{2-}) = G(Mn^{2+}) + 4G(H_2O) - 4G(H_2) + 4(E_0 + (0.0592/4)\log([MnO_4^{2-}]/[Mn^{2+}]))$	$E_0 = 1.74$ [9]	
	$4 = MnO_4^-$	$G(MnO_4^-) = G(Mn^{2+}) + 4G(H_2O) - 4G(H_2) + 5(E_0 + (0.0592/5)\log([MnO_4^-]/[Mn^{2+}]))$	$E_0 = 1.51$ [9]	
	$5 = MnO_4^{-3}$	$G(MnO_4^{3-}) = G(MnO_4^{2-}) + E_0 + (0.0592)\log([MnO_4^{3-}]/[MnO_4^{2-}])$	$E_0 = -0.27$ [20]	
Fe	$1 = Fe^{2+}$	$G(Fe^{2+}) = E_{Fe}(bulk) + 2(E_0 + (0.0592/2)\log[Fe^{2+}])$	$E_0 = -0.45$ [9]	-5.65
	$2 = Fe^{3+}$	$G(Fe^{3+}) = E_{Fe}(bulk) + 3(E_0 + (0.0592/3)\log[Fe^{3+}])$	$E_0 = -0.04$ [9]	
	$3 = HFeO_4^-$	$G(HFeO_4^-) = G(Fe^{3+}) + 4G(H_2O) - (3/2)G(H_2) + 3(E_0 + (0.0592/3)\log([HFeO_4^-]/[Fe^{3+}]))$	$E_0 = 2.07$ [9]	
	$4 = FeO_4^{-2}$	$G(FeO_4^{2-}) = G(Fe^{3+}) + 4G(H_2O) - 4G(H_2) + 3(E_0 + (0.0592/3)\log([FeO_4^{2-}]/[Fe^{3+}]))$	$E_0 = 2.20$ [9]	
	$5 = FeOH^{2+}$	$G(FeOH^{2+}) = G(Fe^{3+}) + G(H_2O) – (1/2)G(H_2) + 2.3026\ k_BT\ pH_0$	$pH_0 = 2.43$ [19]	
	$6 = HFeO_2^-$	$G(HFeO_2^-) = G(Fe^{2+}) + 2G(H_2O) - (3/2)G(H_2) + 2.3026\ k_BT\ pH_0$	$pH_0 = 31.58$ [19]	
	$7 = FeO_2^-$	$G(FeO_2^-) = G(HFeO_2^-) - (1/2)G(H_2) + E_0 + (0.0592)\log([FeO_2^-]/[HFeO_2^-])$	$E_0 = -0.69$ [19]	
Co	$1 = Co^{2+}$	$G(Co^{2+}) = E_{Co}(bulk) + 2(E_0 + (0.0592/2)\log[Co^{2+}])$	$E_0 = -0.28$ [9]	-4.29
	$2 = Co^{3+}$	$G(Co^{3+}) = G(Co^{2+}) + E_0 + (0.0592)\log([Co^{3+}]/[Co^{2+}])$	$E_0 = 1.92$ [9]	
	$3 = HCoO_2^-$	$G(HCoO_2^-) = G(Co^{2+}) + 2G(H_2O) - (3/2){*}G(H_2) + 2.3026\ k_BT\ pH_0$	$pH_0 = 31.70$ [19]	
Ni	$1 = Ni^{2+}$	$G(Ni^{2+}) = E_{Ni}(bulk) + 2(E_0 + (0.0592/2)\log[Ni^{2+}])$	$E_0 = -0.26$ [9]	-2.53
	$2 = Ni^{3+}$	$G(Ni^{3+}) = G(Ni^{2+}) + E_0 + (0.0592)\log([Ni^{3+}]/[Ni^{2+}])$	$E_0 = 2.30$ [21]	
	$3 = HNiO_2^-$	$G(HNiO_2^-) = G(Ni^{2+}) + 2G(H_2O) - (3/2)G(H_2) + 2.3026\ k_BT\ pH_0$	$pH_0 = 30.40$ [19]	
Cu	$1 = Cu^{2+}$	$G(Cu^{2+}) = E_{Cu}(bulk) + 2(E_0 + (0.0592/2)\log[Cu^{2+}])$	$E_0 = 0.34$ [9]	-0.64
	$2 = Cu^{+1}$	$G(Cu^+) = E_{Cu}(bulk) + E_0 + (0.0592)\log[Cu^+]$	$E_0 = 0.34$ [9]	
	$3 = Cu^{3+}$	$G(Cu^{3+}) = G(Cu^{2+}) + E_0 + (0.0592)\log([Cu^{3+}]/[Cu^{2+}])$	$E_0 = 2.40$ [9]	
	$4 = CuO_2^-$	$G(CuO_2^-) = G(Cu^{2+}) + 2G(H_2O) - 2G(H_2) + 2.3026\ k_BT\ pH_0$	$pH_0 = 39.88$ [19]	
	$5 = HCuO_2^-$	$G(HCuO_2^-) = G(Cu^{2+}) + 2G(H_2O) - (3/2)G(H_2) + 2.3026\ k_BT\ pH_0$	$pH_0 = 26.72$ [19]	
Zn	$1 = Zn^{2+}$	$G(Zn^{2+}) = E_{Zn}(bulk) + 2(E_0 + (0.0592/2)\log[Zn^{2+}])$	$E_0 = -0.76$ [9]	2.06
	$2 = ZnOH^{+1}$	$G(ZnOH^{+1}) = G(Zn^{2+}) - (1/2)G(H_2) + G(H_2O) + 2.3026\ k_BT\ pH_0$	$pH_0 = 9.67$ [19]	
	$3 = HZnO_2^-$	$G(HZnO_2^-) = G(Zn^{2+}) + 2G(H_2O) - (3/2){*}G(H_2) + 2.3026\ k_BT\ pH_0$	$pH_0 = 27.63$ [19]	
	$4 = ZnO_2^{-2}$	$G(ZnO_2^{2-}) = G(HZnO_2^-) - (1/2)G(H_2) + 2.3026\ k_BT\ pH_0$	$pH_0 = 13.17$ [19]	
Mo	$1 = Mo^{3+}$	$G(Mo^{3+}) = E_{Mo}(bulk) + 3(E_0 + (0.0592/3)\log[Mo^{3+}])$	$E_0 = -0.20$ [9]	-8.17
	$2 = HMoO_4^-$	$G(HMoO_4^-) = G(Mo^{3+}) + 4G(H_2O) + 3(E_0 + (0.0592/3)\log([HMoO_4^-]/[Mo^{3+}])) - (7/2)G(H_2)$	$E_0 = 0.39$ [19]	
	$3 = MoO_4^{-2}$	$G(MoO_4^{2-}) = G(Mo^{3+}) + 4G(H_2O) + 3(E_0 + (0.0592/3)\log([MoO_4^{2-}]/[Mo^{3+}])) - 4G(H_2)$	$E_0 = 0.51$ [9]	

metal	ion	reaction	E_0 (V)	E_M(bulk) [a]
Ru	1 = Ru^{2+}	$G(Ru^{2+}) = E_{Ru}(bulk) + 2(E_0 + (0.0592/2) \log[Ru^{2+}])$	$E_0 = 0.46$ [9]	-6.26
	2 = Ru^{3+}	$G(Ru^{3+}) = G(Ru^{2+}) + E_0 + (0.0592) \log([Ru^{3+}]/[Ru^{2+}])$	$E_0 = 0.25$ [9]	
	3 = RuO_4^{-2}	$G(RuO_4^{2-}) = G(Ru^{2+}) + 4G(H_2O) - 4G(H_2) + 4(E_0 + (0.0592/4) \log([RuO_4^{2-}]/[Ru^{2+}]))$	$E_0 = 1.56$ [9]	
	4 = RuO_4^-	$G(RuO_4^-) = G(Ru^{2+}) + 4G(H_2O) - 4G(H_2) + 5(E_0 + (0.0592/5) \log([RuO_4^-]/[Ru^{2+}]))$	$E_0 = 1.37$ [9]	
Rh	1 = Rh^{+1}	$G(Rh^+) = E_{Rh}(bulk) + E_0 + (0.0592) \log[Rh^+]$	$E_0 = 0.60$ [9]	-4.24
	2 = Rh^{2+}	$G(Rh^+) = G(Rh^+) + E_0 + (0.0592) \log([Rh^{2+}]/[Rh^+])$	$E_0 = 0.60$ [9]	
	3 = Rh^{3+}	$G(Rh^{3+}) = E_{Rh}(bulk) + 3(E_0 + (0.0592/3) \log[Rh^{3+}])$	$E_0 = 0.76$ [9]	
	4 = RhO_4^{-2}	$G(RhO_4^{-2}) = G(Rh^{2+}) + 4G(H_2O) - 4G(H_2) + 4(E_0 + (0.0592/4) \log([RhO_4^{-2}]/[Rh^{2+}]))$	$E_0 = 2.00$ [19]	
	5 = $RhOH^{2+}$	$G(RhOH^{2+}) = G(Rh^+) + G(H_2O) - (1/2)G(H_2) + 5(E_0 + (0.0592/5) \log([RuOH^{2+}]/[Ru^+]))$	$E_0 = 0.23$ [9]	
Pd	1 = Pd^{2+}	$G(Pd^{2+}) = E_{Pd}(bulk) + 2(E_0 + (0.0592/2) \log[Pd^{2+}])$	$E_0 = 0.95$ [9]	-1.96
Ag	1 = Ag^{+1}	$G(Ag^+) = E_{Ag}(bulk) + E_0 + (0.0592) \log[Ag^+]$	$E_0 = 0.80$ [9]	0.55
	2 = Ag^{2+}	$G(Ag^{2+}) = G(Ag^+) + E_0 + (0.0592) \log([Ag^{2+}]/[Ag^+])$	$E_0 = 1.98$ [9]	
	3 = Ag^{3+}	$G(Ag^{3+}) = G(Ag^{2+}) + E_0 + (0.0592) \log([Ag^{3+}]/[Ag^+])$	$E_0 = 1.80$ [9]	
	4 = AgO^-	$G(AgO^-) = G(Ag^+) - G(H_2) + G(H_2O) + 2.3026\ k_BT\ pH_0$	$pH_0 = 24.04$ [19]	
	5 = AgO^{+1}	$G(AgO^+) = G(Ag^+) - G(H_2) + G(H_2O) + 2(E_0 + (0.0592/2) \log([AgO^+]/[Ag^+]))$	$E_0 = 2.00$ [19]	
W	1 = W^{3+}	$G(W^{3+}) = E_W(bulk) + 3(E_0 + (0.0592/3) \log[W^{3+}])$	$E_0 = 0.10$ [9]	-0.43
	2 = WO_4^{-2}	$G(WO4^{2-}) = G(W^{3+}) + 4G(H_2O) - 4G(H_2) + 3(E_0 + (0.0592/3) \log([WO_4^{2-}]/[W^{3+}]))$	$E_0 = 0.15$ [19]	
Re	1 = Re^{3+}	$G(Re^{3+}) = E_{Re}(bulk) + 3(E_0 + (0.0592/3) \log[Re^{3+}])$	$E_0 = 0.30$ [9]	-9.59
	2 = Re^-	$G(Re^-) = G(Re^{3+}) + 4(E_0 + (0.0592/4) \log([Re^-]/[Re^{3+}]))$	$E_0 = 0.13$ [19]	
	3 = ReO_4^-	$G(ReO_4^-) = G(Re^-) + 4G(H_2O) - 4G(H_2) + 8(E_0 + (0.0592/8) \log([ReO_4^-]/[Re^-]))$	$E_0 = 0.27$ [19]	
	4 = ReO_4^{-2}	$G(ReO_4^{2-}) = G(Re^-) + 4G(H_2O) - 4G(H_2) + 7(E_0 + (0.0592/7) \log([ReO_4^{2-}]/[Re^-]))$	$E_0 = 0.41$ [19]	
Os	1 = OsO_4^{-2}	$G(OsO_4^{2-}) = E_{Os}(bulk) + 4G(H_2O) - 4G(H_2) + 6(E_0 + (0.0592/6) \log[OsO_4^{2-}])$	$E_0 = 0.99$ [19]	-8.28
	2 = OsO_5^{-2}	$G(OsO_5^{2-}) = G(OsO_4^{2-}) + G(H_2O) - G(H_2) + 2(E_0 + (0.0592/2) \log([OsO_5^{2-}]/[OsO_4^{2-}]))$	$E_0 = 1.14$ [19]	
	3 = $HOsO_4^-$	$G(HOsO_4^-) = G(OsO_4^{2-}) + G(H_2O) - (1/2)G(H_2) + 2(E_0 + (0.0592/2) \log([HOsO_4^-]/[OsO_4^{2-}]))$	$E_0 = 0.71$ [19]	
Ir	1 = Ir^{3+}	$G(Ir^{3+}) = E_{Ir}(bulk) + 3(E_0 + (0.0592/3) \log[Ir^{3+}])$	$E_0 = 1.16$ [9]	-5.82
	2 = IrO_4^{-2}	$G(IrO_4^{2-}) = G(Ir^{3+}) - 4G(H_2) + 4G(H_2O) + 3(E_0 + (0.0592/3) \log([IrO_4^{2-}]/[Ir^{3+}]))$	$E_0 = 1.45$ [19]	
Pt	1 = Pt^{2+}	$G(Pt^{2+}) = E_{Pt}(bulk) + 2(E_0 + (0.0592/2) \log[Pt^{2+}])$	$E_0 = 1.18$ [9]	-3.13
Au	1 = Au^{+1}	$G(Au^+) = E_{Au}(bulk) + E_0 + (0.0592) \log[Au^+]$	$E_0 = 1.70$ [9]	-0.25
	2 = Au^{2+}	$G(Au^{2+}) = G(Au^+) + E_0 + (0.0592) \log([Au^{2+}]/ [Au^+])$	$E_0 = 1.80$ [9]	
	3 = Au^{3+}	$G(Au^{3+}) = E_{Au}(bulk) + 3(E_0 + (0.0592/3) \log[Au^{3+}])$	$E_0 = 1.50$ [9]	
	4 = $AuOH^{2+}$	$G(AuOH^{2+}) = G(Au^+) + G(H_2O) - (1/2)G(H_2) + 2(E_0 + (0.0592/2) \log([AuOH^{2+}]/[Au^+]))$	$E_0 = 1.32$ [9]	
	5 = $H_2AuO_3^-$	$G(H_2AuO_3^-) = G(Au^+) + 3G(H_2O) - 2G(H_2) + 2(E_0 + (0.0592/2) \log([H_2AuO_3^-]/[Au^+]))$	$E_0 = 1.85$ [19]	
	6 = $HAuO_3^{-2}$	$G(HAuO_3^{2-}) = G(Au^+) + 3G(H_2O) - (5/2)G(H_2) + 2(E_0 + (0.0592/2) \log([HAuO_3^{-2}]/[Au^+]))$	$E_0 = 2.24$ [19]	
	7 = AuO_3^{-3}	$G(AuO_3^{3-}) = G(HAuO_3^{2-}) - (1/2)G(H_2) + 2.3026\ k_BT\ pH_0$	$pH_0 = 15.99$ [19]	
Sn	1 = Sn^{2+}	$G(Sn^{2+}) = E_{Sn}(bulk) + 2(E_0 + (0.0592/2) \log[Sn^{2+}])$	$E_0 = -0.14$ [9]	-1.18
	2 = Sn^{+4}	$G(Sn^{4+}) = G(Sn^{2+}) + 2(E_0 + (0.0592/2) \log([Sn^{4+}]/[Sn^{2+}]))$	$E_0 = 0.15$ [9]	
	3 = SnO_3^{-2}	$G(SnO_3^{2-}) = G(Sn^{2+}) + 3G(H_2O) - 3G(H_2) + 2(E_0 + (0.0592/2) \log([SnO_3^{2-}]/[Sn^{2+}]))$	$E_0 = 0.84$ [9]	
	4 = $HSnO_2^-$	$G(HSnO_2^-) = G(SnO_3^{2-}) - G(H_2O) + (3/2)G(H_2) - 2(E_0 + (0.0592/2) \log([HSnO_2^-]/[SnO_3^{2-}]))$	$E_0 = 0.37$ [9]	
	5 = $SnOH^{+1}$	$G(SnOH^+) = G(Sn^{3+}) + G(H_2O) - (1/2)G(H_2) + 2.3026\ k_BT\ pH_0$	$pH_0 = 0.56$ [9]	

metal	ion	reaction	E_0 (V)	E_M(bulk) [a]
Sb	1 = SbO^{+1}	$G(SbO^+) = E_{Sb}(bulk) + 2G(H_2O) – G(H_2) + 3(E_0 + (0.0592/3) \log[SbO^+])$	$E_0 = 0.21$ [9]	-2.09
	2 = $HSbO_2$	$G(HSbO_2) = G(SbO^+) - (1/2)G(H_2) + G(H_2O) + 2.3026\ k_BT\ pH_0$	$pH_0 = 0.87$ [19]	
	3 = SbO_2^-	$G(SbO_2^-) = G(HSbO_2) - (1/2)G(H_2) + 2.3026\ k_BT\ pH_0$	$pH_0 =11.00$ [19]	
	4 = SbO_2^{+1}	$G(SbO_2^+) = G(SbO^-) + G(H_2O) – G(H_2) + 2(E_0 + (0.0592/2) \log([SbO_2^+]/[SbO_2^-]))$	$E_0 = 0.72$ [19]	
	5 = SbO_3^-	$G(SbO_3^-) = G(SbO^-) + 2G(H_2O) - 2G(H_2) + 2(E_0 + (0.0592/2) \log([SbO_3^-]/[SbO_2^-]))$	$E_0 = 0.70$ [19]	
Bi	1 = Bi^{+1}	$G(Bi^+) = E_{Bi}(bulk) + E_0 + (0.0592) \log[Bi^+]$	$E_0 = 0.50$ [9]	-1.19
	2 = Bi^{3+}	$G(Bi^{3+}) = E_{Bi}(bulk) + 3(E_0 + (0.0592/3) \log[Bi^{3+}])$	$E_0 = 0.38$ [9]	
	3 = $BiOH^{2+}$	$G(BiOH^{2+}) = G(Bi^{3+}) - (1/2)G(H_2) + G(H_2O) + 2.3026\ k_BT\ pH_0$	$pH_0 = 2.00$ [19]	
	4 = BiO^{+1}	$G(BiO^+) = G(Bi^{3+}) - (1/2)G(H_2) + 2.3026\ k_BT\ pH_0$	$pH_0 = 3.37$ [19]	

[a] Calculated from the stable bulk structure of each metal taken from Material project[22].

5. Electrochemical Stability

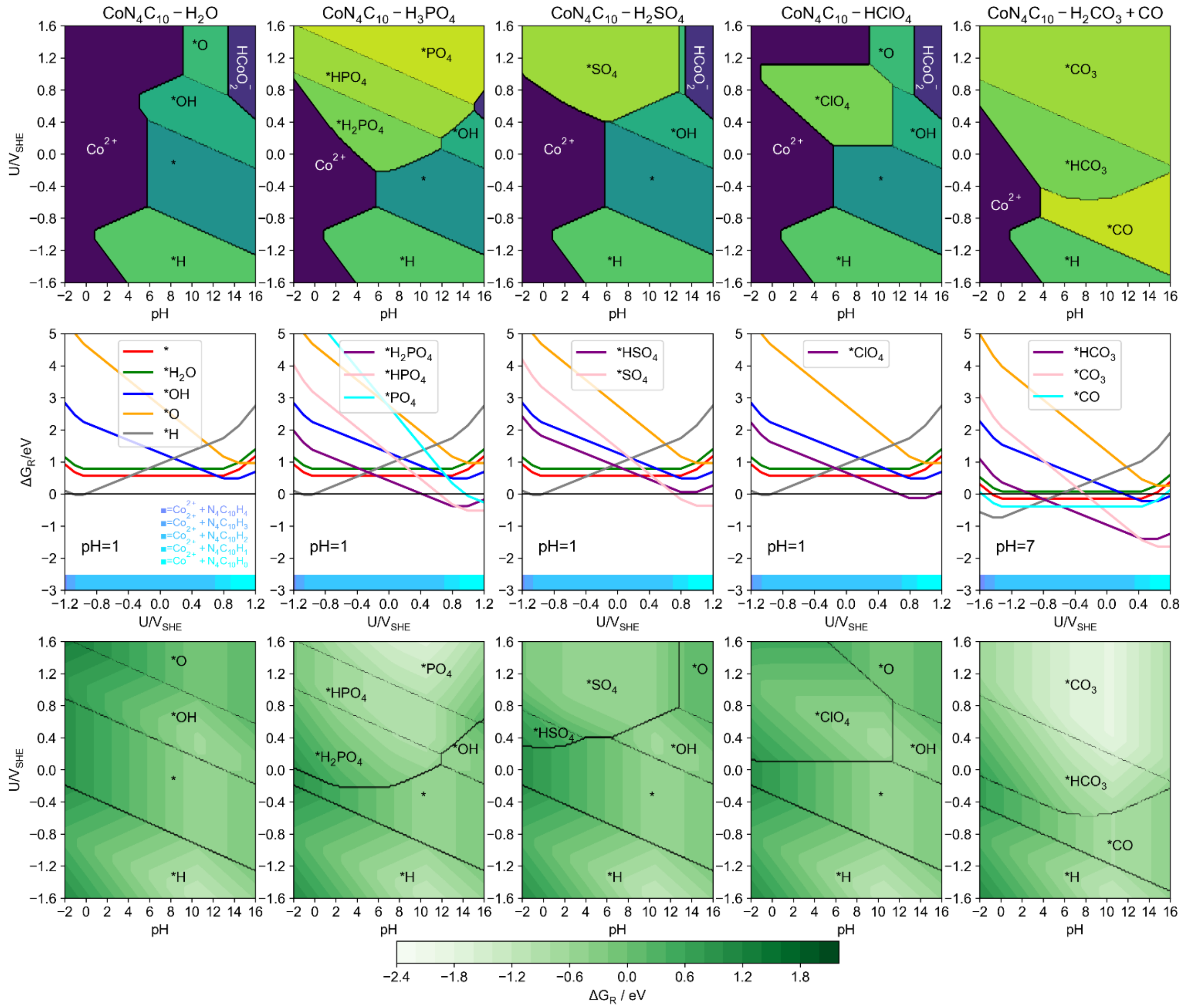

Figure S4 CoN_4C_{10} site in different 0.1 M electrolyte**:** (top) Stability diagram, (middle) ΔG_R of the surfaces at specific pH. The most stable dissolved species for each applied potential which is used as a reference for ΔG_R are superimposed as horizontal bars at the bottom., and (bottom) ΔG_R of the most stable surface.

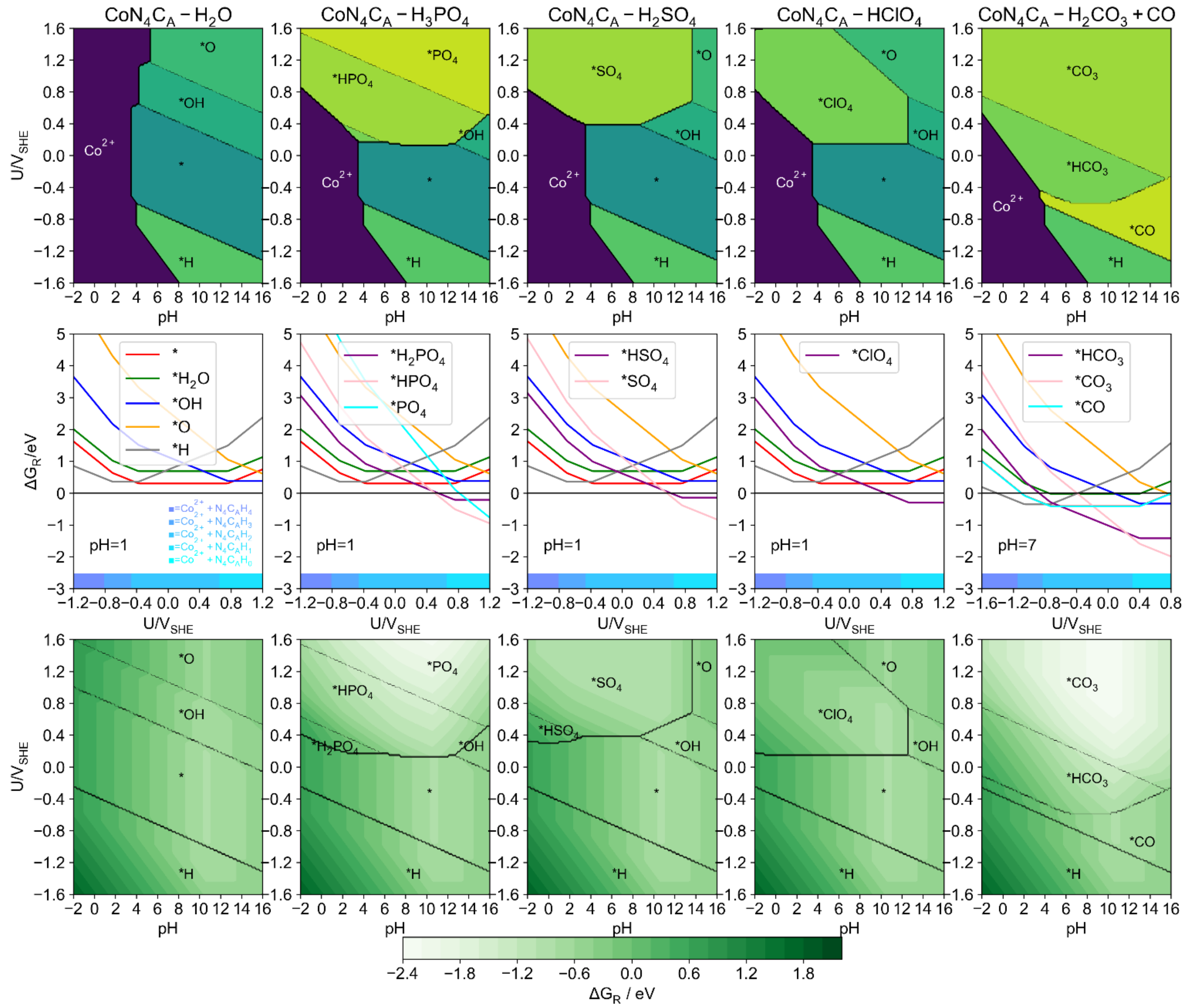

Figure S5 CoN_4C_A site in different 0.1 M electrolytes**:** (top) Stability diagram, (middle) ΔG_R of the surfaces at specific pH. The most stable dissolved species for each applied potential which is used as a reference for ΔG_R are superimposed as horizontal bars at the bottom., and (bottom) ΔG_R of the most stable surface.

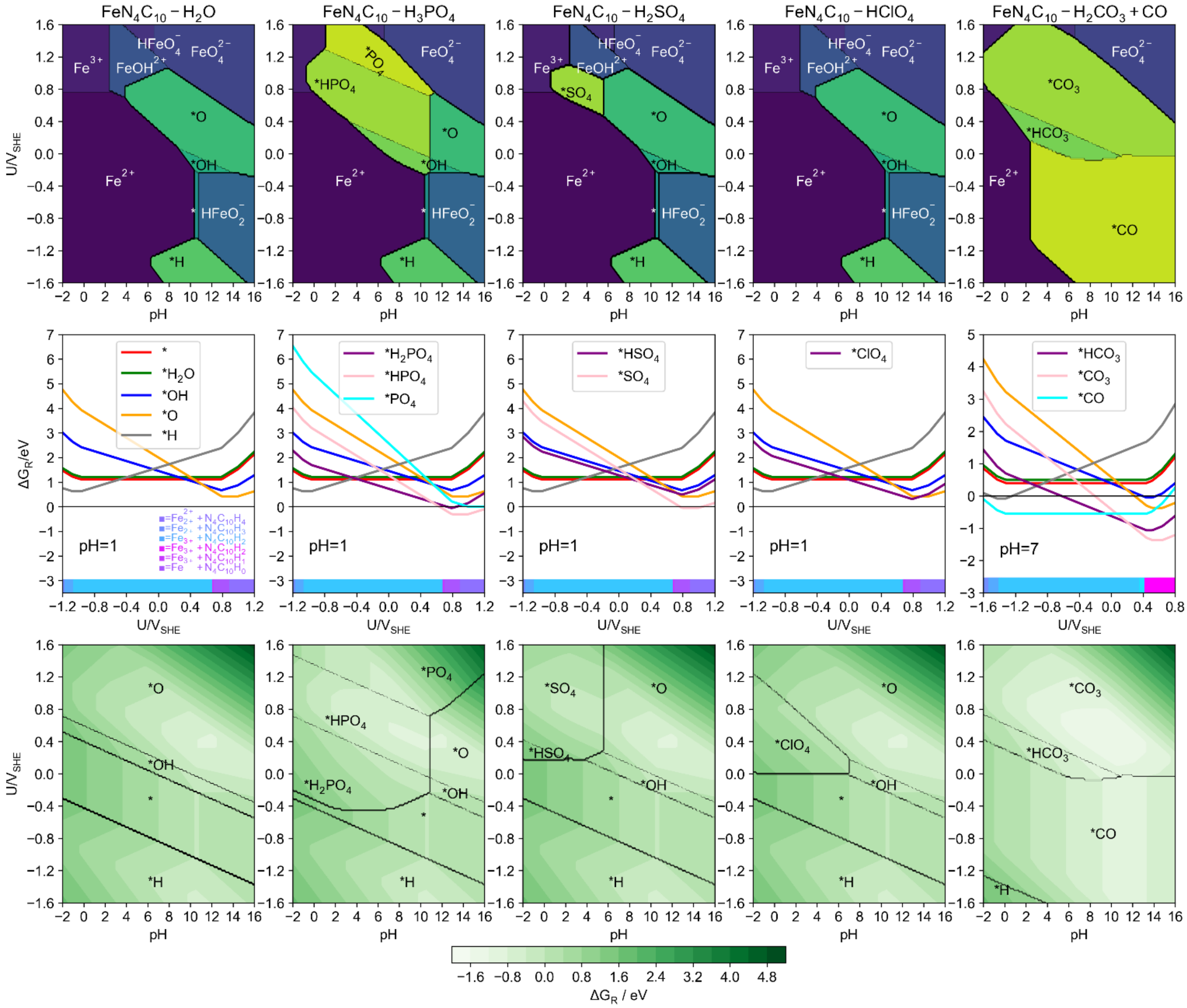

Figure S6 FeN_4C_{10} site in different 0.1 M electrolytes**:** (top) Stability diagram, (middle) ΔG_R of the surfaces at specific pH. The most stable dissolved species for each applied potential which is used as a reference for ΔG_R are superimposed as horizontal bars at the bottom., and (bottom) ΔG_R of the most stable surface.

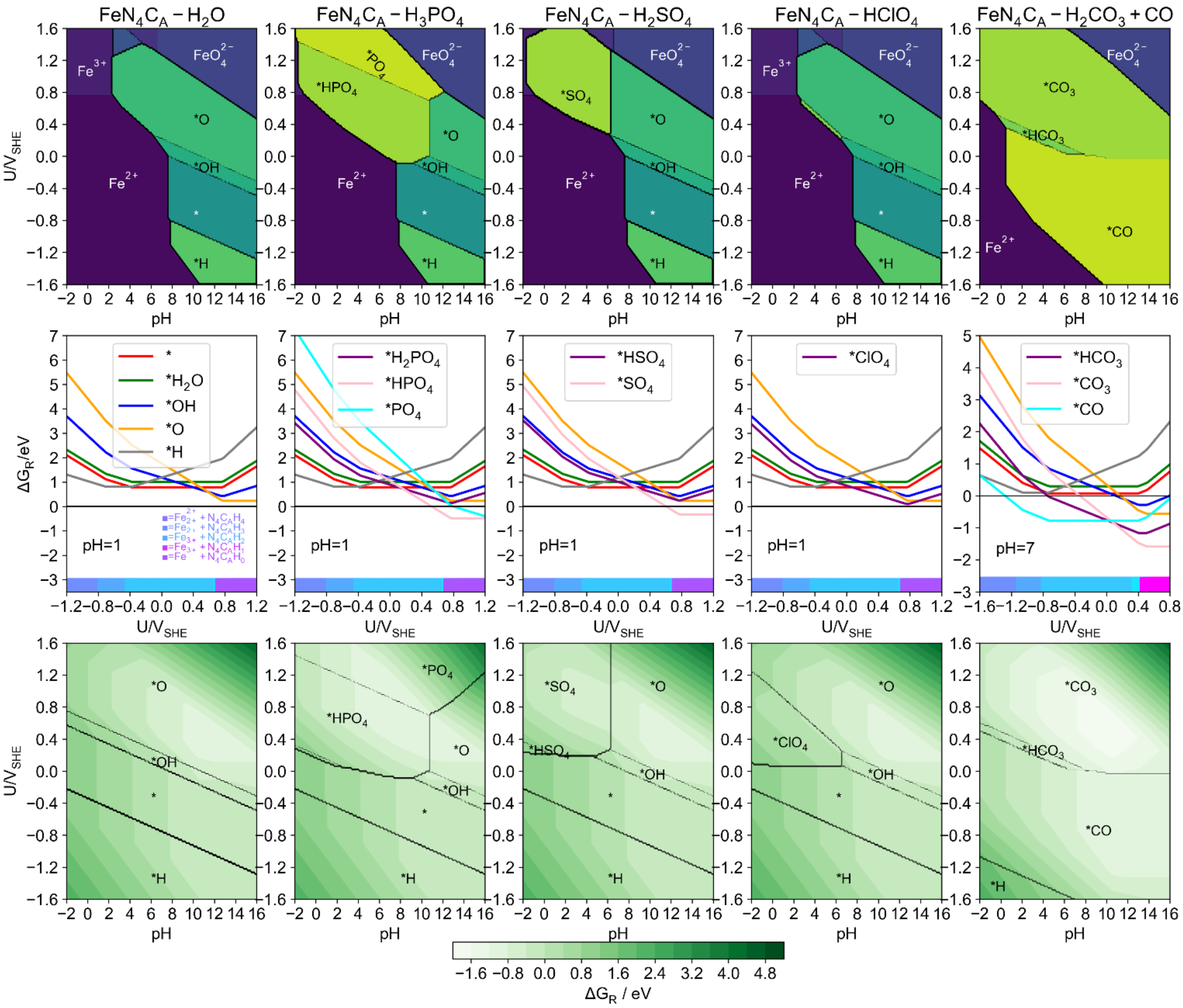

Figure S7 FeN_4C_A site in different 0.1 M electrolytes**:** (top) Stability diagram, (middle) ΔG_R of the surfaces at specific pH. The most stable dissolved species for each applied potential which is used as a reference for ΔG_R are superimposed as horizontal bars at the bottom., and (bottom) ΔG_R of the most stable surface.

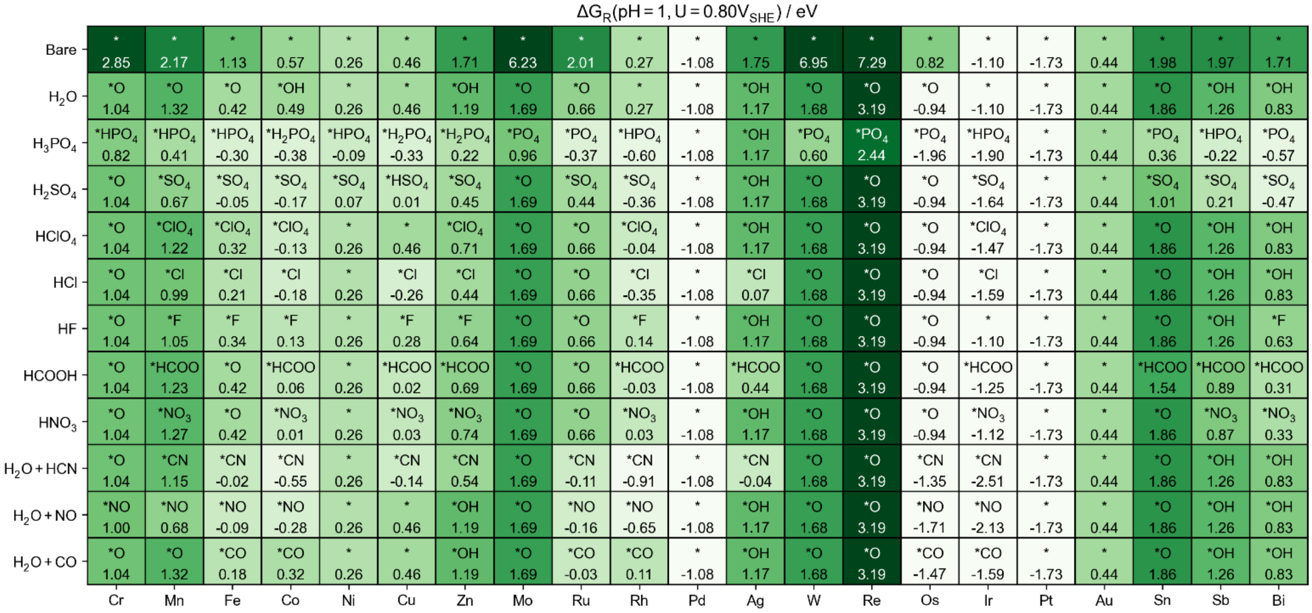

$\Delta G_R(pH = 1, U = 0.80V_{SHE})$ / eV

	Cr	Mn	Fe	Co	Ni	Cu	Zn	Mo	Ru	Rh	Pd	Ag	W	Re	Os	Ir	Pt	Au	Sn	Sb	Bi
Bare	* 2.85	* 2.17	* 1.13	* 0.57	* 0.26	* 0.46	* 1.71	* 6.23	* 2.01	* 0.27	* -1.08	* 1.75	* 6.95	* 7.29	* 0.82	* -1.10	* -1.73	* 0.44	* 1.98	* 1.97	* 1.71
H_2O	*O 1.04	*O 1.32	*O 0.42	*OH 0.49	* 0.26	* 0.46	*OH 1.19	*O 1.69	*O 0.66	* 0.27	* -1.08	*OH 1.17	*O 1.68	*O 3.19	*O -0.94	* -1.10	* -1.73	* 0.44	*O 1.86	*OH 1.26	*OH 0.83
H_3PO_4	*HPO_4 0.82	*HPO_4 0.41	*HPO_4 -0.30	*H_2PO_4 -0.38	*HPO_4 -0.09	*H_2PO_4 -0.33	*H_2PO_4 0.22	*PO_4 0.96	*PO_4 -0.37	*HPO_4 -0.60	* -1.08	*OH 1.17	*PO_4 0.60	*PO_4 2.44	*PO_4 -1.96	*HPO_4 -1.90	* -1.73	* 0.44	*PO_4 0.36	*HPO_4 -0.22	*PO_4 -0.57
H_2SO_4	*O 1.04	*SO_4 0.67	*SO_4 -0.05	*SO_4 -0.17	*SO_4 0.07	*HSO_4 0.01	*SO_4 0.45	*O 1.69	*SO_4 0.44	*SO_4 -0.36	* -1.08	*OH 1.17	*O 1.68	*O 3.19	*O -0.94	*SO_4 -1.64	* -1.73	* 0.44	*SO_4 1.01	*SO_4 0.21	*SO_4 -0.47
$HClO_4$	*O 1.04	*ClO_4 1.22	*ClO_4 0.32	*ClO_4 -0.13	* 0.26	* 0.46	*ClO_4 0.71	*O 1.69	*O 0.66	*ClO_4 -0.04	* -1.08	*OH 1.17	*O 1.68	*O 3.19	*O -0.94	*ClO_4 -1.47	* -1.73	* 0.44	*O 1.86	*OH 1.26	*OH 0.83
HCl	*O 1.04	*Cl 0.99	*Cl 0.21	*Cl -0.18	* 0.26	*Cl -0.26	*Cl 0.44	*O 1.69	*O 0.66	*Cl -0.35	* -1.08	*Cl 0.07	*O 1.68	*O 3.19	*O -0.94	*Cl -1.59	* -1.73	* 0.44	*O 1.86	*OH 1.26	*OH 0.83
HF	*O 1.04	*F 1.05	*F 0.34	*F 0.13	* 0.26	*F 0.28	*F 0.64	*O 1.69	*O 0.66	*F 0.14	* -1.08	*OH 1.17	*O 1.68	*O 3.19	*O -0.94	* -1.10	* -1.73	* 0.44	*O 1.86	*OH 1.26	*F 0.63
HCOOH	*O 1.04	*HCOO 1.23	*O 0.42	*HCOO 0.06	* 0.26	*HCOO 0.02	*HCOO 0.69	*O 1.69	*O 0.66	*HCOO -0.03	* -1.08	*HCOO 0.44	*O 1.68	*O 3.19	*O -0.94	*HCOO -1.25	* -1.73	* 0.44	*HCOO 1.54	*HCOO 0.89	*HCOO 0.31
HNO_3	*O 1.04	*NO_3 1.27	*O 0.42	*NO_3 0.01	* 0.26	*NO_3 0.03	*NO_3 0.74	*O 1.69	*O 0.66	*NO_3 0.03	* -1.08	*OH 1.17	*O 1.68	*O 3.19	*O -0.94	*NO_3 -1.12	* -1.73	* 0.44	*O 1.86	*NO_3 0.87	*NO_3 0.33
$H_2O + HCN$	*O 1.04	*CN 1.15	*CN -0.02	*CN -0.55	* 0.26	*CN -0.14	*CN 0.54	*O 1.69	*CN -0.11	*CN -0.91	* -1.08	*CN -0.04	*O 1.68	*O 3.19	*CN -1.35	*CN -2.51	* -1.73	* 0.44	*O 1.86	*OH 1.26	*OH 0.83
$H_2O + NO$	*NO 1.00	*NO 0.68	*NO -0.09	*NO -0.28	* 0.26	* 0.46	*OH 1.19	*O 1.69	*NO -0.16	*NO -0.65	* -1.08	*OH 1.17	*O 1.68	*O 3.19	*NO -1.71	*NO -2.13	* -1.73	* 0.44	*O 1.86	*OH 1.26	*OH 0.83
$H_2O + CO$	*O 1.04	*O 1.32	*CO 0.18	*CO 0.32	* 0.26	* 0.46	*OH 1.19	*O 1.69	*CO -0.03	*CO 0.11	* -1.08	*OH 1.17	*O 1.68	*O 3.19	*CO -1.47	*CO -1.59	* -1.73	* 0.44	*O 1.86	*OH 1.26	*OH 0.83

Figure S8 ΔG_R of the most stable surface of MN_4C_{10} in 0.1 M electrolytes under ORR-related conditions (pH=1, U=0.80 V_{SHE}). The text insert shows the most stable adsorbate on the metal atom and its corresponding relative stability in eV. The background color corresponds to the ΔG_R value. The brighter the background color, the more stable the MN_4C_{10} site is against the dissolution.

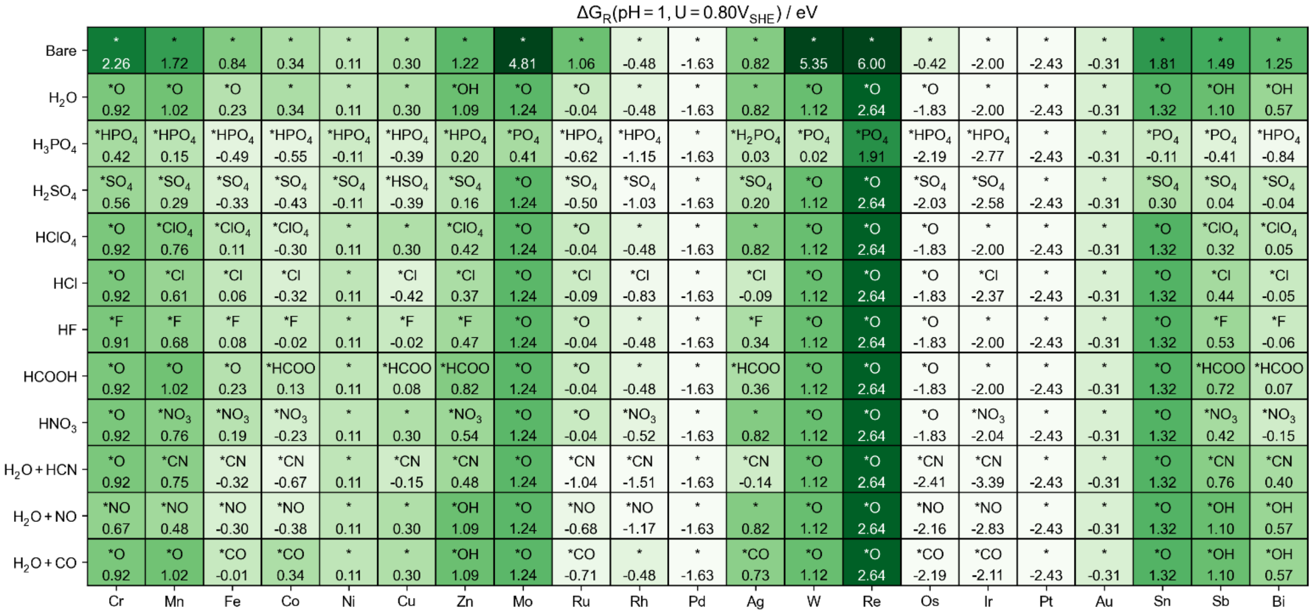

$\Delta G_R(pH = 1, U = 0.80V_{SHE})$ / eV

	Cr	Mn	Fe	Co	Ni	Cu	Zn	Mo	Ru	Rh	Pd	Ag	W	Re	Os	Ir	Pt	Au	Sn	Sb	Bi
Bare	* 2.26	* 1.72	* 0.84	* 0.34	* 0.11	* 0.30	* 1.22	* 4.81	* 1.06	* -0.48	* -1.63	* 0.82	* 5.35	* 6.00	* -0.42	* -2.00	* -2.43	* -0.31	* 1.81	* 1.49	* 1.25
H_2O	*O 0.92	*O 1.02	*O 0.23	* 0.34	* 0.11	* 0.30	*OH 1.09	*O 1.24	*O -0.04	* -0.48	* -1.63	* 0.82	*O 1.12	*O 2.64	*O -1.83	* -2.00	* -2.43	* -0.31	*O 1.32	*OH 1.10	*OH 0.57
H_3PO_4	*HPO_4 0.42	*HPO_4 0.15	*HPO_4 -0.49	*HPO_4 -0.55	*HPO_4 -0.11	*HPO_4 -0.39	*HPO_4 0.20	*PO_4 0.41	*HPO_4 -0.62	*HPO_4 -1.15	* -1.63	*H_2PO_4 0.03	*PO_4 0.02	*PO_4 1.91	*HPO_4 -2.19	*HPO_4 -2.77	* -2.43	* -0.31	*PO_4 -0.11	*PO_4 -0.41	*HPO_4 -0.84
H_2SO_4	*SO_4 0.56	*SO_4 0.29	*SO_4 -0.33	*SO_4 -0.43	*SO_4 -0.11	*HSO_4 -0.39	*SO_4 0.16	*O 1.24	*SO_4 -0.50	*SO_4 -1.03	* -1.63	*SO_4 0.20	*O 1.12	*O 2.64	*SO_4 -2.03	*SO_4 -2.58	* -2.43	* -0.31	*SO_4 0.30	*SO_4 0.04	*SO_4 -0.04
$HClO_4$	*O 0.92	*ClO_4 0.76	*ClO_4 0.11	*ClO_4 -0.30	* 0.11	* 0.30	*ClO_4 0.42	*O 1.24	*O -0.04	* -0.48	* -1.63	* 0.82	*O 1.12	*O 2.64	*O -1.83	* -2.00	* -2.43	* -0.31	*O 1.32	*ClO_4 0.32	*ClO_4 0.05
HCl	*O 0.92	*Cl 0.61	*Cl 0.06	*Cl -0.32	* 0.11	*Cl -0.42	*Cl 0.37	*O 1.24	*Cl -0.09	*Cl -0.83	* -1.63	*Cl -0.09	*O 1.12	*O 2.64	*O -1.83	*Cl -2.37	* -2.43	* -0.31	*O 1.32	*Cl 0.44	*Cl -0.05
HF	*F 0.91	*F 0.68	*F 0.08	*F -0.02	* 0.11	*F -0.02	*F 0.47	*O 1.24	*O -0.04	* -0.48	* -1.63	*F 0.34	*O 1.12	*O 2.64	*O -1.83	* -2.00	* -2.43	* -0.31	*O 1.32	*F 0.53	*F -0.06
HCOOH	*O 0.92	*O 1.02	*O 0.23	*HCOO 0.13	* 0.11	*HCOO 0.08	*HCOO 0.82	*O 1.24	*O -0.04	* -0.48	* -1.63	*HCOO 0.36	*O 1.12	*O 2.64	*O -1.83	* -2.00	* -2.43	* -0.31	*O 1.32	*HCOO 0.72	*HCOO 0.07
HNO_3	*O 0.92	*NO_3 0.76	*NO_3 0.19	*NO_3 -0.23	* 0.11	* 0.30	*NO_3 0.54	*O 1.24	*O -0.04	*NO_3 -0.52	* -1.63	* 0.82	*O 1.12	*O 2.64	*O -1.83	*NO_3 -2.04	* -2.43	* -0.31	*O 1.32	*NO_3 0.42	*NO_3 -0.15
$H_2O + HCN$	*O 0.92	*CN 0.75	*CN -0.32	*CN -0.67	* 0.11	*CN -0.15	*CN 0.48	*O 1.24	*CN -1.04	*CN -1.51	* -1.63	*CN -0.14	*O 1.12	*O 2.64	*CN -2.41	*CN -3.39	* -2.43	* -0.31	*O 1.32	*CN 0.76	*CN 0.40
$H_2O + NO$	*NO 0.67	*NO 0.48	*NO -0.30	*NO -0.38	* 0.11	* 0.30	*OH 1.09	*O 1.24	*NO -0.68	*NO -1.17	* -1.63	* 0.82	*O 1.12	*O 2.64	*NO -2.16	*NO -2.83	* -2.43	* -0.31	*O 1.32	*OH 1.10	*OH 0.57
$H_2O + CO$	*O 0.92	*O 1.02	*CO -0.01	*CO 0.34	* 0.11	* 0.30	*OH 1.09	*O 1.24	*CO -0.71	* -0.48	* -1.63	*CO 0.73	*O 1.12	*O 2.64	*CO -2.19	*CO -2.11	* -2.43	* -0.31	*O 1.32	*OH 1.10	*OH 0.57

Figure S9 ΔG_R of the most stable surface of MN_4C_A in 0.1 M electrolytes under ORR-related conditions (pH=1, U=0.80 V_{SHE}). The text insert shows the most stable adsorbate on the metal atom and its corresponding relative stability in eV. The background color corresponds to the ΔG_R value. The brighter the background color, the more stable the MN_4C_A site is against the dissolution.

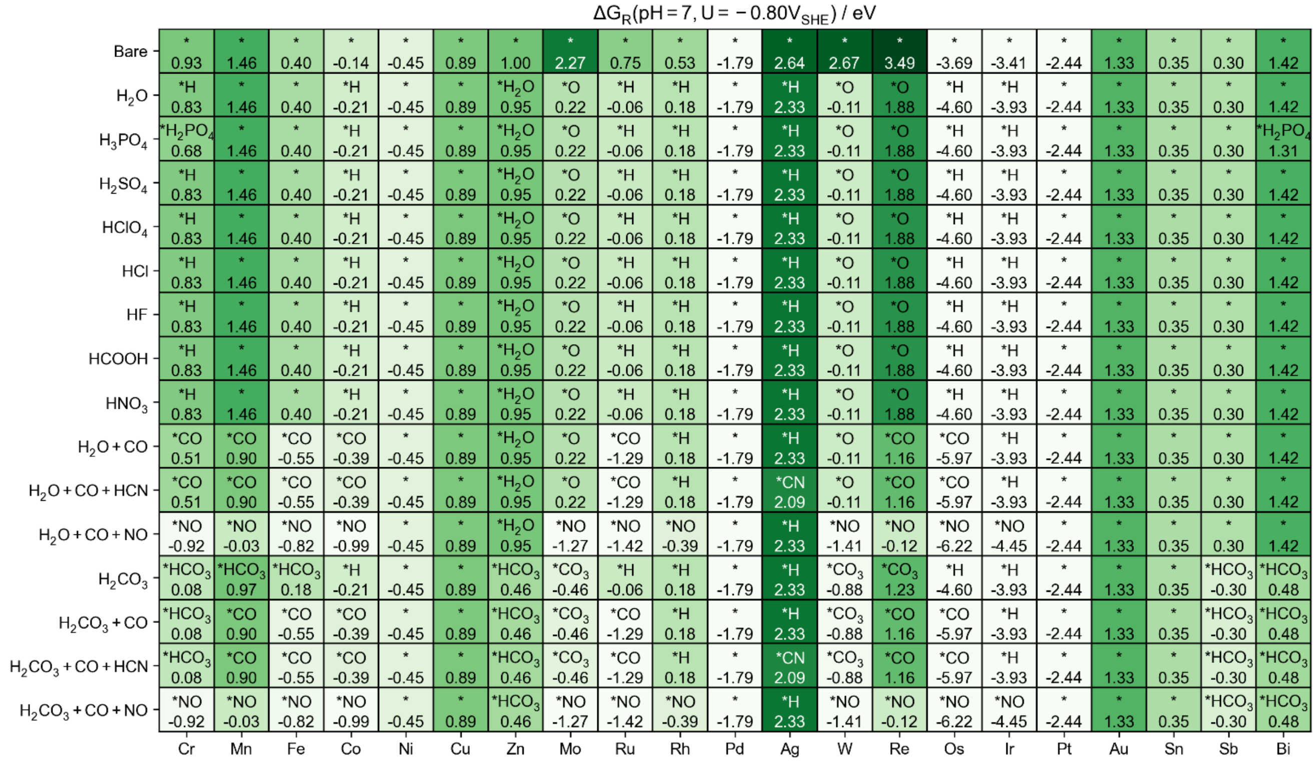

	Cr	Mn	Fe	Co	Ni	Cu	Zn	Mo	Ru	Rh	Pd	Ag	W	Re	Os	Ir	Pt	Au	Sn	Sb	Bi
Bare	* 0.93	* 1.46	* 0.40	* -0.14	* -0.45	* 0.89	* 1.00	* 2.27	* 0.75	* 0.53	* -1.79	* 2.64	* 2.67	* 3.49	* -3.69	* -3.41	* -2.44	* 1.33	* 0.35	* 0.30	* 1.42
H_2O	*H 0.83	* 1.46	* 0.40	*H -0.21	* -0.45	* 0.89	*H_2O 0.95	*O 0.22	*H -0.06	*H 0.18	* -1.79	*H 2.33	*O -0.11	*O 1.88	*H -4.60	*H -3.93	* -2.44	* 1.33	* 0.35	* 0.30	* 1.42
H_3PO_4	*H_2PO_4 0.68	* 1.46	* 0.40	*H -0.21	* -0.45	* 0.89	*H_2O 0.95	*O 0.22	*H -0.06	*H 0.18	* -1.79	*H 2.33	*O -0.11	*O 1.88	*H -4.60	*H -3.93	* -2.44	* 1.33	* 0.35	* 0.30	*H_2PO_4 1.31
H_2SO_4	*H 0.83	* 1.46	* 0.40	*H -0.21	* -0.45	* 0.89	*H_2O 0.95	*O 0.22	*H -0.06	*H 0.18	* -1.79	*H 2.33	*O -0.11	*O 1.88	*H -4.60	*H -3.93	* -2.44	* 1.33	* 0.35	* 0.30	* 1.42
$HClO_4$	*H 0.83	* 1.46	* 0.40	*H -0.21	* -0.45	* 0.89	*H_2O 0.95	*O 0.22	*H -0.06	*H 0.18	* -1.79	*H 2.33	*O -0.11	*O 1.88	*H -4.60	*H -3.93	* -2.44	* 1.33	* 0.35	* 0.30	* 1.42
HCl	*H 0.83	* 1.46	* 0.40	*H -0.21	* -0.45	* 0.89	*H_2O 0.95	*O 0.22	*H -0.06	*H 0.18	* -1.79	*H 2.33	*O -0.11	*O 1.88	*H -4.60	*H -3.93	* -2.44	* 1.33	* 0.35	* 0.30	* 1.42
HF	*H 0.83	* 1.46	* 0.40	*H -0.21	* -0.45	* 0.89	*H_2O 0.95	*O 0.22	*H -0.06	*H 0.18	* -1.79	*H 2.33	*O -0.11	*O 1.88	*H -4.60	*H -3.93	* -2.44	* 1.33	* 0.35	* 0.30	* 1.42
HCOOH	*H 0.83	* 1.46	* 0.40	*H -0.21	* -0.45	* 0.89	*H_2O 0.95	*O 0.22	*H -0.06	*H 0.18	* -1.79	*H 2.33	*O -0.11	*O 1.88	*H -4.60	*H -3.93	* -2.44	* 1.33	* 0.35	* 0.30	* 1.42
HNO_3	*H 0.83	* 1.46	* 0.40	*H -0.21	* -0.45	* 0.89	*H_2O 0.95	*O 0.22	*H -0.06	*H 0.18	* -1.79	*H 2.33	*O -0.11	*O 1.88	*H -4.60	*H -3.93	* -2.44	* 1.33	* 0.35	* 0.30	* 1.42
$H_2O + CO$	*CO 0.51	*CO 0.90	*CO -0.55	*CO -0.39	* -0.45	* 0.89	*H_2O 0.95	*O 0.22	*CO -1.29	*H 0.18	* -1.79	*H 2.33	*O -0.11	*CO 1.16	*CO -5.97	*H -3.93	* -2.44	* 1.33	* 0.35	* 0.30	* 1.42
$H_2O + CO + HCN$	*CO 0.51	*CO 0.90	*CO -0.55	*CO -0.39	* -0.45	* 0.89	*H_2O 0.95	*O 0.22	*CO -1.29	*H 0.18	* -1.79	*CN 2.09	*O -0.11	*CO 1.16	*CO -5.97	*H -3.93	* -2.44	* 1.33	* 0.35	* 0.30	* 1.42
$H_2O + CO + NO$	*NO -0.92	*NO -0.03	*NO -0.82	*NO -0.99	* -0.45	* 0.89	*H_2O 0.95	*NO -1.27	*NO -1.42	*NO -0.39	* -1.79	*H 2.33	*NO -1.41	*NO -0.12	*NO -6.22	*NO -4.45	* -2.44	* 1.33	* 0.35	* 0.30	* 1.42
H_2CO_3	*HCO_3 0.08	*HCO_3 0.97	*HCO_3 0.18	*H -0.21	* -0.45	* 0.89	*HCO_3 0.46	*CO_3 -0.46	*H -0.06	*H 0.18	* -1.79	*H 2.33	*CO_3 -0.88	*CO_3 1.23	*H -4.60	*H -3.93	* -2.44	* 1.33	* 0.35	*HCO_3 -0.30	*HCO_3 0.48
$H_2CO_3 + CO$	*HCO_3 0.08	*CO 0.90	*CO -0.55	*CO -0.39	* -0.45	* 0.89	*HCO_3 0.46	*CO_3 -0.46	*CO -1.29	*H 0.18	* -1.79	*H 2.33	*CO_3 -0.88	*CO 1.16	*CO -5.97	*H -3.93	* -2.44	* 1.33	* 0.35	*HCO_3 -0.30	*HCO_3 0.48
$H_2CO_3 + CO + HCN$	*HCO_3 0.08	*CO 0.90	*CO -0.55	*CO -0.39	* -0.45	* 0.89	*HCO_3 0.46	*CO_3 -0.46	*CO -1.29	*H 0.18	* -1.79	*CN 2.09	*CO_3 -0.88	*CO 1.16	*CO -5.97	*H -3.93	* -2.44	* 1.33	* 0.35	*HCO_3 -0.30	*HCO_3 0.48
$H_2CO_3 + CO + NO$	*NO -0.92	*NO -0.03	*NO -0.82	*NO -0.99	* -0.45	* 0.89	*HCO_3 0.46	*NO -1.27	*NO -1.42	*NO -0.39	* -1.79	*H 2.33	*NO -1.41	*NO -0.12	*NO -6.22	*NO -4.45	* -2.44	* 1.33	* 0.35	*HCO_3 -0.30	*HCO_3 0.48

Figure S10 ΔG_R of the most stable surface of MN_4C_{10} in 0.1 M electrolytes under CO_2RR-related conditions (pH = 7, U = -0.80 V_{SHE}). The text insert shows the most stable adsorbate on the metal atom and its corresponding relative stability in eV. The background color corresponds to the ΔG_R value. The brighter the background color, the more stable the MN_4C_{10} site is against the dissolution.

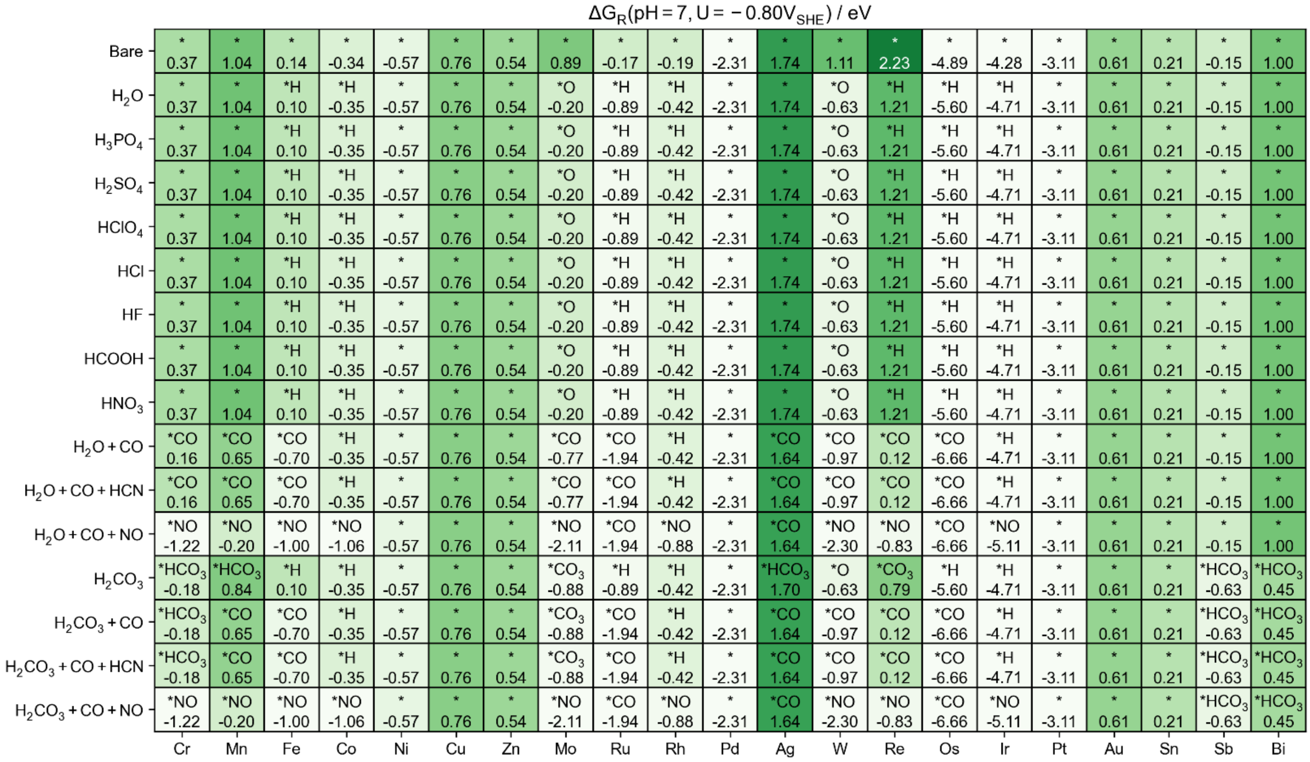

	Cr	Mn	Fe	Co	Ni	Cu	Zn	Mo	Ru	Rh	Pd	Ag	W	Re	Os	Ir	Pt	Au	Sn	Sb	Bi
Bare	* 0.37	* 1.04	* 0.14	* -0.34	* -0.57	* 0.76	* 0.54	* 0.89	* -0.17	* -0.19	* -2.31	* 1.74	* 1.11	* 2.23	* -4.89	* -4.28	* -3.11	* 0.61	* 0.21	* -0.15	* 1.00
H_2O	* 0.37	* 1.04	*H 0.10	*H -0.35	* -0.57	* 0.76	* 0.54	*O -0.20	*H -0.89	*H -0.42	* -2.31	* 1.74	*O -0.63	*H 1.21	*H -5.60	*H -4.71	* -3.11	* 0.61	* 0.21	* -0.15	* 1.00
H_3PO_4	* 0.37	* 1.04	*H 0.10	*H -0.35	* -0.57	* 0.76	* 0.54	*O -0.20	*H -0.89	*H -0.42	* -2.31	* 1.74	*O -0.63	*H 1.21	*H -5.60	*H -4.71	* -3.11	* 0.61	* 0.21	* -0.15	* 1.00
H_2SO_4	* 0.37	* 1.04	*H 0.10	*H -0.35	* -0.57	* 0.76	* 0.54	*O -0.20	*H -0.89	*H -0.42	* -2.31	* 1.74	*O -0.63	*H 1.21	*H -5.60	*H -4.71	* -3.11	* 0.61	* 0.21	* -0.15	* 1.00
$HClO_4$	* 0.37	* 1.04	*H 0.10	*H -0.35	* -0.57	* 0.76	* 0.54	*O -0.20	*H -0.89	*H -0.42	* -2.31	* 1.74	*O -0.63	*H 1.21	*H -5.60	*H -4.71	* -3.11	* 0.61	* 0.21	* -0.15	* 1.00
HCl	* 0.37	* 1.04	*H 0.10	*H -0.35	* -0.57	* 0.76	* 0.54	*O -0.20	*H -0.89	*H -0.42	* -2.31	* 1.74	*O -0.63	*H 1.21	*H -5.60	*H -4.71	* -3.11	* 0.61	* 0.21	* -0.15	* 1.00
HF	* 0.37	* 1.04	*H 0.10	*H -0.35	* -0.57	* 0.76	* 0.54	*O -0.20	*H -0.89	*H -0.42	* -2.31	* 1.74	*O -0.63	*H 1.21	*H -5.60	*H -4.71	* -3.11	* 0.61	* 0.21	* -0.15	* 1.00
HCOOH	* 0.37	* 1.04	*H 0.10	*H -0.35	* -0.57	* 0.76	* 0.54	*O -0.20	*H -0.89	*H -0.42	* -2.31	* 1.74	*O -0.63	*H 1.21	*H -5.60	*H -4.71	* -3.11	* 0.61	* 0.21	* -0.15	* 1.00
HNO_3	* 0.37	* 1.04	*H 0.10	*H -0.35	* -0.57	* 0.76	* 0.54	*O -0.20	*H -0.89	*H -0.42	* -2.31	* 1.74	*O -0.63	*H 1.21	*H -5.60	*H -4.71	* -3.11	* 0.61	* 0.21	* -0.15	* 1.00
$H_2O + CO$	*CO 0.16	*CO 0.65	*CO -0.70	*H -0.35	* -0.57	* 0.76	* 0.54	*CO -0.77	*CO -1.94	*H -0.42	* -2.31	*CO 1.64	*CO -0.97	*CO 0.12	*CO -6.66	*H -4.71	* -3.11	* 0.61	* 0.21	* -0.15	* 1.00
$H_2O + CO + HCN$	*CO 0.16	*CO 0.65	*CO -0.70	*H -0.35	* -0.57	* 0.76	* 0.54	*CO -0.77	*CO -1.94	*H -0.42	* -2.31	*CO 1.64	*CO -0.97	*CO 0.12	*CO -6.66	*H -4.71	* -3.11	* 0.61	* 0.21	* -0.15	* 1.00
$H_2O + CO + NO$	*NO -1.22	*NO -0.20	*NO -1.00	*NO -1.06	* -0.57	* 0.76	* 0.54	*NO -2.11	*CO -1.94	*NO -0.88	* -2.31	*CO 1.64	*NO -2.30	*NO -0.83	*CO -6.66	*NO -5.11	* -3.11	* 0.61	* 0.21	* -0.15	* 1.00
H_2CO_3	*HCO$_3$ -0.18	*HCO$_3$ 0.84	*H 0.10	*H -0.35	* -0.57	* 0.76	* 0.54	*CO$_3$ -0.88	*H -0.89	*H -0.42	* -2.31	*HCO$_3$ 1.70	*O -0.63	*CO$_3$ 0.79	*H -5.60	*H -4.71	* -3.11	* 0.61	* 0.21	*HCO$_3$ -0.63	*HCO$_3$ 0.45
$H_2CO_3 + CO$	*HCO$_3$ -0.18	*CO 0.65	*CO -0.70	*H -0.35	* -0.57	* 0.76	* 0.54	*CO$_3$ -0.88	*CO -1.94	*H -0.42	* -2.31	*CO 1.64	*CO -0.97	*CO 0.12	*CO -6.66	*H -4.71	* -3.11	* 0.61	* 0.21	*HCO$_3$ -0.63	*HCO$_3$ 0.45
$H_2CO_3 + CO + HCN$	*HCO$_3$ -0.18	*CO 0.65	*CO -0.70	*H -0.35	* -0.57	* 0.76	* 0.54	*CO$_3$ -0.88	*CO -1.94	*H -0.42	* -2.31	*CO 1.64	*CO -0.97	*CO 0.12	*CO -6.66	*H -4.71	* -3.11	* 0.61	* 0.21	*HCO$_3$ -0.63	*HCO$_3$ 0.45
$H_2CO_3 + CO + NO$	*NO -1.22	*NO -0.20	*NO -1.00	*NO -1.06	* -0.57	* 0.76	* 0.54	*NO -2.11	*CO -1.94	*NO -0.88	* -2.31	*CO 1.64	*NO -2.30	*NO -0.83	*CO -6.66	*NO -5.11	* -3.11	* 0.61	* 0.21	*HCO$_3$ -0.63	*HCO$_3$ 0.45

Figure S11 ΔG_R of the most stable surface of MN_4C_A in 0.1 M electrolytes under CO_2RR-related conditions (pH = 7, U = -0.80 V_{SHE}). The text insert shows the most stable adsorbate on the metal atom and its corresponding relative stability in eV. The background color corresponds to the ΔG_R value. The brighter the background color, the more stable the MN_4C_{10} site is against the dissolution.

6. ORR activity

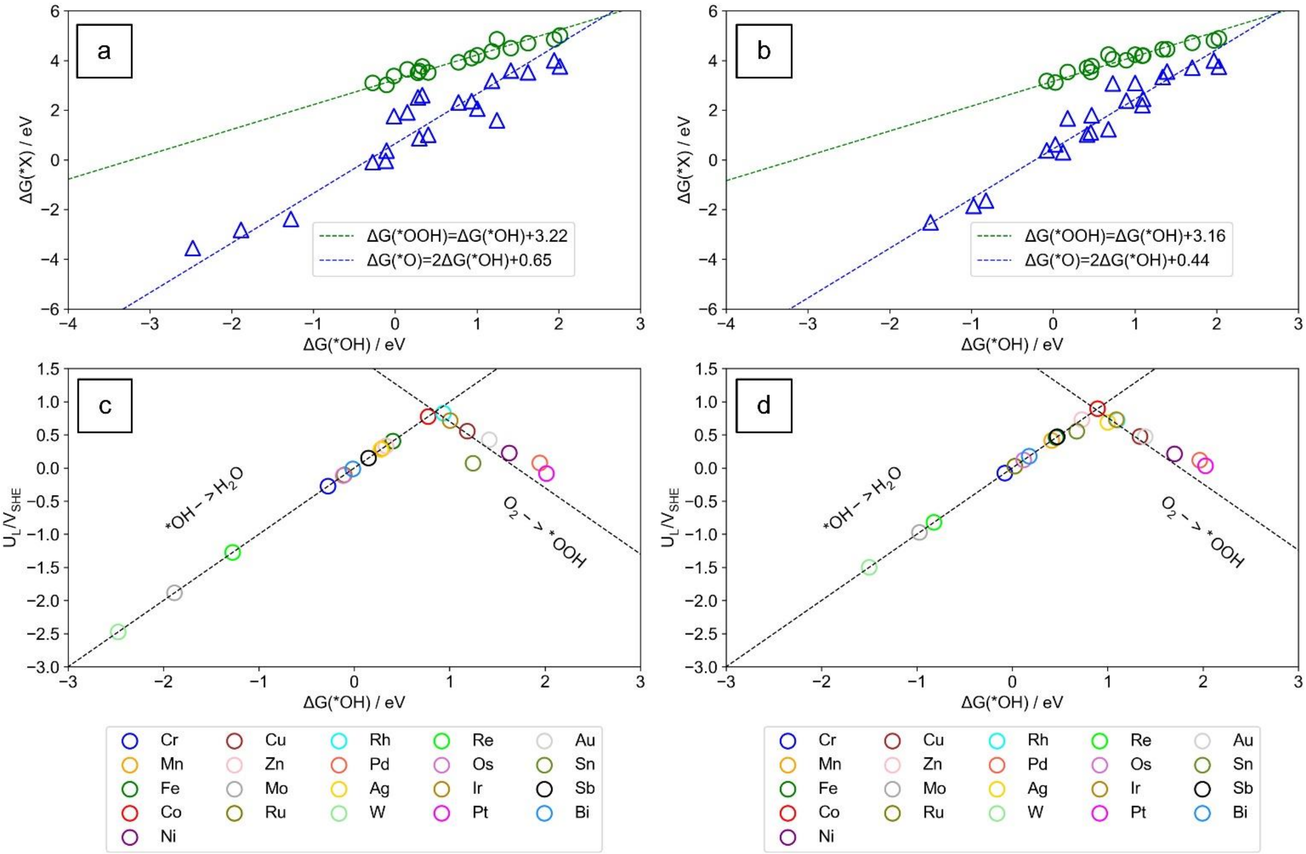

Figure S12 Scaling relation between ΔG(*O) vs. ΔG(*OH) and ΔG(*OH) vs. ΔG(*OOH) on the bare metal site: (a) MN_4C_{10}, (b) MN_4C_A. Activity volcano plot as a function of ΔG(*OH) for the bare metal site: (c) MN_4C_{10} and (d) MN_4C_A.

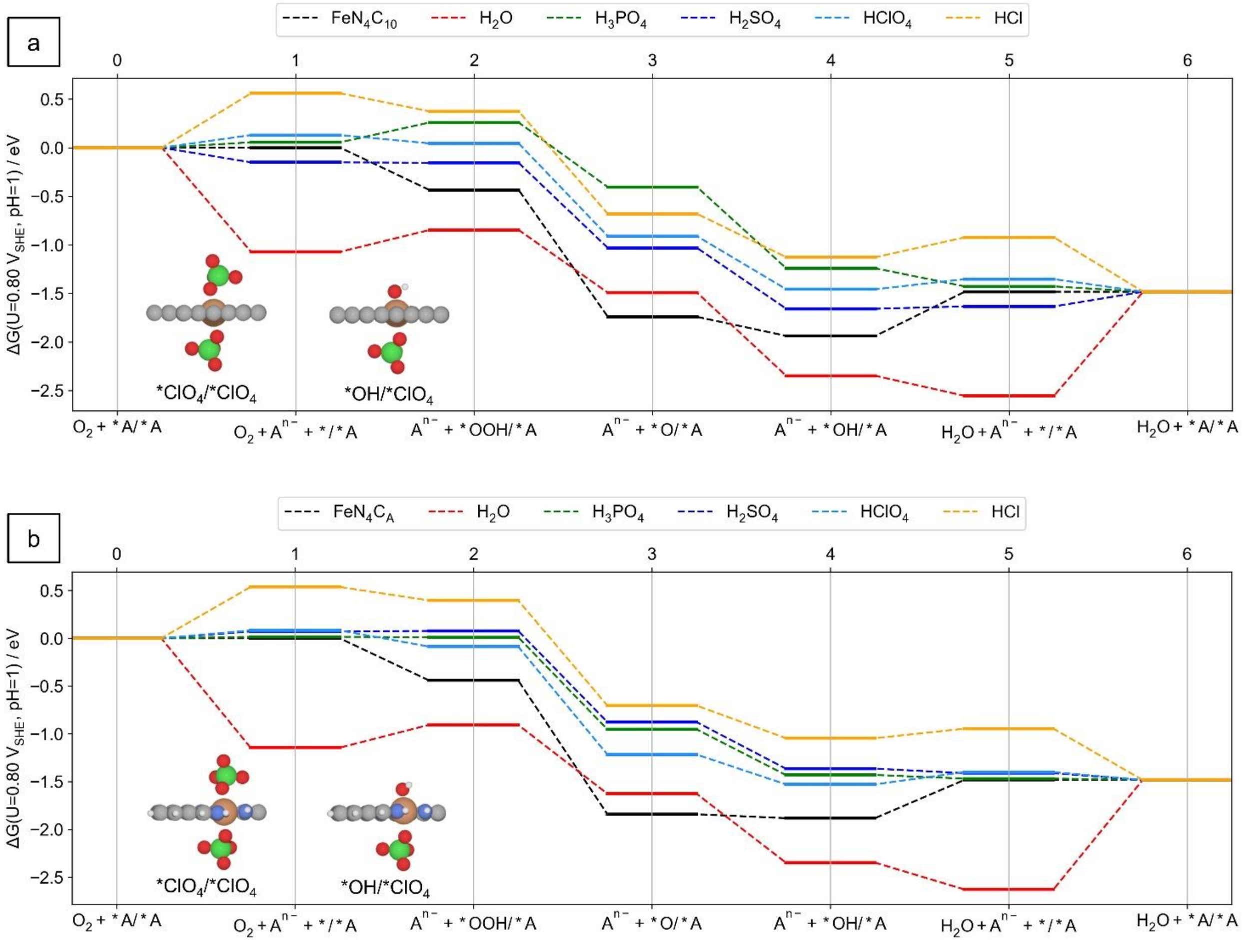

Figure S13 Free energy diagram of the ORR at pH = 1, U = 0.80 V_{SHE} on: (a) FeN_4C_{10}, (b) FeN_4C_A in H_2O, 0.1 M H_3PO_4, 0.1 M $HClO_4$, 0.1 M H_2SO_4 and 0.1M HCl solution. The inset structures show the side view of the $*OH/*ClO_4$ and $*ClO_4/*ClO_4$ on the FeN_4 site. (C = gray, N = blue, H = white, O = red, Fe = orange, Cl = lime green).

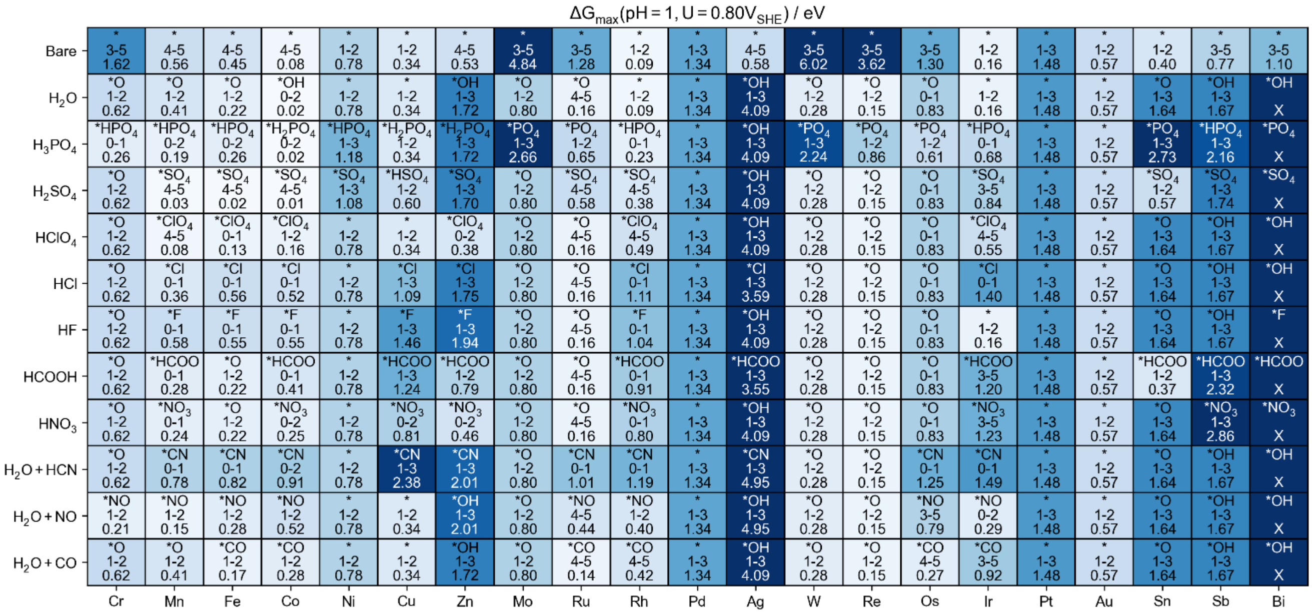

$\Delta G_{max}(pH = 1, U = 0.80V_{SHE})$ / eV

	Cr	Mn	Fe	Co	Ni	Cu	Zn	Mo	Ru	Rh	Pd	Ag	W	Re	Os	Ir	Pt	Au	Sn	Sb	Bi
Bare	* 3-5 1.62	* 4-5 0.56	* 4-5 0.45	* 4-5 0.08	* 1-2 0.78	* 1-2 0.34	* 4-5 0.53	* 3-5 4.84	* 3-5 1.28	* 1-2 0.09	* 1-3 1.34	* 4-5 0.58	* 3-5 6.02	* 3-5 3.62	* 3-5 1.30	* 1-2 0.16	* 1-3 1.48	* 1-2 0.57	* 1-2 0.40	* 3-5 0.77	* 3-5 1.10
H_2O	*O 1-2 0.62	*O 1-2 0.41	*O 1-2 0.22	*OH 0-2 0.02	* 1-2 0.78	* 1-2 0.34	*OH 1-3 1.72	*O 1-2 0.80	*O 4-5 0.16	* 1-2 0.09	* 1-3 1.34	*OH 1-3 4.09	*O 1-2 0.28	*O 1-2 0.15	*O 0-1 0.83	* 1-2 0.16	* 1-3 1.48	* 1-2 0.57	*O 1-3 1.64	*OH 1-3 1.67	*OH X
H_3PO_4	*HPO_4 0-1 0.26	*HPO_4 0-2 0.19	*HPO_4 0-2 0.26	*H_2PO_4 0-2 0.02	*HPO_4 1-3 1.18	*H_2PO_4 1-2 0.34	*H_2PO_4 1-3 1.72	*PO_4 1-3 2.66	*PO_4 1-2 0.65	*HPO_4 0-1 0.23	* 1-3 1.34	*OH 1-3 4.09	*PO_4 1-3 2.24	*PO_4 1-2 0.86	*PO_4 1-2 0.61	*HPO_4 0-1 0.68	* 1-3 1.48	* 1-2 0.57	*PO_4 1-3 2.73	*HPO_4 1-3 2.16	*PO_4 X
H_2SO_4	*O 1-2 0.62	*SO_4 4-5 0.03	*SO_4 4-5 0.02	*SO_4 4-5 0.01	*SO_4 1-3 1.08	*HSO_4 1-2 0.60	*SO_4 1-3 1.70	*O 1-2 0.80	*SO_4 4-5 0.58	*SO_4 4-5 0.38	* 1-3 1.34	*OH 1-3 4.09	*O 1-2 0.28	*O 1-2 0.15	*O 0-1 0.83	*SO_4 3-5 0.84	* 1-3 1.48	* 1-2 0.57	*SO_4 1-2 0.57	*SO_4 1-3 1.74	*SO_4 X
$HClO_4$	*O 1-2 0.62	*ClO_4 4-5 0.08	*ClO_4 0-1 0.13	*ClO_4 1-2 0.16	* 1-2 0.78	* 1-2 0.34	*ClO_4 0-2 0.38	*O 1-2 0.80	*O 4-5 0.16	*ClO_4 4-5 0.49	* 1-3 1.34	*OH 1-3 4.09	*O 1-2 0.28	*O 1-2 0.15	*O 0-1 0.83	*ClO_4 4-5 0.55	* 1-3 1.48	* 1-2 0.57	*O 1-3 1.64	*OH 1-3 1.67	*OH X
HCl	*O 1-2 0.62	*Cl 0-1 0.36	*Cl 0-1 0.56	*Cl 0-1 0.52	* 1-2 0.78	*Cl 1-3 1.09	*Cl 1-3 1.75	*O 1-2 0.80	*O 4-5 0.16	*Cl 0-1 1.11	* 1-3 1.34	*Cl 1-3 3.59	*O 1-2 0.28	*O 1-2 0.15	*O 0-1 0.83	*Cl 0-1 1.40	* 1-3 1.48	* 1-2 0.57	*O 1-3 1.64	*OH 1-3 1.67	*OH X
HF	*O 1-2 0.62	*F 0-1 0.58	*F 0-1 0.55	*F 0-1 0.55	* 1-2 0.78	*F 1-3 1.46	*F 1-3 1.94	*O 1-2 0.80	*O 4-5 0.16	*F 0-1 1.04	* 1-3 1.34	*OH 1-3 4.09	*O 1-2 0.28	*O 1-2 0.15	*O 0-1 0.83	* 1-2 0.16	* 1-3 1.48	* 1-2 0.57	*O 1-3 1.64	*OH 1-3 1.67	*F X
HCOOH	*O 1-2 0.62	*HCOO 0-1 0.28	*O 1-2 0.22	*HCOO 0-1 0.41	* 1-2 0.78	*HCOO 1-3 1.24	*HCOO 1-2 0.79	*O 1-2 0.80	*O 4-5 0.16	*HCOO 0-1 0.91	* 1-3 1.34	*HCOO 1-3 3.55	*O 1-2 0.28	*O 1-2 0.15	*O 0-1 0.83	*HCOO 3-5 1.20	* 1-3 1.48	* 1-2 0.57	*HCOO 1-2 0.37	*HCOO 1-3 2.32	*HCOO X
HNO_3	*O 1-2 0.62	*NO_3 0-1 0.24	*O 1-2 0.22	*NO_3 0-2 0.25	* 1-2 0.78	*NO_3 0-2 0.81	*NO_3 0-2 0.46	*O 1-2 0.80	*O 4-5 0.16	*NO_3 0-1 0.80	* 1-3 1.34	*OH 1-3 4.09	*O 1-2 0.28	*O 1-2 0.15	*O 0-1 0.83	*NO_3 3-5 1.23	* 1-3 1.48	* 1-2 0.57	*O 1-3 1.64	*NO_3 1-3 2.86	*NO_3 X
$H_2O + HCN$	*O 1-2 0.62	*CN 0-1 0.78	*CN 0-1 0.82	*CN 0-2 0.91	* 1-2 0.78	*CN 1-3 2.38	*CN 1-3 2.01	*O 1-2 0.80	*CN 0-1 1.01	*CN 0-1 1.19	* 1-3 1.34	*CN 1-3 4.95	*O 1-2 0.28	*O 1-2 0.15	*CN 0-1 1.25	*CN 0-1 1.49	* 1-3 1.48	* 1-2 0.57	*O 1-3 1.64	*OH 1-3 1.67	*OH X
$H_2O + NO$	*NO 1-2 0.21	*NO 1-2 0.15	*NO 1-2 0.28	*NO 1-2 0.52	* 1-2 0.78	* 1-2 0.34	*OH 1-3 2.01	*O 1-2 0.80	*NO 4-5 0.44	*NO 1-2 0.40	* 1-3 1.34	*OH 1-3 4.95	*O 1-2 0.28	*O 1-2 0.15	*NO 3-5 0.79	*NO 0-2 0.29	* 1-3 1.48	* 1-2 0.57	*O 1-3 1.64	*OH 1-3 1.67	*OH X
$H_2O + CO$	*O 1-2 0.62	*O 1-2 0.41	*CO 1-2 0.17	*CO 1-2 0.28	* 1-2 0.78	* 1-2 0.34	*OH 1-3 1.72	*O 1-2 0.80	*CO 4-5 0.14	*CO 4-5 0.42	* 1-3 1.34	*OH 1-3 4.09	*O 1-2 0.28	*O 1-2 0.15	*CO 4-5 0.27	*CO 3-5 0.92	* 1-3 1.48	* 1-2 0.57	*O 1-3 1.64	*OH 1-3 1.67	*OH X

Figure S14 ΔG_{max} along the ORR pathway at U = 0.80 V_{SHE}, pH = 1 on the MN_4C_{10} site in 0.1 M electrolyte. In each cell, the inserted text in the 1st row shows the electrolyte anion participating in the reaction which is the most stable adsorbate on the MN_4C_{10} site at pH = 1, U = 0.80 V_{SHE}. The inserted text in the 2nd row shows the determining states for ΔG_{max} (number 0-6 is referred to a state in Figure S13). The inserted number in the 3rd row is ΔG_{max} value in eV. The insert 'X' means the second adsorbate moves away from the metal site with a distance > 3.0 Å, thus we consider the metal site is inactive for the ORR. The later cases occur especially on the SbN_4C_{10} and BiN_4C_{10} site. The background color corresponds to the ΔG_{max} value. The brighter the background color, the lower the thermodynamic barrier of the limiting step.

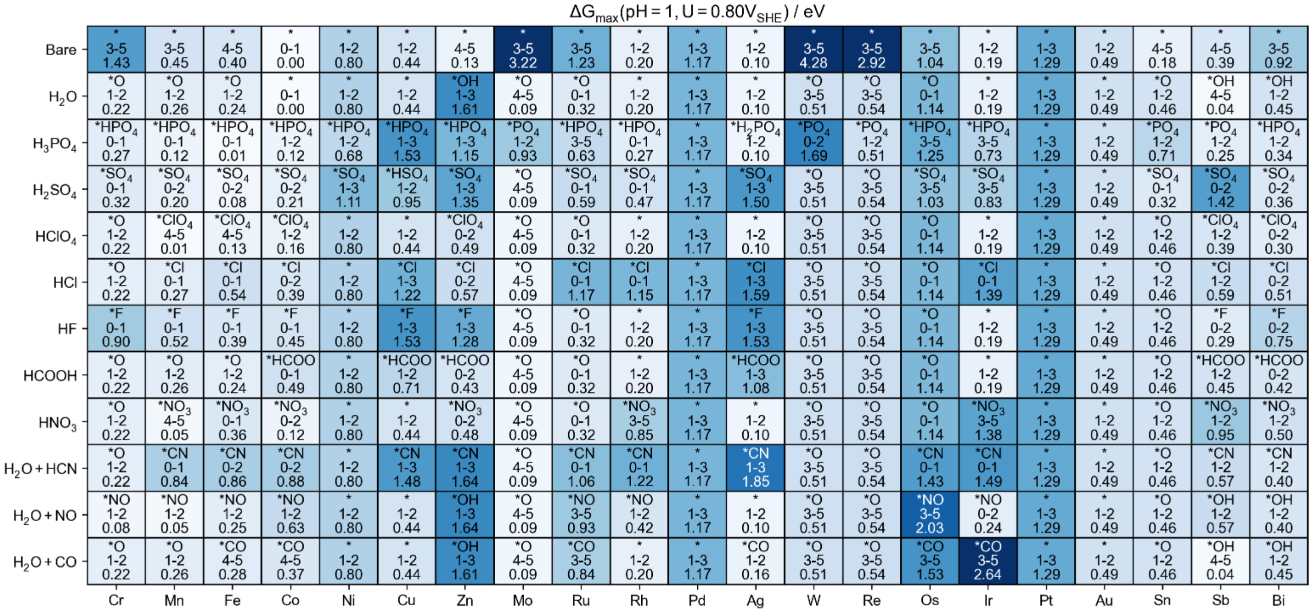

$\Delta G_{max}(pH = 1, U = 0.80V_{SHE})$ / eV

	Cr	Mn	Fe	Co	Ni	Cu	Zn	Mo	Ru	Rh	Pd	Ag	W	Re	Os	Ir	Pt	Au	Sn	Sb	Bi
Bare	* 3-5 1.43	* 3-5 0.45	* 4-5 0.40	* 0-1 0.00	* 1-2 0.80	* 1-2 0.44	* 4-5 0.13	* 3-5 3.22	* 3-5 1.23	* 1-2 0.20	* 1-3 1.17	* 1-2 0.10	* 3-5 4.28	* 3-5 2.92	* 3-5 1.04	* 1-2 0.19	* 1-3 1.29	* 1-2 0.49	* 4-5 0.18	* 4-5 0.39	* 3-5 0.92
H_2O	*O 1-2 0.22	*O 1-2 0.26	*O 1-2 0.24	* 0-1 0.00	* 1-2 0.80	* 1-2 0.44	*OH 1-3 1.61	*O 4-5 0.09	*O 0-1 0.32	* 1-2 0.20	* 1-3 1.17	* 1-2 0.10	*O 3-5 0.51	*O 3-5 0.54	*O 0-1 1.14	* 1-2 0.19	* 1-3 1.29	* 1-2 0.49	*O 1-2 0.46	*OH 4-5 0.04	*OH 1-2 0.45
H_3PO_4	*HPO_4 0-1 0.27	*HPO_4 0-1 0.12	*HPO_4 0-1 0.01	*HPO_4 1-2 0.12	*HPO_4 1-2 0.68	*HPO_4 1-3 1.53	*HPO_4 1-3 1.15	*PO_4 1-2 0.93	*HPO_4 3-5 0.63	*HPO_4 0-1 0.27	* 1-3 1.17	*H_2PO_4 1-2 0.10	*PO_4 0-2 1.69	*PO_4 1-2 0.51	*HPO_4 3-5 1.25	*HPO_4 3-5 0.73	* 1-3 1.29	* 1-2 0.49	*PO_4 1-2 0.71	*PO_4 1-2 0.25	*HPO_4 1-2 0.34
H_2SO_4	*SO_4 0-1 0.32	*SO_4 0-2 0.20	*SO_4 0-2 0.08	*SO_4 0-2 0.21	*SO_4 1-3 1.11	*HSO_4 1-2 0.95	*SO_4 1-3 1.35	*O 4-5 0.09	*SO_4 0-1 0.59	*SO_4 0-1 0.47	* 1-3 1.17	*SO_4 1-3 1.50	*O 3-5 0.51	*O 3-5 0.54	*SO_4 3-5 1.03	*SO_4 3-5 0.83	* 1-3 1.29	* 1-2 0.49	*SO_4 0-1 0.32	*SO_4 0-2 1.42	*SO_4 0-2 0.36
$HClO_4$	*O 1-2 0.22	*ClO_4 4-5 0.01	*ClO_4 4-5 0.13	*ClO_4 1-2 0.16	* 1-2 0.80	* 1-2 0.44	*ClO_4 0-2 0.49	*O 4-5 0.09	*O 0-1 0.32	* 1-2 0.20	* 1-3 1.17	* 1-2 0.10	*O 3-5 0.51	*O 3-5 0.54	*O 0-1 1.14	* 1-2 0.19	* 1-3 1.29	* 1-2 0.49	*O 1-2 0.46	*ClO_4 1-2 0.39	*ClO_4 0-2 0.30
HCl	*O 1-2 0.22	*Cl 0-1 0.27	*Cl 0-1 0.54	*Cl 0-2 0.39	* 1-2 0.80	*Cl 1-3 1.22	*Cl 0-2 0.57	*O 4-5 0.09	*Cl 0-1 1.17	*Cl 0-1 1.15	* 1-3 1.17	*Cl 1-3 1.59	*O 3-5 0.51	*O 3-5 0.54	*O 0-1 1.14	*Cl 0-1 1.39	* 1-3 1.29	* 1-2 0.49	*O 1-2 0.46	*Cl 1-2 0.59	*Cl 0-2 0.51
HF	*F 0-1 0.90	*F 0-1 0.52	*F 0-1 0.39	*F 0-1 0.45	* 1-2 0.80	*F 1-3 1.53	*F 1-3 1.28	*O 4-5 0.09	*O 0-1 0.32	* 1-2 0.20	* 1-3 1.17	*F 1-3 1.53	*O 3-5 0.51	*O 3-5 0.54	*O 0-1 1.14	* 1-2 0.19	* 1-3 1.29	* 1-2 0.49	*O 1-2 0.46	*F 0-2 0.29	*F 0-2 0.75
HCOOH	*O 1-2 0.22	*O 1-2 0.26	*O 1-2 0.24	*HCOO 0-1 0.49	* 1-2 0.80	*HCOO 1-2 0.71	*HCOO 0-2 0.43	*O 4-5 0.09	*O 0-1 0.32	* 1-2 0.20	* 1-3 1.17	*HCOO 1-3 1.08	*O 3-5 0.51	*O 3-5 0.54	*O 0-1 1.14	* 1-2 0.19	* 1-3 1.29	* 1-2 0.49	*O 1-2 0.46	*HCOO 1-2 0.45	*HCOO 0-2 0.42
HNO_3	*O 1-2 0.22	*NO_3 4-5 0.05	*NO_3 0-1 0.36	*NO_3 0-2 0.12	* 1-2 0.80	* 1-2 0.44	*NO_3 0-2 0.48	*O 4-5 0.09	*O 0-1 0.32	*NO_3 3-5 0.85	* 1-3 1.17	* 1-2 0.10	*O 3-5 0.51	*O 3-5 0.54	*O 0-1 1.14	*NO_3 3-5 1.38	* 1-3 1.29	* 1-2 0.49	*O 1-2 0.46	*NO_3 1-2 0.95	*NO_3 1-2 0.50
$H_2O + HCN$	*O 1-2 0.22	*CN 0-1 0.84	*CN 0-2 0.86	*CN 0-2 0.88	* 1-2 0.80	*CN 1-3 1.48	*CN 1-3 1.64	*O 4-5 0.09	*CN 0-1 1.06	*CN 0-1 1.22	* 1-3 1.17	*CN 1-3 1.85	*O 3-5 0.51	*O 3-5 0.54	*CN 0-1 1.43	*CN 0-1 1.49	* 1-3 1.29	* 1-2 0.49	*O 1-2 0.46	*CN 1-2 0.57	*CN 1-2 0.40
$H_2O + NO$	*NO 1-2 0.08	*NO 1-2 0.05	*NO 1-2 0.25	*NO 1-2 0.63	* 1-2 0.80	* 1-2 0.44	*OH 1-3 1.64	*O 4-5 0.09	*NO 3-5 0.93	*NO 1-2 0.42	* 1-3 1.17	* 1-2 0.10	*O 3-5 0.51	*O 3-5 0.54	*NO 3-5 2.03	*NO 0-2 0.24	* 1-3 1.29	* 1-2 0.49	*O 1-2 0.46	*OH 1-2 0.57	*OH 1-2 0.40
$H_2O + CO$	*O 1-2 0.22	*O 1-2 0.26	*CO 4-5 0.28	*CO 4-5 0.37	* 1-2 0.80	* 1-2 0.44	*OH 1-3 1.61	*O 4-5 0.09	*CO 3-5 0.84	* 1-2 0.20	* 1-3 1.17	*CO 1-2 0.16	*O 3-5 0.51	*O 3-5 0.54	*CO 3-5 1.53	*CO 3-5 2.64	* 1-3 1.29	* 1-2 0.49	*O 1-2 0.46	*OH 4-5 0.04	*OH 1-2 0.45

Figure S15 ΔG_{max} along the ORR pathway at U = 0.80 V_{SHE}, pH = 1 on the MN_4C_A site in 0.1 M electrolyte. In each cell, the inserted text in the 1st row shows the electrolyte anion participating in the reaction which is the most stable adsorbate on the MN_4C_{10} site at pH = 1, U = 0.80 V_{SHE}. The inserted text in the 2nd row shows the determining states for ΔG_{max} (number 0-6 is referred to a state in Figure S13). The inserted number in the 3rd row is ΔG_{max} value in eV. The background color corresponds to the ΔG_{max} value. The brighter the background color, the lower the thermodynamic barrier of the limiting step.

.

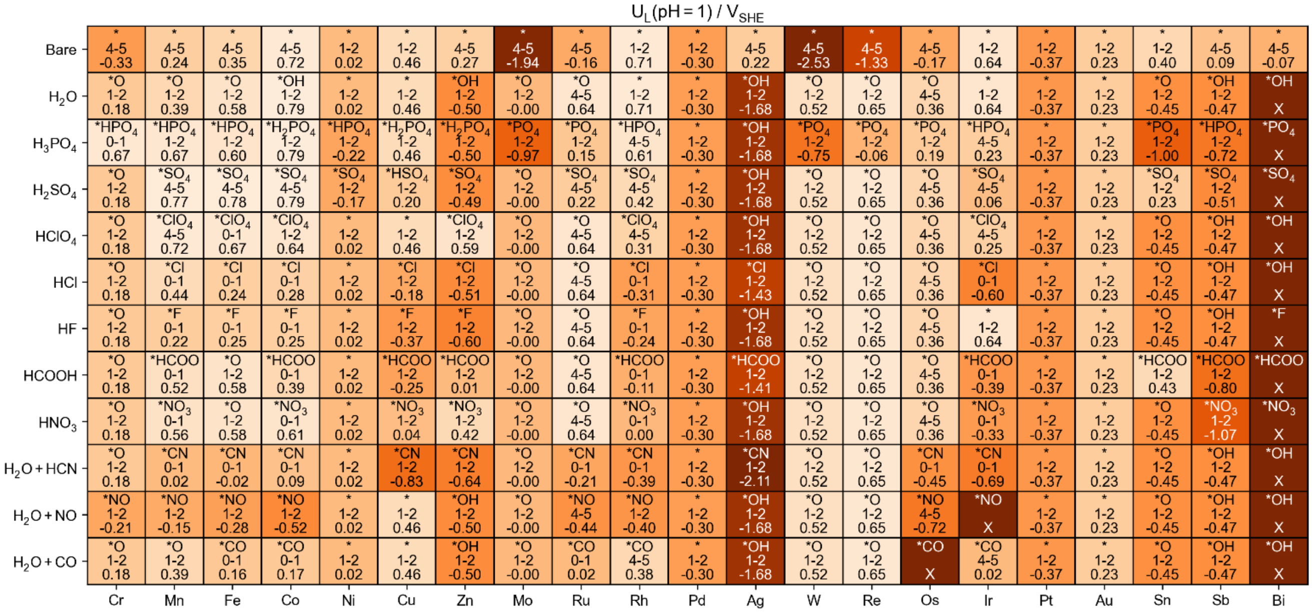

U_L (pH = 1) / V_{SHE}

	Cr	Mn	Fe	Co	Ni	Cu	Zn	Mo	Ru	Rh	Pd	Ag	W	Re	Os	Ir	Pt	Au	Sn	Sb	Bi
Bare	* 4-5 -0.33	* 4-5 0.24	* 4-5 0.35	* 4-5 0.72	* 1-2 0.02	* 1-2 0.46	* 4-5 0.27	* 4-5 -1.94	* 4-5 -0.16	* 1-2 0.71	* 1-2 -0.30	* 4-5 0.22	* 4-5 -2.53	* 4-5 -1.33	* 4-5 -0.17	* 1-2 0.64	* 1-2 -0.37	* 1-2 0.23	* 1-2 0.40	* 4-5 0.09	* 4-5 -0.07
H_2O	*O 1-2 0.18	*O 1-2 0.39	*O 1-2 0.58	*OH 1-2 0.79	* 1-2 0.02	* 1-2 0.46	*OH 1-2 -0.50	*O 1-2 -0.00	*O 4-5 0.64	* 1-2 0.71	* 1-2 -0.30	*OH 1-2 -1.68	*O 1-2 0.52	*O 1-2 0.65	*O 4-5 0.36	* 1-2 0.64	* 1-2 -0.37	* 1-2 0.23	*O 1-2 -0.45	*OH 1-2 -0.47	*OH X
H_3PO_4	*HPO_4 0-1 0.67	*HPO_4 1-2 0.67	*HPO_4 1-2 0.60	*H_2PO_4 1-2 0.79	*HPO_4 1-2 -0.22	*H_2PO_4 1-2 0.46	*H_2PO_4 1-2 -0.50	*PO_4 1-2 -0.97	*PO_4 1-2 0.15	*HPO_4 4-5 0.61	* 1-2 -0.30	*OH 1-2 -1.68	*PO_4 1-2 -0.75	*PO_4 1-2 -0.06	*PO_4 1-2 0.19	*HPO_4 4-5 0.23	* 1-2 -0.37	* 1-2 0.23	*PO_4 1-2 -1.00	*HPO_4 1-2 -0.72	*PO_4 X
H_2SO_4	*O 1-2 0.18	*SO_4 4-5 0.77	*SO_4 4-5 0.78	*SO_4 4-5 0.79	*SO_4 1-2 -0.17	*HSO_4 1-2 0.20	*SO_4 1-2 -0.49	*O 1-2 -0.00	*SO_4 4-5 0.22	*SO_4 4-5 0.42	* 1-2 -0.30	*OH 1-2 -1.68	*O 1-2 0.52	*O 1-2 0.65	*O 4-5 0.36	*SO_4 4-5 0.06	* 1-2 -0.37	* 1-2 0.23	*SO_4 1-2 0.23	*SO_4 1-2 -0.51	*SO_4 X
$HClO_4$	*O 1-2 0.18	*ClO_4 4-5 0.72	*ClO_4 0-1 0.67	*ClO_4 1-2 0.64	* 1-2 0.02	* 1-2 0.46	*ClO_4 1-2 0.59	*O 1-2 -0.00	*O 4-5 0.64	*ClO_4 4-5 0.31	* 1-2 -0.30	*OH 1-2 -1.68	*O 1-2 0.52	*O 1-2 0.65	*O 4-5 0.36	*ClO_4 4-5 0.25	* 1-2 -0.37	* 1-2 0.23	*O 1-2 -0.45	*OH 1-2 -0.47	*OH X
HCl	*O 1-2 0.18	*Cl 0-1 0.44	*Cl 0-1 0.24	*Cl 0-1 0.28	* 1-2 0.02	*Cl 1-2 -0.18	*Cl 1-2 -0.51	*O 1-2 -0.00	*O 4-5 0.64	*Cl 0-1 -0.31	* 1-2 -0.30	*Cl 1-2 -1.43	*O 1-2 0.52	*O 1-2 0.65	*O 4-5 0.36	*Cl 0-1 -0.60	* 1-2 -0.37	* 1-2 0.23	*O 1-2 -0.45	*OH 1-2 -0.47	*OH X
HF	*O 1-2 0.18	*F 0-1 0.22	*F 0-1 0.25	*F 0-1 0.25	* 1-2 0.02	*F 1-2 -0.37	*F 1-2 -0.60	*O 1-2 -0.00	*O 4-5 0.64	*F 0-1 -0.24	* 1-2 -0.30	*OH 1-2 -1.68	*O 1-2 0.52	*O 1-2 0.65	*O 4-5 0.36	* 1-2 0.64	* 1-2 -0.37	* 1-2 0.23	*O 1-2 -0.45	*OH 1-2 -0.47	*F X
HCOOH	*O 1-2 0.18	*HCOO 0-1 0.52	*O 1-2 0.58	*HCOO 0-1 0.39	* 1-2 0.02	*HCOO 1-2 -0.25	*HCOO 1-2 0.01	*O 1-2 -0.00	*O 4-5 0.64	*HCOO 0-1 -0.11	* 1-2 -0.30	*HCOO 1-2 -1.41	*O 1-2 0.52	*O 1-2 0.65	*O 4-5 0.36	*HCOO 0-1 -0.39	* 1-2 -0.37	* 1-2 0.23	*HCOO 1-2 0.43	*HCOO 1-2 -0.80	*HCOO X
HNO_3	*O 1-2 0.18	*NO_3 0-1 0.56	*O 1-2 0.58	*NO_3 0-1 0.61	* 1-2 0.02	*NO_3 1-2 0.04	*NO_3 1-2 0.42	*O 1-2 -0.00	*O 4-5 0.64	*NO_3 0-1 0.00	* 1-2 -0.30	*OH 1-2 -1.68	*O 1-2 0.52	*O 1-2 0.65	*O 4-5 0.36	*NO_3 0-1 -0.33	* 1-2 -0.37	* 1-2 0.23	*O 1-2 -0.45	*NO_3 1-2 -1.07	*NO_3 X
$H_2O + HCN$	*O 1-2 0.18	*CN 0-1 0.02	*CN 0-1 -0.02	*CN 0-1 0.09	* 1-2 0.02	*CN 1-2 -0.83	*CN 1-2 -0.64	*O 1-2 -0.00	*CN 0-1 -0.21	*CN 0-1 -0.39	* 1-2 -0.30	*CN 1-2 -2.11	*O 1-2 0.52	*O 1-2 0.65	*CN 0-1 -0.45	*CN 0-1 -0.69	* 1-2 -0.37	* 1-2 0.23	*O 1-2 -0.45	*OH 1-2 -0.47	*OH X
$H_2O + NO$	*NO 1-2 -0.21	*NO 1-2 -0.15	*NO 1-2 -0.28	*NO 1-2 -0.52	* 1-2 0.02	* 1-2 0.46	*OH 1-2 -0.50	*O 1-2 -0.00	*NO 4-5 -0.44	*NO 1-2 -0.40	* 1-2 -0.30	*OH 1-2 -1.68	*O 1-2 0.52	*O 1-2 0.65	*NO 4-5 -0.72	*NO X	* 1-2 -0.37	* 1-2 0.23	*O 1-2 -0.45	*OH 1-2 -0.47	*OH X
$H_2O + CO$	*O 1-2 0.18	*O 1-2 0.39	*CO 0-1 0.16	*CO 0-1 0.17	* 1-2 0.02	* 1-2 0.46	*OH 1-2 -0.50	*O 1-2 -0.00	*CO 0-1 0.02	*CO 4-5 0.38	* 1-2 -0.30	*OH 1-2 -1.68	*O 1-2 0.52	*O 1-2 0.65	*CO X	*CO 4-5 0.02	* 1-2 -0.37	* 1-2 0.23	*O 1-2 -0.45	*OH 1-2 -0.47	*OH X

Figure S16 U_L for ORR on MN_4C_{10} in 0.1 M electrolyte at pH = 1. In each cell, the inserted text in the 1st row shows the electrolyte anion participating in the reaction which is the most stable adsorbate on the MN_4C_{10} site at pH=1, U=0.80 V_{SHE}. The inserted text in the 2nd row shows the potential determining states for U_L (the number 0-6 is referred a state in Figure S13). The inserted number in the 3rd row is U_L value in V_{SHE}. The insert 'X' means the neutral gas molecules are thermodynamic stable on both sides of the metal atom or the second adsorbate moves away from the metal site with the distance > 3.0 Å, thus we considered the metal site is inactive for the ORR. The later cases occur especially on the SbN_4C_{10} and BiN_4C_{10} sites, The background color corresponds to the U_L value. The brighter the background color, the higher the limiting potential.

.

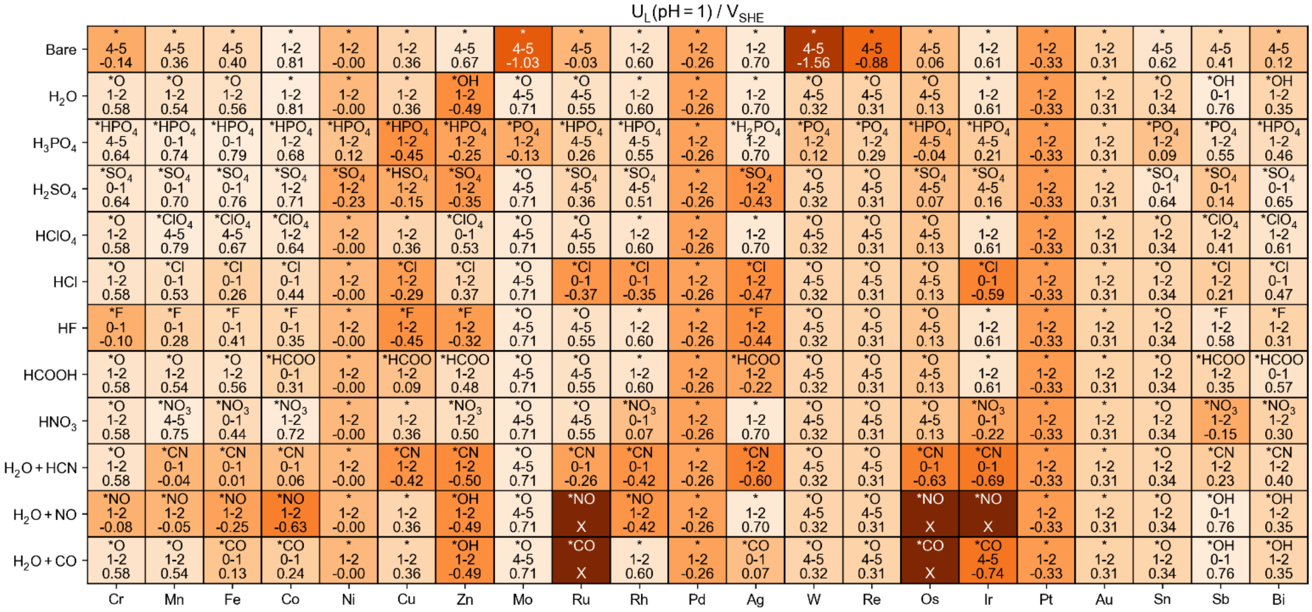

$U_L (pH = 1) / V_{SHE}$

	Cr	Mn	Fe	Co	Ni	Cu	Zn	Mo	Ru	Rh	Pd	Ag	W	Re	Os	Ir	Pt	Au	Sn	Sb	Bi
Bare	* 4-5 -0.14	* 4-5 0.36	* 4-5 0.40	* 1-2 0.81	* 1-2 -0.00	* 1-2 0.36	* 4-5 0.67	* 4-5 -1.03	* 4-5 -0.03	* 1-2 0.60	* 1-2 -0.26	* 1-2 0.70	* 4-5 -1.56	* 4-5 -0.88	* 4-5 0.06	* 1-2 0.61	* 1-2 -0.33	* 1-2 0.31	* 4-5 0.62	* 4-5 0.41	* 4-5 0.12
H_2O	*O 1-2 0.58	*O 1-2 0.54	*O 1-2 0.56	* 1-2 0.81	* 1-2 -0.00	* 1-2 0.36	*OH 1-2 -0.49	*O 4-5 0.71	*O 4-5 0.55	* 1-2 0.60	* 1-2 -0.26	* 1-2 0.70	*O 4-5 0.32	*O 4-5 0.31	*O 4-5 0.13	* 1-2 0.61	* 1-2 -0.33	* 1-2 0.31	*O 1-2 0.34	*OH 0-1 0.76	*OH 1-2 0.35
H_3PO_4	*HPO$_4$ 4-5 0.64	*HPO$_4$ 0-1 0.74	*HPO$_4$ 0-1 0.79	*HPO$_4$ 1-2 0.68	*HPO$_4$ 1-2 0.12	*HPO$_4$ 1-2 -0.45	*HPO$_4$ 1-2 -0.25	*PO$_4$ 1-2 -0.13	*HPO$_4$ 4-5 0.26	*HPO$_4$ 4-5 0.55	* 1-2 -0.26	*H$_2$PO$_4$ 1-2 0.70	*PO$_4$ 1-2 0.12	*PO$_4$ 1-2 0.29	*HPO$_4$ 4-5 -0.04	*HPO$_4$ 4-5 0.21	* 1-2 -0.33	* 1-2 0.31	*PO$_4$ 1-2 0.09	*PO$_4$ 1-2 0.55	*HPO$_4$ 1-2 0.46
H_2SO_4	*SO$_4$ 0-1 0.64	*SO$_4$ 0-1 0.70	*SO$_4$ 0-1 0.76	*SO$_4$ 1-2 0.71	*SO$_4$ 1-2 -0.23	*HSO$_4$ 1-2 -0.15	*SO$_4$ 1-2 -0.35	*O 4-5 0.71	*SO$_4$ 4-5 0.36	*SO$_4$ 4-5 0.51	* 1-2 -0.26	*SO$_4$ 1-2 -0.43	*O 4-5 0.32	*O 4-5 0.31	*SO$_4$ 4-5 0.07	*SO$_4$ 4-5 0.16	* 1-2 -0.33	* 1-2 0.31	*SO$_4$ 0-1 0.64	*SO$_4$ 0-1 0.14	*SO$_4$ 0-1 0.65
$HClO_4$	*O 1-2 0.58	*ClO$_4$ 4-5 0.79	*ClO$_4$ 4-5 0.67	*ClO$_4$ 1-2 0.64	* 1-2 -0.00	* 1-2 0.36	*ClO$_4$ 0-1 0.53	*O 4-5 0.71	*O 4-5 0.55	* 1-2 0.60	* 1-2 -0.26	* 1-2 0.70	*O 4-5 0.32	*O 4-5 0.31	*O 4-5 0.13	* 1-2 0.61	* 1-2 -0.33	* 1-2 0.31	*O 1-2 0.34	*ClO$_4$ 1-2 0.41	*ClO$_4$ 1-2 0.61
HCl	*O 1-2 0.58	*Cl 0-1 0.53	*Cl 0-1 0.26	*Cl 0-1 0.44	* 1-2 -0.00	*Cl 1-2 -0.29	*Cl 1-2 0.37	*O 4-5 0.71	*Cl 0-1 -0.37	*Cl 0-1 -0.35	* 1-2 -0.26	*Cl 1-2 -0.47	*O 4-5 0.32	*O 4-5 0.31	*O 4-5 0.13	*Cl 0-1 -0.59	* 1-2 -0.33	* 1-2 0.31	*O 1-2 0.34	*Cl 1-2 0.21	*Cl 0-1 0.47
HF	*F 0-1 -0.10	*F 0-1 0.28	*F 0-1 0.41	*F 0-1 0.35	* 1-2 -0.00	*F 1-2 -0.45	*F 1-2 -0.32	*O 4-5 0.71	*O 4-5 0.55	* 1-2 0.60	* 1-2 -0.26	*F 1-2 -0.44	*O 4-5 0.32	*O 4-5 0.31	*O 4-5 0.13	* 1-2 0.61	* 1-2 -0.33	* 1-2 0.31	*O 1-2 0.34	*F 1-2 0.58	*F 1-2 0.31
HCOOH	*O 1-2 0.58	*O 1-2 0.54	*O 1-2 0.56	*HCOO 0-1 0.31	* 1-2 -0.00	*HCOO 1-2 0.09	*HCOO 1-2 0.48	*O 4-5 0.71	*O 4-5 0.55	* 1-2 0.60	* 1-2 -0.26	*HCOO 1-2 -0.22	*O 4-5 0.32	*O 4-5 0.31	*O 4-5 0.13	* 1-2 0.61	* 1-2 -0.33	* 1-2 0.31	*O 1-2 0.34	*HCOO 1-2 0.35	*HCOO 0-1 0.57
HNO_3	*O 1-2 0.58	*NO$_3$ 4-5 0.75	*NO$_3$ 0-1 0.44	*NO$_3$ 1-2 0.72	* 1-2 -0.00	* 1-2 0.36	*NO$_3$ 1-2 0.50	*O 4-5 0.71	*O 4-5 0.55	*NO$_3$ 0-1 0.07	* 1-2 -0.26	* 1-2 0.70	*O 4-5 0.32	*O 4-5 0.31	*O 4-5 0.13	*NO$_3$ 0-1 -0.22	* 1-2 -0.33	* 1-2 0.31	*O 1-2 0.34	*NO$_3$ 1-2 -0.15	*NO$_3$ 1-2 0.30
$H_2O + HCN$	*O 1-2 0.58	*CN 0-1 -0.04	*CN 0-1 0.01	*CN 0-1 0.06	* 1-2 -0.00	*CN 1-2 -0.42	*CN 1-2 -0.50	*O 4-5 0.71	*CN 0-1 -0.26	*CN 0-1 -0.42	* 1-2 -0.26	*CN 1-2 -0.60	*O 4-5 0.32	*O 4-5 0.31	*CN 0-1 -0.63	*CN 0-1 -0.69	* 1-2 -0.33	* 1-2 0.31	*O 1-2 0.34	*CN 1-2 0.23	*CN 1-2 0.40
$H_2O + NO$	*NO 1-2 -0.08	*NO 1-2 -0.05	*NO 1-2 -0.25	*NO 1-2 -0.63	* 1-2 -0.00	* 1-2 0.36	*OH 1-2 -0.49	*O 4-5 0.71	*NO X	*NO 1-2 -0.42	* 1-2 -0.26	* 1-2 0.70	*O 4-5 0.32	*O 4-5 0.31	*NO X	*NO X	* 1-2 -0.33	* 1-2 0.31	*O 1-2 0.34	*OH 0-1 0.76	*OH 1-2 0.35
$H_2O + CO$	*O 1-2 0.58	*O 1-2 0.54	*CO 0-1 0.13	*CO 0-1 0.24	* 1-2 -0.00	* 1-2 0.36	*OH 1-2 -0.49	*O 4-5 0.71	*CO X	* 1-2 0.60	* 1-2 -0.26	*CO 0-1 0.07	*O 4-5 0.32	*O 4-5 0.31	*CO X	*CO 4-5 -0.74	* 1-2 -0.33	* 1-2 0.31	*O 1-2 0.34	*OH 0-1 0.76	*OH 1-2 0.35

Figure S17 U_L for ORR on MN_4C_A in 0.1 M electrolyte at pH = 1. In each cell, the inserted text in the 1st row shows the electrolyte anion participating in the reaction which is the most stable adsorbate on the MN_4C_{10} site at pH=1, U=0.80 V_{SHE}. The inserted text in the 2nd row shows the potential determining states for U_L (the number 0-6 is referred a state in Figure S13). The inserted number in the 3rd row is U_L value in V_{SHE}. The insert 'X' means the neutral gas molecules are thermodynamic stable on both sides of the metal atom or the second adsorbate moves away from the metal site with the distance > 3.0 Å, thus we considered the metal site is inactive for the ORR. The later cases occur especially on the SbN_4C_{10} and BiN_4C_{10} sites, The background color corresponds to the U_L value. The brighter the background color, the higher the limiting potential.

7. CO_2RR to CO activity

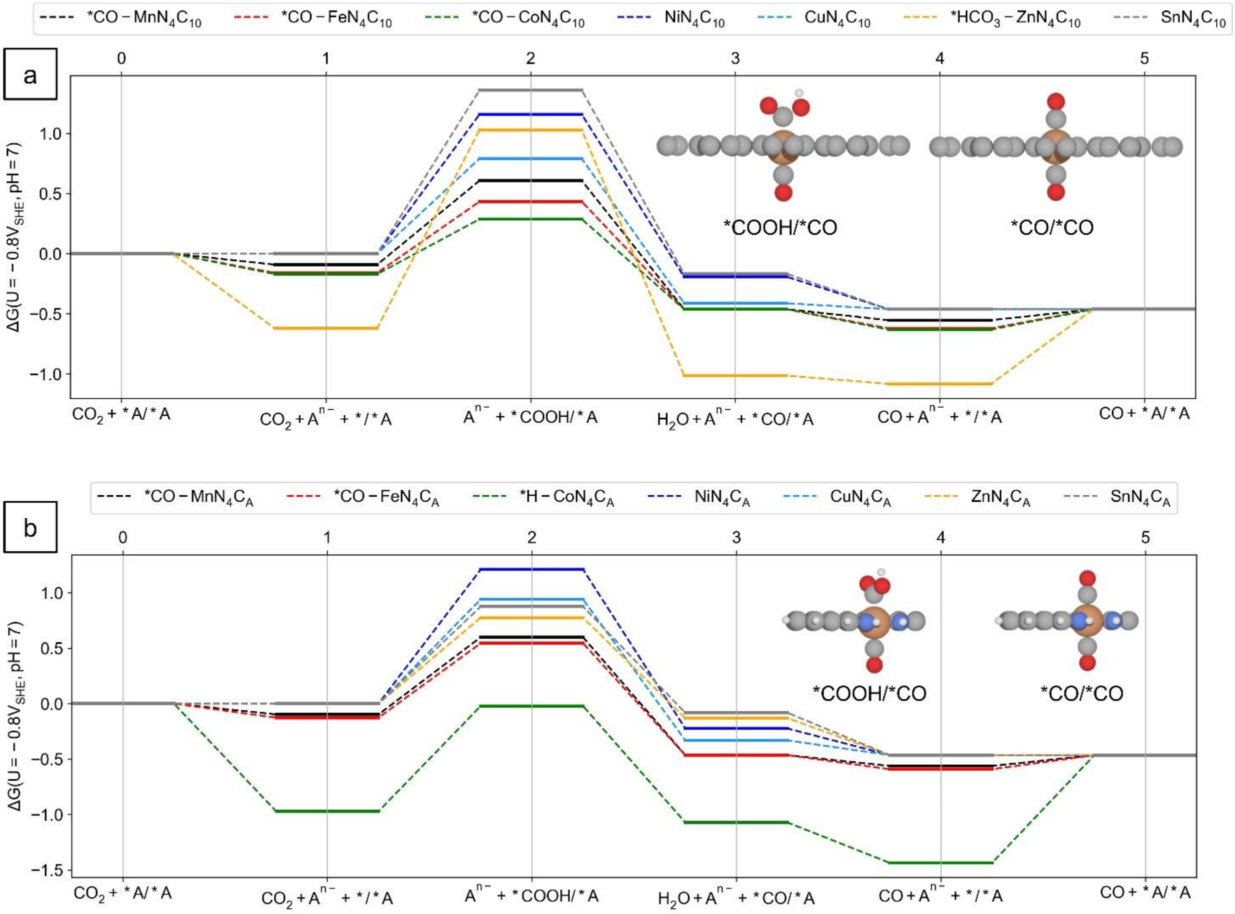

Figure S18 Free energy diagram of the CO_2RR to CO at pH = 7, U = -0.80 V_{SHE} on: (a) MN_4C_{10}, (b) MN_4C_A in 0.1 M H_2CO_3+CO solution, where M = Mn, Fe, Co, Ni, Zn, Cu and Sn. The inset structures show the side view of the *COOH/*CO and *CO/*CO on the FeN_4 site. (C = gray, N = blue, H = white, O = red, Fe = orange).

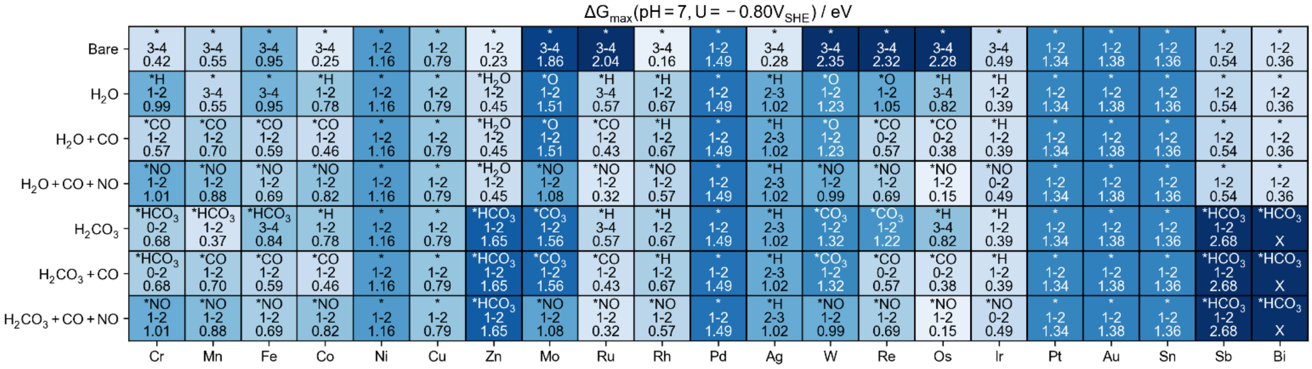

	Cr	Mn	Fe	Co	Ni	Cu	Zn	Mo	Ru	Rh	Pd	Ag	W	Re	Os	Ir	Pt	Au	Sn	Sb	Bi
Bare	* 3-4 0.42	* 3-4 0.55	* 3-4 0.95	* 3-4 0.25	* 1-2 1.16	* 1-2 0.79	* 1-2 0.23	* 3-4 1.86	* 3-4 2.04	* 3-4 0.16	* 1-2 1.49	* 3-4 0.28	* 3-4 2.35	* 3-4 2.32	* 3-4 2.28	* 3-4 0.49	* 1-2 1.34	* 1-2 1.38	* 1-2 1.36	* 1-2 0.54	* 1-2 0.36
H_2O	*H 1-2 0.99	* 3-4 0.55	* 3-4 0.95	*H 1-2 0.78	* 1-2 1.16	* 1-2 0.79	*H_2O 1-2 0.45	*O 1-2 1.51	*H 3-4 0.57	*H 1-2 0.67	* 1-2 1.49	*H 2-3 1.02	*O 1-2 1.23	*O 1-2 1.05	*H 3-4 0.82	*H 1-2 0.39	* 1-2 1.34	* 1-2 1.38	* 1-2 1.36	* 1-2 0.54	* 1-2 0.36
$H_2O + CO$	*CO 1-2 0.57	*CO 1-2 0.70	*CO 1-2 0.59	*CO 1-2 0.46	* 1-2 1.16	* 1-2 0.79	*H_2O 1-2 0.45	*O 1-2 1.51	*CO 1-2 0.43	*H 1-2 0.67	* 1-2 1.49	*H 2-3 1.02	*O 1-2 1.23	*CO 0-2 0.57	*CO 0-2 0.38	*H 1-2 0.39	* 1-2 1.34	* 1-2 1.38	* 1-2 1.36	* 1-2 0.54	* 1-2 0.36
$H_2O + CO + NO$	*NO 1-2 1.01	*NO 1-2 0.88	*NO 1-2 0.69	*NO 1-2 0.82	* 1-2 1.16	* 1-2 0.79	*H_2O 1-2 0.45	*NO 1-2 1.08	*NO 1-2 0.32	*NO 1-2 0.57	* 1-2 1.49	*H 2-3 1.02	*NO 1-2 0.99	*NO 1-2 0.69	*NO 1-2 0.15	*NO 0-2 0.49	* 1-2 1.34	* 1-2 1.38	* 1-2 1.36	* 1-2 0.54	* 1-2 0.36
H_2CO_3	*HCO_3 0-2 0.68	*HCO_3 1-2 0.37	*HCO_3 3-4 0.84	*H 1-2 0.78	* 1-2 1.16	* 1-2 0.79	*HCO_3 1-2 1.65	*CO_3 1-2 1.56	*H 3-4 0.57	*H 1-2 0.67	* 1-2 1.49	*H 2-3 1.02	*CO_3 1-2 1.32	*CO_3 1-2 1.22	*H 3-4 0.82	*H 1-2 0.39	* 1-2 1.34	* 1-2 1.38	* 1-2 1.36	*HCO_3 1-2 2.68	*HCO_3 X
$H_2CO_3 + CO$	*HCO_3 0-2 0.68	*CO 1-2 0.70	*CO 1-2 0.59	*CO 1-2 0.46	* 1-2 1.16	* 1-2 0.79	*HCO_3 1-2 1.65	*CO_3 1-2 1.56	*CO 1-2 0.43	*H 1-2 0.67	* 1-2 1.49	*H 2-3 1.02	*CO_3 1-2 1.32	*CO 0-2 0.57	*CO 0-2 0.38	*H 1-2 0.39	* 1-2 1.34	* 1-2 1.38	* 1-2 1.36	*HCO_3 1-2 2.68	*HCO_3 X
$H_2CO_3 + CO + NO$	*NO 1-2 1.01	*NO 1-2 0.88	*NO 1-2 0.69	*NO 1-2 0.82	* 1-2 1.16	* 1-2 0.79	*HCO_3 1-2 1.65	*NO 1-2 1.08	*NO 1-2 0.32	*NO 1-2 0.57	* 1-2 1.49	*H 2-3 1.02	*NO 1-2 0.99	*NO 1-2 0.69	*NO 1-2 0.15	*NO 0-2 0.49	* 1-2 1.34	* 1-2 1.38	* 1-2 1.36	*HCO_3 1-2 2.68	*HCO_3 X

Figure S19 ΔG_{max} along the CO_2RR to CO pathway at U=-0.80 V_{SHE}, pH=7 on the MN_4C_{10} site in 0.1 M electrolyte. In each cell, the inserted text in the 1st row shows the electrolyte anion participating in the reaction which is the most stable adsorbate on the MN_4C_{10} site at pH=7, U=-0.80 V_{SHE}. The inserted text in the 2nd row shows the determining states for ΔG_{max} (number 0-5 is referred to state in Figure S18). The inserted number in the 3rd row is ΔG_{max} value in eV. The insert 'X' means the second adsorbate moves away from the metal site with the distance > 3.0 Å, thus we considered the metal site is inactive for the ORR. The later cases occur especially on the SbN_4C_{10} and BiN_4C_{10} site.

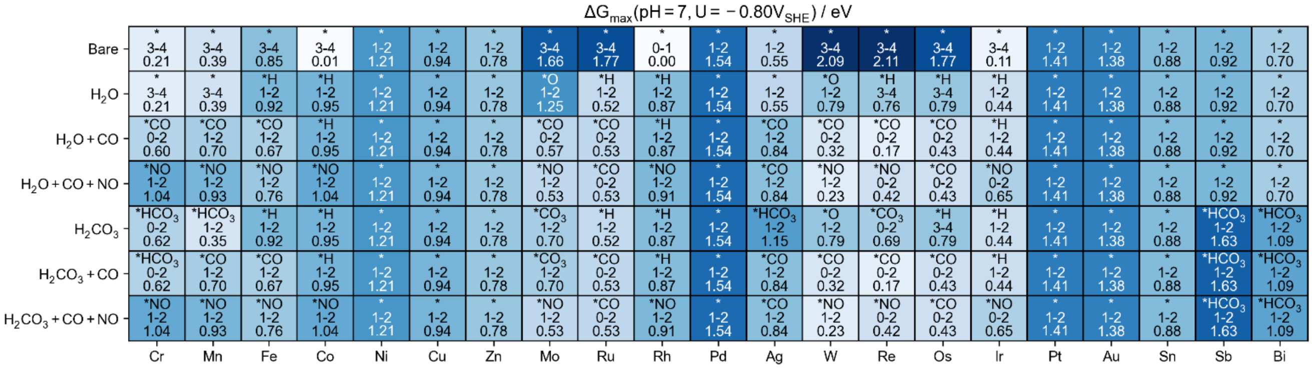

	Cr	Mn	Fe	Co	Ni	Cu	Zn	Mo	Ru	Rh	Pd	Ag	W	Re	Os	Ir	Pt	Au	Sn	Sb	Bi
Bare	* 3-4 0.21	* 3-4 0.39	* 3-4 0.85	* 3-4 0.01	* 1-2 1.21	* 1-2 0.94	* 1-2 0.78	* 3-4 1.66	* 3-4 1.77	* 0-1 0.00	* 1-2 1.54	* 1-2 0.55	* 3-4 2.09	* 3-4 2.11	* 3-4 1.77	* 3-4 0.11	* 1-2 1.41	* 1-2 1.38	* 1-2 0.88	* 1-2 0.92	* 1-2 0.70
H_2O	* 3-4 0.21	* 3-4 0.39	*H 1-2 0.92	*H 1-2 0.95	* 1-2 1.21	* 1-2 0.94	* 1-2 0.78	*O 1-2 1.25	*H 1-2 0.52	*H 1-2 0.87	* 1-2 1.54	* 1-2 0.55	*O 1-2 0.79	*H 3-4 0.76	*H 3-4 0.79	*H 1-2 0.44	* 1-2 1.41	* 1-2 1.38	* 1-2 0.88	* 1-2 0.92	* 1-2 0.70
$H_2O + CO$	*CO 0-2 0.60	*CO 1-2 0.70	*CO 1-2 0.67	*H 1-2 0.95	* 1-2 1.21	* 1-2 0.94	* 1-2 0.78	*CO 0-2 0.57	*CO 0-2 0.53	*H 1-2 0.87	* 1-2 1.54	*CO 1-2 0.84	*CO 0-2 0.32	*CO 0-2 0.17	*CO 0-2 0.43	*H 1-2 0.44	* 1-2 1.41	* 1-2 1.38	* 1-2 0.88	* 1-2 0.92	* 1-2 0.70
$H_2O + CO + NO$	*NO 1-2 1.04	*NO 1-2 0.93	*NO 1-2 0.76	*NO 1-2 1.04	* 1-2 1.21	* 1-2 0.94	* 1-2 0.78	*NO 1-2 0.53	*CO 0-2 0.53	*NO 1-2 0.91	* 1-2 1.54	*CO 1-2 0.84	*NO 1-2 0.23	*NO 0-2 0.42	*CO 0-2 0.43	*NO 0-2 0.65	* 1-2 1.41	* 1-2 1.38	* 1-2 0.88	* 1-2 0.92	* 1-2 0.70
H_2CO_3	*HCO_3 0-2 0.62	*HCO_3 1-2 0.35	*H 1-2 0.92	*H 1-2 0.95	* 1-2 1.21	* 1-2 0.94	* 1-2 0.78	*CO_3 1-2 0.70	*H 1-2 0.52	*H 1-2 0.87	* 1-2 1.54	*HCO_3 1-2 1.15	*O 1-2 0.79	*CO_3 0-2 0.69	*H 3-4 0.79	*H 1-2 0.44	* 1-2 1.41	* 1-2 1.38	* 1-2 0.88	*HCO_3 1-2 1.63	*HCO_3 1-2 1.09
$H_2CO_3 + CO$	*HCO_3 0-2 0.62	*CO 1-2 0.70	*CO 1-2 0.67	*H 1-2 0.95	* 1-2 1.21	* 1-2 0.94	* 1-2 0.78	*CO_3 1-2 0.70	*CO 0-2 0.53	*H 1-2 0.87	* 1-2 1.54	*CO 1-2 0.84	*CO 0-2 0.32	*CO 0-2 0.17	*CO 0-2 0.43	*H 1-2 0.44	* 1-2 1.41	* 1-2 1.38	* 1-2 0.88	*HCO_3 1-2 1.63	*HCO_3 1-2 1.09
$H_2CO_3 + CO + NO$	*NO 1-2 1.04	*NO 1-2 0.93	*NO 1-2 0.76	*NO 1-2 1.04	* 1-2 1.21	* 1-2 0.94	* 1-2 0.78	*NO 1-2 0.53	*CO 0-2 0.53	*NO 1-2 0.91	* 1-2 1.54	*CO 1-2 0.84	*NO 1-2 0.23	*NO 0-2 0.42	*CO 0-2 0.43	*NO 0-2 0.65	* 1-2 1.41	* 1-2 1.38	* 1-2 0.88	*HCO_3 1-2 1.63	*HCO_3 1-2 1.09

Figure S20 ΔG_{max} along the CO_2RR to CO pathway at U=-0.80 V_{SHE}, pH=7 on the MN_4C_A site in 0.1 M electrolyte. In each cell, the inserted text in the 1st row shows the electrolyte anion participating in the reaction which is the most stable adsorbate on the MN_4C_A site at pH=7, U=-0.80 V_{SHE}. The inserted text in the 2nd row shows the determining states for ΔG_{max} (number 0-5 is referred to state in Figure S18). The inserted number in the 3rd row is ΔG_{max} value in eV.

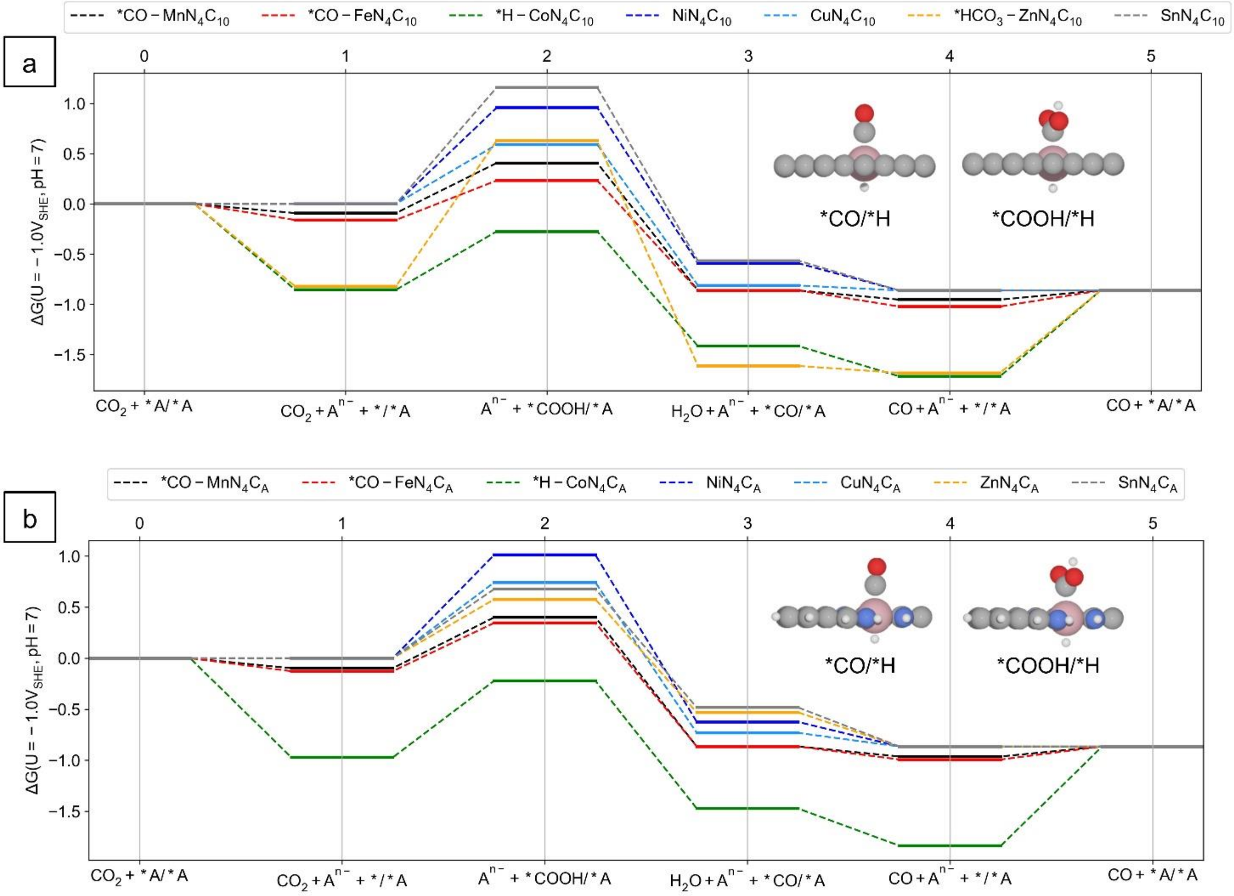

Figure S21 Free energy diagram of the CO_2RR to CO at pH = 7, U = -1.0 V_{SHE} on: (a) MN_4C_{10}, (b) MN_4C_A in 0.1 M H_2CO_3+CO solution, where M = Mn, Fe, Co, Ni, Zn, Cu and Sn. The inset structures show the side view of the *COOH/*H and *CO/*H on the FeN_4 site. (C = gray, N = blue, H = white, O = red, Co = pink).

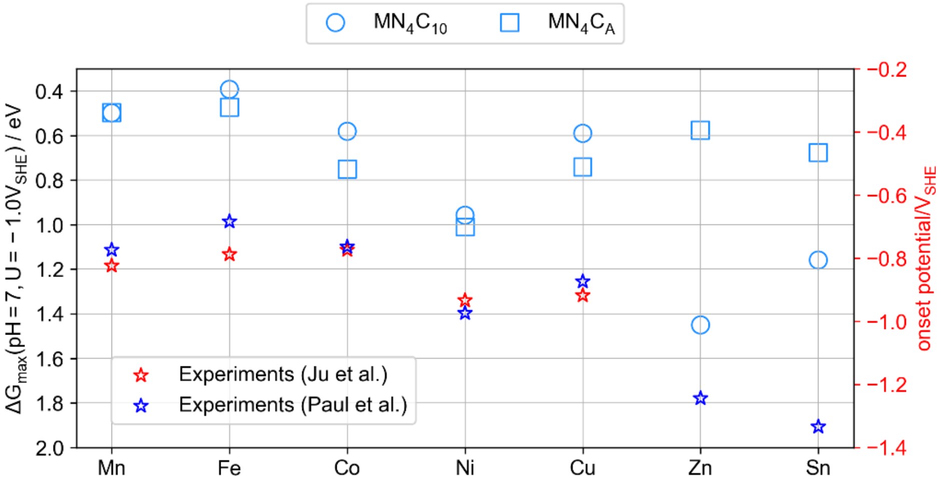

Figure S22 ΔG_{max} for the CO_2RR to CO on MN_4C_{10} (circle) and MN_4C_A (square) at pH = 7 and U= -1.0 V_{SHE} with M = Mn, Fe, Co, Ni, Cu, Zn, and Sn. The onset potentials from the experiments are marked with stars and use the y-axis on the right.

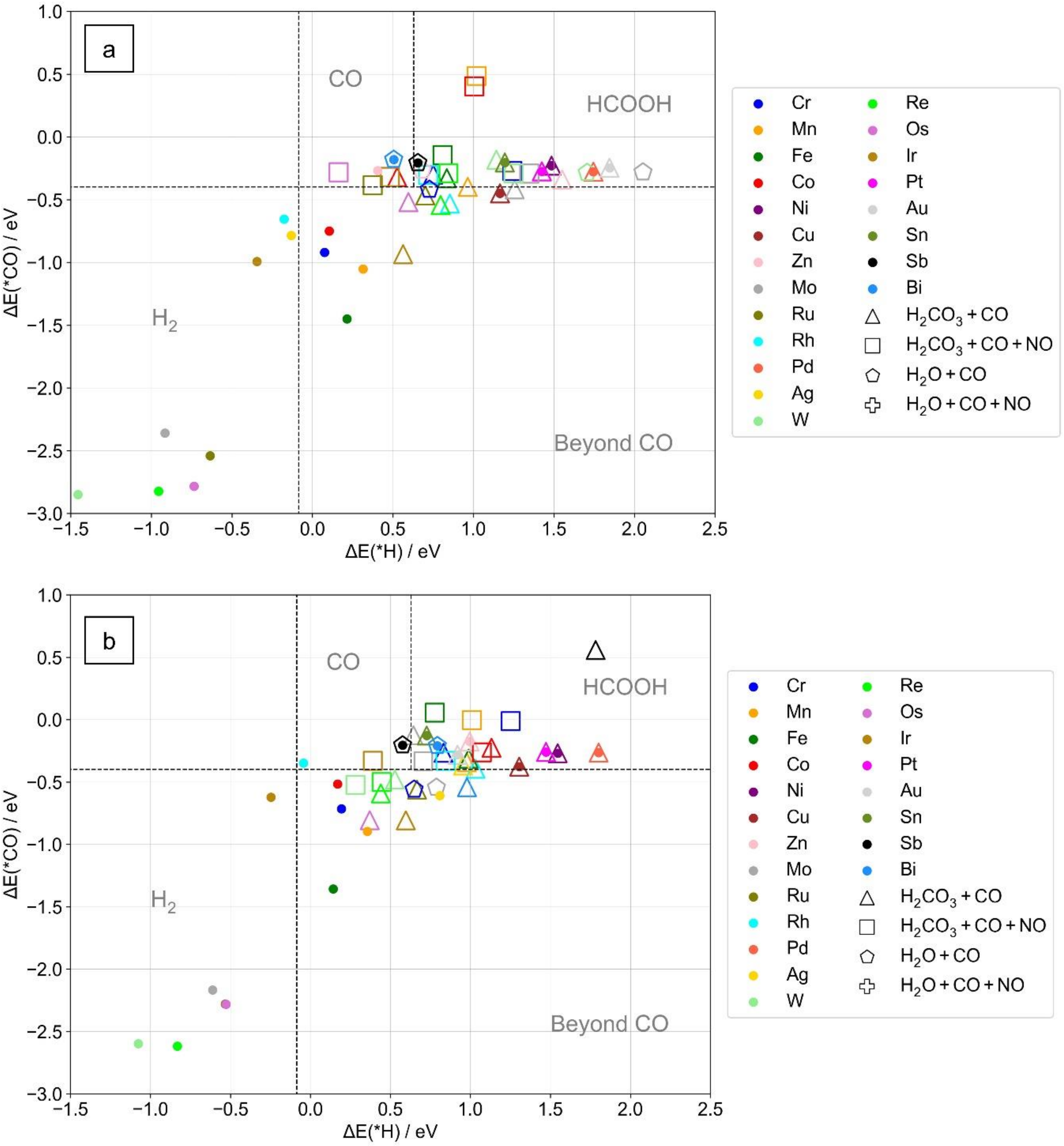

Figure S23 Classification of possible product from CO_2RR on promising candidates ($\Delta G_R < 1$ eV and $\Delta G_{max} < 0.8$ eV) and bare MN_4 sites based on ΔE(*H) and ΔE(*CO): (a) MN_4C_{10}, (b) MN_4C_A. The binding energy of the bare metal sites is marked with filled color dots.

8. Electronic structure

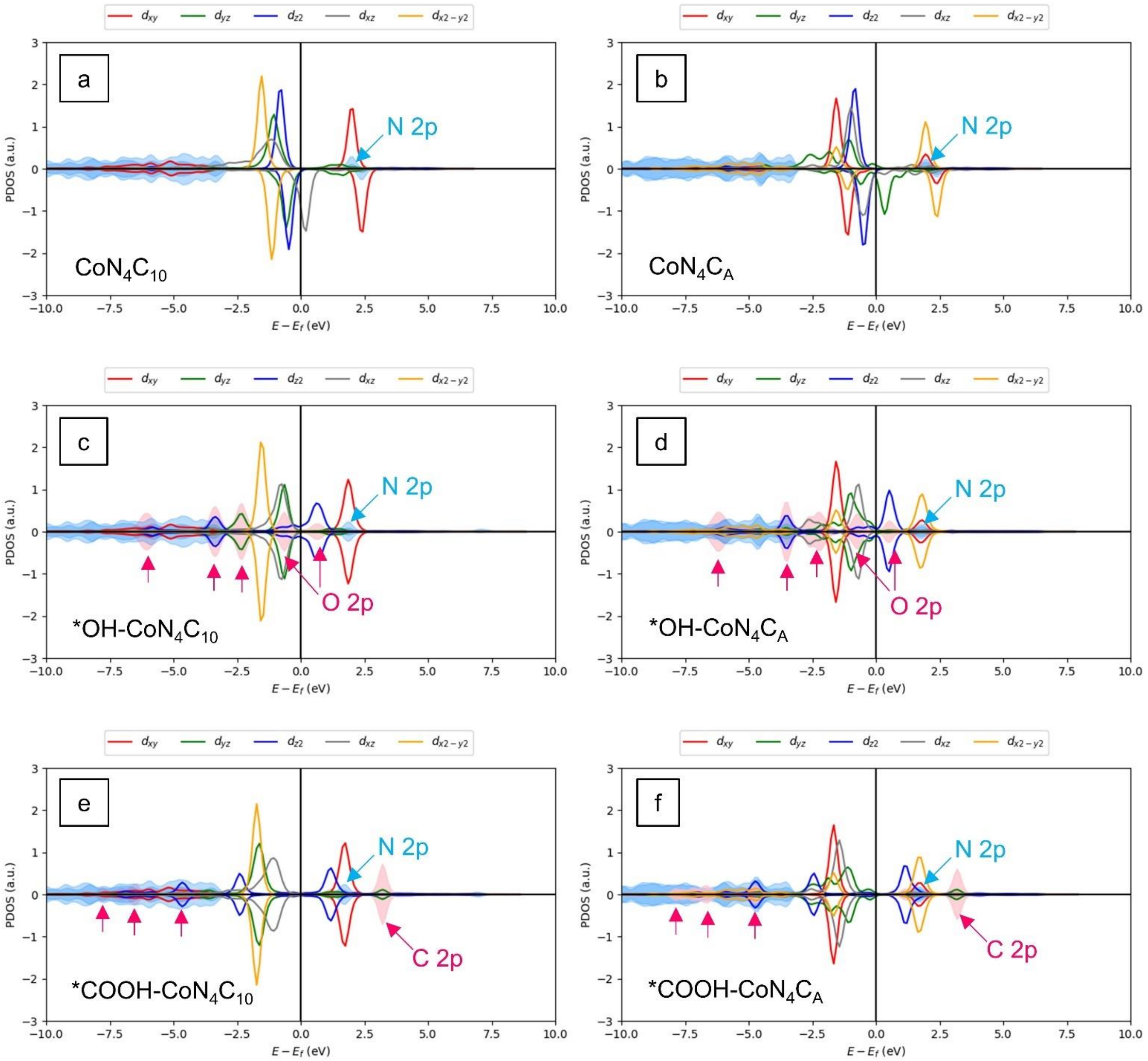

Figure S24 Spin-polarized density of states for pristine CoN_4 site projected onto Co 3d, N 2p orbital: (a) CoN_4C_{10}, (b) CoN_4C_A. Spin-polarized density of states for CoN_4 site with ∗OH projected onto Co 3d, N 2p and O 2p (∗OH) orbital: (c) CoN_4C_{10}, (d) CoN_4C_A. Spin-polarized density of states for CoN_4 site with ∗COOH projected onto Co 3d, N 2p and C 2p (∗COOH) orbital: (d) CoN_4C_{10}, (e) CoN_4C_A.

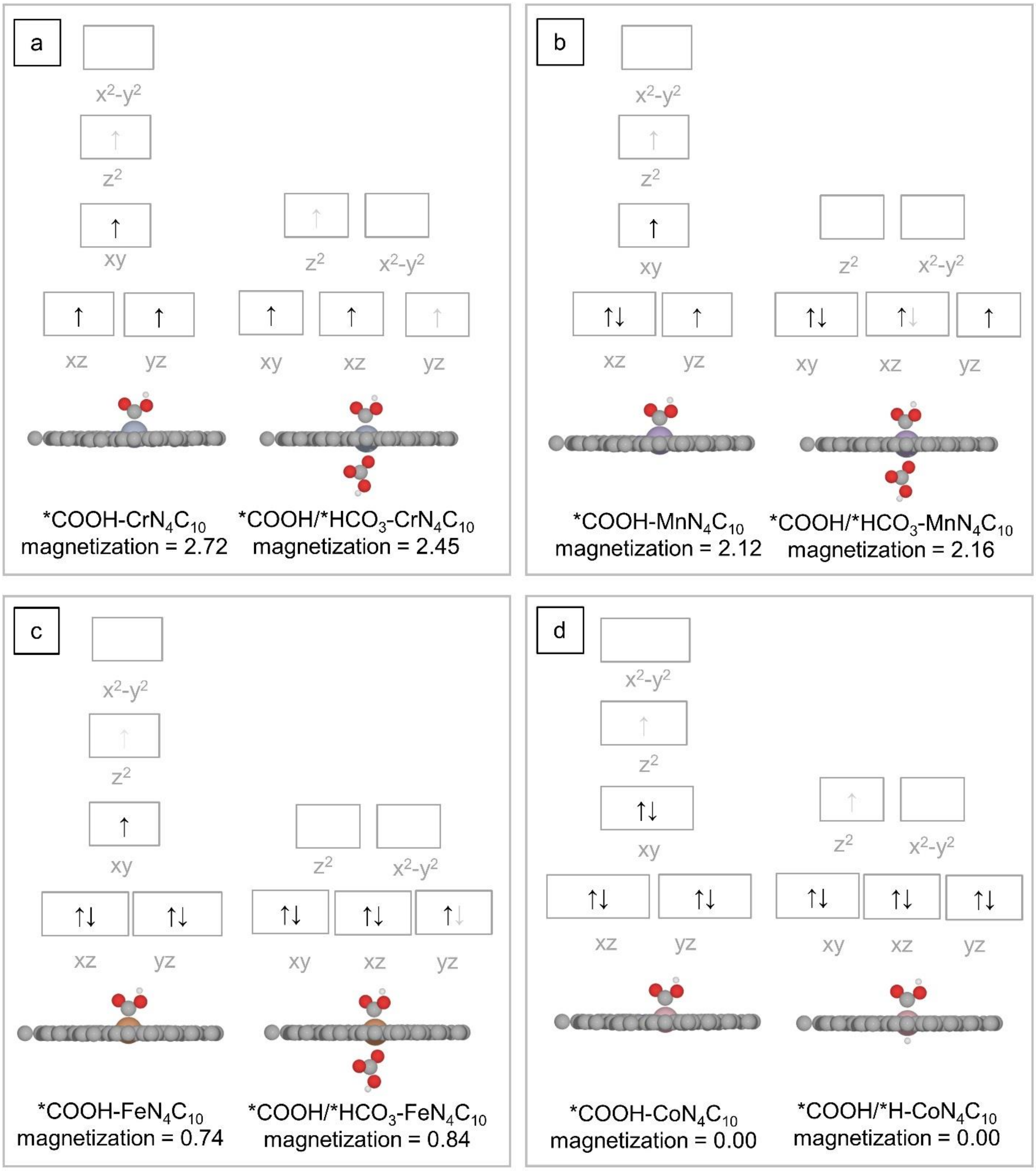

Figure S25 Illustration of d-orbital splitting and possible electronic configurations for a single metal atom on bulk graphene (MN_4C_{10}) in square pyramidal geometry (with one adsorbate), octahedral geometry (two adsorbates): (a) Cr, (b) Mn, (c) Fe and (d) Co. The possible electron configuration is based on the converged magnetization (# spin up - # spin down) and we assume that the oxidation of the metal center atom of the pristine structure (without adsorbates) is 2+. Only electrons in black arrows remain on the metal center atom while the electrons in grey arrows are donated to the adsorbates. The relative position of energy level is qualitative only.

RFERENCES

(1) Kresse, G.; Hafner, J. *Ab. Initio Molecular Dynamics for Liquid Metals*; Vol. 47.

(2) Kresse, G.; Joubert, D. *From Ultrasoft Pseudopotentials to the Projector Augmented-Wave Method*.

(3) Wellendorff, J.; Lundgaard, K. T.; Møgelhøj, A.; Petzold, V.; Landis, D. D.; Nørskov, J. K.; Bligaard, T.; Jacobsen, K. W. Density Functionals for Surface Science: Exchange-Correlation Model Development with Bayesian Error Estimation. *Phys Rev B Condens Matter Mater Phys* **2012**, *85* (23). https://doi.org/10.1103/PhysRevB.85.235149.

(4) Hjorth Larsen, A.; JØrgen Mortensen, J.; Blomqvist, J.; Castelli, I. E.; Christensen, R.; Dułak, M.; Friis, J.; Groves, M. N.; Hammer, B.; Hargus, C.; Hermes, E. D.; Jennings, P. C.; Bjerre Jensen, P.; Kermode, J.; Kitchin, J. R.; Leonhard Kolsbjerg, E.; Kubal, J.; Kaasbjerg, K.; Lysgaard, S.; Bergmann Maronsson, J.; Maxson, T.; Olsen, T.; Pastewka, L.; Peterson, A.; Rostgaard, C.; SchiØtz, J.; Schütt, O.; Strange, M.; Thygesen, K. S.; Vegge, T.; Vilhelmsen, L.; Walter, M.; Zeng, Z.; Jacobsen, K. W. The Atomic Simulation Environment - A Python Library for Working with Atoms. *Journal of Physics Condensed Matter*. Institute of Physics Publishing June 7, 2017. https://doi.org/10.1088/1361-648X/aa680e.

(5) Hansen, H. A.; Patniboon, T. Acid-Stable and Active M−N−C Catalysts for the Oxygen Reduction Reaction: The Role of Local Structure. *ACS Catal* **2021**, *11* (21), 13102–13118. https://doi.org/10.1021/acscatal.1c02941.

(6) Mathew, K.; Sundararaman, R.; Letchworth-Weaver, K.; Arias, T. A.; Hennig, R. G. Implicit Solvation Model for Density-Functional Study of Nanocrystal Surfaces and Reaction Pathways. *Journal of Chemical Physics* **2014**, *140* (8). https://doi.org/10.1063/1.4865107.

(7) Mortensen, J.; Gjerding, M.; Thygesen, K. MyQueue: Task and Workflow Scheduling System. *J Open Source Softw* **2020**, *5* (45), 1844. https://doi.org/10.21105/joss.01844.

(8) P.J. Linstrom; W.G. Mallard, Eds. *NIST Chemistry WebBook, NIST Standard Reference Database Number 69*; National Institute of Standards and Technology: Gaithersburg MD, 2022.

(9) *CRC Handbook of Chemistry and Physics*, 97th Edition.; W. M. Haynes, David R. Lide, Thomas J. Bruno, Eds.; CRC Press: Boca Raton, 2016.

(10) Nørskov, J. K.; Rossmeisl, J.; Logadottir, A.; Lindqvist, L.; Kitchin, J. R.; Bligaard, T.; Jónsson, H. Origin of the Overpotential for Oxygen Reduction at a Fuel-Cell Cathode. *Journal of Physical Chemistry B* **2004**, *108* (46), 17886–17892. https://doi.org/10.1021/jp047349j.

(11) Christensen, R.; Hansen, H. A.; Vegge, T. Identifying Systematic DFT Errors in Catalytic Reactions. *Catal Sci Technol* **2015**, *5* (11), 4946–4949. https://doi.org/10.1039/c5cy01332a.

(12) Christensen, R.; Hansen, H. A.; Dickens, C. F.; Nørskov, J. K.; Vegge, T. Functional Independent Scaling Relation for ORR/OER Catalysts. *Journal of Physical Chemistry C* **2016**, *120* (43), 24910–24916. https://doi.org/10.1021/acs.jpcc.6b09141.

(13) Holst-Olesen, K.; Silvioli, L.; Rossmeisl, J.; Arenz, M. Enhanced Oxygen Reduction Reaction on Fe/N/C Catalyst in Acetate Buffer Electrolyte. *ACS Catal* **2019**, *9* (4), 3082–3089. https://doi.org/10.1021/acscatal.8b04609.

(14) Svane, K. L.; Reda, M.; Vegge, T.; Hansen, H. A. Improving the Activity of M−N4 Catalysts for the Oxygen Reduction Reaction by Electrolyte Adsorption. *ChemSusChem* **2019**, *12* (23), 5133–5141. https://doi.org/10.1002/cssc.201902443.

(15) Atkins, P. W.; de Paula, Julio. *Physical Chemistry*, 8th ed.; W.H. Freeman: New York, 2006.

(16) Ruscic, B.; Pinzon, R. E.; von Laszewski, G.; Kodeboyina, D.; Burcat, A.; Leahy, D.; Montoy, D.; Wagner, A. F. Active Thermochemical Tables: Thermochemistry for the 21st Century. In *Journal of Physics: Conference Series*; Institute of Physics Publishing, 2005; Vol. 16, pp 561–570. https://doi.org/10.1088/1742-6596/16/1/078.

(17) C W Davies. *Ion Association*; London, Butterworths, 1962.

(18) Holby, E. F.; Wang, G.; Zelenay, P. Acid Stability and Demetalation of PGM-Free ORR Electrocatalyst Structures from Density Functional Theory: A Model for “Single-Atom Catalyst” Dissolution. *ACS Catal* **2020**, *10* (24), 14527–14539. https://doi.org/10.1021/acscatal.0c02856.

(19) Marcel Pourbaix. *Atlas of Electrochemical Equilibria in Aqueous Solutions*, 2nd ed.; National Association of Corrosion Engineers: Houston, Tex, 1974.

(20) Bard, A. J.; Parsons, R.; Jordan, J. *Standard Potentials in Aqueous Solution*, 1st ed.; Routledge, 2017. https://doi.org/10.1201/9780203738764.

(21) Bratsch, S. G. Standard Electrode Potentials and Temperature Coefficients in Water at 298.15 K. *J Phys Chem Ref Data* **1989**, *18* (1), 1–21. https://doi.org/10.1063/1.555839.

(22) Jain, A.; Ong, S. P.; Hautier, G.; Chen, W.; Richards, W. D.; Dacek, S.; Cholia, S.; Gunter, D.; Skinner, D.; Ceder, G.; Persson, K. A. Commentary: The Materials Project: A Materials Genome Approach to Accelerating Materials Innovation. *APL Materials*. American Institute of Physics Inc. 2013. https://doi.org/10.1063/1.4812323.

D.3 Paper III

Degradation of Polybenzimidazole in Alkaline Solution with First-principles Modeling
Tipaporn Patniboon and Heine Anton Hansen
Electrochimica Acta, 2021, 398, 139329,

Electrochimica Acta 398 (2021) 139329

Contents lists available at ScienceDirect

Electrochimica Acta

journal homepage: www.elsevier.com/locate/electacta

Degradation of polybenzimidazole in alkaline solution with first-principles Modeling

Tipaporn Patniboon, Heine Anton Hansen*

Department of Energy Conversion and Storage, Technical University of Denmark, Anker Engelunds Vej, Kongens Lyngby 2800, Denmark

ARTICLE INFO

Article history:
Received 7 July 2021
Revised 9 September 2021
Accepted 25 September 2021
Available online 30 September 2021

Keywords:
Density Functional Theory
Polybenzimidazole
Solvation
Degradation
Electrolysis

ABSTRACT

Membrane-based polybenzimidazole (mPBI) emerges as an exciting electrolyte membrane for alkaline fuel cells and water electrolyzers due to its useful ion conductivity range after being doped with aqueous KOH. However, the polymer degradation at highly alkaline concentrations limits its practical use. Herein, the density functional theory (DFT) calculations are used to study the degradation mechanism of mPBI molecule in an alkaline solution. The pristine mPBI molecule deprotonates to form an ionized molecule in an alkaline solution, with the ionized form being predominant at high pH. The nucleophilic hydroxide at the C2 position initiates the degradation, whereas the formation of the fully deprotonated ionic form suppresses the hydroxide ion attack. The degradation reaction then proceeds by ring-opening and chain scission reactions. The ring-opening reaction is preferred with an ancillary hydroxide ion or water molecule during the proton transfer process. The rate-determining state is the transition state involving the amide cleavage during the chain scission. Combining implicit-explicit solvation models is found to stabilize intermediate and transition states, lowering the energy barrier. With one or two explicit water molecules, the free energy barrier agrees well with experimental polymer lifetimes. An increase in KOH concentration increases the degradation rate, agreeing with experiments.

1. Introduction

Alkaline anion exchange membranes have gained increased attention due to their potential to integrate with a wide range of electrochemical energy storage and conversion technologies. The advantage of an alkaline condition is a broad selection of electrocatalysts based on abundant and cheap materials, in contrast to noble metal-based electrocatalysts required in acidic conditions [1].

In the cell design, the electrodes are separated by an electrolyte membrane where hydroxide ions are transported. Cations, such as ammonium [2,3] and imidazolium cation [4–6], are commonly attached to the polymer backbone to allow hydroxide ion-conduction. However, the hydroxide ion can react irreversibly with the polymer backbone and cations, causing ionic conductivity degradation over time [7–9]. Therefore, chemical stability remains a significant challenge for anion conducting membranes. An alternative is to use an ion-solvating membrane where an aqueous electrolyte is dissolved in a polymer matrix [10] so that it utilizes the uptake of an aqueous alkaline to achieve ionic conductivity and does no need for cation moieties [11,12].

The poly(2,2′-(m-phenylene)-5,5′-bibenzimidazole) (mPBI) equilibrated in aqueous potassium hydroxide (KOH) can form an ion-solvating polymer system composed of KOH and water dissolved in the polymer matrix; the ternary mPBI/KOH/H_2O electrolyte system [13]. This alkaline doped mPBI system has been reported to have high ionic conductivity and excellent chemical stability in alkaline conditions. It has been tested as an anion exchange membrane in direct alkaline alcohol fuel cells [14,15], alkaline fuel cells [16–18], water electrolyzers [10,19], and vanadium redox flow batteries [20] with remarkable performance.

The ternary mPBI/KOH/H_2O electrolyte composite is strongly dependent on the KOH concentration, which significantly determines the ionic conductivity of the membrane. The system exhibits high ionic conductivity and chemical stability at low KOH concentration (5–10 wt% KOH at 88 °C). The ionic conductivity can be increased by two orders of magnitude and reach a peak at 20–25 wt% KOH [21]. However, increasing KOH concentration enhances the degradation of the polymer, as evidenced by the gradually reduced molecular weight, mechanical strength, ionic conductivity, and structural change [10,21]. Thus, the actual use is limited.

Experimental studies have suggested that the polybenzimidazole-based membrane may degrade in an alkaline environment by a hydrolysis reaction [10,21,22]. The postulated

---

* Corresponding author.
E-mail address: heih@dtu.dk (H.A. Hansen).

https://doi.org/10.1016/j.electacta.2021.139329

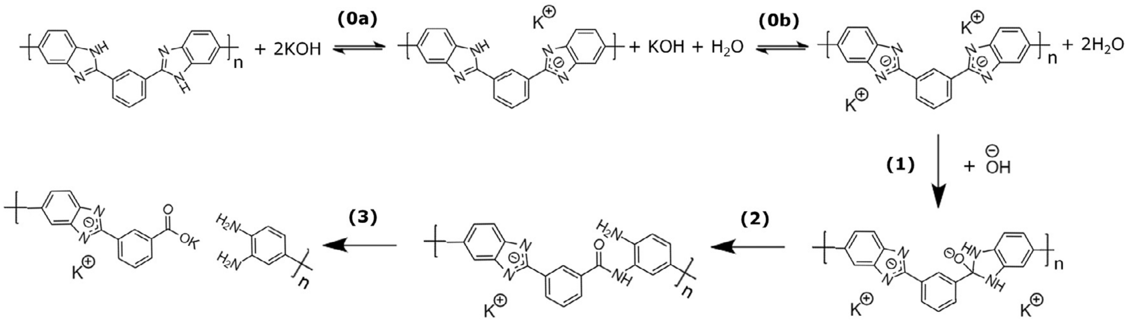

Fig. 1. Schematic illustration: (0) acid-base equilibrium of mPBI and (1)–(3) postulated degradation pathway of mPBI in aqueous KOH.

degradation pathway is shown in Fig. 1, where (1) the nucleophilic addition of hydroxide ions at the benzimidazole ring initiates the degradation, followed by (2) the ring-opening and (3) chain scissors [11,23]. This postulated reaction path is similar to the degradation of imidazolium and benzendazolium cations [8,9,24,25], which have also been suggested as a promising candidate for anion exchange membranes. However, the degradation mechanism of the mPBI membrane in alkaline solution has not been presented in detail. Additionally, the mPBI has been reported to deprotonate when submerged in aqueous KOH [13]. The equilibrium between the pristine and deprotonated form is shown as reaction (0a) and (0b) in Fig. 1. Unlike the imidazole cation, the negative charge may be delocalized over the benzimidazole ring of the deprotonated mPBI. Thus, the mPBI and hydroxide ion interaction may differ from that occurs with the imidazolium cations, resulting in different degradation mechanisms and degradation rates. Also, it is unclear which form of mPBI is most vulnerable and undergoes degradation in an alkaline environment as the equilibrium between the pristine and deprotonated forms strongly depends on the KOH concentration [13,26].

In this work, we use first-principles modeling with density functional theory (DFT) to evaluate the predominant species and the degradation mechanism of mPBI in an alkaline solution. The postulated degradation pathway of the mPBI, as shown in Fig. 1, is investigated where the first step of the degradation involves the nucleophilic addition reaction, followed by the ring-opening and chain scission. A low-barrier degradation pathway for mPBI molecules in an alkaline solution is catalyzed by hydroxide ions or water molecules. We study the role of explicit water molecules on the free energy barrier in each reaction step and investigate the effect of hydroxide ion concentration on the degradation rate. Comparing experiment and theory is achieved by computing the theoretical free energy barrier against those estimated from the experimental results. Our investigation provides a clearer understating of how the mPBI-based membranes degrade in an alkaline environment.

2. Computational details

All calculations are performed using B3LYP [27] functional and 6-311++G(d, p) basis sets as implement in Q-Chem 5.2 [28] for both optimized geometries and calculated energies. The threshold for the maximum gradient and the self-consistent field (SCF) energy change between consecutive optimization cycles is 3.0×10^{-3} Hartree/Bohr and 1×10^{-8} Hartree, respectively. The geometry optimizations for intermediate and transition states are carried out in the gas phase. A freezing string method (FSM) [29,30] is used to approximate the reaction path connecting each intermediate state pair. The highest energy point on the reaction path is taken as the first approximation for a transition state which is then refined to the actual transition state by using the Baker's partitioned rational-function optimization (P-RFO) algorithm [31] implemented in Q-chem 5.2. Each transition state is verified to connect the designated reactant and product by performing an intrinsic reaction coordinate (IRC) calculation [32]. The vibrational frequencies are calculated to confirm the local minima on the potential energy surface with no imaginary frequencies for all intermediates and one single imaginary frequencies for all transition states. Single point energies are computed with the conductor-like polarization continuum model (C-PCM) [33–35] based on the optimized gas-phase geometries. A dielectric constant of 78.39 corresponds to the bulk water used to include the surrounding water medium.

Free reaction energy and free energy barrier are calculated at $T = 88$ °C and 1 atm, which is the same as the experimental condition [21]. For the reaction between A and B, the reaction goes through a transition state TS and results in the product C.

$$\mathrm{A} + \mathrm{B} \ \rightarrow \mathrm{TS} \ \rightarrow \mathrm{C} \tag{1}$$

The free energy reaction ($\Delta G_{(sol)}$) and the free energy barrier ($\Delta G^{TS}{}_{(sol)}$) in the solution are defined as follows.

$$\Delta G_{(sol)} = G\left(C_{(sol)}\right) - G\left(A_{(sol)}\right) - G\left(B_{(sol)}\right) = \ \Delta E_{(sol)} + \Delta G^{corr}_{(gas)} \tag{2}$$

$$\Delta G^{TS}_{(sol)} = G\left(TS_{(sol)}\right) - G\left(A_{(sol)}\right) - G\left(B_{(sol)}\right) = \Delta E^{TS}_{(sol)} + \Delta G^{TScorr}_{(gas)} \tag{3}$$

where

$$\Delta E_{(sol)} = E\left(C_{(sol)}\right) - E\left(A_{(sol)}\right) - E\left(B_{(sol)}\right) \tag{4}$$

$$\Delta E^{TS}_{(sol)} = E\left(TS_{(sol)}\right) - E\left(A_{(sol)}\right) - E\left(B_{(sol)}\right) \tag{5}$$

$\Delta E_{(sol)}$ and $\Delta E^{TS}{}_{(sol)}$ are the reaction energy and the energy barrier, respectively, computed as the energy difference between the species in the gas phase geometry with the presence of the continuum solvent. $\Delta G^{corr}{}_{(gas)}$ ($=\Delta H_{(gas)}$ - $T\Delta S_{(gas)}$) and $\Delta G^{TScorr}{}_{(gas)}$ are thermal corrections, including zero-point vibration energy (ZPVE) and vibrational, translational, and rotational entropies and enthalpies computed from the vibration analysis assuming vibrational modes are non-interacting quantum mechanical harmonic oscillators.

An estimate of the reaction rate constant is obtained from transition state theory.

$$k = \frac{k_B T}{h} e^{\frac{-\Delta G^{TS}}{RT}} \tag{6}$$

k is the rate constant for a given reaction, k_B is Boltzmann's constant, h is Planck's constant, ΔG^{TS} is the free energy difference between the transition state and the reactants, R is the gas constant, and T is the temperature.

As a hydrogen atom can be described as a wave packet, it can penetrate regions forbidden for classical particles. The inclusion of quantum mechanical tunnelling effects in the calculations has been reported to increases the proton transfer rate [36]. Therefore, in our calculations, a proton tunnelling effect is included in the rate constant involved in the proton transfer reaction. The reaction rate constant, including the tunnelling effect, can be written as follows.

$$k = \kappa \frac{k_B T}{h} e^{\frac{-\Delta G^{TS}}{RT}} \tag{7}$$

κ is tunnelling correction used to account for the tunnelling effect along the reaction coordinate and obtained as the ratio between the quantum mechanical and the classical rate constant. If $\kappa = 1$, there is no tunnelling, and if $\kappa > 1$, the tunnelling effect contributes to the rate constant. The tunnelling correction (κ) [37] is defined as follows.

$$\kappa = e^{\left(\frac{\Delta E^{TS}}{k_B T}\right)} \int_0^\infty \frac{1}{k_B T} e^{\left(\frac{-E}{k_B T}\right)} P(E) dE \tag{8}$$

P(E) is a tunnelling probability of a particle with mass m and energy E to penetrate the barrier with height ΔE^{TS}. In this work, P(E) is approximated by using WKB approximation [38] and can be written as follows.

$$P(E) = e^{-\frac{\pi^2 w}{h}\sqrt{2m\left(\Delta E^{TS} - E\right)}};\, 0 < E < \Delta E^{TS} \tag{9}$$

$$P(E) = 1;\;\; E > \Delta E^{TS} \tag{10}$$

w is barrier width, $\Delta E^{TS} - E$ is the energy deficiency of the proton with respect to the top of the barrier. The barrier width (w) is estimated from the reaction path obtained from the IRC calculations.

3. Results and discussion

3.1. Deprotonation reaction of mPBI in alkaline solution

The dissociation of an acidic proton of the mPBI-based molecule in KOH solution has been observed in experiments, and the ionized form has been found to dominate at concentrations higher than 15 wt% KOH [13]. The ionized form leads to the ternary mPBI/KOH/H_2O electrolyte system, which is responsible for a high ionic conductivity of the membrane. Further increasing the KOH concentration has been found to cause membrane degradation [13]; thus, the degradation has been suggested to start from the ionized form of the mPBI [11,22].

To identify the predominant form of the mPBI in the alkaline solution where the degradation occurs, we first consider an acid dissociation constant (pK_a) of the mPBI molecule. The stepwise dissociation constant is defined for losing a single proton and is illustrated as reaction (0a) and (0b) in Fig. 1. The dissociation constant for the first proton is denoted as pK_{a1}, and the successive proton is pK_{a2}. Thus, the acid deprotonation reaction of the mPBI molecule can be written as follows.

$$\mathrm{mPBI}(0) \rightleftarrows \mathrm{mPBI}(1) + H^+ \rightleftarrows \mathrm{mPBI}(2) + 2H^+ \tag{11}$$

The number in parenthesis indicates the total negative charge on the molecule; thus, mPBI(0) is the pristine molecule, mPBI(1) is the first ionized form after losing one proton, and mPBI(2) is the second ionized form after losing two protons. The pK_a can be calculated from the Gibbs free energy of the deprotonation reaction.

$$pK_a = \frac{\Delta G_{dep(sol)}}{2.303RT} \tag{12}$$

$\Delta G_{dep(sol)}$ is the Gibbs free energy of the deprotonation reaction in the solution obtained from a thermodynamic cycle as shown in Figure S1.

Table 1
Calculated ΔG_{dep} and pK_a value for mPBI molecule at $T = 88$ °C.

	ΔG_{dep} (eV)	pk_a
mPBI(0)	0.89	$pK_{a1} = 12.46$
mPBI(1)	0.92	$pK_{a2} = 12.85$

Table 1 shows the calculated pK_a for the mPBI(0) and mPBI(1), implying that the mPBI(2) is the major species at high pH. However, there is a slight difference between successive pK_a values, so there can be an overlap between the species' pH range and existence. Figure S2 shows the calculated percentage of formation for each mPBI species as a function of pH at T = 88 °C. The mPBI(1) starts to form at pH ~ 10. The mPBI(2) begins to form at pH ~ 12 and becomes the predominant species at pH > 13 (about 5 wt% KOH [39,40]). Still, all three mPBI species can be found in the solution at pH between 12–13. At pH = 13, approximately 10% of mPBI(0) and 40% of mPBI(1) are in the solution and at pH = 14, the solution consists of approximately 10% of mPBI(1) and 90% of mPBI(2).

The concentration of the ionized form (mPBI(1) + mPBI(2)) increases as pH increases. Therefore, by increasing KOH bulk concentration, the ion conductivity can be expected to increase. In the experimental study by Kraglund et al., the ionic conductivity of the mPBI based-membrane at $T = 80$ °C increases by two orders of magnitude from 0.7 to 72 $mS{\bullet}cm^{-1}$ when the bulk solution concentration is increased from 5 to 15 wt% KOH with limited structural changes and the ionic conductivity can be peak at KOH concentration around 20–25 wt% KOH while the membrane shows signs of structural change [10].

The conversion between the pH and KOH bulk concentration in the above approximation might not be directly applicable to the ternary mPBI/KOH/H_2O system. Hou et al. suggest that protons from the mPBI molecule can combine with hydroxide ions in the environment and form a more stable water molecule [41]. At the same time, potassium ions could interact with the negatively charged nitrogen or carbon atom, subsequently integrating with the mPBI molecule [26,42]. Therefore, the internal KOH concentration of the ternary mPBI/KOH/H_2O system can slightly be different from the bulk solution [21].

4. Nucleophilic addition reaction

The degradation of mPBI based membranes in alkaline solutions has been suggested via hydrolysis reaction [23]. The first reaction step involves the nucleophilic addition at the carbon atom of the five-membered ring [11,21]. A carbon atom at the C2 position [11,22,24] (Fig. 2a) has been suggested as the susceptible point of the mPBI to hydroxide ion attack.

All three forms of the mPBI molecule can be present in the alkaline solution at a high pH range (pH ~ 12-14) where the degradation has been reported; thus, we first consider the free reaction energy for the first reaction step (ΔG_1) for all three mPBI forms as follows.

$$\Delta G_1 = G\left(\mathrm{OHmPBI}(n)_{(sol)}\right) - G\left(\mathrm{mPBI}(n)_{(sol)}\right) - G\left(OH^-_{(sol)}\right) \tag{13}$$

OHmPBI denotes the mPBI molecule with a hydroxide ion bound to one of the carbon atoms of the five-membered ring.

There are three possible distinct carbon atoms, marked as C2, C4, and C5 in Fig. 2b, where hydroxide ions can attack the mPBI(0) molecule. There are five possible positions for the mPBI(1) molecule at C2, C4, C5, C2*, and C4*, where the * denotes atoms located at the ionized part of the mPBI molecule. For the mPBI(2) molecule, hydroxide attack on the carbon atom at the C2* or C5*

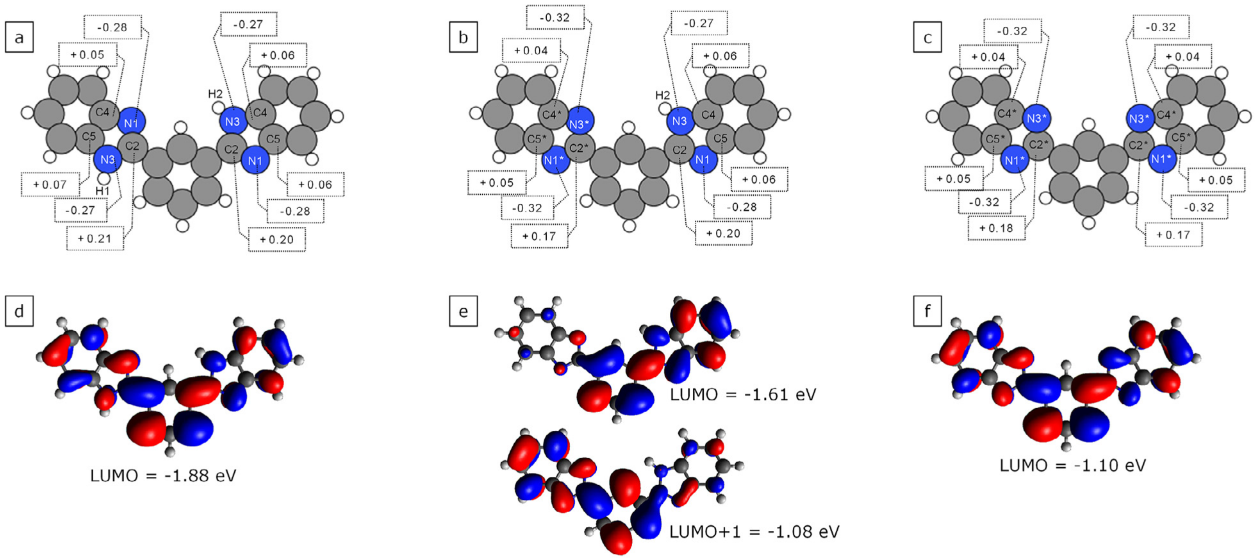

Fig. 2. (a–c) Optimized structures and NBO atomic charge on atoms for each mPBI species: (a) mPBI(0), (b) mPBI(1), and (c) mPBI(2). (d-f) LUMO (and LUMO+1) isosurface for each mPBI species: (d) mPBI(0), (e) mPBI(1), and (f) mPBI(2). Colors code for atoms: H-white, C-gray and N-blue.

Table 2
ΔG_1 for hydroxide ion attack at different carbon atoms of the five-membered ring for each species of mPBI at T = 88 °C.

molecule	attack position	Atomic partial charge (electron)	ΔG_1 (eV)
mPBI(0)	C2	0.20	1.31
	C4	0.06	1.99
	C5	0.06	2.26
mPBI(1)	C2*	0.17	2.43
	C4*	0.04	2.88
	C2	0.20	1.38
	C4	0.06	2.02
	C5	0.06	2.25
mPBI(2)	C2*	0.17	2.66
	C4*	0.05	2.99

position is possible, while the carbon atoms at C4* and C5* are symmetry equivalent.

Table 2 presents calculated ΔG_1 at different carbon positions. The hydroxide ion attack at the C2 position in either the mPBI(0) or mPBI(1) is more accessible than in other positions. Since carbon at the C2 (or C2*) position is between two nitrogen atoms, which has higher electronegativity, the atomic charges obtained from the natural bond orbital (NBO) analysis [43] on these carbon atoms are more positive than the others (Fig. 2). The more positive charge can make the attack of the hydroxide anions more favorable. On the contrary, the ionized part of the molecule is less vulnerable to hydroxide ions. Considering the mPBI(1), the hydroxide ion attacks at the C2* position are more difficult than those at the C2 position. After deprotonation, the lowest unoccupied molecular orbital (LUMO) energy of the ionized molecule increases, and the atomic charge of atoms near the ionized position becomes more negative. Fig. 2(d–f) shows LUMO isosurfaces for mPBI molecules in different protonation states. The LUMO isosurface has weight on carbon atoms at the C2 position of the mPBI(0). For the mPBI(1), the LUMO isosurface has mainly weight near the C2 position and not on the ionized part near the C2* position. However, the LUMO+1 isosurface with higher energy localizes on the carbon atom at the C2* position. For the mPBI(2), the LUMO energy is highest among considered species, and the attack by hydroxide ion is also most difficult. This suggests that the susceptibility to hydroxide anion attack of the mPBI based-molecule can be related to the LUMO energy and the LUMO isosurface [4,44], and the formation of the deprotonated mPBI form can suppress hydroxide ion attack.

For the nucleophilic addition reaction at the C2 position, the forward free energy barrier is 1.42 eV for the mPBI(1) and 1.35 eV for the mPBI(0) but only 0.04 eV for both mPBI(1) and mPBI(0) in the reverse direction. Thus, the first step is highly reversible. The free energy barrier for the nucleophilic addition reaction at the other positions of the mPBI(0) and mPBI(1) as well as at the mPBI(2) molecule is 2.0 eV or greater, making the degradation from the other parts and the mPBI(2) unlikely. As there are more percentages of mPBI(1) in solution than mPBI(0) at high pH range, we think that the overall degradation is significantly due to the degradation of the mPBI(1) species, and we investigate the further degradation reaction from the hydroxide ion bond with a carbon atom at the C2 position in the mPBI(1).

5. Ring-opening reaction

A ring-opening reaction follows the hydroxide ion attack. The possible mechanism for the mPBI(1) degradation is that a hydroxyl proton at the C2 position is transferred to the nitrogen atom at the N1 or N3 position, followed by a C-N bond breaking.

5.1. Hydroxyl proton transferred to the nitrogen atom at the N3 position

We first consider that the hydroxyl proton is transferred to the nitrogen atom at the N3 position, followed by a C2-N3 bond breaking, as shown in Fig. 3.

First, we consider that this ring-opening reaction occurs in a single step, as shown in reaction path 1.1, Fig. 3. The free energy barrier for this single-step reaction is 0.83 eV, and a transition state TS2-1.1 locates at 2.22 eV in the quantitative reaction profile. The hydrogen tunnelling effect in this single-step reaction is negligible as we find the calculated tunnelling correction (κ) of 1.00 (Table S1).

Alternatively, as the degradation occurs in an alkaline solution, water molecules and hydroxide ions are available in the environment, and both can participate and assist the reaction [24,25].

For reaction path 1.2 in Fig. 3, one hydroxide ion is added into the simulation explicitly. The additional hydroxide ion spon-

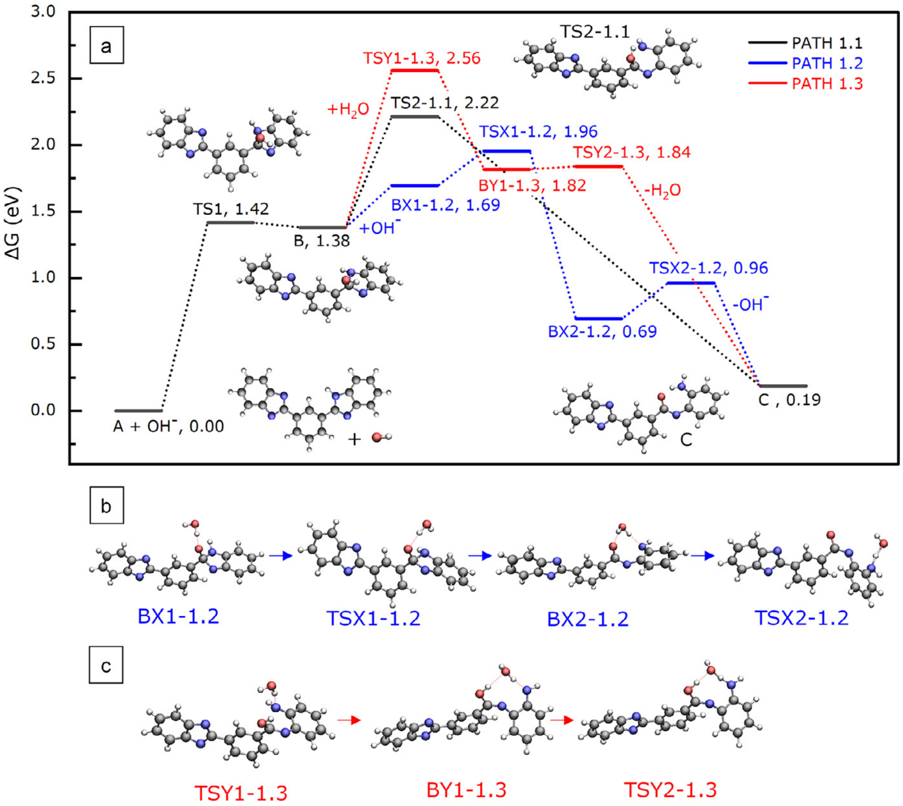

Fig. 3. (a) Quantitative reaction profile for the ring-opening reaction of mPBI(1) via reaction path 1 at $T = 88$ °C. The reference zero energy state for energies reported is A+OH^- and the relative energies of the intermediates and transition state are in eV. The insets show optimized structures for intermediate and transition states involved in the reaction path 1.1. The optimized structures for intermediate and transition states involved: (b) reaction path 1.2 and (c) 1.3. Colors code for atoms: H-white, C-grey, N-blue, O-red.

taneously reacts with the hydroxyl proton at the C2 position, resulting in intermediate state BX1-1.2, where one water molecule is formed. A transition state between the intermediate B and BX1-1.2 cannot be found. However, the intermediate BX1-1.2 state is 0.31 eV, less stable than the intermediate state B. The resulting water molecule further participates in the C2-N3 bond breaking, giving intermediate state C and one hydroxide ion. Thus, the additional hydroxide ion acts as a catalyst in this reaction path. For the two successive reactions, free energy barriers $\Delta G^{TSX1\text{-}1.2}$ and $\Delta G^{TSX2\text{-}1.2}$ are 0.26 and 0.27 eV, respectively. The last step for the BX2-1.2 → C+OH^- step involves the proton transfer from the water molecule to the N3 nitrogen atom, where we find the tunnelling correction (κ) of 1.07. Thus, the proton tunnelling contributes to the rate constant increased from 1.33×10^9 s^{-1} to 1.43×10^9 s^{-1} when including the tunnelling correction. The highest transition state along this reaction path is TSX1-1.2, locating at 1.96 eV in the quantitative reaction profile. Although the TSX1-1.2 is lower than the TS2-1.1 in the quantitative reaction profile, the energy relative to the initial reactant is still high.

For reaction path 1.3 in Fig. 3, we consider the hydroxyl proton transfer through one explicit water molecule. The reaction first goes through a transition state TSY1-1.3, where the C2-N3 bond is broken. The transition vector of a single imaginary frequency of the TSY1-1.3 state relates to the C-N bond breaking (Fig. S3a). The free energy barrier for this step is 1.18 eV which includes the free formation energy for hydrogen-bond structure between the intermediate structure B and one explicit water of 0.25 eV. After that, the hydroxyl proton at the C2 position is transferred to the nitrogen atom at the N3 position via the additional water molecule, giving the intermediate C and one water molecule at the end of the process. The free energy barrier for the hydroxyl proton transfer is only 0.02 eV, and the tunnelling correction (κ) for the BY1-1.3 → C+H_2O step is 1.73, implying that the proton tunnelling can significantly contribute to the rate constant. The rate constant before applying the tunnelling correction is 3.67×10^{12} s^{-1}, and it is increased to 6.36×10^{12} s^{-1} after applying the tunnelling correction. However, the highest transition state in the reaction path 1.3, which is the TSY1-1.3 locating at 2.56 eV in the quantitative reaction profile, is higher than the previously considered reaction path.

5.2. Hydroxyl proton transferred to the nitrogen atom at the N1 position

An alternative path for the ring-opening reaction is shown in Fig. 4. The hydroxyl proton is transferred to a nitrogen atom at the N1 position. Then either the C2-N1 or C2-N3 bond is broken.

We first consider the intramolecular proton transfer process where the hydroxyl proton at the C2 position is directly transferred to the nitrogen atom at the N1 position, as shown in reaction path 2.1, Fig. 4. The optimized structures related to this reaction path are shown in Fig. 5a. A relatively high free energy barrier (0.91 eV) is found for this intramolecular proton transfer process, and a TS2-2.1 state locates at 2.29 eV in the quantitative reaction profile. The rate constant for the proton transfer along this reaction path (for B→C step) is 1.43 s^{-1}, and the inclusion of the tunnelling effect gives a rate constant of 1.48 s^{-1} (κ =1.04).

We also investigate whether the hydroxyl proton is transferred to the nitrogen atom at the N1 position via a nearby hydroxide ion or water molecule.

The quantitative reaction profile for the hydroxyl proton transfer through the water molecule is shown in reaction path 2.2, Fig. 4. A single imaginary frequency transition vector for a tran-

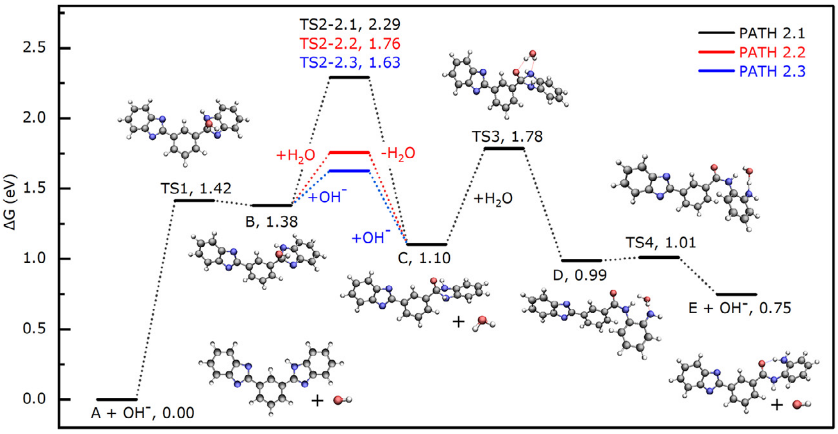

Fig. 4. Quantitative reaction profile for the ring-opening reaction of mPBI(1) via reaction path 2 at $T = 88$ °C. The reference zero energy state for energies reported is A+OH⁻ and the relative energies of the intermediates and transition state are in eV. The insets show optimized structures for the intermediate and transition states involved in the reaction path. Colors code for atoms: H-white, C-grey, N-blue, O-red

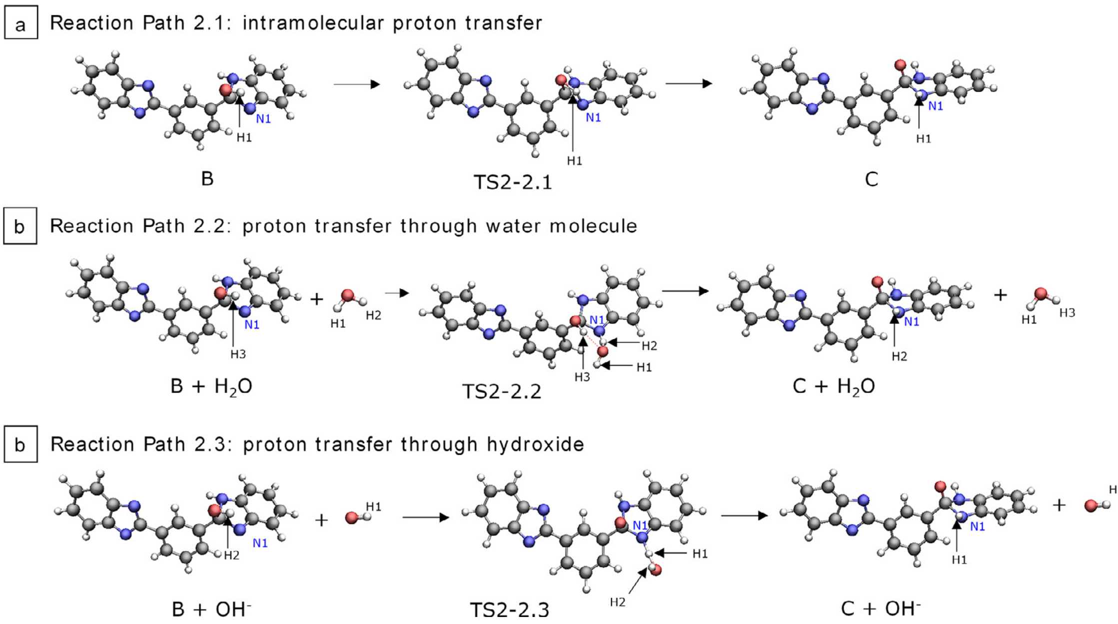

Fig. 5. Optimized structures for the intermediate and transition states related to the hydroxyl proton transfer for mPBI(1) during the ring-opening reaction path: (a) 2.1 (b) 2.2 and (c) 2.3. Colors code for atoms: H-white, C-grey, N-blue, O-red

sition state TS2-2.1 corresponds to a proton transfer via a water molecule (Fig. S4b). First, the water molecule donates one of its protons to the nitrogen atom at the N1 position, and then one hydroxide ion is obtained. After that, the resulting hydroxide ion reacts with the hydroxyl proton at the C2 position, giving intermediate structure C and a water molecule at the end of the process. The optimized structures along this reaction path are shown in Fig. 5b. The free energy barrier for the hydroxyl proton transfer is 0.37 eV, including the free formation energy for hydrogen-bond structure between intermediate structure B and one explicit water of 0.25 eV. Therefore, the TS2-2.1 state is 0.54 eV lower than TS2-2.1 in the quantitative reaction profile, and the rate constant (for B+H_2O→C+H_2O step) without the tunnelling correction ($k = 4.42 \times 10^7$ s^{-1}) is already higher than that of the intermolecular proton transfer. Furthermore, in this reaction path, the tunnelling correction (κ) is 1.26, resulting in a higher rate constant for the hydroxyl proton transfer of 5.55×10^7 s^{-1} when the proton tunnelling effect is included.

For the hydroxyl proton transfer through a hydroxide ion, the qualitative reaction profile is shown in reaction path 2.3, Fig. 4. First, the additional hydroxide ion reacts with the hydroxyl proton at the C2 position, produces one water molecule. This water molecule later donates one of its protons to the nitrogen atom at the N1 position (Fig. 5c). Then, the intermediate state *C* and a hydroxide ion are obtained. The transition vector for a single imaginary frequency of a transition state TS2-2.3 mainly corresponds to a proton transfer from the produced water molecule to the nitrogen atom at the N1 position (Fig. S4c). The free energy barrier for this hydroxyl proton transfer is 0.25 eV (0.66 eV lower than the TS2-2.1 and only 0.13 eV lower than the TS2-2.2 in the qualitative reaction profile). Like the previous water assists the process, the rate constant (for B+OH^-→C+OH^- step) without tunnelling correction ($k = 2.68 \times 10^9$ s^{-1}) is higher than the intermolecular proton transfer. Also, the tunnelling correction (κ) of 1.33 along this reaction path increases the rate constant to 3.57×10^9 s^{-1}.

The results show that the water molecule and hydroxide ion play an important role in reducing the energy barrier for the hydroxyl proton transfer during the ring-opening reaction. Also, along a water molecule or hydroxide ion-assisted pathway, the proton can tunnel through the energy barrier. Thus, the tunnelling increases the rate constant, improving the ability of water or hydroxide to facilitate the process (Table S2).

After forming the intermediate state C, the next step involves breaking the C-N bond. Note that for the intermediate structure C, the C2-N1 bond is symmetric with the C2-N3 bond. The cleavage of the C-N bond creates an unstable N dangling bond in the intermediate structure D. This unstable N dangling bond can be stabilized by receiving a proton from an available water molecule in its environment. Thus, the next ring-opening step involves the intermediate C and water molecules. This process results in an intermediate structure E and a hydroxide ion. The free energy barrier for breaking the C-N bond is 0.68 eV, including the free formation energy for hydrogen-bond structure between intermediate structure C and one explicit water of 0.23 eV. The free energy barrier for the proton transfer from the water molecule to the unstable N dangling bond is only 0.02 eV, with the tunnelling correction (κ) of 1.33. Thus, the proton tunnelling effect also contributes to the reaction rate constant in this step, increasing the rate constant from 3.50×10^{12} s^{-1} to 4.65×10^{12} s^{-1}

For reaction path 2.2 and 2.3 in Fig. 4, the highest transition state is TS3 which locates at 1.78 eV in the quantitative reaction profile, and it relates to the C-N bond-breaking. The highest transition state along this reaction path is lower than reaction path 1 in Fig. 3. Thus, the ring-opening reaction of the mPBI(1) molecules possibly occurs through reaction path 2.2 or 2.3 with the assistance of either a water molecule or hydroxide ion. However, the additional hydroxide ion is unstable for the latter case as it is likely to spontaneously react with the hydroxyl proton at the C2 position. It is also possible that if we added an explicit potassium ion, this additional hydroxide ion could spontaneously combine with the potassium ion instead of catalyzing the reaction. Still, as there are available water molecules in the environment, the reaction is expected to occur with the assistance of a water molecule.

We also investigate the ring-opening reaction for the mPBI(0) as shown in Figure S6a and S6b. The results conclude that the ring-opening reaction is likely to occur via reaction path 2.2 or 2.3. In reaction path 2 for the mPBI(0), the TS2-2.2 and TS2-2.3 are 0.52 and 0.67 eV lower than the TS2-2.1 in the quantitative reaction profile. Also, the highest transition state along the ring-opening reaction (reaction path 2.2 or 2.3) for the mPBI(0) is the TS3.

6. Chain scission reaction

The C2-N1 bond in the intermediate E is the amide linkage (Fig. 6a) which can be further hydrolyzed, leading to complete chain scission. As the degradation occurs in an alkaline solution, we consider the chain scission involving hydroxide ions. In Fig. 6b, the chain scission begins with the nucleophilic hydroxide ion attack at the C2 carbon atom in the intermediate structure E as it has the most positive charge. The nucleophilic addition goes through a transition state TS5 with the free energy barrier of 1.03 eV in the forward direction and only 0.13 eV in the reverse direction. Thus, this step is highly reversible. The next step involves the amide cleavage, as shown in reaction path 3.1, Fig. 6b. The reaction goes through a transition state TS6-3.1 with a free energy barrier of 0.40 eV. The transition vector corresponded to a single imaginary frequency for the TS6-3.1 state mainly relates to the C2-N1 bond breaking (Fig. S5a). After the C2-N1 bond is broken, the hydroxyl proton at the C2 position transferred to the nitrogen atom at the N1 position occurs without a transition state, so no tunnelling effect is considered along this reaction step. The final product G is 1.25 eV, more stable than the intermediate E+OH^- state.

The chain scission reaction considered here is the same as the alkaline hydrolysis of an amide [45,46]. A previous study by Lopez et al. has suggested that the explicit water molecule lowers the energy barrier by either acting as a proton bridge between hydroxyl and nitrogen or stabilizing the molecule via hydrogen bonding [45]. Cheshmedzhieva et al. conducted a theoretical study on alkaline hydrolysis of three different secondary amides. They found that the stabilization, whether via proton bridging or hydrogen bonds, depending on the molecular structure containing the amide bond [46].

We consider the effect of explicit water on the amide cleavage energy profile as shown in reaction path 3.2, Fig. 6b. One explicit water molecule is placed near the amide linkage in the intermediate E structure. The amide cleavage goes through a transition state TS6-3.2. The transition vector corresponded to a single imaginary frequency for TS6-3.2 still mainly relates to the C2-N1 bond breaking (Fig. S5b) similar to the previous TS6-3.1 state. After the C2-N1 bond is broken, the hydroxyl proton at the C2 position is also spontaneously transferred to the N1 nitrogen atom. The hydroxyl proton transfer can occur either with or without passing the proton through the explicit water molecule; still, they are a barrierless and exothermic process. The free energy barrier for the C2-N1 bond cleavage along the reaction path 3.2 is 0.70 eV, including the free formation energy for hydrogen-bond structure between intermediate structure F and one explicit water molecule of 0.31 eV. The free energy barrier is lowered by ~ 0.01 eV with the presence of one explicit water molecule. Thus the explicit water molecule has a minor effect on the amid cleavage energy barrier for the mPBI(1).

Furthermore, we consider the amid cleavage with an additional hydroxide ion as shown in reaction path 3.3, Fig. 6b. We find that the additional hydroxide ion near the amide linkage in the intermediate E spontaneously reacts with a hydroxyl proton at the C2 position, forming a water molecule. The hydroxyl proton abstraction leads to the cleavage of the C2-N1 bond, and the H4 hydrogen atom is transferred back and forth between the N3 nitrogen atom and the O2 oxygen atom along this process (Fig. 6d). The reaction undergoes a transition state TS6-3.3, locating at 1.88 eV in the quantitative reaction profile. The tunnelling correction (κ) along this reaction step is 1.02, resulting in the rate constant of 1.50×10^{-1} s^{-1}. The breaking of the C2-N1 bond creates an unstable N dangling bond at the N1 position in intermediate structure FX2-3.3. This unstable N dangling bond can be stabilized by receiving a proton from an available water molecule in its environment. The free energy barrier of the last step is found to be only 0.01 eV with the tunnelling correction of 1.51, implying a significant proton tunnelling facilitating this step. The final products, structure G, and one hydroxide ion are obtained at the end of the process. However, along reaction path 3.3 in Fig. 6b, the free energy barrier for the amide breaking is higher than the previous considerations. Therefore, the rate constant for the amide cleavage (for F→G step) along the reaction path 3.3, even including the proton tunnelling effect, is much lower than the others (Table S3).

The chain scission reaction of the mPBI(0) is shown in Fig. S6c. Like the amide cleavage of the mPBI(1), the transition vector corresponded to a single imaginary frequency for TS6-3.1 and TS6-3.2 state of the mPBI(0) mainly relates to the C2-N1 bond breaking (Fig. S10). Also, the hydroxyl proton transfer from the C2 carbon atom to the N1 nitrogen atom spontaneously occurs after the C-N bond breaking. The free energy barrier for the amide cleavage without explicit water molecules is 0.48 eV. In comparison, the free energy barrier for the amide cleavage with one explicit water molecule is 0.86 eV, including the free formation energy for hydrogen-bond structure between intermediate structure F and explicit water of 0.41 eV. Thus, the free energies barrier is lower ~ 0.03 eV with the presence of one explicit water molecule.

The final product from the chain scion reaction contains free amino groups and a carbonyl group, agreeing with the experimental results by Aili et al., where the mPBI membrane structures soaked in KOH solution at $T = 88$ °C were studied with FTIR

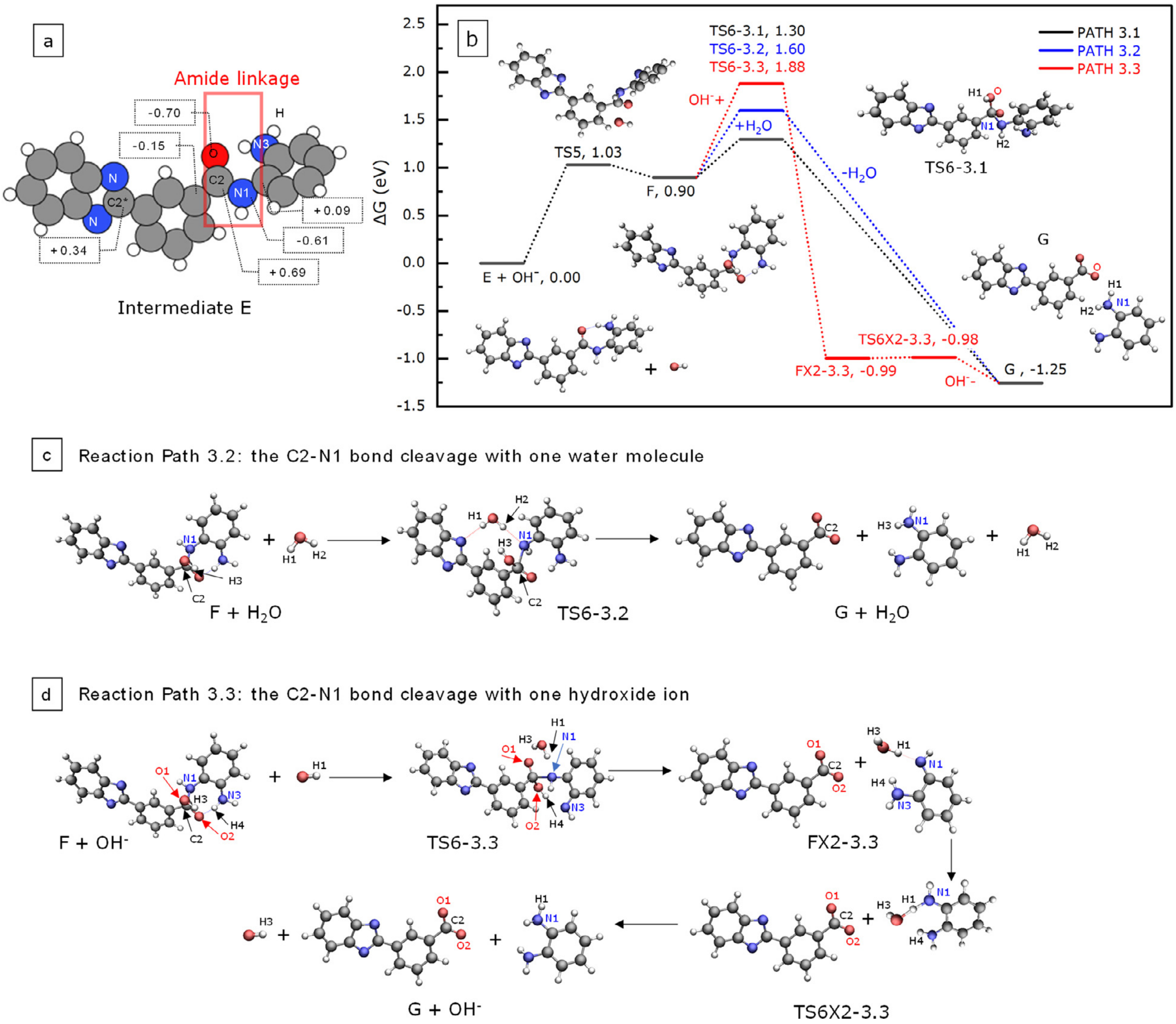

Fig. 6. (a) Optimized structure and NBO atomic charges on intermediate structure E. (b) Quantitative reaction profile for the chain scission reaction of mPBI(1) at $T = 88$ °C. The reference zero energy state for energies reported is E+OH⁻, and the relative energies of the intermediates and transition states are in eV. The insets show optimized structures for the intermediate and transition states involved in the reaction path 3.1. (c–d) Optimized structures for the intermediate and transition state related to the C2-N1 bond cleavage along reaction path: (c) 3.2 (d) 3.3. Colors code for atoms: *H*-white, *C*-grey, *N*-blue, *O*-red.

and ^{1}H NMR spectra. The mPBI structures soaked in 15–50 wt% KOH for 200 days were reported to the structure changes assigned to the free amino group formation [21]. Kraglund et al. also reported forming free amino groups and carbonyl moieties in the mPBI membrane structure after operating in a water electrolyzer at 2.0 V in 30 wt% KOH, 80°C for 48h [10].

The quantitative reaction profile for the entire degradation process of the mPBI(1), is shown in the black line, Fig. 7a. A water molecule catalyzes this reaction pathway during the ring-opening reaction, and there is no explicit water included during the chain scission reaction. The highest transition state is the TS6-3.1 located at 2.04 eV in the quantitative reaction profile. This state is predicted to be the rate-limiting state and the effective barrier for the degradation reaction is 2.04 eV.

The same reaction path for the entire degradation reaction of mPBI(0) is shown in Fig. S11 (the black line). The highest transition state, in this case, is also the TS6-3.1 (TS6) located at 2.02 eV in the quantitative reaction profile, so the effective energy barrier for the degradation reaction differs only by 0.02 eV from that of the mPBI(1).

When the chain scission occurs, the reaction is irreversible. The hydroxide ion is consumed during the degradation as well as the mPBI(1) partially loses the ability to hold the aqueous KOH. Eventually, the degradation reaction can lead to the gradual drop of the ionic conductivity of the membrane. Also, the degradation reaction can lead to a reduced molecular weight of the mPBI polymer, as evidenced by the experimental results by Aili et al. [21]. The stability study of mPBI membrane in KOH solution at $T = 88$ °C has been found that the average molecular weight of mPBI soaked in 50 wt% KOH for 200 days was about 21-25% of the initial molecular weight [21].

7. Reaction with implicit-explicit solvation model

So far, we employ the PCM implicit solvation model to approximately account for the effect of a dielectric constant surrounding the reaction center. However, it does not incorporate specific short-range solute-solvent interactions such as hydrogen bonding, which can be particularly important for anions [47–49]. A combined implicit-explicit solvation approach by including few explicit

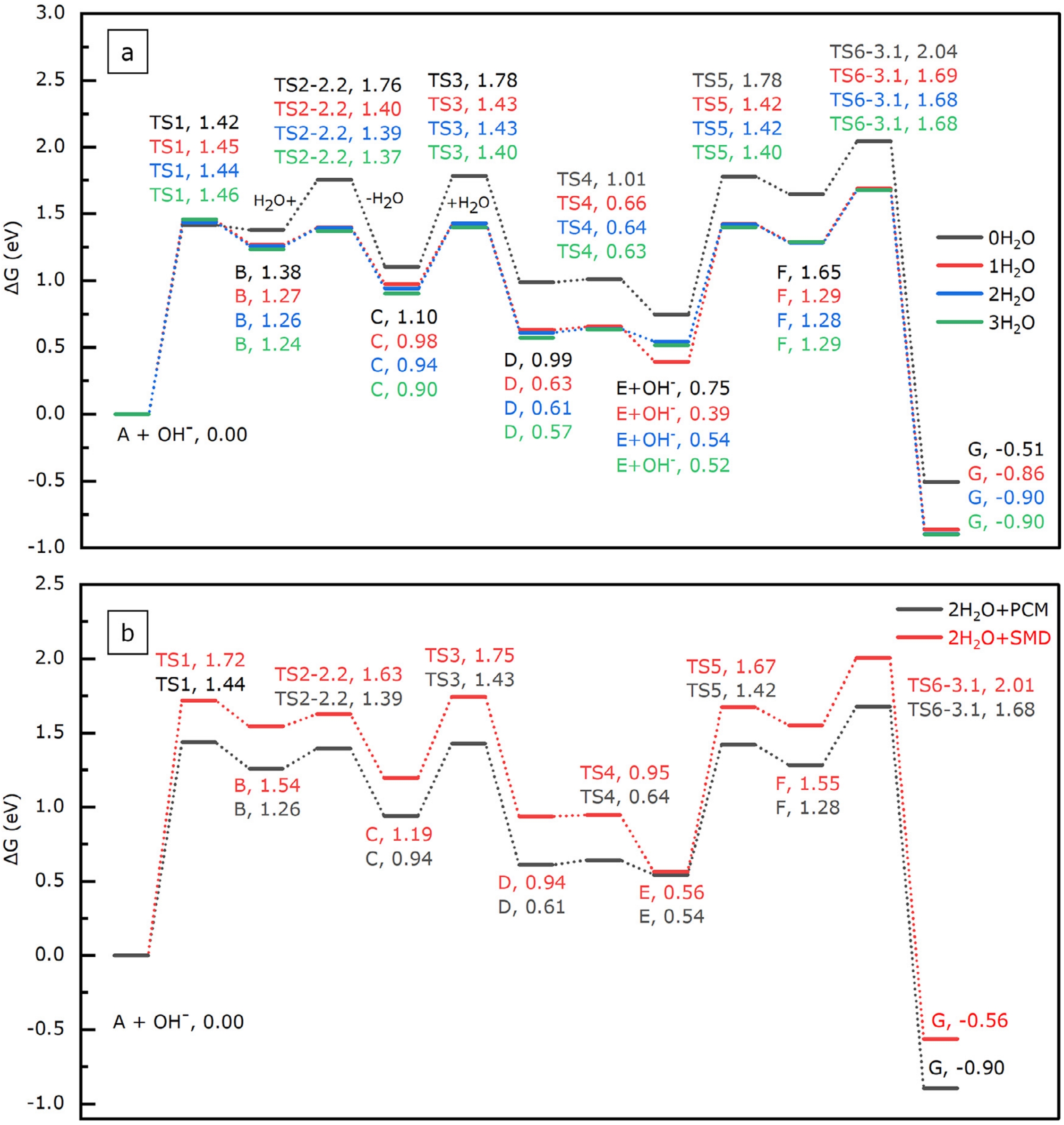

Fig. 7. Quantitative reactive profile for the degradation path of mPBI(1) at $T = 88$ °C (a) with a different number of explicit water molecules using PCM implicit solvation model and (b) with two explicit water molecules using PCM and SMD implicit solvation model. The reference zero energy state for energies reported is A+OH$^-$, and the relative energies of the intermediates and transition state are in eV.

water molecules in the implicit solvation model has been found to improve the agreement between theoretical calculations and experimental data such as solvation energies and pK_a for neutral, cation, and anion molecules [47–51]. For alkaline hydrolysis of amide bonds, the explicit water molecule has been reported to assist the proton-transfer process and stabilize the critical transition states via hydrogen bonding [45,46]. Subsequently, the explicit water molecule alters the activation energy.

7.1. Reaction with one explicit water molecule

The first hydroxide ion attack at the C2 carbon atom of the mPBI(1) or ΔG_1 with one explicit water molecule at different hydrogen-bonding sites is shown in Table S7. The results clearly show that a hydrogen bonding site can contribute significantly to ΔG_1 while placing one explicit water molecule near the N1 position gives the lowest energy for ΔG_1. Thus, when we consider the entire degradation pathway of the mPBI(1) with one explicit water molecule, the explicit water molecule is placed near the nitrogen atom at the N1 position in structure A which is also close to where the expected degradation reaction occurs and participates in the reaction as a reactant.

With one explicit water molecule through the entire degradation process, only the initial reactant structure A, intermediate structure B, C, and transition structure TS1 are different from those previously considered. The optimized structures for the entire degradation process with one explicit water molecule are shown in Fig. S13.

The free energy diagram of mPBI(1) degradation with one explicit water molecule is plotted in Fig. 7a (the red lines). The one explicit water molecule does not substantially affect the free energy barrier during the first nucleophile addition reaction, but it still lowers the free reaction energy for this step (0.11 eV lower than without explicit water molecule). The free energy barrier related to the water-assisted hydroxyl proton transfer ($\Delta G^{TS2\text{-}2.2}$) and the cleavage of the C2-N1 bond (ΔG^{TS3}) during the ring-opening reaction is about 0.25 and 0.23 eV lower than that in the reaction path without explicit water molecule. The ΔG^{TS4} and other relative free energies during the chain scissor reaction are the same as the previous consideration since the explicit water molecule is not included in these steps. The highest transition state for the entire degradation pathway with one explicit solvation for the mPBI(1) is TS6-3.1, locating at 1.69 eV in the quantitative reaction profile, which is 0.35 eV lower than the degradation pathway without the explicit water molecule. The explicit water molecule lowers the energy barrier by stabilizing via hydrogen bonds with the intermediate state structure along the reaction path.

7.2. *Reaction with two and three explicit water molecules*

More water molecules (up to three water molecules) were explicitly included in the simulation. With two explicit water molecules, we find that the configuration with at least one explicit water molecule near the nitrogen at the N1 position results in lower energy for ΔG_1 (Table S7). An increasing number of explicit water molecules from zero to three (with at least one explicit water molecule is near the N1 nitrogen atom) reduced ΔG_1 from 1.38 to 1.24 eV. Thus, when we add more explicit water molecules along the simulated reaction path, the first explicit water molecule is placed near the nitrogen atom at the N1 position and participates as a reactant. The second and third water molecules are placed near the nitrogen atom at the N3* or N1* position in structure A, forming a hydrogen bond with deprotonated site. Besides, the additional explicit water molecules keep forming the hydrogen bond at the same site throughout the degradation process.

It is important to mention that we only consider some specific configurations between the limited amount of explicit water molecules and the mPBI(1) molecule in the reaction pathway. More explicit water molecules and other possible hydrogen bonding positions would require considering a more elaborate model. Increasing the number of explicit water molecules to achieve at least the first solvation shell has been reported to agree with the experimental results as it can provide a more accurate treatment of the short-range solvation interactio [52–54]. The complete first solvation shell can be obtained by ab initio molecular dynamics simulations, which typically require a large number of water molecules (~10–100 molecules) and long simulation times [55,56]; such calculations are beyond the scope of the present study.

The quantitative reaction profile for the mPBI(1) degradation with two and three explicit water molecules is shown in Fig. 7a (the blue and green line, respectively), exhibiting a similar reaction profile to that with one explicit water molecule. However, the free reaction energy for the proton transfer reaction (for D→E+OH⁻ step) along the degradation with two and three explicit water molecules is about 0.14 less negative than that with one explicit water molecule. Also, the free energy barrier and free energy reaction for the second nucleophilic addition step (for E+OH⁻→TS5→F step) along the reaction path with two and three explicit water molecules are about 0.15 and 0.14 eV lower than those in the reaction pathway with one explicit water molecule, respectively. This is results can imply that the specific hydrogen bonding at the deprotonate site significantly affects these steps. Hydrogen bonds between the explicit water molecules and the structure along the reaction path are likely to result in a lower energy barrier.

The free energy difference for each reaction step along the degradation pathway with two and three explicit water molecules is less than 0.1 eV. This can suggest that a further increase in explicit water molecules may have no practical effect on the reaction profile. The highest transition state along the degradation pathway with two and three explicit water molecules is the TS6-3.1 state, which is only 0.1 eV lower than that of the degradation pathway with one explicit water molecule, but it is 0.36 eV lower than the degradation pathway without the explicit water molecule.

To test the sensitivity to the choice of implicit solvation model, we employed the SMD implicit solvation model [57] based on the same optimized structures in the gas phase, and the solvent remains water. Fig. 7b presents the quantitative reaction profile for the degradation pathway of the mPBI(1) molecule with two explicit water molecules using PCM and SMD implicit solvation. The reaction profiles obtained from both implicit solvation are similar, except that all states from the SMD implicit solvation are higher in the quantitative reaction profile. Still, the highest transition state with the SMD implicit solvation is the TS6-3.1 state but locates at 0.33 eV higher than that obtained from the PCM implicit solvation. However, similar results in which the effective barrier becomes smaller when including the explicit water molecules along the reaction pathway are also found for the SMD implicit solvation (Fig. S16).

The same degradation pathway for the mPBI(0) with up to two explicit water molecules using the PCM implicit solvation is shown in Fig. S11, leading to the same conclusion. The rate-determining state is the TS6-3.1 (TS6) state, regardless of the number of explicit water molecules. The effective free energy barrier along the degradation pathway for the mPBI(0) is reduced from 2.02 eV to 1.63 and 1.60 eV when the number of explicit water molecules increases from zero to one and two, respectively.

8. Comparison with experimental degradation rates

The degradation of the mPBI membrane depends on the KOH concentration. The experimental studies by Aili et al. [21] and Kraglund et al. [10] both reported that the mPBI membrane was stable at low KOH concentration (up to 5 wt% KOH at T = 80–88 °C). At higher KOH concentrations, the mPBI membrane degrades, and the degradation rate increases with increasing KOH concentration. To consider the KOH concentration dependency, we take the hydroxide ion concentration into account and reconsider the free reaction energy (ΔG) and free energy barrier (ΔG^{TS}), i.e., for the first nucleophilic reaction between structure A and OH^-, the reaction goes through TS1 and results in intermediate B.

$$A + OH^- \rightarrow \ TS1 \ \rightarrow B \tag{14}$$

$$\Delta G_1 = \Delta G_1^c - RT\ln\left[OH^-\right] = \ \Delta G_1^c - 2.303RT(pH - pK_w) \tag{15}$$

$$\Delta G^{TS1} = \Delta G^{TS1c} - RT\ln\left[OH^-\right] = \Delta G^{TS1c} - 2.303RT(pH - pK_w) \tag{16}$$

ΔG^c and ΔG^{TSc} are the free reaction energy and free energy barrier at a standard concentration, pK_W is the acid dissociation constant of water at T = 88 °C which is taken from the literature ($pK_W = 12.46$ [40]).

Based on the above calculation, the free reaction energy along the water-assisted degradation pathway in the first, fourth and fifth reaction steps depends on pH, and only the first and the fifth free energy barrier changes with pH. Besides, all previous calculations are applied for pH = 12.46.

Fig. 8a shows the quantitative reaction profile for the mPBI(1) degradation with two explicit water molecules at different pH. For all considered pH values, the overall degradation rate is still determined by the TS6-3.1 state, which is decreased as pH increases. Thus, the effective energy barrier is reduced, and the degradation of mPBI(1) becomes more facile with increased hydroxide ion concentration.

Even though at a high pH range (pH= 13–14), the dominant species is mPBI(2) which is unlikely to degrade, the degradation

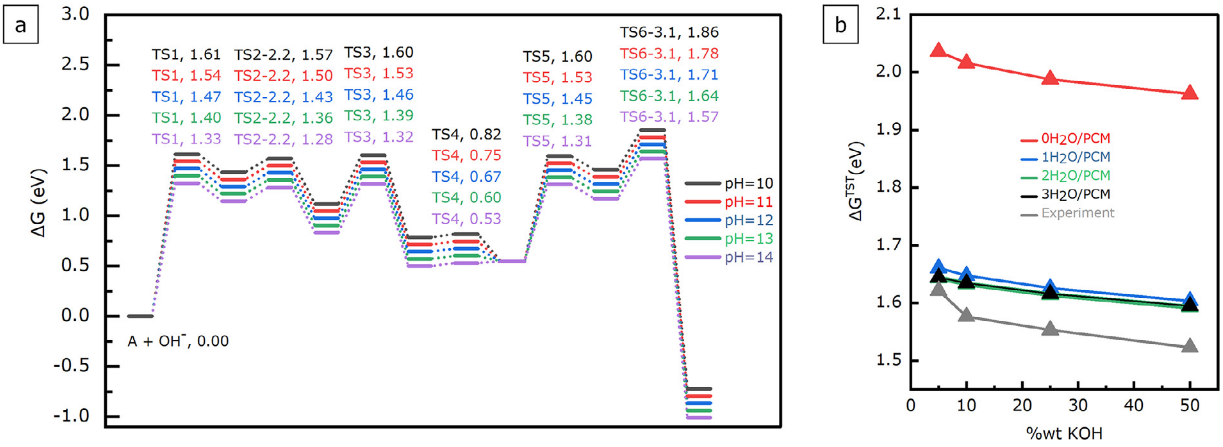

Fig. 8. (a) Quantitative reaction profile for the mPBI(1) degradation at $T = 88$ °C with two explicit water molecules and the PCM implicit solvation model at different pH. The reference zero energy state for energies reported is A+OH^- and the relative energies of the intermediates and transition state are in eV. (b) the calculated effective free energy barrier and the apparent energy barrier from the experiments [21] (ΔG^{TST}) at different KOH concentrations and $T = 88$ °C.

still occurs through the mPBI(1) species which accounts for 10–20% of the PBI molecules. The number of mPBI(1) in the solution can be quickly reduced as the degradation reaction is also facile at this high pH. Some mPBI(2) species then can change to mPBI(1) species to maintain the equilibrium between all mPBI species. The degradation can further proceed, and the number of ionized species and mobile hydroxide ions in the solution is also reduced. Thus, the reduction in the ionic conductivity and the changes in membrane structure are unavoidable. Working at a lower pH range to minimize degradation can be possible. However, this comes with a lower ionic conductivity as the percentage of the ionized form in the solution becomes lower at a lower pH.

The reaction rate constant can be estimated from transition state theory, as shown in Eq. (6). The effective rate constant for the over degradation is calculated from the effective free energy barrier, the free energy difference between the highest transition state (TS6-3.1) and the initial reactant state (A+OH^-).

Furthermore, given an experimentally observed reaction rate, one could estimate an apparent free energy barrier. The apparent free energy barrier is derived from the molecular weight loss of the mPBI membrane after being soaked in 5, 10, 25, 50 wt% KOH at $T = 88$ °C for 200 days reported by Aili et al. [21]. The rate of the molecular weight loss of the mPBI at a specific KOH concentration (in s^{-1} unit) is approximated as follows.

$$\text{rate} = \frac{1}{\Delta t}\left(1 - \frac{m_{200}}{m_1}\right) = k_0 f_{mPBI(0)} + k_1 f_{mPBI(1)} \tag{17}$$

where k_0, and k_1, are an apparent reaction rate constant (in s^{-1} units) for the degradation of mPBI(0), and mPBI(1), respectively; $f_{mPBI(0)}$, $f_{mPBI(1)}$ are the mole fraction of mPBI(0), and mPBI(1) at considered KOH concentrations, respectively; Δt is the duration for storing the mPBI in KOH solution (Δt= 200 days); m_1 and m_{200} are a molecular weight of mPBI before storing in KOH solution (day1) and after storing in KOH solution for 200 days (in g mol^{-1}).

The mPBI(2) molecule is unlikely to degrade with the initial degradation step on the mPBI(2) molecule > 2 eV, about 1.30 eV higher than those of the mPBI(1) and mPBI(0). For simplicity, we assume that the contribution of the mPBI(2) to the total rate constant is insignificant, and we neglect the apparent reaction rate and the mole fraction of the mPBI(2) into Eq. (17). Fig. S17 shows the approximated rate including the mPBI(2) contribution, demonstrating that there is no further improvement in the approximated rate compared to the rate using Eq. 17.

Fig. 8b shows the apparent energy barrier derived from the experimental results and the effective free energy barrier from different implicit-explicit solvation models (Table S11). The effective energy barrier from the theoretical model is a weighted average value, taking the mole fraction of mPBI(0) and mPBI(1) at each KOH concentration into account. We find that both the apparent and effective free energy barriers decrease as the KOH concentration increases, implying the increasing degradation rate of mPBI as the KOH concentration increases. Without the explicit water molecules, the PCM implicit solvation model predicts a much larger effective free energy barrier than the experiments, resulting in an MAE of 0.43 eV. The MAE is reduced to below 0.1 eV when including explicit water molecules in the simulation. The results clearly show that the combination of implicit and explicit solvation models makes the predicted effective free energy barrier move toward the experimental results.

9. Conclusion

A comprehensive DFT study of the degradation mechanism of the mPBI molecule in an alkaline solution is carried out in this work. The impact of continuum solvation and explicit water molecules on the reaction mechanism and energy profile is examined. The theoretical results are compared to the experimental work by determining the activation energy barrier for the degradation reaction.

The mPBI molecule deprotonates when submerged into an alkaline solution. At the high pH where the degradation occurs, the ionized forms, mPBI(2), is the predominant species, but the degradation is possibly initiated by the hydroxide ion attack at the C2 carbon position in the mPBI(1) or mPBI(0). The formation of a fully ionized molecule suppresses the hydroxide ion attack. The following ring-opening reaction is associated with hydroxyl proton transfer, the C-N bond breaking, and the stabilization of the N dangling bond. The hydroxyl proton transfer during the ring-opening reaction likely occurs via an ancillary hydroxide ion or water molecule. The amide linkage is a product from the ring-opening reaction, which subsequently undergoes alkaline hydrolysis, leading to a complete chain scissor. The rate-determining state is associated with the amide cleavage during the chain scission reaction. A continuum solvation model predicts a relatively high effective barrier compared to the experiment. While combining explicit water molecules and implicit solvation lower the calculated effective barrier for the degradation, giving a good agreement between experiment and theoretical results. The explicit water molecules reduce the energy barrier mainly by forming hydrogen bonds with the intermediate state structure along the reaction path. The proposed model additionally captures the experimental trend in which the degradation rate increased with increased KOH concentration.

These studies point to the dominant degradation pathway for the mPBI membranes in alkaline solution and the importance of evaluating the reaction pathway with explicit water molecules. This insight is expected to be useful in designing degradation-resistant anion exchange membranes for alkaline water electrolyzers and fuel cells. In addition, a polymer structure optimization of the polybenzimidazole membrane is expected to affect the alkaline stability of the membrane.

Declaration of Competing Interest

The authors declare that they have no known competing financial interests or personal relationships that could have appeared to influence the work reported in this paper.

Credit authorship contribution statement

Tipaporn Patniboon: Conceptualization, Methodology, Formal analysis, Investigation, Data curation, Writing – original draft, Visualization. **Heine Anton Hansen:** Conceptualization, Methodology, Formal analysis, Writing – review & editing, Supervision.

Acknowledgments

Funding from the Villum Foundation V-SUSTAIN grant 9455 to the Villum Center for the Science of Sustainable Fuels and Chemicals, the Innovation Fund Denmark Grand Solutions Grant 9067-00055B to the project DREAME, and a scholarship from the Ministry of Science and Technology, Royal Thai Government, is acknowledged.

Supplementary materials

Supplementary material associated with this article can be found, in the online version, at doi:10.1016/j.electacta.2021.139329.

References

[1] S. Gottesfeld, DR. Dekel, M. Page, et al., Anion exchange membrane fuel cells: current status and remaining challenges, J. Power Sources 375 (2018) 170–184, doi:10.1016/j.jpowsour.2017.08.010.

[2] Y. Leng, G. Chen, AJ. Mendoza, TB. Tighe, MA. Hickner, CY. Wang, Solid-state water electrolysis with an alkaline membrane, J. Am. Chem. Soc. 134 (22) (2012) 9054–9057, doi:10.1021/ja302439z.

[3] YC. Cao, X. Wu, K. Scott, A quaternary ammonium grafted poly vinyl benzyl chloride membrane for alkaline anion exchange membrane water electrolysers with no-noble-metal catalysts, Int. J. Hydrog. Energy 37 (12) (2012) 9524–9528, doi:10.1016/j.ijhydene.2012.03.116.

[4] B. Lee, D. Yun, JS. Lee, CH. Park, TH. Kim, Development of highly alkaline stable OH–conductors based on imidazolium cations with various substituents for anion exchange membrane-based alkaline fuel cells, J. Phys. Chem. C 123 (22) (2019) 13508–13518, doi:10.1021/acs.jpcc.9b02991.

[5] J. Fan, S. Willdorf-Cohen, EM. Schibli, et al., Poly(bis-arylimidazoliums) possessing high hydroxide ion exchange capacity and high alkaline stability, Nat. Commun. 10 (1) (2019) 2306, doi:10.1038/s41467-019-10292-z.

[6] OD. Thomas, KJWY. Soo, TJ. Peckham, MP. Kulkarni, S. Holdcroft, A stable hydroxide-conducting polymer, J. Am. Chem. Soc. 134 (26) (2012) 10753–10756, doi:10.1021/ja303067t.

[7] MR. Sturgeon, CS. Macomber, C. Engtrakul, H. Long, BS. Pivovar, Hydroxide based benzyltrimethylammonium degradation: quantification of rates and degradation technique development, J. Electrochem. Soc. 162 (4) (2015) F366–F372, doi:10.1149/2.0271504jes.

[8] D. Henkensmeier, HR. Cho, HJ. Kim, et al., Polybenzimidazolium hydroxides-structure, stability and degradation, Polym. Degrad. Stab. 97 (3) (2012) 264–272, doi:10.1016/j.polymdegradstab.2011.12.024.

[9] D. Henkensmeier, HJ. Kim, HJ. Lee, et al., Polybenzimidazolium-based solid electrolytes, Macromol. Mater Eng. 296 (10) (2011) 899–908, doi:10.1002/mame.201100100.

[10] MR. Kraglund, D. Aili, K. Jankova, E. Christensen, Q. Li, JO. Jensen, Zero-Gap alkaline water electrolysis using ion-solvating polymer electrolyte membranes at reduced KOH concentrations, J. Electrochem. Soc. 163 (11) (2016) F3125–F3131, doi:10.1149/2.0161611jes.

[11] JO. Jensen, D. Aili, MK. Hansen, Q. Li, NJ. Bjerrum, E. Christensen, (Invited) a stability study of alkali doped PBI membranes for alkaline electrolyzer cells, ECS Trans. 64 (3) (2014) 1175–1184, doi:10.1149/06403.1175ecst.

[12] MR. Kraglund, M. Carmo, G. Schiller, et al., Ion-solvating membranes as a new approach towards high rate alkaline electrolyzers, Energy Environ. Sci. 12 (11) (2019) 3313–3318, doi:10.1039/c9ee00832b.

[13] D. Aili, K. Jankova, J. Han, NJ. Bjerrum, JO. Jensen, Q. Li, Understanding ternary poly(potassium benzimidazolide)-based polymer electrolytes, Polymer 84 (2016) 304–310 (Guildf), doi:10.1016/j.polymer.2016.01.011.

[14] AD. Modestov, MR. Tarasevich, AY. Leykin, VY. Filimonov, MEA for alkaline direct ethanol fuel cell with alkali doped PBI membrane and non-platinum electrodes, J. Power Sources 188 (2) (2009) 502–506, doi:10.1016/j.jpowsour.2008.11.118.

[15] RN. Couto, J.J. Linares, KOH-doped polybenzimidazole for alkaline direct glycerol fuel cells, J. Memb. Sci. 486 (2015) 239–247, doi:10.1016/j.memsci.2015.03.031.

[16] JH. Park, JS. Park, KOH-doped porous polybenzimidazole membranes for solid alkaline fuel cells, Energies 13 (3) (2020), doi:10.3390/en13030525.

[17] H. Luo, G. Vaivars, B. Agboola, S. Mu, M. Mathe, Anion exchange membrane based on alkali doped poly(2,5-benzimidazole) for fuel cell, Solid State Ion. 208 (2012) 52–55, doi:10.1016/j.ssi.2011.11.029.

[18] B. Xing, O. Savadogo, Hydrogen/oxygen polymer electrolyte membrane fuel cells (PEMFCs) based on alkaline-doped polybenzimidazole (PBI), Electrochem. Commun. 2 (10) (2000) 697–702, doi:10.1016/j.memsci.2019.01.026.

[19] L. Zeng, TS. Zhao, L. An, G. Zhao, XH. Yan, A high-performance sandwiched-porous polybenzimidazole membrane with enhanced alkaline retention for anion exchange membrane fuel cells, Energy Environ. Sci. 8 (9) (2015) 2768–2774, doi:10.1039/c5ee02047f.

[20] C. Noh, D. Serhiichuk, N. Malikah, Y. Kwon, D. Henkensmeier, Optimizing the performance of meta-polybenzimidazole membranes in vanadium redox flow batteries by adding an alkaline pre-swelling step, Chem. Eng. J. 407 (July 2020) (2021) 126574, doi:10.1016/j.cej.2020.126574.

[21] D. Aili, K. Jankova, Q. Li, NJ. Bjerrum, JO. Jensen, The stability of poly(2,2'-(m-phenylene)-5,5'-bibenzimidazole) membranes in aqueous potassium hydroxide, J. Memb. Sci. 492 (2015) 422–429, doi:10.1016/j.memsci.2015.06.001.

[22] D. Aili, AG. Wright, MR. Kraglund, K. Jankova, S. Holdcroft, JO. Jensen, Towards a stable ion-solvating polymer electrolyte for advanced alkaline water electrolysis, J. Mater Chem. A 5 (10) (2017) 5055–5066, doi:10.1039/c6ta10680c.

[23] D. Aili, MK. Hansen, RF. Renzaho, et al., Heterogeneous anion conducting membranes based on linear and crosslinked KOH doped polybenzimidazole for alkaline water electrolysis, J. Memb. Sci. 447 (2013) 424–432, doi:10.1016/j.memsci.2013.07.054.

[24] H. Long, B. Pivovar, Hydroxide degradation pathways for imidazolium cations: a DFT study, J. Phys. Chem. C 118 (19) (2014) 9880–9888, doi:10.1021/jp501362y.

[25] W. Wang, S. Wang, X. Xie, Y. lv, VK. Ramani, Hydroxide-ion induced degradation pathway for dimethylimidazolium groups in anion exchange membranes, J. Memb. Sci. 462 (2014) 112–118, doi:10.1016/j.memsci.2014.03.026.

[26] E. Babcock, N. Szekely, A. Konovalova, et al., Using neutron methods SANS and PGAA to study evolution of structure and composition of alkali-doped polybenzimidazole membranes, J. Memb. Sci. 577 (January) (2019) 12–19, doi:10.1016/j.memsci.2019.01.026.

[27] AD. Becke, A new mixing of Hartree-Fock and local density-functional theories, J. Chem. Phys. 98 (2) (1993) 1372–1377, doi:10.1063/1.464304.

[28] Y. Shao, Z. Gan, E. Epifanovsky, et al., Advances in molecular quantum chemistry contained in the Q-Chem 4 program package, Mol. Phys. 113 (2) (2015) 184–215, doi:10.1080/00268976.2014.952696.

[29] S. Mallikarjun Sharada, PM. Zimmerman, AT. Bell, M. Head-Gordon, Automated transition state searches without evaluating the hessian, J. Chem. Theory Comput. 8 (12) (2012) 5166–5174, doi:10.1021/ct300659d.

[30] S. Maeda, K. Ohno, K. Morokuma, An automated and systematic transition structure explorer in large flexible molecular systems based on combined global reaction route mapping and microiteration methods, J. Chem. Theory Comput. 5 (10) (2009) 2734–2743, doi:10.1021/ct9003383.

[31] J. Baker, An algorithm for the location of transition states, J. Comput. Chem. 7 (4) (1986) 385–395, doi:10.1002/jcc.540070402.

[32] K. Fukui, Formulation of the reaction coordinate, J. Phys. Chem. 74 (23) (1970) 4161–4163, doi:10.1021/j100717a029.

[33] M. Cossi, N. Rega, G. Scalmani, V. Barone, Energies, structures, and electronic properties of molecules in solution with the C-PCM solvation model, J. Comput. Chem. 24 (6) (2003) 669–681, doi:10.1002/jcc.10189.

[34] V. Barone, M. Cossi, Conductor solvent model, J. Phys. Chem. A 102 (97) (1998) 1995–2001, doi:10.1021/jp9716997.

[35] TN. Truong, EV. Stefanovich, A new method for incorporating solvent effect into the classical, ab initio molecular orbital and density functional theory frameworks for arbitrary shape cavity, Chem. Phys. Lett. 240 (4) (1995) 253–260, doi:10.1016/0009-2614(95)00541-B.

[36] K. Jana, B. Ganguly, DFT studies on quantum mechanical tunneling in tautomerization of three-membered rings, Phys. Chem. Chem. Phys. 20 (44) (2018) 28049–28058, doi:10.1039/c8cp03963a.

[37] RP. Bell, The tunnel effect correction for parabolic potential barriers, Trans. Faraday Soc. 55 (0) (1959) 1–4, doi:10.1039/TF9595500001.

[38] DJ. Griffiths, PDJ. Griffiths, Introduction to Quantum Mechanics, Pearson Prentice Hall, 2005 https://books.google.dk/books?id=z4fwAAAAMAAJ.

[39] WR. Kelly, PF. Borza, RD. Harriger, Densities and viscosities of potassium hy-

droxide solutions at low temperatures, J. Chem. Eng. Data 10 (3) (1965) 233–234, doi:10.1021/je60026a006.

[40] FH. Sweeton, RE. Mesmer, CF. Baes, Acidity measurements at elevated temperatures. VII. dissociation of water, J. Solut. Chem. 3 (3) (1974) 191–214, doi:10.1007/BF00645633.

[41] H. Hou, S. Wang, Q. Jiang, W. Jin, L. Jiang, G. Sun, Durability study of KOH doped polybenzimidazole membrane for air-breathing alkaline direct ethanol fuel cell, J. Power Sources 196 (6) (2011) 3244–3248, doi:10.1016/j.jpowsour.2010.11.104.

[42] L. Zeng, TS. Zhao, L. An, G. Zhao, XH. Yan, Physicochemical properties of alkaline doped polybenzimidazole membranes for anion exchange membrane fuel cells, J. Memb. Sci. 493 (2015) 340–348, doi:10.1016/j.memsci.2015.06.013.

[43] ED. Glendening, CR. Landis, F. Weinhold, NBO 6.0: natural bond orbital analysis program, J. Comput. Chem. 34 (16) (2013) 1429–1437, doi:10.1002/jcc.23266.

[44] K. Matsuyama, H. Ohashi, S. Miyanishi, H. Ushiyama, T. Yamaguchi, Quantum chemical approach for highly durable anion exchange groups in solid-state alkaline fuel cells, RSC Adv. 6 (43) (2016) 36269–36272, doi:10.1039/c5ra27939a.

[45] X. Lopez, JI. Mujika, GM. Blackburn, M. Karplus, Alkaline hydrolysis of amide bonds: effect of bond twist and nitrogen pyramidalization, J. Phys. Chem. A 107 (13) (2003) 2304–2315, doi:10.1021/jp022014s.

[46] D. Cheshmedzhieva, S. Ilieva, B. Hadjieva, B. Galabov, The mechanism of alkaline hydrolysis of amides: a comparative computational and experimental study of the hydrolysis of N-methylacetamide, N-methylbenzamide, and acetanilide, J. Phys. Org. Chem. 22 (6) (2009) 619–631, doi:10.1002/poc.1492.

[47] CP. Kelly, CJ. Cramer, DG. Truhlar, Adding explicit solvent molecules to continuum solvent calculations for the calculation of aqueous acid dissociation constants, J. Phys. Chem. A 110 (7) (2006) 2493–2499, doi:10.1021/jp055336f.

[48] L. Xu, ML. Coote, Methods to improve the calculations of solvation model density solvation free energies and associated aqueous p Ka values: comparison between choosing an optimal theoretical level, solute cavity scaling, and using explicit solvent molecules, J. Phys. Chem. A 123 (34) (2019) 7430–7438, doi:10.1021/acs.jpca.9b04920.

[49] B. Thapa, HB. Schlegel, Calculations of pKa's and redox potentials of nucleobases with explicit waters and polarizable continuum solvation, J. Phys. Chem. A 119 (21) (2015) 5134–5144, doi:10.1021/jp5088866.

[50] B. Thapa, H. Bernhard Schlegel, Theoretical calculation of pKa's of selenols in aqueous solution using an implicit solvation model and explicit water molecules, J. Phys. Chem. A 120 (44) (2016) 8916–8922, doi:10.1021/acs.jpca.6b09520.

[51] B. Thapa, HB. Schlegel, Density functional theory calculation of pKa's of thiols in aqueous solution using explicit water molecules and the polarizable continuum model, J. Phys. Chem. A 120 (28) (2016) 5726–5735, doi:10.1021/acs.jpca.6b05040.

[52] BL. Eggimann, JI. Siepmann, Size effects on the solvation of anions at the aqueous liquid−vapor interface, J. Phys. Chem. C 112 (1) (2008) 210–218, doi:10.1021/jp076054d.

[53] H. Dong, W. Liu, DJ. Doren, RH. Wood, Structure of an accurate ab initio model of the aqueous Na+ Ion at high temperatures, J. Phys. Chem. B 112 (43) (2008) 13552–13560, doi:10.1021/jp8057405.

[54] O. Hollóczki, P. Terleczky, D. Szieberth, G. Mourgas, D. Gudat, L. Nyulászi, Hydrolysis of imidazole-2-ylidenes, J. Am. Chem. Soc. 133 (4) (2011) 780–789, doi:10.1021/ja103578y.

[55] T. Zelovich, Z. Long, M. Hickner, SJ. Paddison, C. Bae, ME. Tuckerman, Ab initio molecular dynamics study of hydroxide diffusion mechanisms in nanoconfined structural mimics of anion exchange membranes, J. Phys. Chem. C 123 (8) (2019) 4638–4653, doi:10.1021/acs.jpcc.8b10298.

[56] L. Wu, X. Zhou, G. Zhang, et al., Tunable OH− transport and alkaline stability by imidazolium-based groups of Poly(2,6-dimethyl-1,4-phenylene oxide) anion exchange membranes: a molecular dynamics simulation, Ind. Eng. Chem. Res. 60 (6) (2021) 2481–2491, doi:10.1021/acs.iecr.1c00230.

[57] AV. Marenich, CJ. Cramer, DG. Truhlar, Universal solvation model based on solute electron density and on a continuum model of the solvent defined by the bulk dielectric constant and atomic surface tensions, J. Phys. Chem. B 113 (18) (2009) 6378–6396, doi:10.1021/jp810292n.